GARRETT
AIRESEARCH MANUFACTURING COMPANY
A DIVISION OF THE GARRETT CORPORATION
9851-9951 SEPULVEDA BLVD. • LOS ANGELES, CALIFORNIA 90009
TELEPHONE: SPRING 6-1010, ORCHARD 0-0131 • CABLE: GARRETTAIR LOS ANGELES

AIRESEARCH MANUFACTURING COMPANY
Los Angeles, California

HYPERSONIC RESEARCH ENGINE PROJECT - PHASE II COMBUSTOR PROGRAM, FINAL TECHNICAL DATA REPORT (U)

DATA ITEM NO. 55-2.11
3 FEBRUARY 1967 THROUGH 31 OCTOBER 1969
NASA CONTRACT NO. NAS1-6666

Document No. AP-70-6054

Group
Downgr... at ... ear intervals;
declassi... er 12 years
DO... AR ...

...SIFIED DOCUMENT - UN...SIFIED TITLE
This material co... ...ing the national defense of the United States within the ... ... laws, Title 18, U.S.C., Sections 793 a..., the transmissi... ...lation of which in any manne... unauthorized person is proh... law.

Number of pages 310

Original date 23 March 1970

Prepared by Engineering Staff

Edited by L. F. Jilly

Approved by Henry J. Lopez
HRE Program Manager

Revision	Date	Pages Affected (Revised, Added, Eliminated)

CONFIDENTIAL
THIS PAGE IS UNCLASSIFIED

FORM 23 77, 8-70

FOREWORD

This final technical data report is submitted to the NASA Langley Research Center by the AiResearch Manufacturing Company, Los Angeles, California. The document was prepared in accordance with the guidelines established by paragraph 5.7.3.2.2 of NASA Statement of Work L-4947-B (Revised).

This report summarizes the entire combustor program development effort and encompasses the period of 3 February 1967 through 31 October 1969.

ACKNOWLEDGEMENTS

Acknowledgements for completion of this report are extended to the following contributors:

R. B. Chapman	Test coordination
W. C. Sainio	Aerodynamic analysis
G. R. Short	Overall coordination
J. G. Sotter	Aerodynamic analysis
Y. H. Sun	Technical direction
T. T. Yang	Aerodynamic analysis

CONTENTS

CONTENTS (Continued)

CONTENTS (Continued)

AiResearch Drawings Attached to Back of Report

PA 106770	ML 2340	ML 2409 Sht 2
PA 106772	ML 2407	ML 2485
0565-901 (FluiDyne)	ML 2409 Sht 1	ML 2499

ILLUSTRATIONS

ILLUSTRATIONS (Continued)

ILLUSTRATIONS (Continued)

ILLUSTRATIONS (Continued)

ILLUSTRATIONS (Continued)

ILLUSTRATIONS (Continued)

TABLES

I. SUMMARY

Subsonic combustion and supersonic combustion of hydrogen were studied experimentally using a water-cooled, variable geometry, two-dimensional model. Hydrogen-oxygen vitiation was used to bring the inlet air to total temperatures simulating flight Mach numbers from 3 to 7; combustor inlet total pressures ranged from 20 to 300 psia. Subsonic combustion was maintained at inlet total temperatures as low as 820°R with normal fuel injection and a step flameholder 0.25 in. in height. Supersonic combustion chemical efficiencies close to 100 percent were achieved with single-stage cross-stream injection and with an inlet Mach number of approximately 2.6. The total internal viscous drag was determined from thrust and static pressure measurements; corresponding average friction coefficients between 0.004 and 0.0062 were obtained from calculations based on a one-dimensional analytical model. Supersonic combustion chemical efficiency in the constant-area first stage was found to be a function of jet penetration and spreading parameters. The pressure difference between the combustor's inlet and exit was correlated with chemical efficiency, average friction coefficient, and combustor area ratio. In the diverging second stage, chemical efficiency was less than 60 percent under all conditions. Gas-sampling data indicated that this problem was not caused by poor jet mixing on a macroscopic, time-averaged basis; on the other hand, chemical kinetic calculations incorporating measured test parameters indicated that the inefficiency was not a result of slow specific reaction rates. The hypothesis suggested is that the low chemical efficiency in the second stage was due to insufficient turbulence intensity on the scale required to lead to good mixing at the molecular level.

2. PROBLEM STATEMENT

The experiments described in this report were directed toward obtaining the combustor design information for the NASA Hypersonic Ramjet Engine (HRE). This engine is a hydrogen-fueled ramjet designed for operation over the Mach 3.0 to 8.0 range with equivalence ratios of 0.3 to 1.5. It is to be capable of employing subsonic combustion for flight Mach numbers from 3 to 6 and supersonic combustion from Mach 5 to 8.

Combustor component test data were needed in order to check design methods and to indicate necessary design modifications. Test data were to include sufficient information to determine extent of mixing, combustion rates, heat transfer and viscous drag at the chamber walls, characteristics of various injection systems, ignition requirements, and combustion stability. The tests were to cover a range of chamber geometries and inlet conditions so that the HRE combustor could be tailored to an inlet design suitable for use throughout the appropriate flight regime.

3. BACKGROUND

Despite intensive experimental and analytical activity during recent years, a great deal more information is needed to optimize combustor design for a hypersonic ramjet. Although some excellent basic studies have been carried out, much of the available work cannot be applied directly to engine design. In particular, additional design data were needed in the following areas:

- Lateral spreading of normally injected fuel jets
- Effects of area variation, and of combustion, on jet penetration, spreading, and mixing
- Ignition of supersonic combustible gases at temperatures below the autoignition point
- Effects of shock waves and of various boundary layer profiles on the mixing and combustion processes
- Flame stabilization in subsonic flow
- Combustion stability
- Frictional losses in a supersonic combustor

The proposed AiResearch Phase IIA HRE design provided a guideline for the general combustor geometry and inlet parameters to be studied. Combustor inlet conditions were determined by the approximate engine inlet performance expected. Cross-stream fuel injection, with equivalence ratios up to 1.5, was to be achieved with fuel manifold pressures of 350 psia or less.

The HRE Combustor design has several fuel injection stages. At Mach 8 most of all of the fuel is to be injected at the first stage. At lower Mach numbers the combustor inlet static temperature is lower; to avoid choking, it is necessary to inject part of the fuel at the downstream injection stations. For subsonic combustion all the fuel is to be introduced at a single injection stage, with a normal shock being stabilized between that stage and the inlet throat.

4. OVERALL APPROACH

A diverging duct of rectangular cross-section was selected in order to simulate a circumferential segment of an annular combustor. Wide flexibility in design parameters was to be one of the features of the segment combustor.

The following parameters were believed to significantly affect combustor performance:

(a) Injector size and spacing

(b) Inlet air temperature and pressure

(c) Fuel temperature

(d) Combustor area ratio

(e) Equivalence ratio

(f) Flame holding ignition characteristics

(g) Heat transfer

The combustor design concept chosen allowed investigation of the effects of these parameters.

5. EXPERIMENTAL APPARATUS

5.1 COMBUSTOR AND SUPPORT EQUIPMENT

The combustor test system is shown in Figures 5.1-1 and 5.1-2. Compressed air was heated in a direct-fired, hydrogen-fueled vitiation heater. Oxygen was added to the supply air prior to combustion to provide a vitiated airstream at the desired combustor inlet total temperature with an oxygen content of 21 percent by volume. Downstream of the vitiation heater were the inlet nozzle, a thrust stand, and the combustor model. All three were water-cooled and 6 in. in width.

The two-dimensional inlet nozzle had interchangeable contoured inserts which allowed inlet Mach number variation.

The first section of the combustor was a constant-area duct which was 12 in. long and could be set at either 2 in. or 0.6 in. in height. Fuel could be injected at three stations in this section: two in the lower wall and one in the upper. The water-cooled injectors were interchangeable inserts. When a station was not being used for fuel injection, the injector could be replaced by an igniter.

The second section was 17 in. long. Its top and bottom plates could be adjusted between runs to change their divergence angle. A third section was also available but was not used in the experiments.

Sixteen wall thermocouples and 42 wall static pressure taps were spaced along the combustor's top and bottom walls.

A hydrogen-oxygen torch igniter was used for some tests. It could be operated continuously when necessary.

Hydrogen was pressure-fed from storage tanks. The hydrogen fuel for the combustor was heated by a natural-gas-fired heater capable of providing fuel temperatures up to 1500°R.

The design and fabrication of the combustor, and details of the test facility, are discussed in Appendix A. Heat transfer design calculations for the nozzle and combustor are summarized in Appendix B.

5.2 INSTRUMENTATION

Instrumentation was provided for obtaining the following information:

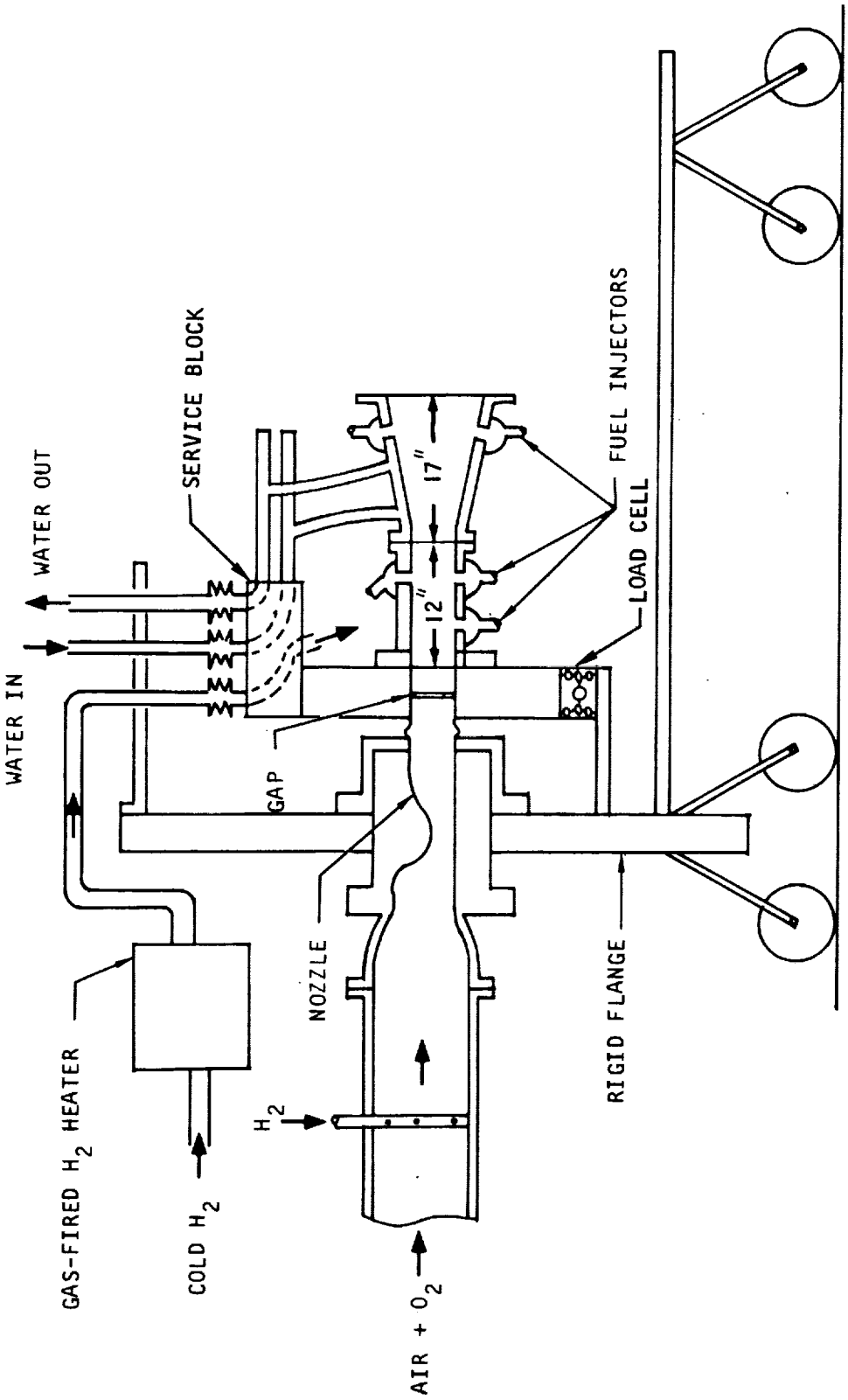

Figure 5.1-1. Schematic of Test System

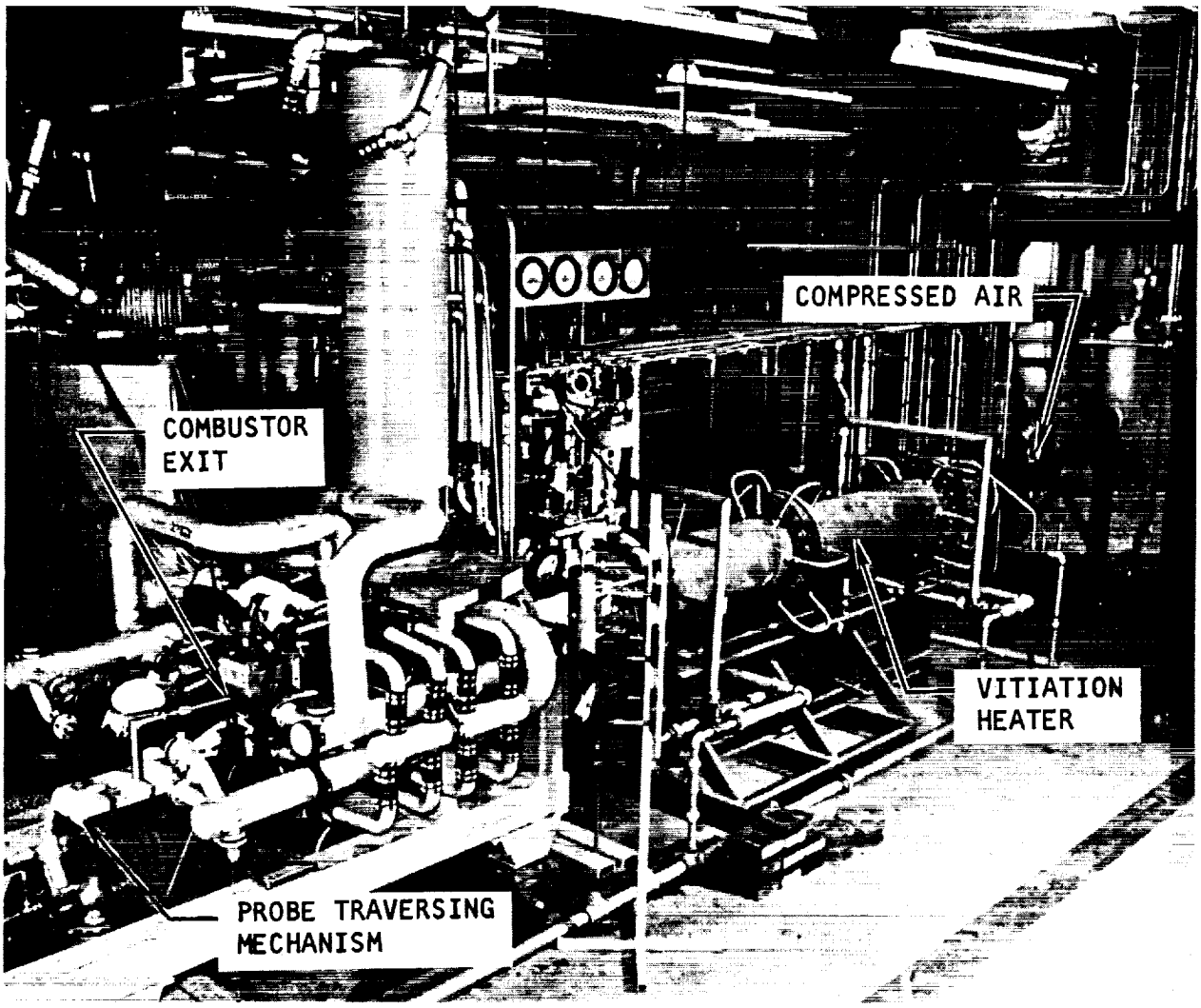

F-11642

Figure 5.1-2. Combustor Test Setup

(a) Inlet total temperature, total pressure and vitiated gas flow rates

(b) Thrust

(c) Static pressure distribution

(d) Wall heat transfer rates

(e) Fuel total temperature and total pressure

(f) Fuel mass flow rates at both stages

(g) Wall temperatures

(h) Local equivalence ratio as a function of position on the combustor exit plane.

For supersonic combustion runs the vitiated air inlet temperature was not measured directly, but the vitiation heater was instrumented such that the exit total temperature could be calculated both from the continuity equation and from an energy balance. Vitiating hydrogen and oxygen flow rates were measured with calibrated choked-flow nozzles; air flow was measured with a flat-plate orifice. All three gases entered the vitiation heater nearly at room temperature. The vitiation heater cooling water temperature differential was measured using copper-constantan thermocouples connected to give an emf proportional to the water temperature rise. Vitiation heater total pressure, which was actually measured as a static pressure in a low-velocity area, was obtained using a pressure transducer accurate to within one-half of 1 percent of full scale.

The thrust system consisted of two major subassemblies: a massive fixed flange and a movable force-pickup ring. The fixed flange formed the upstream portion of the thrust system. It was mounted on rails so that upstream thermal growth would not affect the force balance. The force-pickup ring, located in the downstream portion of the thrust system, was connected to the fixed flange through a load cell. The fixed and movable sections of the air flow duct in the thrust system were separated by a 0.01 in. gap. A flexible rubber seal was provided to prevent flow through the gap.

The rate of heat transfer from the gas to the cooling water was obtained by measuring the water flow rates through the individual plates that comprised the combustor walls, and the water temperature differentials.

Fuel total temperature was measured at the inlets to the fuel manifolds using chromel-alumel thermocouples.

Wall-temperature thermocouples were brazed into the top and bottom panels. The precise location of the thermocouple junction relative to the surface was determined for each. This was necessary because the high heat fluxes involved created temperature gradients across the skin of the order of 10,000°F per in.

Drawing PA 106770, attached at the end of this report, shows the traversing gas sampling probe which was used to determine equivalence ratio as a function of position on a plane slightly downstream of the combustor exit plane. Figure 5.2-1 shows the probe installed at this position. The probe had a blunt (0.3-in.-dia) inlet orifice. The gas samples were analyzed continuously on-line by a mass spectrometer which was calibrated to yield, directly, the volume percentages of H_2, O_2, H_2O, and N_2 in the samples.

The data were recorded on magnetic tape by a digital system which scanned all 100 channels in approximately 30 msec. To aid in detecting unexpected phenomena, most of these parameters were plotted mechanically as functions of time, using one reading (of each parameter) per second of run time.

Further information on the instrumentation system is given in Appendix C.

5.3 VITIATION HEATER CALIBRATION

The vitiated air total temperature at the combustor inlet plane was obtained from chemical equilibrium calculations. The assigned enthalpy used was based on measured flow rates and temperatures of the air, vitiation hydrogen, and oxygen. As a check on the assumption that combustion was complete, a "continuity" temperature was also calculated using the measured total flow, total pressure, nozzle throat area, and heat losses up to the throat.

Figures 5.3-1 and 5.3-2 give total temperature and normalized mass flow per unit throat area, respectively, for a vitiation heater with various values of heat loss. The heat loss is expressed in terms of Btu per lb of vitiating hydrogen, which is found by dividing the rate of heat loss by the vitiation hydrogen flow rate. In the calculations for Figures 5.3-1 and 5.3-2, the following assumptions were made:

(a) The flow is steady and one-dimensional.

(b) The equilibrium isentropic stagnation pressure at the point of interest is 300 psia.

(c) The compressed air, oxygen, and vitiating hydrogen enter the vitiation heater at a total temperature of 77°F.

(d) The gases at the plane of interest are perfectly mixed and in chemical equilibrium.

(e) The vitiating gases have been added at the correct oxygen-to-hydrogen weight-flow ratio of 12.2:1.

Figure 5.3-1 is valid at any plane provided the assumptions given above are true and the heat loss up to the given plane is considered. In Figure 5.3-1 all heat losses up to the nozzle throat must be accounted for. Note also that the flow per unit area has been normalized with respect to the total pressure, P_T.

Due to the construction of the variable Mach number inlet nozzle, some of the gas passed not through the throat, but along the water-cooled sides of

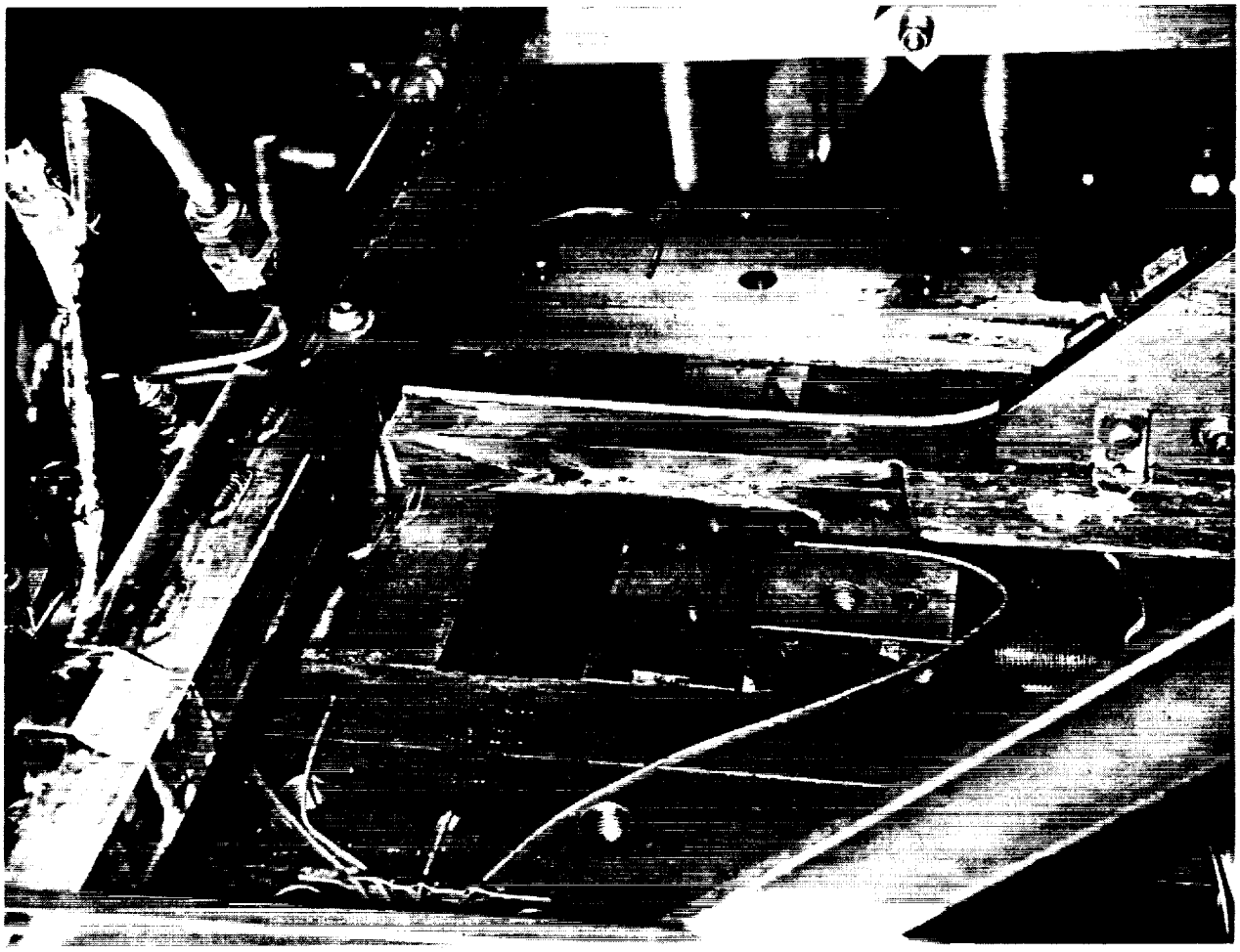

F-11620

Figure 5.2-1. Traversing Gas Sampling Probe

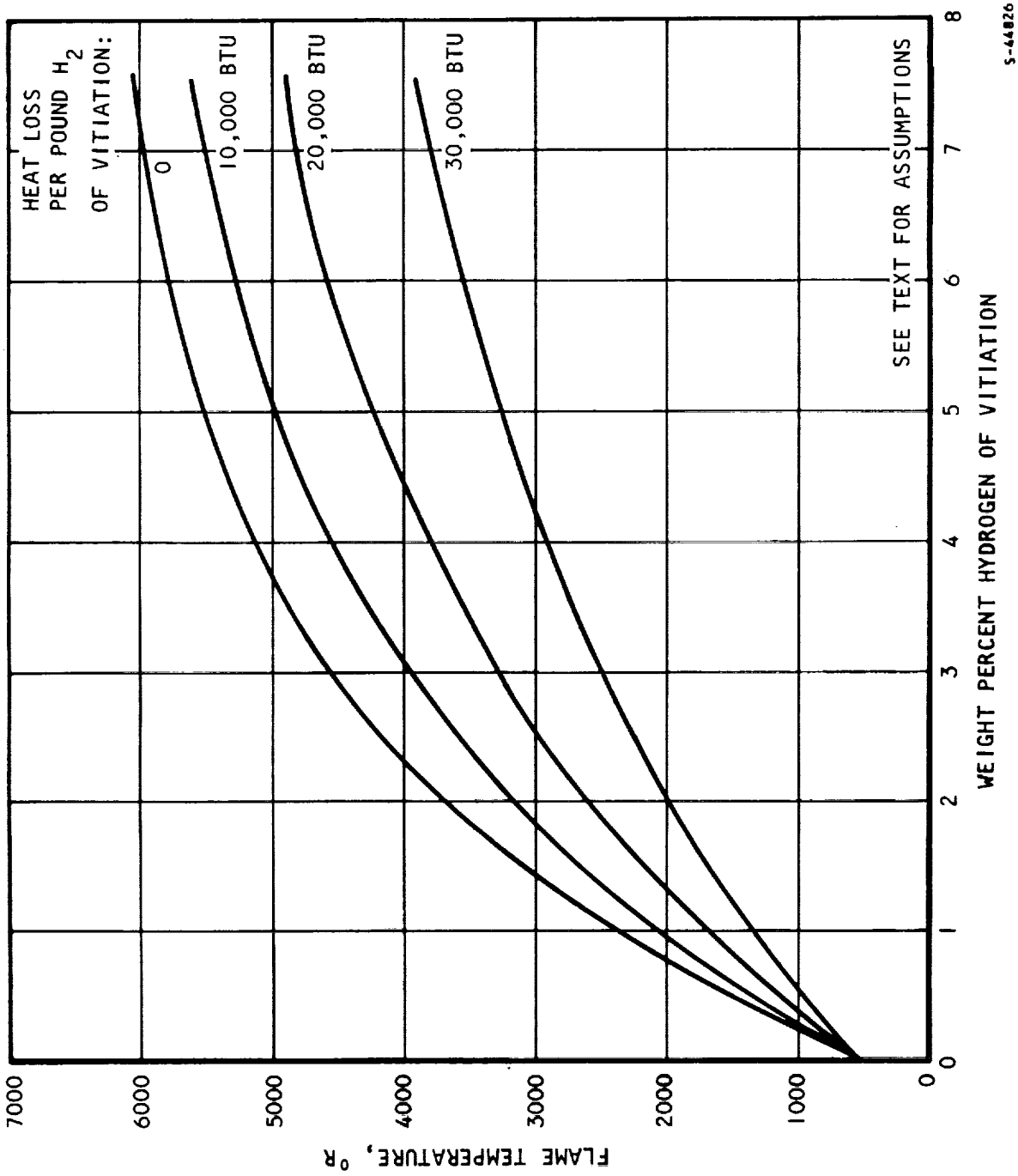

Figure 5.3-1. Total Temperature in Vitiation Heater

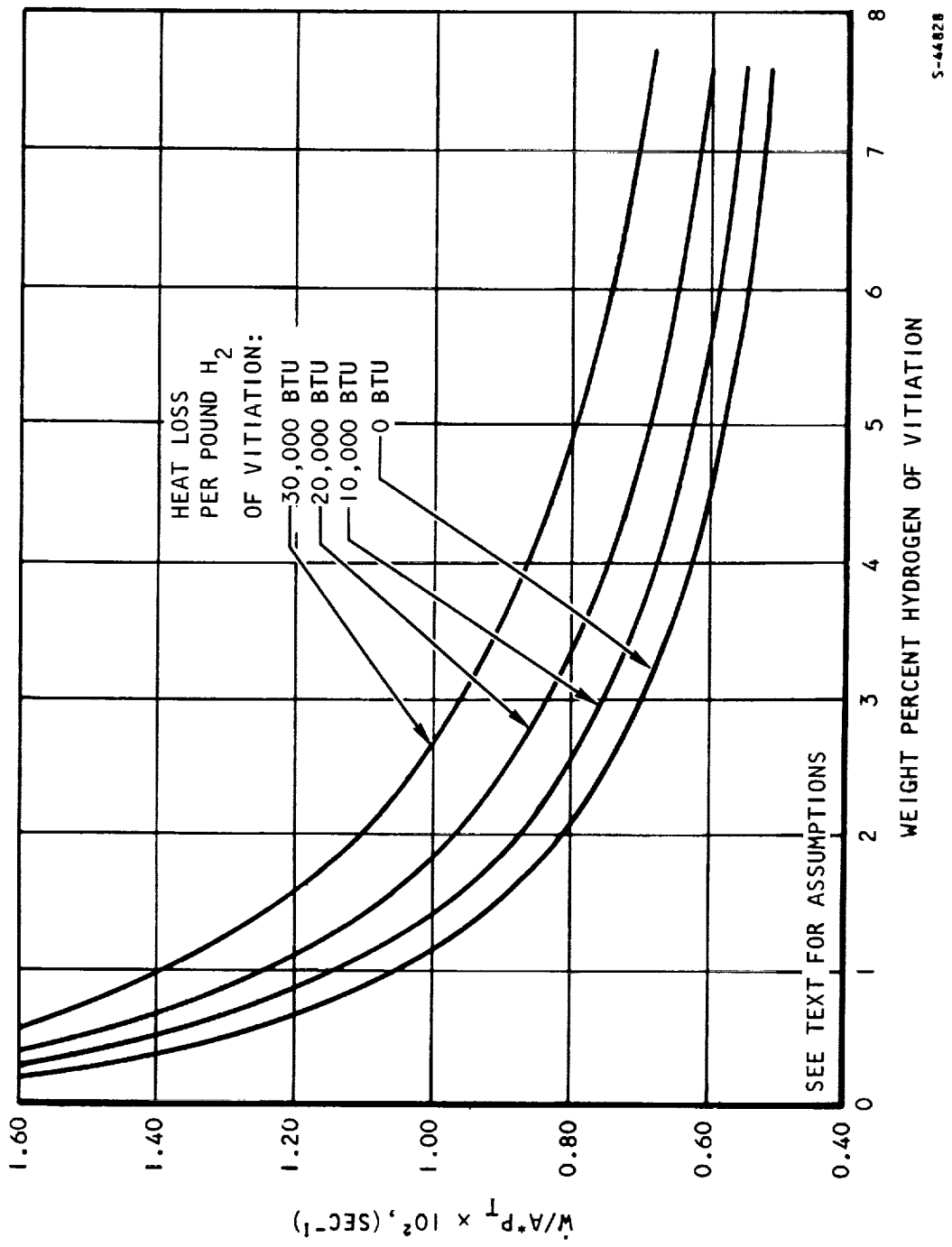

Figure 5.3-2. Normalized Weight Flow of Vitiated Air in Choked Throat

the nozzle insert. A correction was made for the effect of this leakage by using a nozzle discharge coefficient measured for cold flow, together with the assumption that the leakage flow always reentered the main flow "choked" and at the temperature of the water-cooled wall.

The temperatures computed using the two different methods indicated that complete combustion was attained in the vitiation heater. Conditions obtained in the calibration runs were used as a guide in setting desired conditions in subsequent runs.

6. COMBUSTOR TESTING

Combustor testing was divided into several test series. The first series was the subsonic tests using the 2- by 6-in. configuration of the combustor model. These tests were primarily to examine autoignition and flameholding. The second series was supersonic combustion tests using the 2- by 6-in. configuration and were conducted at an air inlet Mach number of 2.9. The third, fourth, and fifth series of tests were conducted using the true-scale version of the combustor, with a nominal inlet Mach number of 2.7, and at total temperatures simulating freestream Mach numbers of 5, 6, and 7. Gas sampling was conducted during the true-scale tests.

6.1 TEST PROCEDURE

The overall test procedure is described below in general terms. Detailed procedures dealing with the combustor only are given in References 6-1 through 6-4.

First, the supporting equipment (such as the hydrogen heater and air compressor) was started at least two hours prior to the commencement of testing. Water pumps that supplied the combustor, probe, and test facility were turned on, and the flow rates checked and recorded. During the same time period the quantities of nitrogen, oxygen, and hydrogen were checked and recorded.

The thrust stand was calibrated, then the test cell cleared and pre-test zeros recorded with the data acquisition system. The vitiation heater was started, and at the same time, tape in the data acquisition system started. After setting the required vitiated air total temperature and total pressure, hydrogen flow into the combustor was initiated. In many cases progress was stopped at this point to wait for the hydrogen temperature to come up to the desired value. The various equivalence ratios in the combustor were then set and each held for approximately one minute each. If gas sampling was to be done, a pre-selected equivalence ratio was held constant until the exit plane traverse was completed or the tape on the data acquisition system was expended. Early in the usage of the gas-sampling probe only a portion of the traverse of the exit plane could be completed within the time span allowable by the duration of the tape--about 20 min. With experience, more probe activity was fit in to the available time. Once the test was complete, the hydrogen fuel to the combustor was shut off, followed by the termination of the hydrogen and oxygen flows to the vitiation heater. The cell was then checked for residual hydrogen, and if safe to enter, the cell was opened and the supporting systems were shut down.

6.2 TEST SUMMARY

The combustor tests are summarized by the run log given in Table 6.2-I. The listed run numbers start from the first subsonic pre-test calibration, then restart when the vitiation heater used for the subsonic tests was replaced. The columns under the heading "Injector" refer to injector location in the combustor, the number of orifices in the injector, the orifice diameter (size) and the orifice spacing. T_{T0} is the vitiated air total temperature, ϕ_1 is the first-stage equivalence ratio, and ϕ_2 is the second-stage equivalence ratio.

TABLE 6.2-1

SUMMARY OF TEST CONDITIONS

Run No.	Injector				T_{TO}, °R	ϕ_1	ϕ_2	Ignitor Location	Purpose	Remarks
	Loc	No.	Size	Spacing						
1	1b 1c	3 3	.16 .16	1.5 1.5	1810	0	-	2f	Check out test facility. Subsonic model (2-in.-high duct)	Pre-run calibration
2	1b 1c	3 3	.16 .16	1.5 1.5	1810-1910	0,.1,.3	-	2f	Measure auto-ignition temperature	No burning at 1810°R, auto-ignition at 1910°R
3	1b 1c 1a	3 3	.16 .16 flameholder	1.5 1.5	1810-1860	0,.3	-	2f	Determine if flameholder affects auto-ignition	Auto-ignition took place at 1860°R
4 & 5	1b 1c 1a	3 3	.16 .16 flameholder	1.5 1.5	1083	0,.4	-	2f	Determine flameholding characteristics	Flame extinguished immediately when ignitor turned off
6	1b 1c 1a	3 3	.16 .16 flameholder	1.5 1.5	1083	0,.4,.5,.7,1.0	-	2f	Determine if higher step (0.4-in. high) would be more effective in flame holding	Flame never reached the step flameholder
7 & 8	1b 1c 1a	3 3	.16 .16 flameholder	1.5 1.5	1083-1133	0,.4,.6,.8,.9	-	2f	Determine if flame would hold once actually established just downstream of step	Flame held at step
9 & 10	1b 1a	3	.16 flameholder	1.5	1860-1133		-	1c	Verify original step flameholder height	Flame held satisfactorily
-	Vitiation heater modified and test sequence renumbered.									
1-21									Vitiation heater checkout, calibration and temperature survey	Air-cooled liner failed, went to water-cooled liner
22	1a 1c	3 3	.25 .25	1.5 1.5	2800	0,.2,.3	-	-	Measure gross effects of fuel temperature	Thrust stand failed. First test with 2-in.-high duct
23	1a 1c	3 3	.25 .25	1.5 1.5	2800	0,.15,.2,.3	-	-	Choke the combustor	Test terminated when pressures indicated boundary layer separation
24					4000				Airflow calibration at higher inlet temperature	
25					4960				Airflow calibration at Mach 8 temperature	
26					4960				Combustor run at high temperatures	Heater failed
27-57									Checkout and calibrate new vitiation heater design	Heater calibrated
58	1a 1c	3 3	.25 .25	1.5 1.5	3800	0-.6	-	-	Measure performance of 2-in.-high combustor over range of ϕ's	
59 & 60	1a 1c	3 3	.25 .25	1.5 1.5	3800	0-.9	-	-	Find ϕ where choking occurs	Reached ϕ = .9 before N_2 leakage aborted test
61-119									Checkout "redesigned" new heater for true-scale combustor tests 5-in. heater	SUE-type heater design chosen and calibrated
120	1a 1c 2e 2f	8 7 3 2	.1 .1 .16 .16	.55 .55 1.8 1.8	2900	0,.9,1.0 (N_2)	0,.65 (N_2)	-	True-scale combustor dry run. Checkout gas sampling probe	Total pressure surveys made with and without N_2 (gaseous)
121 & 122	1a 1c 2e 2f	8 7 3 2	.1 .1 .16 .16	.55 .55 1.8 1.8	3300, 3630	0,.9,1.1 (N_2)	0,.4,.6 (N_2)	-	Correlate sampling with different air temperatures	Total pressure and gas-sampling traverses made

TABLE 6.2-1 (Continued)

Run No.	Loc	Injector No.	Injector Size	Injector Spacing	T_{TO}, °R	ϕ_1	ϕ_2	Ignitor Location	Purpose	Remarks
123									Map exit total temperatures	Total temperature map completed
124 & 125									Cowl leading edge heat flux model test	
126-136									Vitiation heater calibration	
137	1a 1c 2e 2f	8 7 2 3	.1 .1 .16 .16	.55 .55 1.8 1.8	3800	0,.4,.5, .6,.76	-	Off	Test true-scale combustor over wide range of ϕ's. Exit height = 2.2 in.	Thrust stand seal failed at the high-ϕ point
138-140	↓	↓	↓	↓	↓	0-.6	-	↓	Test with broken seal over wide ϕ range	Good pressure rise
141 & 142	↓	↓	↓	↓	↓	.5-.7	0-.75	↓	Test second stage injectors	No appreciable pressure rise at second stage, even at high ϕ
143	1a 1c 2e 2f	8 7 2 3	.1-60°↑ .1-60°↑ .16 .16	.55 .55 1.8 1.8	3800	0-.5	-	Off	Obtain effects of angle injection	Similar pressure distribution to normal injection case
144	1a 1c 2e 2f	8 7 2 3	.1-60°↑ .1-60°↑ .16 .16	.55 .55 1.8 1.8	3800	.5	0-.6	Off	Obtain effects of 2nd-stage injectors and compare with Run 142	No large pressure rise in second stage
145	2e 2f	2 3	.25 .25	1.5 1.5	3800	-	.4-.9	Off	Measure effects of combustion at higher Mach number	Pressure disturbance small
146										Poor run
147	1a 1c	4 3	.15-60°↑ .15-60°↑	1.25 1.25	3800	0-.5	-	Off	Evaluate effect of fuel total pressure	No thrust measurement
148	1a 1c	5 4	.15-60°↑ .15-60°↑	.825 .825	3800	0-.6	-	Off	Investigate effects of injector diameter	Similar to Run 147
149	1a 1c 2e 2f	5 4 2 3	.15-60°↑ .15-60°↑ .25 .25	.825 .825 1.5 1.5	3800	0,.3,.5, .8	0,.7	Off	Further investigate two-stage combustion	Similar results to previous 2nd-stage tests
150										Poor run
151	1a 1c	5 4	.1-60°↑ .1-60°↑	.95 .95	3800	0-.5	-	Off	Evaluate effect of injector spacing	Thrust measurement erratic
152-154									Vitiation heater calibration	
155-157	1b 1c	7 6	.1 .1	.6 .6	2200	0-.2	-	1a	Run Mach 5 simulation prior to smaller combustor exit height	Each time ignitor turned off, flame went out
158	1b 1c	7 6	.1 .1	.6 .6	2940	0,.2,.4	-	1a	Measure effects of fuel temperature	Burning continued when ignitor turned off
159	1a 1c	7 6	.1 .1	.6 .6	2940	0,.05, .15,.25	-	1b	Examine ignition characteristics at low ϕ	At ϕ = .1, burning stopped with ignitor off; at ϕ = .2, burning maintained but moved downstream
160										Poor run
161-177									Vitiation heater checkout, profile testing and calibration with new transition section	
178	1a 1c 2e 2f	3 2 2 3	.2 .2 .25 .25	1.9 1.9 1.5 1.5	2940	-	0,.4,.5, .6,.8, .6,0	-	Second stage combination only. Combustor exit height = 1.56 in.	Good pressure rise

TABLE 6.2-1 (Continued)

Run No.	Injector				T_{TO}, °R	ϕ_1	ϕ_2	Ignitor Location	Purpose	Remarks
	Loc	No.	Size	Spacing						
179	1a 1c 2e 2f	3 2 2 3	.2 .2 .25 .25	1.9 1.9 1.5 1.5	2940	-	0,.7,.8, .9,1.0, 1.1,.8,0	-	Same as 178 with higher ϕ	Good pressure rise
180	1a 1c 2e 2f	3 2 2 3	.2 .2 .25 .25	1.9 1.9 1.5 1.5	3830	-	0,.4,.5, .6,.7,.8, .9,1.0, 1.1,.6,0	-	Mach 7 inlet temperature	Good pressure rise
181	1a 1c 2e 2f	3 2 3 2	.2 .2 .16 .16	1.9 1.9 1.8 1.8	3830	0,.3,.4, .5,.6,.7, .8,3.0	-	-	First stage combination only, larger jet dia than previous tests	Ignition delay behavior at ϕ = .3, suspect ϕ reading not correct
182	1b 1c 2e 2f	3 2 3 2	.2 .2 .16 .16	1.9 1.9 1.8 1.8	2940	0,.1,.2, .3,.4,.1, 0	-	1a	Mach 6 inlet temperature	Test looked good, first cold flow point is bad
183	1b 1c 2e 2f	3 2 3 2	.2 .2 .16 .16	1.9 1.9 1.8 1.8	2940	0,.3,.4, .5,.6,max, .3,0	-	1a	Same as 182 with higher ϕ	
184	↓	↓	↓	1.9	3830	0,.8,.9, 1.0,1.0+, 1.0+,abort	-	1a	Attempt to choke combustor	Blew out FluiDyne seal
185	1b 1c 2e 2f	3 2 3 plug	.2 .2 .16	1.9 1.9 1.8	2940	0,.1,.2, .3,.4,.4+, .1,0	-	1a	Repeat 182 after seal failure	No ign at ϕ = .10 w/o ignitor separation flip flop seen, deposits in nozzle
186	1b 1c 2e 2f	7 6 plug plug	.1 .1	.6 .6	2940	0,.1,.2, .3,.4,.4+, .2,.1,0	-	1a	Evaluate design point injectors; compare with 185	Flame oscillation at combustor exit from ϕ = .2 up
187	1b 1c 2e 2f	7 6 plug plug	.1 .1	.6 .6	2204	0,.1,.2, .3,.3+,.2, .1,0	-	1a	Mach 5 inlet temperature	Stays lit at ϕ = .2 when ignitor off, at higher ϕ's get flameout
188	1b 1c 2e 2f	3 2 3 2	.2 .2 .16 .16	1.9 1.9 1.8 1.8	2940	0,.1,.2, .3,.4,.2, .1,0	-	1a	Repeat 182 and 185	At ϕ = .1 some fuel appeared to be burning outside
189	1b 1c 2e 2f	3 2 3 2	.2 .2 .16 .16	1.9 1.9 1.8 1.8	2940	0,.1,.2, .3,.4,.2, .1,0	-	1a	Repeat 182 and 185	Flame looks different, burning in center this time
190	1b 1c 2e 2f	7 6 3 2	.1 .1 .16 .16	.6 .6 1.8 1.8	2204	0,.2	0,.4,.6, .8,1., 1.2,0	1a	Study two-stage combustion	No flame out upstream with ignitor off at ϕ = 1.1
191	1b 1c 2e 2f	7 6 3 2	.1 .1 .16 .16	.6 .6 1.8 1.8	2204	.3	0,.4,.6, .8,1.0, 1.2,0	1a	Two-stage combustion at Mach 5 temperature	
192	1b 1c 2e 2f	7 6 3 2	.1 .1 .16 .16	.6 .6 1.8 1.8	2940	0,.1,.2	-	1a	Repeatability test compare with Run 186	
193	1b 1c 2e 2f	7 6 3 2	.1 .1 .16 .16	.6 .6 1.8 1.8	2940	.2	.4,.6,.8, 1.0	1a	Two-stage combustion with Mach 6 inlet temperature	Compressor trouble; test aborted at ϕ_T = 1.2
194	1b 1c 2e 2f	7 6 2 2	.1 .1 .16 .16	.6 .6 1.8 1.8	2940	.2	.4,.6,.8	1a	Repeat Run 193	Ignitor no good

TABLE 6.2-1 (Continued)

Run No.	Injector				T_{TO}, °R	ϕ_1	ϕ_2	Ignitor Location	Purpose	Remarks
	Loc	No.	Size	Spacing						
195	1b	7	.1	.6	2940	.3	0,.4,.6, .8,1.0, 1.2,1.4, 0	1a	Two stage combustion at Mach 6 inlet temperature	
	1c	6	.1	.6						
	2e	3	.16	1.8						
	2f	2	.16	1.8						
196	1b	7	.1	.6	2940	.2	0,.4,.6, .8,1.0, 1.2,1.4, .2,0	1a	Two stage with high EQ ratio	
	1c	6	.1	.6						
	2e	3	.16	1.8						
	2f	2	.16	1.8						
197	1b	7	.1	.6	2940			1a	Fuel temperature effects	Aborted due to malfunction of fuel control system
	1c	6	.1	.6						
	2e	3	.16	1.8						
	2f	2	.16	1.8						
198	1b	7	.1	.6	2940	.2	-	1a	Fuel temperature	Fuel temperature change very slow
	1c	6	.1	.6		.4				
	2e	3	.16	1.8						
	2f	2	.16	1.8						
199	1b	7	.1	.6	2940	.2	-	1a	Fuel temperature	
	1c	6	.1	.6		.4				
	2e	3	.16	1.8						
	1f	2	.16	1.8						
200					540				30 min. run for aerodynamic loading and vibration checkout of wedge probe No. 1	No digital data taken
201					2940				10 min. run for checkout of wedge probe No. 1	
202	1b	7	.1	.6	2940	0	0	1a	Checkout run for wedge probe No. 1	Run aborted at ϕ_T = .5 because sparks were observed
	1c	6	.1	.6		.3	0			
	2e	3	.16	1.8		.3	.2			
	2f	2	.16	1.8						
203	1b	7	.1	.6	2940	0,.25,.3	0,.2,.5, .8	1a	Continuation of checkout of wedge probe No. 1	Good light at both stages. Run aborted during shutdown
	1c	6	.1	.6						
	2e	3	.16	1.8						
	2f	2	.16	1.8						
204	1b	7	.1	.6	2204	0,.1,2	-	1a	Obtain gas samples and pitot pressures	Took samples, have new silicone rubber seal in thrust stand
	1c	6	.1	.6						
	2e	3	.16	1.8						
	2f	2	.16	1.8						
205 & 206					540	-	-	-	Thrust checkout vs. line temperature	Zero shift when lines heated
207					2940	-	-	-	Vitiation heater calibration	
208					2204	-	-	-	Vitiation heater calibration	
209	1b	7	.1	.6	2940	0,.1,.2, .3	-	1a	Gas sample - obtain map at combustor exit	Not enough time to gas sample, but mapped pitot pressure. Good light
	1c	6	.1	.6						
	2e	3	.16	1.8						
	2f	2	.16	1.8						
210	1b	7	.1	.6	2940	0,.3,0	-	1a	Repeat missed points of Run 209	Took gas samples, pitot pressure
	1c	6	.1	.6						
	2e	3	.16	1.8						
	2f	2	.16	1.8						
211 & 212	1b	7	.1	.6	2940	.21	0,.47,.65, .88,1.1,0	1a	Obtain gas sample with two-stage injection	Good light both stages. Probe appears to affect 2nd stage pressures
	1c	6	.1	.6						
	2e	3	.16	1.8						
	2f	2	.16	1.8						
213	1b	7	.1	.6	2940	.2	0,.47,.65	1a	Obtain gas samples with double 2nd stage injector area	Probe moved 3/4 in. downstream of combustor exit. Good light both stages
	1c	6	.1	.6						
	2e	7	.142	.6						
	2f	6	.142	.6						

TABLE 6.2-I (Continued)

Run No.	Injector				T_{TO}, °R	ϕ_1	ϕ_2	Ignitor Location	Purpose	Remarks
	Loc	No.	Size	Spacing						
214	1b	7	.1	.6	2940	.2	0,.47,.65, .88,1.2, 1.3,1.41, 0	1a	Remove probe to observe effect on pressure	Good light, data incomplete
	1c	6	.1	.6						
	2e	7	.142	.6						
	2f	6	.142	.6						
215	1b	7	.1	.6	2940	.2	0,.47,.65, .88,1.2, 1.3,1.41, 0	1a	Test without probe with same geometry as Run 209-212	Smaller pressure rise at high ϕ's
	1c	6	.1	.6						
	2e	3	.16	1.8						
	2f	2	.16	1.8						
216	1b	7	.1	.6	2940	.2	0,.47,.65, .88,1.2, 1.3,1.41, 0	1a	Test with 2nd stage injectors pointing 30° upstream from vertical to improve pressure rise	No large change in measured pressures
	1c	6	.1	.6						
	2e	7-60°↑	.1	.6						
	2f	6-60°↑	.1	.6						
217	1b	7	.1	.6	2940	.2	0,.47,.65, .88,1.2, 1.3,1.41, 0	1a	2nd stage injectors pointing 45° upstream to improve pressure rise	Slight increase in pressure downstream of injectors
	1c	6	.1	.6						
	2e	7-45°↑	.1	.6						
	2f	6-45°↑	.1	.6						
218	1b	7-60°↑	.1	.6	2940	.2	0,.47,.65, .88,1.2, 1.3,1.41., 0	1a	Inject 2nd stage normal for a reference point	Pressures similar to previous tests, except near injectors where lower
	1c	6-60°↑	.1	.6						
	2e	7	.1	.6						
	2f	6	.1	.6						
219	1b	7-60°↑	.1	.6	2940	0,.1,.2, .29,.21, .1,0	-	1a	Vary 1st stage injection	Very little burning inside combustor at ϕ = .1
	1c	6-60°↑	.1	.6						
	2e	7	.1	.6						
	2f	6	.1	.6						
220	Bad run (seal blew)									
221	1b	7	.1	.6	2940	.2	0,.47,.65, .88,1.1, 1.3,1.4,0	1a	Try to improve pressure rise with supersonic injectors	Lower pressure rise than previous test Run 215
	1c	6	.1	.6						
	2e	3	.16	1.8						
	2f	2	.16	1.8						
222	1b	7	.1	.6	2940	.2	0,.47,.65, .88,1.1, 1.3,1.4,0	1a	Point larger holes 45° upstream to raise static pressures	Lower pressure rise than .1 in. dia injectors
	1c	6	.1	.6						
	2e	3-45°↑	.16	1.8						
	2f	2-45°↑	.16	1.8						
223	1b	3-45°↑	.16	1.8	2940	0,.1,.2, .3,.2, .1,0	-	1a	Compare pressure rise with larger holes	Pressure rise looked low
	1c	2-45°↑	.16	1.8						
	2e	plugged								
	2f	plugged								
224	1b	3-45°↑	.16	1.8	3830	0,.2,.4 .6,.2,0	-	1a	See if higher temperatures improve combustion	Flame at combustor exit throughout test
	1c	2-45°↑	.16	1.8						
	2e	plugged								
	2f	plugged								
225 & 226	1b	3	.16	1.8	2940	0,.1,.2, .3,.2, .1,0	-	1a	Check normal injection with larger holes	Run looked better than .16 in. dia - 45°↑, but not as good as .1 in. dia holes
	1c	2	.16	1.8						
	2e	plugged								
	2f	plugged								
227	1b	3	.16	1.8	3830	0,.2,.4, .6,.2,0	-	1a	Check at higher temperature to improve efficiency	Some flame at combustor exit throughout test
	1c	2	.16	1.8						
	2e	plugged								
	2f	plugged								
228	1b	7	.1	.6	3830	0,.2,.4, .6,.2,0	-	1a	Check pressure rise with smaller holes	Pressure rise better
	1c	6	.1	.6						
	2e	plugged								
	2f	plugged								
229	1b	7	.1	.6	2940	.2	0,.47,.65, .79,.88,0	1a	Try to keep 2nd stage injectors out of combustion gases to improve pressure rise	No noticeable improvement in measured pressures
	1c	plugged								
	2e	3	.16	1.8						
	2f	plugged								
230 & 231	1b	7	.1	.6	2940	0	0	-	Gas sampling	
	1c	6	.1	.6						
	2e	3	.16	1.8						
	2f	2	.16	1.8						

TABLE 6.2-1 (Continued)

Run No.	Injector Loc	Injector No.	Injector Size	Injector Spacing	$T_{TO'}$ °R	ϕ_1	ϕ_2	Ignitor Location	Purpose	Remarks
232	1b	7	.1	.6	2940	.2	.8	1a	Obtain gas samples to establish comparison point	No major changes from previous tests. Peak fuel concentration in middle
	1c	6	.1	.6						
	2e	3	.16	1.8						
	2f	2	.16	1.8						
233	1b	7	.1	.6	2940	.2	.8	1a	Add two orifices in 2nd stage to inject fuel to sides of combustor	No improvement in static pressures. Peak concentration shifted to sides
	1c	6	.1	.6						
	2e	3	.16	1.8						
	2f	2	.16	1.8						
		2-45°↓	.18	1.8						
234 & 235	1b	7	.1	.6	2940	.2	.48	1a	Check exit profiles with gas sampling probe with only one side injection	Two distinct peaks in gas samples opposite 2nd stage injectors
	1c	6	.1	.6						
	2e	3	.16	1.8						
	2f	plugged								
236	1b	7	.1	.6	2940	.2	.8	1a	Try to improve concentration profile	Still have peak concentration in middle, but profile has spread out more
	1c	6	.1	.6						
	2e	7-45°↓	.1	.6						
	2f	6-45°↓	.1	.6						
237	1b	7	.1	.6	2940	.2	.8	1a	Check profiles with ignitor turned off	Profiles changed from previous run
	1c	6	.1	.6						
	2e	7-45°↓	.1	.6						
	2f	6-45°↓	.1	.6						
238	1b	7	.1	.6	2940	.2	.4	1a	Obtain profiles at a lean equivalence ratio	Profiles fairly flat
	1c	6	.1	.6						
	2e	7-45°↓	.1	.6						
	2f	6-45°↓	.1	.6						
239	1b	7	.1	.6	2940	.2	.8	1a	Repeat Run 237; had fuel leaks previous tests	Similar profile to Run 237
	1c	6	.1	.6						
	2e	7-45°↓	.1	.6						
	2f	6-45°↓	.1	.6						
240	1b	7	.1	.6	2940	.2	.4	1a	Repeat Run 238 with leaks fixed	Similar profile to Run 238
	1c	6	.1	.6						
	2e	7-45°↓	.1	.6						
	2f	6-45°↓	.1	.6						
241 & 242	1b	7	.1	.6	3830	.2	.4,.8	1a	Try to improve combustion at higher temperature	Visible flame throughout test, flame unsteady at ϕ_{total} = .6, flame steady at ϕ_{total} = 1.0
	1c	7	.1	.6						
	2e	7-45°↓	.1	.6		.3	.3,.7			
	2f	6-45°↓	.1	.6						
243 & 244	1b	7	.1	.6	2940	0	.65,.92	1a	Obtain profiles with 2nd stage injection only	Tests aborted prior to completion; once due to sparks from probe, and another due to electrical failure
	1c	6	.1	.6						
	2e	3	.16	1.8						
	2f	plugged								
245	1b	7	.1	.6	3000	0	.92	1a	Repeat Run 243	First time through map, exhaust separated and unstable. Raised ϕ to 1.0. Combustor stable
	1c	6	.1	.6						
	2e	3	.16	1.8						
	2f	plugged								
246	1b	7	.1	.6	3000	0	1.2	1a	Obtain profiles at rich ϕ, run for spreading comparison	High concentrations near combustor bottom, peaks opposite injectors
	1c	6	.1	.6						
	2e	3	.16	1.8						
	2f	plugged								
247	1b	7	.1	.6	3000	0	1,2	1a	Compare with Run 246 to observe spreading	Profile changed at centerline. 2nd stage pressure profile moved slightly downstream of Run 246
	1c	6	.1	.6						
	2e	3	.228	1.8						
	2f	plugged								
248	1b	7	.1	.6	3000	.2 - cold H_2	0 - GN_2 injection	1a	Test with N_2 injection to see if combustion influences profiles	First stage flamed out when GN_2 added in 2nd stage. Still peaks in middle
	1c	6	.1	.6						
	2e	7-45°↓	.1	.6						
	2f	6-45°↓	.1	.6						

TABLE 6.2-1 (Continued)

Run No.	Injector				T_{TO}, °R	ϕ_1	ϕ_2	Ignitor Location	Purpose	Remarks
	Loc	No.	Size	Spacing						
249	1b	7	.1	.6	3000	.2 - cold H_2	.2,.4,.6, .8 - cold H_2	1a	Gas sample using cold H_2 to bypass leakage problem	Flameout of 1st stage when 2nd stage fuel came on
	1c	6	.1	.6						
	2e	7-45°	.1	.6						
	2f	6-45°	.1	.6						
250	1b	7	.1	.6	3000	.2	.2,.4,.6, .8	1a	Run with 50 percent excess O_2 in heater to improve pressures	Pressure profile practically identical to Run 249. Orange flame instead of usual blue-green
	1c	6	.1	.6						
	2e	7-45°	.1	.6						
	2f	6-45°	.1	.6						
251	1a	plugged			3000	.2,.3	0,.4	2f	See if ignitor in 2nd stage will improve pressure profile	1st stage did not light even when increased to ϕ = .3, no significant pressure change
	1b	6	.1	.6						
	1c	plugged								
	2e	7-45°	.1	.6						
252	1b	6	.1	.6	3000	.2	0, .2,.4,.6, .8,0	1a	Try to keep 2nd stage injectors out of combustion gases	Pressure profile lower than Run 250. Burning outside combustor - at ϕ = 1.0 large flame outside
	1c	plugged								
	2e	7-45°	.1	.6						
	2f	plugged								
253 & 254	1a	7	.1	.6	3000	.3	-	1b	Change 1st stage injector location to see effect on pressures	Pressures appear higher in 1st stage and farther upstream
	1c	plugged								
	2e	not used								
	2f	not used								
255	1b	7	.1	.6	3000	.3	-	1a	Vary 1st stage location and compare with previous runs	Combustor pressures lower and farther downstream than Run 254
	1c	plugged								
	2e	not used								
	2f	not used								
256	1a	7	.1	.6	3000	.3	-	1b	Repeat Runs 253 and 254 - suspect fuel leak these runs	Similar results to Runs 253 and 254
	1c	plugged								
	2e	not used								
	2f	not used								

7. RESULTS AND ANALYSIS - SUBSONIC COMBUSTION TESTS

The subsonic combustion tests were run in a constant-area duct 2 in. high. The principal objectives of these tests were to determine the autoignition temperature and to determine whether a step that simulated the engine inlet trailing edge would operate as a suitable flameholder in the Mach 3 to 6 range. Fuel was injected from injectors at 1b and 1c through three 0.16-in.-dia. holes, in each row, spaced 1.5-in. apart. The step was placed at row 1a and varied in height from 0.25 to 0.40 in.

Autoignition took place with an air total temperature of 1750°R at the flameholder station. The flow Mach number was 0.45 and the static pressure and temperature were approximately 60 psia and 1715°R respectively.

Preliminary tests showed that with the igniter located at position 2f the flame would not propagate to the step, which was approximately 15 inches upstream from the igniter. Therefore, autoignition was used to initiate the flame at the step for some of the later tests. Flame was held satisfactorily by both the 0.40- and 0.25-in. flameholder with the air total temperature reduced to 1080°R. Therefore, using a flameholder of 0.25 in., burning was sustained at pressures and temperatures corresponding to high-altitude flight at Mach 3, and at combustor inlet Mach numbers of approximately 0.4 to 0.3.

The inlet temperature was then further reduced to the point where the vitiation heater was no longer controllable (approximately 820°R). Combustion was still sustained by the flameholder.

A typical pressure and wall temperature distribution with the 0.25-in. flameholder installed is presented in Figure 7.0-1. Additional plots can be found in Reference 7-1. The amount of heat release at each station inside the combustor was computed one-dimensionally, using the static pressure distribution along the wall. The results of this one-dimensional calculation are presented in Figure 7.0-2. The combustor was choked. The calculations appear valid since the calculated Mach number was near unity at the combustor exit plane. A chemical efficiency of 100 percent was reached about 18 inches from the fuel injection point.

In these tests, the main purpose was to evaluate flameholding, not to optimize fuel injection. Thus, the 18-in. combustion length should not be considered typical of what subsonic combustor lengths are required for complete combustion. With the autoignition temperature established and a flameholder design verified, subsonic combustion tests were discontinued in favor of the supersonic tests. It was concluded that having demonstrated the adequacy of the flameholder system, obtaining high combustion efficiencies in the allotted length would not be a problem.

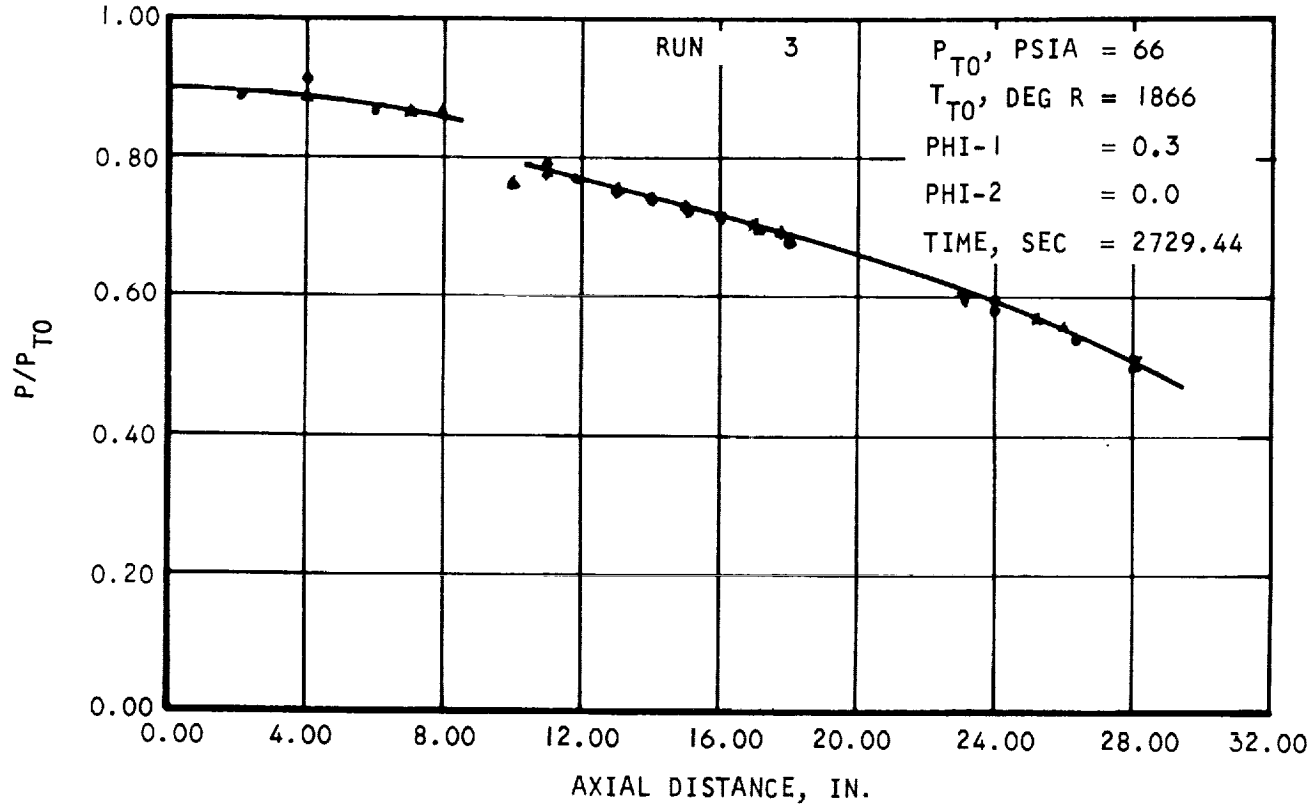

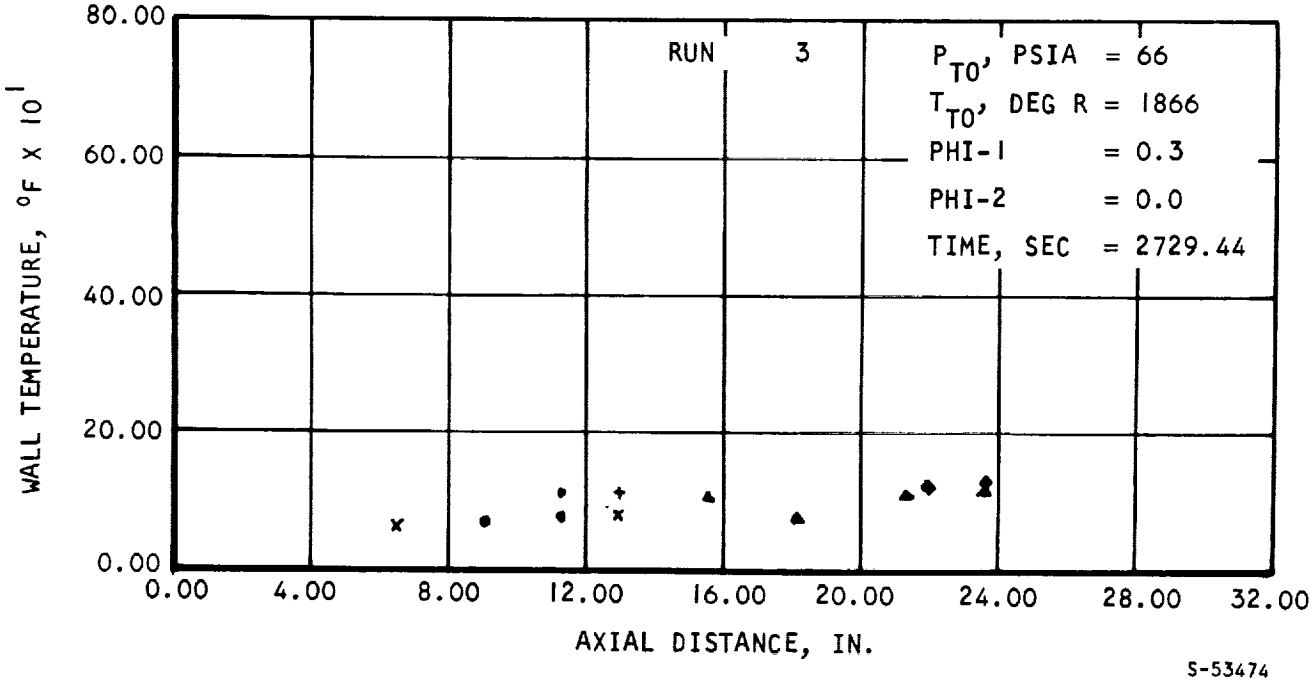

Figure 7.0-1. Pressures and Wall Temperatures During Autoignition (U)

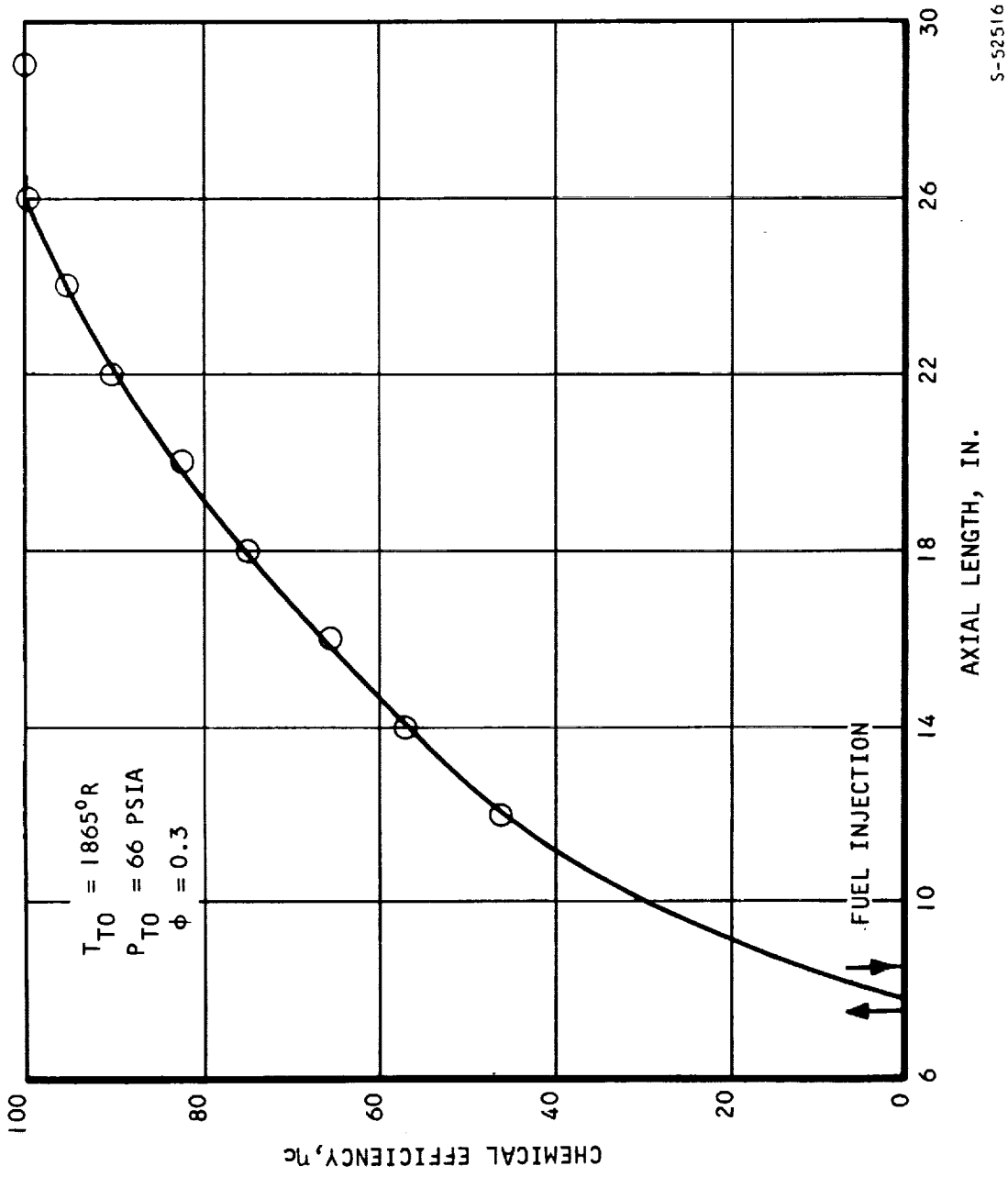

Figure 7.0-2. Subsonic Combustion Chemical Efficiency (U)

8. RESULTS AND ANALYSIS - SUPERSONIC COMBUSTION TESTS

The supersonic test results will be discussed in two main categories:

(a) Single-stage injection - in both a constant-area duct and a divergent duct.

(b) Two-stage injection - with part injected in a constant-area duct and the remainder injected farther downstream in a divergent duct.

Combustor area ratios of 3.68 and 1.60 were used in conjunction with the true-scale version, and 1.32 with the 2-in.-high version (See Figure 8.0-1).

A wide variety of injectors was tested. Hole spacing, number of holes, hole diameter and angle were varied. Total temperatures corresponding to freestream Mach numbers of 5, 6, and 7 were used. The temperatures corresponding to these Mach numbers were 2204°, 2940°, and 3830°R respectively. One-stage and two-stage combustion were investigated. The equivalence ratio at each stage was varied. The fuel temperature was also varied in order to evaluate its effect on the combustion process.

8.1 PERFORMANCE DATA REDUCTION METHOD

Combustor performance for the two-dimensional test rig was calculated, using a one-dimensional flow model, from measured static pressures, mass flows, heat loss, and thrust.

Below is a sketch of the combustor model geometry used in the analysis:

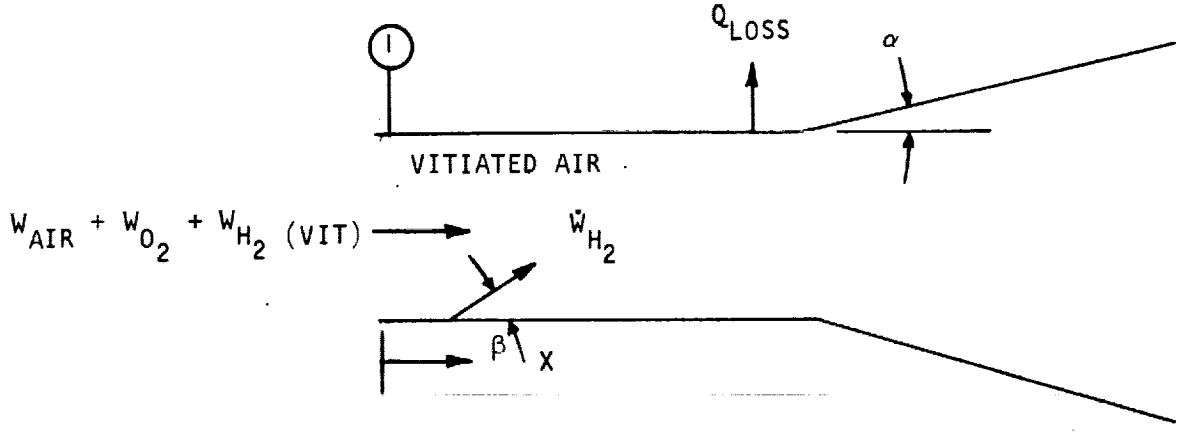

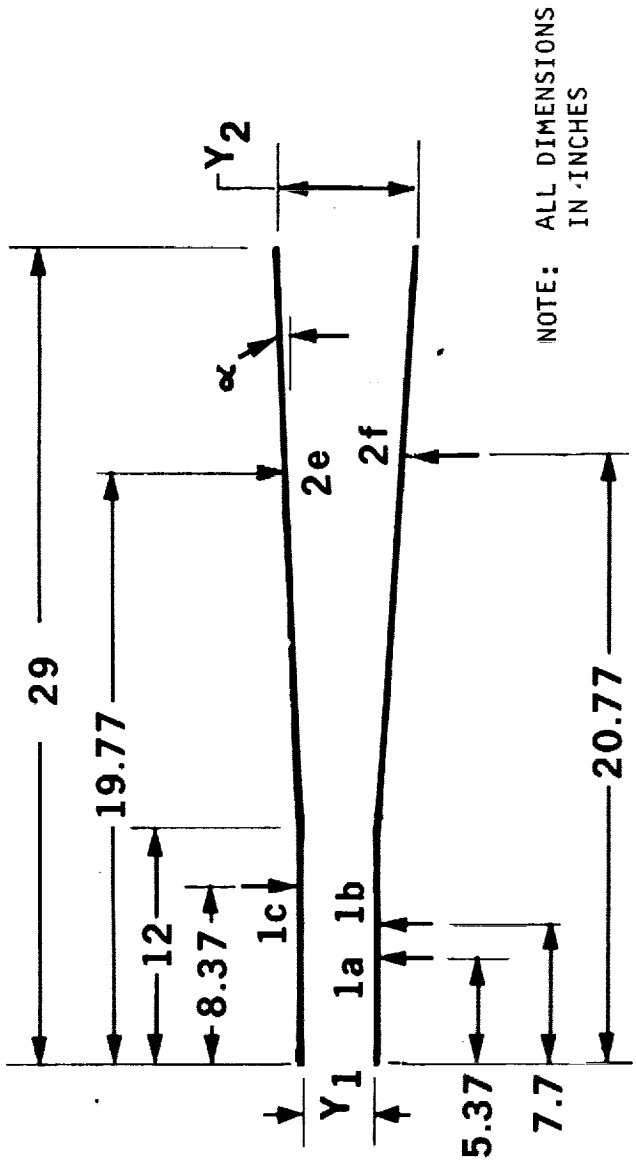

TEST GEOMETRY	Y_1	Y_2	α	
1	2	2.64	$1^0 5'$	SUPERSONIC COMBUSTION TESTS
2	0.6	2.2	$2^0 42'$	
3	0.6	1.56	$1^0 37'$	
4	2	2	0	SUBSONIC COMBUSTION TESTS

Figure 8.0-1. Combustor Test Geometry

Static pressures were measured along the combustor length and from these, combustor efficiency was determined. The heat loss, Q_{loss}, was determined from measured cooling water flow rates and temperature rises. The entrance conditions to the combustor (Station 1) such as Mach number, velocity, and static temperature were obtained by satisfying equations of continuity and energy assuming 100 percent combustion efficiency in the vitiation heater.

Once the entering vitiated air properties are determined, the velocity distribution along the combustor length can be calculated as follows:

Momentum Balance

$$F_1 + \left(P_f A_f + \frac{\dot{W}_{H_2}}{g} V_f\right) \cos \beta + \left(\frac{P_1 + P_x}{2}\right)\left(A_x - A_1\right) - \frac{C_f}{2g}\left(\frac{P_1 V_1^2 + P_x V_x^2}{2}\right) A_W \cos \alpha = P_x A_x + \frac{\dot{W}_x}{g} V_x \qquad (8\text{-}1)$$

Where A_W is wetted area, subscript (f) denotes fuel, and C_f is an average friction coefficient which is considered constant for any one test point.

Continuity

$$\dot{W}_1 + \dot{W}_{H_2} = \dot{W}_x = \rho_x V_x A_x \qquad (8\text{-}2)$$

In the above two equations, the only unknowns are ρ_x and V_x (an iteration was made for friction coefficient so that the calculated total frictional force was equal to the measured frictional force). Linearity of pressure between pressure taps is assumed. Thus the one-dimensional ρ_x and V_x can be calculated vs axial position (note that the value of A_x used was the geometric cross-sectional area) assuming that static pressure is uniform across the duct. The total enthalpy, H_{T_x}, can be found from:

$$H_{T_x} = \frac{H_{T_1} + \frac{\dot{W}_{H_2}}{\dot{W}_1} H_{T_f}}{1 + \dot{W}_{H_2}/\dot{W}_1} - \frac{Q_{loss}}{\dot{W}_x} \qquad (8\text{-}3)$$

The vacuum specific impulse, I_{vac}, can also be calculated:

$$I_{vac} = \frac{P_x}{(W/A)_x} + \frac{V_x}{g} \qquad (8\text{-}4)$$

Combustor performance is then determined by iterating on combustor chemical efficiency (η_c) defined as:

$$\eta_c = \frac{\dot{W}_{H_2 \text{ reacted}}}{\dot{W}_{H_2 \text{ injected}}} \qquad \text{for } \phi \leq 1 \qquad (8\text{-}5)$$

and

$$\eta_c = \frac{\dot{W}_{H_2 \text{ reacted}}}{\dot{W}_{H_2 \text{ stoichiometric}}} \qquad \text{for } \phi > 1$$

The combusted species are obtained by setting fuel which reacts at $\eta_c \dot{W}_{H_2}$ and then allowing the reactants to come to equilibrium (the unreacted fuel is assumed to be perfectly mixed with the combustion products).

In the iteration for η_c and p_t at each combustor station, the known quantities I_{vac} and W/A are the dependent variables. With initial guesses for $\eta_c^{(1)}$ and $p_t^{(1)}$, the total conditions are determined by solving the pressure enthalpy problem. An isentropic expansion is made to the measured pressure and $I_{vac}^{(1)}$ and $(W/A)^{(1)}$ are calculated. The initial values $\eta_c^{(1)}$ and $p_t^{(1)}$ are perturbed separately to obtain the Jacobian matrix which is inverted to obtain the next values of η_c and p_t. The iteration is continued until:

$$\frac{(W/A) - (W/A)^{(n)}}{(W/A)} < \epsilon$$

and

$$\frac{I_{vac} - I_{vac}^{(n)}}{I_{vac}} < \epsilon$$

8.2 SINGLE-STAGE INJECTION

Single-stage injection tests were conducted in both a constant-area and a diverging section. Large static pressure rises over a wide range of air and fuel temperatures were obtained when fuel was injected into the constant-area combustor section. However, when fuel was injected into the diverging section, the static pressure rises were significantly lower.

8.2.1 Fuel Injection Into A Constant-Area Section

A typical pressure distribution with fuel injection into the 2-in.-high constant-area section is shown in Figure 8.2-1. A distinct pattern is observed: at low equivalence ratios, ignition delay and chemical reaction time are long (approximately 5 in. or 70 micro-seconds); at higher equivalence ratios, combustion takes place almost immediately. Furthermore, at high equivalence ratios local flow separation occurred and extended upstream into the thrust stand. In the vicinity of the injector, the flow probably contained both subsonic and supersonic regions. The negative slope of the pressure-versus-distance profiles in the diverging combustor section indicates that the overall mixed flow behaves supersonically.

This same phenomenon occurred in the 0.6-in.-high duct, but in that case peak pressures in the constant area section increased as shown in Figure 8.2-2. The general characteristics of these tests were similar to those of the 2-in.-high duct. The pressure profiles showed wider spreads of peaks and valleys indicating stronger supersonic waves. A direct comparison of data from these two geometries is shown in Figure 8.2-3. Results from the one-dimensional data reduction program indicated that the peak flow blockages due to separation were approximately equal (40 percent). However, the blockage for the 0.6-in. duct increased much more abruptly from inlet to the peak value resulting in a higher total pressure loss and a higher static pressure.

This peak pressure varied with geometry and with total temperature as shown in Figure 8.2-4 and 8.2-5. At any particular equivalence ratio as total temperature increased the peak pressures decreased. This is a direct consequence of the increase in specific heat and initial temperature of the flow.

A principal objective in conducting tests with fuel injection into the constant-area section was to determine effects of injector geometry. A summary of those tests is in Table 8.2-1. A brief description of some of these runs follows. Further details can be found in Reference 8-1.

8.2.2 Effect of Injection Angle

In the two runs relating to Figure 8.2-6 two injector rows were used; one on the bottom wall and one on the top wall, axially spaced 3 in. apart. The first row had eight 0.1-in.-dia injection holes spaced 0.55 in. apart, while the second row consisted of seven holes with the same size and spacing, but staggered with respect to the holes in the first row. All orifices were 0.31 in. in length; i.e., drilled through a piece of material 0.31 in. thick. In run 143 the orifices pointed downstream at an angle of 60 deg to the combustor centerline, and in run 140 injection was normal to the main stream.

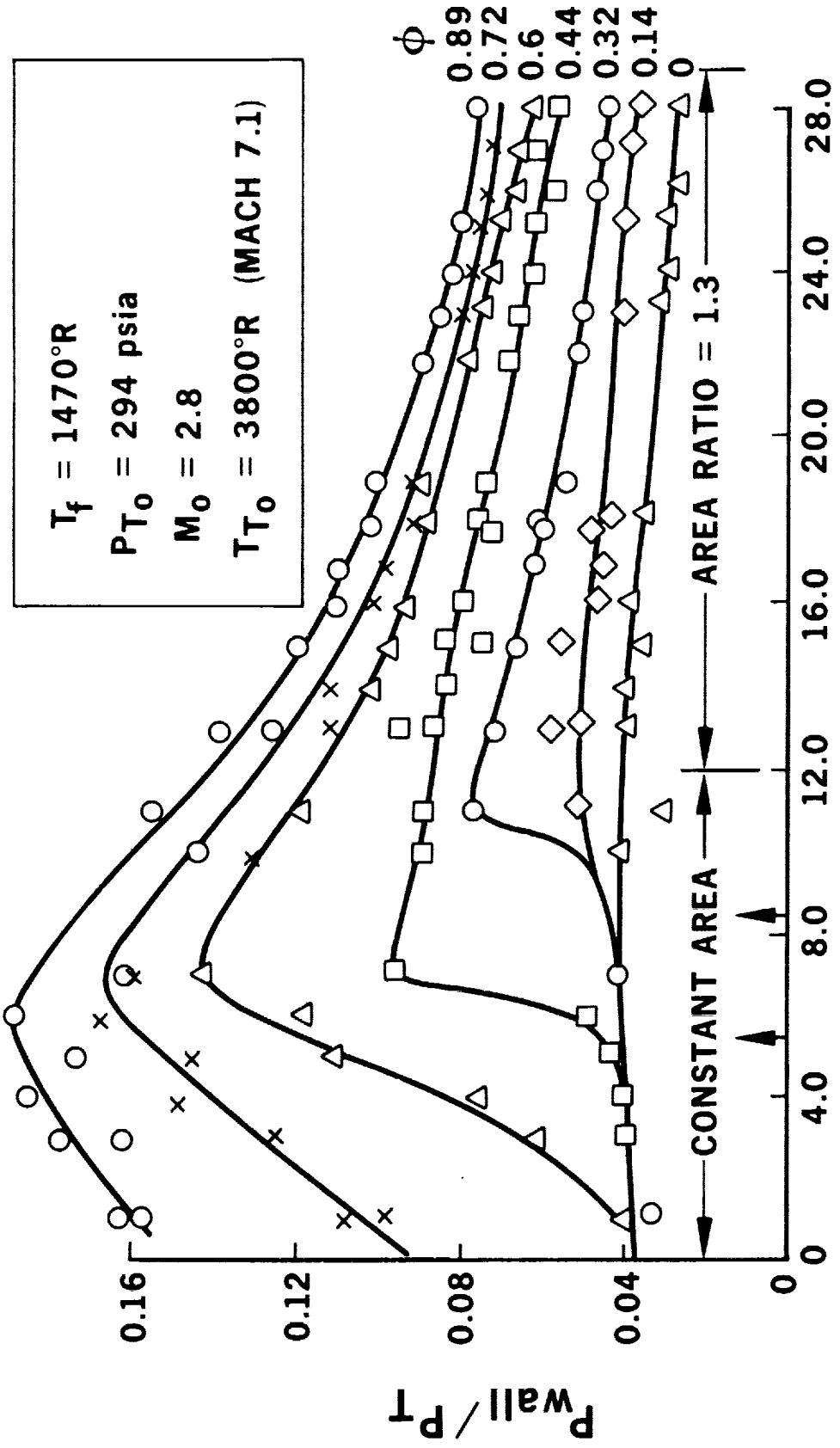

Figure 8.2-1. Combustor Pressure Distribution (U)

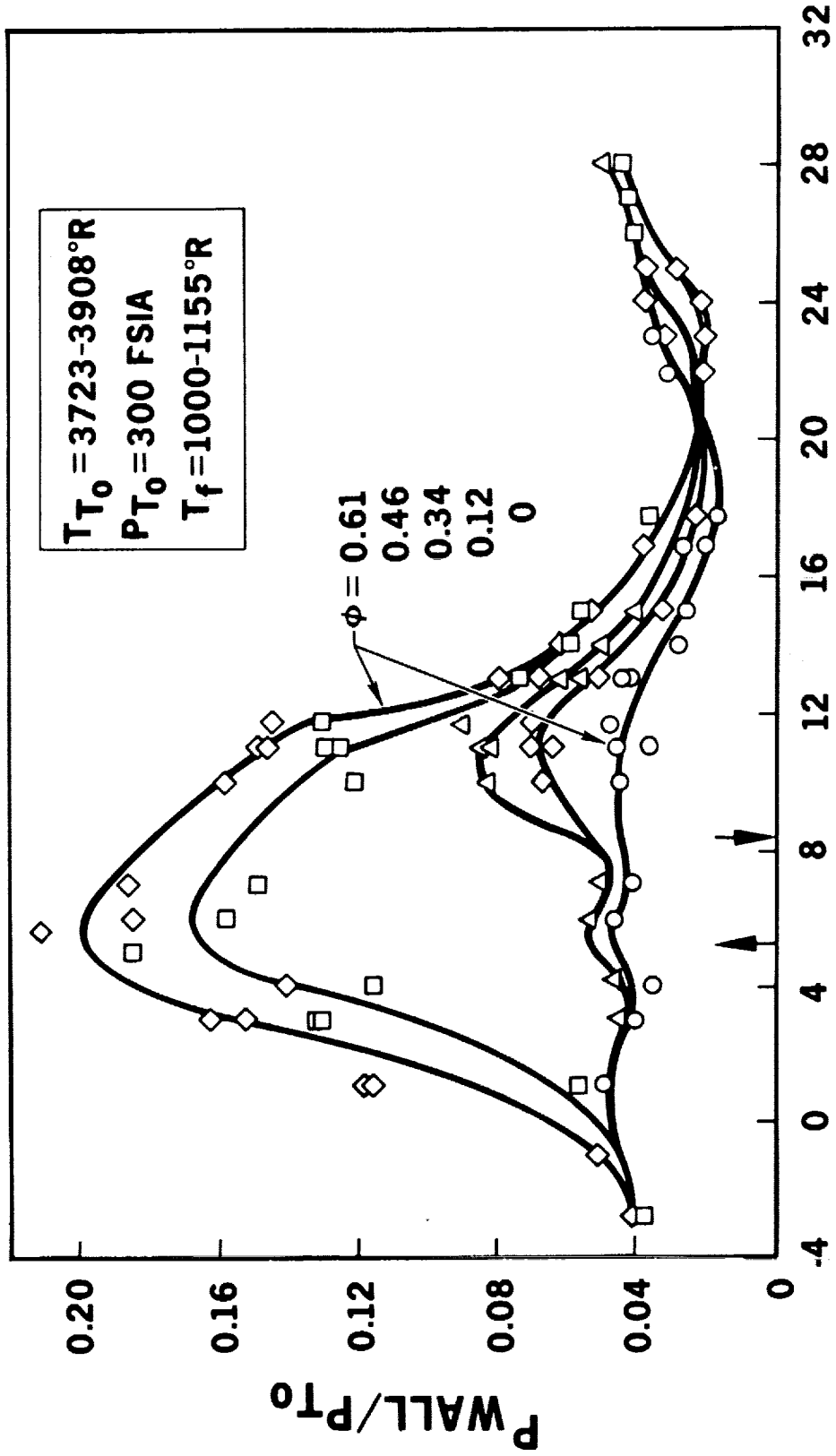

Figure 8.2-2. True-Scale Pressure Distribution (U)

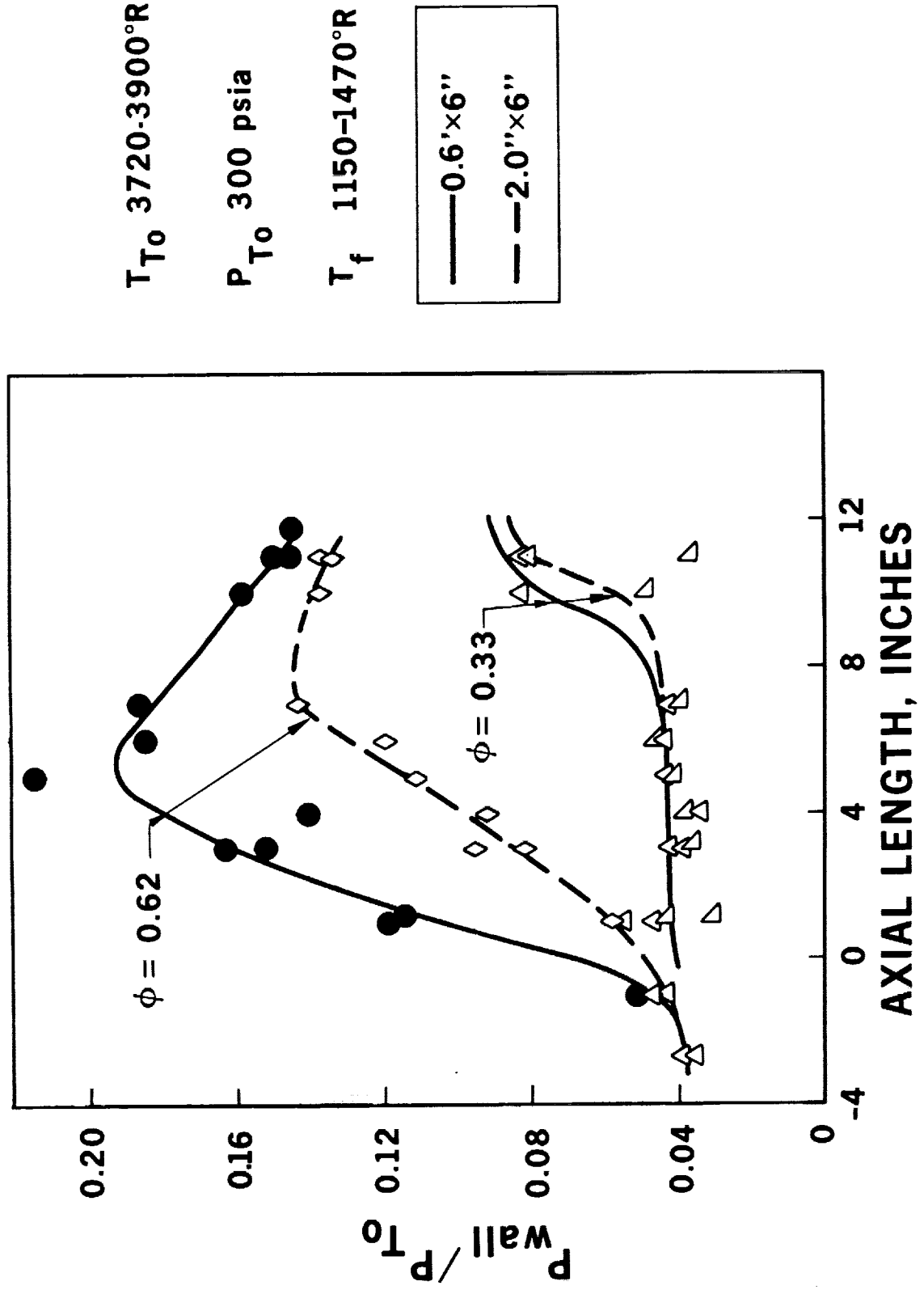

Figure 8.2-3. Combustor Scale Effect (U)

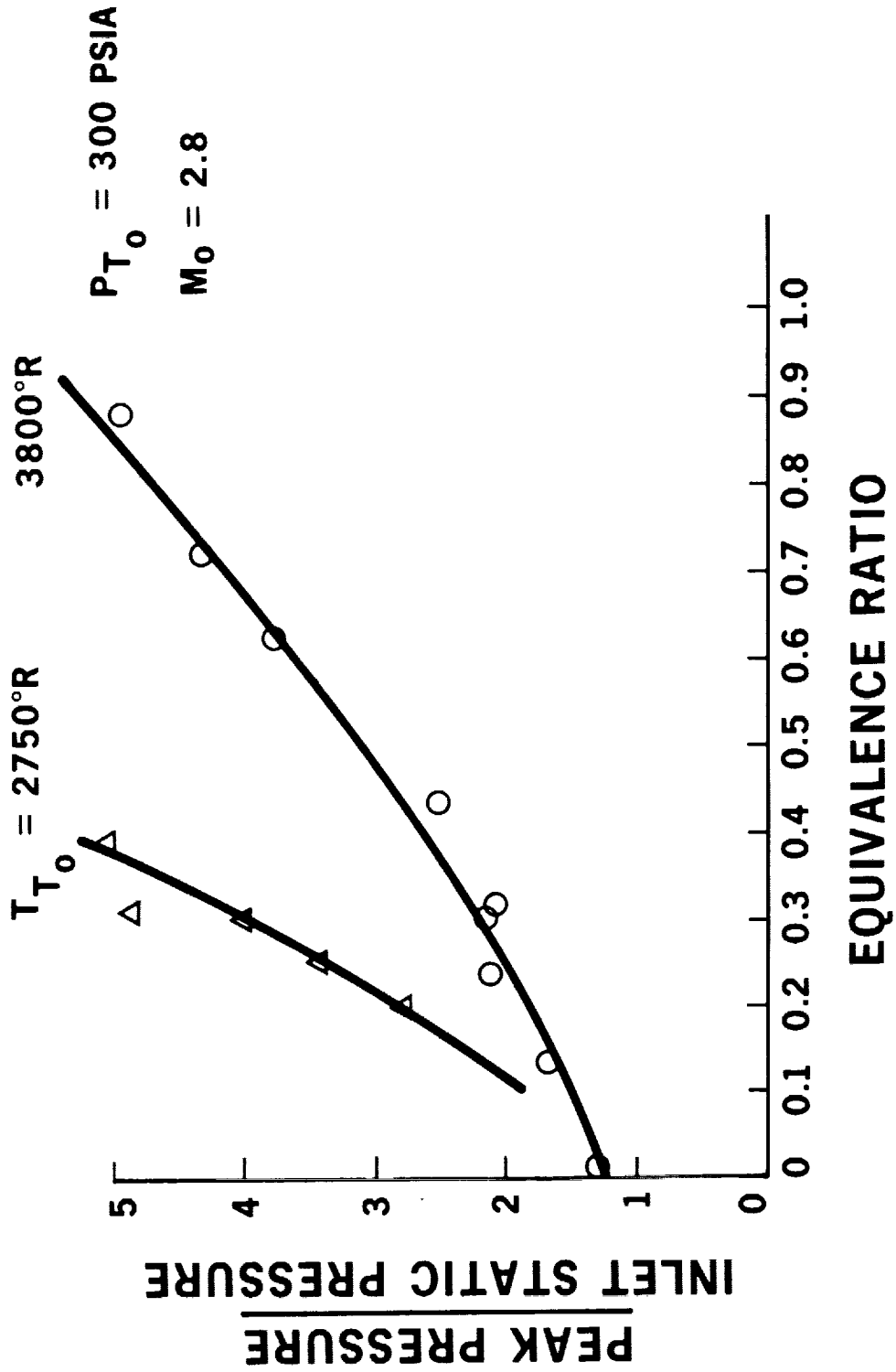

Figure 8.2-4. Peak Pressure Ratios - Two-Inch-High Constant-Area Section (U)

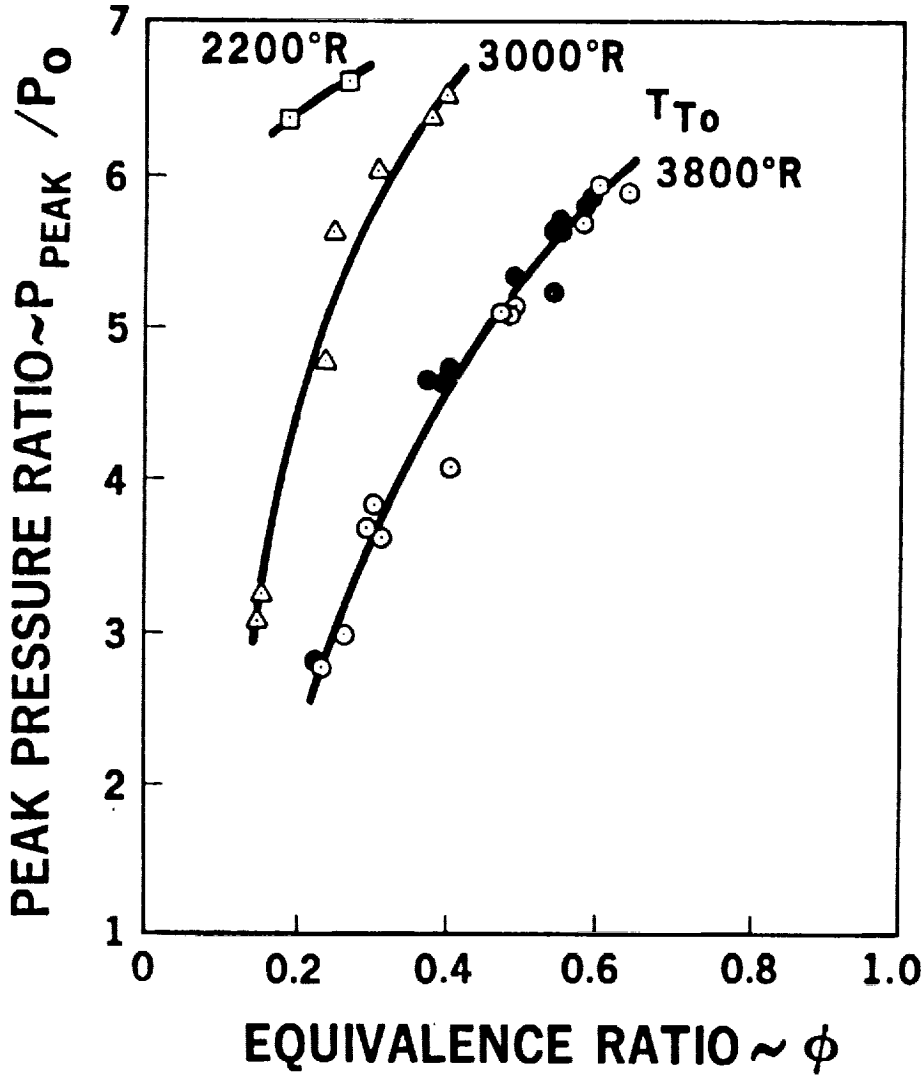

Figure 8.2-5. Peak Combustor Pressure Rise - 0.6-Inch-High Constant-Area Section (U)

TABLE 8.2-I

FUEL INJECTION INTO A CONSTANT AREA

Summary of Combustor Tests

Purpose	Injector Diameter	Injector Spacing	Injection Angle	Fuel Pressure	Equivalence Ratio
Effect of angular injection	Same	Same	Different	Different	Same
Effect of injector spacing	Same	Different	Same	Different	Same
Effect of injector diameter	Different	Different	Same	Same	Same
Effect of injector diameter	Different	Same	Same	Different	Same

Combustor Tests At Mach 7 Simulation

$T_{To} \approx 3800^{\circ}R$ $P_{To} \approx 300$ psia

Runs	Injector Diameter, in.	Number of Injectors	Injector Spacing, in.	S/D	Injection Angle, deg.
137 139 140 141 142	0.1	15	0.55	5.5	90
143 144	0.1	15	0.55	5.5	60
147	0.15	7	1.25	8.33	60
148	0.15	9	0.825	5.5	60
151	0.1	9	0.95	9.5	60

Note: Injectors Ia and Ic only.

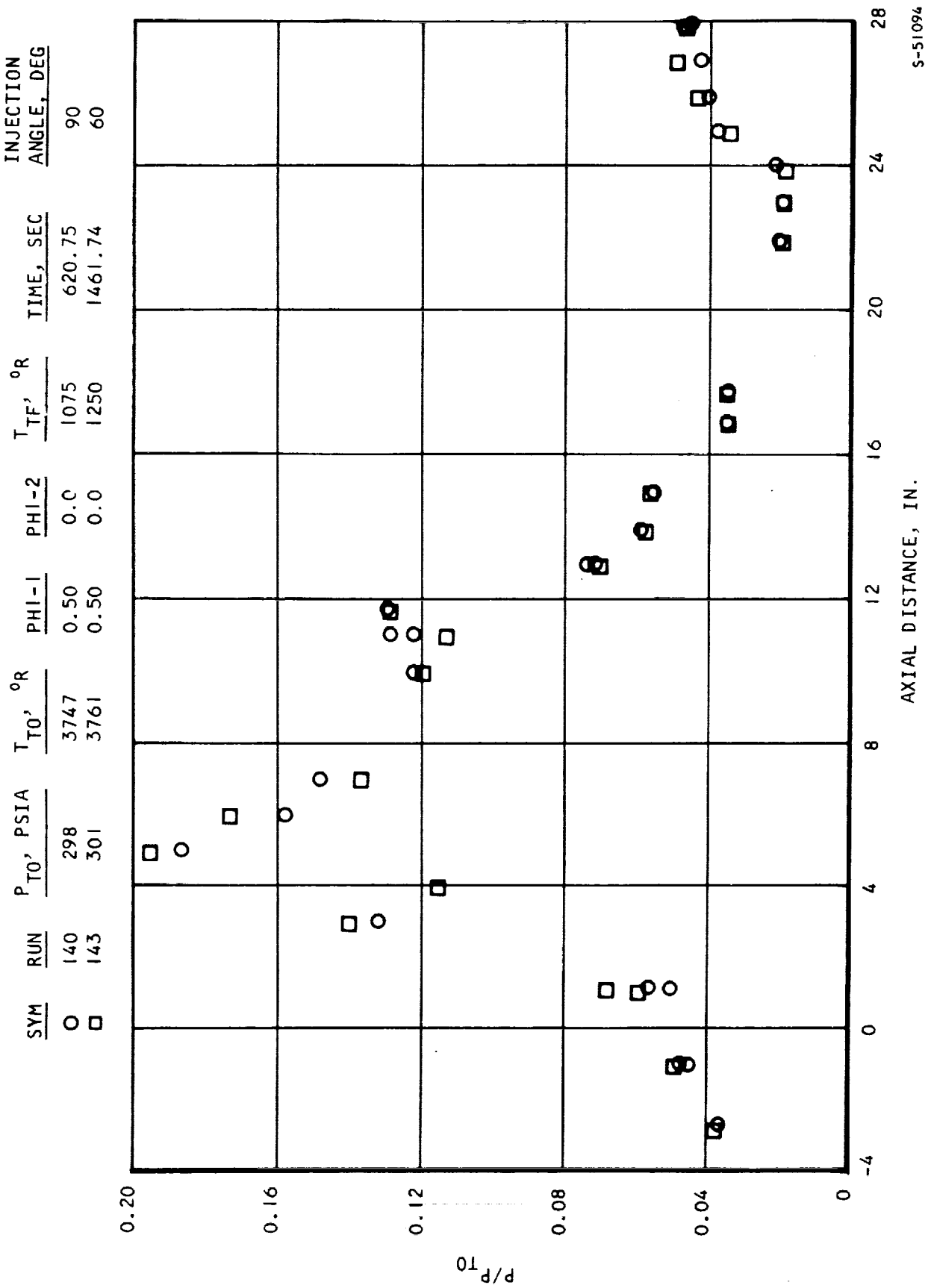

Figure 8.2-6. Static Pressure Distribution - Effect of Injection Angle (U)

The pressure distributions were not significantly different for these two cases. The angled-injection case seems to yield slightly higher static pressure rises than those from normal injection, particularly upstream of the first injector row. The fuel-manifold pressure for angled injection was 92 psia , as compared to 81 psia for normal injection, due to a lower discharge coefficient for angled injection holes.

The chemical efficiencies computed from the one-dimensional data reduction program indicated that efficiency for normal injection was slightly higher than that for angled injection, presumably due to higher jet penetration.

8.2.3 Effect of Orifice Spacing

The effects of orifice spacing at an equivalence ratio of 0.55 are shown in Figure 8.2-7. In this comparison, orifice diameter and injection angle were 0.1 in. and 60 deg, respectively. The pressure profile was higher for the injector with the larger hole spacing (Δ) up to Station 14. Downstream of this station, the pressures were similar. Because of the greater spacing between injector holes in run 151, the number of holes was less (9 vs 15). Consequently, the fuel pressure required for the same equivalence ratio was higher, which in turn resulted in a 20 percent increase in fuel jet penetration.

The chemical efficiency for the injector with the larger hole spacing is approximately 15 percent higher as shown in Figure 8.2-8. This is also supported by the wall temperature measurements, particularly at Station 13, where in run 151 the wall temperature was 685^0R as compared with 575^0R in run 143. Also, measured total heat losses in run 151 are 15 percent higher. It is apparent that penetration and spacing are interrelated in this case, and both appear to affect combustion.

8.2.4 Effect of Orifice Diameter - Same Spacing-to-Diameter Ratio

The effects of increasing orifice diameter at the same orifice spacing-to-diameter ratio are shown in Figures 8.2-9 and 8.2-10. Run 148 has nine injection holes, as compared with 15 for run 143. It is interesting to note that the efficiency at an equivalence ratio (ϕ) of 0.6 (d_j = 0.15 in.) is higher than at ϕ of 0.4 (d_j = 0.1 in.) up to Station 15. This agrees with wall static pressures and temperatures. However, downstream of Station 15 the efficiency of the smaller-diameter injector is higher. The smaller injector diameter, with inherently better mixing characteristics, appears to have more efficient combustion even though the fuel penetration for these two cases is the same. Thus, it appears that the chemical efficiency cannot be dictated by penetration alone.

8.2.5 Effect of Orifice Diameter - Same Manifold Pressure

The two runs in Figure 8.2-11 were originally intended to determine the effect of injector diameter at the same manifold pressure and equivalence ratio, varying injector spacing and number of holes. The injector with the larger hole spacing (7 holes) appears to have a higher chemical efficiency than

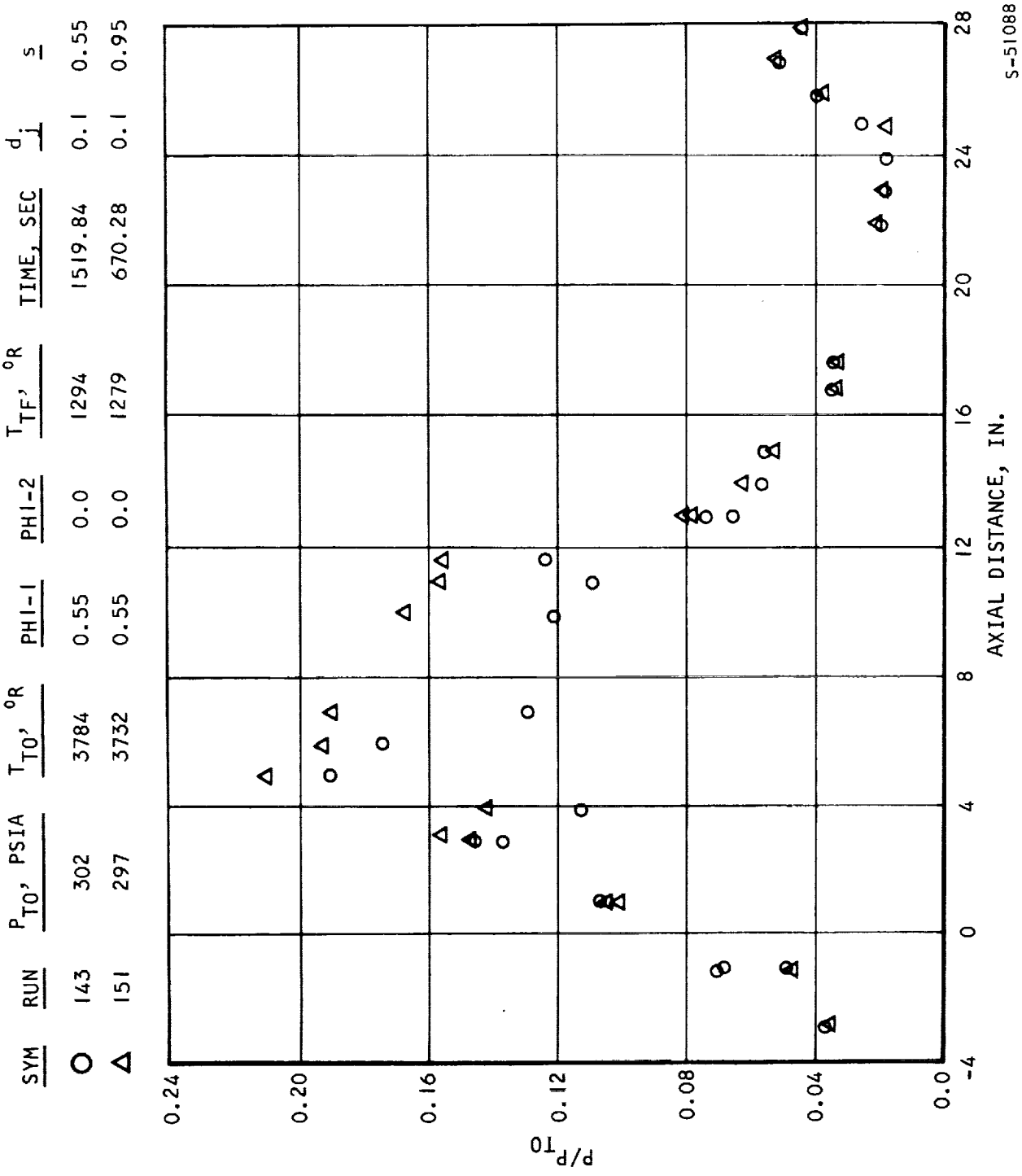

Figure 8.2-7. Static Pressure Distribution - Effect of Spacing, Same Equivalence Ratio (U)

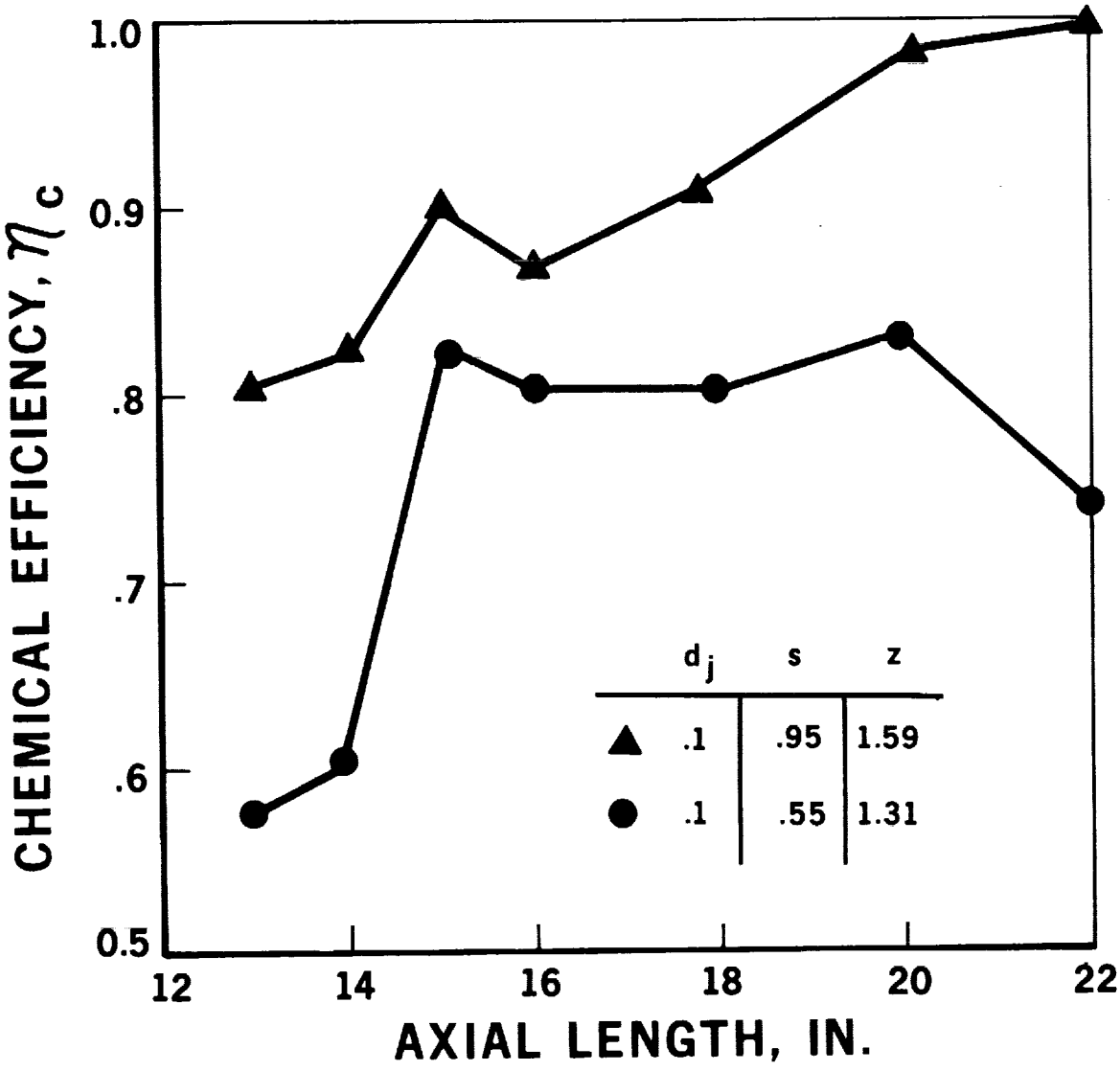

Figure 8.2-8. Effect of Hole Spacing (N_c) (U)

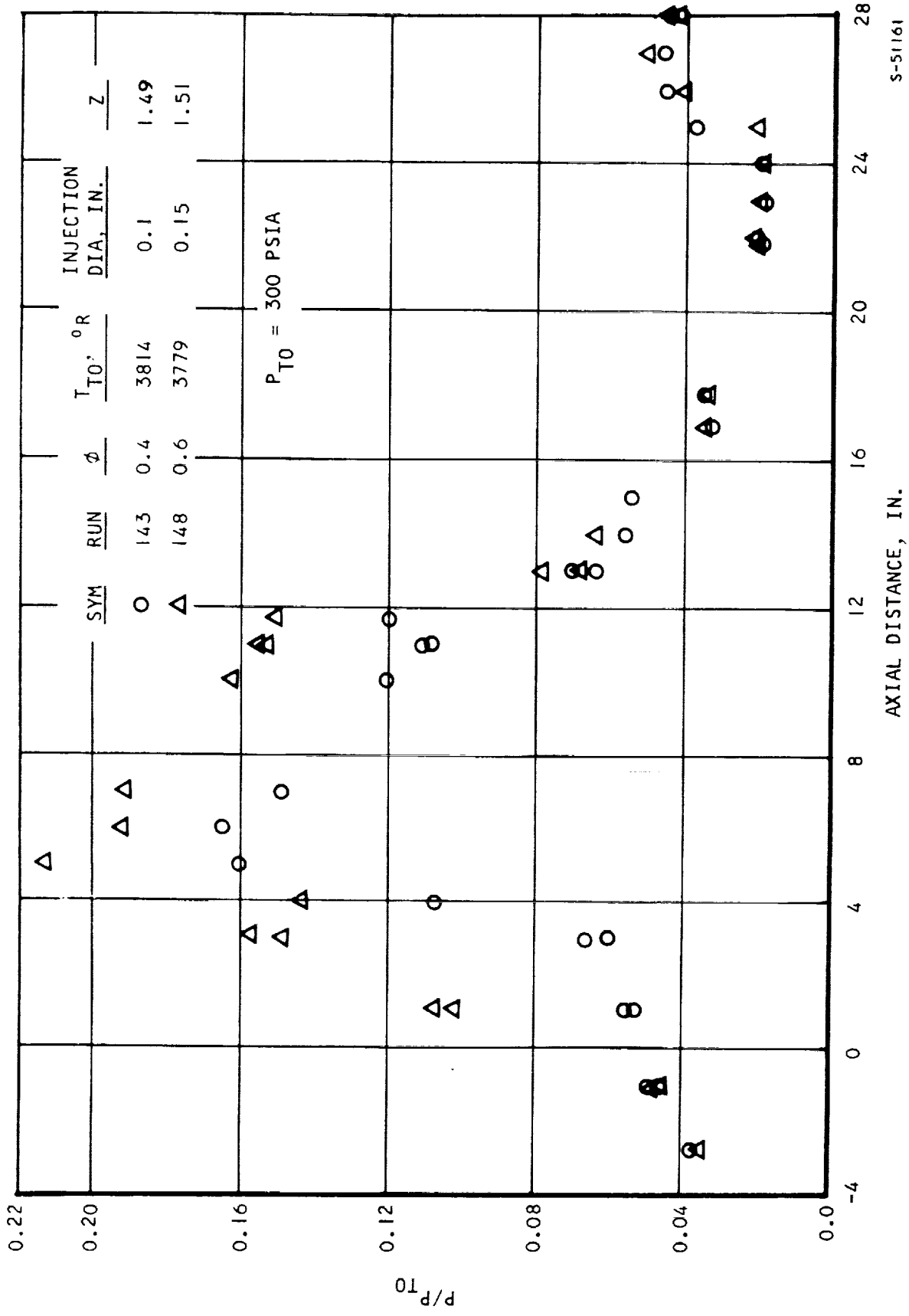

Figure 8.2-9. Static Pressure Distribution (U)

Z	SYM	RUN	Ø	T_{TO}, °R	D	S/D	⊀	T_{TF}, °R	P_{TF}, PSIA
1.49	●	143	0.40	3814	0.1	5.5	60°	1131	75.2
1.51	▲	148	0.60	3779	0.15	5.5	60°	1297	87.0

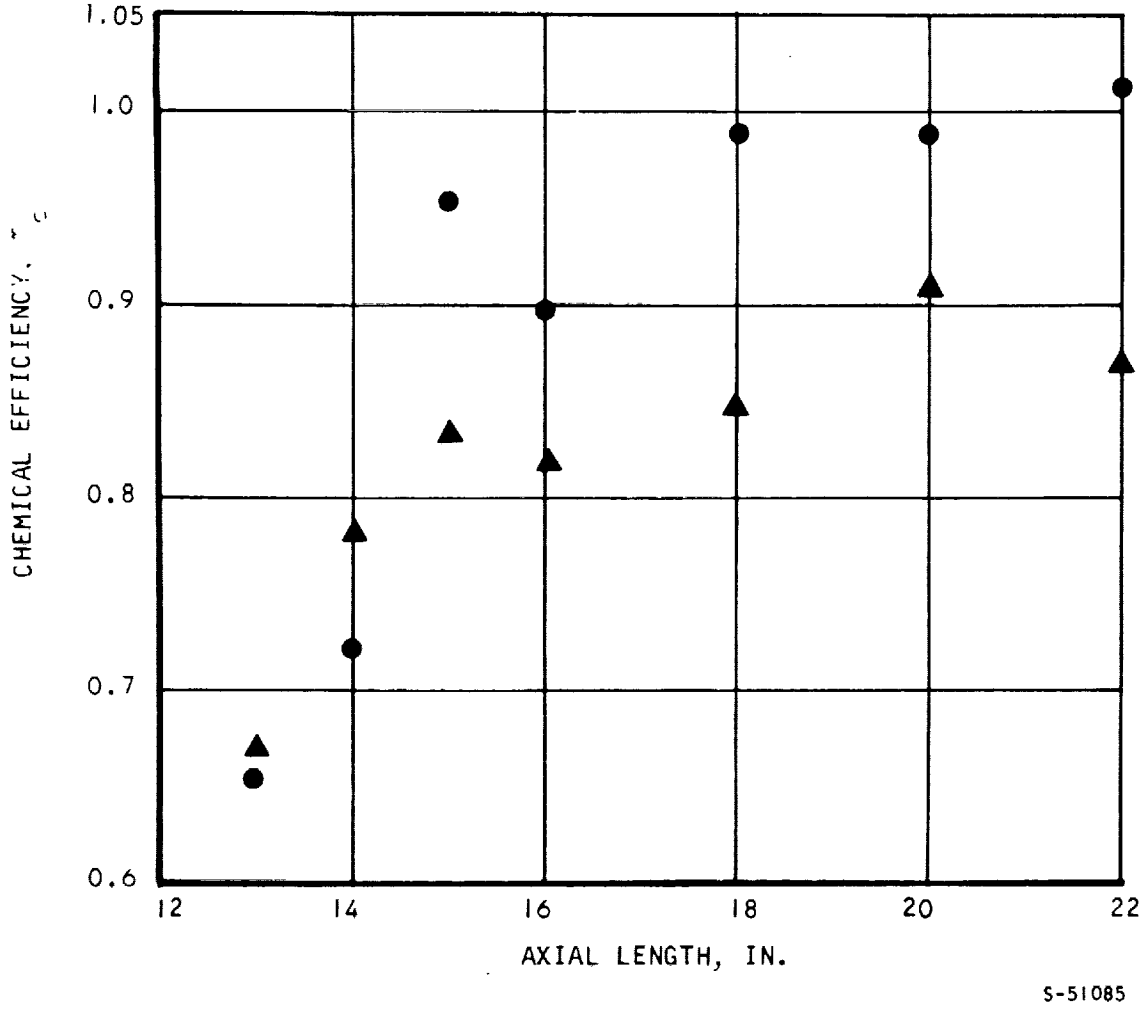

Figure 8.2-10. Combustor Chemical Efficiency (U)

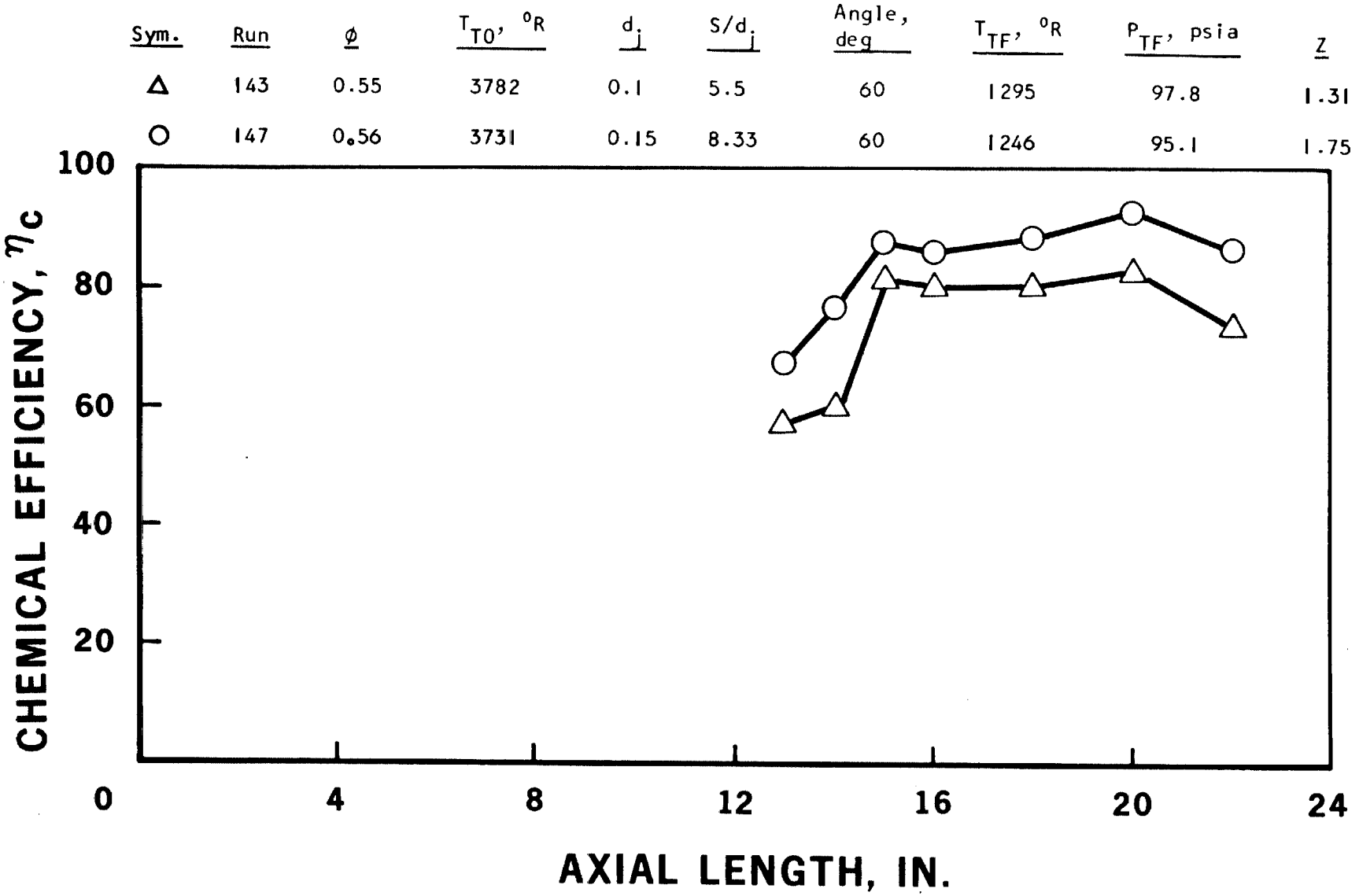

Figure 8.2-11. Effect of Injector Diameter - Same Manifold Pressure (U)

the injector with smaller hole spacing (15 holes). It can be shown that the jet penetration is a function of number of holes; the fewer the holes, the higher the penetration. Therefore, in this case the effect of larger spacing in run 147 was more than compensated for by the higher jet penetration (34 percent higher than run 143), resulting in a higher chemical efficiency.

For fuel injection into the constant-area section, high chemical efficiencies were obtained about 10 to 12 inches downstream of the injection point for most of the injector configurations tested. Also, all injector configurations tested gave similar pressure profiles with their characteristic peak pressure occurring in the constant-area duct.

8.2.6 Effect of Constant-Area Length

The importance of combustor length was illustrated by injecting fuel into the constant-area section at two different locations. An equivalence ratio of 0.29 was injected from location 1a, 6.6 in. before the beginning of a 1-deg-37-min divergence. The pressure distribution (Figure 8.2-12) shows the characteristic peak pressure occurring near injection. However, when the same amount of fuel was injected from 1b, 4.3 in. before the divergence, the measured peak pressure was about 20 percent lower than previously. It is possible that this may not be the true peak pressure due to lack of instrumentation near location 1b. Also, the pressures in the diverging section were slightly lower with injection from 1b for a length of about five inches from the exit of the constant-area section. Thus, this 2.3-in.-shorter constant-area section, prior to injection, affected combustion.

8.2.7 Fuel Injection Into a Diverging Section

When fuel was injected into a diverging area, quite different results were obtained. Initial tests were conducted in the true-scale combustor (0.6 in. high at the nozzle exit), which had a divergence angle of 2 deg 42 min. A typical result is shown in Figure 8.2-13 which indicates no pressure rise at a high equivalence ratio. The slight change in pressure profile is due to the separation point being moved downstream. In this run fuel was injected from injector stations 2e and 2f only. The injector holes at 2e and 2f were interdigitized, with two holes at 2e and three holes at 2f. The holes were 0.25 in. in diameter, spaced 1.5 in. apart. When fuel was injected into the duct using the same injector geometry at the same location, but with a divergence angle of 1 deg 37 min, a noticeable difference in pressure rise occurred (Figure 8.2-14).

The divergence angle did not appear to affect combustion when fuel was injected only into the first-stage constant-area section (for the two values of divergence tested). Comparing pressures (Figure 8.2-15) at a combustor divergence of 1 deg 37 min with those at a divergence of 2 deg 42 min (Figure 8.2-2) shows that divergence did not significantly change the pressure distribution in the constant-area section. Apparently, the short constant-area section prior to divergence provided enough stay time to get combustion going.

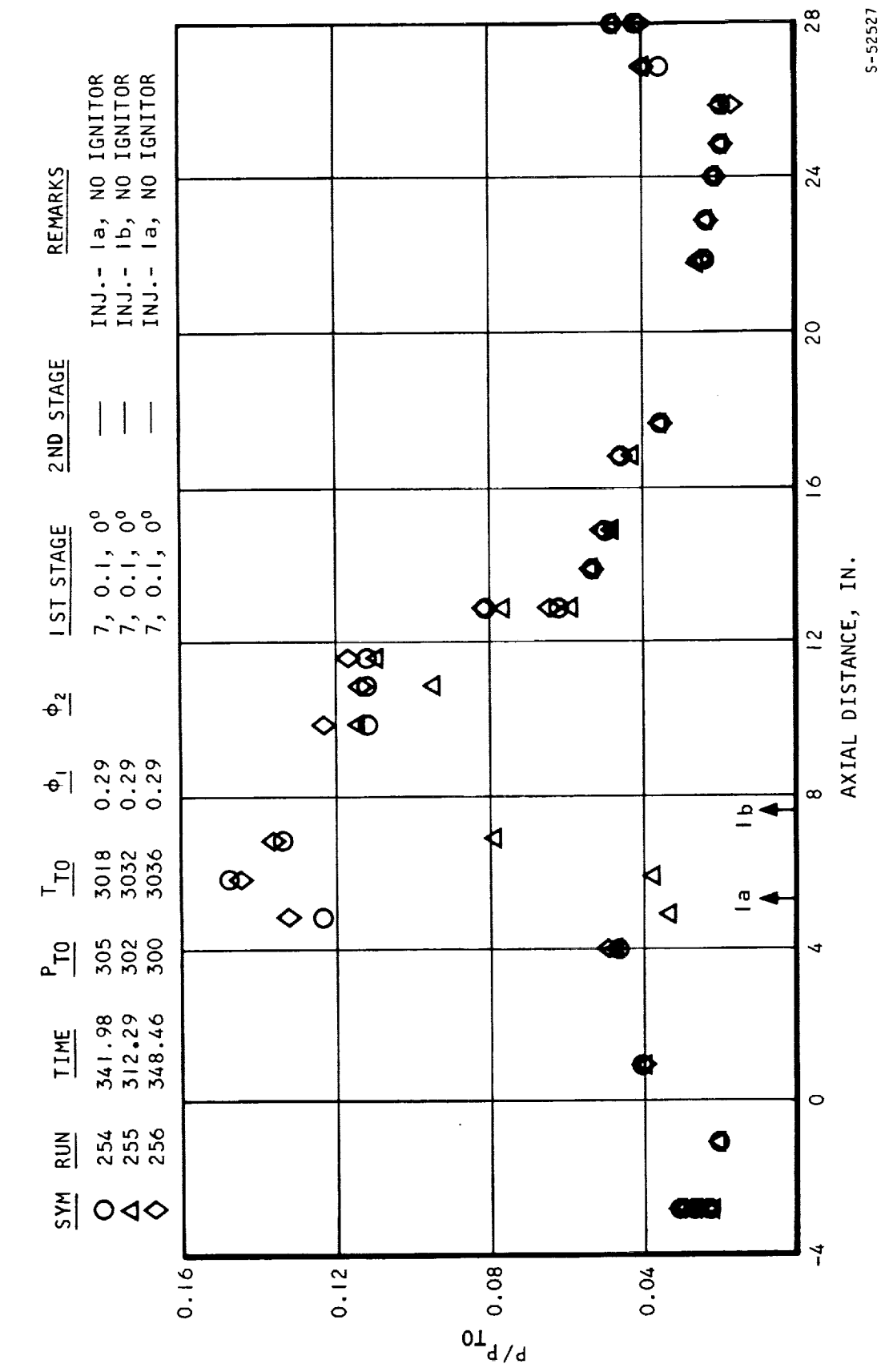

Figure 8.2-12. Static Pressure Distribution (U)

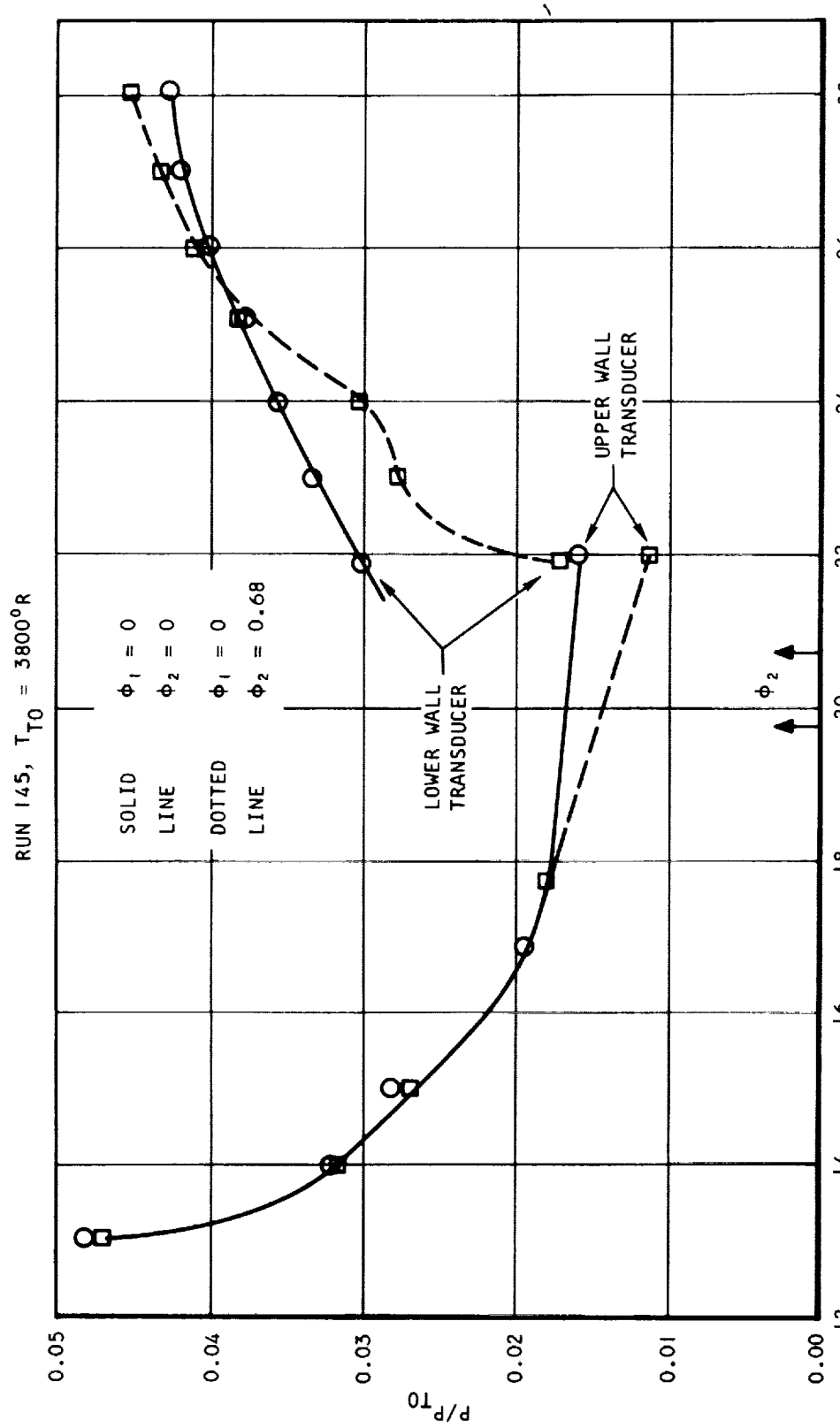

Figure 8.2-13. Pressure Profile for Second-Stage Injection Only (U)

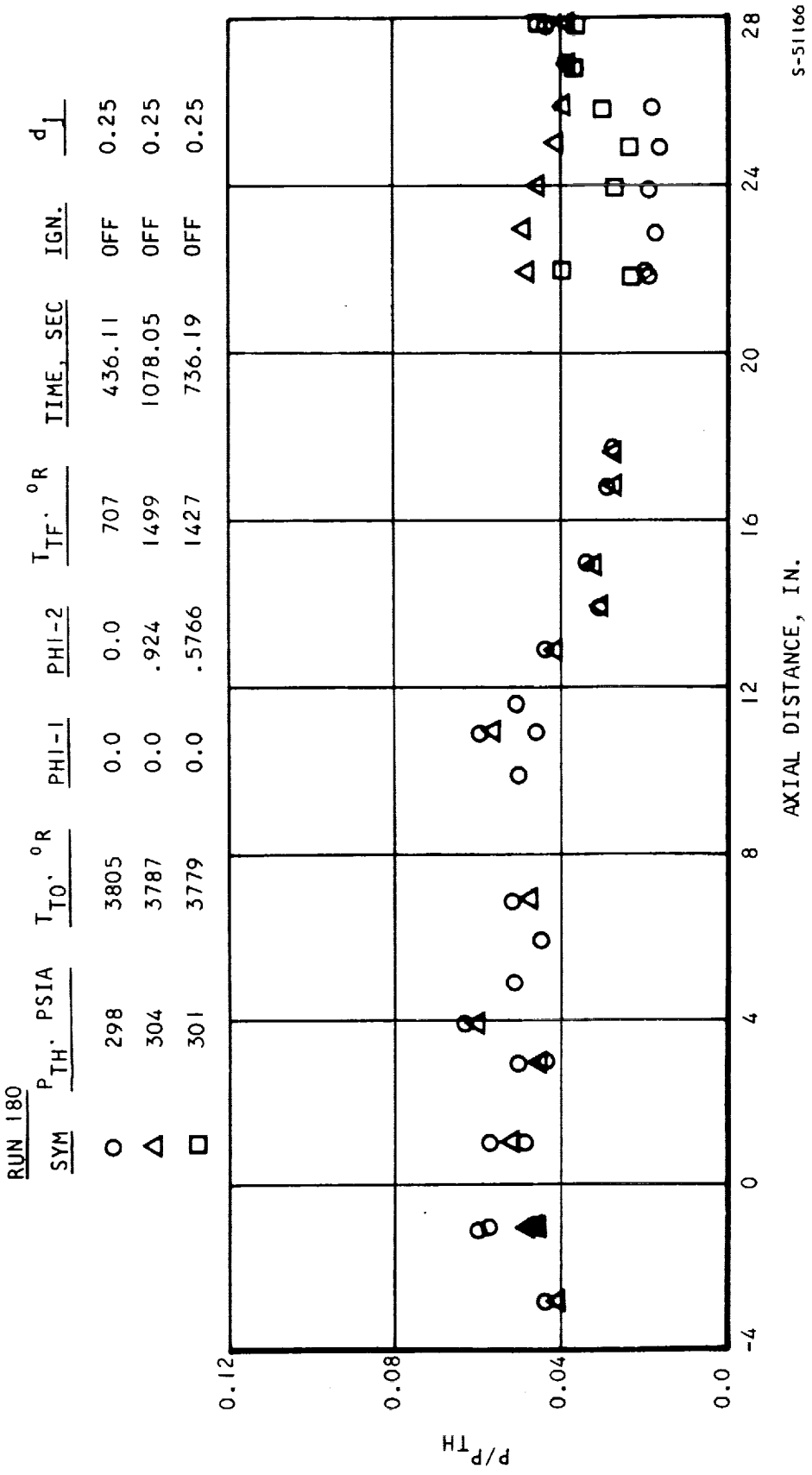

Figure 8.2-14. Static Pressure Distributions, Run 180 - Second Stage Only (U)

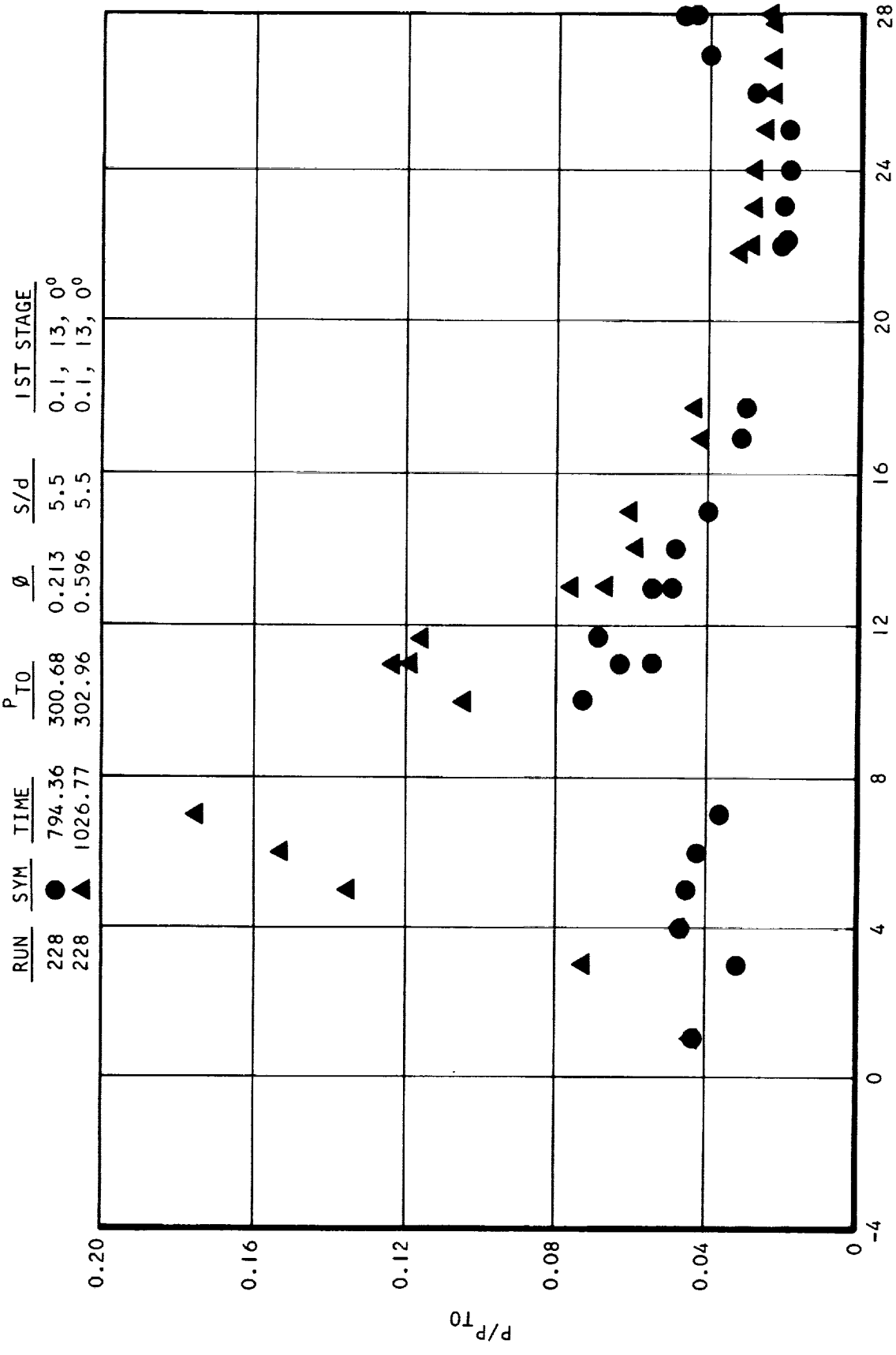

Figure 8.2-15. Static Pressure Distribution at Lower Second-Stage Divergence (U)

When fuel was injected only into a diverging section at a lower air total temperature (Figure 8.2-16), a larger pressure rise was observed than previously (Figure 8.2-14). The peak pressure ratio at both total temperatures (3000^0 and 3800^0R)--that is, the peak pressure divided by the undisturbed pressure ahead of the injectors and prior to combustion--was significantly lower than that obtained with fuel injection into the constant-area section. Also, chemical efficiencies were much lower with fuel injection into the diverging-area section.

Typical values for chemical efficiency in the diverging section were 40 percent to 55 percent as compared with 80 percent to 100 percent when fuel was injected only into the constant-area section. A representative plot of efficiency versus combustor length is shown in Figure 8.2-17 for the two types of fuel injection. The efficiency is much lower with injection into the diverging-area section.

8.3 TWO-STAGE INJECTION

At flight Mach numbers below 8 it becomes difficult to add heat near the inlet throat in a single stage due to thermal choking and inlet unstarting problems. Therefore, two-stage injection is required. This type of injection was simulated in the two-dimensional combustor test rig with part of the fuel injected into the constant-area section and part into the diverging-area section. In general, low efficiencies were obtained with two-stage injection as was the case with injection only into the diverging section. The various parameters which were investigated are shown below:

(a) Injector diameter and spacing

(b) Injection angle - Downstream and upstream injection

(c) One-sided injection

(d) Supersonic injection

(e) Oxygen-rich mixtures

(f) Air total temperature

As was the case for injection only into the diverging duct, there was an insignificant pressure rise with two-stage injection in a 2 deg 42 min divergent combustor. Results in Figure 8.3-1 actually show a pressure decrease even at fuel-rich equivalence ratios.

A typical two-stage pressure distribution for the duct of smaller divergence is shown in Figure 8.3-2 with a divergence angle of 1 deg 37 min.

The injectors for the first stage were located at 1b and 1c with 0.1-in.-dia holes. There were seven holes at injector 1b spaced 0.6 in. apart, and six holes at injector 1c with the same spacing but staggered with respect to the holes in 1b. The second stage also had two rows of orifices (2e and 2f). There were three 0.16-in.-dia holes at 2e spaced 1.8 in. apart, and two holes at 1f with the same diameter and spacing but staggered with respect to the holes at 2e. The fuel injected from the first stage varied from an equivalence ratio of 0.2 to 0.3, and from 0.4 to 1.4 at the second stage. The pressure

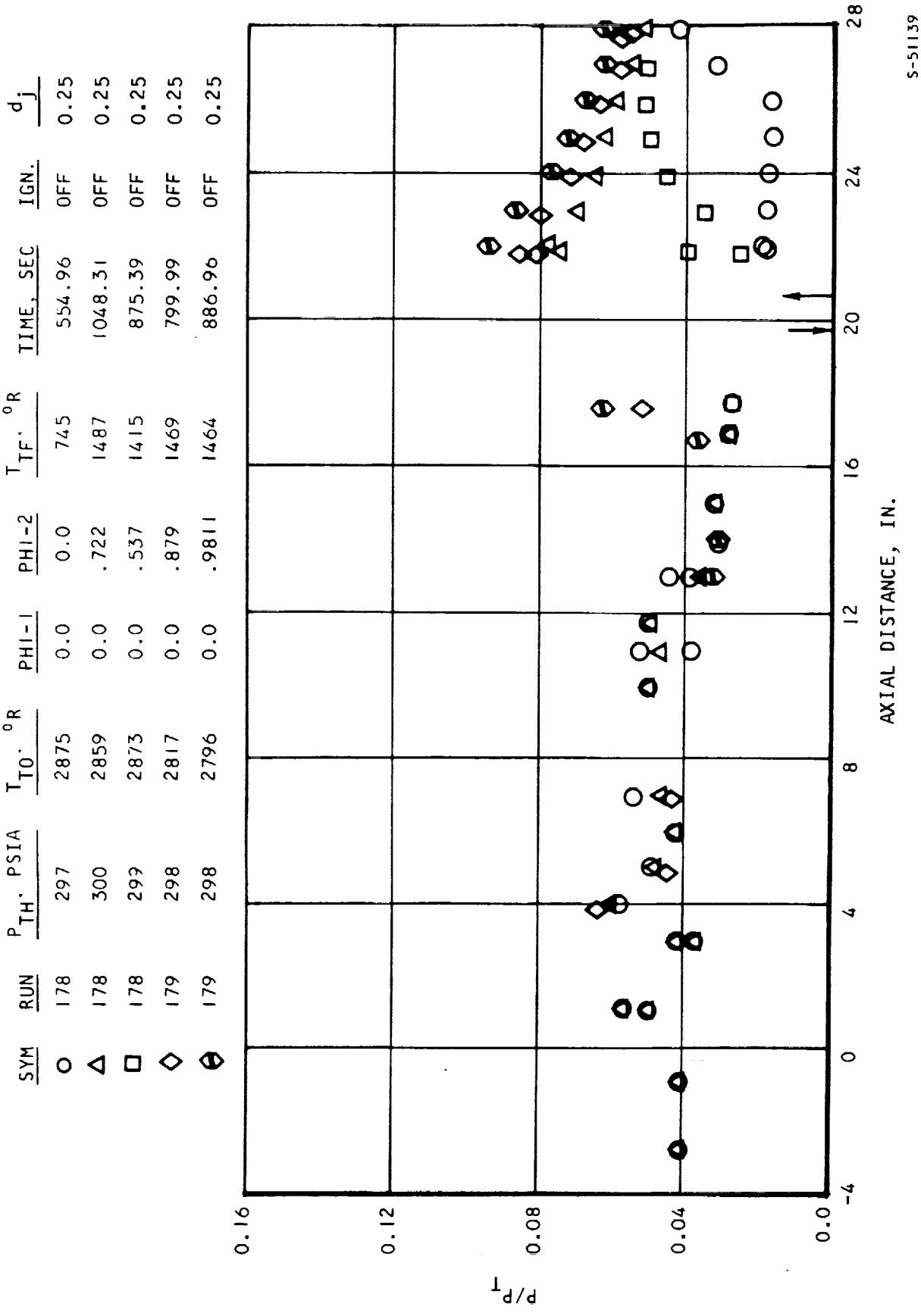

Figure 8.2-16. Static Pressure Distributions - Second Stage Only (U)

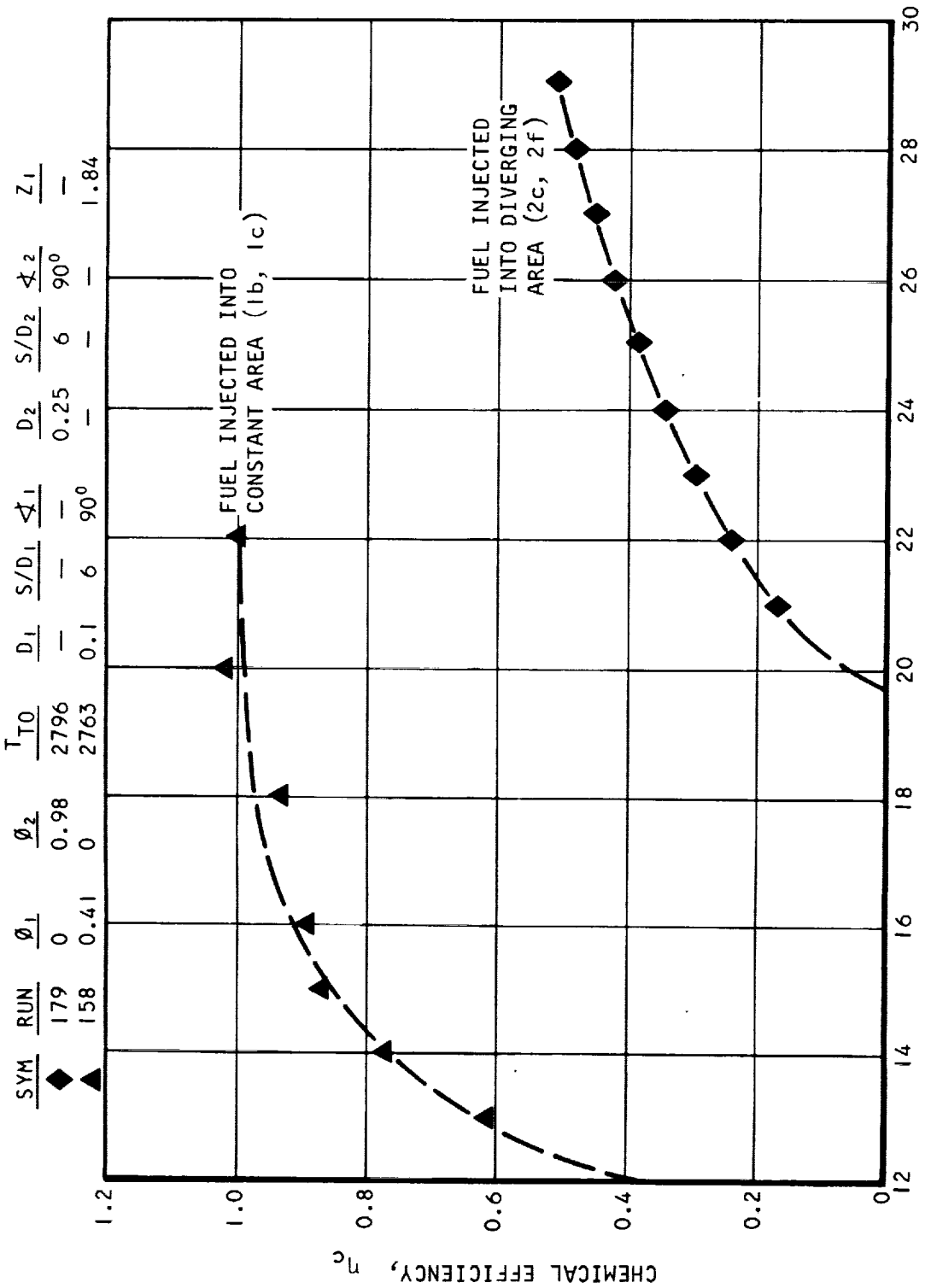

Figure 8.2-17. Combustor Chemical Efficiency (U)

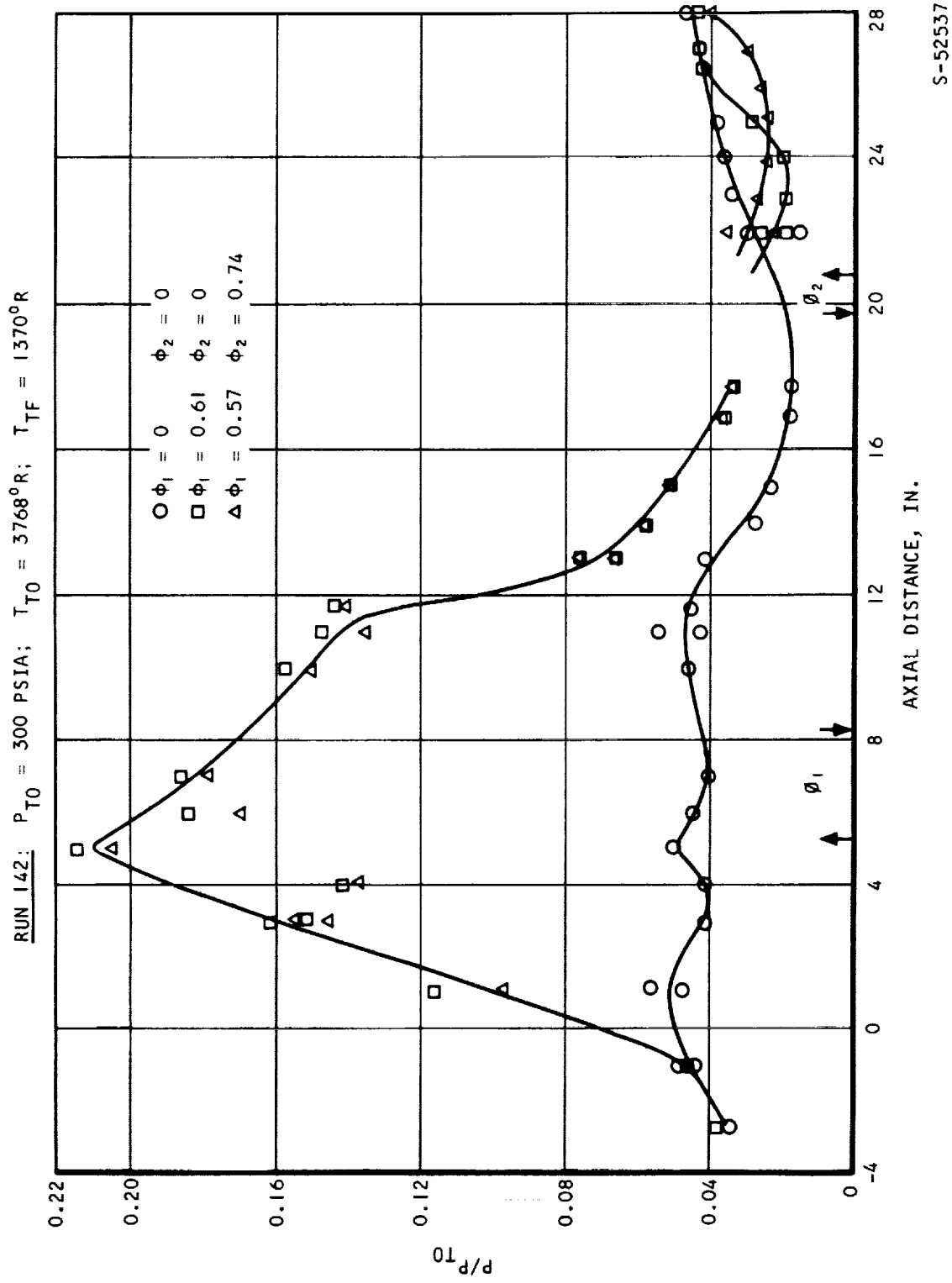

Figure 8.3-1. Second-Stage Injection (U)

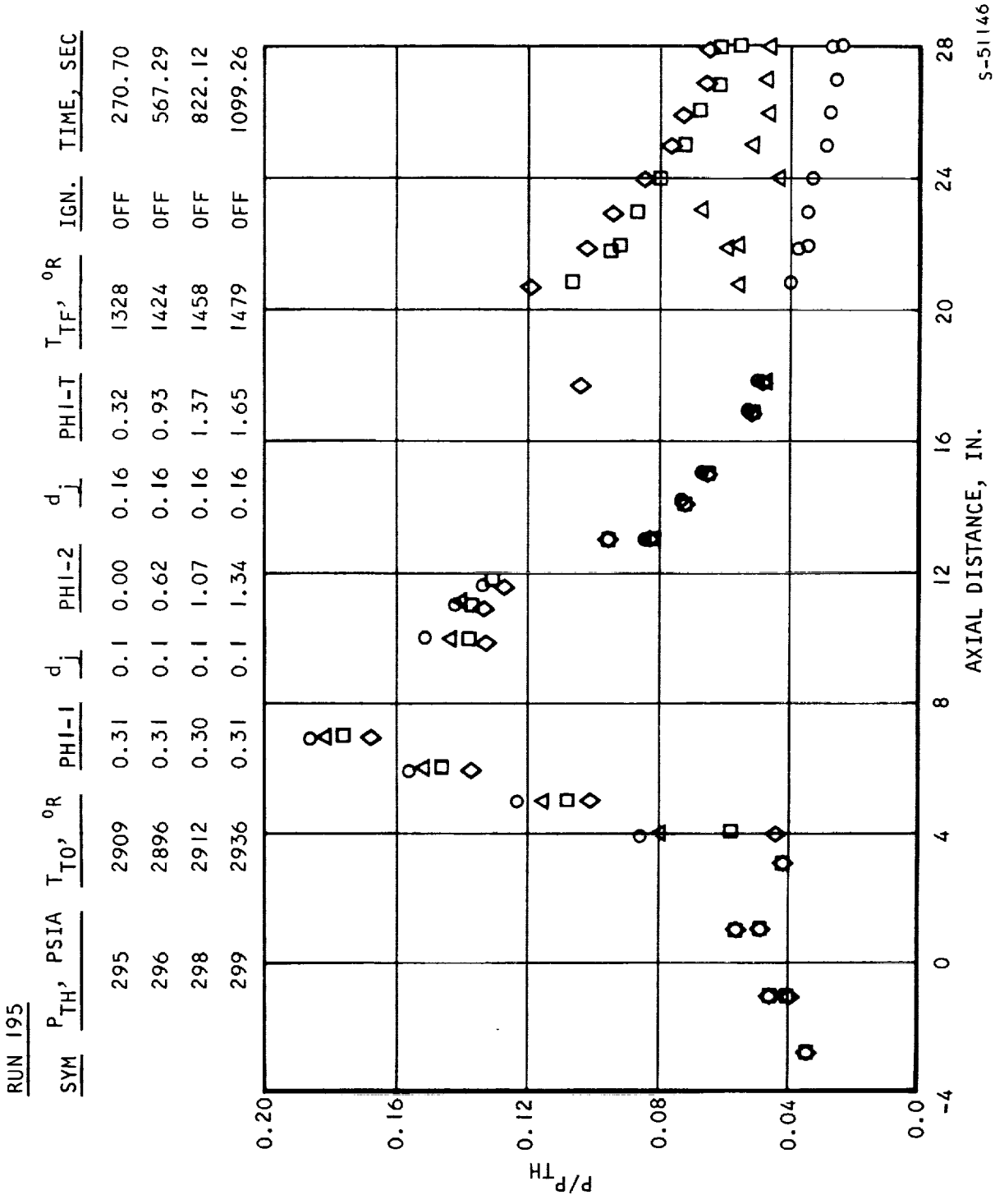

Figure 8.3-2. Static Pressure Distributions, Run 195 - Two-Stage, Various ϕ_2's (U)

rise from the second stage was significantly lower than that from the first stage, and the pressure disturbance from the second stage appears to be limited to the region downstream of the second fuel injector except at very high equivalence ratios. The interaction between stages is small as compared to that between the inlet flow and combusted flow. Again, the chemical efficiency for the second stage was very low. No noticeable change in pressure occurred at the second stage when the equivalence ratio in the first stage was decreased to 0.2, as indicated in Figure 8.3-3. As previously, the chemical efficiencies (Figure 8.3-4) fell in the 50-70 percent range.

Because of the low chemical efficiency in the second stage, a number of exploratory tests were conducted using various injector geometries to improve the penetration and mixing qualities of the second stage.

8.3.1 Effects of Upstream Angle Injection

In Reference 8-2 angled injection pointing upstream was shown to have better penetration than normal injection. Pressure distributions of normal, 30 deg and 45 deg upstream angle injections are shown in Figure 8.3-5. The injector diameters in both stages were 0.1 in. spaced 0.6 in. apart. Injector rows 1b and 2e had 7 orifices, rows 1c and 2f had 6 orifices. It appeared that angled injection had higher static pressures downstream of the second stage. Therefore, the chemical efficiency was slightly higher, but with no significant improvement.

The second-stage equivalence ratio was increased to 1.35 (Figure 8.3-6) with still no significant improvement in chemical efficiency. The range of efficiencies was still low--in the 50-70 percent range as shown in Figure 8.3-7 (increasing the diameter in the secone stage gave lower pressures than the 0.1-in.-dia injector when both were pointed 45 deg upstream).

8.3.2 Effects of Supersonic Injection

Supersonic injectors, with an exit Mach number of two, were designed to improve the jet penetration. The supersonic injectors consisted of three and two holes staggered with respect to each other. The throat diameter for these injectors was 0.16 in. with 6-deg half-cone angles. The calculated jet penetration was 20 percent higher than that from normal injection.

The pressure distribution for this injector (Figure 8.3-8) was even lower than that from normal sonic injection. This indicated that the low chemical efficiency for the second stage may not have been caused by low penetration.

8.3.3 One-Sided Injection

In an attempt to increase chemical efficiency, fuel was injected normally only from the bottom row of injectors in the first stage (1b), and only from the top row of injectors in the second stage (2e). Row 1b had seven 0.1-in.-dia injectors and row 2e had three 0.16-in.-dia injectors. It was reasoned that with this type of injection, the second-stage fuel would not be injected into combustion gases. In this manner fuel would not have to penetrate through a

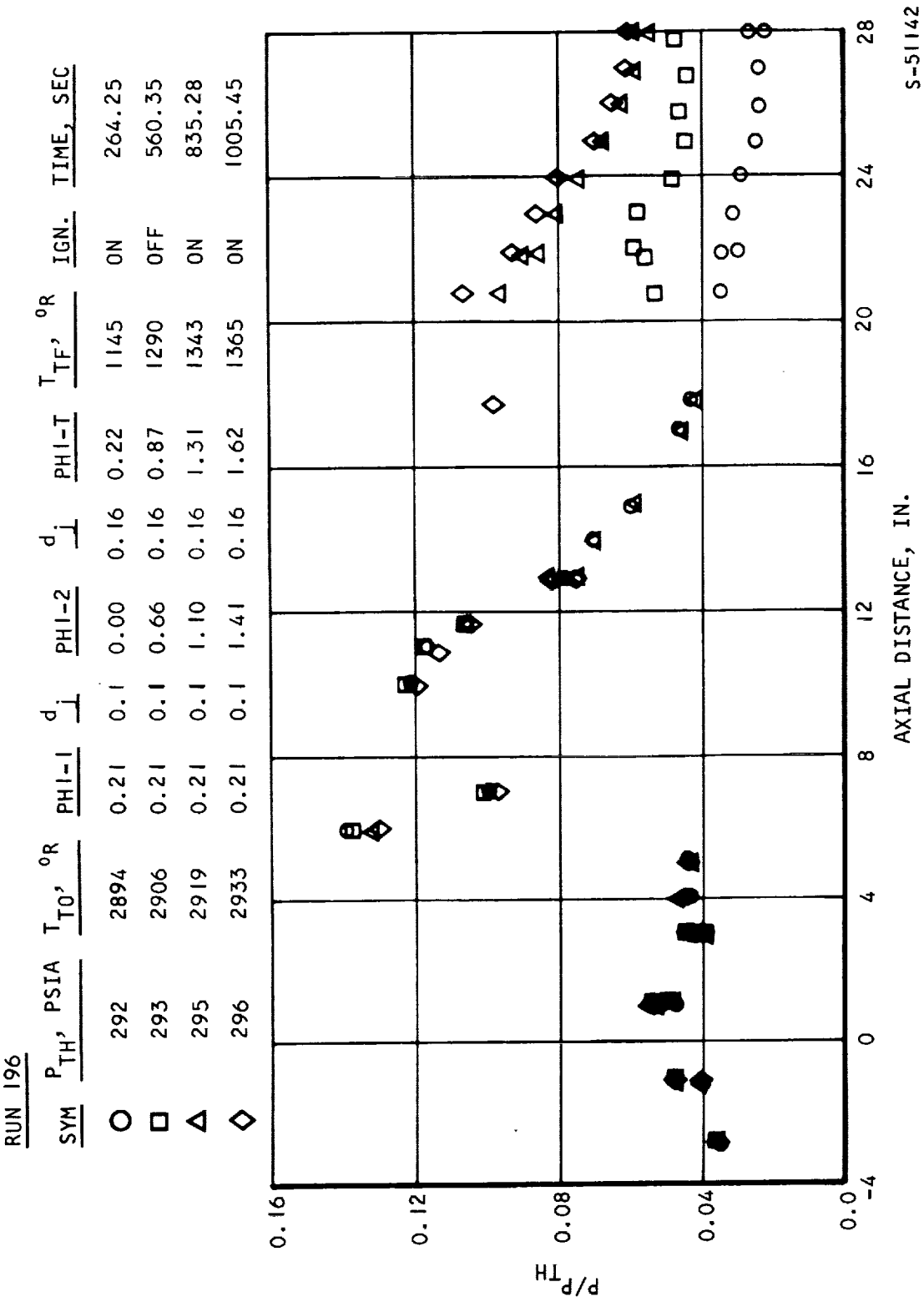

Figure 8.3-3. Static Pressure Distributions, Run 196 - Two-Stage, Various ϕ_2's (U)

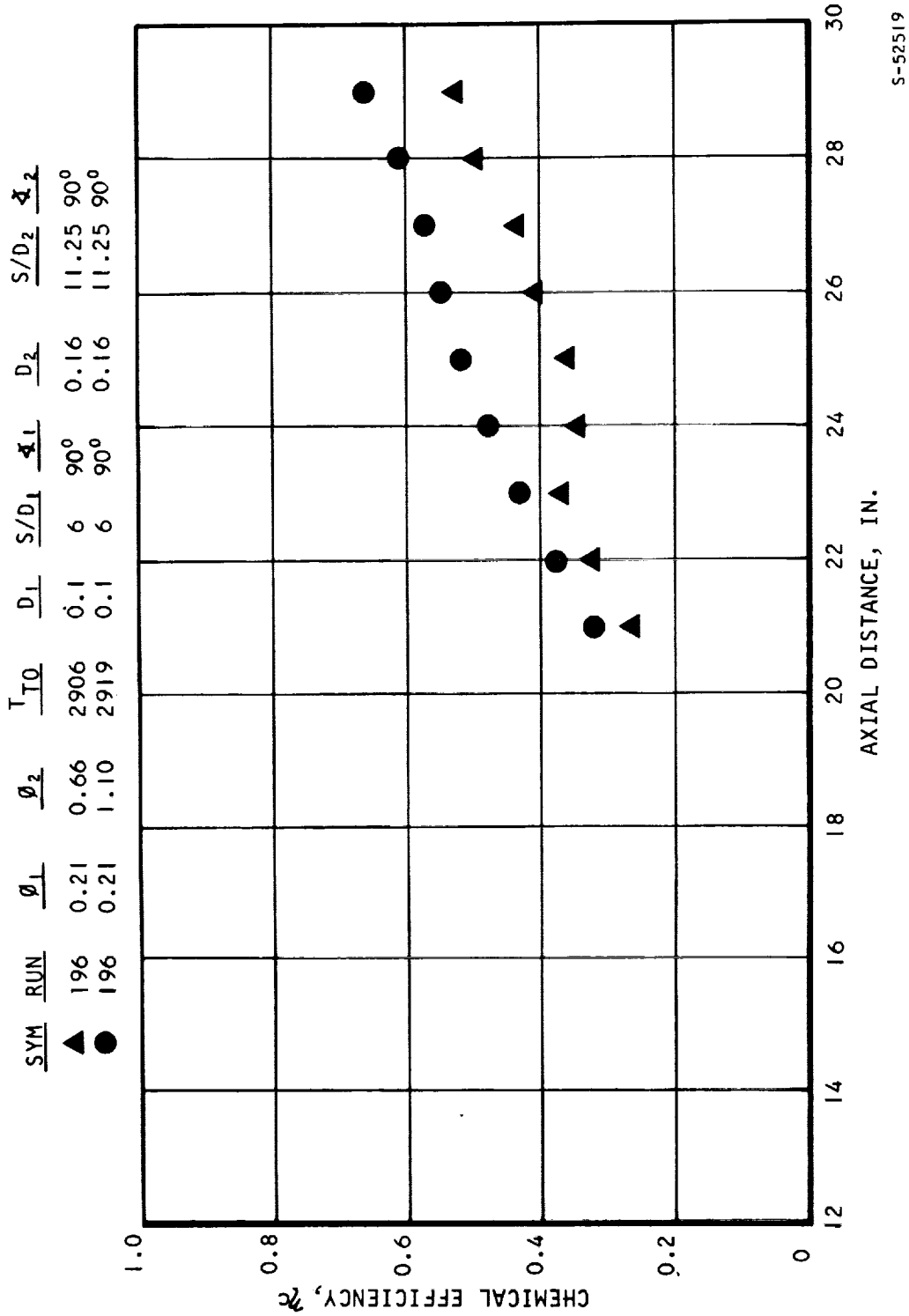

Figure 8.3-4. Combustor Chemical Efficiency (U)

Sym.	P_{TO}, psia	T_{TO}, °R	ϕ_1	d_j	ϕ_2	d_j	Run	Time
⊙	300.0	2946	0.21	0.1	0.68	0.1	218	630.68
△	300.7	2946	0.21	0.1	0.66	0.1	217	620.8
⊡	299.2	2950	0.22	0.1	0.69	0.1	216	610.76

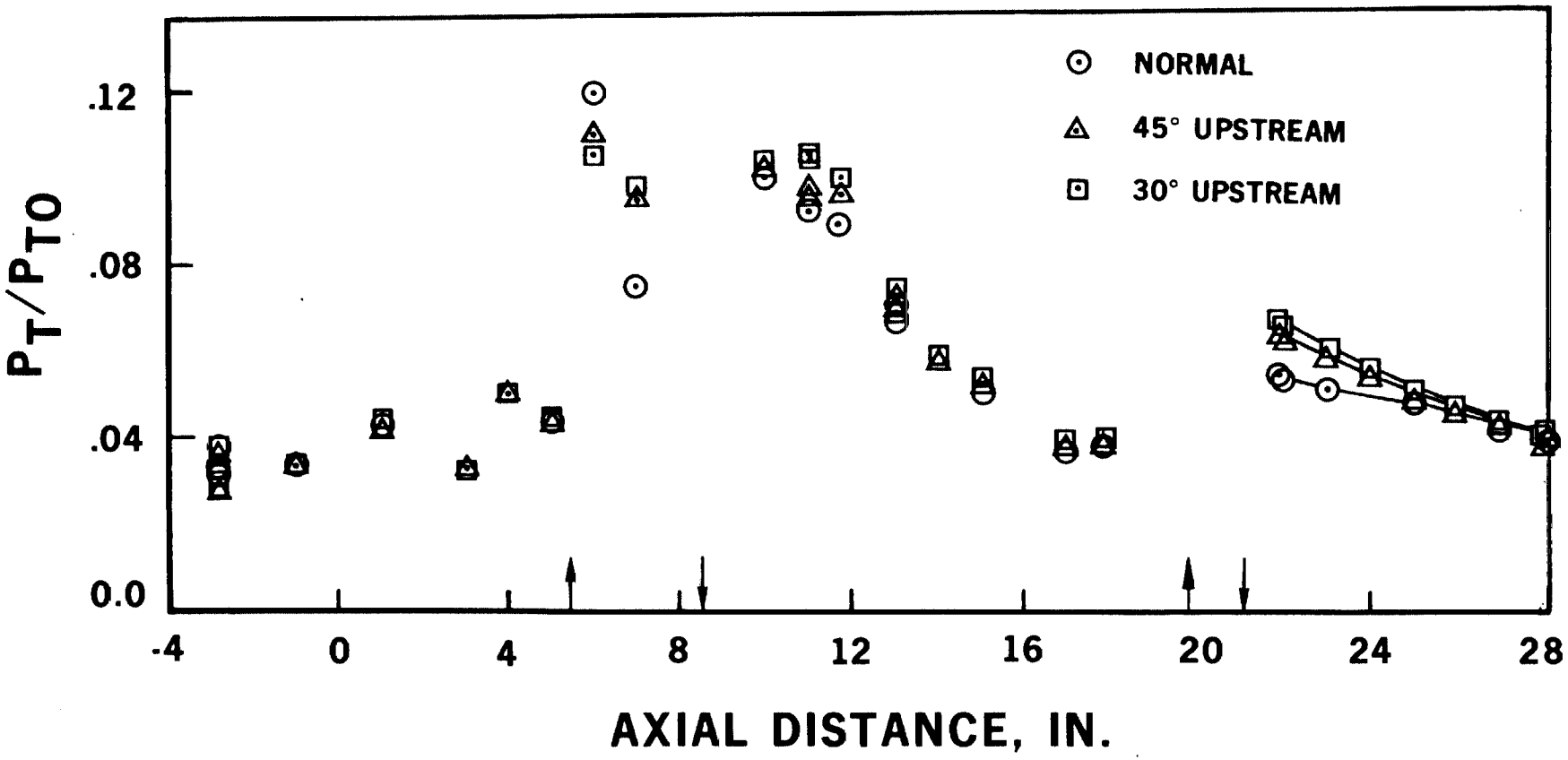

Figure 8.3-5. Effects of Upstream Angle Injection (U)

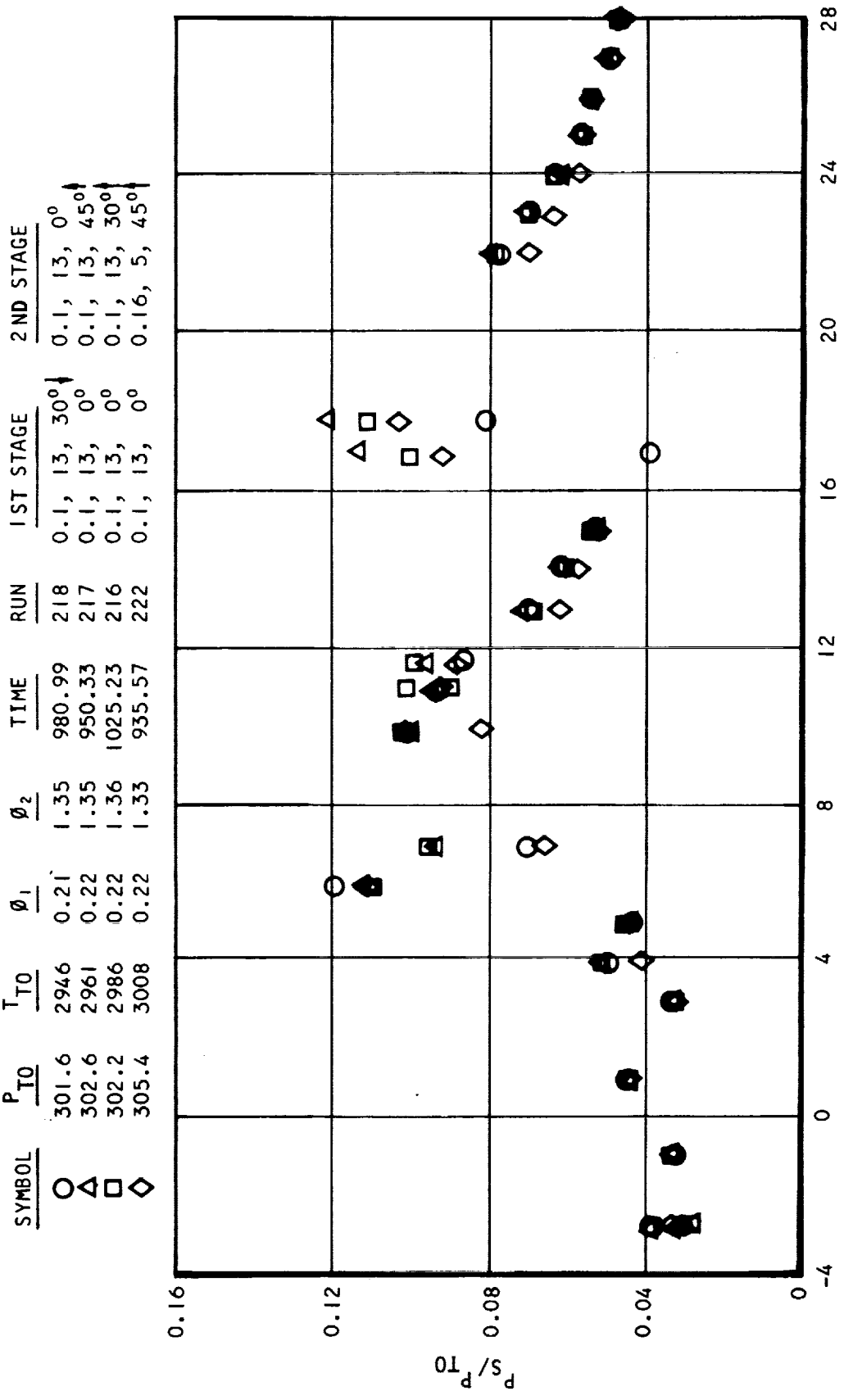

Figure 8.3-6. Effect of Angle Injection (U)

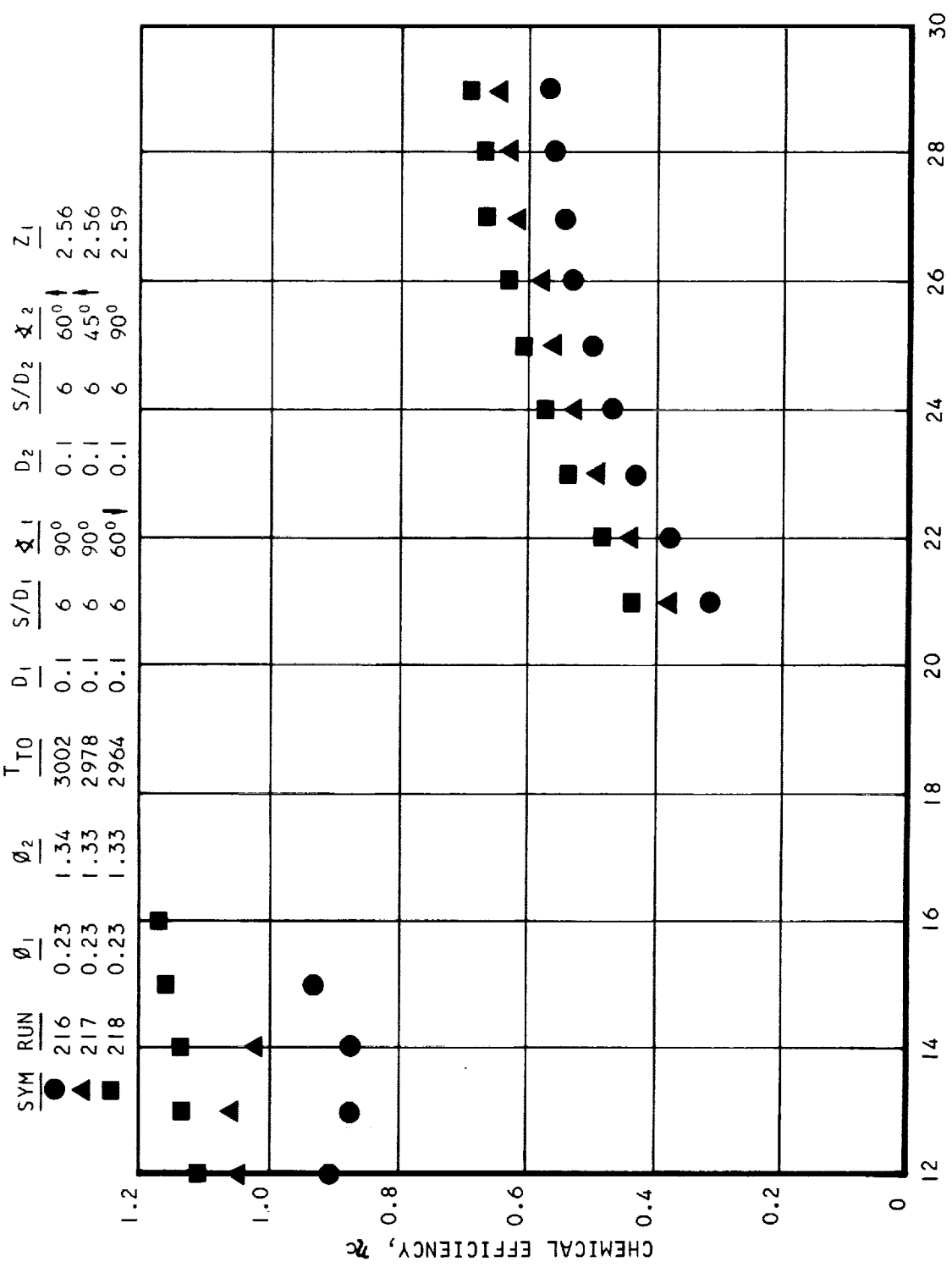

Figure 8.3-7. Combustor Chemical Efficiency (U)

Sym.	Run	P_{TO}, psia	T_{TO}, °R	ϕ_1	ϕ_2	T_{TF}, °R	Time	Second Inj.
○	217	300	2947	0.22	0.67	1252	525.58	45° upstream
▲	221	298	3028	0.22	0.66	1180	596 39	Supersonic
□	218	299	2939	0.21	0.67	1240	556.64	Normal

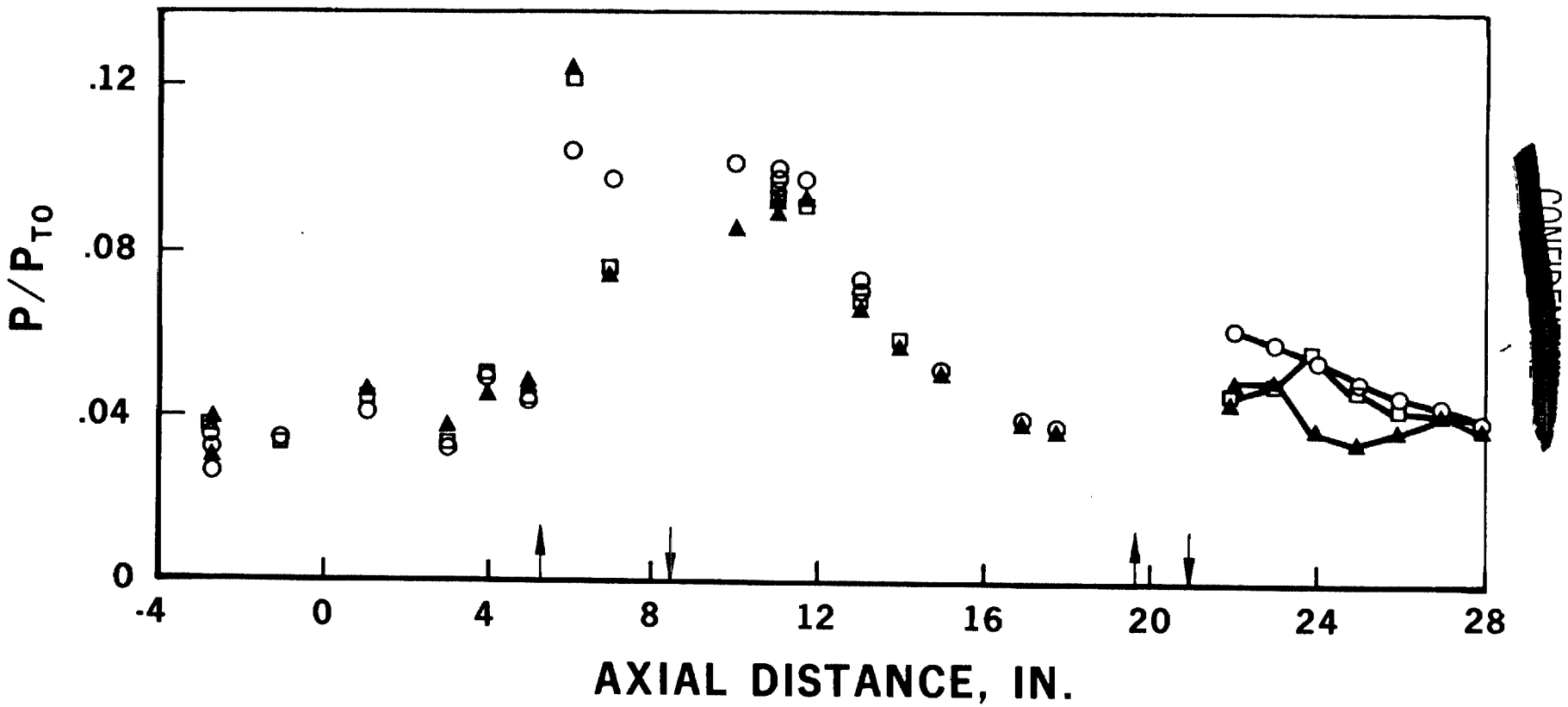

Figure 8.3-8. Effects of Supersonic Injection (U)

combusted region in order to come in contact with oxygen. The results in Figure 8.3-9 show that measured wall static pressures were actually lower than with normal injection from both sides in each stage.

The increased penetration, using fewer injectors, gave results similar to those obtained using supersonic injectors. Both of these tests indicated that low penetration may not have been the cause of poor pressure rises.

8.3.4 Added Orifices

The fuel injectors could not be placed across the full 6-in. width. Fuel could only be injected across a 4-in. width, leaving a 1-in. gap at each side. It was felt that lack of fuel in these sides could be the cause of the low efficiencies. To remedy this situation, two fuel injectors were added to fill this open area at the sides as shown below:

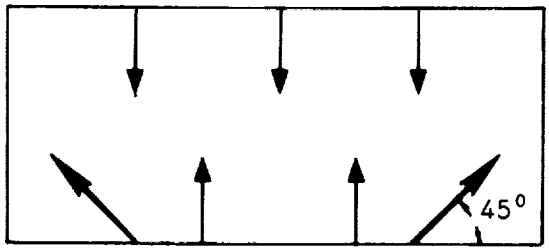

The results using these additional orifices (Figure 8.3-10) indicated no improvement.

8.3.5 Other Exploratory Tests

An igniter was added at the 2e injection location to insure positive ignition. The injector configuration was changed to one-sided injection, with six 0.1-in. dia injectors in row 1b and seven 0.1-in. dia injectors, pointing 45^0 upstream in row 2e. The pressure distribution is shown in Figure 8.3-11. The first stage pressures are low indicating that the fuel injected in the constant-area section did not burn properly, because the igniter was not used in the first stage. However, it appears that the fuel from the first stage started to burn about three inches upstream of the igniter. The pressures downstream of station 21 were unchanged, however, from run 217, which didn't have a downstream igniter. The resulting chemical efficiency (Figure 8.3-12) shows no improvement and is of the same order of magnitude as that from other exploratory tests.

Runs with a higher inlet total temperature and with an oxygen-rich mixture (with 50 percent excess oxygen in the vitiation heater) were made. These runs should have respectively reduced the reaction time and promoted better mixing. However, the second stage static pressure rise was not improved.

Thus after these exploratory runs, the reason for the low chemical efficiency was still not certain. It was not resolved by these tests whether the low combustor efficiency was due to insufficient residence time, poor mixing,

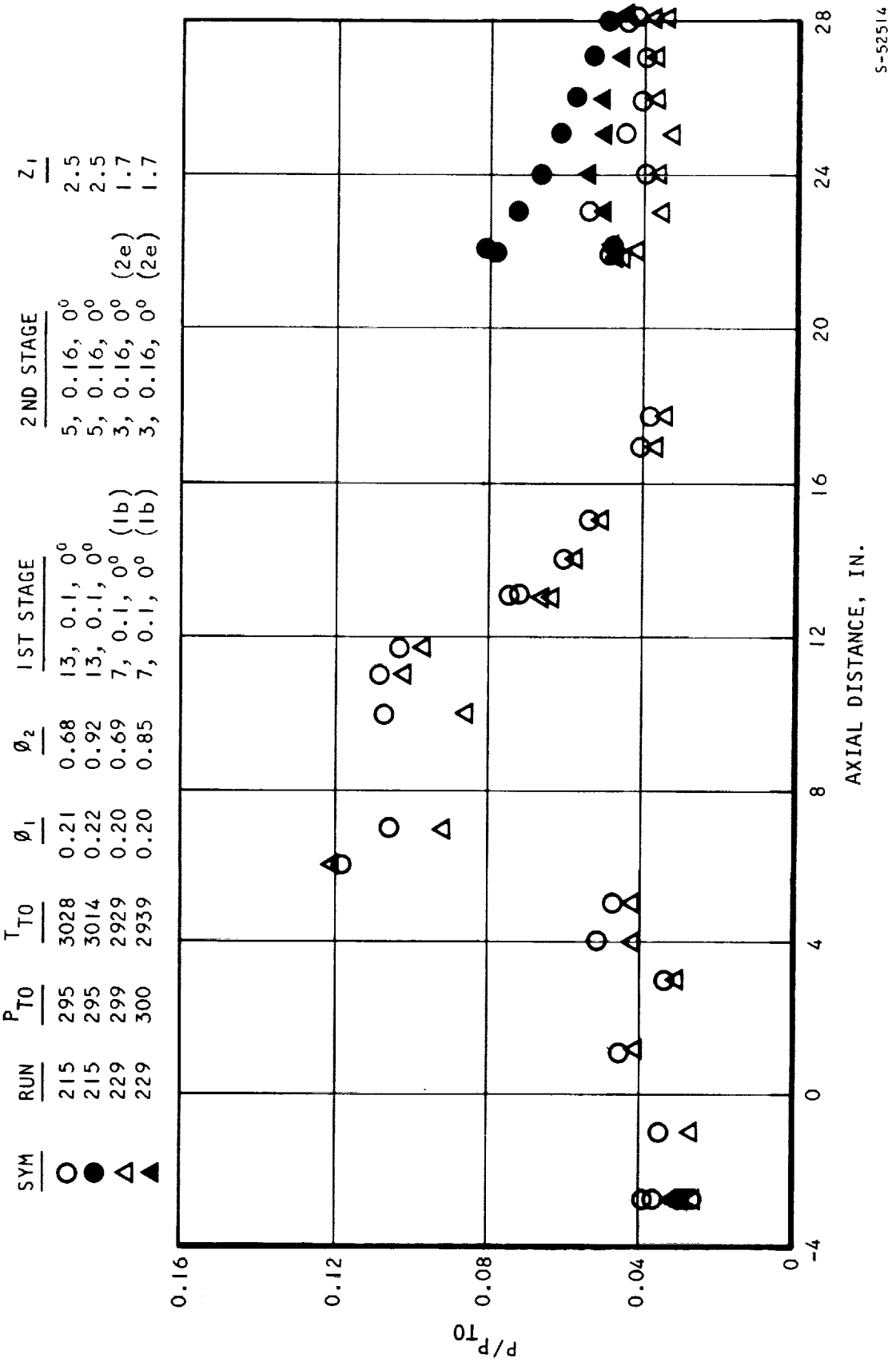

Figure 8.3-9. Comparison with One-Sided Injection (U)

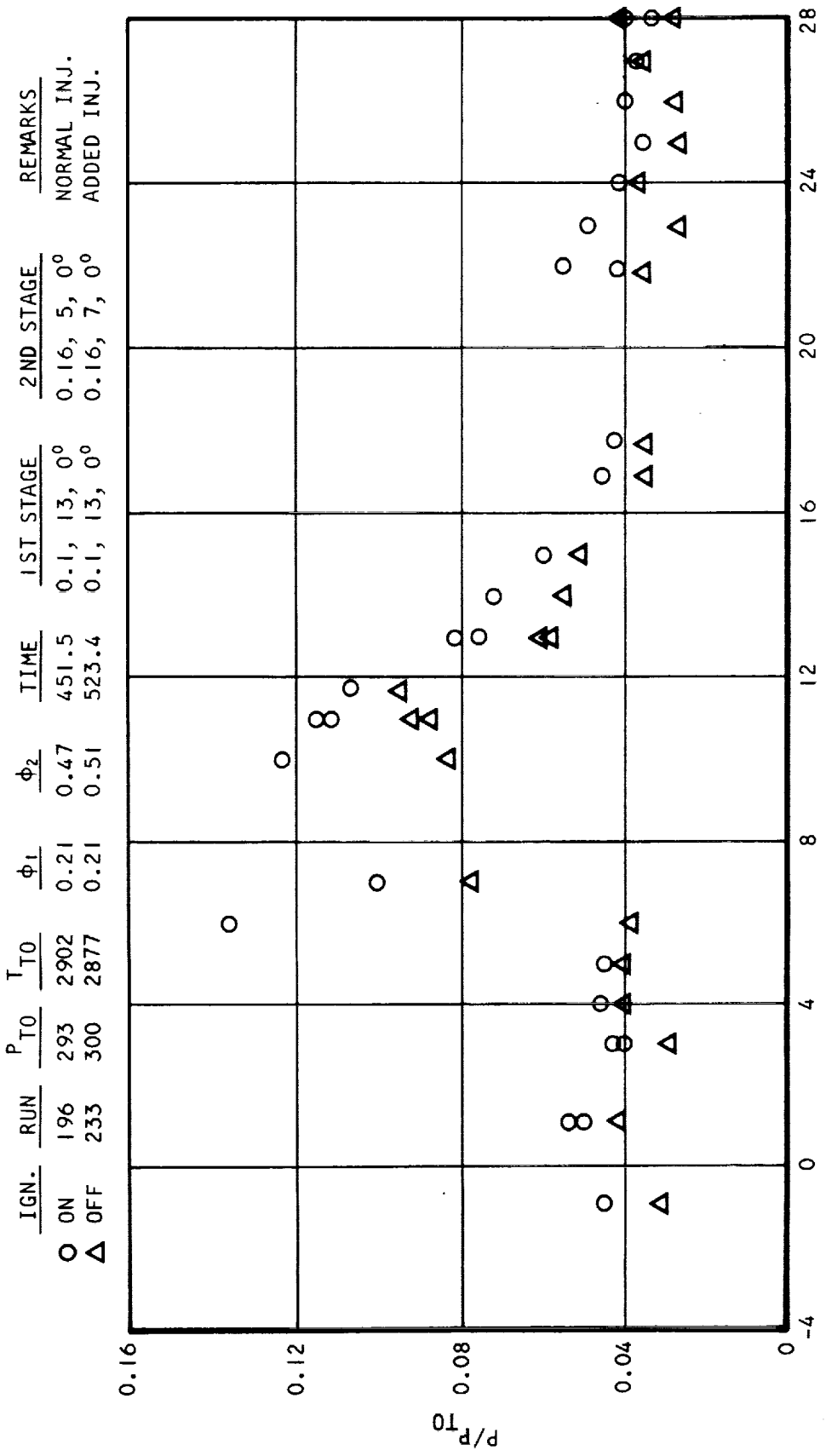

Figure 8.3-10. Static Pressure Distribution (U)

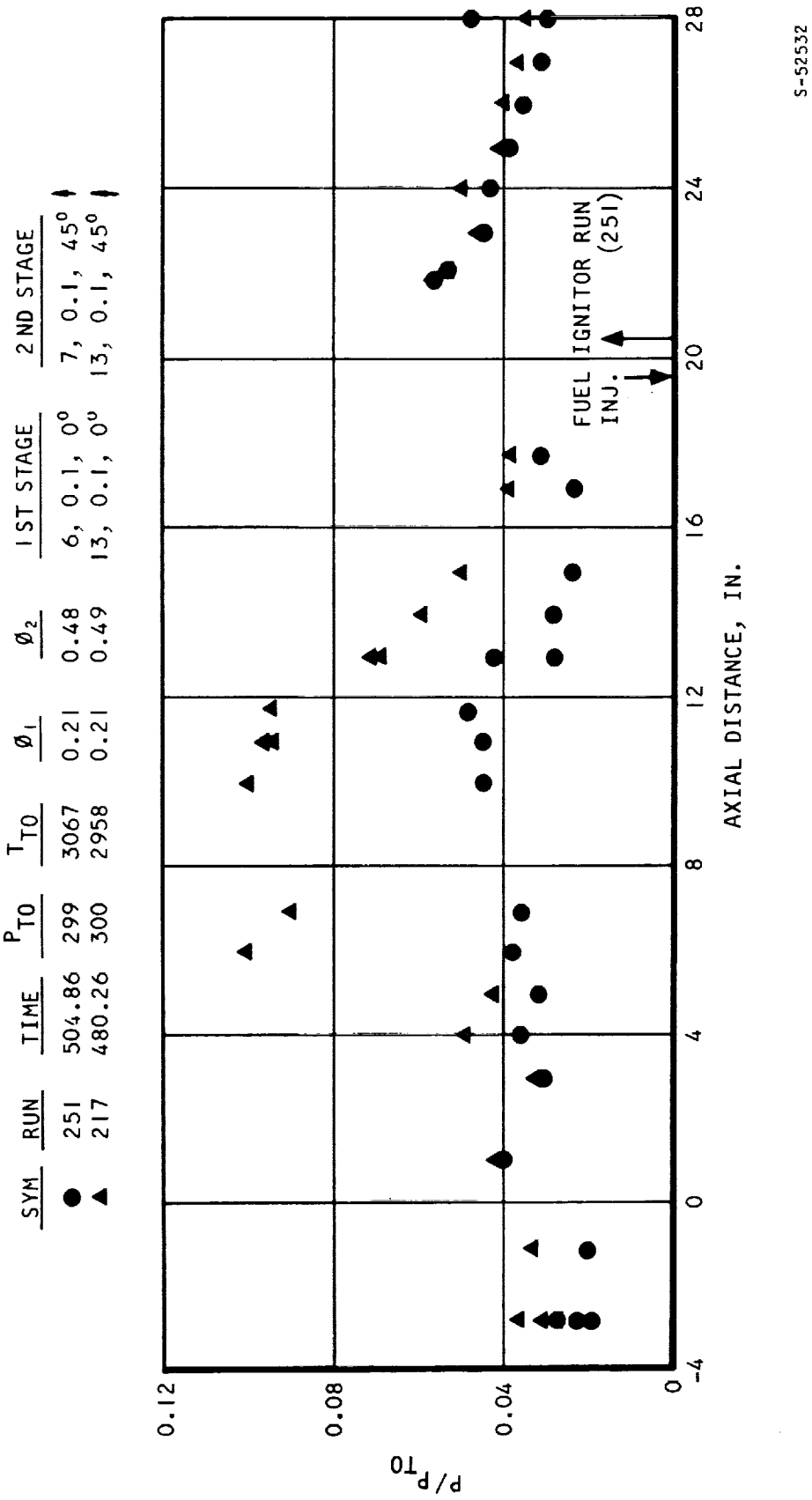

Figure 8.3-11. Static Pressure Distribution (U)

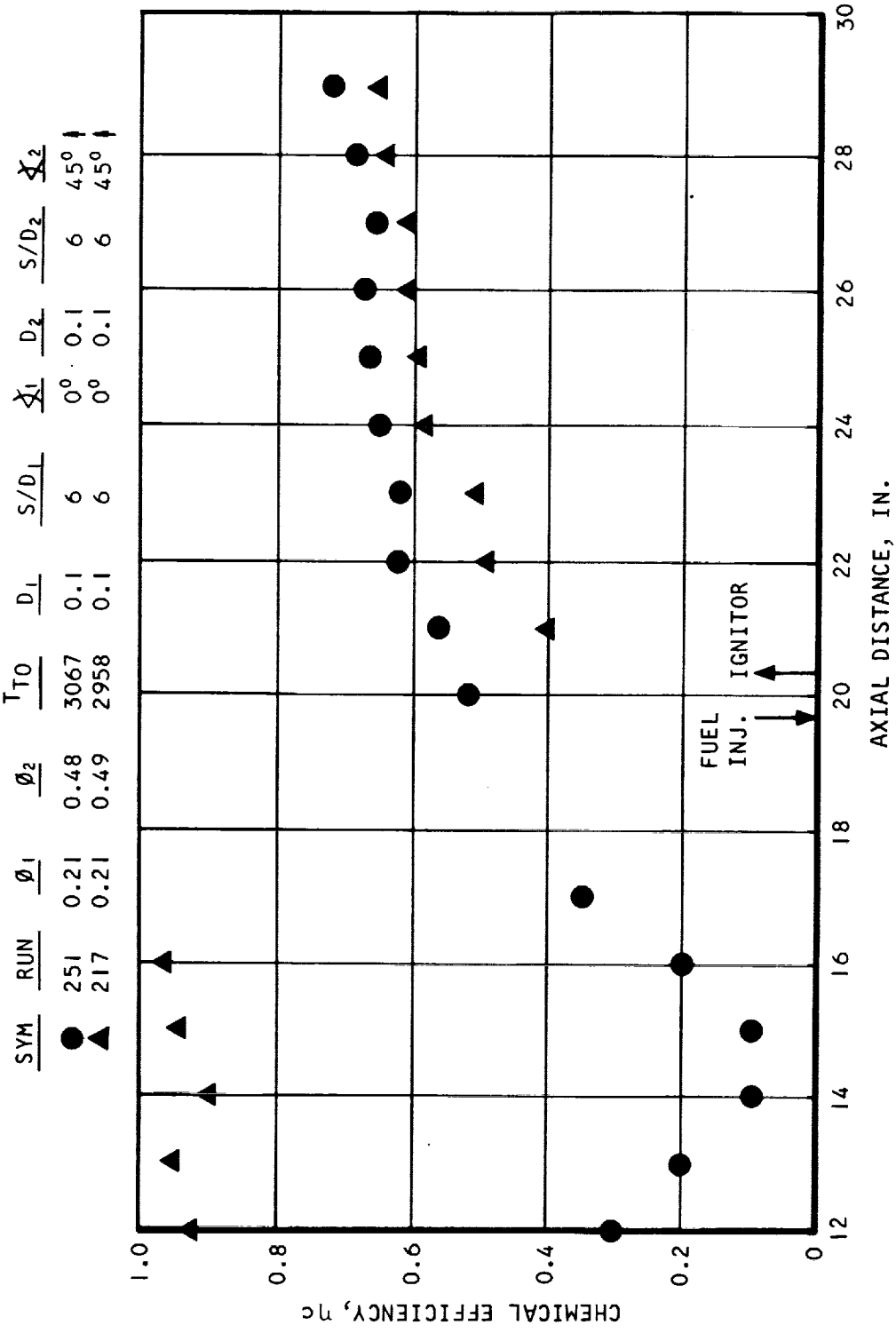

Figure 8.3-12. Combustor Chemical Efficiency (U)

or a combination of both.

The bands of efficiencies for the overall and the second-stage combustors with various injector geometries used are in Figure 8.3-13. Within nine inches of second-stage length, the highest overall efficiency was 66 percent. This was substantiated in that flame at the combustor exit was observed during all second-stage combustion tests. This was contrary to the visual observations for first-stage combustion, where no flame was observed during the tests.

8.3.6 Interference Effect of the Probe

An interesting observation was made when the sampling probe was placed 0.25 in. from the combustor exit. The wedge probe had a blunt nose with a 0.3-in. leading edge radius and gave a flow blockage of approximately 13 percent based on the projected area.

At a total equivalence ratio of 1.03, the pressure distribution is similar to those previously observed, as shown in Figure 8.3-14. However, at a slightly higher equivalence ratio (ϕ_T = 1.12), the second-stage pressure is significantly higher. It appears that the probe initiated combustion when the equivalence ratio changed from 1.03 to 1.12. Thus, a combination of flow separation caused by the probe blockage and high equivalence ratio was necessary for good combustion in the second stage.

The chemical efficiency at an equivalence ratio of 1.12 rises rapidly as shown in Figure 8.3-15. This chemical efficiency is based on all of the fuel injected from both the first and second stages. Also, the efficiencies have been corrected to a base of ϕ = 1.0; i.e., at a ϕ of 1.12, the highest overall efficiency that can be attained is 1/1.12 or 89 percent. The efficiencies shown, therefore, are based on ϕ = 1.12 divided by 0.89. Note that an extrapolation of the data would yield an efficiency above 90 percent with a combustor 2 in. longer.

A comparison of the pressure distributions with and without the probe at the combustor exit is shown in Figure 8.3-16. It must be pointed out that the last three static pressure taps near the exit were spaced 2 in. apart laterally; i.e., the pressure tap at station 27 is on the centerline of the combustor, while pressure taps on stations 26 and 28 are 2 in. from the centerline. It is not clear whether the pressure rise near the exit is due to combustion or to a local flow separation phenomenon.

8.4 OVERALL PERFORMANCE

8.4.1 Typical First- and Second-Stage Flow Parameters

Typical calculated velocity, static temperature and chemical efficiency profiles are shown in Figures 8.4-1 and 8.4-2 for (1) an equivalence ratio of 0.39 injected only into the first stage constant-area section, and for (2) an equivalence ratio of 0.22 injected into the first stage and an equivalence ratio of 0.65 injected into the second stage. Air total temperature for both cases was about 3000°R.

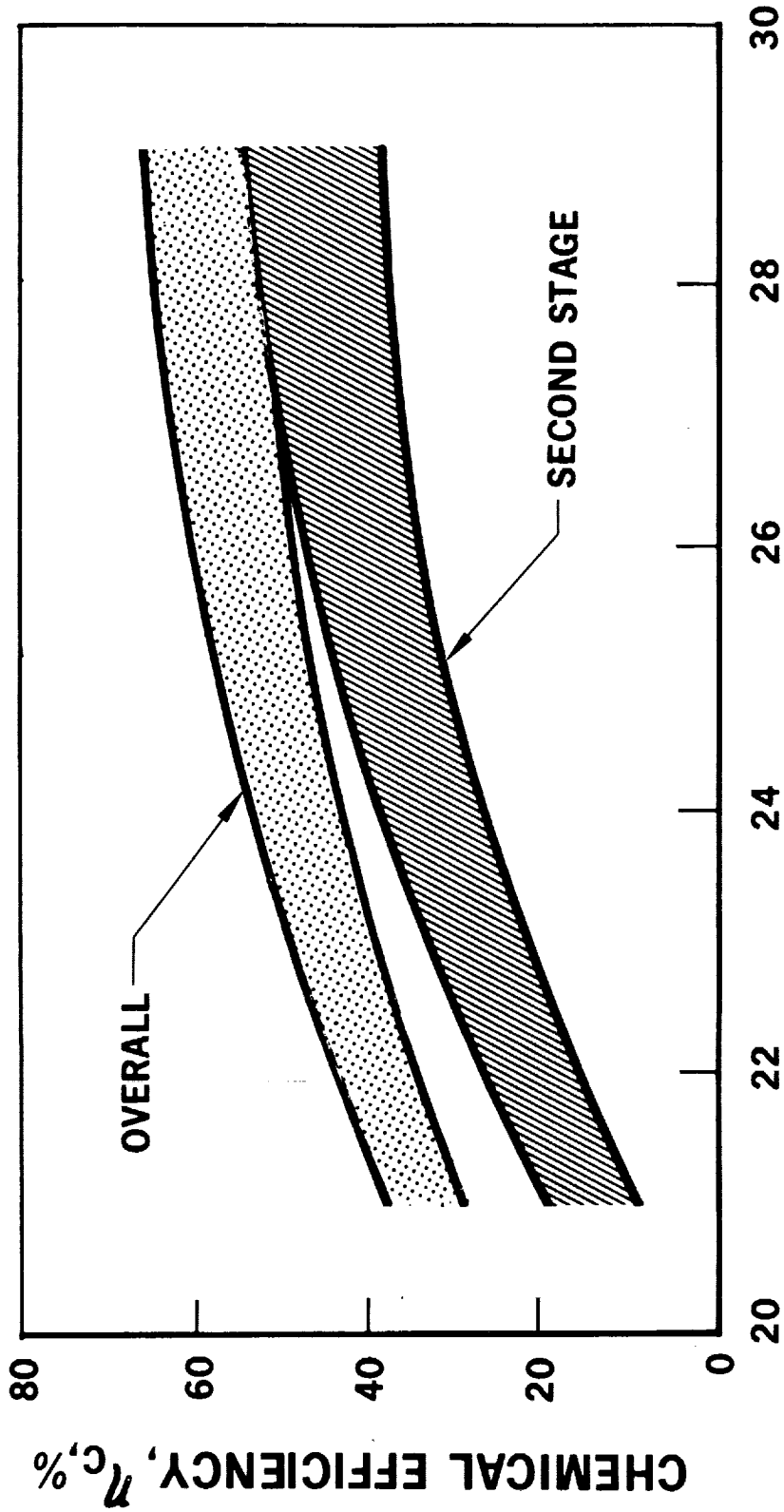

Figure 8.3-13. Overall and Second-Stage Chemical Efficiencies (U)

Sym.	P_{T0}, psia	T_{T0}, °R	ϕ_1	ϕ_2	ϕ_T	T_{TF}, °R	Run	Time
▲	300	2951	0.22	0.90	1.12	1287	211	910.65
●	290	2931	0.22	0.81	1.03	1226	211	656.08
■	297	2933	0.22	0.00	0.22	1003	211	273.9

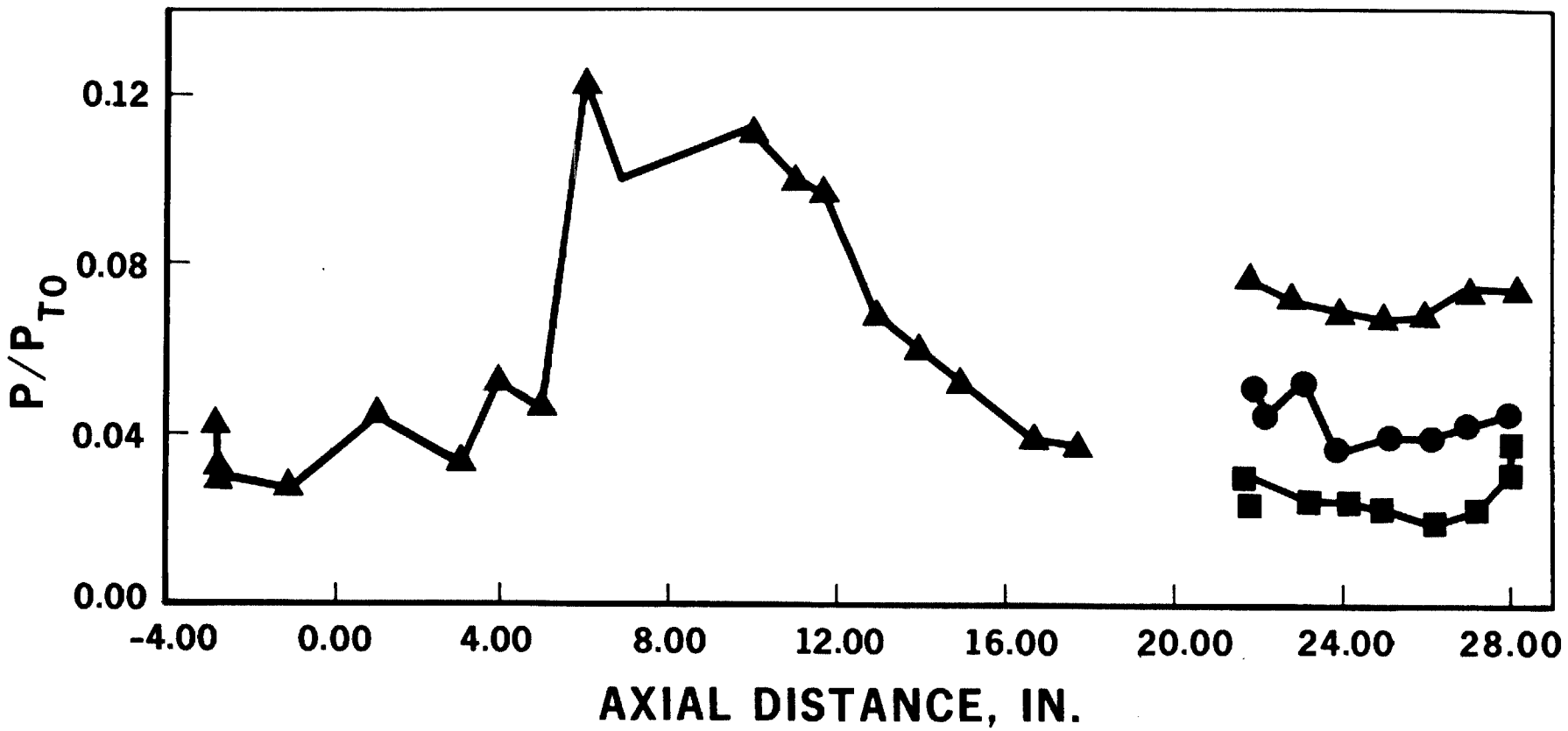

Figure 8.3-14. Interference Effects - Sampling Probe (Pressure) (U)

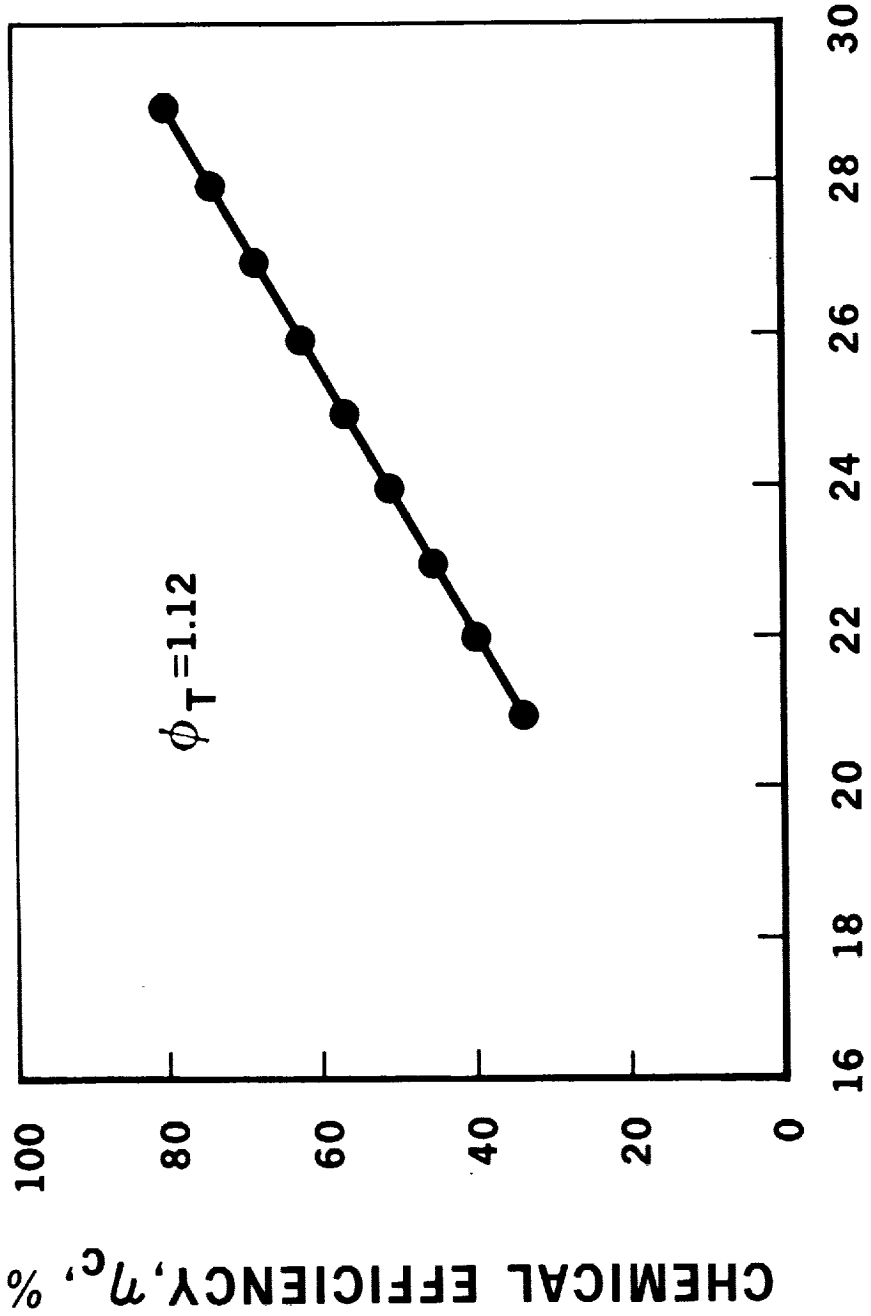

Figure 8.3-15. Interference Effects - Sampling Probe (Efficiency) (U)

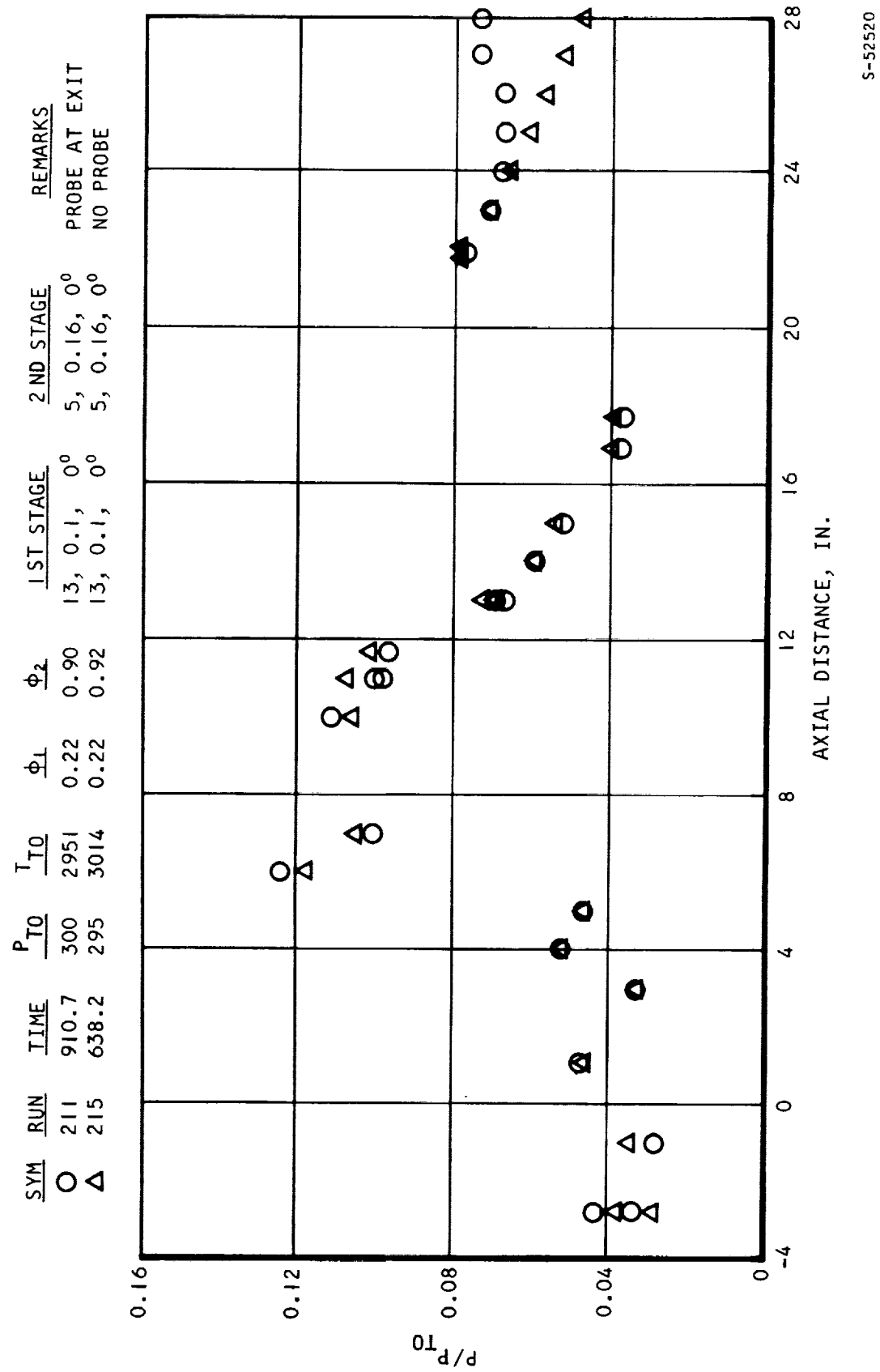

Figure 8.3-16. Static Pressure Distribution - Two-Stage Injection (U)

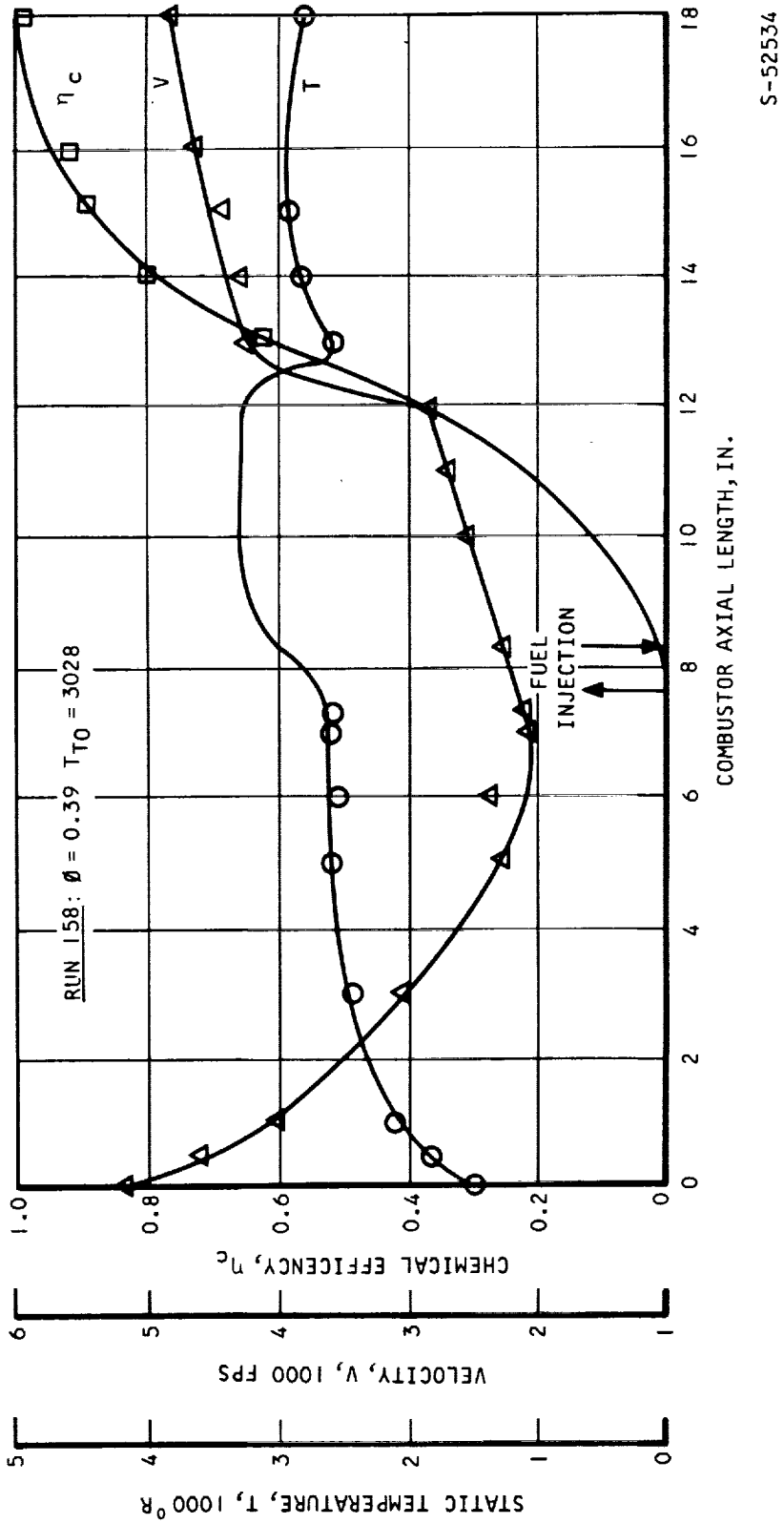

Figure 8.4-1. Typical First-Stage Profiles (U)

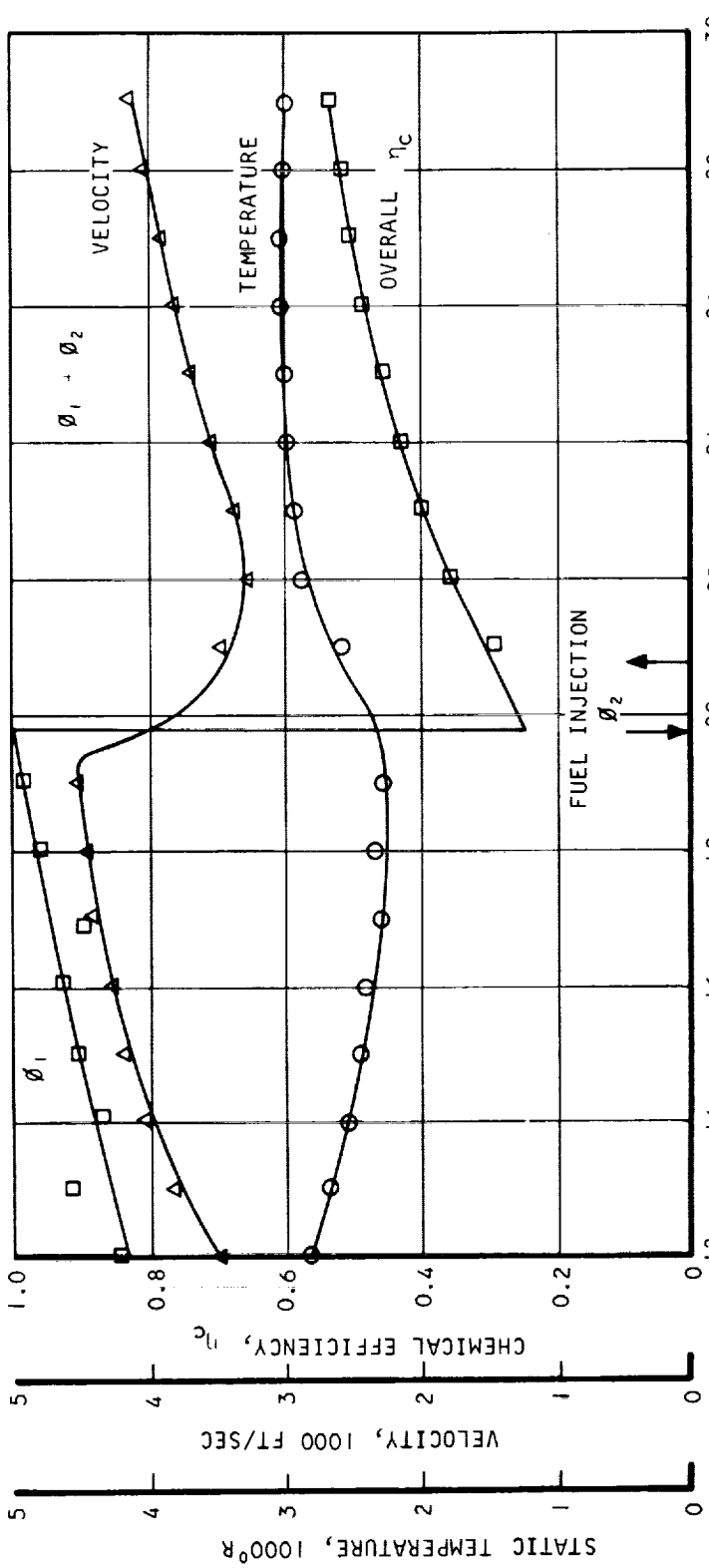

Figure 8.4-2. Typical Second-Stage Profiles (U)

When fuel was injected, at an equivalence ratio of 0.39, into the constant-area section (Figure 8.4-1) it created an aerodynamic blockage. This blockage caused a decrease in velocity prior to injection with a corresponding rise in static temperature. For this particular case, air static temperature rose to 2600°R upstream of the injection point from 1500°R at the combustor entrance. The low velocity and high static temperature initiated rapid combustion with the result that combustion was apparently nearly complete 10 in. from fuel injection.

With two-stage injection, the static temperature at the injection plane is about the same as that in the first stage. As shown in Figure 8.4-2, static temperature in the second stage before fuel is injected is about 2300°R. However, the aerodynamic blockage was not as great as in the first stage.

8.4.2 Combustor Exit Total Pressure

A plot of calculated combustor total pressure recovery versus combustor length is shown in Figure 8.4-3 for both single and multiple stage injection for typical equivalence ratios. There is a steady decrease in total pressure without fuel injection, due to friction alone. When fuel is added in the constant-area section, an aerodynamic blockage sets up a shock system resulting in a rapid decrease in total pressure; then, there is a less rapid decay in total pressure once fuel starts burning because the Mach number at which combustion occurs is lower. When fuel is added in the diverging section, a similar pattern is observed. With fuel added in both stages it appears that the total pressure losses are larger.

This is more clearly seen in Figure 8.4-4 where combustor exit total pressures for single-stage and two-stage injection are compared. Adding fuel in the second stage gives greater losses than if this fuel had been added in the first stage. Additionally, at higher equivalence ratios, the total pressure decreases less rapidly. Without fuel injection there is 55 percent loss in total pressure due to friction alone.

Superimposed is the total pressure loss predicted for constant-pressure combustion. Since the two-dimensional combustor is a diverging combustor, its performance is expected to lie between the constant-pressure and constant-area processes. Because of thermal choking, the performance of the constant-area process could not be calculated.

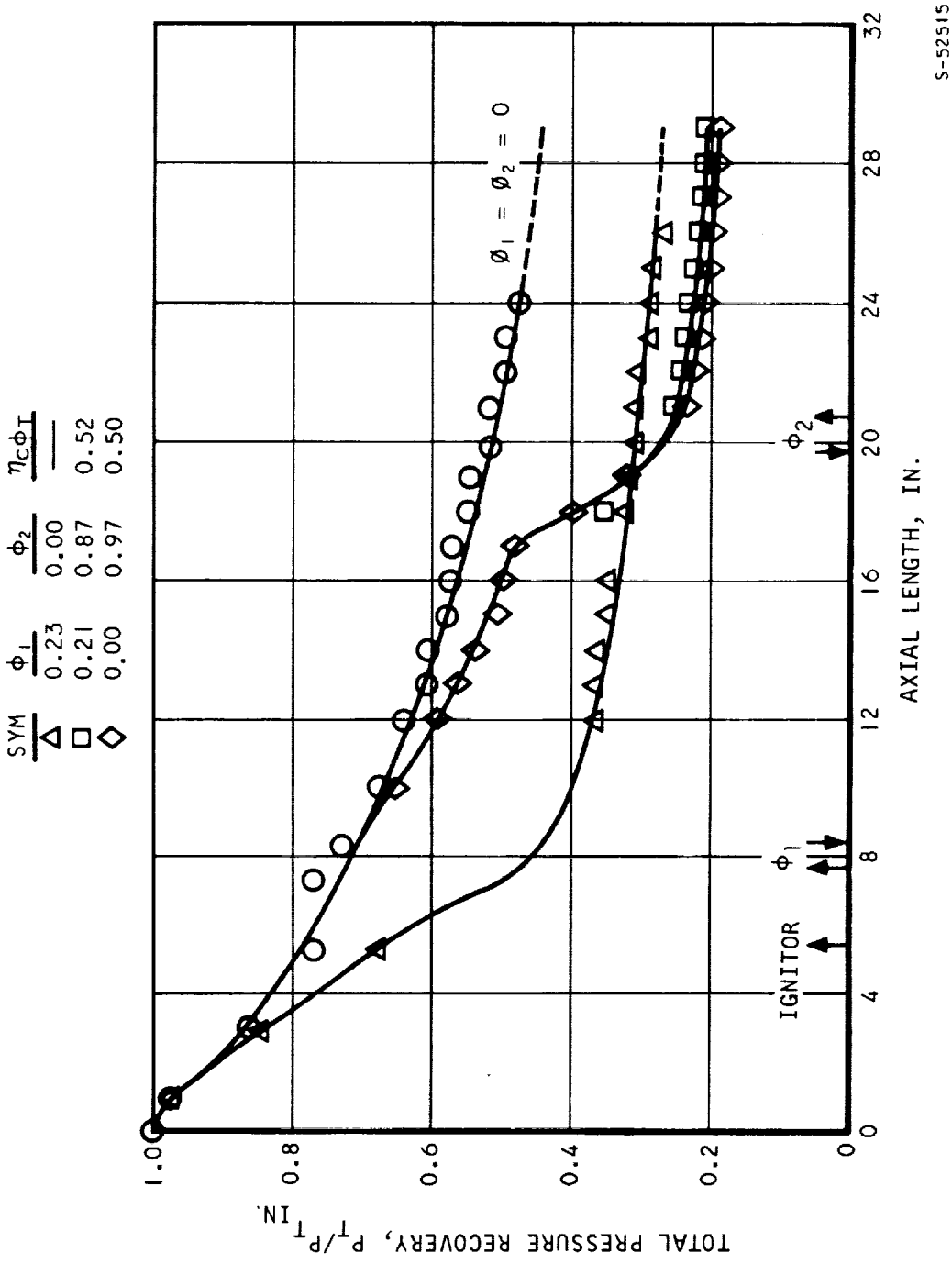

Figure 8.4-3. Combustor Total Pressure Recovery (U)

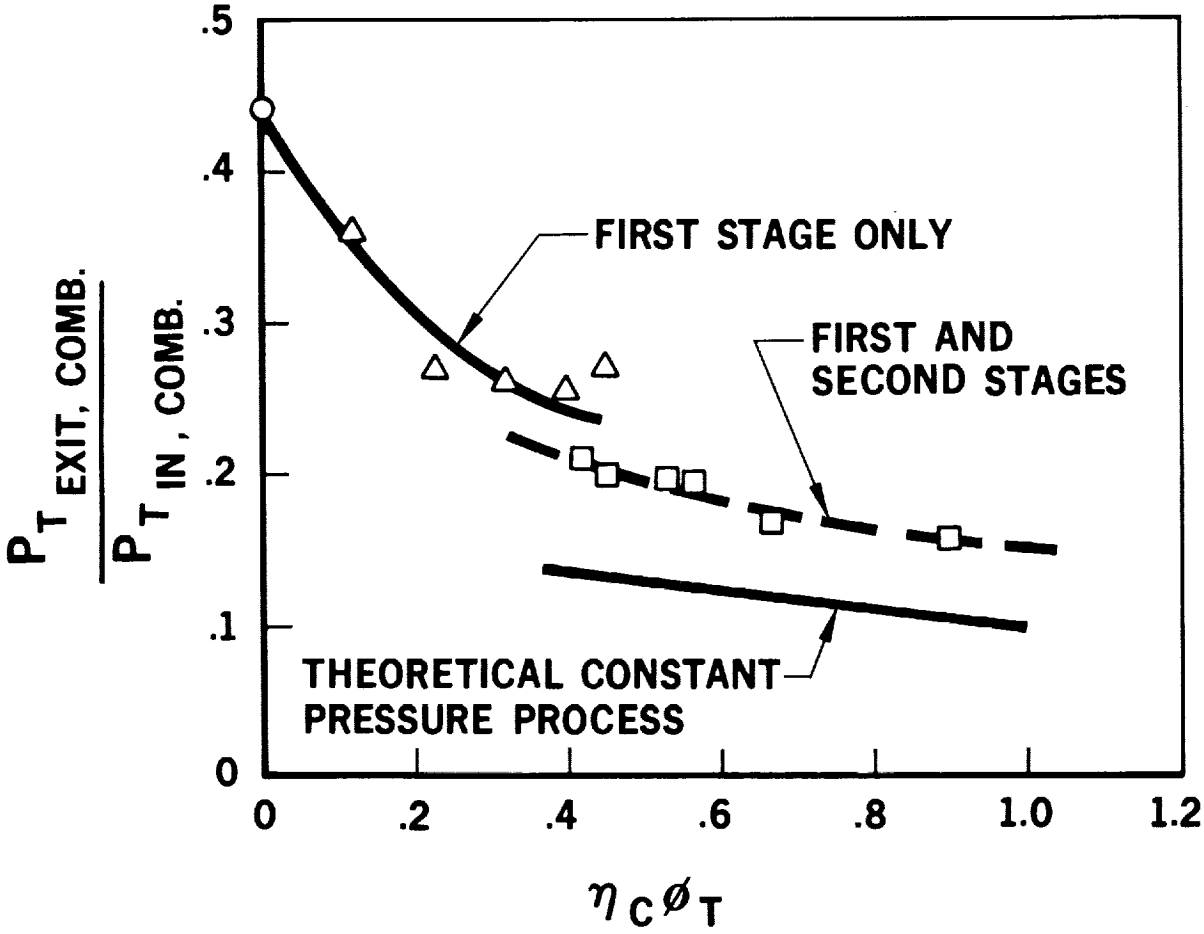

Figure 8.4-4. Combustor Exit Total Pressure (U)

8.4.3 Error Analysis of Chemical Efficiency Calculation Method

The accuracy of the combustor efficiency calculations is affected by a number of parameters as shown in Table 8.4-1. Because the chemical efficiency is determined from momentum, the accuracy in determining the stream momentum will have a direct influence on the level of chemical efficiency. The combustor inlet static pressure and the axial measured pressures determine the inlet stream thrust and pressure integral, respectively. The errors incurred in these two measurements are significantly smaller than that in the friction force. The large error in the friction force is due to the inaccuracy of internal thrust, because it is determined from the difference of measured thrust and the pressure integral term. Difficulties encountered in isolating the thermal stress from the heated hydrogen lines was the largest-contributing factor in the inaccuracy of the thrust measurement.

The estimated total experimental error of chemical efficiency based on rms value is ± 10.4 percent. Mathematical tolerances allow a further 2-percent error.

A brief sensitivity study was made to see if measurement inaccuracies or computer errors were the cause of the low calculated efficiencies. As indicated in Figure 8.4-5, to reach 90 percent chemical efficiency at the combustor exit would have required static pressures 30 percent higher than measured. This is much greater than the percentage error introduced by mathematical approximations and measurement inaccuracy. Even decreasing the friction coefficient to 0.0025 instead of the nominal 0.005 measured (Figures 8.4-6 and 8.4-7) gave no significant improvement in chemical efficiency. Thus other causes for the low calculated efficiencies were sought.

8.5 DATA CORRELATION PARAMETERS

8.5.1 Chemical Efficiency Correlation

Since difficulties were encountered in injection into a diverging duct (the second stage), most of the data correlated comes from test results with fuel injection into the constant-area section (from the first stage) only. A summary of these tests was listed in Table 6.2-1. These tests had pressure profiles in the combustor similar to those in Figure 8.2-2 and they were analyzed with the aid of the one-dimensional data reduction program. The relative merit of each injector design was assessed by using the level of efficiency and the distance in which this efficiency was achieved.

If one assumes that the flow is truly two-dimensional and the combustion mixing-controlled, penetration of the jet will then be a dominating factor in achieving good combustion efficiency. The data therefore can be correlated with the jet penetration parameter normalized with respect to the equivalence ratio. The penetration parameter is defined as the outer boundary of the jet penetration where hydrogen concentration is 1/2 of one percent by volume divided by the minimum penetration height required for complete combustion. For example, if the duct height is one inch and the equivalence ratio is 0.5, then the minimum

TABLE 8.4-1

ERROR ANALYSIS

Parameter	Change in Parameter, %	Change in η_c, %	Instrumentation Error, %	Error, η_c, %
Inlet static Pressure	+10	-8	0.8	0.6
Heat loss	+10	+5	5.4	2.7
Friction coefficient	+10	-5	20.0	10.0
Axial measured pressures	+10	+14	0.8	1.1

Estimated Total η_c Error = ±10.4%

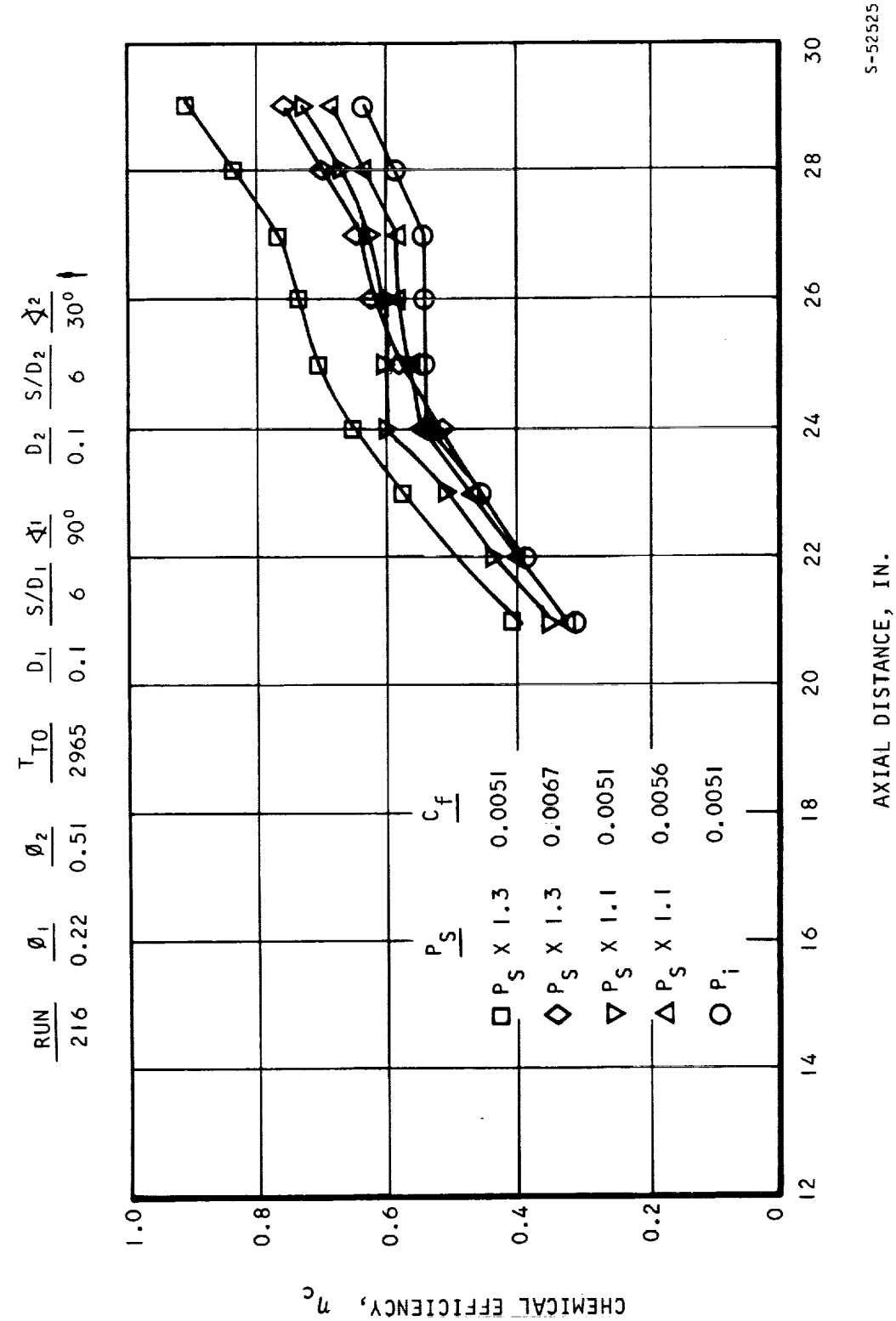

Figure 8.4-5. Combustor Chemical Efficiency (U)

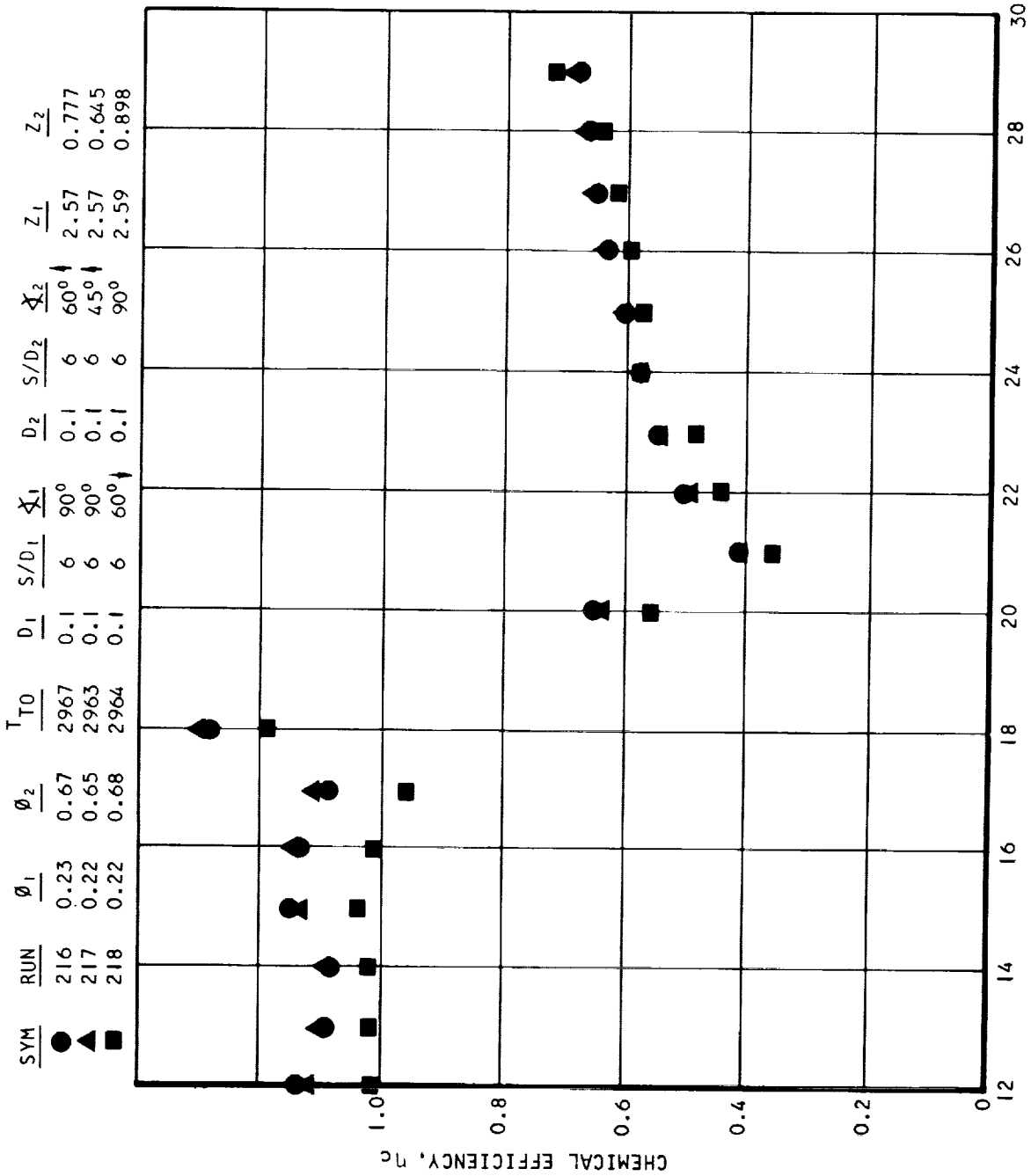

Figure 8.4-6. Combustor Chemical Efficiency (U)

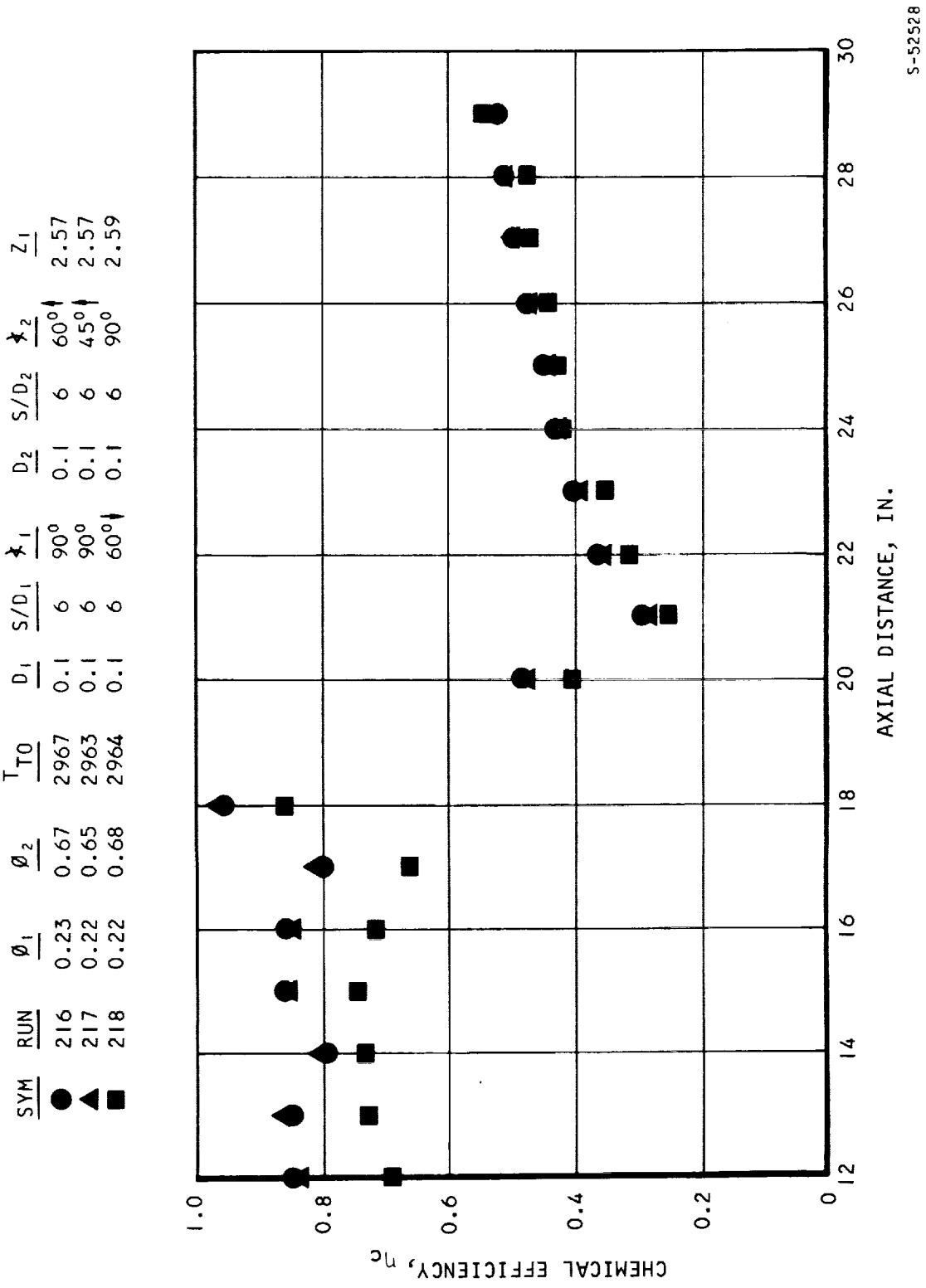

Figure 8.4-7. Combustor Chemical Efficiency (U)

penetration height required for complete combustion is one-half inch or one-quarter inch depending on whether the fuel is injected from one side or both sides.

A sketch illustrating this concept is shown below:

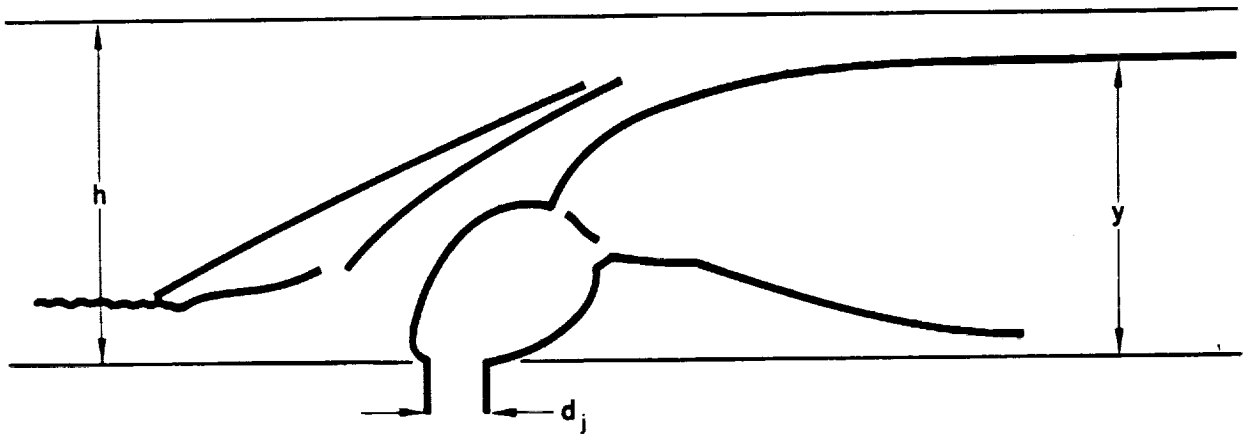

$$z = \text{PENETRATION PARAMETER} = \frac{y}{h\phi}$$

(Reference 8-3)

$$y = 2.91 \left(\frac{\rho_j v_j^2}{\rho_0 v_0^2}\right)^{.5} \left(\frac{x}{d_{j_*}}\right)^{.0866} d_{j_*}, \quad d_{j_*} = d_j\sqrt{C_D}$$

S-53287

Since the jet boundary is calculated from open literature based on non-reacting gas in an unconfined stream, this penetration parameter cannot be construed as the true penetration height, but can only be used as a reference parameter.

The decrease in chemical efficiency with increasing equivalence ratio as shown in Figure 8.5-1, for example, can be explained by the penetration parameter. A total of 15 injector holes was used for these runs. The chemical efficiencies as shown decrease sharply as equivalence ratio is increased, but it can be shown that the penetration parameter decreases with increasing equivalence ratio. It must be remembered that the absolute penetration height increases with equivalence ratio, but the increase cannot keep pace with the required penetration for complete combustion. This correlation is further substantiated by the two solid symbols showing that they both have approximately the same equivalence ratio (0.56 and 0.55), but with different penetration parameters of 1.59 and 1.31; their chemical efficiencies are 98 and 81 respectively. On the other hand, with the same penetration parameters (● and △, or ▲ and ▽), but with different equivalence ratios, the efficiencies are about the same.

Comparing two different diameters at the same Z, Ø, and essentially the same physical spacing (Figure 8.5-2) shows that chemical efficiency versus length

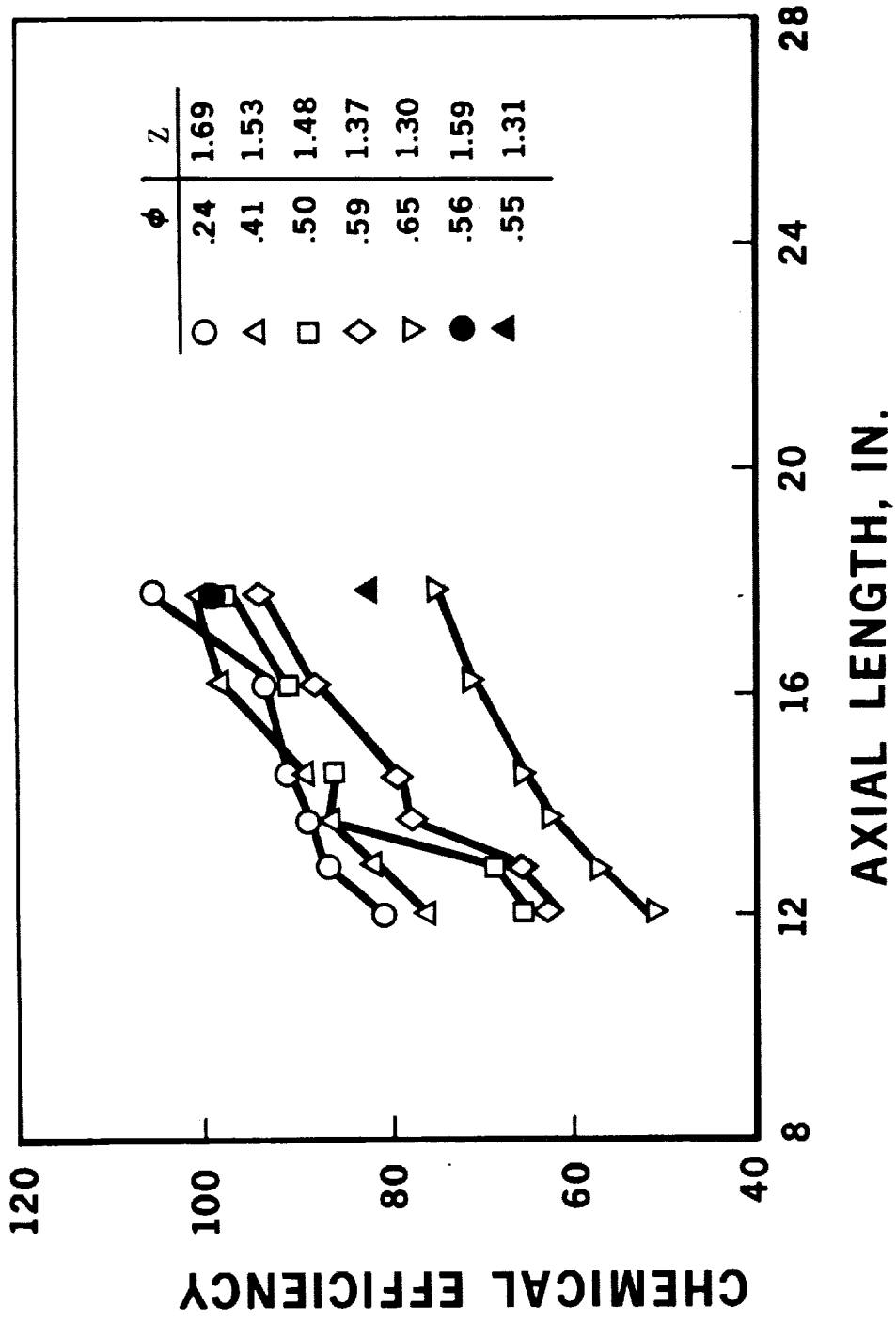

Figure 8.5-1. Correlation of Penetration Parameters (U)

SYM	RUN	ϕ_1	ϕ_2	T_{TO}	D_1	S/D_1	$\measuredangle_1$	SPACING, IN.	Z_1
●	148	0.55	—	3775	0.15	5.5	60°	0.825	1.52
▲	151	0.55	—	3759	0.10	9.5	60°	0.95	1.59

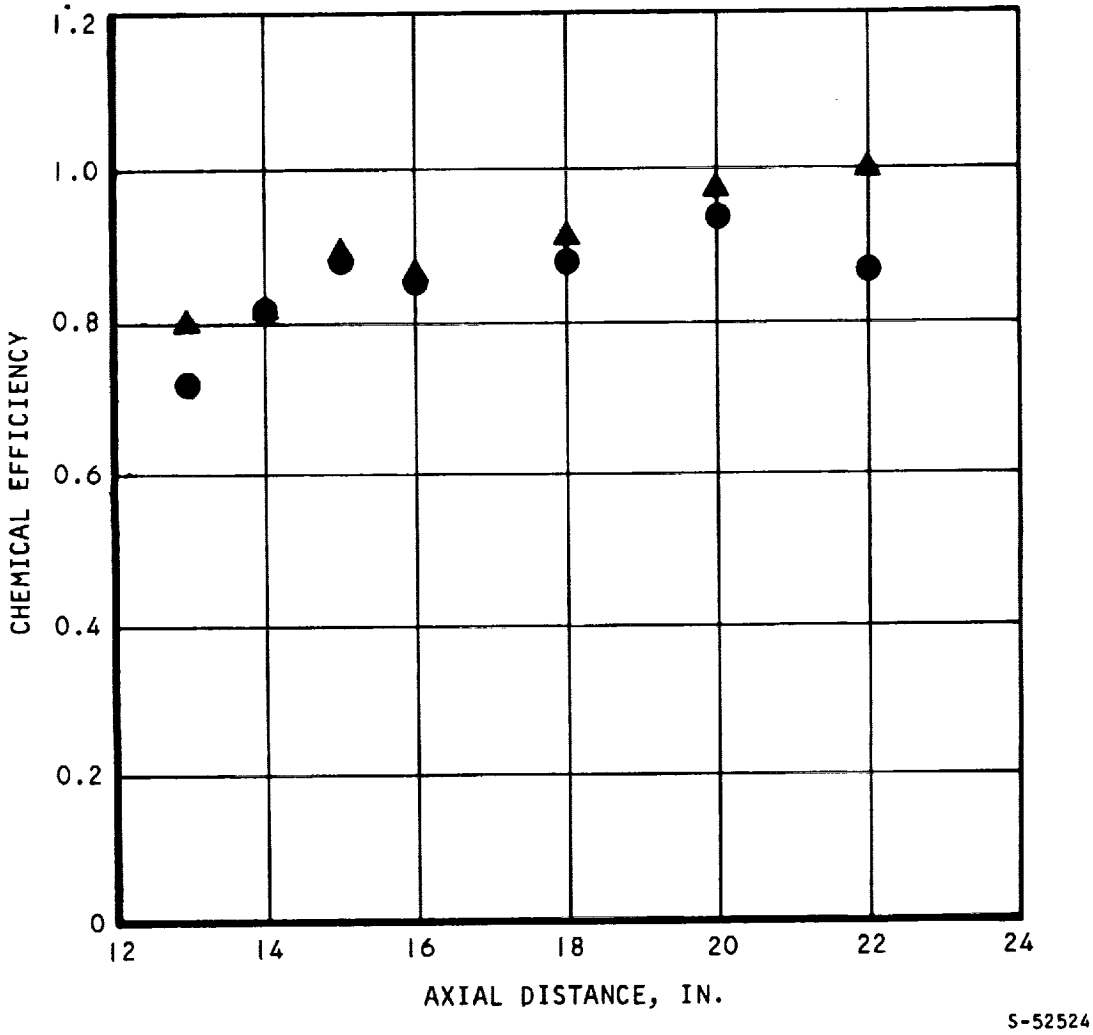

Figure 8.5-2. Combustor Chemical Efficiency - Effect of Spacing (U)

does not vary significantly.

However, if two different diameter injectors with the same penetration parameter are compared at the same spacing-to-diameter ratio (S/d), the smaller diameter injector has higher efficiency as previously shown in Figure 8.2-10. It thus appears that the penetration parameter alone cannot correlate the chemical efficiency.

First attempts to correlate penetration with lateral spreading are given in Figures 8.5-3 and 8.5-4. These are plots for particular distances downstream of injection. In these plots, the effects of injector spacing and diameter are not clear.

Another correlation was attempted using peak chemical efficiencies, no matter at what axial length from injection they occurred. A summary of the effects of injector geometry and penetration parameter for different inlet temperatures on peak chemical efficiency is shown in Figure 8.5-5. The following observations may be made;

(a) The peak chemical efficiency is a strong function of penetration parameter, but levels off when the penetration parameter reaches 1.7.

(b) The peak chemical efficiency is a weak function of hole-spacing-to-diameter ratios, but the correlation is inconclusive.

(c) At the same penetration parameter and spacing-to-diameter ratio, smaller diameter injectors give better chemical efficiency.

The results in Figure 8.5-5 indicated that a more refined correlation was needed since the mixing process in a combustor is truly a three-dimensional phenomenon. This two-dimensional concept using a penetration parameter was not adequate to evaluate this problem.

Therefore, one may go one step further to correlate the chemical efficiency with a three-dimensional mixing model. As shown in Figure 8.5-6, the jet penetrates into the stream by a distance (y) and at the same time spreads out laterally by a width (b). Then the actual fuel-air mixing area is a function of (y) and (b). The ideal minimum mixing area required for 100 percent combustion is the height of the duct multiplied by the hole-spacing and equivalence ratios. The ratio of these two areas defines the mixing parameter.

The lateral spreading characteristic is not fully predictable. Two different methods of determining the spreading parameters, along with the modified penetration, were combined to correlate the combustion efficiency. Since the large number of factors involved made satisfactory theoretical solutions difficult to achieve, an attempt was made to correlate the dependent variable, chemical efficiency, with the independent variable in a manner similar to that used in the correlation of heat transfer coefficients, friction coefficients, etc. Briefly, the procedure consisted of two parts, (1) deciding what groups are important in the description of the flow process, and (2) assuming a functional

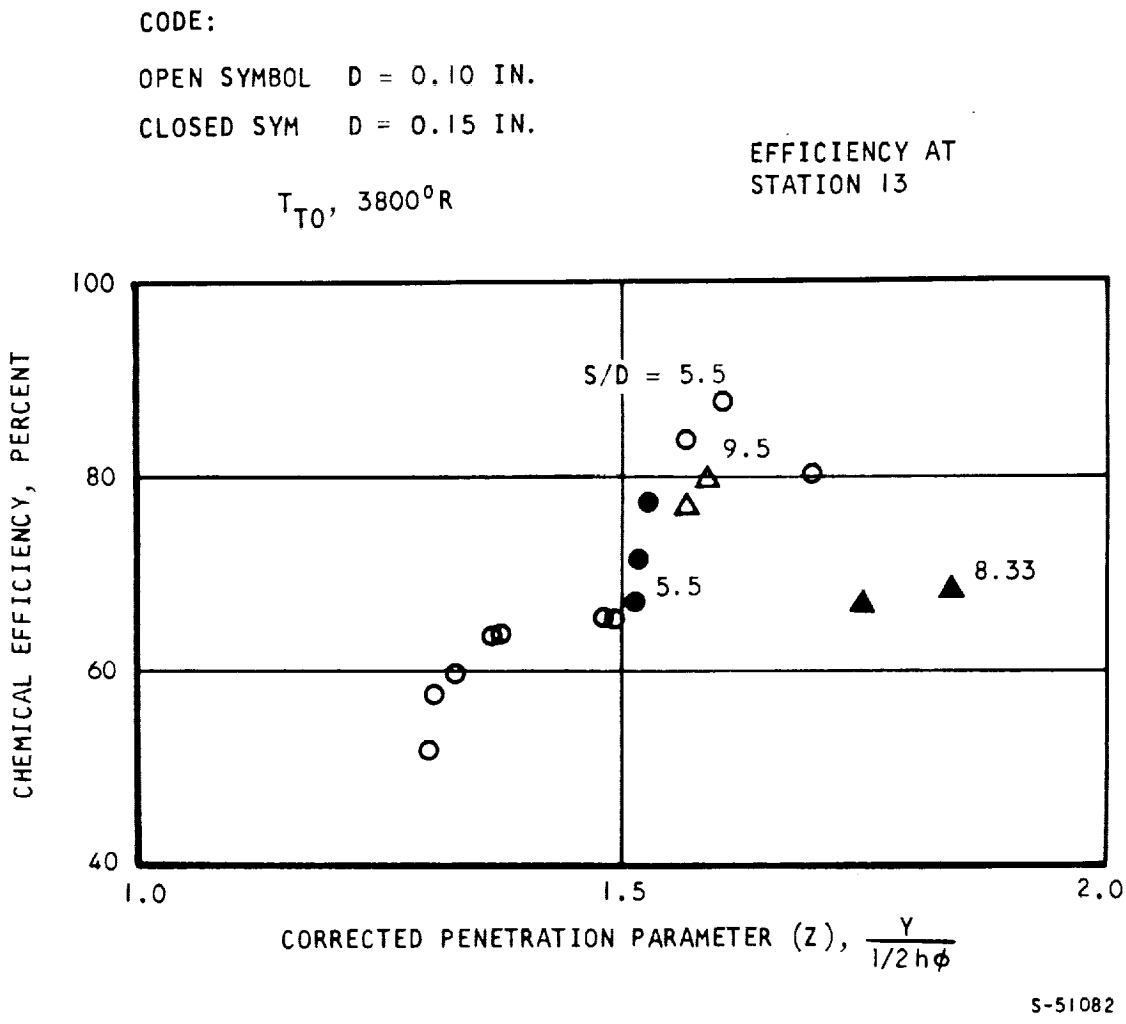

Figure 8.5-3. Effect of Injector Diameter on the Corrected Penetration Parameter and Chemical Efficiency (U)

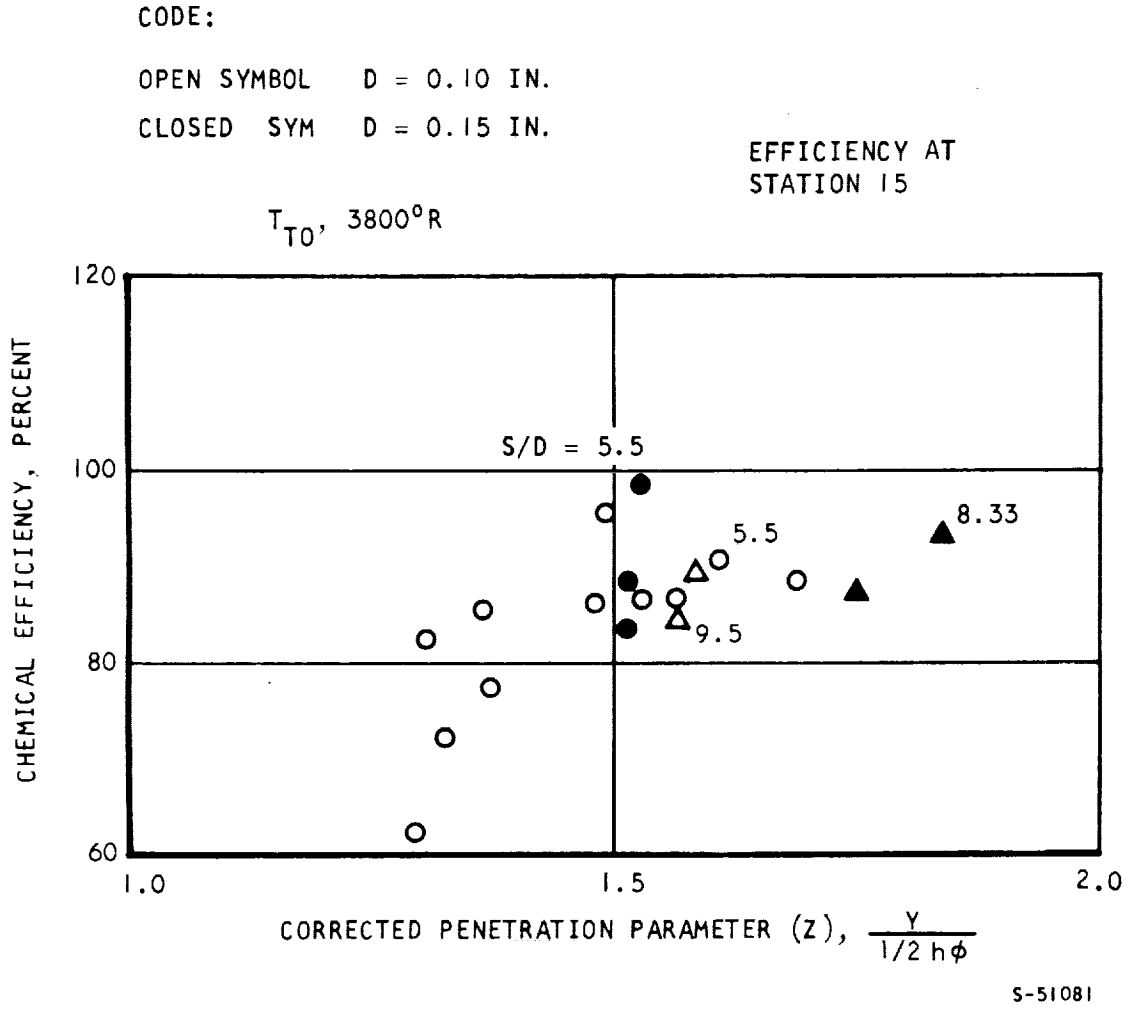

Figure 8.5-4. Effect of Injector Diameter on the Corrected Penetration Parameter and Chemical Efficiency (U)

CODE

OPEN SYMBOLS - D = 0.10 IN.
CLOSED SYMBOLS - D = 0.15 IN.

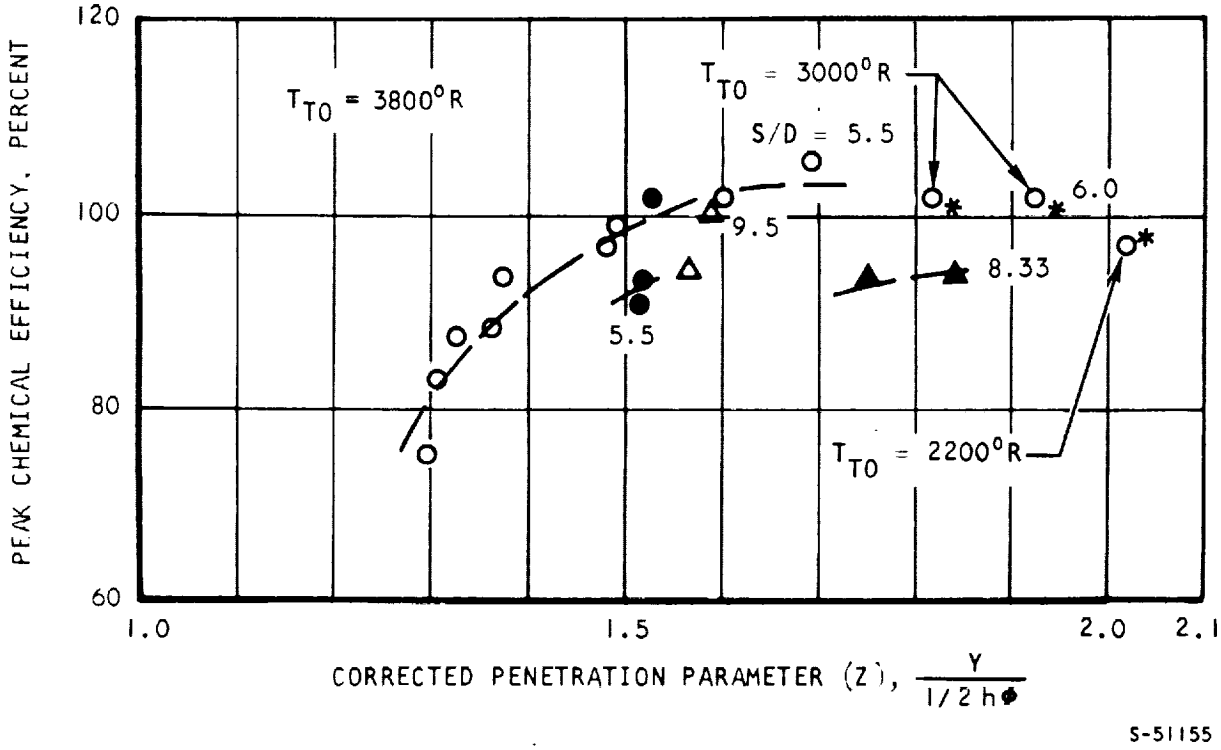

Figure 8.5-5. Effect of Injector Diameter on the Corrected Penetration Parameter and Chemical Efficiency (U)

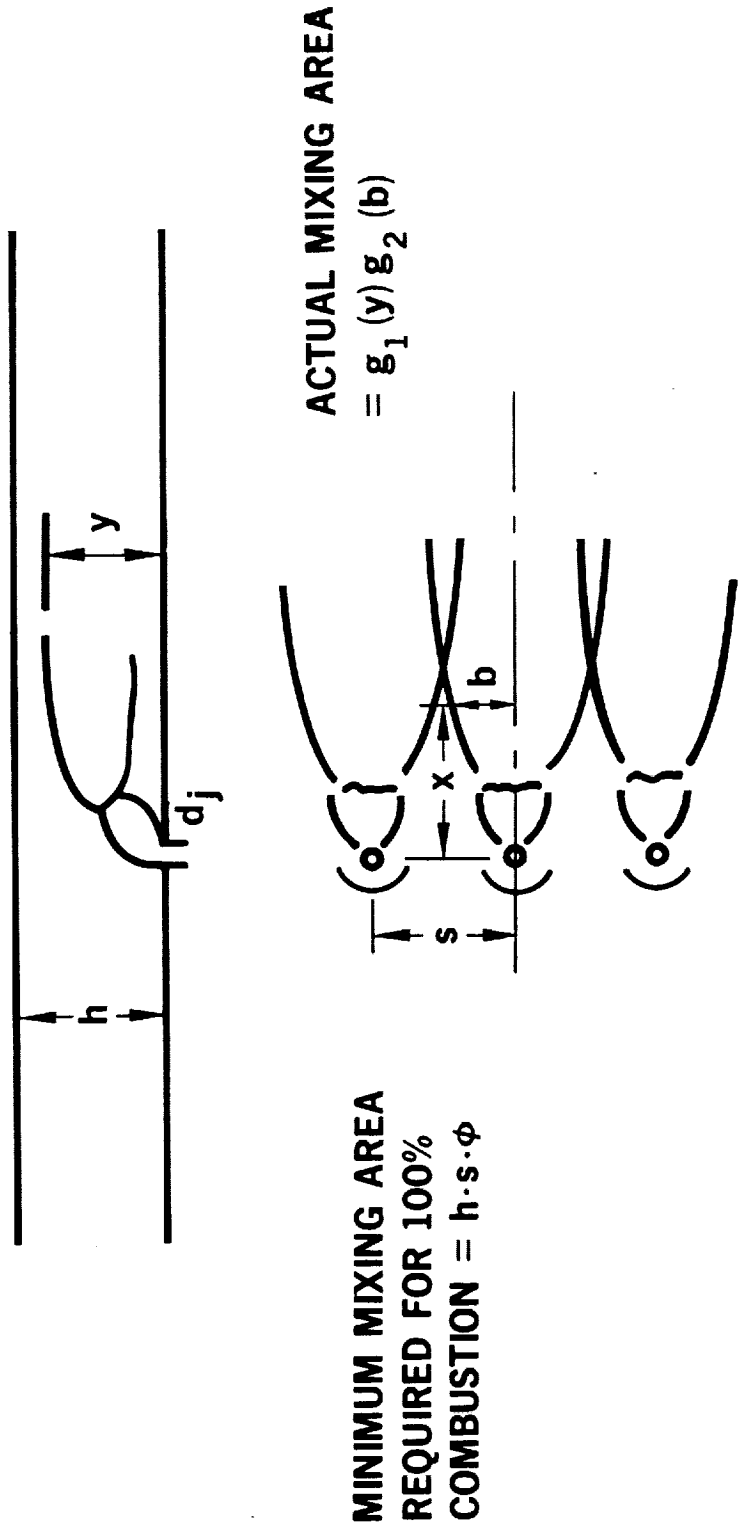

Figure 8.5-6. Concept of Mixing Parameter

relationship between the dependent variable (e.g., chemical efficiency) and the independent variable (the dimensionless group) subject to the determination of certain empirical constants.

It was assumed that mixing rates, and not chemical kinetics, would govern combustion rates over most of the conditions anticipated in supersonic hydrogen combustion. In other words, the success of combustion depended upon how well the fuel is mixed with air. The major characteristic parameters in the mixing were the depth of jet penetration and its spreading width.

Method I: The spreading characteristic (b) was selected similar to the spreading width of a two-dimensional turbulent jet (Reference 8-4) which meant that the lateral spreading width of the mixing zone associated with transverse injection was proportional to the distance from the injection point. In order to make b a useful parameter for the injector row design, it was necessary to include the geometric effects on b. It was assumed that the lateral spreading is completed when the injection flow patterns merge.

A correlation of a two-dimensional region for the normal injector is: (Reference 8-2).

$$\left(\frac{X}{D}\right)_c \quad vs \left(\frac{P_{TO}}{P_{T_j}}\right)^{\frac{1}{2}} \left(\frac{S}{D}\right)\left(\frac{1}{1+\gamma M_o^2}\right) \tag{8-6}$$

where S is the hole spacing and D is the hole diameter. This correlation is shown in Figure 8.5-7, and can be modified and expressed approximately by

$$\left(\frac{X}{D}\right)_c = K\left(\frac{S}{D}\right)^2 \frac{P_o}{P_{T_j}} \tag{8-7}$$

Assuming the jet spreads linearly with X, a spreading parameter b/S is obtained as

$$\frac{b}{S} = K\left(\frac{X}{D}\right)\left(\frac{D}{S}\right)^2 \frac{P_{T_j}}{P_o} \tag{8-8}$$

Although knowledge of b/S yields no details of the spreading flow field, this parameter has several advantages. It is a normalized parameter that has the value of unity when the spreading is completed (i.e., injected flow patterns merge) and zero before the spreading is started. In addition it is a parameter which allows easy computation of the spreading for different total pressure ratios and injection configurations.

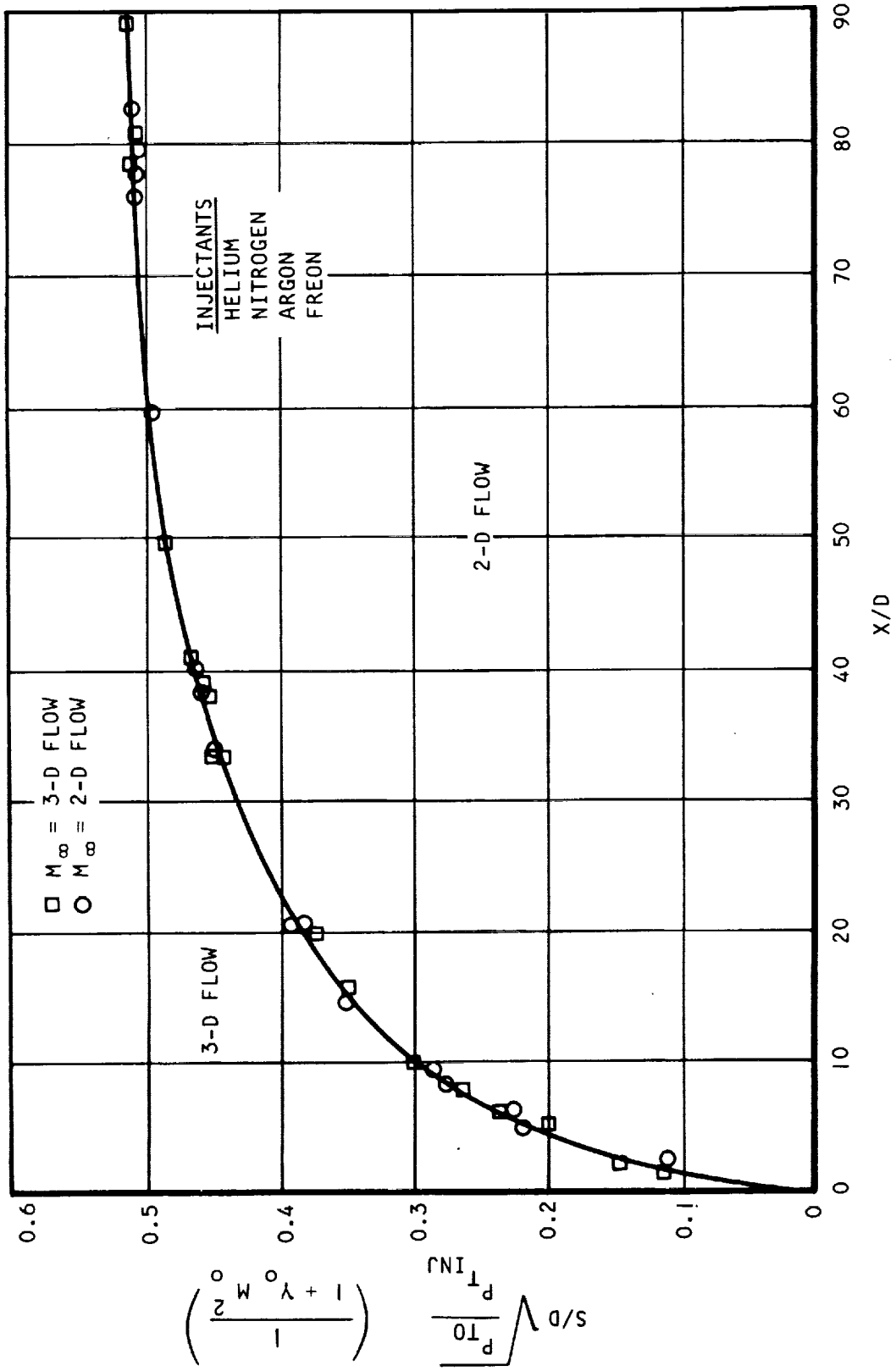

Figure 8.5-7. Correlation of Two-Dimensional Flow Boundary Normal Sonic Injection Into Supersonic Mainstream

The mixing parameter, which was defined previously as the area ratio of the calculated mixing area divided by the minimum area required for complete combustion, can then be expressed as

$$\text{Mixing Parameter} = \frac{g_1(g)g_2(b)}{hs\ \phi}$$

$$= g_2(Z)g_4\left(\frac{b}{s}\right)$$

Because the functions g_2 and g_4 are not known, the chemical efficiency is plotted as a contour map against Z and b/S as the independent variables in Figure 8.5-8. The tests used for this correlation are tabulated in Tables 8.5-1 and 8.5-2.

The correlation is reasonably good for injectors of different diameters, spacings, and angles. For a fixed spreading parameter, the chemical efficiency increases almost linearly with the penetration parameter up to about 85-90 percent efficiency. After this, it levels off rapidly. At a high penetration parameter, the required spreading parameter for a fixed efficiency is lower than that required at low penetration parameter. This agrees with the concept of mixing area. Inspection of Figure 8.5-8 shows that for a fixed chemical efficiency the increase in penetration decreases the spreading or vice versa. The exact dependence of the combustion efficiency on these parameters is not known. However, from the experimental data previously presented it seems that the penetration has a stronger effect than spreading on the combustion efficiency.

Thus this plot implies that it is easier to achieve high chemical efficiency at high penetration parameters than low penetration parameters. For example, if one wishes to improve the chemical efficiency from 60 to 80 percent at a penetration parameter of 1.73, it is necessary to improve the spreading parameter from 6 to 8. However, if the penetration parameter were 1.5, it would be necessary to improve the spreading parameter from 12 to 18. The dotted lines represent lower air inlet total temperature cases lying on the right of the higher total temperatures. Physically, this means that in order to obtain the same efficiency, the case of lower air inlet total temperature requires a higher penetration or larger spreading.

A cross-plot for a constant chemical efficiency of 90 percent is shown in Figure 8.5-9 for two different temperatures simulating Mach 6 and 7 flight conditions. For a fixed penetration parameter (2.0) the required spreading parameter increases almost fourfold when inlet total temperature decreases from 3800° to 2900°R. This clearly indicates the chemical kinetics effects, requiring greater combustor lengths at lower temperatures.

Method II: From Figure 8.5-7 (Reference 8-4) and some experimental observations, it is possible to show that the spreading parameter depends on

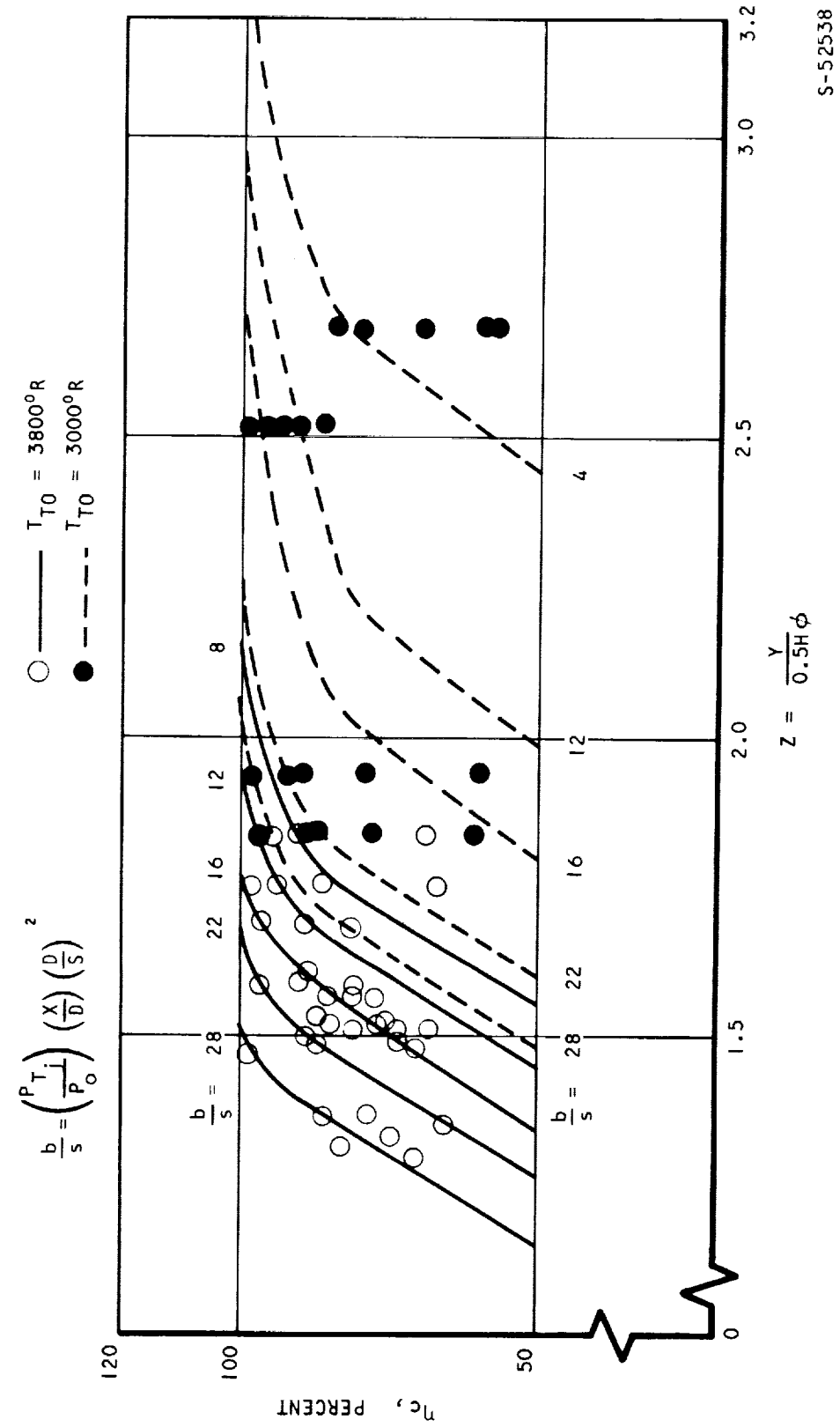

Figure 8.5-8. Chemical Efficiency Correlation with Mixing Parameters (U)

TABLE 8.5-1

SUMMARY OF COMBUSTOR TESTS

Runs	Injector Diameter, in.	Number of Injectors	Injector Spacing, in.	S/D	Injection Angle, deg.
140	0.1	15	0.55	5.5	90
141	0.1	15	0.55	5.5	90
142	0.1	15	0.55	5.5	90
143	0.1	15	0.55	5.5	90
147	0.15	7	1.25	8.33	60
148	0.15	9	0.825	5.5	60
151	0.1	9	0.95	9.5	60
158	0.1	9	0.95	9.5	60
185	0.2	5	1.9	9.5	90
217	0.1	13	0.6	6	90

TABLE 8.5-2

COMBUSTOR TESTS

Runs	ϕ	$\frac{P_{T_j}}{P_{T0}}$	$Z = \frac{Y}{0.5H}$	T_{T0}, °R
140	0.41	0.287	1.528	3800
140	0.50	0.346	1.480	3800
140	0.59	0.3920	1.373	3800
141	0.24	0.1847	1.694	3800
141	0.61	0.3869	1.328	3800
142	0.65	0.4123	1.297	3800
143	0.27	0.215	1.568	3800
143	0.32	0.2536	1.604	3800
143	0.40	0.320	1.492	3800
143	0.50	0.3906	1.367	3800
143	0.55	0.4162	1.309	3800
147	0.49	0.354	1.837	3800
147	0.56	0.4047	1.75	3800
148	0.48	0.3174	1.528	3800
148	0.55	0.3515	1.515	3800
148	0.60	0.3702	1.511	3800
151	0.56	0.5728	1.589	3800
151	0.59	0.6179	1.565	3800
158	0.39	0.363	1.920	3000
158	0.41	0.380	1.84	3000
217	0.216	0.280	2.52	3000

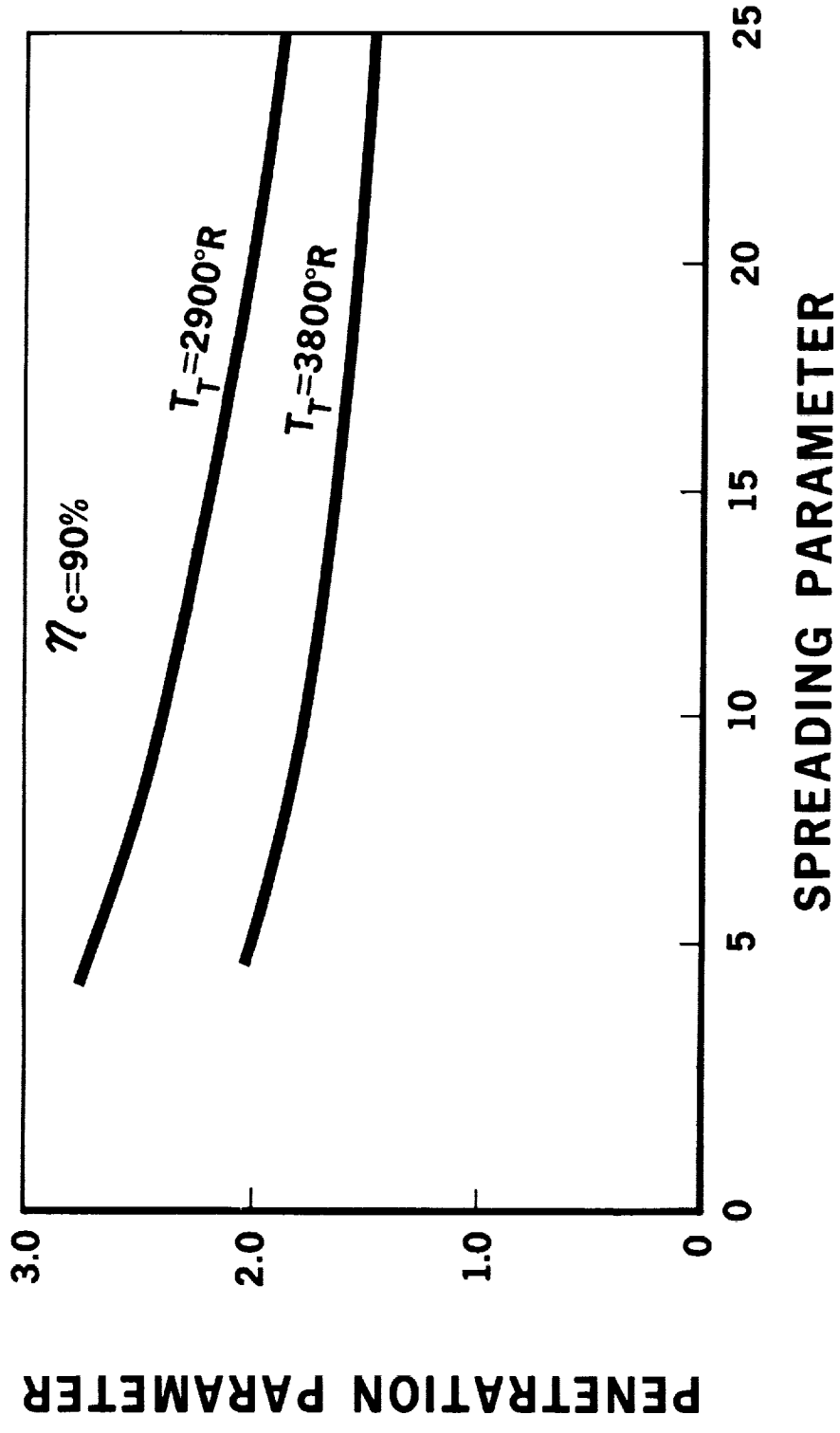

Figure 8.5-9. Correlation of Spreading and Penetration Parameters (U)

the following dimensionless groups:

$$\frac{P_{T_j}}{P_{T0}}, \frac{D}{S}, \frac{X}{D}, \frac{T_{T_j}}{T_{T0}}, \frac{M_j}{M_o}, \frac{\gamma_j}{\gamma_o}, \frac{W_j}{W_o}$$

A general functional relationship of spreading parameter b/S may then be written,

$$\frac{b}{S} = f\left(\frac{P_{T_j}}{P_{T0}}, \frac{D}{S}, \frac{X}{D}, \frac{T_{T_j}}{T_{T0}}, \frac{M_j}{M_o}, \frac{\gamma_j}{\gamma_o}, \frac{W_j}{W_o}\right) \qquad (8-9)$$

This expression can be simplified further. It is believed that the penetration is relatively insensitive to the molecular weight and specific heat ratios; this same assumption will also be made for the spreading parameter. It is further assumed that the effects of stagnation temperature and Mach number are negligible. The expression then simplifies to:

$$\frac{b}{S} = f\left(\frac{P_{T_j}}{P_{T0}}, \frac{D}{S}, \frac{X}{D}\right) \qquad (8-10)$$

A new penetration parameter is defined as

$$Z = \frac{Y}{H} \qquad (8-11)$$

Based on the mixing controlled combustion concept, the chemical efficiency η_c was first assumed to correlate as

$$\eta_c \text{ vs } (Z)^{\delta_1}\left(\frac{P_{T_j}}{P_{T0}}\right)^{\delta_2}\left(\frac{D}{S}\right)^{\delta_3}\left(\frac{X}{D}\right)^{\delta_4} \quad \frac{1}{\phi} \qquad (8-12)$$

It was observed from the test data that the combustion efficiency depends on X rather than X/D. In order to have a dimensionless group, X/D was replaced by X/H:

$$\eta_c \text{ vs } \frac{1}{\phi}\left\{(Z)^{\delta_1}\left(\frac{P_{T_j}}{P_{T0}}\right)^{\delta_2}\left(\frac{D}{S}\right)^{\delta_3}\left(\frac{X}{H}\right)^{\delta_4}\right\} \qquad (8-13)$$

The δ_1's were determined by the method of cut and try to fit the experimental data. The resultant correlation was

$$\eta_c \text{ vs } \frac{1}{\phi} Z^{\frac{1}{2}} \left(\frac{P_{T_j}}{P_{T0}}\right)^{\frac{1}{4}} \left(\frac{D}{S}\right)^{\frac{1}{2}} \left(\frac{X}{H}\right)^{\frac{1}{2}} \tag{8-14}$$

or

$$\eta_c \text{ vs } \frac{\sqrt{Zb/s}}{\phi} \tag{8-15}$$

where

$$Z = \frac{Y}{H} = \text{penetration parameter}$$

$$b/S = \left(\frac{P_{T_j}}{P_{T0}}\right)^{\frac{1}{2}} \left(\frac{D}{S}\right)\left(\frac{X}{D}\right) = \text{spreading parameter}$$

Figure 8.5-10 shows this correlation, which does not include effects of combustor inlet temperature.

Substituting in Equation (8-14) the initial definition for Z , the following is obtained.

$$\eta_c \text{ vs } \left(\frac{P_{T_j}}{P_{T0}}\right)^{\frac{1}{2}} \left(\frac{X}{H}\right)^{\frac{1}{2}} \left(\frac{D}{S}\right)^{\frac{1}{2}} \frac{1}{\phi} \tag{8-16}$$

where air and fuel are at constant Mach numbers.

Effects of the air inlet total temperature can now be included in this correlation. The chemical kinetic effects of temperature can be evaluated using the ignition delay and chemical reaction time based on an empirical correlation (Reference 8-5), i.e.,

$$\tau_{ID} = \frac{9.522}{P} \exp\left(\frac{1800}{T}\right)$$

$$\tau_R = 105 \left(\frac{2116}{P}\right)^{1.7} \exp\left(\frac{0.622T}{1000}\right) \tag{8-17}$$

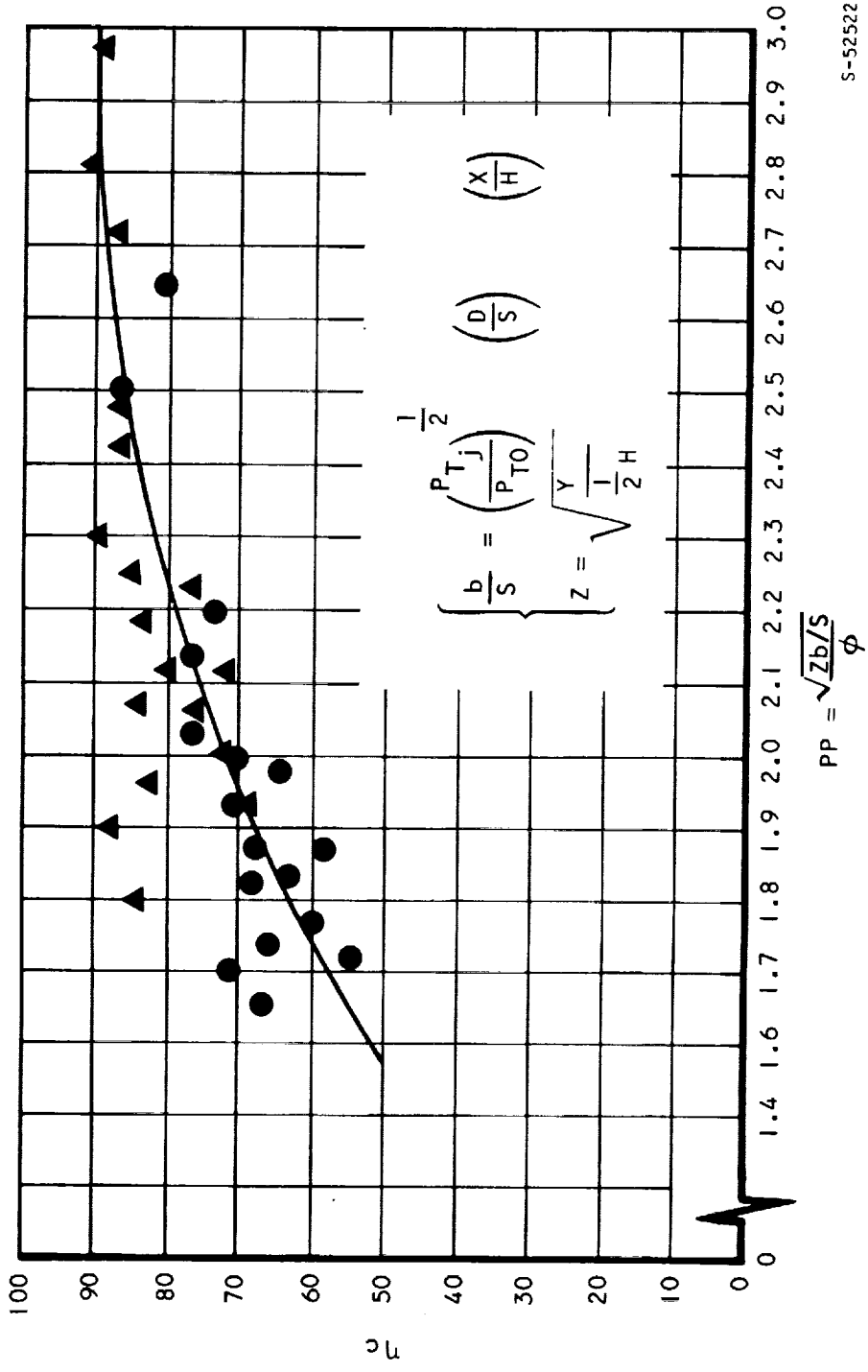

Figure 8.5-10. Correlation of Spreading and Penetration Parameters (U)

where τ_{ID} and τ_R are the ignition delay and chemical reaction time respectively. Chemical efficiency is a function of τ_{ID} and τ_R, and they are related exponentially to the local temperature. Therefore, it is expected that the inlet total temperature effect would enter into the correlation in some exponential form. By the method of cut and try, the correlation including the inlet total temperature effect is

$$\eta_c \quad vs \quad \frac{\sqrt{Zb/s}}{\phi} \quad \exp\left(-\frac{T_{TO}-T_T}{2T_{TO}}\right) \tag{8-18}$$

where T_{TO} = the reference total temperature of air. The open symbols in Figure 8.5-11 are the data for $T_T = 3800^0R$, whereas, the data of $T_T = 3000^0R$ is plotted in closed symbols. It is seen that correlation is reasonably good.

Similar to Method II, except defining the parameters based on the equivalence ratio, we have

$$\text{spreading parameter} = \frac{b}{S} = \frac{1}{\phi}\left(\frac{P_{T_j}}{P_{TO}}\right)^{\frac{1}{2}}\left(\frac{D}{S}\right)\left(\frac{X}{H}\right)$$

$$\text{penetration parameter} \quad Z = \frac{1}{\phi}\left(\frac{Y}{.5H}\right)$$

and the resultant correlation is obtained as

$$\eta_c \quad vs \quad \left[\frac{1}{\phi}\left(\frac{Y}{.5H}\right)^2\right]\left[\frac{1}{\phi}\left(\frac{P_{T_j}}{P_{TO}}\right)^{\frac{1}{4}}\left(\frac{D}{S}\right)^{\frac{1}{2}}\left(\frac{X}{H}\right)^{\frac{1}{2}}\right] \tag{8-19}$$

This equation differs slightly from Equation (8-14). Again to include the inlet total temperature effect, we get

$$\eta_c \quad vs \quad \left[\frac{1}{\phi}\left(\frac{Y}{.5H}\right)^2\right]\left[\frac{1}{\phi}\left(\frac{P_{T_j}}{P_{TO}}\right)^{\frac{1}{4}}\left(\frac{D}{S}\right)^{\frac{1}{2}}\left(\frac{X}{H}\right)^{\frac{1}{2}}\right]\exp\left\{-\frac{2(T_{TO}-T_T)}{T_{TO}}\right\} \tag{8-20}$$

In Figure 8.5-12, the results for $T_T = 3800^0R$ and $T_T = 3000^0R$ are plotted in open symbols and closed symbols respectively. The data scatter is about as large as that in Figure 8.5-11.

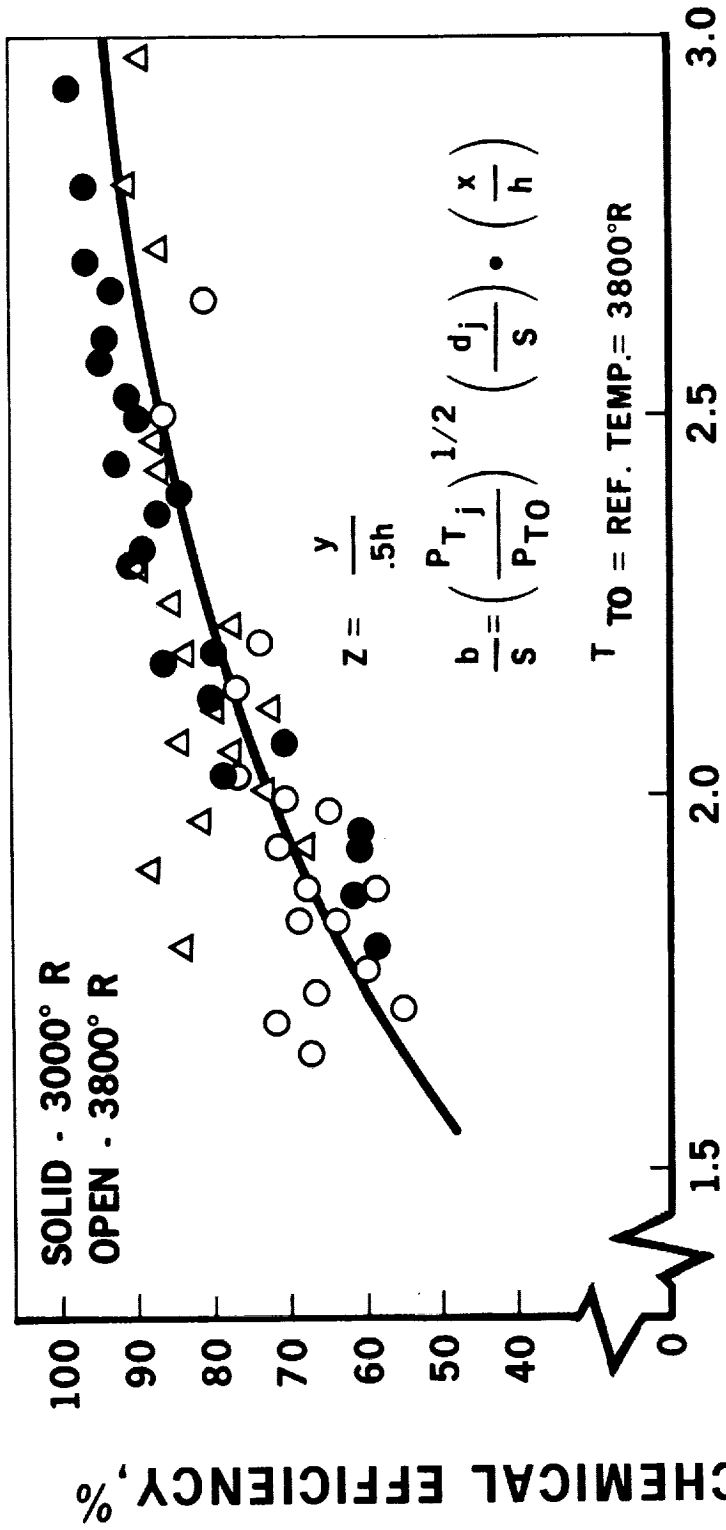

Figure 8.5-11. Lumped Correlation Parameter (U)

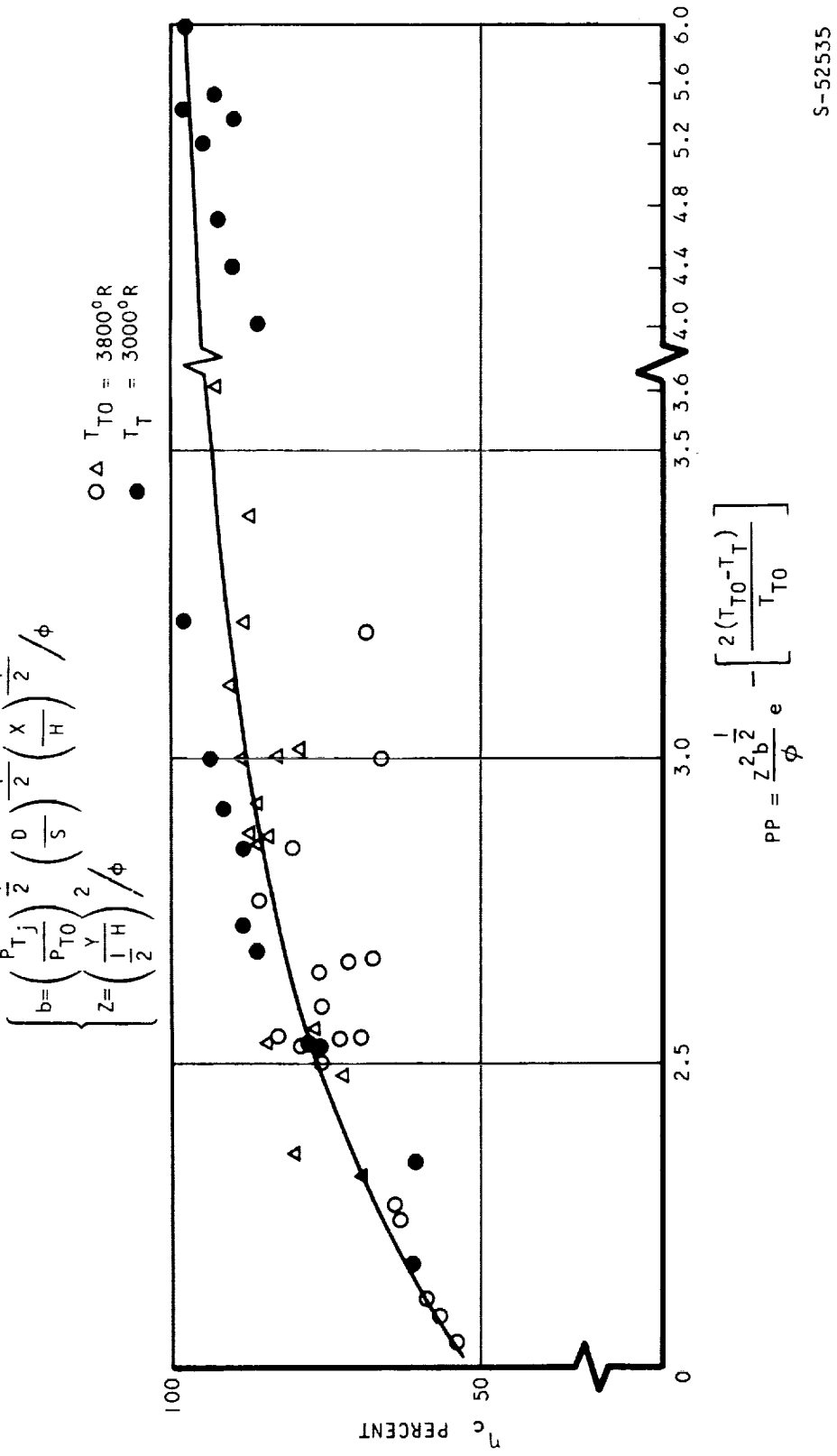

Figure 8.5-12. Correlation of Spreading and Penetration Parameters (U)

In summary:

(a) Based on the mixing-controlled combustion concept, a simple power law relationship can be used to correlate the combustion efficiency for the fuel injector design.

(b) Three correlations were obtained with the basic independent dimensionless groups the same.

(c) Although the simple relationships did not give the detailed functional dependence on the spreading and penetration, the trends shown by the correlations may be useful in designing fuel injectors for a scramjet combustor.

8.5.2 Pressure Rise Correlation

Supersonic combustor performance is reduced by the effects from three major sources:

(a) Incomplete combustion

(b) Losses due to combustion, shock, flow separation and mixing

(c) Viscous drag

The first source is concerned with energy while the latter two concern the entropy. It is desirable to define these losses in terms of parameters which can be directly measured. However, this is very difficult because of severe instrumentation limitations, both in measuring local gas dynamic properties and in determining the temperature and the composition of the gas. Therefore, an alternative method must be used. Incomplete combustion is assessed by the chemical efficiency as discussed in previous sections. In the earlier phase of the HRE study, the losses due to combustion, shock, flow separation, and mixing were assessed by a lumped parameter-pressure integral--which is indicative of the change of momentum. Although this parameter was convenient mathematically, it did not seem to be ideally suited to correlation of experimental results. For this reason an alternative method was sought.

The method proposed is based on the difference in static pressure between the combustor inlet and exit. It is assumed that heat addition, heat loss to the walls, and viscous drag are the dominant influences in determining the combustor static pressure for a given combustor area ratio. This can be readily explained by influence coefficients.

The influence coefficients given by Shapiro (Reference 8-6) are

$$\frac{dP}{P} = \frac{KM^2}{1-M^2}\frac{dA}{A} - \frac{KM^2}{1-M^2}\frac{dQ + dH}{C_pT} - \frac{KM^2\left[1 + (K-1)M^2\right]}{2(1-M^2)}\,4f\frac{dX}{D} \qquad (8\text{-}21)$$

or

$$\frac{1-M^2}{KM^2}\frac{dP}{P} = \frac{dA}{A} - \frac{dQ + dH}{C_pT} - \left[1 + (K-1)M^2\right]2f\frac{dX}{D} \qquad (8\text{-}22)$$

where

A = area

C_p = specific heat at constant pressure

D = hydraulic diameter

f = friction factor

H = the heat added to the flow

K = specific heat ratio

M = Mach number

P = static pressure

Q = the heat loss through the walls

T = static temperature

X = axial coordinate

The simplified form of Equation (8-22) used for correlation is

$$\left(\frac{P_4}{P_3} - 1\right)\left(\frac{M_3^2 - 1}{\gamma_3 M_3^2}\right) = f\left\{\frac{Q_n}{C_{P_3} T_3} + 2\left[1 + (\gamma_3 - 1) M_3^2\right]\frac{C_f L}{D}\right\} \quad (8\text{-}23)$$

where Q_n is the net heat added to the flow as a result of combustion and heat loss to the walls.

C_f is the average friction coefficient.

D is combustor hydraulic diameter.

L is combustor length.

Subscript 3 refers to the combustor entrance plane.

Subscript 4 refers to the combustor exit plane.

A plot based on the above equation is given in Figure 8.5-13 for combustor area ratios of 1.0 to 2.9. The test conditions used include several inlet total temperatures and combustor geometries, and a range of equivalence ratios less than unity. The degree of correlation is encouraging, particularly when the large number of measured parameters is considered.

The effect of combustor exit pressure on engine performance can be seen by a review of a continuity-momentum diagram, an example of which is given in Figure 8.5-14. A continuity-momentum diagram gives the spectrum of combustor exit states for one-dimensional flow at a given energy level. (Energy level is specified in terms of flight Mach number, hydrogen equivalence ratio, and chemical efficiency.) Inlet performance data give the flow per unit area (W/A) and static pressure (p) at the combustor entrance. Once the equivalence ratio and chemical efficiency are specified, the flow per unit area and static pressure at the combustor exit complete the information needed to locate a point on the continuity-momentum diagram, and thus determine combustor performance.

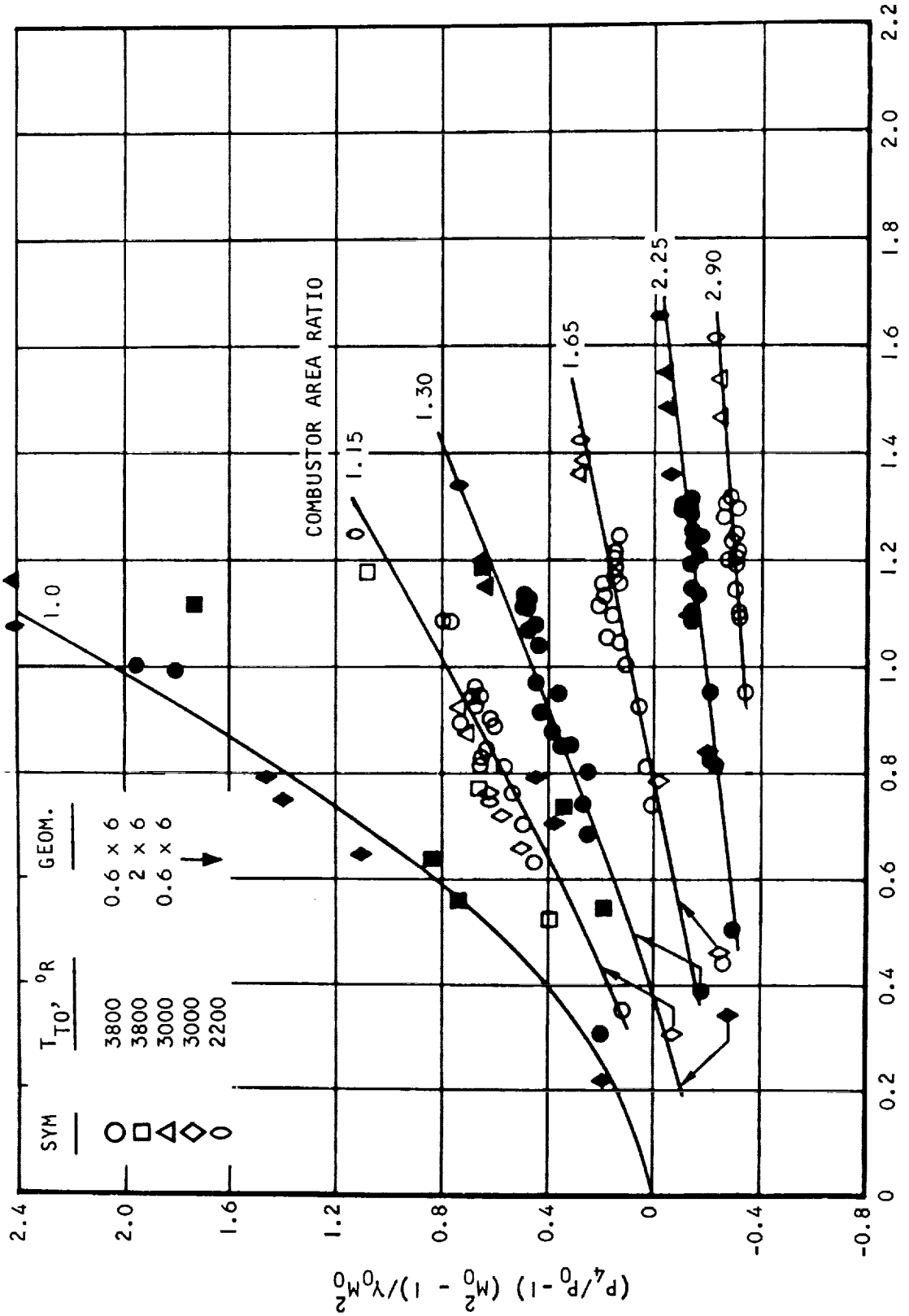

Figure 8.5-13. Combustor Pressure Rise Correlation (U)

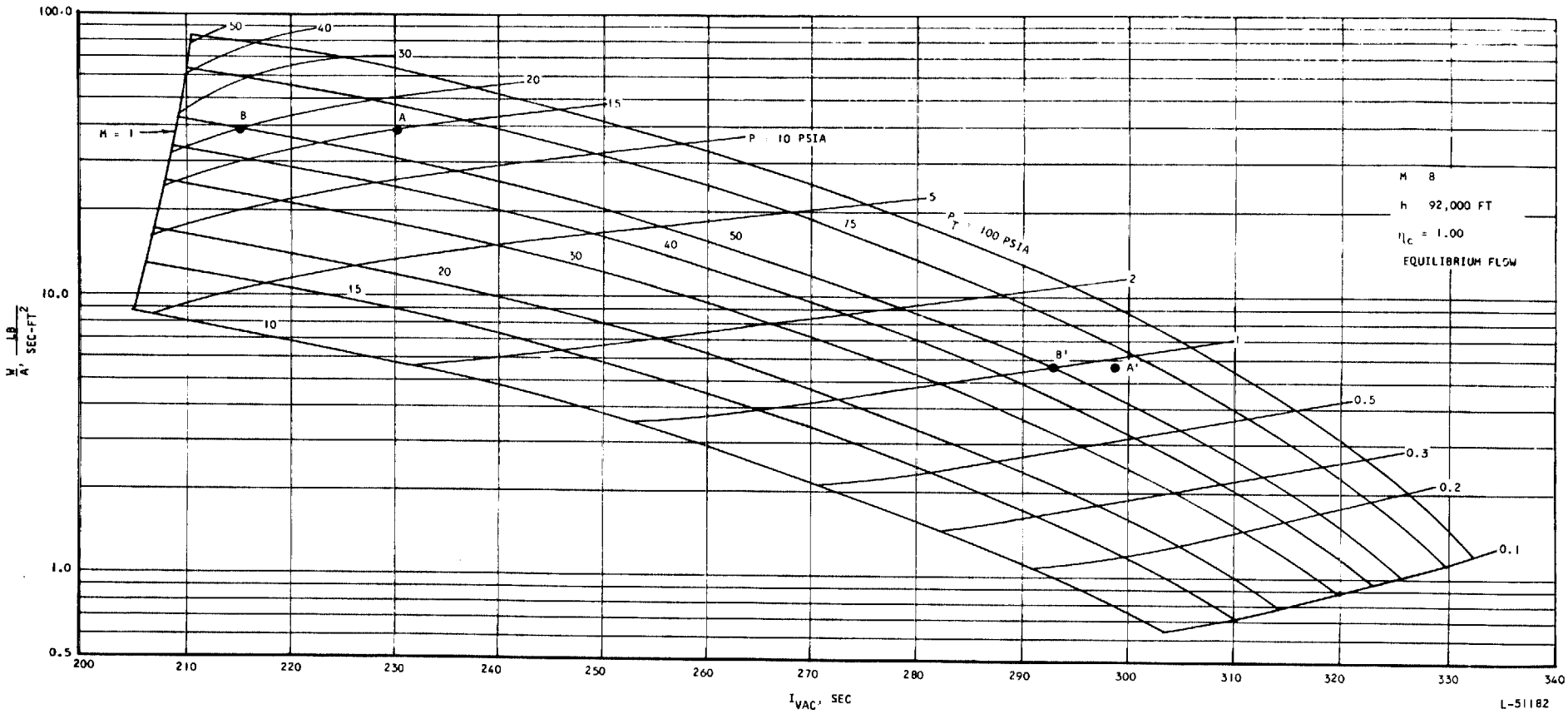

FOLDOUT FRAME 1

FOLDOUT FRAME 2

Figure 8.5-14. Continuity-Momentum Diagram for Mach 8, ϕ = 1 (U)

AIRESEARCH MANUFACTURING COMPANY
Los Angeles, California

An idea of the accuracy needed can be obtained from Figure 8.5-14 (note that for a given energy and mass flow, lower static pressures yield better performance). Assume that the predicted pressure is 15 psia with W/A = 39 lb/sec ft^2 (point A). Ideal expansion of the flow to W/A = 5.7 lb/sec ft^2, or a static pressure slightly below 1 psia (point A'), would give a vacuum gross specific impulse (I_{vac}) of approximately 299 sec.

If the actual combustor exit pressure were 20 psia (point B in Figure 8.5-14) instead of the predicted 15 psia, expansion through the same area ratio to point B' would give a vacuum gross specific impulse of 293 sec. At Mach 8 this corresponds to an error of approximately 11 percent in the net internal thrust. Thus, for the condition cited each three percent of error in the predicted combustor exit pressure gives, on the average, a one percent error in predicted internal thrust. (Note that chemical efficiency is assumed to be accurately known.)

8.5.3 Average Friction Factor

A dominant factor in determining combustor exit pressure is combustor friction. The combustor friction drag, as determined from thrust measurements, varied from 45 to 65 lb, with the majority of data occurring at a drag of about 50 lb. The data are translated into combustor friction coefficient in Figure 8.5-15. The range of friction coefficients is 0.004 to 0.0062, with most of the values near 0.005.

SOLID = 3800°R
OPEN = 3000°R
○ FIRST STAGE INJECTION ONLY
△ FIRST AND SECOND STAGE INJECTION
* 2 X 6 IN. COMBUSTOR

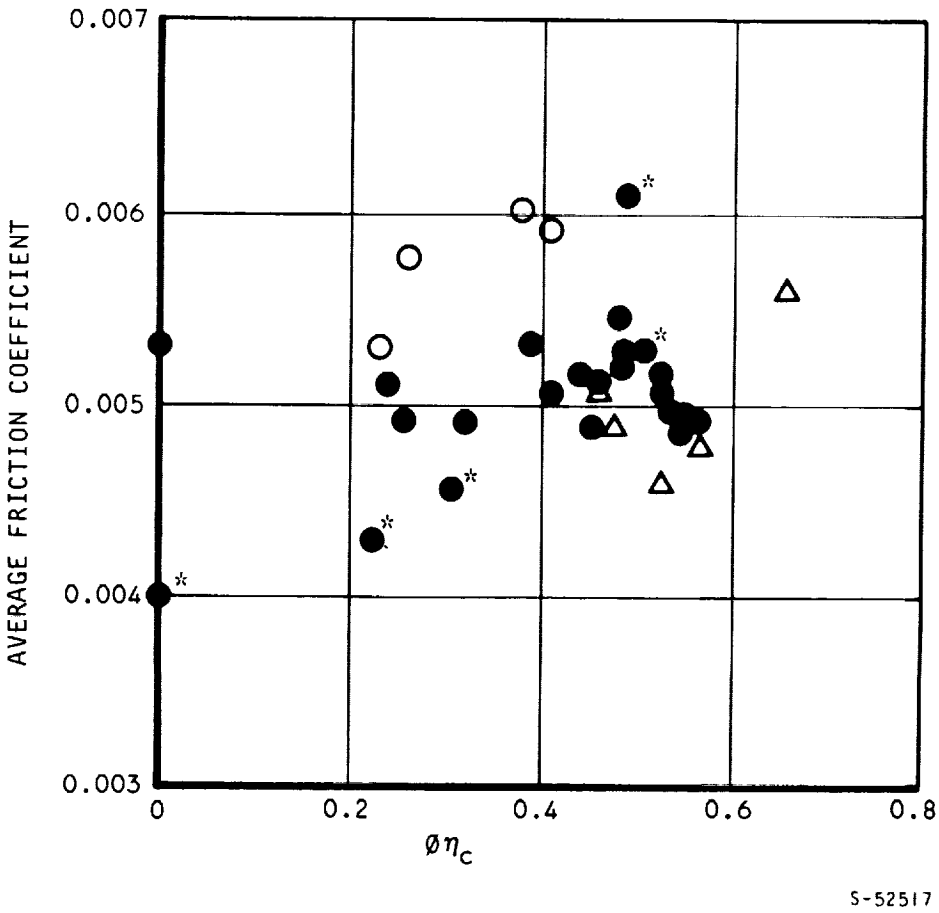

Figure 8.5-15. Combustor Friction Coefficient (U)

8.6 GAS SAMPLING

The gas sampling probe was used to determine the time-averaged local equivalence ratio at various points in the combustor. No attempt was made to freeze chemical reactions in the sample.

Because the gas sampling system required several seconds to respond to a change in sample composition, no fluctuations on a smaller time scale could be measured.

The sampling period for each point was about 20 sec. This allowed sufficient time for the sample flow composition to stabilize and for several gas analyses to be made.

A typical probe traverse map is shown in Figure 8.6-1. The number of points at which samples were taken during any given run depended on the time available, and in some cases was considerably less than the 34 points shown in the figure.

The gas composition is expressed in terms of the local equivalence ratio, ϕ_L. The data reduction methods used are described in Appendix C.

Unless otherwise noted, the probe was positioned 3/4-in. (one probe width) downstream of the combustor exit, and the inlet total temperature corresponded to Mach 6 flight.

Several Mach 6 test runs were made in which gas sampling data were taken with fuel injection at the first stage only, at equivalence ratios in the range 0.2 to 0.3. Injection was from seven 0.100-in.-dia orifices on the lower wall only. The gas sampling data for the combustor exit gases indicated fairly uniform mixing; however, the data are suspect because the flow was separated at the exit. The data will therefore not be reviewed here; the only conclusion being that any gross heterogeneities in composition at these conditions could not be detected by using the probe at the combustor exit.

For all the two-stage gas sampling results to be discussed below, the first-stage injectors had 13 0.100-in.-dia orifices--seven on the lower wall and six on the upper wall. Injection in the first stage was normal to the vitiated air stream.

In run 235 most of the fuel was introduced through the second-stage injectors ($\phi_1 = 0.2$, $\phi_2 = 0.5$). In the second stage, three orifices, all 0.160 in. in dia and on the top wall, were used. The gas sampling results, shown in Figure 8.6-2, indicate poor mixing in the second stage. The left-hand plot shows ϕ_L vs horizontal distance, X. Peaks corresponding to two of the injector orifices can be seen. (No points were sampled directly downstream of the third orifice.) The second-stage injection scheme is indicated schematically by the arrows at the top of the figure.

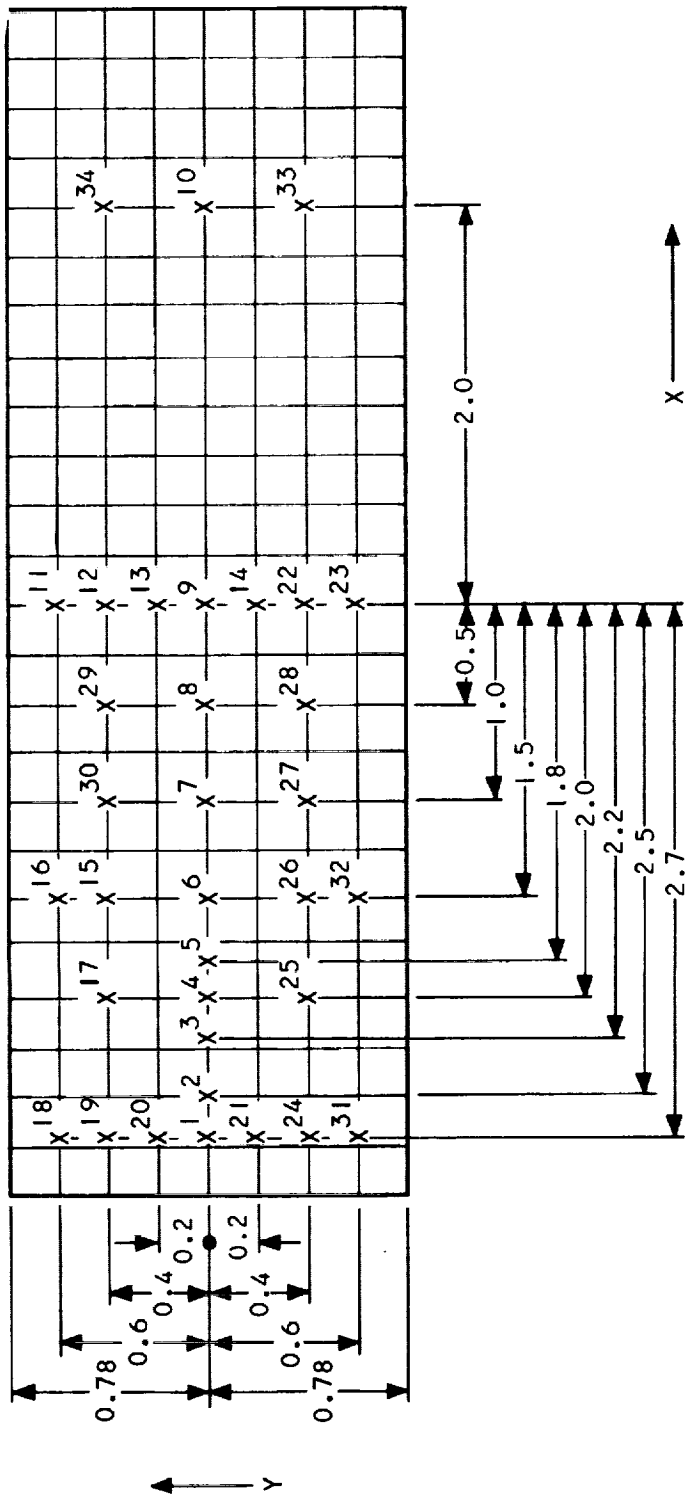

Figure 8.6-1. Typical Gas Sampling Traverse Map

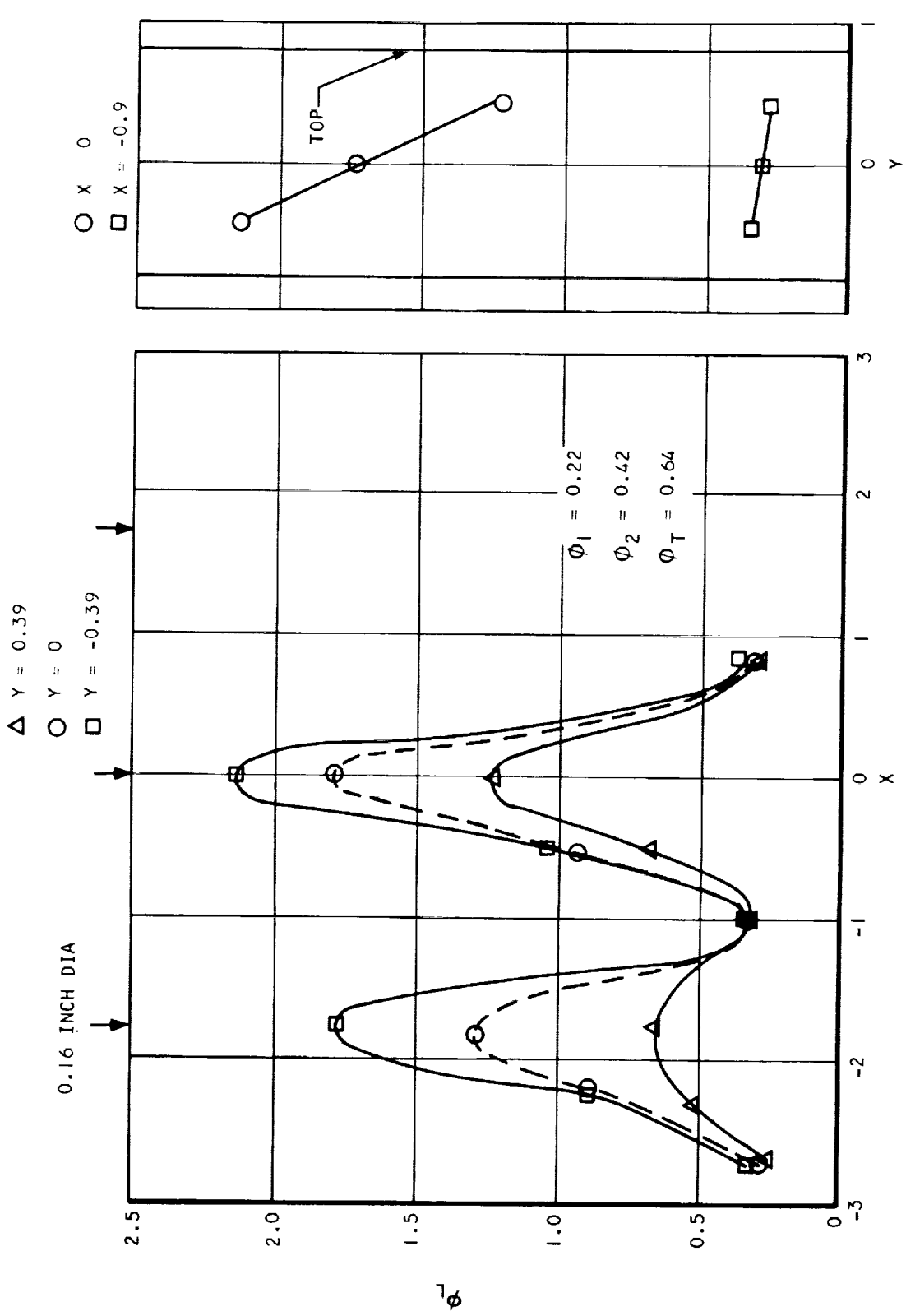

Figure 8.6-2. Gas Sampling Data From Run 235

The existence of regions where $\phi_L > 1$ indicates a priori that chemical efficiency was less than unity for this run. Three of the points gave gas samples with over 20 percent H_2 by volume. Note that the samples were taken more than 60 orifice diameters downstream of the injectors.

The higher peak from the center orifice may indicate that some of the air was diverted around the injector toward the combustor's side walls. More evidence of this will be seen later.

The right-hand plot in Figure 8.6-2, showing ϕ_L vs vertical distance, Y, indicates that the fuel jets penetrated well past the combustor's centerline (Y = 0). Jet spreading appears to be a limiting process for the second stage in this case, indicating that injectors with a larger number of more-closely-spaced orifices might give an improved mixing profile.

In run 238, each of the two injection stages had 13 0.100-in.-dia orifices. In the first stage, injection was normal to the airstream; in the second stage, the orifices were angled 45 deg upstream.

The gas sampling data are shown in Figure 8.6-3. The absence of points for $\phi_L > 1$ seems to indicate that at least on a time-averaged, macroscopic basis, the gases are mixed well enough to allow complete combustion of the fuel. The gas sampling data thus eliminate one possible explanation for the low second-stage chemical efficiency calculated for this run (about 60 percent).

In run 240 the test conditions were similar to those of run 238. The gas sampling results are shown in Figure 8.6-4 and indicate that the profile reproduces reasonably well from run to run.

In run 237 an equivalence ratio near unity was run with the same injectors; Figure 8.6-5 shows the gas sampling results. In Figure 8.6-6, similar results are shown for a higher equivalence ratio. In both cases the equivalence ratio along the vertical centerline of the combustor is much higher than the overall equivalence ratio. A simple calculation indicates that this effect is not due solely to poor lateral spreading of the fuel from the injectors toward the combustor side walls. The injection orifices span 3.7 in. of the combustor's width. If the fuel does not spread beyond this region, the average equivalence ratio in the fuel-rich zone at $\phi_T = 1.12$ would be (1.12 x 6/3.7), or 1.81. The measured mixing profiles in Figures 8.6-5 and 8.6-6 indicate no local rich regions due to individual jets (in other words, fuel spreading between jets seems to be adequate) and one might expect the local equivalence ratio to be no larger than 1.81 in Figure 8.6-6. In fact the measured centerline ϕ_L's were 2.18 or greater. This may indicate that large amounts of the oxidant are being diverted around the sides of the injectors.

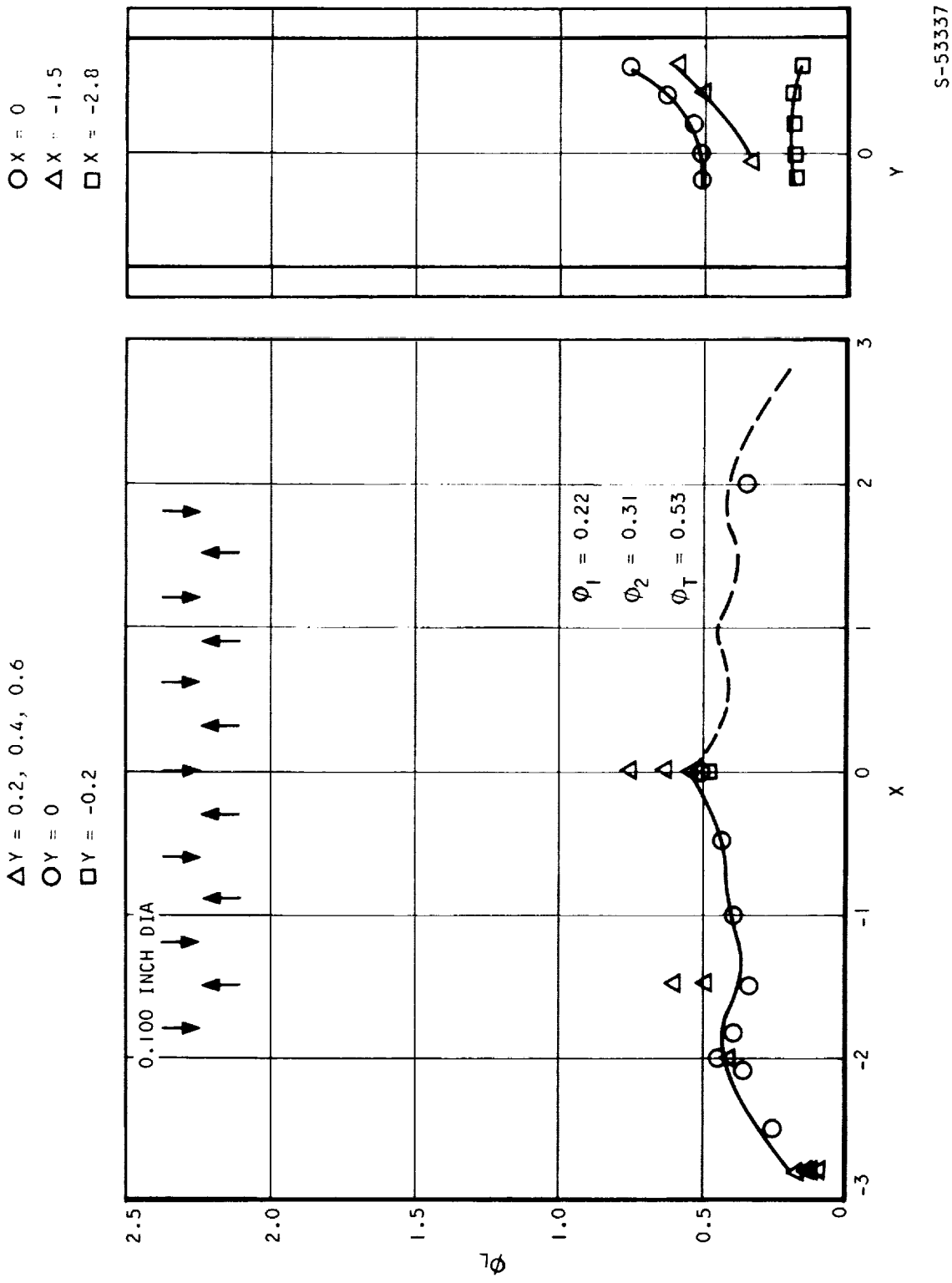

Figure 8.6-3. Gas Sampling Data From Run 238

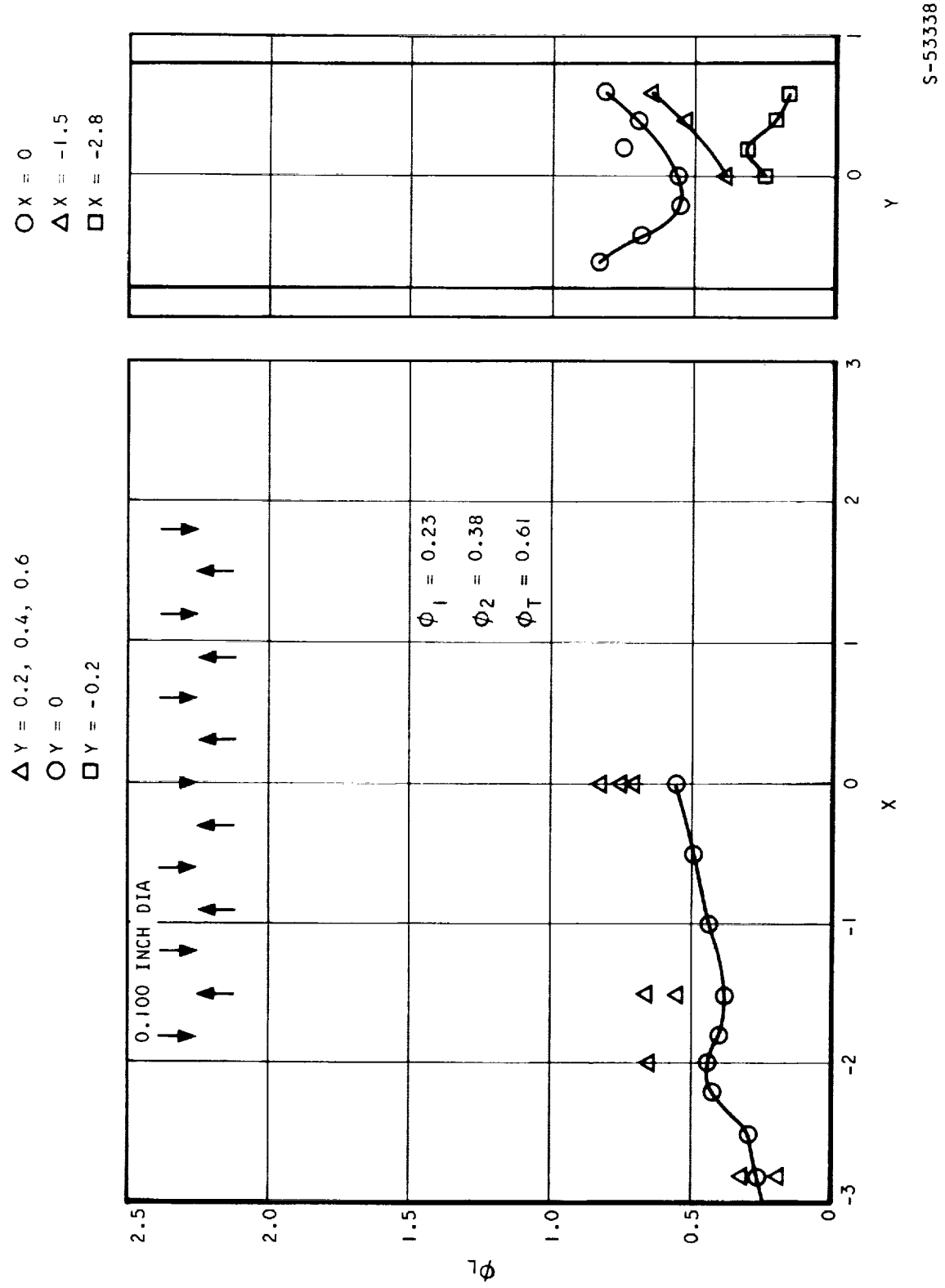

Figure 8.6-4. Gas Sampling Data From Run 240

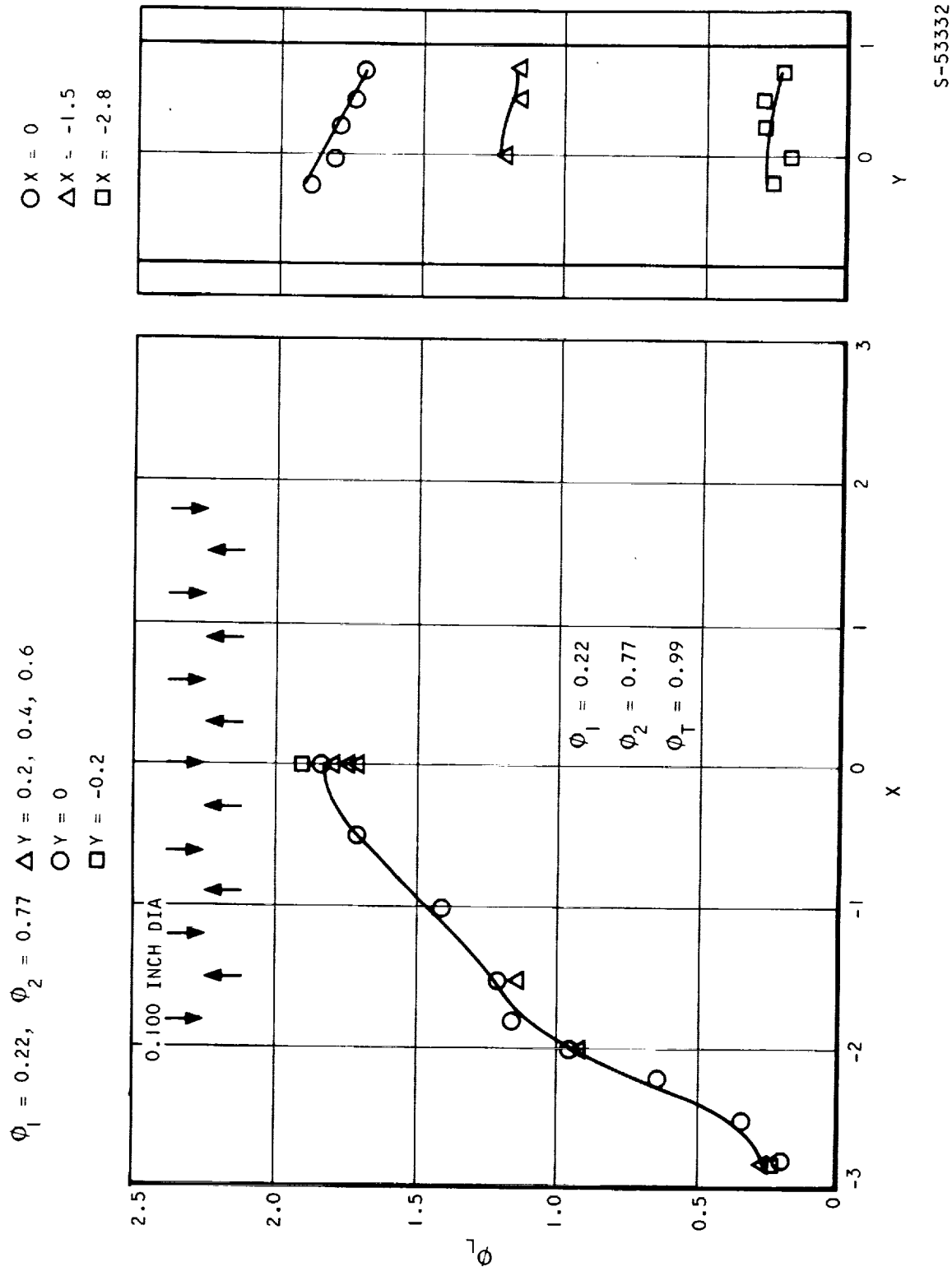

Figure 8.6-5. Gas Sampling Data From Run 237

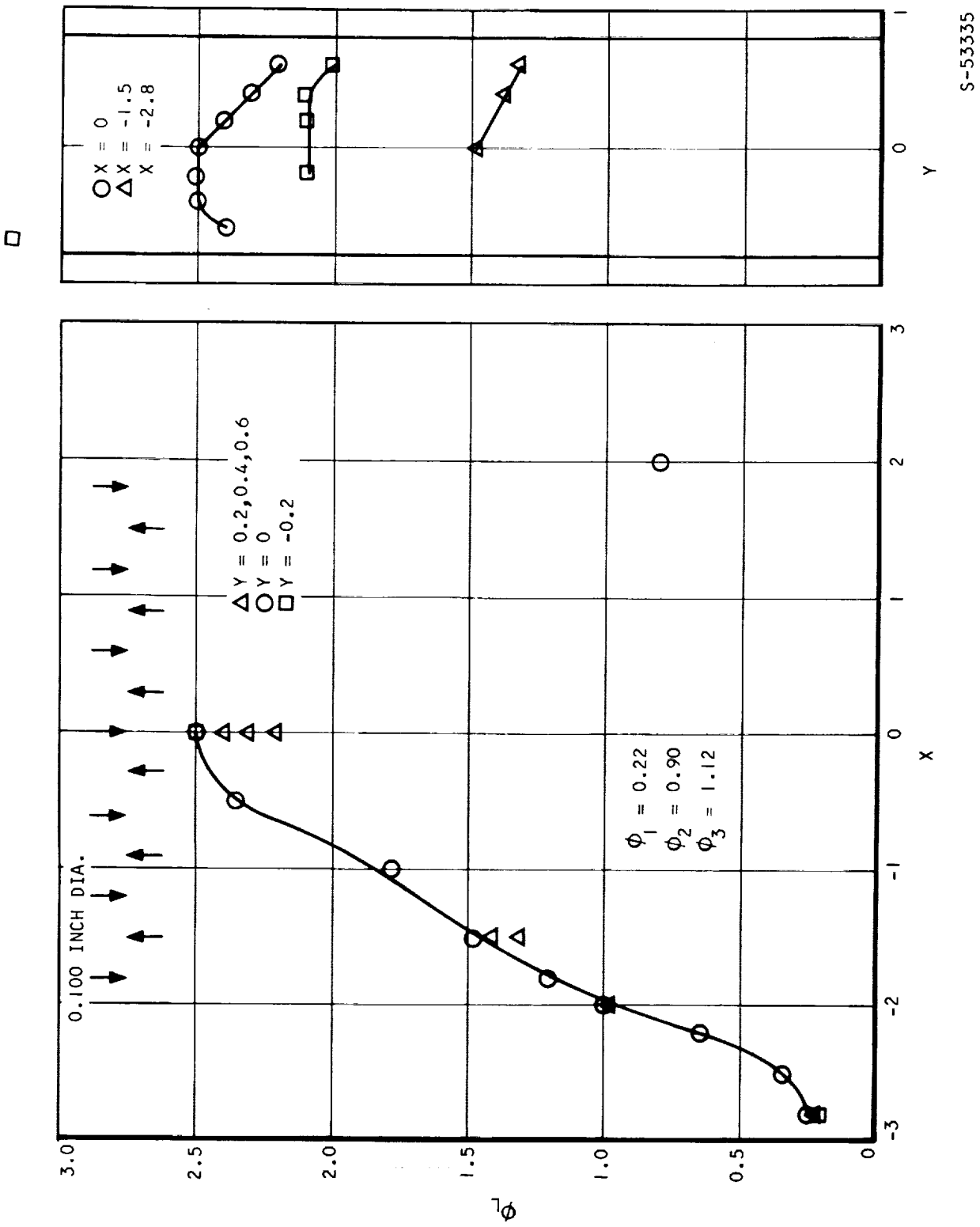

Figure 8.6-6. Gas Sampling Data From Run 239

The existence of a large region where $\phi_L > 1$ indicates that this injector combination cannot be expected to give good chemical efficiency in the two-dimensional combustor for equivalence ratios near unity. This gross maldistribution of fuel is due to the mechanical design of the two-dimensional combustor and is not expected to be present in the HRE.

In two-dimensional combustor run 212 the equivalence ratio was 1.55. The second-stage injector had only five orifices, each 0.160 in. in dia. The mixing profile, shown in Figure 8.6-7, does not show as pronounced a maldistribution as that in the previous figure: the peak equivalence ratios in the two figures are about equal despite the large difference in total equivalence ratio. The two runs are not strictly comparable, however, because in run 212 the probe was only 0.1 in. downstream of the combustor exit, and interfered with the flow in the combustor.

The five-orifice second-stage configuration was used at a lower equivalence ratio in run 232. The mixing profile is shown in Figure 8.6-8. In this case the central region of the combustor was again fuel-rich, but with large vertical gradients as well as horizontal variations.

In an attempt to improve the horizontal fuel distribution from this configuration, two 0.180-in.-dia orifices were added to one of the injectors. The new orifices were at either end of the injector and were angled at 45 deg toward the side walls of the combustor. The resulting mixing profile is shown in Figure 8.6-9. Although the equivalence ratio peak was shifted somewhat, the special injector did not give an even fuel distribution. The chemical efficiency was still low (see Section 8.3.4).

In run 245, all the fuel was injected from three 0.160-in. orifices in the upper wall at the second stage (injector station 2e). The gas sampling data are shown in Figure 8.6-10. The same configuration was also run at a slightly higher equivalence ratio. The results are shown in Figure 8.6-11. Figure 8.6-12 gives similar results obtained using three 0.228-in-dia orifices. In both cases the jets penetrated well beyond the combustor centerline. For most points the difference between the two patterns is small enough to be attributed to experimental error. The conclusion from this experiment is that the difference in mixing resulting from enlarging the orifice area by a factor of two was small.

A single traverse was made for the Mach 5 inlet total temperature. Fuel was injected at the first stage only. The results, shown in Figure 8.6-13, indicate a high equivalence ratio in the center of the combustor's width; this again is attributed to diversion of the air around the injectors. During this run there may have been a small separation region at the combustor exit.

Pitot pressures were measured for Mach 6 conditions at a high equivalence ratio in run 212. The profiles, shown in Figure 8.6.14, show a variation in pitot pressure only near the combustor wall. The points traversed were on the vertical and horizontal centerlines only, however.

The mixing profile for run 212 is shown in Figure 8.6-7. It is known the position of the probe affected the flow in the combustor during this run.

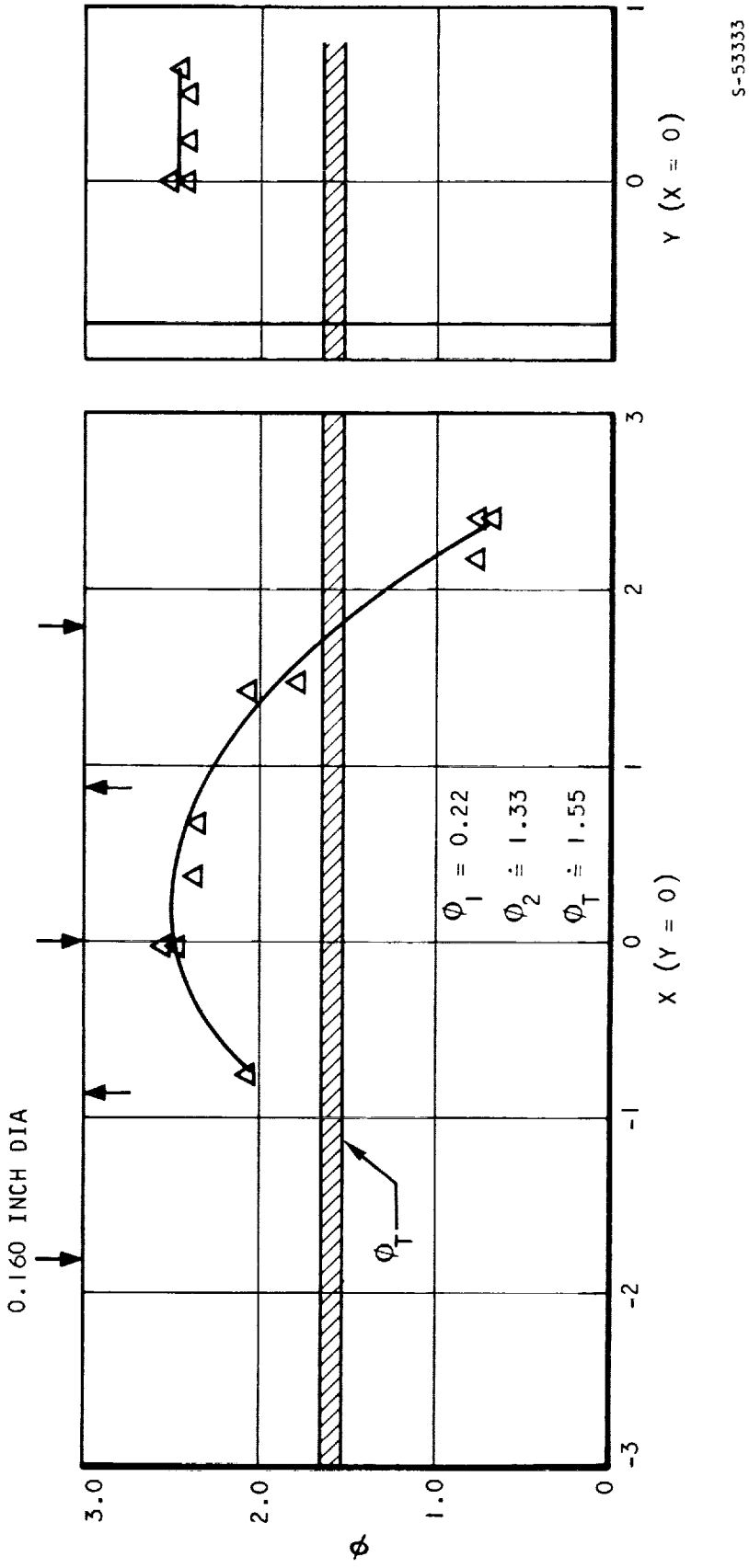

Figure 8.6-7. Gas Sampling Data From Run 212

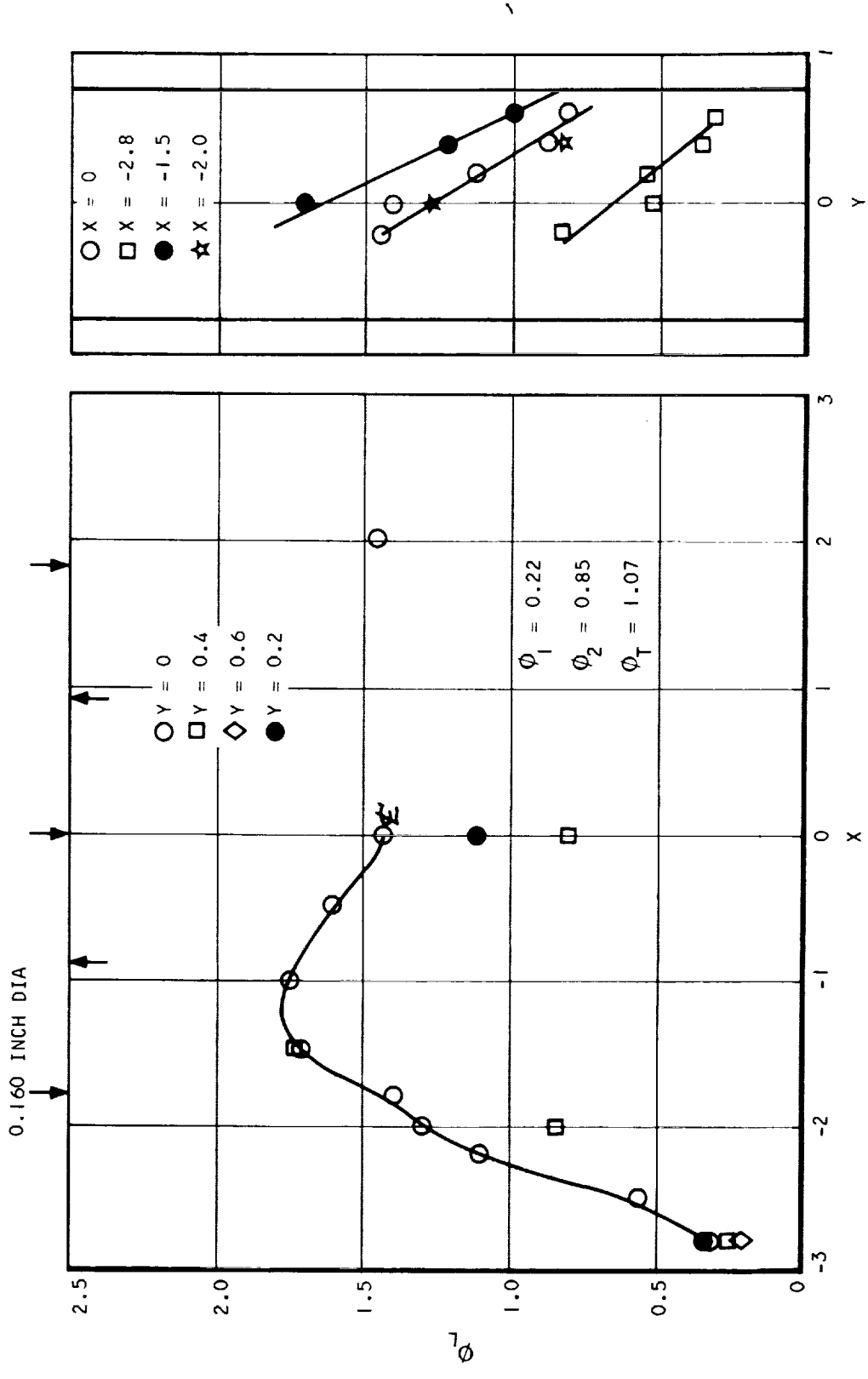

Figure 8.6-8. Gas Sampling Data From Run 232

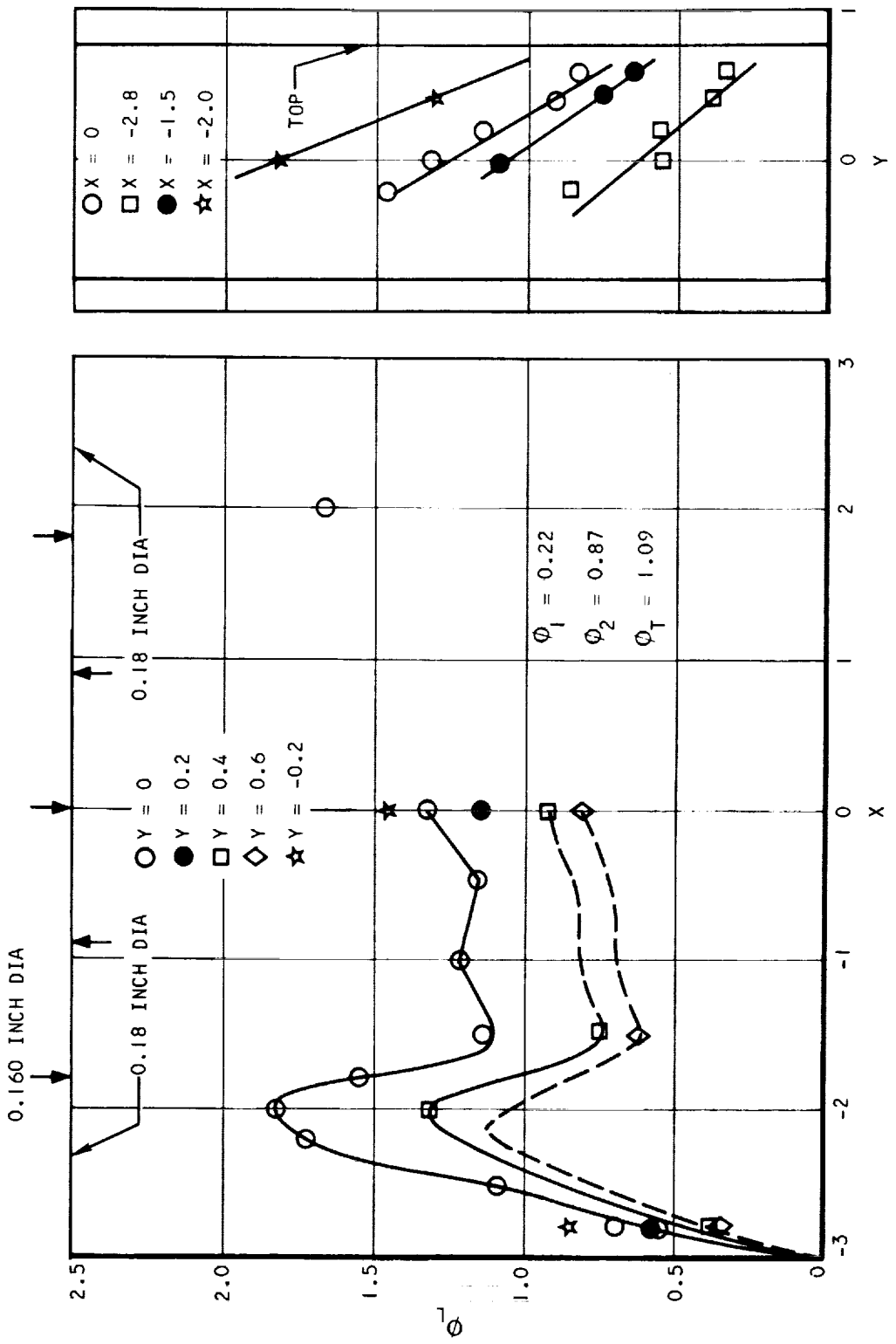

Figure 8.6-9. Gas Sampling Data From Run 233

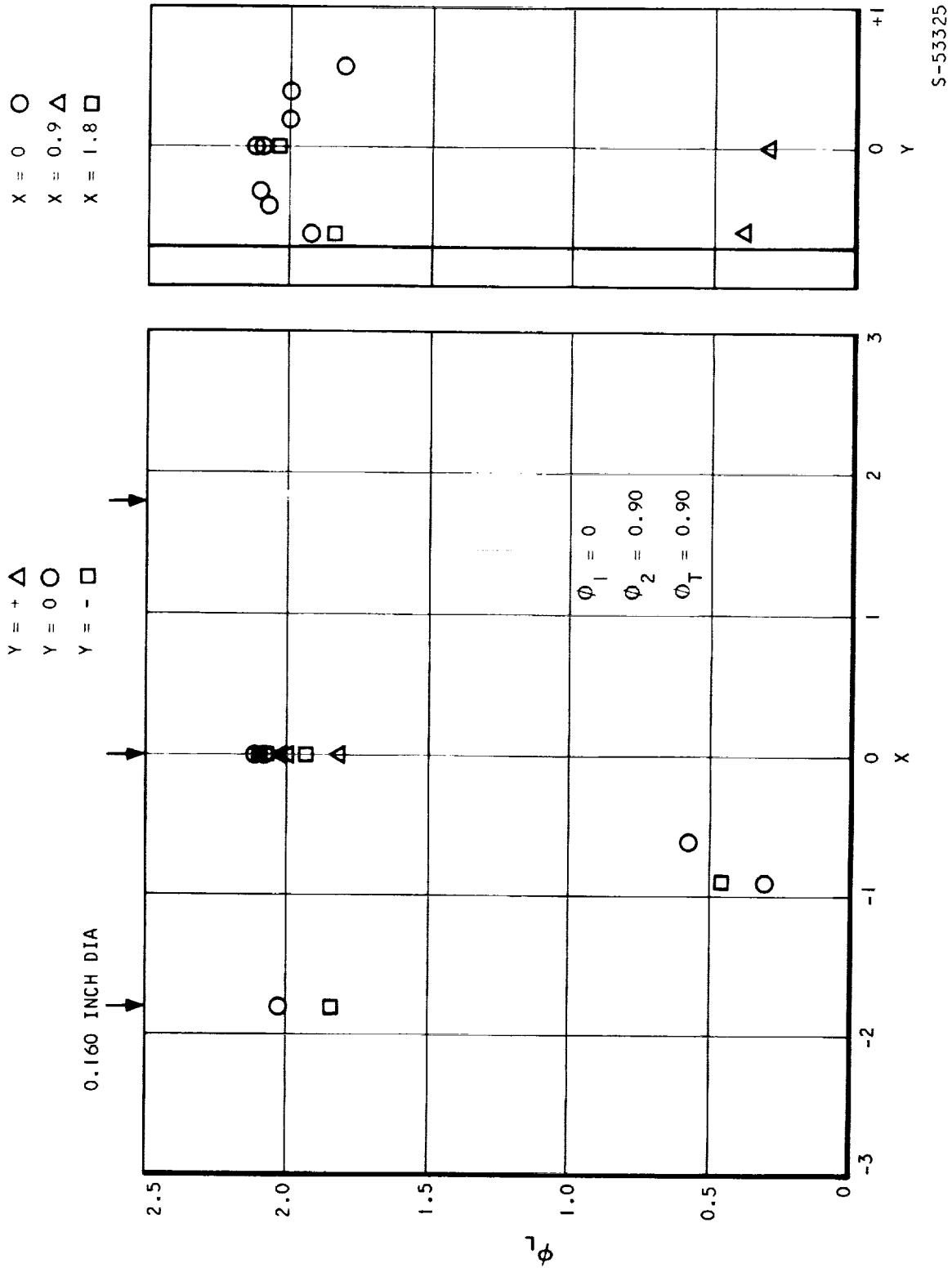

Figure 8.6-10. Gas Sampling Data From Run 245

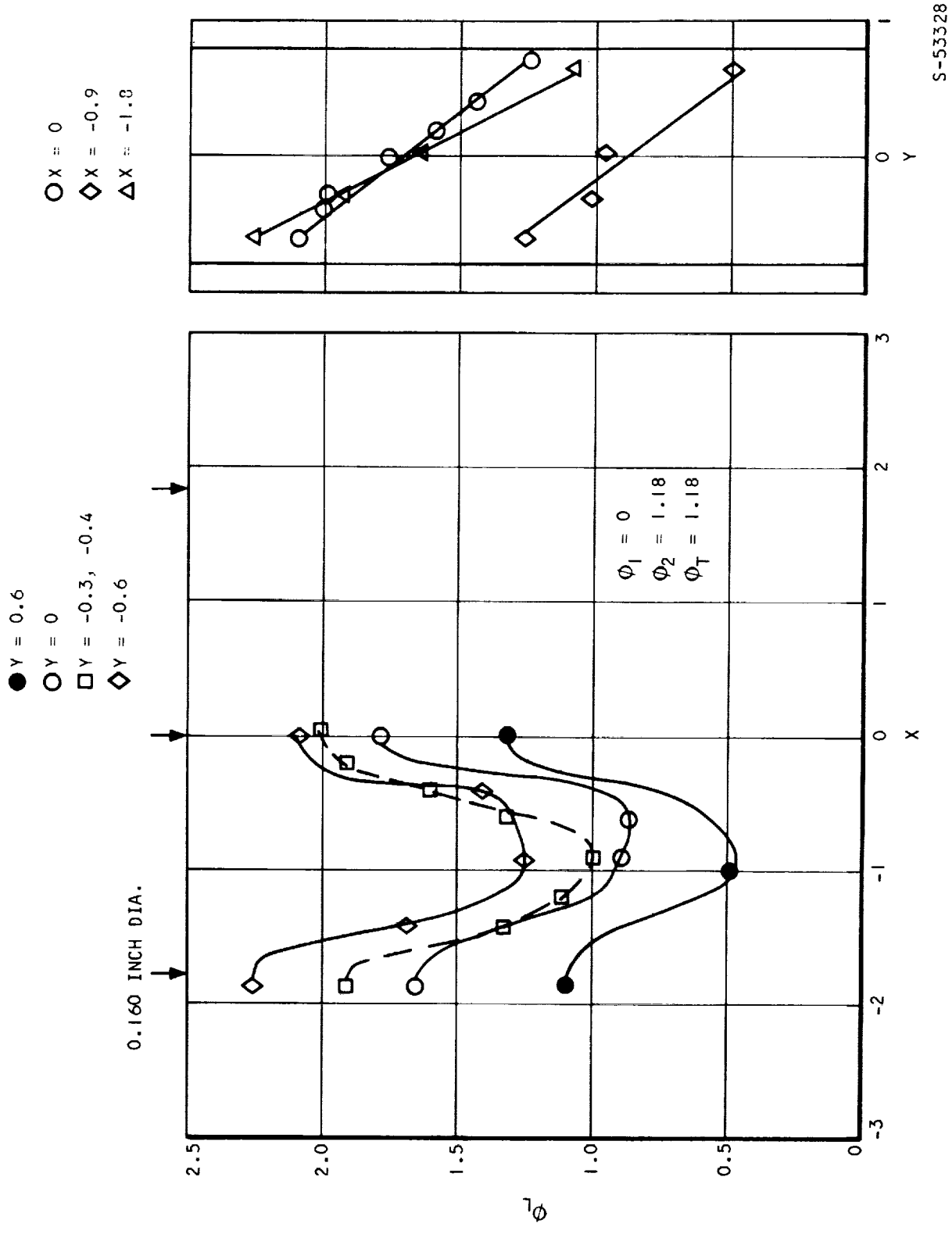

Figure 8.6-11. Gas Sampling Data From Run 246

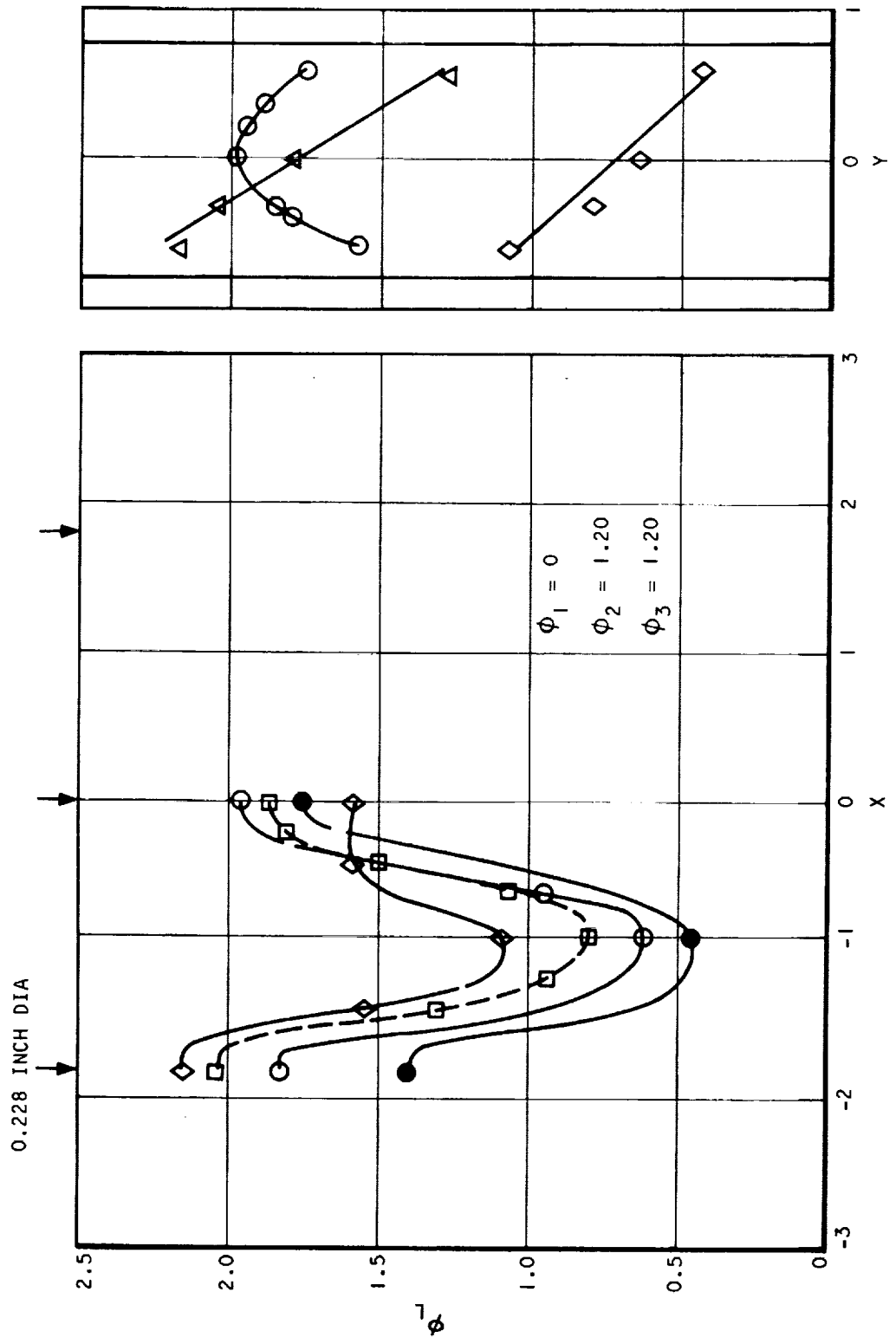

Figure 8.6-12. Gas Sampling Data From Run 247

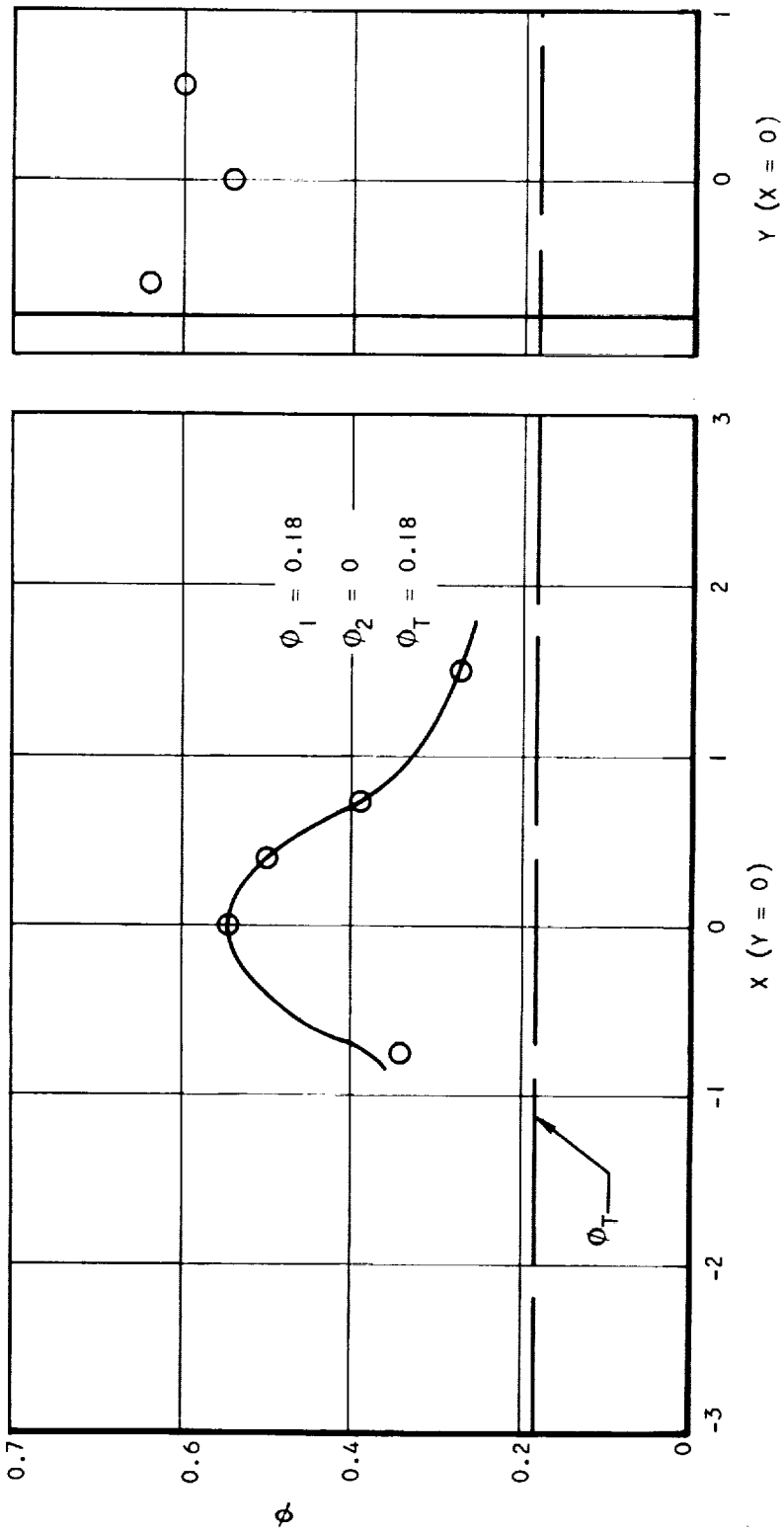

Figure 8.6-13. Gas Sampling Data From Run 204

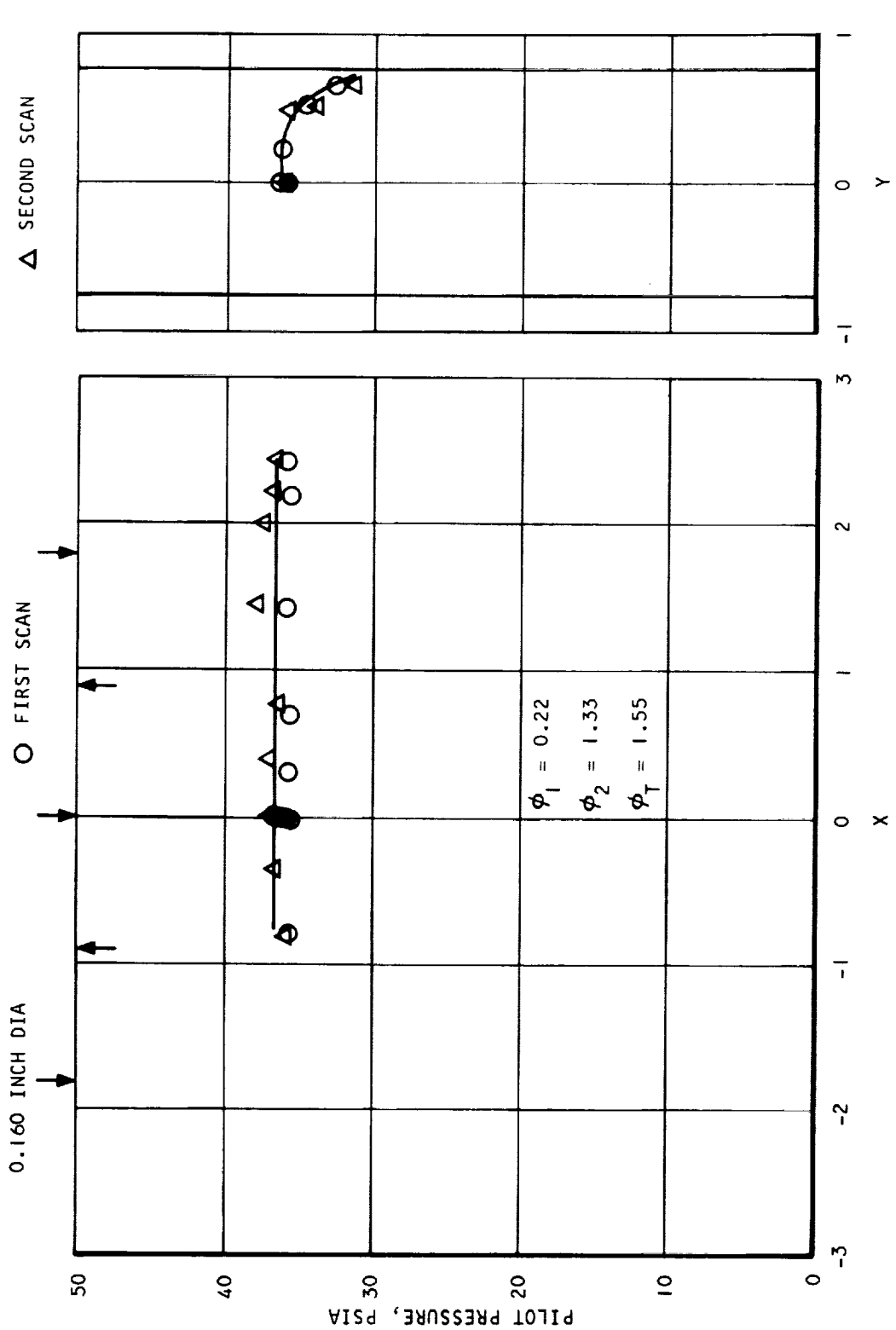

Figure 8.6-14. Gas Sampling Data From Run 212

8.7 HEAT TRANSFER

8.7.1 Heat Flux Measurement

The combustor water jacket included several circuits in both the upper and lower walls, as shown in Figure 8.7-1. The water flow rates and water inlet and outlet temperature differences were measured separately for each circuit.

The wall thermocouple locations are indicated on Figure 8.7-2, and the installation is shown in the insert of Figure 8.7-3. Holes of 0.25 in. dia were drilled using electrical-discharge machining (EDM) through the 1-in.-thick outer wall of the combustor water jacket and the fin to permit the installation of the thermocouple and fitting. The thermocouple junction was formed by welding the wires to the sheath after removal of the magnesium oxide, using type 347 steel welding material. The depth of the junction (the interface between the welding material and the MgO) was determined by X-ray. The welded end was trimmed to a depth of approximately 0.032 in.--the same as the thickness of the combustor hot wall. When the installation was completed, the end of the thermocouple was flush with the coolant side of the hot wall.

Data were recorded for nine thermocouples in the lower wall and six thermocouples in the upper wall of the combustor. The relationship between measured-wall temperature and heat flux was established analytically from the detailed conduction model in the vicinity of the thermocouples. The conduction of heat through the combustor wall to the thermocouple and the water in the cooling jacket was analyzed with the aid of a steady-state thermal analyzer computer program. The continuous conduction path was divided into 120 finite elements to facilitate the numerical analysis. Since the system is symmetrical about the centerline of the thermocouple, the metal was divided into either cylinders or concentric shells. The model used for the cross section of the thermocouple installation is shown in Figure 8.7-4. The heat transfer coefficient for the hot-gas side was assumed to be uniform over the general area of the thermocouple. This implies that the non-isothermal wall effects were neglected. The heat transfer coefficient for the water side was analyzed for the thermocouple sheath as well as for the combustor wall. Heat transfer to the combustor wall is a function of water-flow rate, wall-to-bulk temperature difference, and fin efficiency. For wall nodes 51, 56, 61, 65, and 67, water properties were evaluated at the film temperature defined as the average of the node temperature and the 62^{0}F water bulk temperature. Heat transfer to the thermocouple tubing (sheath) was calculated, using a flow model of a cylinder with cross-flow (flow normal to the cylinder). Since the flow was highly turbulent in the water jacket, the cylinder stagnation film coefficient was raised to 1.8-times the value when the approaching flow is turbulence-free (Reference 8-7). Thermocouple junction temperature is a function of heat flux, water temperature, and water flow rate for a given installation. The results were presented in Figure 8.7-3 as the thermocouple ΔT (junction temperature-water temperature) as a function of the combustor wall heat flux at different water flow rates in a 6-in.-wide water passage. The local heat fluxes can be determined from this figure using the wall thermocouple data, the water flow rate, and the bulk water temperature. A sample computer output

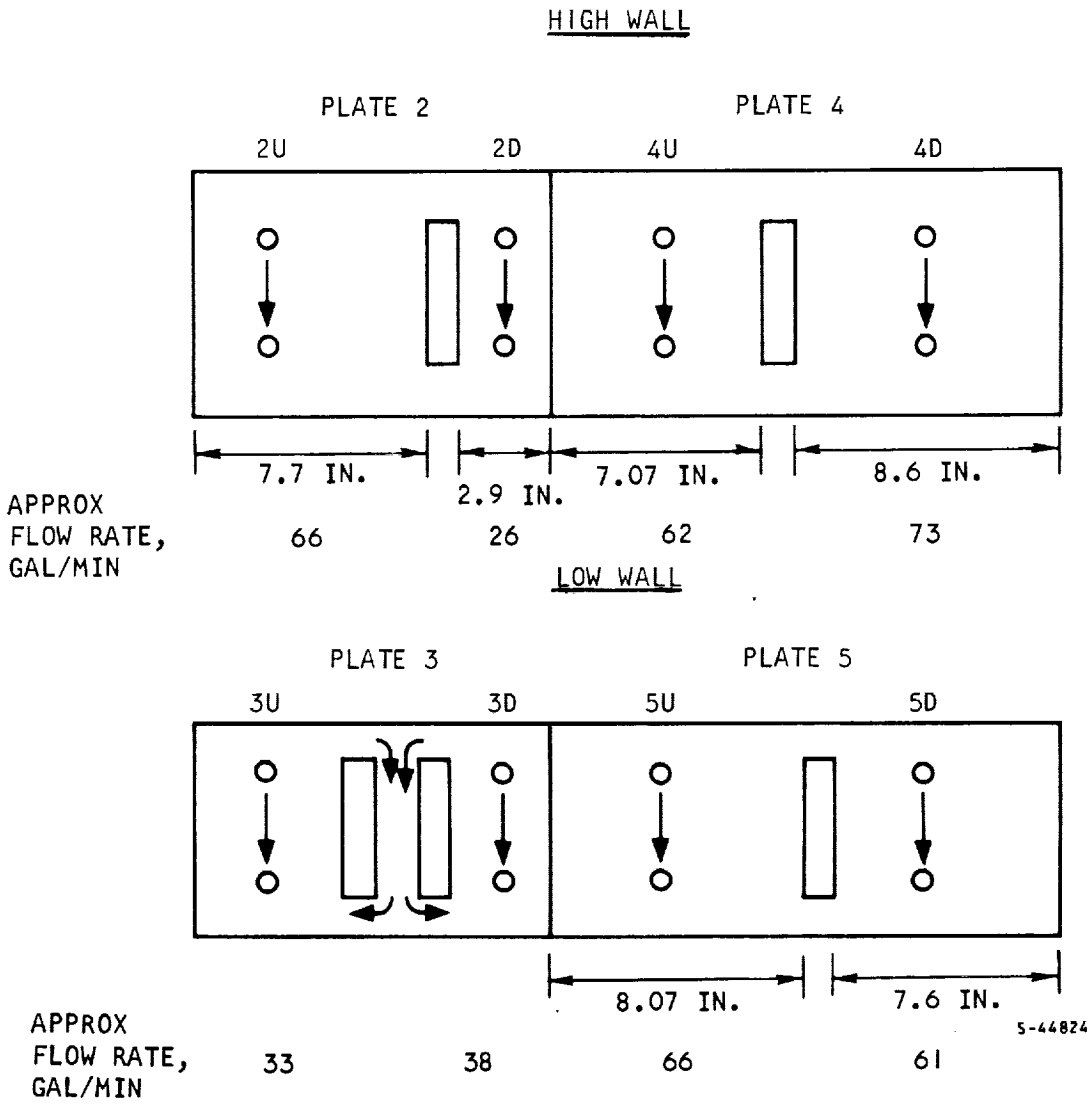

Figure 8.7-1. Combustor Coolant Path Identification

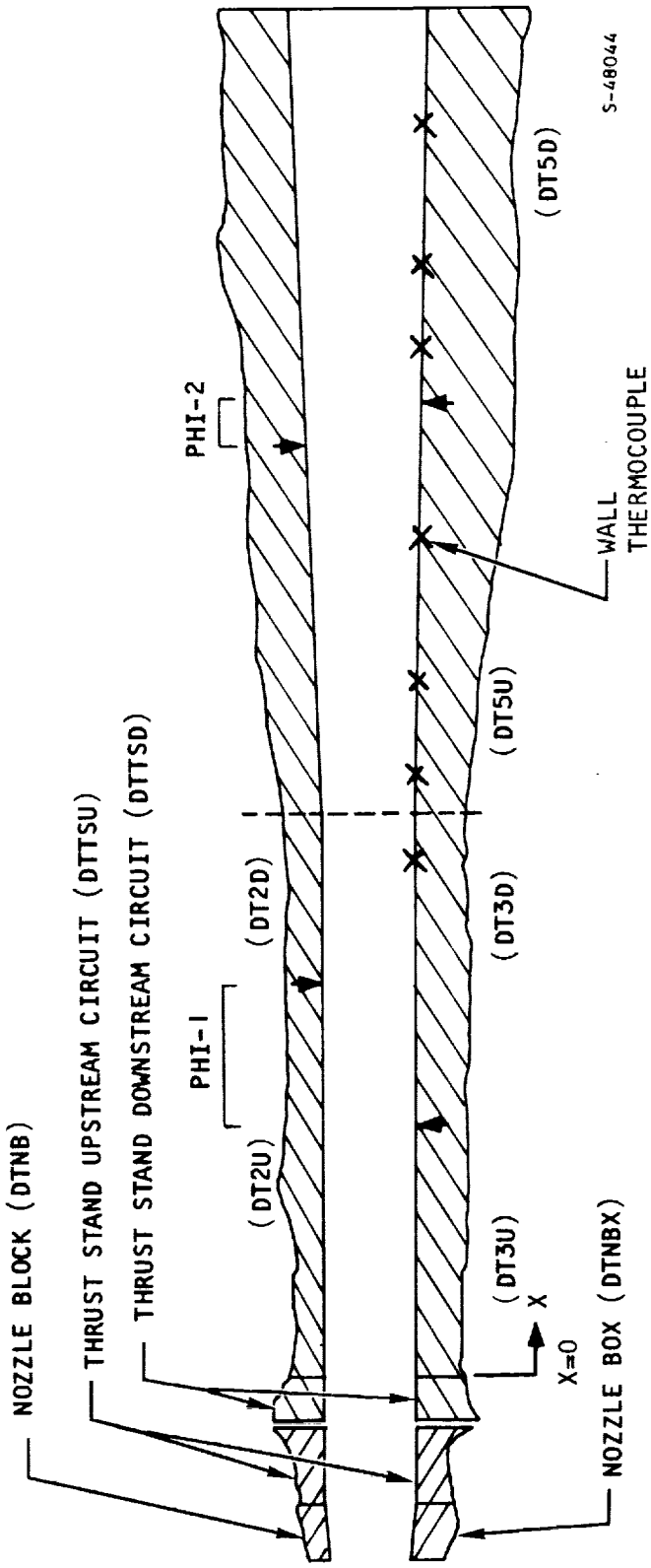

Figure 8.7-2. Schematic of 2-In.-Height Combustor Configuration, Including Coolant Temperature-Rise Nomenclature

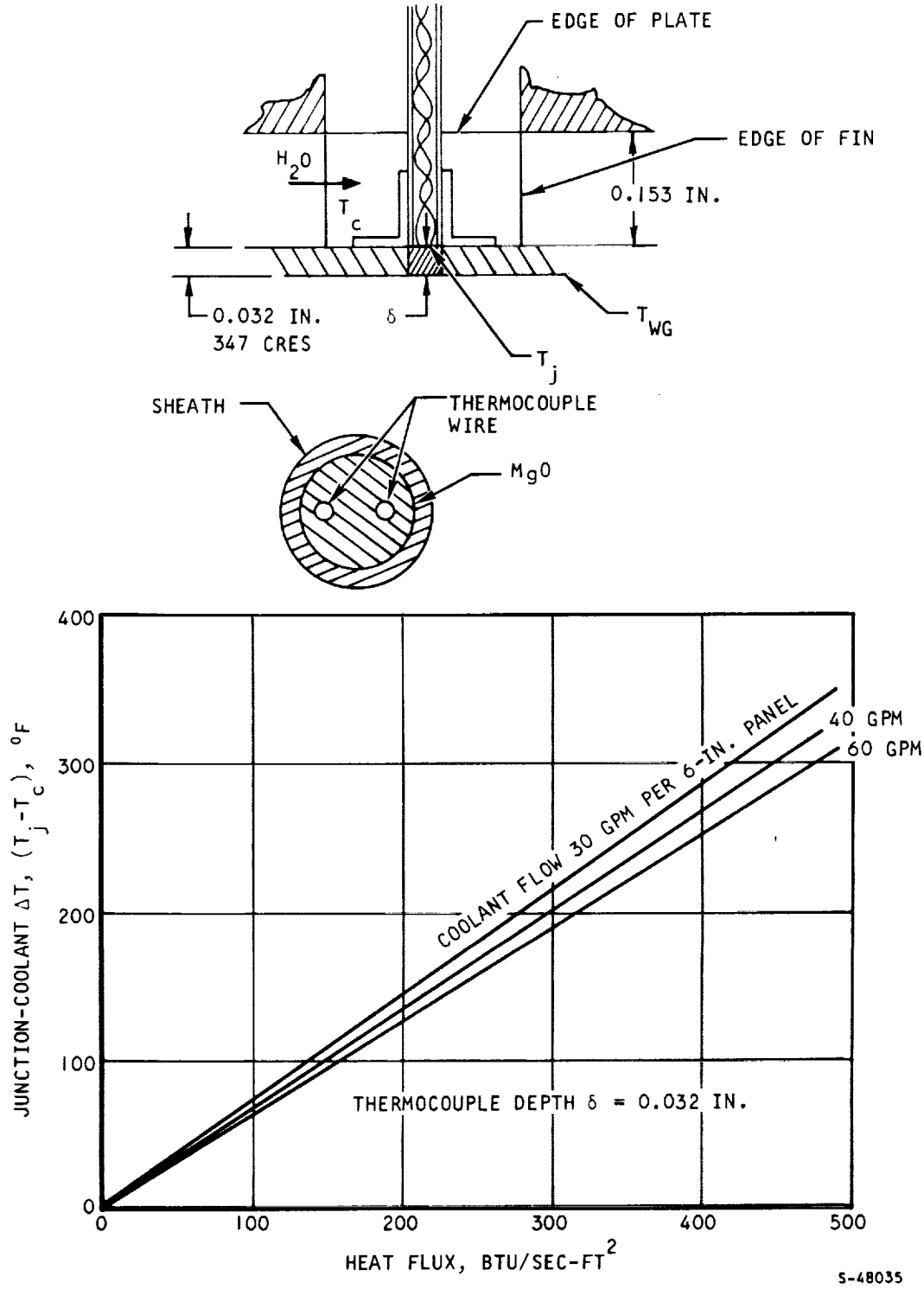

Figure 8.7-3. Combustor Wall Heat Flux vs Thermocouple ΔT

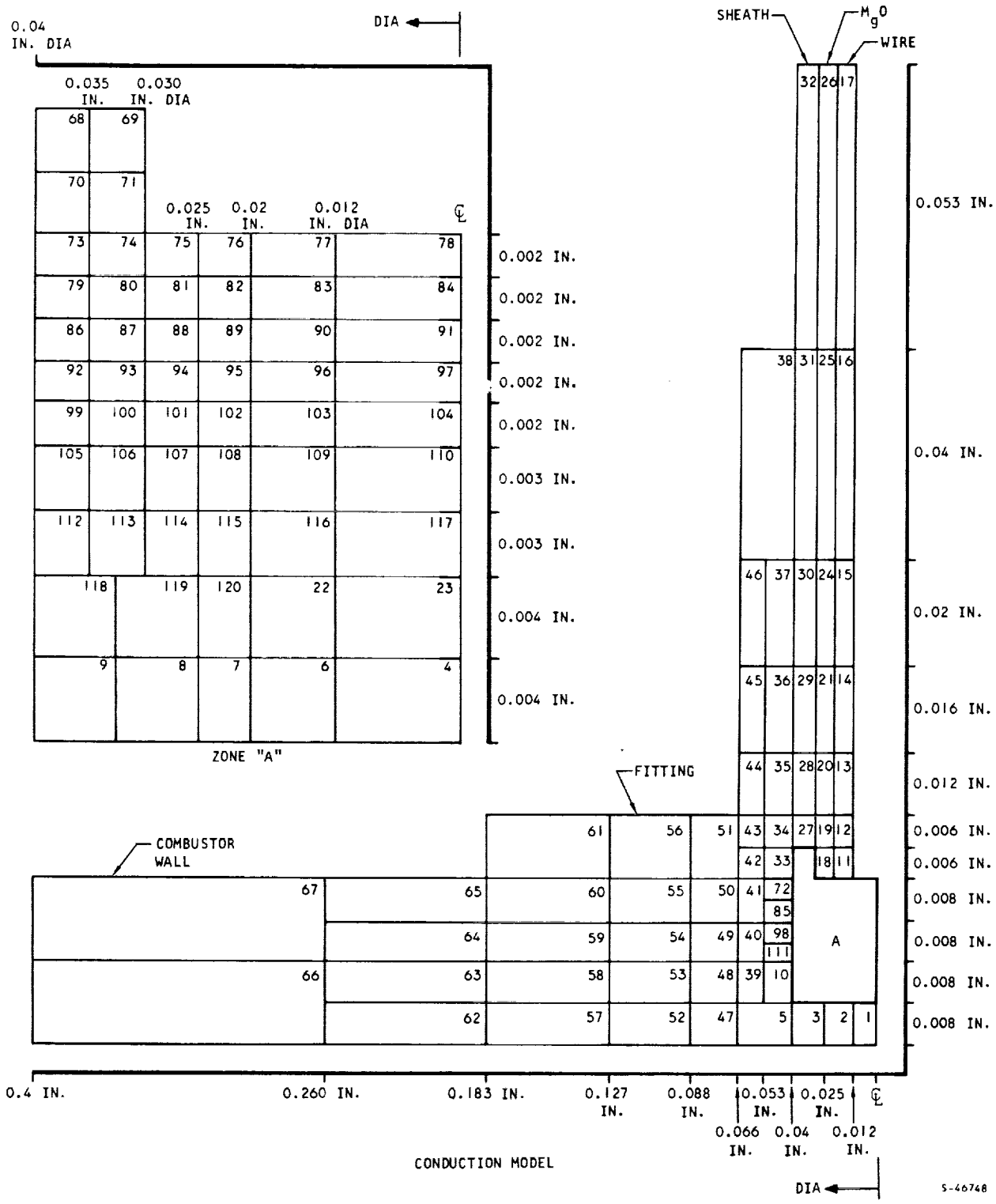

Figure 8.7-4. Analytical Conduction Model Used for the Chromel-Alumel Wall Thermocouple Installation

is shown in Table 8.7-I for an internal coolant flow of 60 gpm per 6-in.-wide panel. The heat flux at locations free of the interference of the thermocouple is 350 Btu/sec-ft^2.

8.7.2 Correlation Method

The theoretical heat transfer rates were computed with either a duct-flow equation or Blasius equation for a flat plate. To account for gas compressibility, the reference enthalpy was used to evaluate the fluid properties. The duct equation used is (Reference 8-8)

$$\frac{q}{A} = .023\ (\rho^* u)^{0.8}\left(\frac{\mu^*}{D}\right)^{0.2} Pr^*\left(-\frac{2}{3}\right)(H_r - H_w) \qquad (8\text{-}24)$$

and the flat-plate equation used is (Reference 8-9)

$$\frac{q}{A} = 0.0296\ (\rho^* u)^{0.8}\left(\frac{\mu^*}{X}\right)^{0.2} Pr^*\left(-\frac{2}{3}\right)(H_r - H_w) \qquad (8\text{-}25)$$

The equilibrium gas enthalpy--which is a function of the gas composition, pressure and temperature--is shown in Figure 8.7-5. Aero properties for run 143 were computed with a variable combustion efficiency, η_c, until the calculated thrust matched that of the experimental value. The aero properties for runs 142 and 147 were computed with an arbitrary combustion efficiency ($\eta = 0.9$ was assumed) and the flow properties were obtained by solving the continuity, state, and energy equations:

Continuity: $G = \frac{W}{A}$

State: $H = H_T - \frac{1}{2gJ}\left(\frac{RTG}{P}\right)^2$

Energy: $H_T = H_i - \Delta H_D + \eta\ \frac{W_{H_2} \times 52{,}000}{W}$

where ΔH_D is the heat loss to the water jacket.

If the combustion efficiency is $\eta_c = 0.8$ instead of 0.9, then the predicted heat flux for runs 142 and 147 will be decreased by 4 to 5 percent.

TABLE 8.7-I

SAMPLE COMPUTER OUTPUT*

Node	Temp, °F	Node	Temp, °F	Node	Temp, °F
1=	537.27	44=	103.74(h_c=0.0259)	87=	332.07
2=	535.45	45=	74.26(h_c=0.0259)	88=	341.63
3=	529.28	46=	65.09(h_c=0.0259)	89=	350.07
4=	482.28	47=	502.66	90=	358.73
5=	520.78	48=	428.09	91=	365.58
6=	481.96	49=	348.53	92=	339.83
7=	478.94	50=	264.44	93=	347.39
8=	474.62	51=	147.83(h_c=0.031)	94=	354.81
9=	467.59	52=	499.36	95=	361.56
10=	446.66	53=	417.28	96=	368.97
11=	287.36 = T_J	54=	333.61	97=	374.60
12=	237.82	55=	247.73	98=	357.90
13=	179.24	56=	135.64(h_c=0.031)	99=	358.50
14=	115.15	57=	479.01	100=	363.41
15=	79.38	58=	395.56	101=	369.16
16=	64.16	59=	311.93	102=	374.62
17=	62.12	60=	229.17	103=	380.84
18=	275.27	61=	128.29(h_c=0.031)	104=	385.50
19=	224.16	62=	425.96	105=	378.28
20=	162.15	63=	337.20	106=	383.28
21=	105.21	64=	242.28	107=	388.01
22=	447.55	65=	143.76(h_c=0.031)	108=	392.37
23=	449.37	66=	340.25	109=	397.35
24=	75.65	67=	143.59(h_c=0.031)	110=	401.04
25=	63.62	68=	239.22	111=	389.31
26=	62.08	69=	240.46	112=	403.45
27=	200.31	70=	262.14	113=	408.33
28=	135.97	71=	268.28	114=	412.15
29=	88.24	72=	287.02	115=	415.66
30=	69.13	73=	289.45	116=	419.56
31=	62.66	74=	298.99	117=	422.34
32=	62.01(h_c=0.0259)	75=	321.92	118=	438.70
33=	240.40	76=	335.17	119=	441.58
34=	190.55	77=	343.87	120=	444.65
35=	125.22	78=	355.06		
36=	83.07	79=	306.32		
37=	67.53	80=	316.27		
38=	62.37(h_c=0.0259)	81=	330.11		
39=	440.11	82=	340.85		
40=	362.76	83=	350.36		
41=	286.21	84=	358.87		
42=	221.36	85=	318.93		
43=	175.77	86=	324.39		

(h_c - coolant heat transfer coefficient = $\frac{\text{Btu}}{\text{in.}^2\text{-sec-}^\circ\text{R}}$)

*The node numbers in this table correspond to those shown in Figure 8.7-4

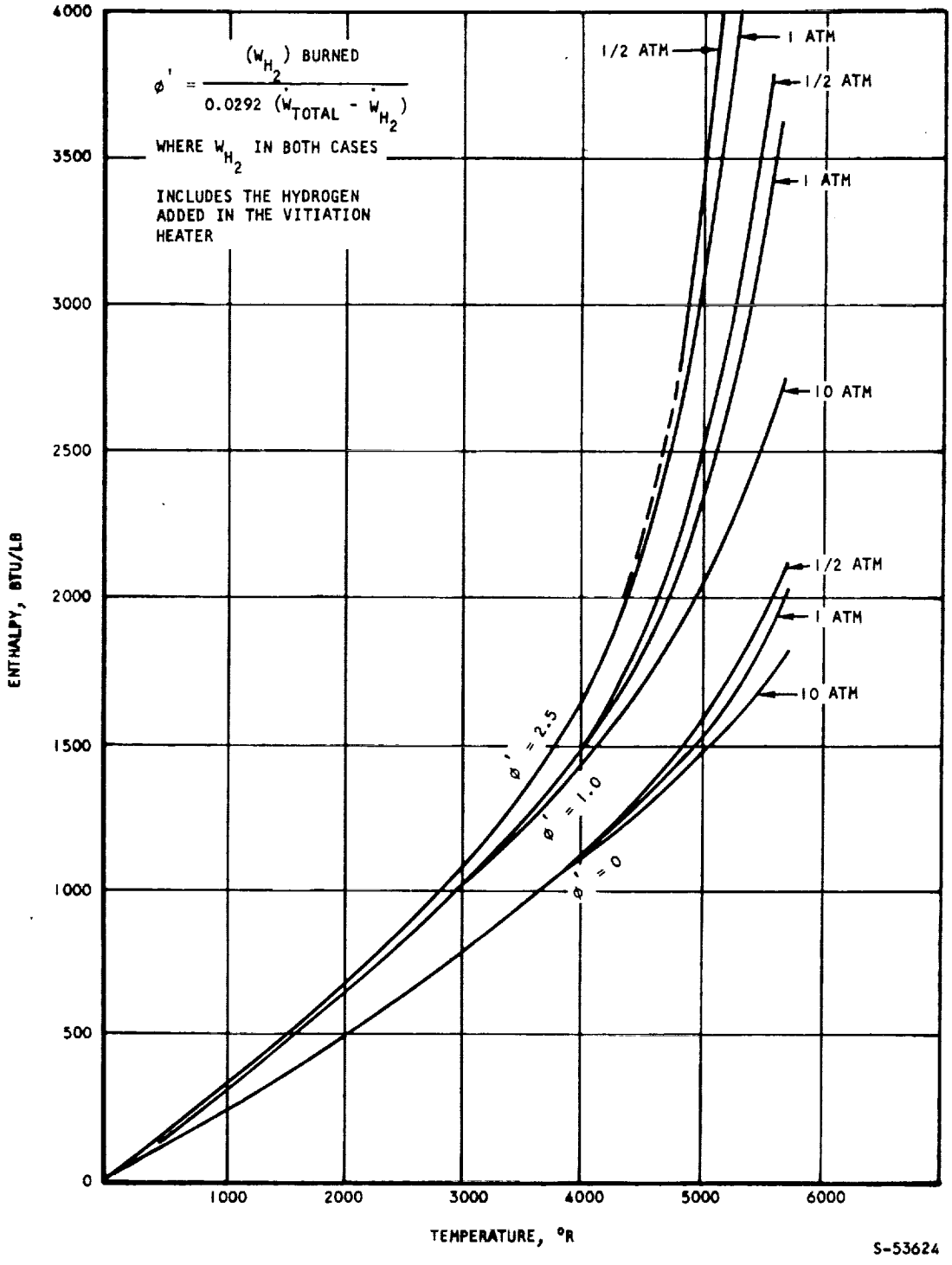

Figure 8.7-5. Gas Enthalpy vs Gas Temperature

8.7.3 Data Interpretation

The heat transfer data was analyzed for the purpose of developing a more accurate analytic technique for the prediction of heat transfer during combustion. The specific questions to be resolved were (1) will the conventional duct equation using a reference enthalpy be acceptable for combustor heat transfer analysis?, and (2) which reference enthalpy equation is more accurate--Eckert's reference enthalpy equation or the modified form which is obtained by replacing the wall enthalpy term in Eckert's equation by the adiabatic wall enthalpy? The raw data indicated that the experimental correlation with heating predictions using only the duct equations was inadequate. This conclusion is based on the unusual nature of the combustor wall temperature readings. All combustor wall thermocouples registered a drop in the temperature when the first injector fuel flow was increased up to a value of about $\phi = 0.3$. The wall temperature increased when the fuel flow was reduced from a high ϕ to a ϕ of 0.3. This phenomenon is most pronounced near the injectors. Typical examples of temperature reversal are shown in Figures 8.7-6 to 8.7-8 for runs 142, 143 and 147, respectively. These are plots of equivalence ratio and the wall temperature vs the running time. Combustor wall temperature vs fuel flow is shown in Figure 8.7-9. Since the wall temperature reversal occurred over the entire duct where thermocouple data was available (x greater than 11), this phenomenon cannot be explained by the fuel mixing-and-burning pattern within the boundary layer. Any acceptable explanation must be applicable over the entire affected area.

A proposed explanation consistent with the experimental heat transfer data is as follows. The injection and burning of fuel induces a pressure rise. At a sufficiently large fuel injection rate, the induced pressure rise will cause the boundary layer flow to separate. The boundary layer reattachment point is the peak pressure location. The peak pressure point was not fixed relative to the combustor duct stations. At a ϕ of 0.3 or lower, the peak pressure occurred at approximately X = 10 to 12 inches. As ϕ is increased, the peak pressure point moved gradually upstream until at $\phi > 0.4$ the peak pressure point moved to approximately X = 5. This characteristic is shown in Figures 8.7-10, 8.7-11, and 8.7-12 for runs 142, 143 and 147, respectively. This shift of the peak pressure location (and also the reattachment point) has a significant influence on the heat transfer coefficient. It is hypothesized that at the reattached point, a new sub-layer is formed. At a given station (e.g. X = 11.3) the boundary layer running length changes as the peak pressure point shifts. When the peak pressure is at X = 10, the distance between the peak pressure point and the first thermocouple (X = 11.3) is only 1.3 in. When, due to increasing fuel flow, the peak pressure point shifts to X = 5, the same thermocouple is now 6.3 in. away. Since the turbulent heat transfer rate is inversely proportional to the one-fifth power of the running length, the shift of the running length from 1.3 to 6.3 will reduce the heat transfer coefficient by 37 percent (everything else being constant). Therefore, as ϕ is increased from $\phi = 0.3$ to $\phi = 0.4$, the net effect at X = 11.3 is to reduce the heat transfer rate. Note also that the gas total enthalpy is increased by approximately 150 Btu/lb (or about 10 to 15 percent), while the heat transfer coefficient decreases by 37 percent. Proof of this concept can be seen from

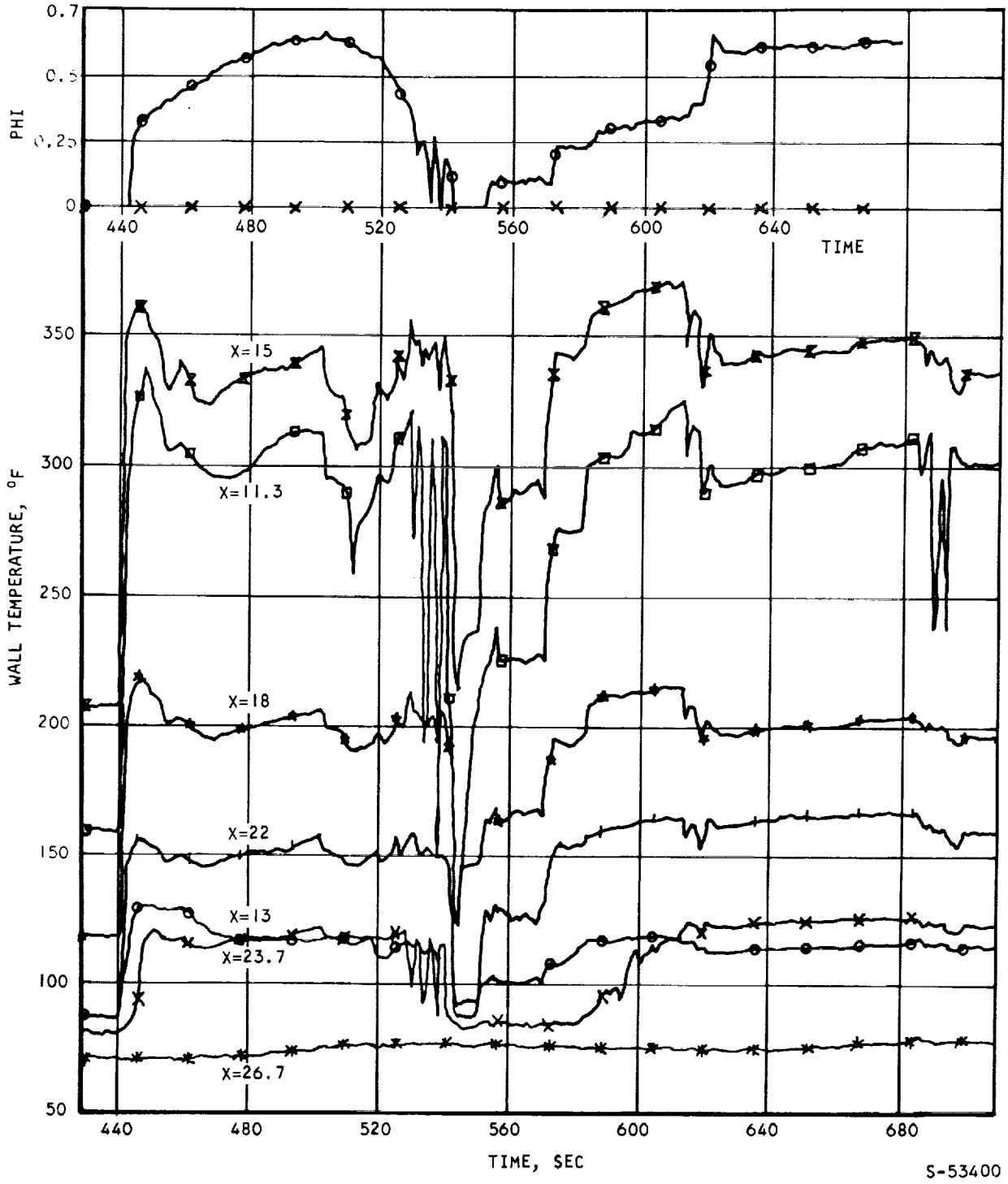

Figure 8.7-6. Wall Temperature and Fuel Flow vs Time, Run 142 (U)

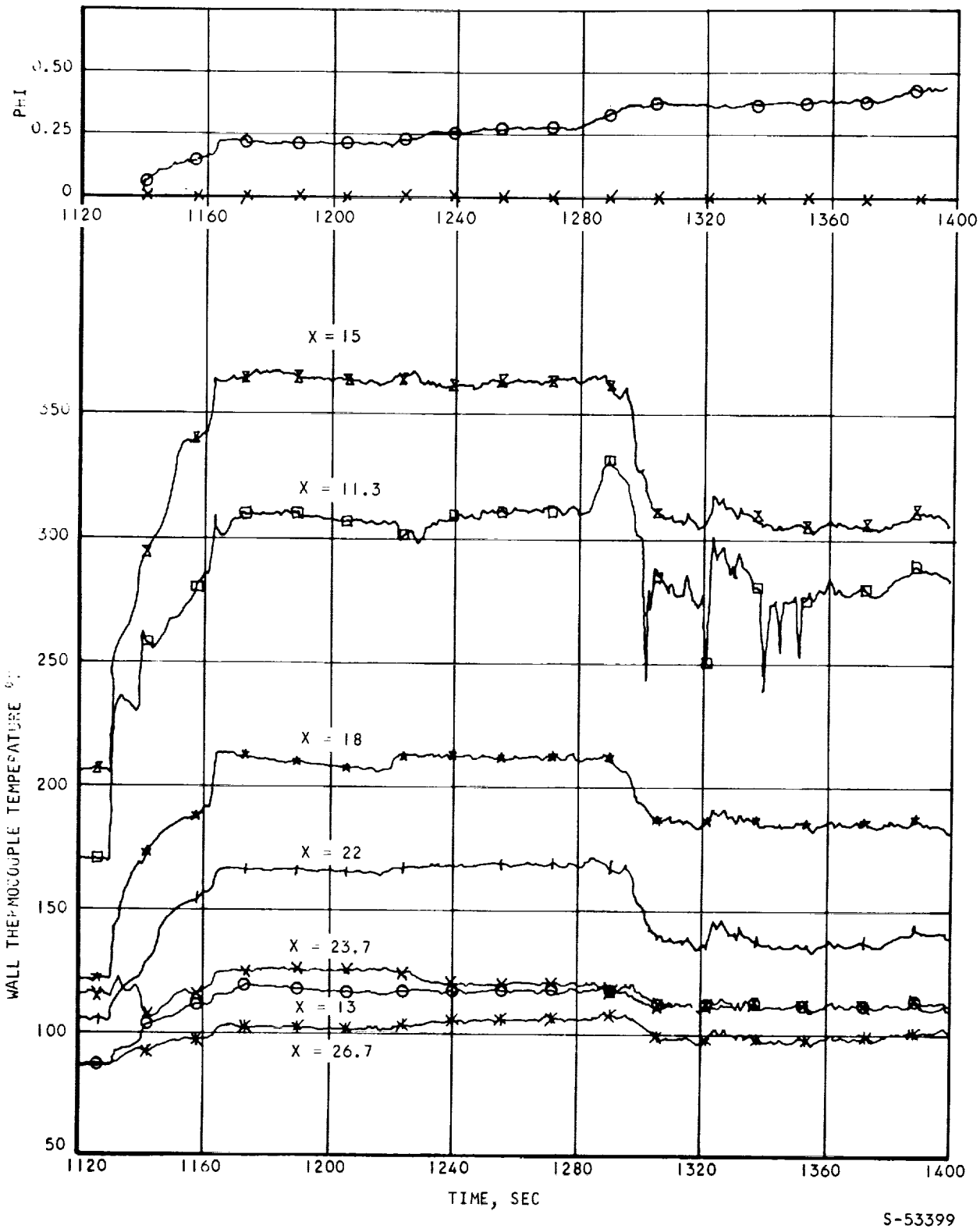

Figure 8.7-7. Wall Temperature and Fuel Flow vs Time, Run 143 (U)

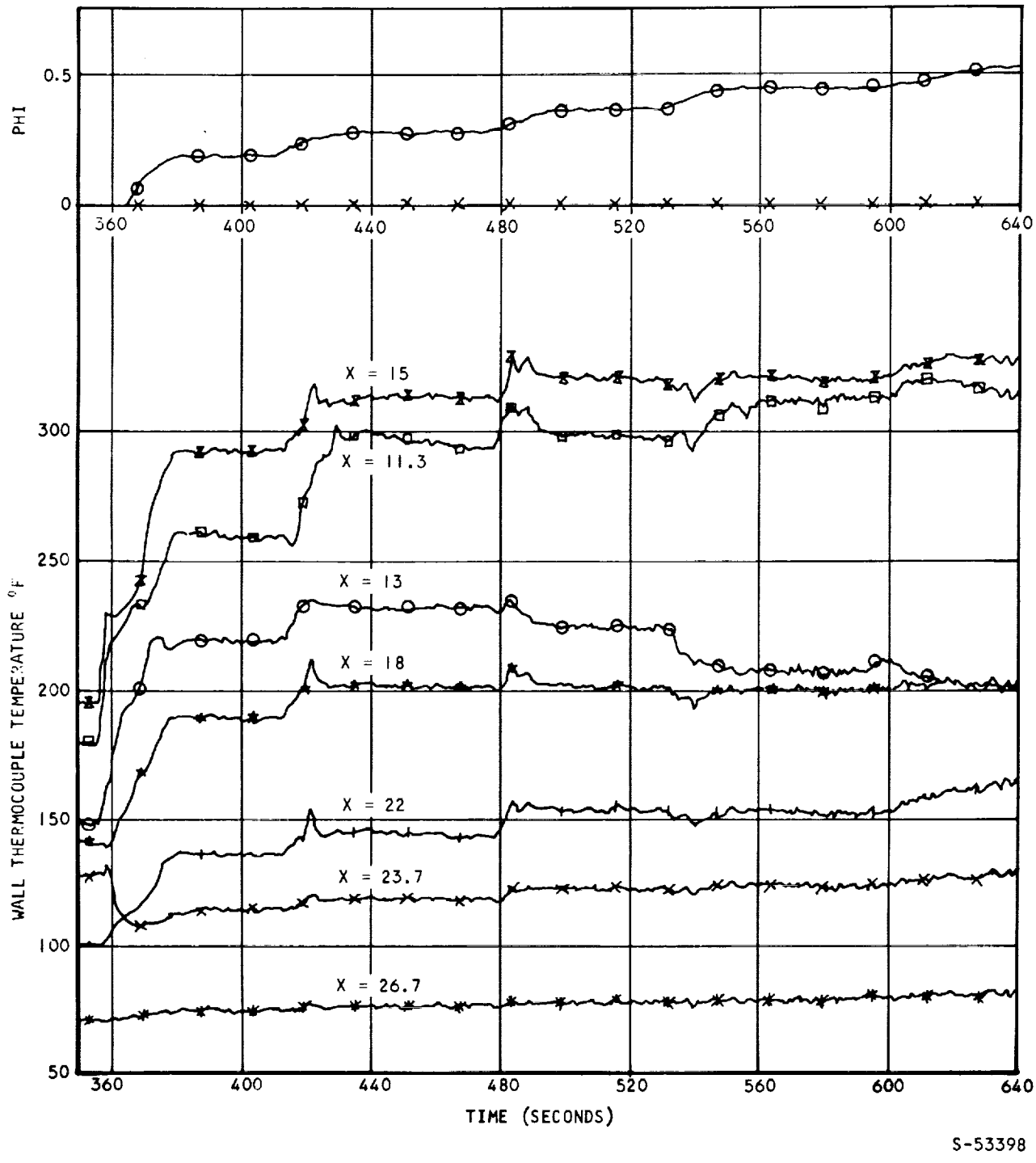

Figure 8.7-8. Wall Temperature and Fuel Flow vs Time, Run 147 (U)

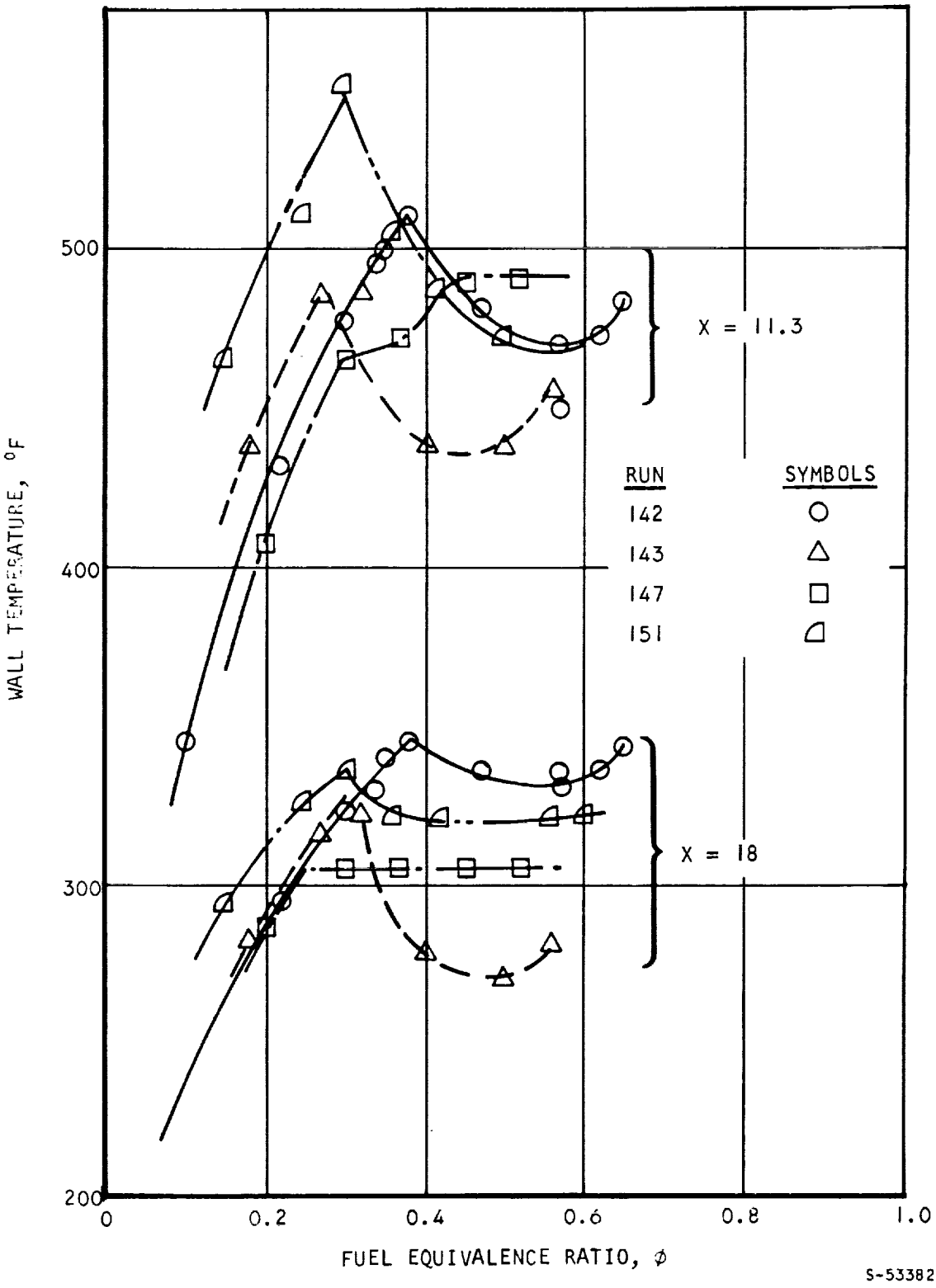

Figure 8.7-9. Wall Temperature vs Fuel Equivalence Ratio (U)

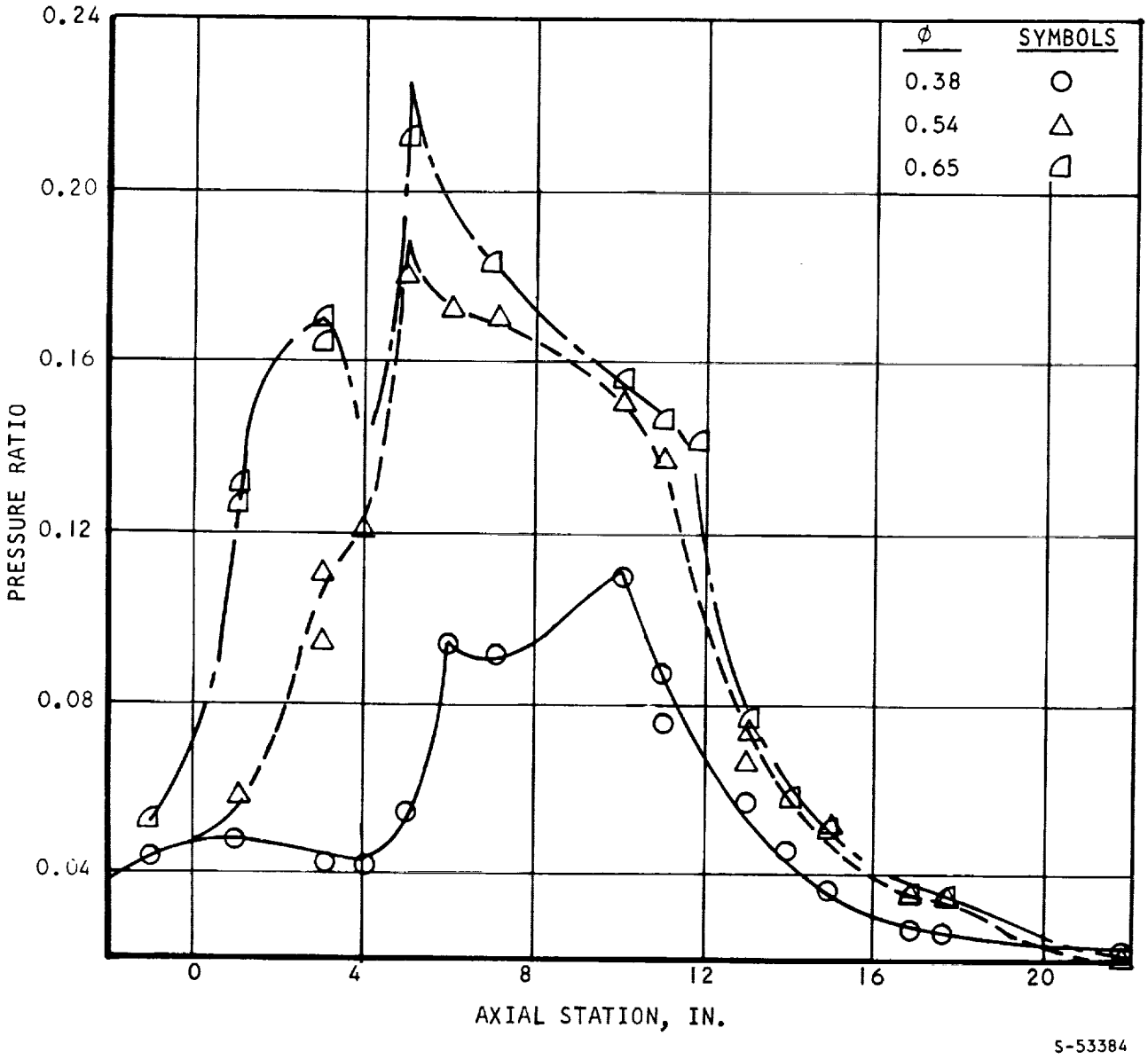

Figure 8.7-10. Pressure Distribution Run 142 (U)

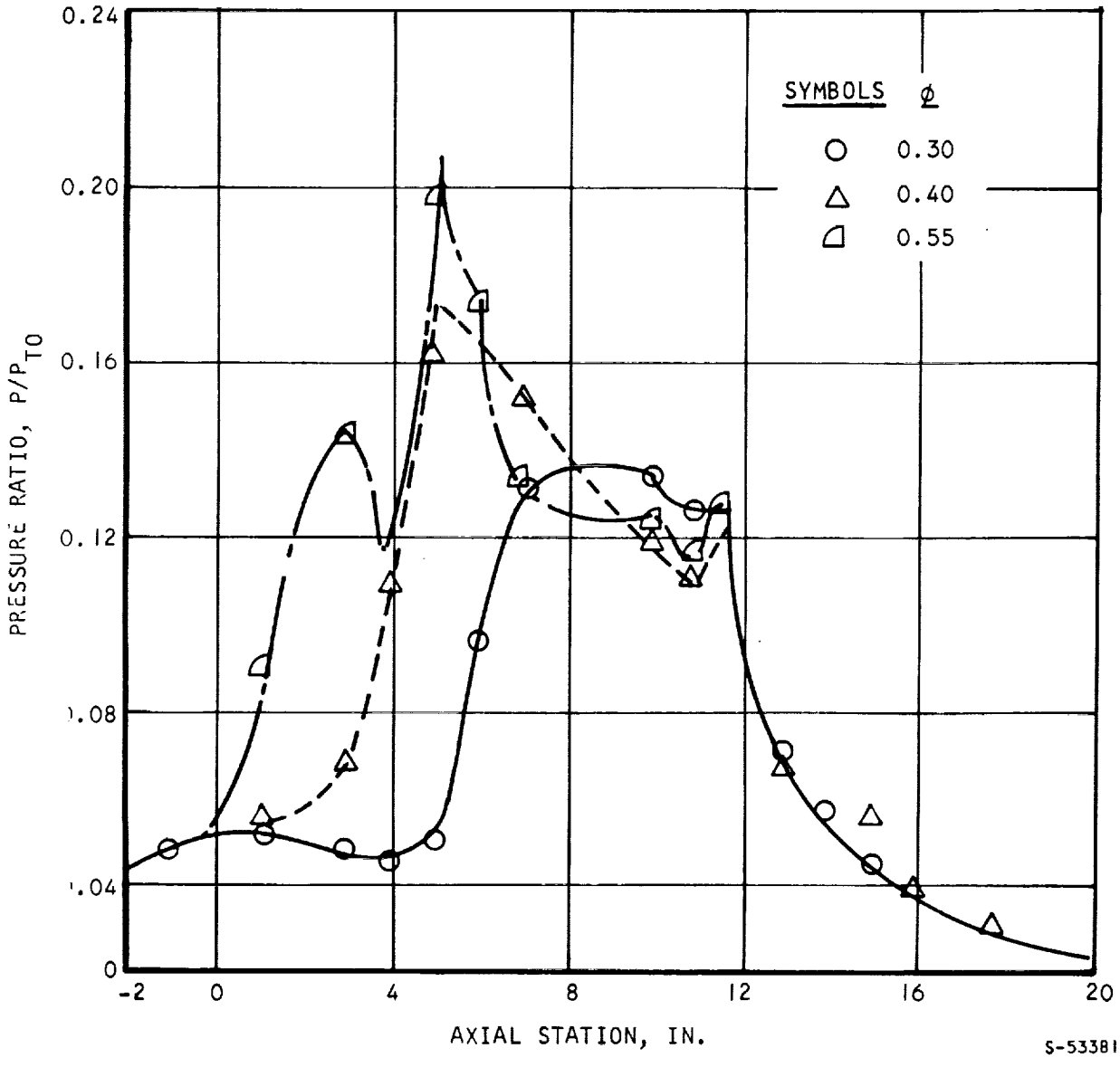

Figure 8.7-11. Pressure Distribution, Run 143 (U)

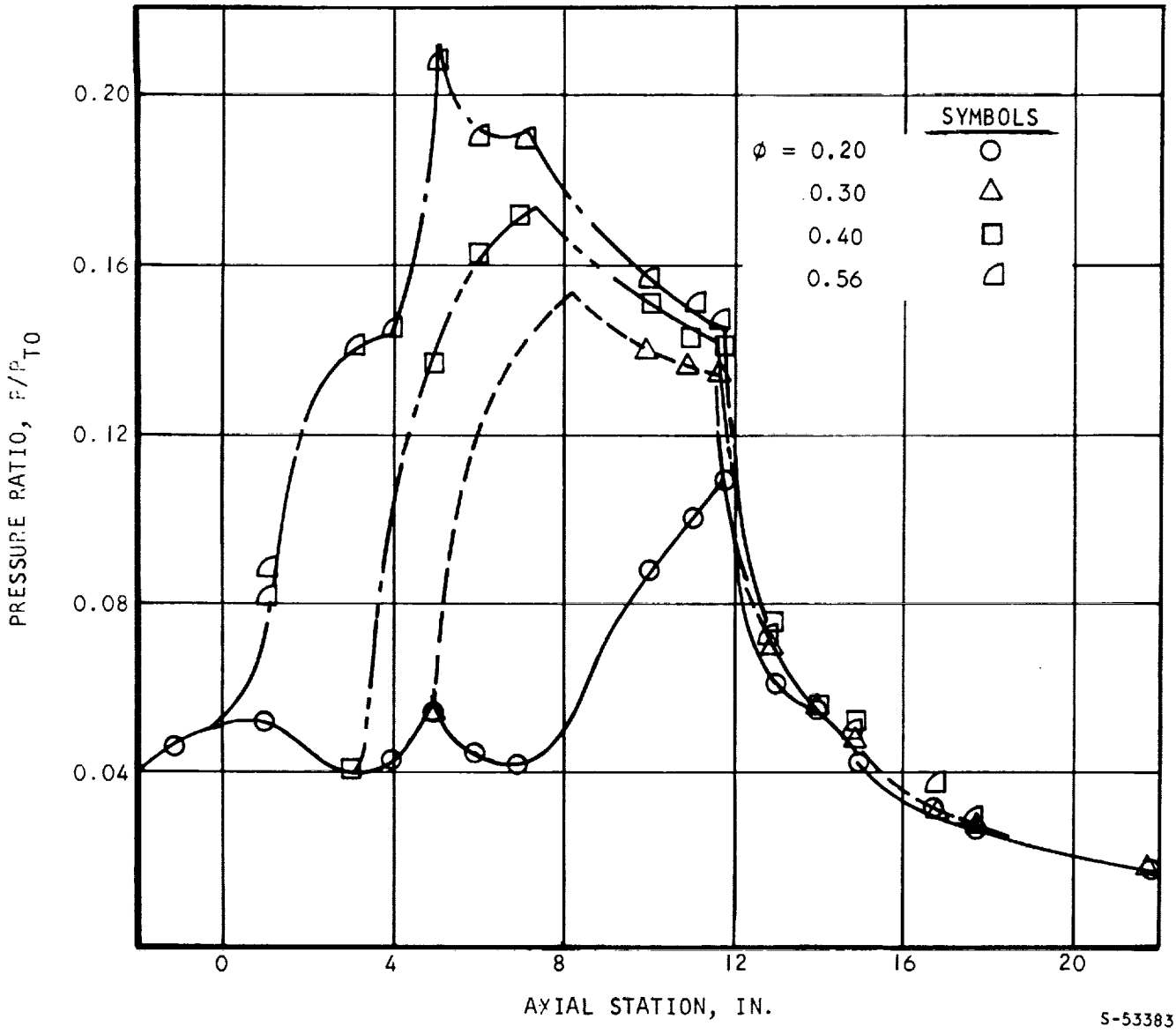

Figure 8.7-12. Pressure Distribution, Run 147 (U)

Figure 8.7-13, which shows the theoretical heat transfer coefficients computed by two different methods--the duct equation and the new-boundary layer method. The new-boundary-layer method is a flat-plate solution, with the running length originating from the peak-pressure location. The test data was taken from runs 142, 143 and 147 over a range of ϕ varying from 0.3 to 0.6. The new-boundary-layer method showed good agreement with the experimental heat transfer rates. On the other hand, the duct equation increasingly under-predicted the heat transfer rate as the distance between the peak pressure location and the thermocouple station is decreased. The two predicting methods yielded the same value when the peak pressure location was 6.5 in. forward of the thermocouple. At a distance of 6.5 in., the equivalent of 6 duct-hydraulic diameters, the flow became fully developed again. The shift of the peak pressure location from X = 10 to X = 5 also affected the heat transfer rate at Stations 18 and 22. The section aft of Station X = 12 is a divergent duct with a half-angle of 2.7 deg. When the peak pressure occurs at a station greater than 7, the heat transfer data exhibits the entrance effects. This is shown in Figure 8.3-14. The experimental heat transfer rates at Stations X = 18 and 22 show fair agreement with the duct equation only when the peak pressure point is at X = 5. The duct equation under-predicts the experimental data by approximately 30 percent when the peak pressure occurs at stations larger than 7. The new-boundary-layer concept can also provide a reasonable explanation to these results. When the peak pressure occurs at X = 5, the new boundary layer will become fully developed by the time the flow enters the diverging section. For such condition the duct equation is applicable to the diverging section. When the peak pressure point occurs at a Station X = 7 or larger, the new boundary layer has not become fully developed before entering the divergent section. The duct equation is not applicable to the divergent section for this latter condition.

The above results were computed using Eckert's reference-enthalpy equation:

$$H^{*} \equiv H + 0.5\,(H_w - H) + 0.22\,(H_r - H) \qquad \text{(Reference 8-10)}$$

The modified form is defined as:

$$H' \equiv H + 0.72\,(H_r - H)$$

When the modified form was used, the resulting heat transfer coefficients were significantly lower than the experimental data as shown in Figures 8.7-15 and 8.7-16. These results do not agree with the experimental results of Reference 8-11, which show a better agreement was obtained using the modified form of the reference-enthalpy equation. It is to be noted that in Reference 8-11 the heat flux vs the thermocouple reading curve was calculated using a one-dimensional conduction model, whereas a more complex conduction model was used in the present calculations. Applying the above new-boundary-layer concept, the calculated heat transfer rate for run 142 is compared with experimental results

RUN	ϕ	SYMBOLS
142	0.38	○
	0.54	◁
	0.65	◁
143	0.30	△
	0.40	◇
	0.48	◇
147	0.30	□
	0.40	◇
	0.56	∩

SOLID SYMBOLS

HEAT TRANSFER CALCULATIONS BASED ON DUCT HYDRAULIC DIAMETER

OPEN SYMBOLS

HEAT TRANSFER CALCULATIONS BASED ON A DISTANCE X EQUAL TO THE DISTANCE BETWEEN STATION 11.3 AND THE PEAK PRESSURE LOCATION

HALF SYMBOL

DESIGNATES THAT THE SOLID SYMBOL AND THE OPEN SYMBOL COINCIDE

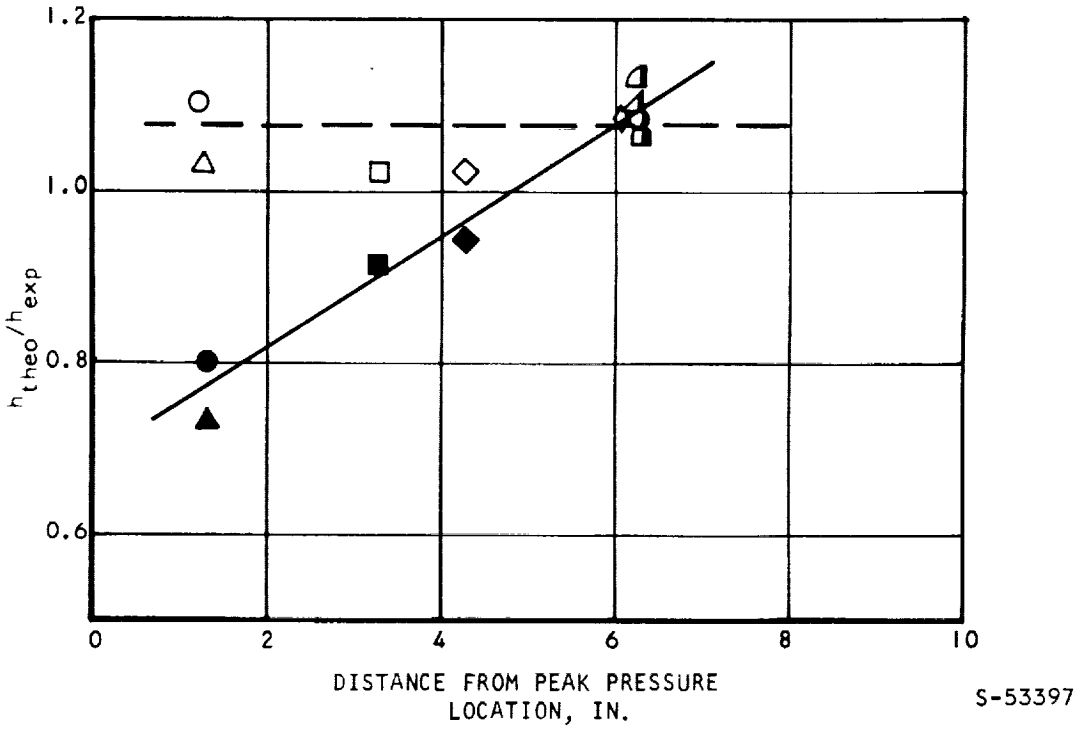

Figure 8.7-13. Theoretical-to-Experimental Heat Transfer Ratio at X = 11.3 (U)

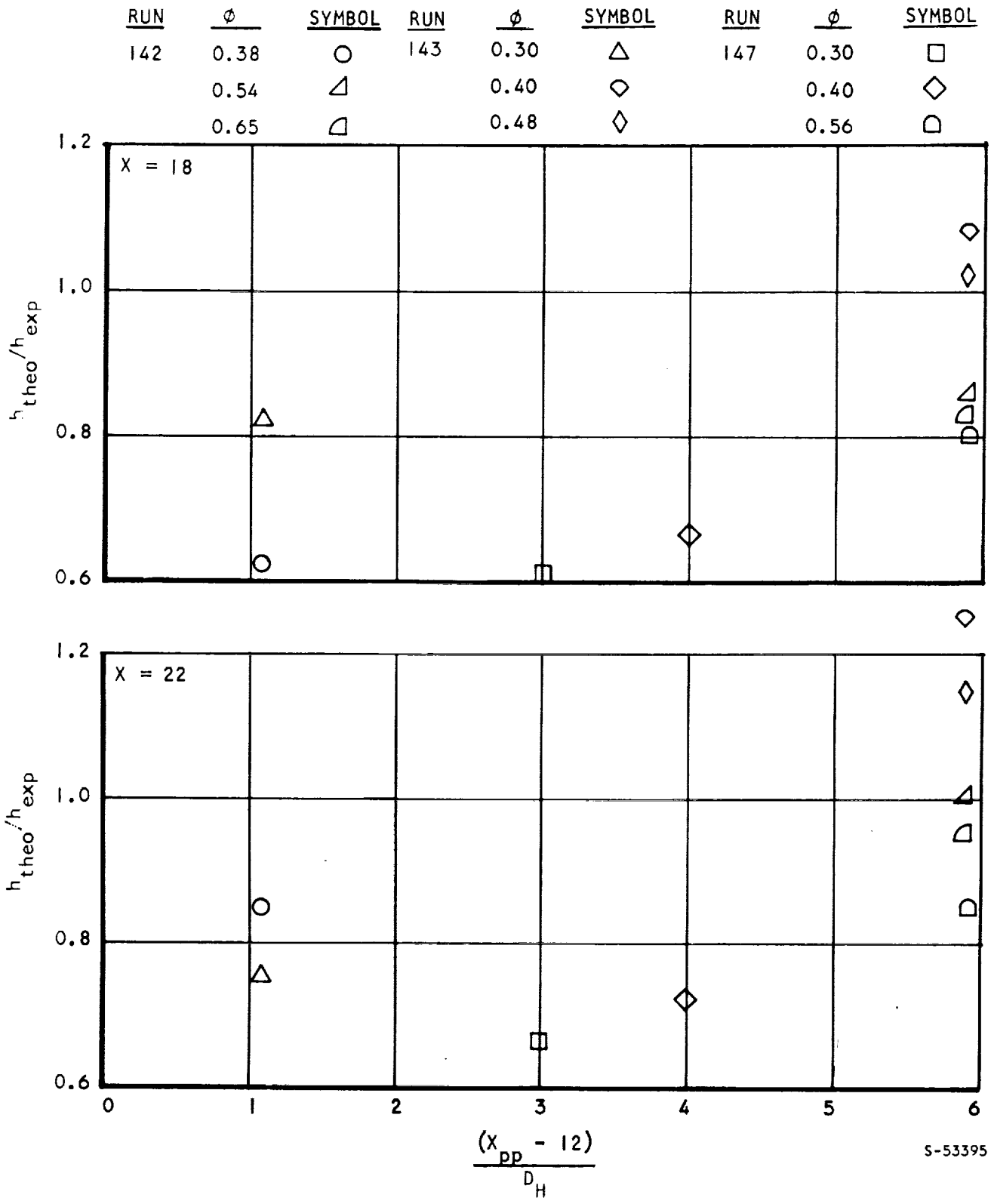

Figure 8.7-14. Theoretical-to-Experimental Heat Transfer Ratio (U)

SOLID SYMBOLS - CALCULATED BASED ON ECKERT'S REFERENCE TEMPERATURE T*

OPEN SYMBOLS - CALCULATED BASED ON T'

RUN	$\bar{r}$	SYMBOLS
142	0.38	○
	0.54	△
	0.65	◁
147	0.30	□
	0.40	◇

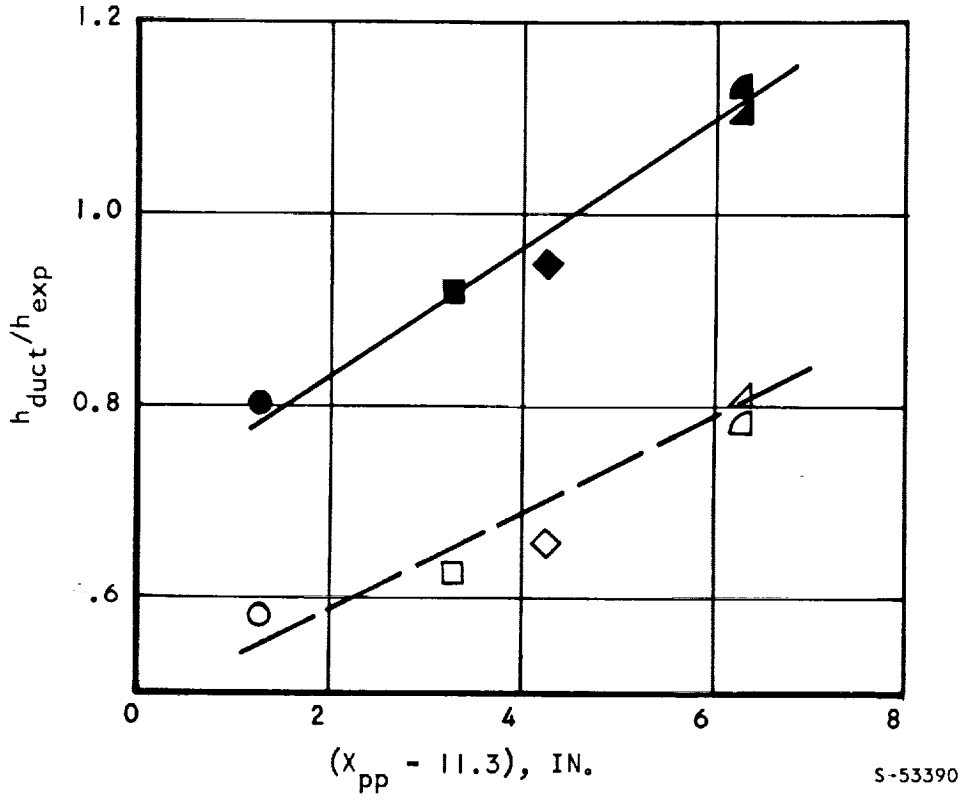

Figure 8.7-15. Theoretical to Experimental Heat Transfer Ratio at X = 11.3 (U)

$H^* = H + 0.5\ (H_w - H) + 0.22\ (H_r - H)$

$H' = H + 0.72\ (H_r - H)$

$T^* = T^*\ (H^*, \phi, P)$

$T' = T'\ (H^*, \phi, P)$

RUN	ϕ	SYMBOLS
142	0.38	○
	0.54	◿
	0.65	◿
147	0.3	□
	0.4	◇

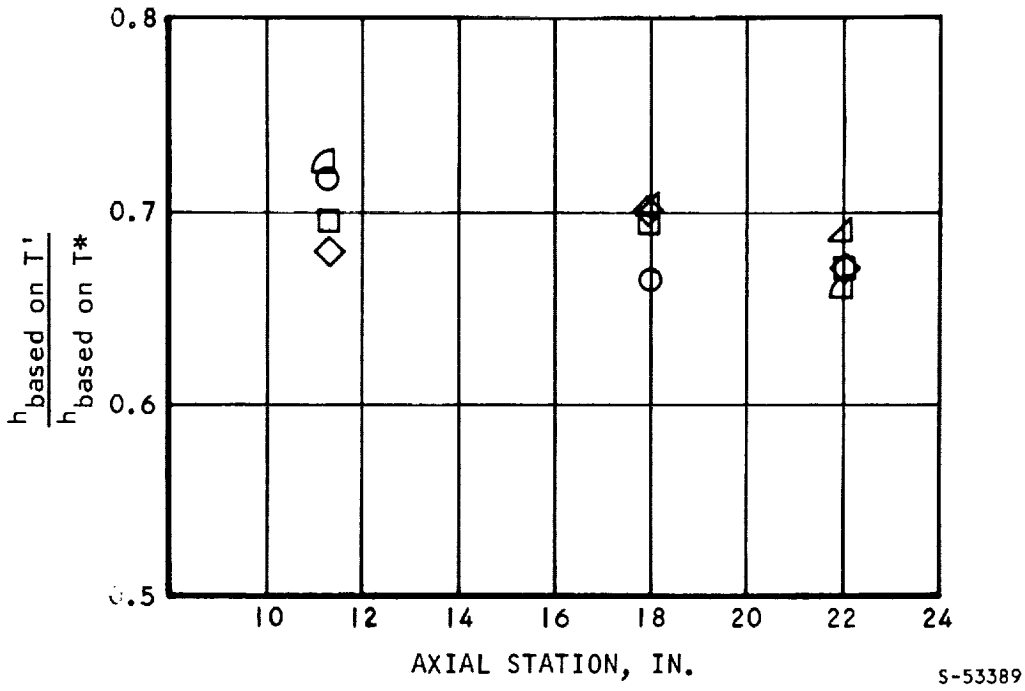

Figure 8.7-16. Comparison of Heat Transfer Coefficients by Eckert's and Modified Reference Temperatures (U)

in Figure 8.7-17. As shown in Figure 8.7-17, the peak heating location coincides with the peak pressure location. The magnitude of the peak heat flux was computed with the shock impinging equation as shown below:

$$\left(\frac{q}{A}\right)_{shock} = \left(\frac{q}{A}\right)_{undisturbed} \left(\frac{P_{peak}}{P_{\infty}}\right)^{0.9}$$

The water jacket data as shown in Figure 8.7-17, are average values over the entire water panel. Good agreement between the water jacket data and the thermocouple data is seen in Figure 8.7-17. Similar graphs for runs 143 and 147 are shown in Figure 8.7-18.

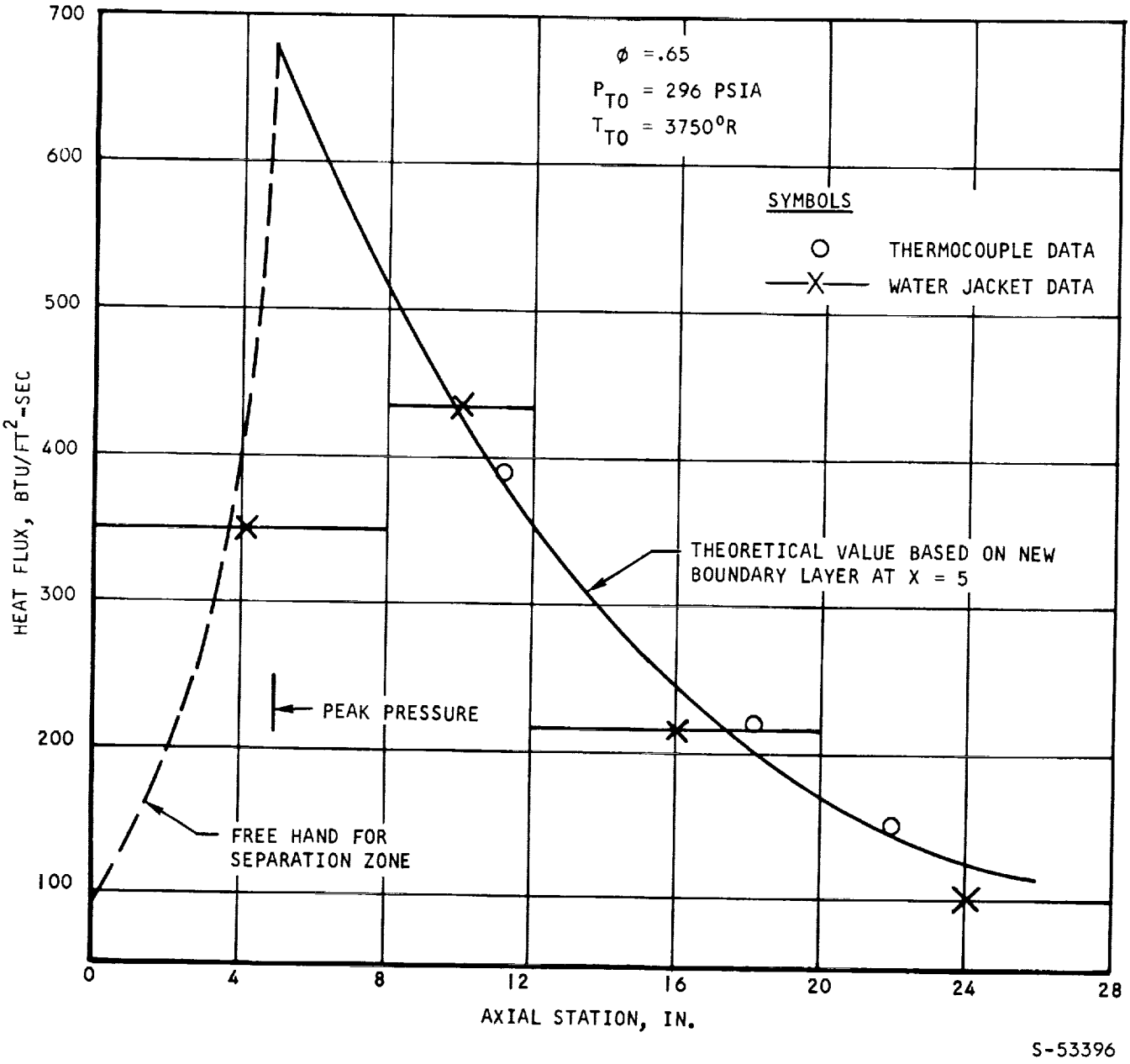

Figure 8.7-17. Run 142 Heat Flux Comparison (U)

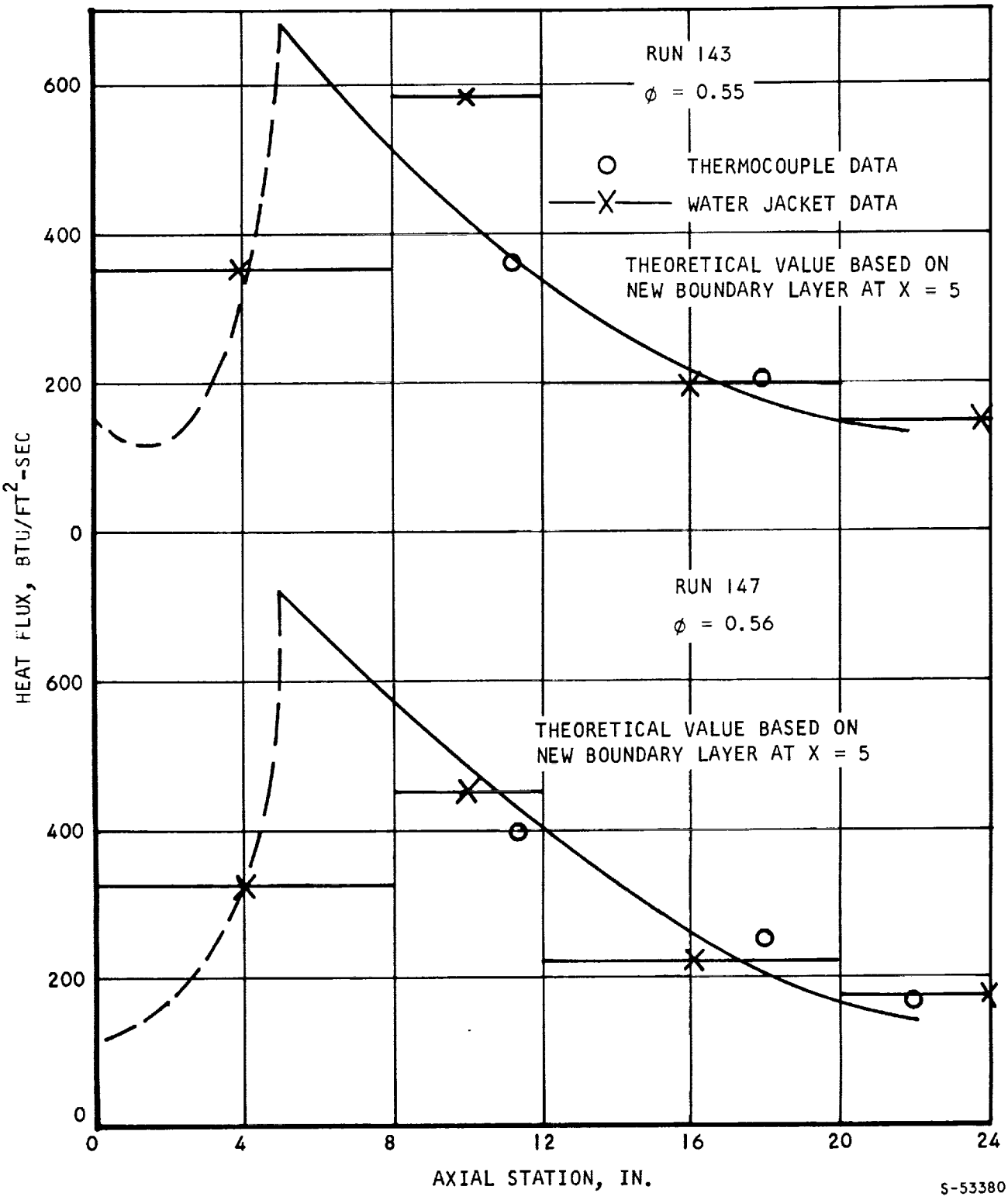

Figure 8.7-18. Heat Flux Comparison (U)

9. DISCUSSION

9.1 FLAME STABILIZATION FOR SUBSONIC COMBUSTION

The step at the downstream end of the HRE inlet spike offers a convenient means of flame stabilization for subsonic combustion. One objective of the subsonic combustion tests was to evaluate the effectiveness of this step as a flameholder.

Since the two-dimensional combustor at its 2-in. height had a channel height greater than that of the HRE subsonic combustor, it is necessary to know whether the height of the step-flameholder should be adjusted.

For Reynolds numbers greater than 10^4, the required absolute width of a flameholder for subsonic combustion using a given fuel is usually correlated by

$$D = \left(\frac{U_{Bo}}{p^a T^c f(\phi)} \right)^b$$ (Reference 9-1)

where U_{Bo} = blowoff velocity

p = pressure

T = temperature

$f(\phi)$ = a function of equivalence ratio

b = a function of Reynolds number

a, c = positive constants of order unity

The velocity, U_{Bo}, is evaluated just ahead of the step.

The equation indicates that for a given equivalence ratio and inlet Mach number, a step which holds the flame at a given pressure and temperature will also hold the flame at higher pressures and temperatures. The channel width is not important in this respect; thus, it concluded that the smaller step height used successfully in the experiments will be effective in the HRE.

9.2 SUPERSONIC COMBUSTION IN A CONSTANT-AREA SECTION

A high level of performance in the first stage combustor was demonstrated by the two-dimensional combustor test program when fuel was injected into a constant-area duct. Chemical efficiency above 90 percent was achieved within ten inches of combustor length. High chemical efficiency is attributed to the strong shock-boundary layer combustion interaction in maintaining a steep pressure gradient by creating aerodynamic blockage (the equivalent flow blockage area was estimated to be up to 40 percent). The steep pressure gradient not only reduced the flow velocity and increased the static temperature but also provided a strong beneficial effect on the mixing process. The losses induced from shocks and flow separations were compensated for by a more efficient combustion process in a slower moving stream. The phenomenon of flow separation did not impair the overall combustor performance and it is rather a necessity in order to have a better mixing process and shorter combustor length.

It is worthy of note that this type of separation was produced to a large extent by the adverse pressure gradient caused by the combustion process. Figure 9.2-1 shows the pressure distributions before and after the combustion was initiated. Without combustion, no strong separation was observable upstream of the injector. However, once combustion was established, the separation region extended more than 3.5 in. upstream. The strong interaction between combustion and separation represents an essential feature of supersonic combustion in a constant-area duct.

The flow reattached downstream of the separated region, as evidenced by a steep pressure drop in a constant-area section. The amount of heat release in the separated region could not be computed from pressure profiles because both heat release and flow separation are contributing factors in the static pressure rise. However, reasonable chemical efficiency could be computed for the attached flow in the diverging section.

For the same equivalence ratio, due to thermodynamic effect the static pressure rise decreases as the inlet temperature increases. Therefore, the effect of shock-boundary-layer-combustion interaction diminishes as inlet temperature is increased. This could present a basic mixing problem at higher flight Mach numbers.

9.3 SUPERSONIC COMBUSTION IN A DIVERGING DUCT

The problems of supersonic combustion in a diverging duct were evident from this test program. In these tests, low chemical efficiencies of the order of 50 to 60 percent were encountered regardless of injector geometry, equivalence ratio, and inlet total temperature. Various injector geometries, aimed at improving the mixing, and a higher inlet total temperature ($3800^{0}R$), aimed to enhance the chemical reaction, were tried. Both attempts failed to improve the combustor performance. A subsequent survey of the literature indicated that low chemical efficiencies were also obtained by a number of investigators (References 9-2, 9-3, 9-4) whenever a diverging duct was used. Cookson found that a hydrogen diffusion flame could not be maintained in a simple conical combustor of 0.75 deg divergence and 30 in. length.

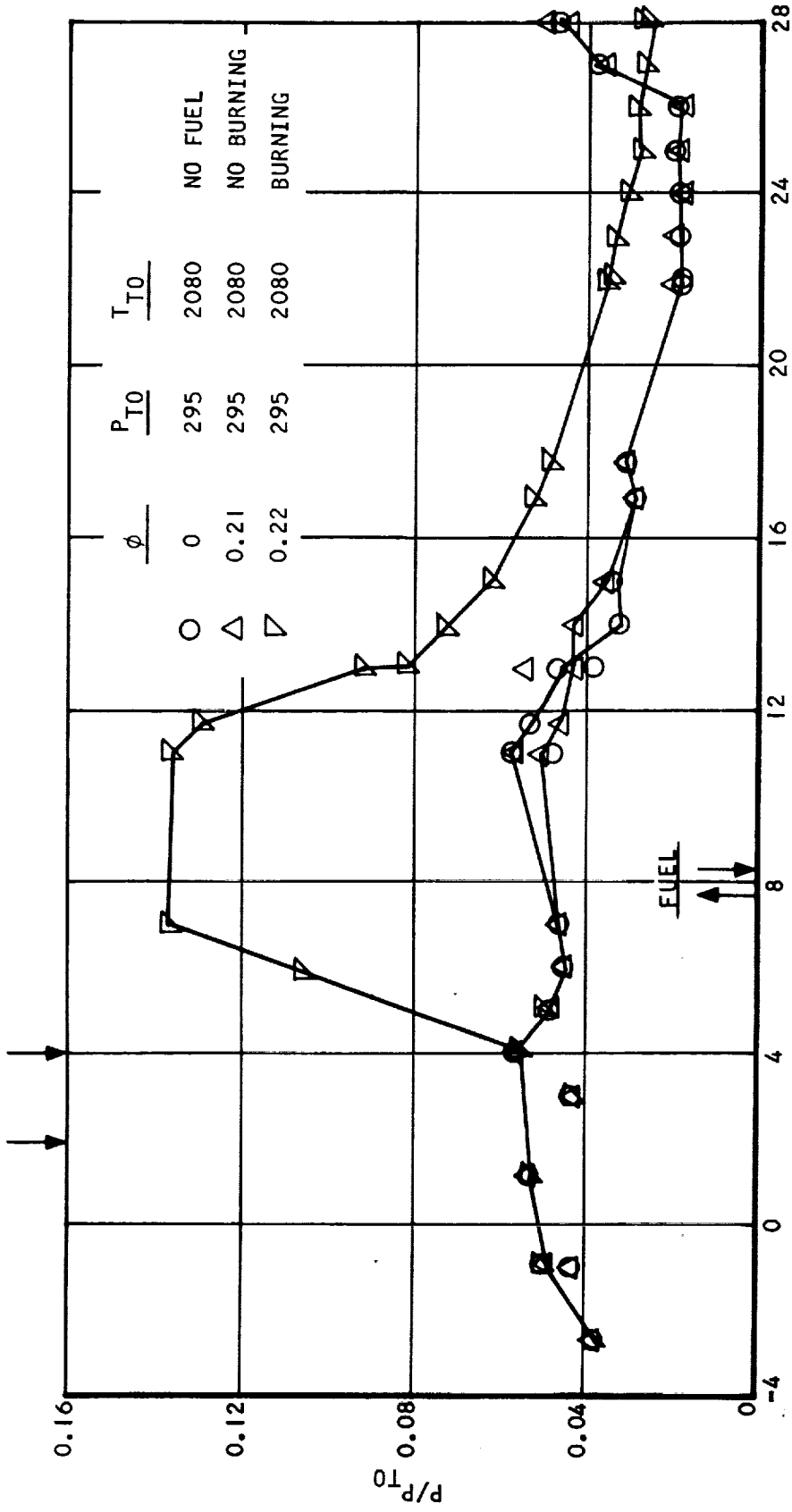

Figure 9.2-1. Effect of Combustion on Upstream Pressure (U)

Combustion was observed to occur after the Mach disc which was formed at the combustor exit. Cookson's experiments suggest that the chemical kinetics have a significant effect on the problem. Therefore, a chemical-kinetic analysis of two-dimensional combustor tests was performed.

Two cases at 3000°R test total temperature with total equivalence ratios of 0.6 and 1.02 were simulated in the Shear Layer Combustion Computer Program (Reference 9-5). This program permits the analysis of complex chemical kinetics systems with arbitrary gas phase reactions and species using a one-dimensional (area or pressure defined) stream tube model. Unique features of this program are (1) its ability to integrate the differential equations governing the chemical kinetic system with complete numerical stability using an implicit integration technique (Reference 9-6); and (2) its ability to consider addition or extraction of mass, momentum, energy, and chemical species at any position along the stream tube.

The two tests chosen for this simulation are listed in the following table, along with their nominal test parameters.

	Run 238	Run 242	
Time, sec	520.30	682.55	
φ	0.6049	1.0267	
T_T, °R	2838	3575	Station 7.3
T, °R	1897	2158	Station 7.3
Chemical Efficiency	60%	60%	

The chemical kinetics calculations were started at Station 7.3, just ahead of the first stage injectors, using equilibrium concentrations of the species. The energy and momentum losses due to heat transfer and wall friction were distributed linearly along the combustor, while the energy, momentum, and mass addition due to fuel injection were input at the appropriate injectors. The pressure-defined stream tube model was employed using measured static pressures from the two tests (see Figure 9.3-1). The resulting calculated flow areas could then be compared with the known combustor duct area.

For the following discussion the chemical efficiency as defined earlier in this report will be referred to as the "combustor efficiency." This is because in the model used combustion is limited by both the amount of fuel-oxidant mixing assumed, and the extent of chemical reaction calculated for that quantity of fuel which has mixed with the fuel. The efficiencies of mixing (η_m) and chemical kinetics (η_k) combined give the combustor efficiency (η_{cr}):

$$\eta_{cr} = \eta_m \cdot \eta_k$$

The simulation of the tests was based on the assumption of two limiting conditions. For the first of these conditions it was assumed that the combustor efficiencies calculated from test data represented chemical kinetic

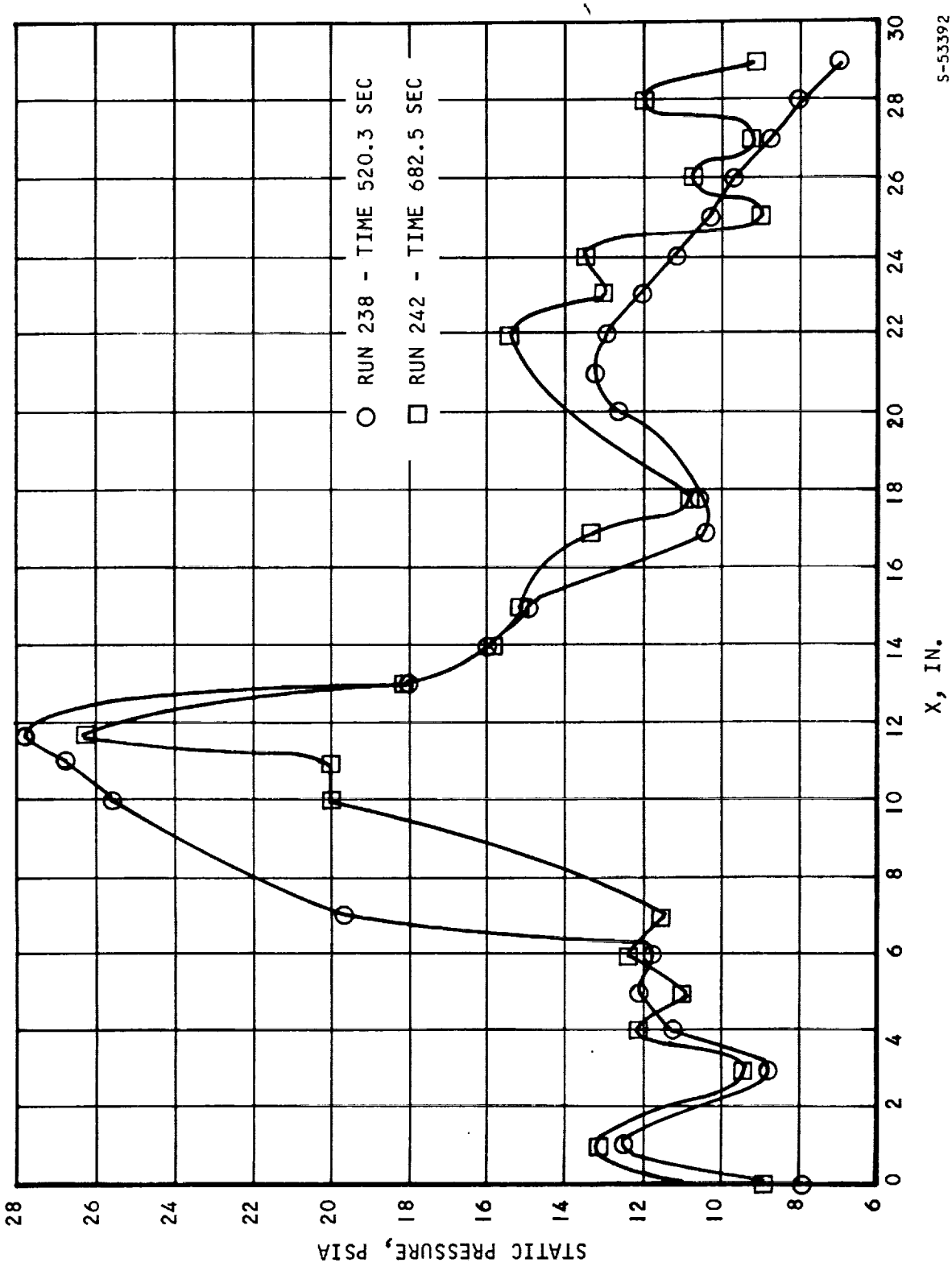

Figure 9.3-1. Measured Static Pressures - Tests 238 and 242 (U)

efficiencies (100 percent mixing efficiency). The second assumed that the combustor efficiencies represented the mixing efficiencies.

The several mixing models used with the two limiting conditions were implemented by the concept of an inert hydrogen molecule denoted by the symbol HZ_2. The inert hydrogen participated in the flow dynamics, but was not permitted to dissociate or react with other species. Mixing was simulated by replacing inert hydrogen (HZ_2) with active hydrogen (H_2) using the species addition feature of the computer program.

The three basic mixing models are shown in the sketch below. Model 1

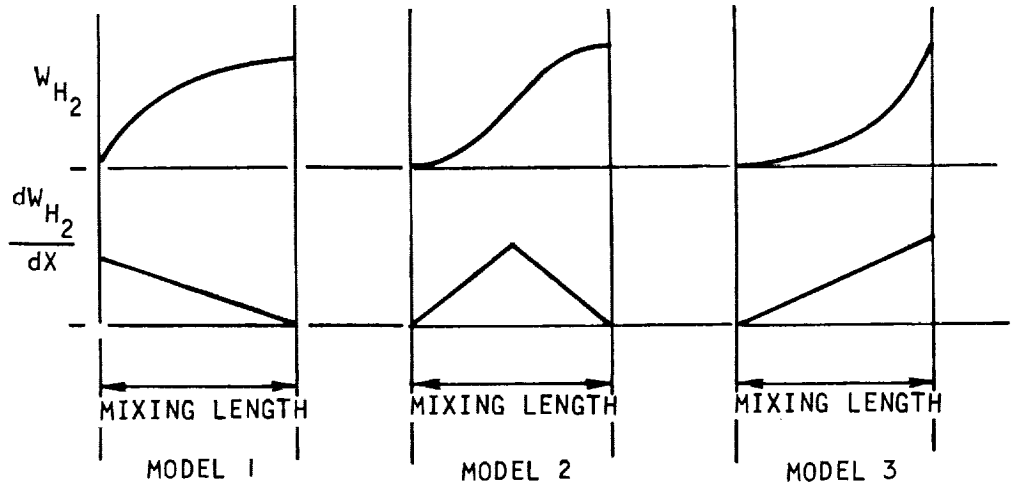

produced early mixing, Model 2 produced a maximum mixing rate at the mid-point of the mixing length, and Model 3 produced late mixing. Further variation within each mixing model was obtained by varying both the mixing length and the amount of hydrogen mixed at the injectors.

The results obtained from imposing the two limiting conditions on the simulation of run 238 in the Shear Layer Combustion Computer Program are presented in Figures 9.3-2 through 9.3-4, where the areas, mixing efficiencies, and chemical efficiencies were plotted as a function of axial position. In all cases 100 percent mixing efficiency (η_m) was assumed in the first stage combustor using mixing Model 2 with 50 percent mixing at the injectors and complete mixing at Station 12. Examination of the calculated areas in Figure 9.3-2 indicated a reasonable blockage (30 percent) in the constant-area portion, and reattachment of the flow near the entrance of the divergent portion of the first-stage combustor. The first-stage calculated results demonstrated chemical efficiencies of 95 percent at Station 13 and nearly 100 percent beyond Station 17 (see Figure 9.3-4).

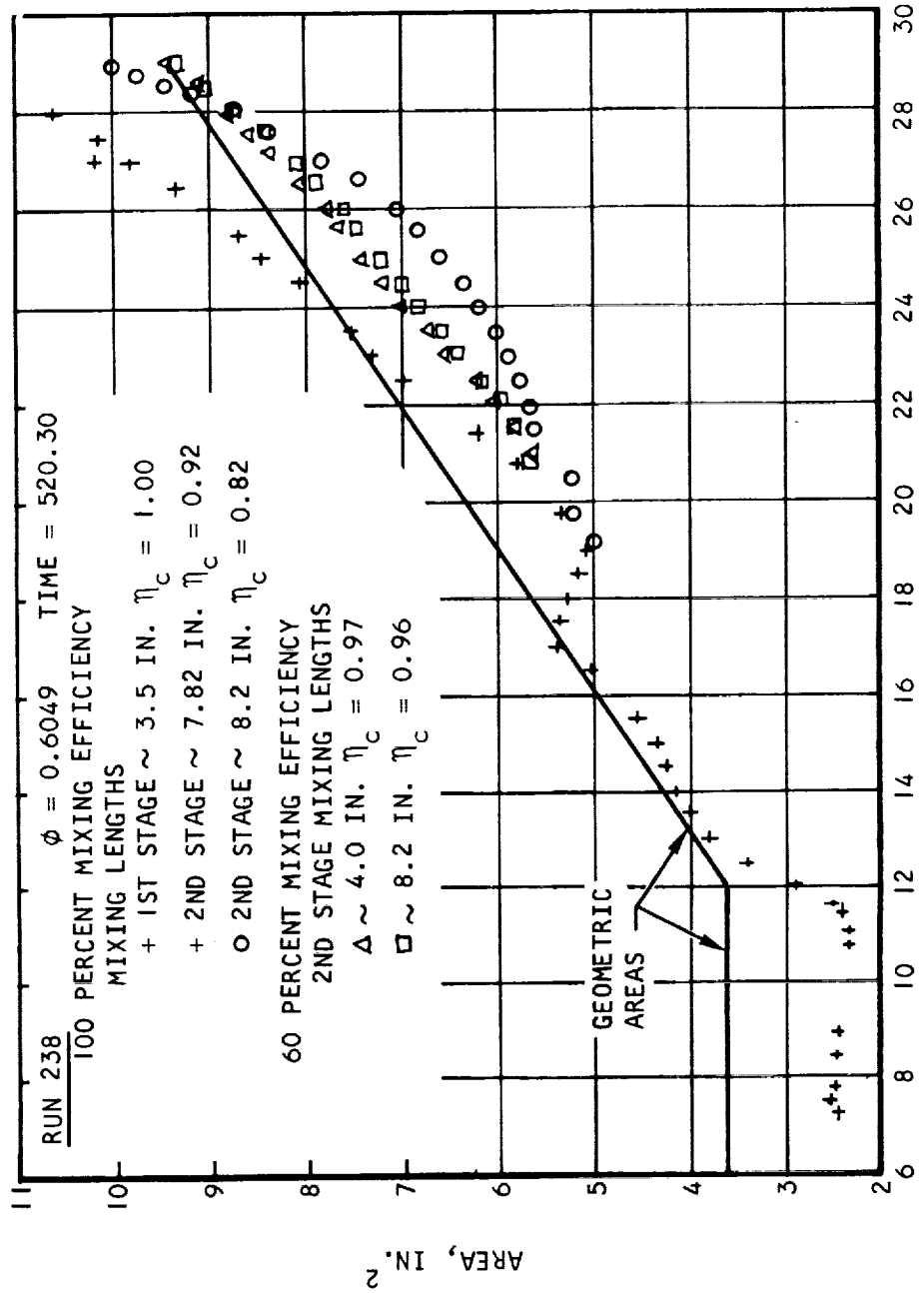

Figure 9.3-2. Geometric and Calculated Areas vs Axial Position - Run 238 (U)

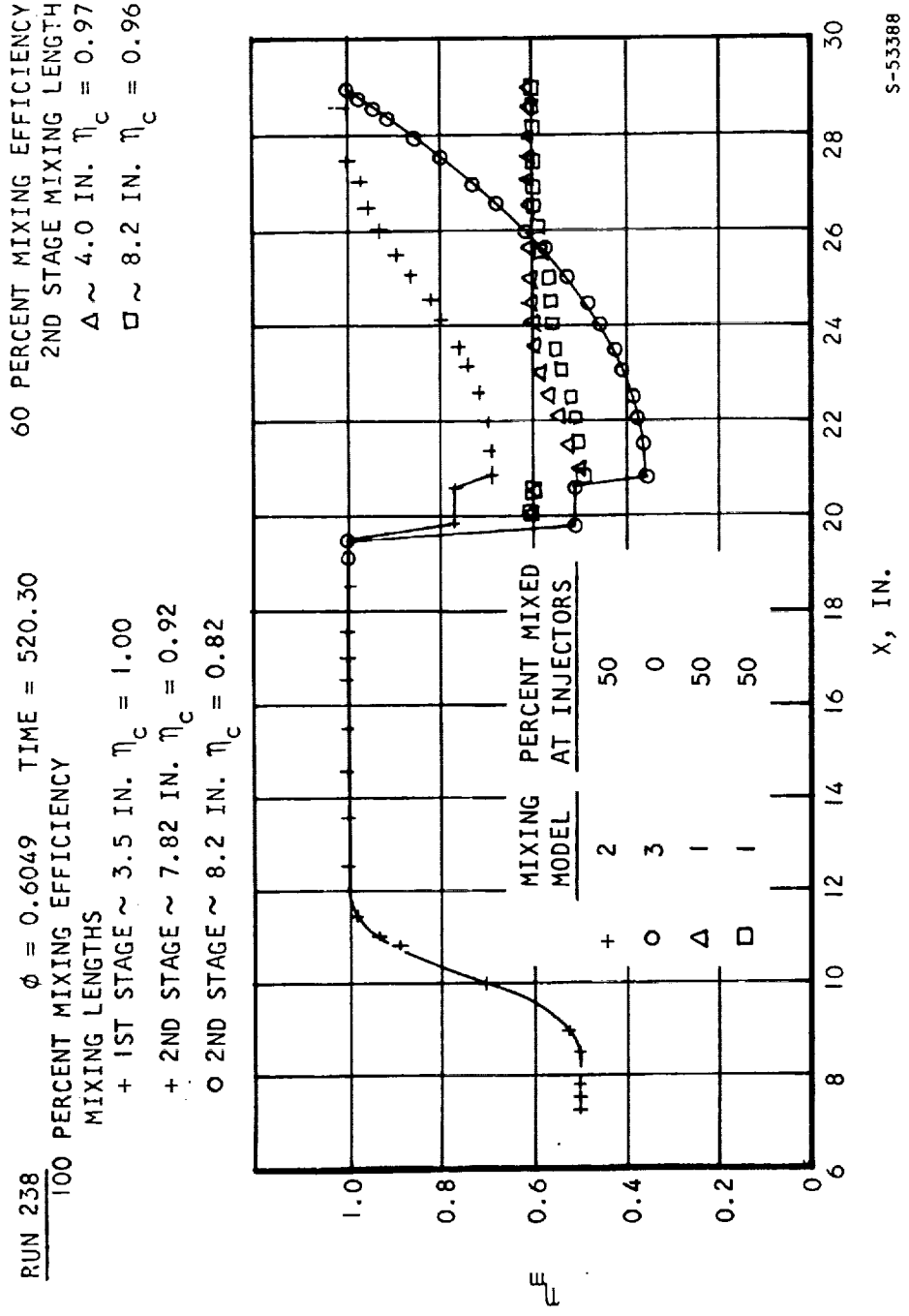

Figure 9.3-3. Mixing Efficiency vs Axial Position - Run 238 (U)

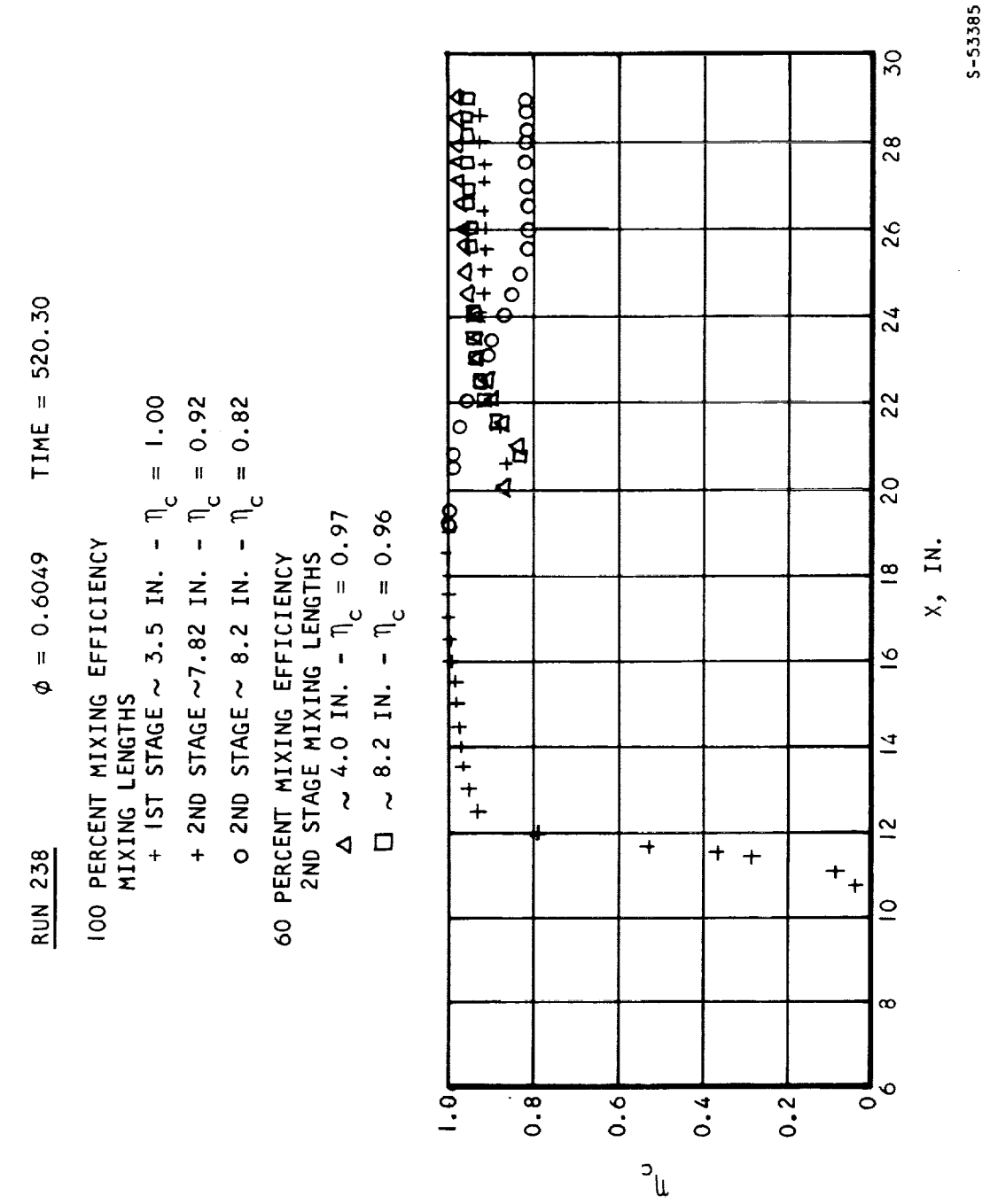

Figure 9.3-4. Chemical Efficiency vs Axial Position (U)

The first limiting condition (100 percent overall mixing efficiency) was imposed on the second-stage combustor using both a 50-percent local mixing efficiency at the injectors with mixing Model 2, and a 0-percent local mixing efficiency at the injectors with mixing Model 3. An overall mixing efficiency of 100 percent was set at Station 29 with both mixing models--the former simulating early mixing, the latter, late mixing.

Examination of the calculated areas (Symbols + and o) in Figure 9.3-2 indicated a reasonable blockage (~15 percent) at the second stage injectors; however, both mixing models eventually required flow areas greater than the geometric areas. Since such flows would be impossible to attain with the measured pressures from run 238, the assumption that the combustor efficiency equaled the chemical efficiency with 100 percent mixing was apparently in error. This argument was further substantiated by the chemical efficiencies in Figure 9.3-4 whose values were 92 percent for early mixing and 82 percent for late mixing compared with the value of 60 percent required to match the test data.

Therefore, the second limiting condition (combustor efficiency = mixing efficiency) was imposed on the second-stage combustor. A 50-percent local mixing efficiency at the injectors, with mixing Model 1 (early mixing), was assumed. An overall mixing efficiency of 60 percent was set at 4 in. and 8.2 in. downstream of the second-stage injectors as shown in Figure 9.3-3.

Again, the calculated flow areas indicated a reasonable blockage in the vicinity of the second-stage injectors, with the blockage gradually decreasing to zero as the flow approached the combustor exit (Figure 9.3-2). The mixing length of 4 in. produced flow areas which more closely matched the geometric areas and resulted in a chemical efficiency, for the mixed fuel, of 97 percent.

The two limiting conditions were imposed on the simulation of run 242 using the same mixing models as in run 238 with the exception that time did not permit the late mixing case to be run. The flow areas, mixing efficiencies, and chemical efficiencies were plotted as a function of axial distance and presented in Figures 9.3-5 through 9.3-7. Examination of the areas in Figure 9.3-5 again indicated that the first limiting condition (chemical efficiency = combustor efficiency) was in error and that the flow areas resulting from the second limiting condition more closely matched the test conditions. The fluctuating flow areas near the exit of the combustor (Figure 9.3-5) were due to fluctuations in the pressure-vs-length profile (see Figure 9.3-1).

While it appeared that the second limiting condition, i.e., incomplete mixing, produced the correct flowfields, the true condition could be found somewhere between the two limiting conditions, but quite close to the second. The relationship

$$\eta_{cr} = \eta_m \cdot \eta_k$$

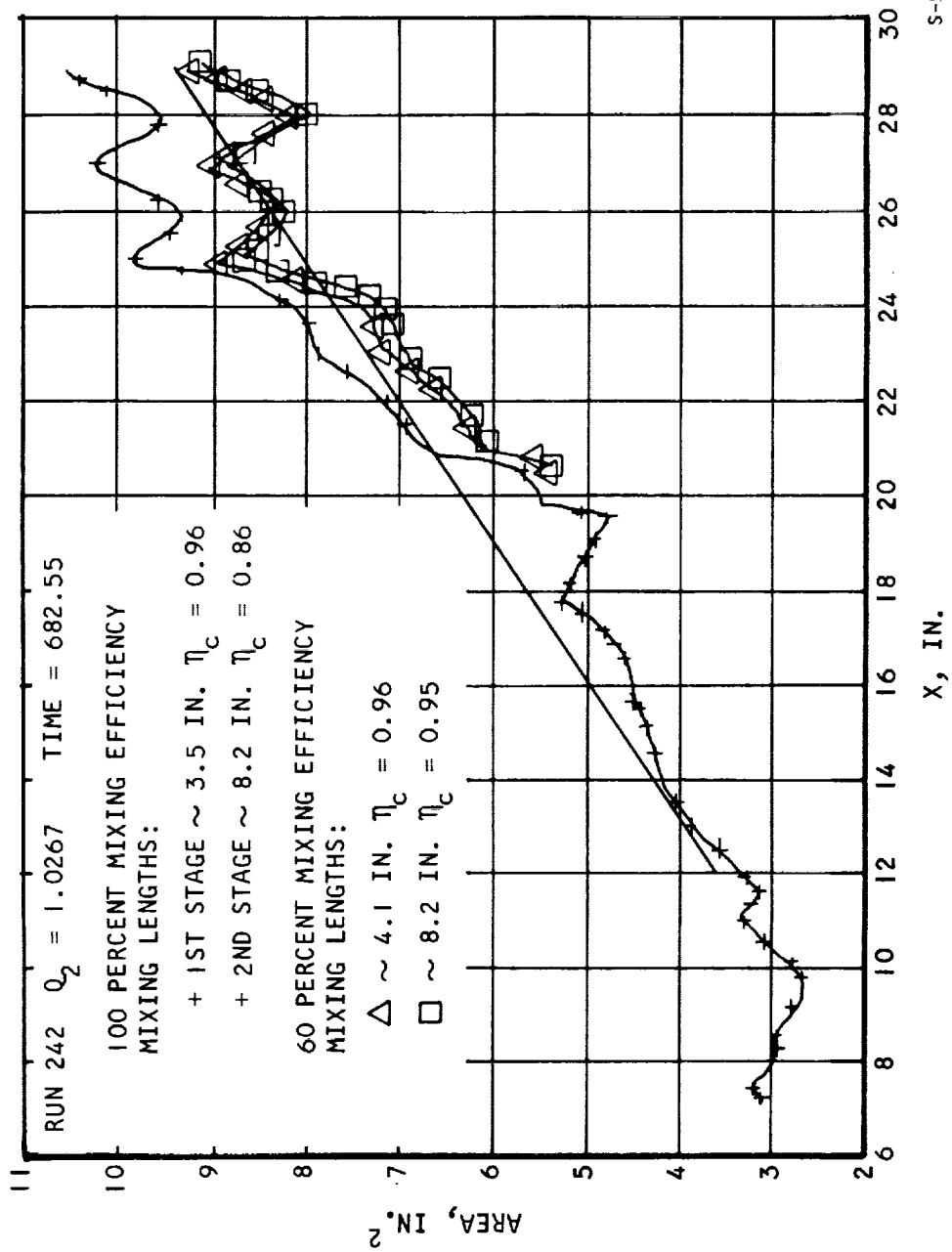

Figure 9.3-5. Geometric and Calculated Areas vs Axial Position - Run 242 (U)

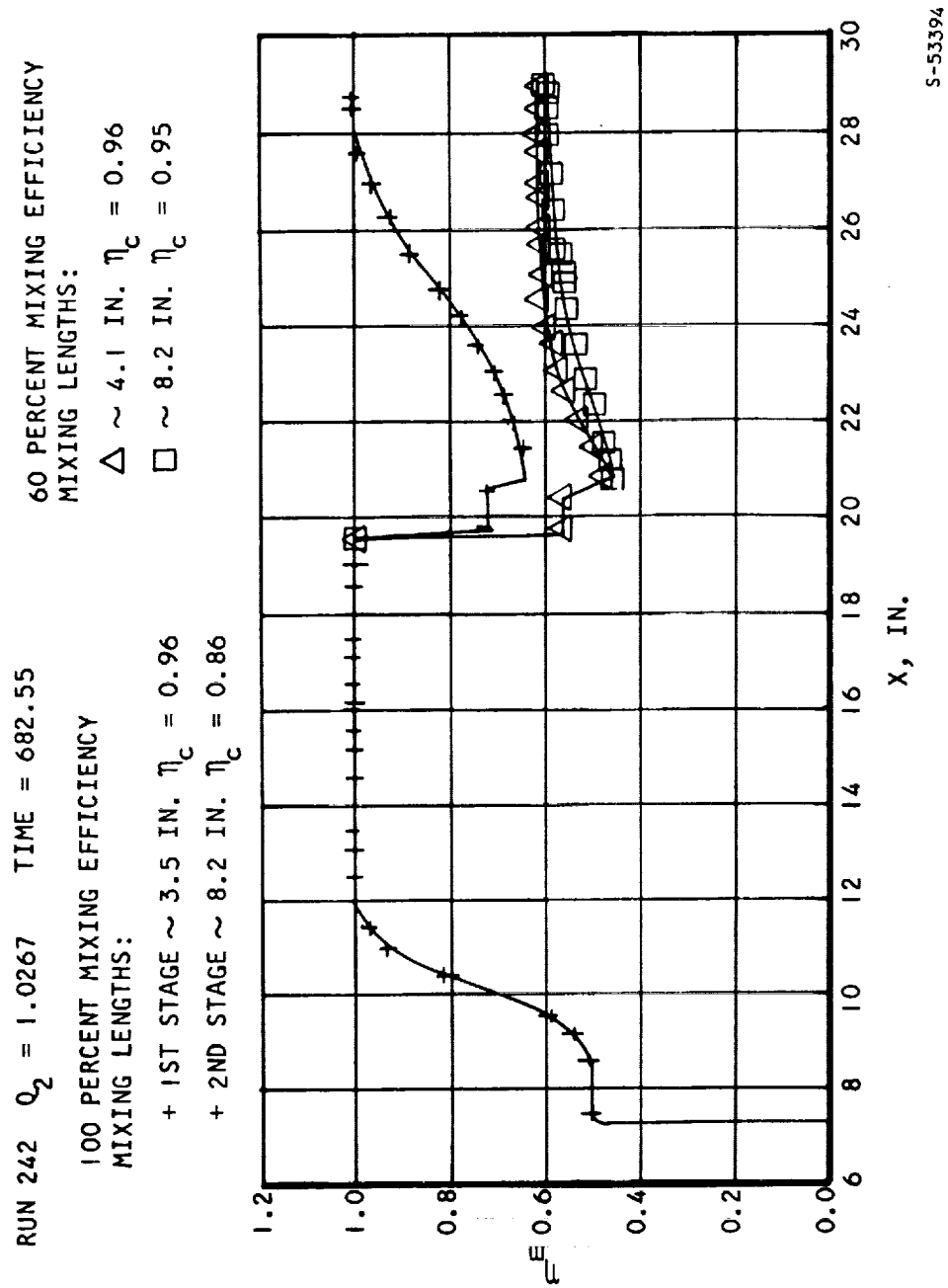

Figure 9.3-6. Mixing Efficiency vs Axial Position - Run 242 (U)

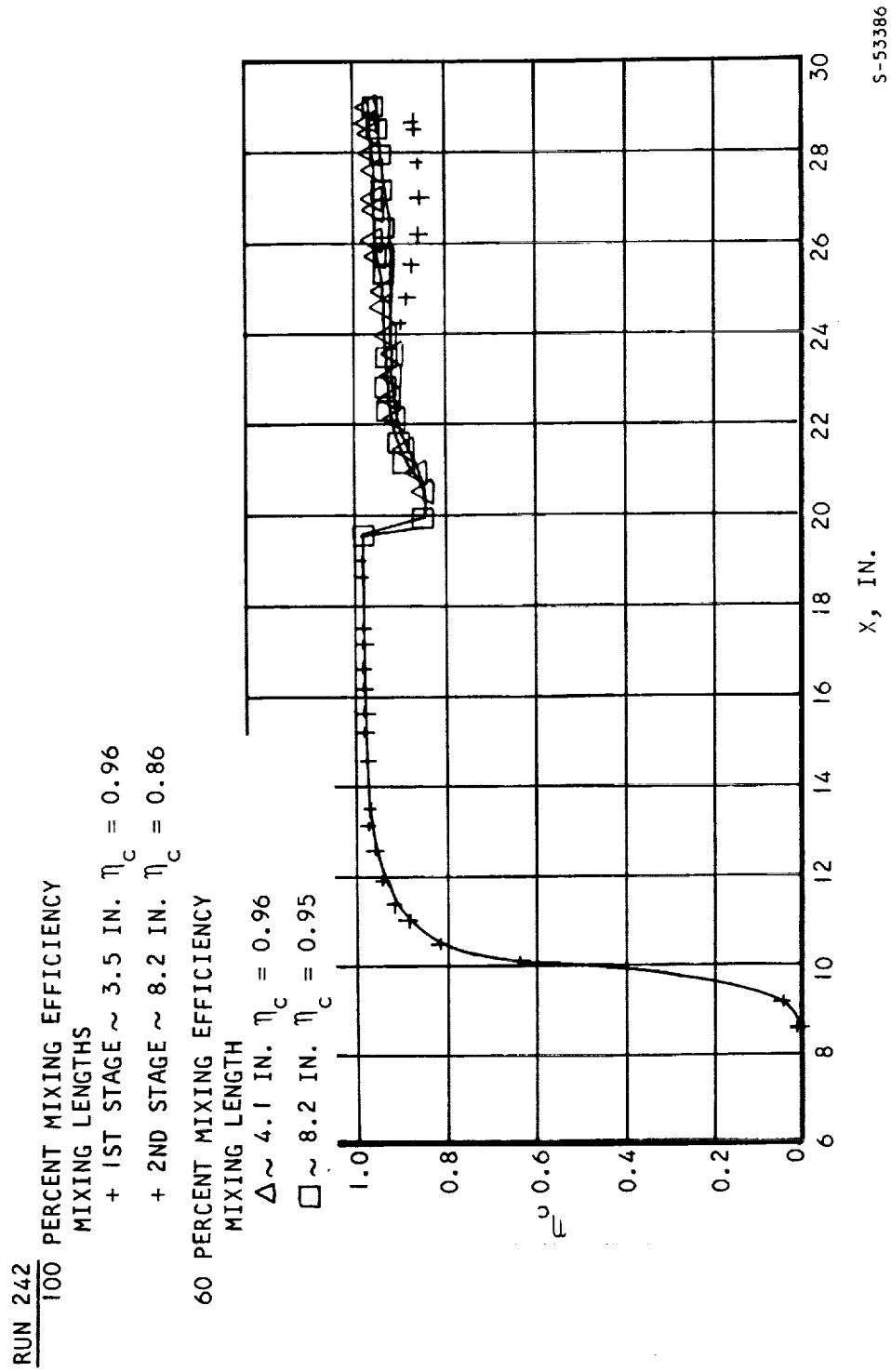

Figure 9.3-7. Chemical Efficiency vs Axial Position (U)

could be used to iterate on a mixing efficiency to produce flows which would more closely match the test results. For example, the next value of mixing efficiency in the iteration for run 238 would be obtained from

$$\eta_m^{(n+1)} = \frac{\eta_{cr}}{\eta_c^{(n)}} = \frac{0.6}{0.97} = 0.62$$

The results from the above test simulations support the conclusion that the low combustor efficiencies experienced in the two-dimensional combustor tests were due to poor mixing in the second stage.

9.4 MIXING IN A SUPERSONIC COMBUSTOR

One of the difficulties in experimental work is the accurate measurement of the mixing process. The measured quantitites are averages of the instantaneous values because the turbulence is a random, fluctuating flow and is three-dimensional. The mixing is not as complete as that indicated by the time-averaged measurement taken over a period of time using a gas sampling probe. The sampling probe mixes rich and lean regions to indicate an average composition. This may explain how low chemical efficiency could result in the two-dimensional combustor tests, despite the fact that gas sampling data indicated uniform mixed flow at the combustor exit.

The mixing process in a supersonic combustor may be divided into three phases: (1) jet penetration, (2) turbulent mixing, and (3) molecular diffusion. Among these, the turbulent mixing is least understood. The function of jet penetration is to properly distribute the fuel stream into the combustor by means of jet momentum. The turbulence which exists in the airstream or is generated by jet penetration and combustion breaks up the fuel stream into many small eddies. Finally, mixing is completed by molecular diffusion, which brings hydrogen and oxygen molecules into intimate contact. The molecular diffusion process is slow. Therefore, in order to shorten the mixing length, it is necessary to generate strong turbulence and small eddies to break up the fuel jet and reduce the distance through which the molecules must diffuse for complete combustion.

The second stage of the combustor test rig was a diverging duct, where the pressure gradient was less conducive to flow separation. Therefore, the required strong pressure disturbances which promote mixing and combustion were absent.

In turbulent flow, there is a bulk motion of large groups of molecules, or eddies. The turbulent mixing process breaks up the larger eddies into smaller eddies. The quality of the turbulence can be described by two characteristics: scale and intensity. The scale corresponds to the size of the eddies. Intensity can be defined in terms of variance of properties existing in a partially mixed gas. Intensity does not decrease until the scale of the non-uniformity becomes small or until molecular diffusion reduces the difference in properties.

(C) For example, in a pipe flow the viscous forces along the wall create large eddies arising from the interaction of the mean flow with the wall. The scale of these large eddies is of the order of one pipe diameter. The motion of the large eddies is unstable and they break up into smaller eddies. The smaller eddies in turn are unstable and will break up into still smaller eddies; this process continues until the smallest eddies are formed. For all but the smallest eddies, the Reynolds number (based on eddy size) is large, and dissipation of energy by viscous force is unimportant. As eddy size decreases, the Reynolds number becomes smaller and smaller, and at some critical point viscous force becomes important. The energy is then transferred from large to progressively smaller eddies until it is lost to heat by the dissipation action associated with the smallest eddies (Reference 9-7). The viscosity is associated with two extremes of this process. It creates the large eddies in the beginning and destroys the smallest eddies at end but does not have any large effect in the intermediate range of energy exchange (from large to smaller eddies). For mixing purposes, we are concerned with the intermediate stage at which strong turbulence has been produced, but dissipation is still negligible. It was observed (Reference 9-8) that approximately 80 percent of the turbulence energy is associated with the small eddies. Therefore it may be reasoned that the ability to achieve mixing will depend largely upon the total turbulence energy generated in the system and independent on the turbulence-producing device (Reference 9-9). Shock waves generated by cross-stream injection dissipate kinetic energy to heat without efficiently producing turbulence. Flow behind the separation bubble is very similar to the wake from a bluff body, which is a very effective turbulence-producing device. In addition, the favorable pressure gradient in a diverging duct may have significant effects in damping the turbulence, as demonstrated by Schubauer-Skramstad (Reference 9-10) for subsonic flows. These reasons may explain why the various injector geometries tried in the second stage would not improve the combustor performance.

9.5 USE OF VITIATED AIR

(U) Several of the features of the test concept must be considered in applying the test results to design of a flight engine. These include (1) the use of vitiated air, (2) the limiting of combustor inlet total pressures to less than 300 psia, (3) differences between the geometry of the flight engine combustor and the simpler geometry of the test combustor, and (4) flow separation at the combustor exit due to discharge into an environment at sea-level pressure. The effects of using vitiated air are discussed in this section.

(U) Vitiation of air can be thought of as the addition of water vapor at the expense of the nitrogen percentage. Unfortunately, besides having different physical properties, water is not as inert, chemically, as nitrogen. Therefore, the chemical properties of vitiated air are different from those of

"clean" air, to an extent which is not well-known for the complex environment in a supersonic combustor. Some factors which must be considered in attempting the extrapolation of vitiated air results to the clean-air case are discussed below.

9.5.1 Physical Properties of Vitiated Air

The quantity of vitiating gases which must be added to air, to give the desired combustor inlet temperature, is dependent upon the initial temperatures of the gases, the local static pressure, and the heat losses in the system. Therefore, it is convenient to treat "weight-percent of vitiating gases", ν, as a parameter which does not depend exclusively on the inlet temperature.

$$\nu = \frac{(\dot{W}_{H_2,\ vit} + \dot{W}_{O_2,\ vit})}{(\dot{W}_{H_2,\ vit} + \dot{W}_{O_2,\ vit}) + \dot{W}_{air}} \times 100 \text{ percent}$$

where $\dot{W}$ is weight flow rate, subscript (vit) signifies that the gases are added to the air in the vitiation heater, and H_2 and O_2 denote hydrogen and oxygen, respectively. The weight percentage of water vapor in the inlet gases (without dissociation) is equal to 0.677 ν.

The molecular weight and γ, the ratio of specific heats, are plotted as functions of static temperature in Figures 9.5-1 and 9.5-2, for vitiated air in chemical equilibrium at static pressures of 0.5 and 10.4 atm, respectively. (These two pressures are near the extremes of pressures which occur in the combustor model inlet and in the vitiation heater.) In each case, results are given for three different values of ν. The $\nu = 0$ case represents clean air.

Since γ is dependent upon ν, the Mach number obtained from a given inlet nozzle will depend to some extent on the factors discussed above which determine ν. The nozzle's Mach number will also depend on gas temperature. This is true even for clean air.

Given identical inlet Mach numbers and static pressures, the dynamic pressure of the vitiated airstream is somewhat lower than that for clean air, again because of γ's dependence on ν. The dynamic pressure, q, is given by

$$q = \frac{\gamma p M^2}{2}$$

where p is static pressure and M is Mach number. A change in q_{air} will affect penetration of the fuel jet into the air stream, since for constant jet and airstream Mach numbers the penetration is roughly proportional to

$$\left(\frac{q_{jet}}{q_{air}}\right)^n$$

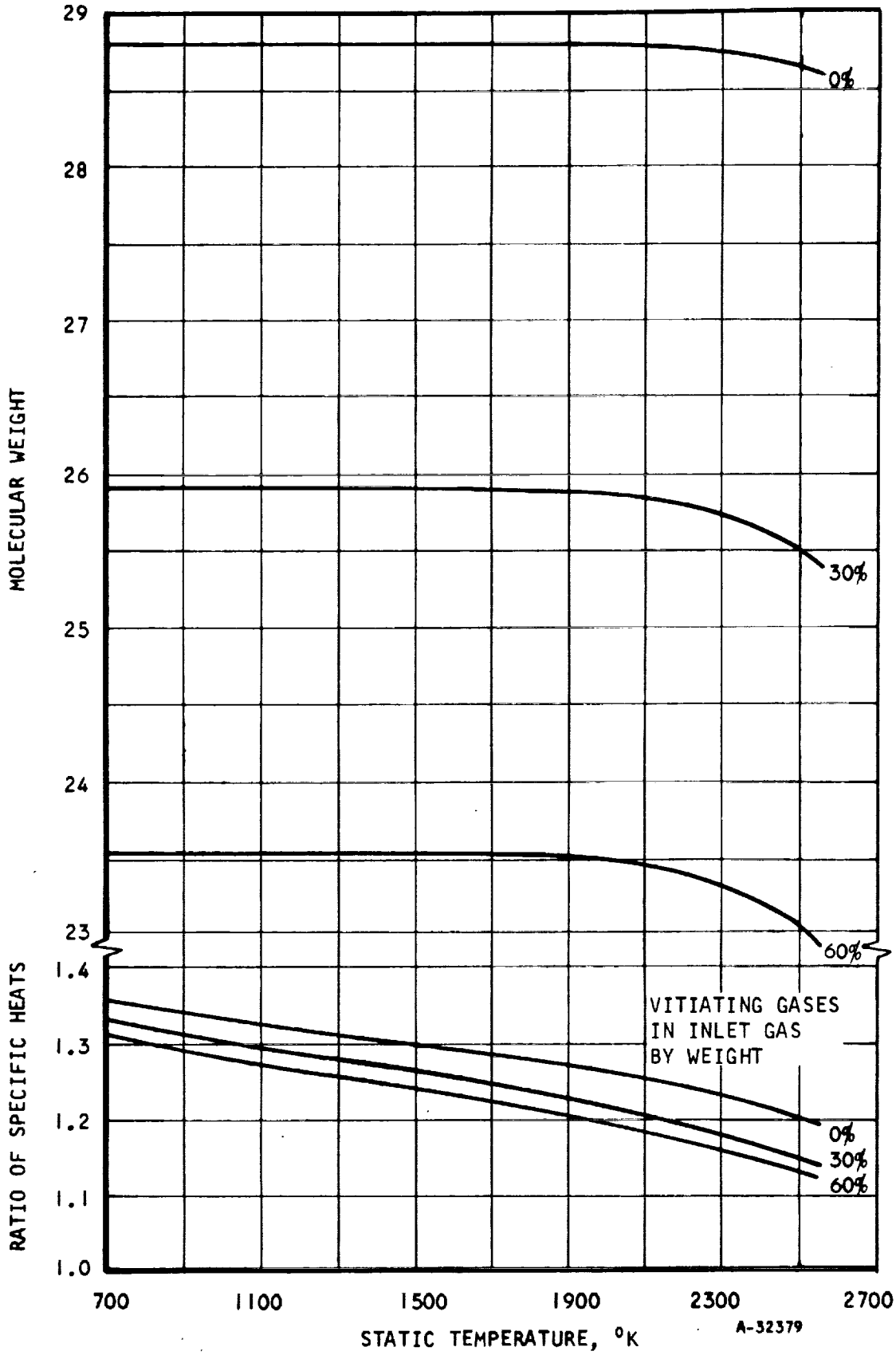

Figure 9.5-1. Properties of Vitiated Air at 0.5 Atm. Assuming Chemical Equilibrium.

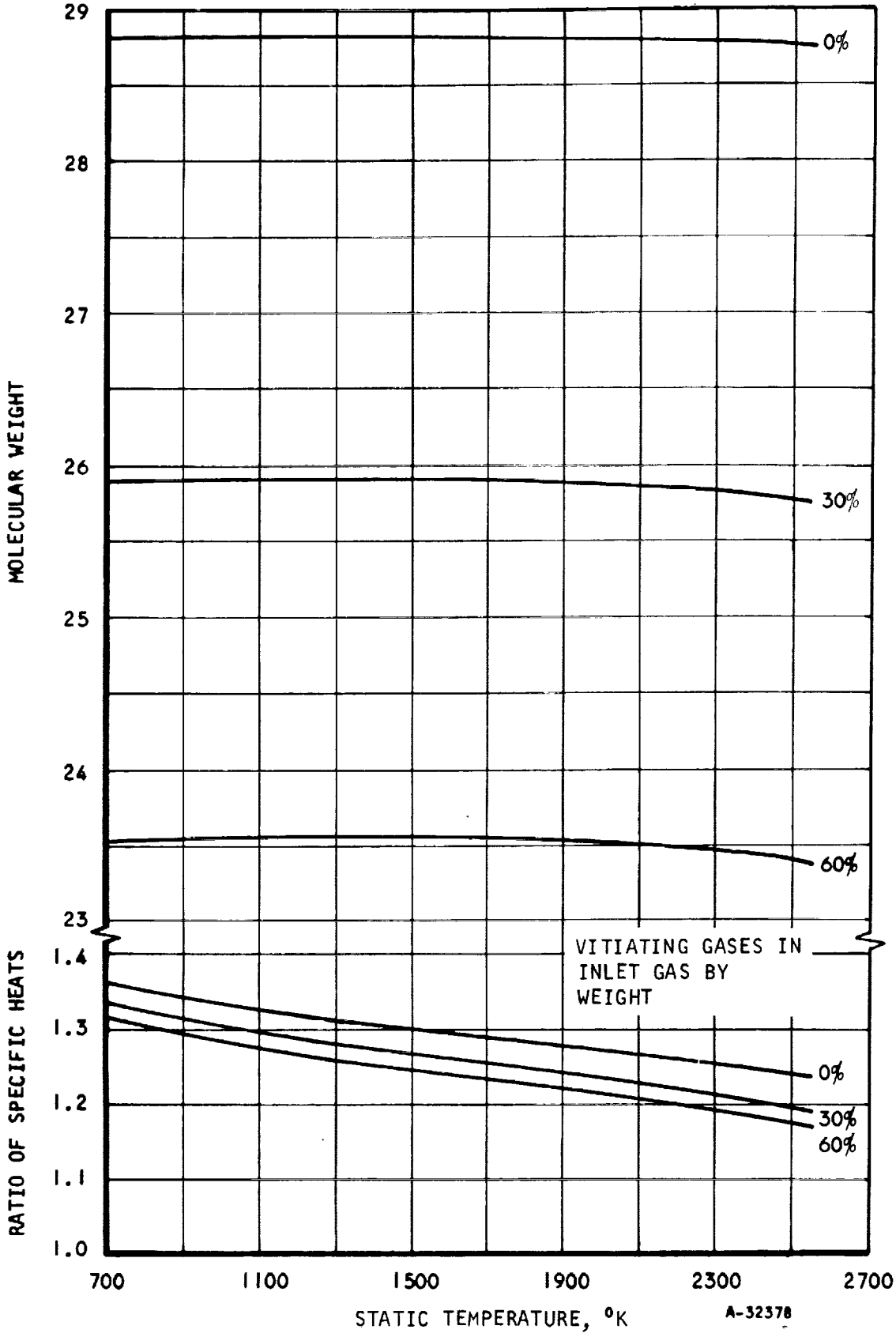

Figure 9.5-2. Properties of Vitiated Air at 20.4 Atm, Assuming Chemical Equilibrium.

where $n \approx 0.33 - 0.5$ (see Reference 9-11). However, since both n and the change in q_{air} due to variation in γ are small, the penetration should differ from that in clean air by less than five percent.

For a given inlet mass flow rate, the dependence of molecular weight of vitiated air on ν affects the weight flow of hydrogen which must be injected to obtain the desired combustor equivalence ratio.

The equivalence ratio, ϕ, for a hydrogen-fueled combustor can be defined as a ratio of mass flows:

$$\phi = \frac{\left(\dot{m}_{H_2}\right)_{\text{combustor}}}{\left(\dot{m}_{H_2}\right)_{\text{stoichiometric}}}$$

where $\left(\dot{m}_{H_2}\right)_{\text{stoichiometric}}$ is referred to the amount of available oxygen entering the combustor. When computing ϕ for vitiated air, the following formula may be used:

$$\phi = \frac{\left(\dot{m}_{H_2}\right)_{\text{combustor}}}{0.0290\left[\dot{m}_{air} + \left(4.35\ \dot{m}_{O_2} - 34.5\ \dot{m}_{H_2,\ vit}\right)\right]}$$

where $\dot{m}_{O_2}$ and $\dot{m}_{H_2,\ vit}$ are the mass flows of oxygen and hydrogen added in vitiation. These two flows are assumed independent, since experimental errors in general prevent exact attainment of the correct ratio between the two. The constants in the above equation are based on the further assumption that the relative humidity in the incoming clean air is about 50 percent.

For a given heat release, the performance obtainable from a supersonic combustor is determined by the entropy rise. Changes in the entropy rise due to using vitiated air are determined, in part, by the physical properties of the mainstream gas, such as specific heats and viscosity. However, perhaps the most important effect on entropy rise is due to the change in the rate of heat release arising from chemical kinetic effects (see Section 9.6).

9.5.2 Equilibrium Thermochemical Effects on Choking Conditions

Designing for supersonic flow throughout the HRE combustor requires a knowledge of the "choking area"; that is, at what flow area the gas stream would become sonic for a given inlet condition and equivalence ratio. Since the choking conditions are a function of the rates of combustion, they must be determined experimentally. Extrapolating subscale combustor test results to flight engine behavior, however, requires knowing to what degree the choking conditions are affected by the use of vitiated air rather than clean air.

For the purpose of analysis, two identical combustors may be considered: one uses vitiated air and the other, clean air. For this example, it is assumed that:

(a) Combustion is complete in both cases, leaving a uniform gas stream at chemical equilibrium

(b) The flows are one-dimensional

(c) The total pressure at the sonic plane is the same in both cases

With these assumptions, the effect of the equilibrium thermochemical properties on choking conditions can be ascertained. Specifically, the ratio of choking areas for the two combustors can be found when both combustors are operated at the same inlet total pressure, inlet total temperature, fuel temperature, and equivalence ratio.

Once these conditions have been prescribed, the weight flow rate, per unit area, of the combustion products at the sonic plane is readily found from thermochemical considerations (using the computer program described in Reference 9-12). These flows will be denoted by (W_{cp}/A^*_{cp}) for the combustion products in the clean air case and by (W_{vp}/A^*_{vp}) in the vitiated air case. The ratio of these, however, must be corrected because the weight flow through a converging-diverging supersonic combustor inlet will not be the same in both cases, nor will the weight flows of fuel added be the same for a given effective equivalence ratio. If the inlet nozzle throat areas are the same for both vitiated and clean air cases, the ratio of choking areas is

$$\frac{A^*_{cp}}{A^*_{vp}} \quad \frac{\left(W_{vp}/A^*_{vp}\right)}{\left(W_{cp}/A^*_{cp}\right)} \times \left[\frac{W_{cp}}{W_{vp}}\right]$$

$$\frac{A^*_{cp}}{A^*_{vp}} = \frac{\left(W_{vp}/A^*_{vp}\right)}{\left(W_{cp}/A^*_{cp}\right)} \times \left[\frac{\left(W_{ca}/A^*_{noz}\right)\left(1 + \frac{W_{cf}}{W_{ca}}\right)}{\left(W_{va}/A^*_{noz}\right)\left(1 + \frac{W_{vf}}{W_{va}}\right)}\right]$$

where W_{vf} and W_{cf} = the weight flows of fuel added in the vitiated and clean-air cases, respectively

W_{ca} and W_{va} = the weight flows of clean and vitiated air, respectively

Typical values of (ν) were used to obtain (A^*_{cp}/A^*_{vp}) vs simulated flight Mach number for $\phi = 1$, using somewhat arbitrary values of inlet total pressure. The total pressure was assumed to decrease by a factor of four in the combustion process. An assumed value of combustor heat loss was set, again arbitrarily, by making the fuel enthalpy equal to that of liquid hydrogen at 36^0R. (This is equivalent to assuming that all the heat lost through the combustor walls is absorbed by the fuel, which has entered the cooling passages as a liquid.) It is to be noted that the arbitrary inlet total pressures do not exceed the

nominal subscale combustor test limit of 300 psia.

Results, given in Figure 9.5-3, indicate that equilibrium thermochemical effects alone affect the choking area by four percent or less and that the clean air combustor is more prone to choking.

9.5.3 Total Pressure Effects on Choking Conditions

The area required to pass a given mass flow at Mach 1 depends on the local total pressure as well as on gas properties and temperature, and the equilibrium gas properties depend somewhat on the pressure.

Total pressure drop in a supersonic combustor depends on the heat release rate and the amounts of skin friction and three-dimensional flow loss associated with the particular combustion-flow process. Previous sections mentioned some reasons for the effect of vitiated air on the combustion processes. A rigorous analysis of the various effects, however, would be complex and, based on the present state of the art, not very reliable, because only detailed knowledge of every phase of the combustion process would provide an accurate idea of the difference in total pressure loss due to vitiation.

9.5.4 Temperature Rise

The temperature rise due to complete combustion is affected by the extent of vitiation. This is primarily due to the high heat capacity of water vapor relative to that of nitrogen. The effect is augmented, at high static temperatures, by the heat-absorbing dissociation of the vitiation water.

Estimated temperatures for various simulated flight Mach numbers are plotted in Figure 9.5-4 for clean air and vitiated air conditions.

9.6 CHEMICAL KINETICS IN THE SUPERSONIC COMBUSTION OF HYDROGEN

The chemical kinetics of supersonic combustion of the premixed hydrogen-air system was investigated analytically. Attention was directed towards clarifying effects of static temperature, static pressure, equivalence ratio, vitiation, initial radical concentration, and channel divergence on chemical kinetics. These effects were determined using a one-dimensional chemical kinetics computer program (Reference 9-13). More complete results will be found in a forthcoming report.

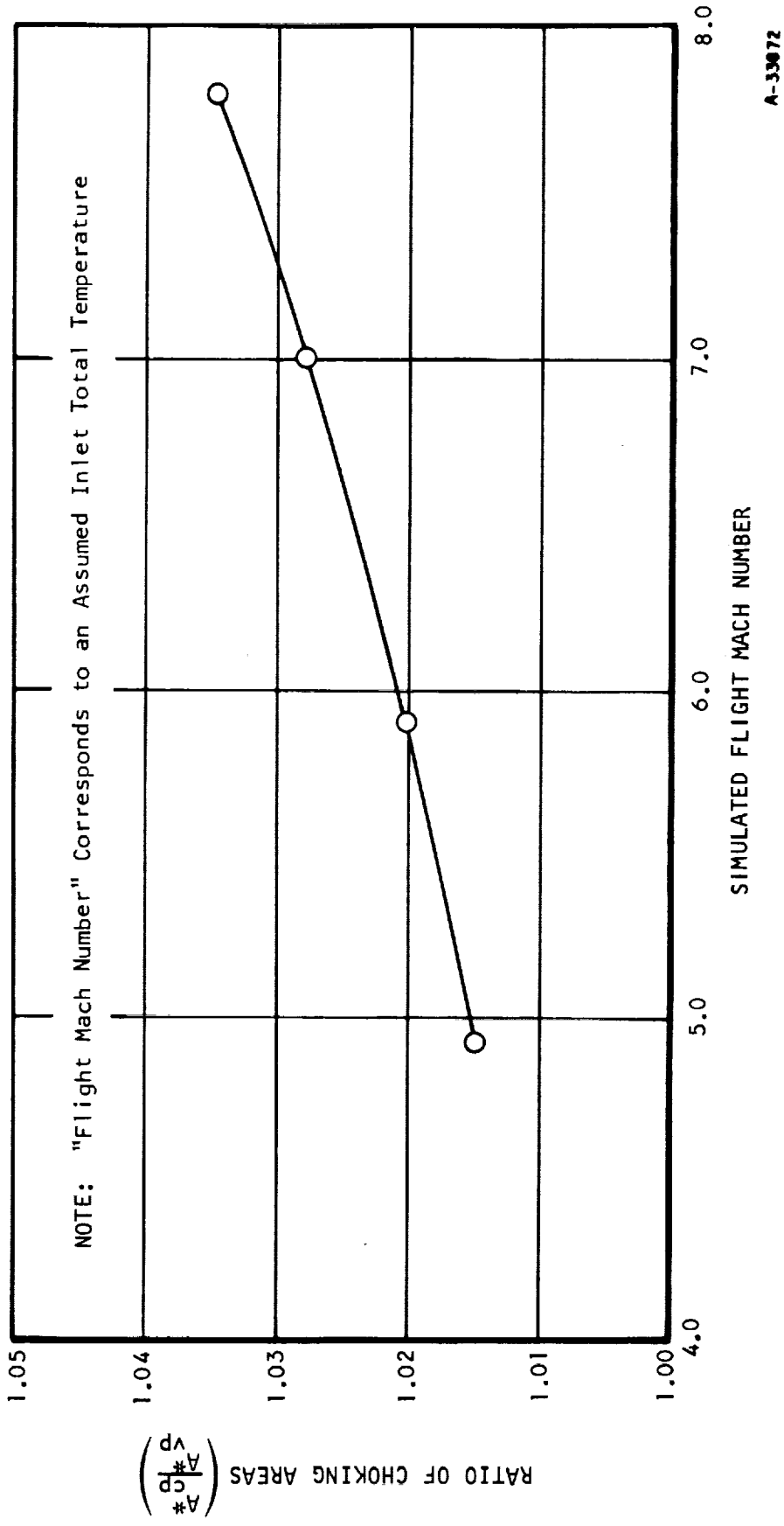

Figure 9.5-3. Choking Area Ratio vs Simulated Flight Mach Number for $\phi = 1$, Using Estimated Values of the Necessary Percentage of Vitiation Gases

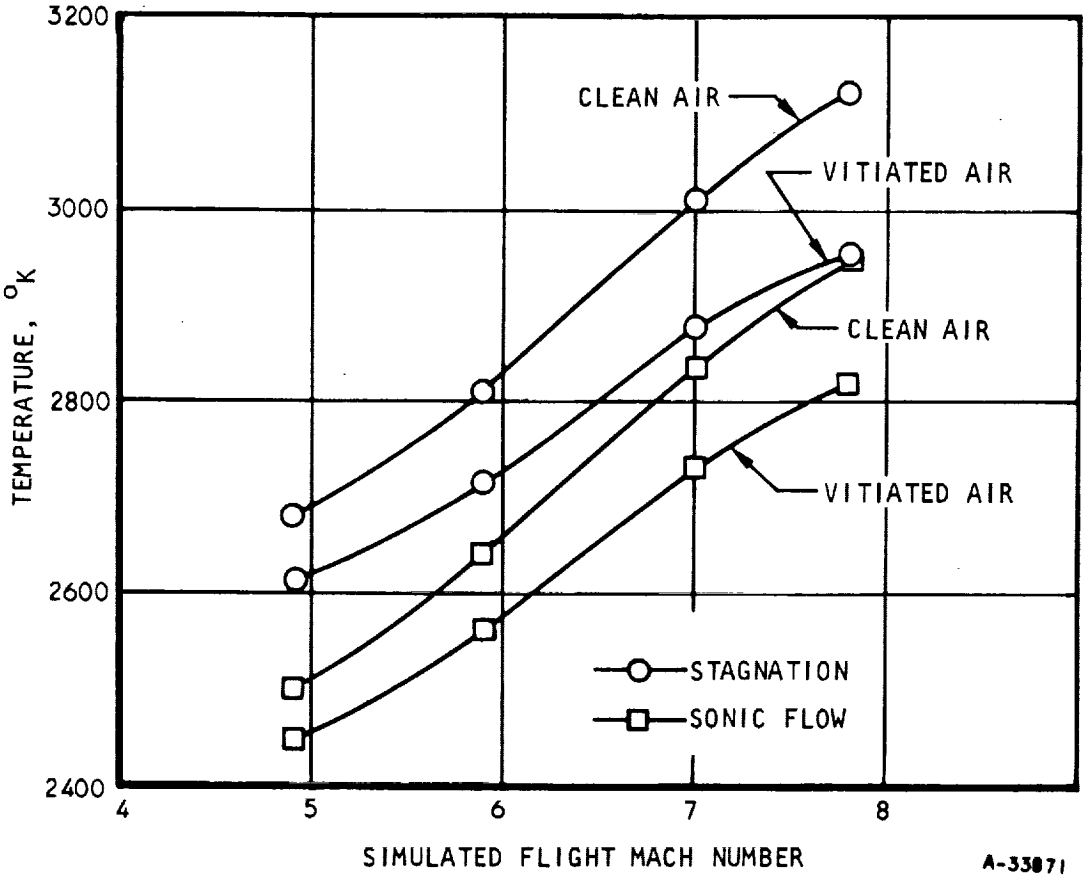

Figure 9.5-4. Effect of Vitiation on Final Temperature

The reaction mechanism of the hydrogen-air mixture was assumed to be comprised of the eleven elementary reactions shown in Table 9.6-1.

TABLE 9.6-1

HYDROGEN-AIR REACTIONS

(4)	$H_2 + M = H + H + M$	(Chain-initiating steps)
(9)	$O_2 + M = O + O + M$	
(11)	$H_2 + O_2 = OH + OH$	
(1)	$H_2 + OH = H_2O + H$	(Chain-carrying steps)
(8)	$O + H + M = OH + M$	
(2)	$H + O_2 = OH + O$	(Chain-branching steps)
(3)	$O + H_2 = OH + H$	
(7)	$H_2O + O = OH + OH$	
(6)	$HO_2 + H_2 = H_2O_2 + H$	
(5)	$H + O_2 + M = HO_2 + M$	(Chain-breaking steps)
(10)	$H + OH + M = H_2O + M$	

The symbol "M" represents a "third body"; i.e., any chemical species. The third body acts as an energy source or sink in chemical reactions.

The reaction rate constants were expressed in the standard Arrhenius form:

$$K_f = DT^E \exp. \frac{F}{T}$$

$$K_b = \frac{K_f}{K_{EQ}}$$

$$K_{Eq} = DCT^{EC} \exp. (FC/T)$$

where D, E, F, DC, EC, and FC are the constants in Table 9.6-2. The constant, D, for reaction 5 was multiplied by the weighted third body efficiency factor, b_w.

TABLE 9.6-2

REACTION-RATE CONSTANTS*

	D	E	F	DC	EC	FC
1	.23000+14	.00000	-.26200+04	.21592-01	.28430-00	.79233+04
2	.10000+15	.00000	-.80500+04	.40779+03	-.41038-00	-.86628+04
3	.12000+14	.00000	-.46300+04	.18825+01	.21810-01	-.91546+03
4	.10000+22	-.15000+01	-.51900+05	.36160+01	.63998-02	-.52421+05
5	.8600+15	.00000	.64400+03	.69905-01	.28001-00	.23858+05
6	.54000+12	.00000	-.12090+05	.66604-00	-.46383-01	-.76370+04
7	.29000+15	.00000	-.94000+04	.87164+02	-.26247-00	-.88387+04
8	.40000+19	-.10000+01	.00000	.51895-00	.15772-01	.51506+05
9	.11370+26	-.25000+01	-.59400+05	.78438+03	-.42620-00	-.60168+05
10	.75000+20	-.10000+01	.00000	.59569-02	.27819-00	.60344+05
11	.25000+13	.00000	-.19630+05	.76439+03	-.38806-00	-.95775+04

$$b_w = 5.0\ X_{H_2} + 1.75\ X_{O_2} + 2.15\ X_{N_2} + 1.00\ X_{AR} + 30.0\ X_{H_2O}$$

*E. A. Lezberg "Ignition and Chemical Kinetics in Hypersonic Ramjets" Conference in Hypersonic Aircraft Technology

9.6.1 Effect of Static Temperature

Chemical kinetic calculations were made as a function of inlet static temperature for clean air as defined in Table 9.6-3. In all of these calculations, the initial static pressure (p = 1 atm.), equivalence ratio (ϕ = 0.5), initial flow velocity (V = 4500 ft/sec), and combustor flow area were held constant.

A significant time delay is necessary before any appreciable temperature rise is observed. This period is referred to as the ignition delay period. During this period, little heat is released, but large changes occur in O, H, and OH concentrations. The two-body reactions are relatively fast and lead to an overproduction of some radicals. At the end of the ignition delay period, the third body reactions begin to play a dominant role leading to recombination

TABLE 9.6-3

MASS FRACTIONS OF REACTING FLOW

(Equivalence Ratio = 0.5)

C_h	Clean Air	5.05% Vitiation		49.25% Vitiation	
		Static Temperature, °R		Static Temperature, °R	
		2000	2300	2000	2300
H	1.000-09	1.000000-09	1.0000-09	1.000000-09	1.000000-09
O	1.0000-09	1.000000-09	0.296-07	1.000000-09	0.346-07
N_2	0.7569-00	0.71959-00	0.71981-00	0.38336-00	0.38348-00
H_2	0.1440-01	0.14634-01	0.14634-01	0.17194-01	0.17194-01
O_2	0.2287-00	0.23228-00	0.23206-00	0.27292-00	0.27279-00
OH	1.0000-09	0.345-06	0.3438-05	0.116-05	0.116-04
H_2O	1.0000-09	0.33491-01	0.33491-01	0.32653-00	0.32653-00
HO_2	1.0000-09	1.000000-09	1.0000-09	1.000000-09	0.330-07
H_2O_2	1.0000-09	1.000000-09	1.0000-09	1.000000-09	1.0000-09

and depletion of radicals with an accompanying energy release. The time required to proceed from the end of ignition delay to an equilibrium state is referred to as reaction time.

There are a number of quantitative definitions of the ignition delay time:

(a) The time required for the concentration of OH radical to reach 10^{-6} mole/liter (Reference 9-14)

(b) The time at which a point of inflection of atomic hydrogen is observed (Reference 8-5)

(c) The location of the intersection of the slopes of the initial and maximum temperature rise (Reference 9-15)

(d) The time at which a point of inflection in the concentration of (OH) radicals is observed

(e) The point of 0.1-percent-density decrease (Reference 9-16)

(f) The time it takes for the temperature to increase five percent of the total temperature rise (Reference 9-17)

All these assumptions in defining the ignition delay period are reasonable and lead to the same conclusion (Reference 9-18). For convenience, definition (a) was used.

At 1 atm initial pressure the calculated ignition delay decreased with temperature as shown in Figure 9.6-1.

9.6.2 Effect of Pressure

Chemical kinetic calculations were made for a hydrogen-air mixture at temperatures from 1900° to 2500°R for several initial pressures. The ignition delays obtained from these calculations are presented in Figure 9.6-2. A reversal in the trend of ignition delay occurred as pressure was increased. When the initial static temperature was increased from 1900° to 2200°R, this reversal occurred at a higher static pressure.

For a hydrogen-air mixture at an initial temperature of 1900°R and at a low pressure in the combustion chamber, the relatively low density gives a low molecular collision rate, leading to long ignition delays. As pressure is increased, the frequency of collisions increases; this results in a decreased ignition delay.

The reversal with increasing pressure is caused by the reaction

$$H + O_2 + M = HO_2 + M$$

which serves to break the hydrogen-oxygen reaction chain by removing free hydrogen atoms from the mixture.

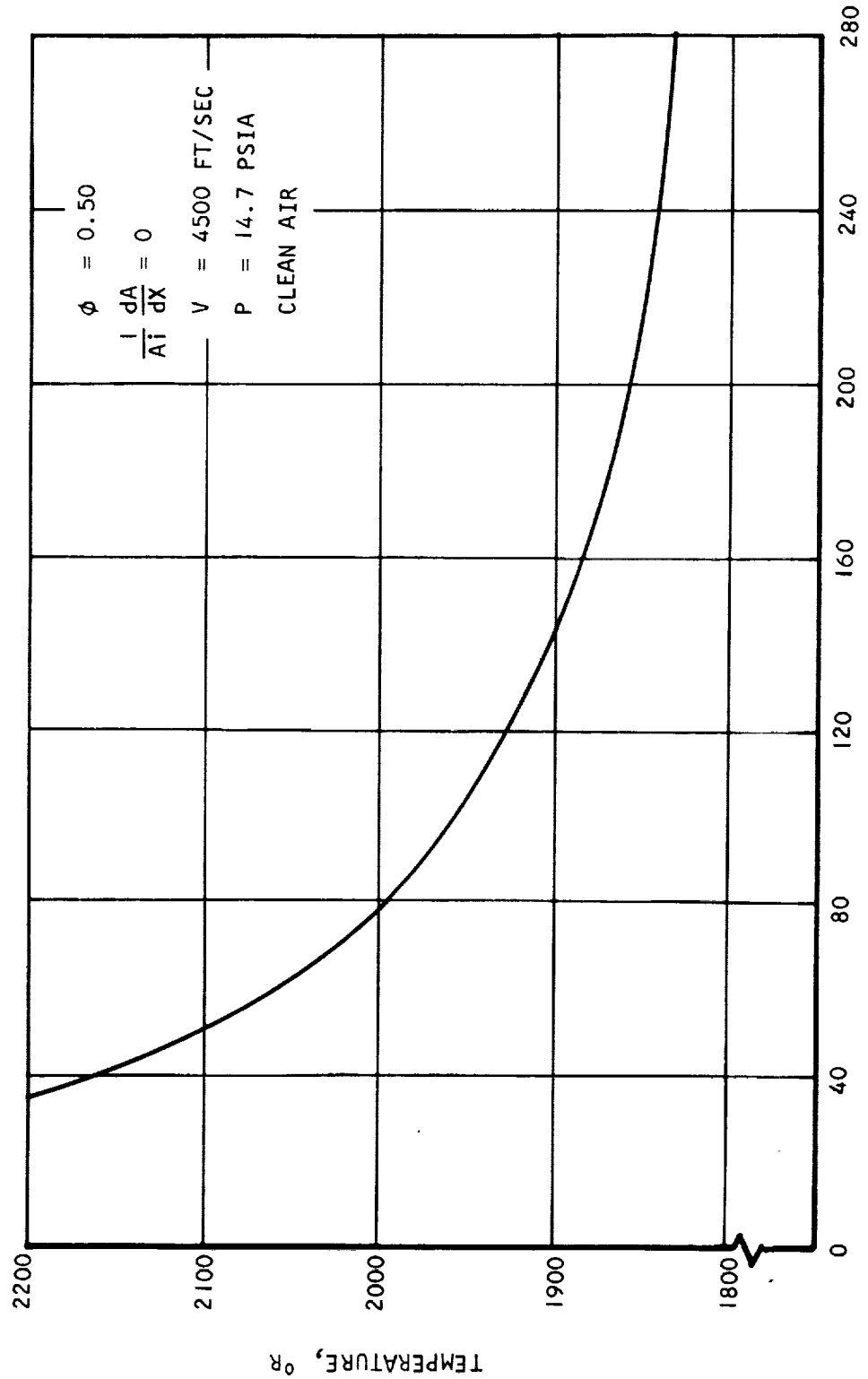

Figure 9.6-1. Effect of Initial Static Temperature on Total Ignition Delay

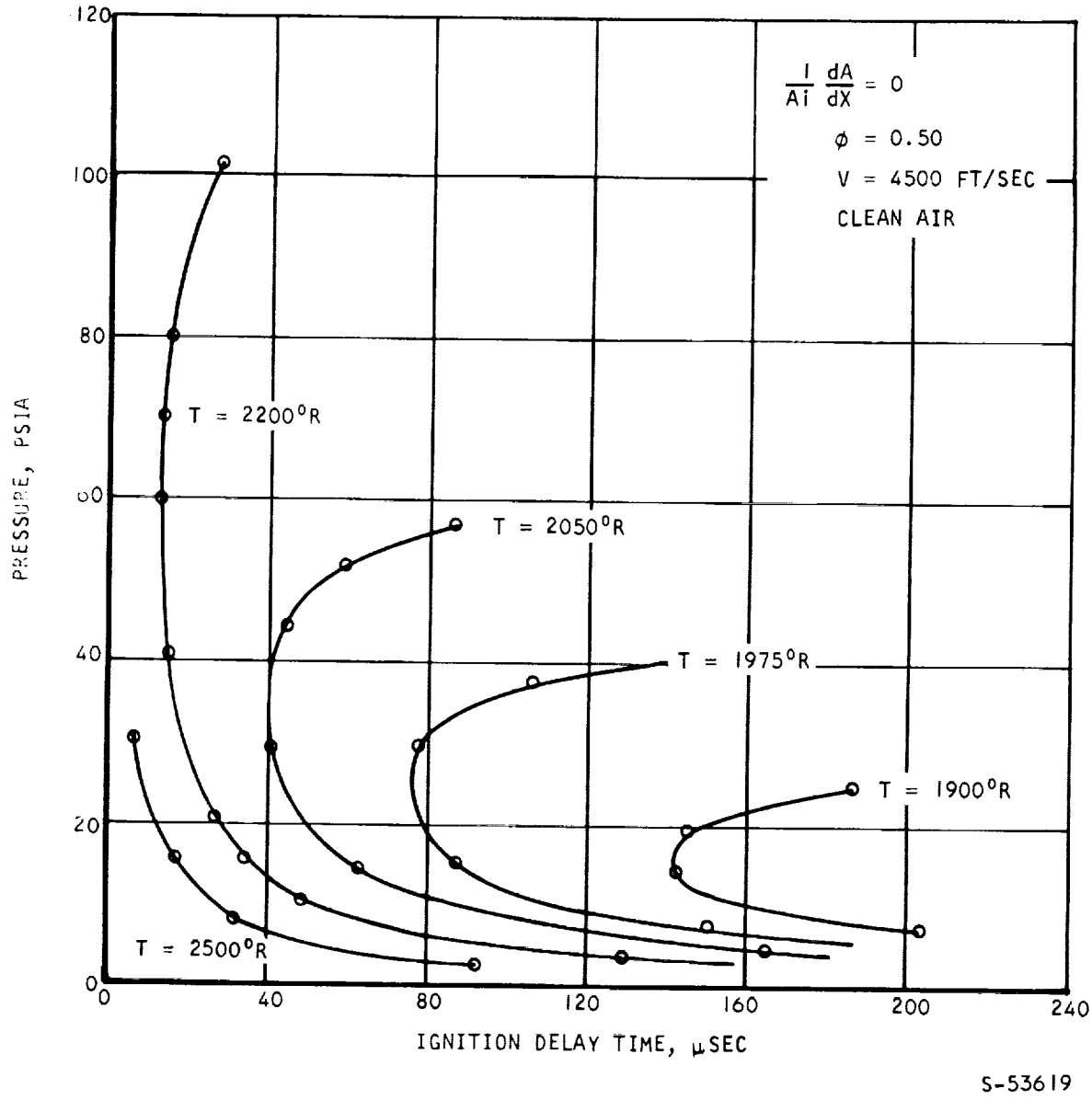

Figure 9.6-2. Effect of Initial Static Pressure and Temperature on Ignition Delay

As shown in Figure 9.6-2 at an initial temperature of 2200°R, no pressure reversal occurs up to a static pressure of 65 psia. The reaction then slows down slightly in the range of 65 to 100 psia. Thus at the higher initial temperature of 2200°R, ignition delay was not affected as much by static pressure as at an initial temperature of 1900°R.

9.6.3 Effect of Equivalence Ratio

At constant initial mixed temperature and pressure, the equivalence ratio was found to have a negligible effect on chemical kinetics. Results at equivalence ratios from 0.25 to 1.25 (Figure 9.6-3) indicated that ignition delays are essentially constant.

9.6.4 Vitiation Effects With Equilibrium Flow in the Inlet Nozzle

Clean air at several initial temperatures was assumed to combust at 20 atm with varying amounts of vitiating gases. The combustion products were then assumed to be expanded to 1 atm pressure in order to obtain their equilibrium compositions. The percent of vitiating gases (H_2 and O_2) by weight (with the weight of O_2 12.1-times that of H_2) was varied from 0 to 50 percent (see Table 9.6-3).

Chemical kinetic calculations were then made starting with the vitiated equilibrium species concentrations. Hydrogen at an equivalence ratio of 0.5 was allowed to react at constant area with the vitiated air. The initial conditions consisted of a static pressure of 1 atm and a velocity of 4500 ft/sec at several initial static temperatures from 1850° to 2300°R. The results of these calculations are presented in Figure 9.6-4. Ignition delays were determined from the time required for the OH concentration to reach 10^{-6} moles/liter. The dotted lines are extrapolations.

Examination of Figure 9.6-5 indicated that the degree of vitiation had a strong effect on ignition delay time at 1850° and 2000°R, but a negligible effect at 2300°R. Even small amounts of vitiation at 1850°R caused the ignition delay time to increase very rapidly. Sharp increases also occurred at 2000°R initial temperature near 25 percent vitiation.

As the amount of vitiation increased, so did the amount of water vapor and OH. The initial concentrations are shown in Table 9.6-3. At low temperatures the amount of OH present initially is small, and the dominant effect is the increase in the rate of reaction 5 due to water being a highly effective third body in this reaction.

At low initial static temperatures, vitiation--assuming equilibrium flow in the inlet nozzle--causes longer ignition delays. At higher initial temperatures the difference in ignition delay caused by using equilibrium vitiated air (rather than clean air) is less than 20 μsec and is therefore considered negligible.

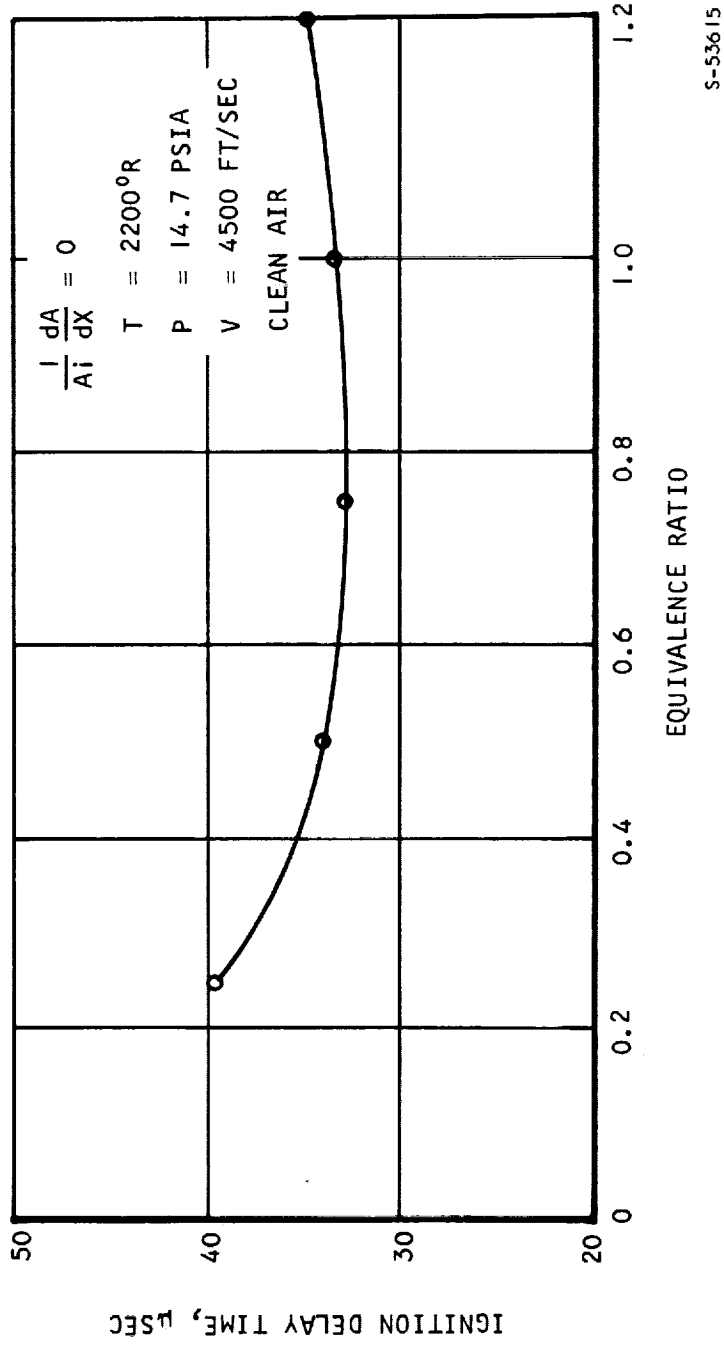

Figure 9.6-3. Effect of Equivalence Ratio on Ignition Delay

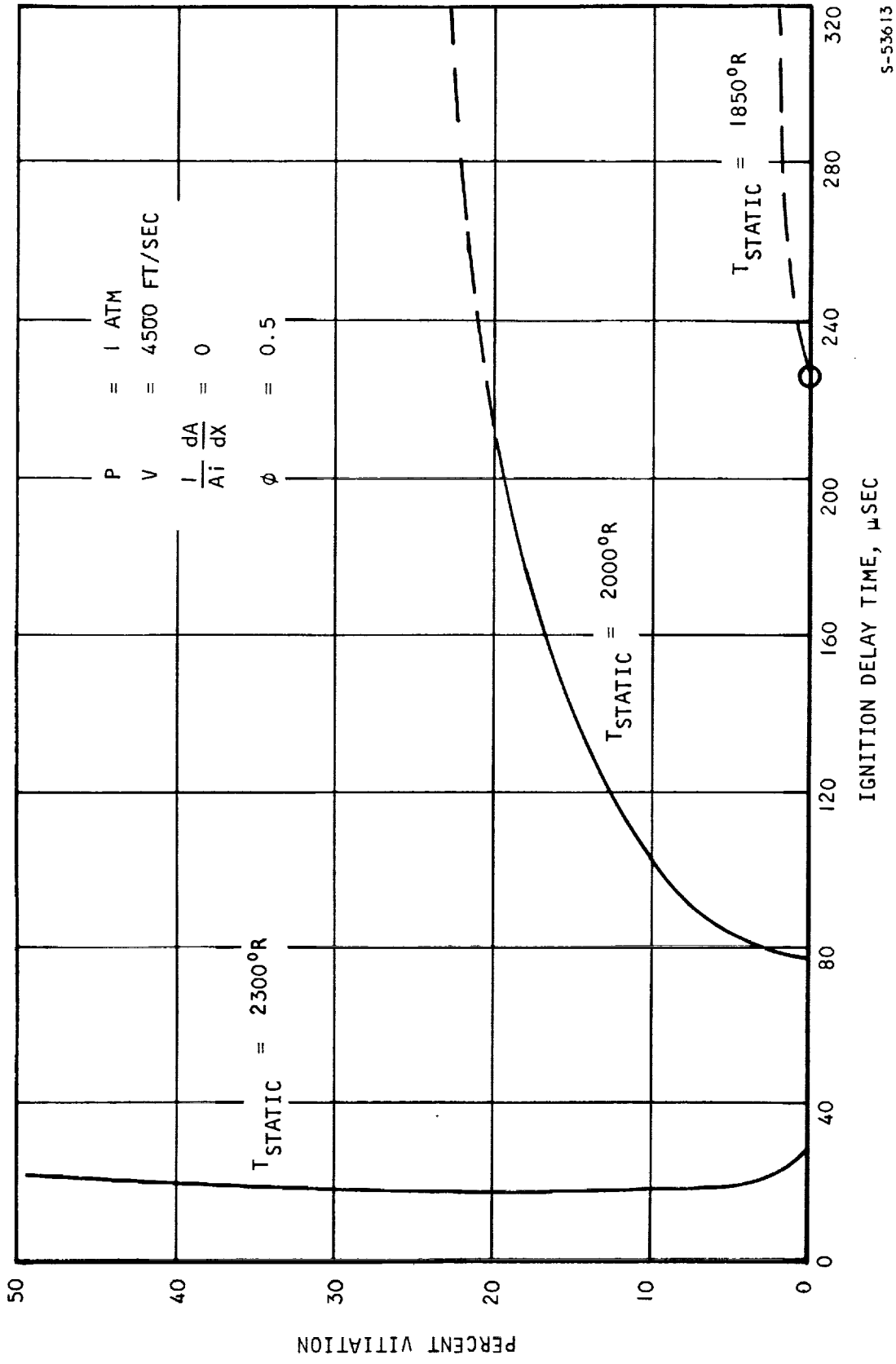

Figure 9.6-4. Effect of Vitiation on Ignition Delay Time

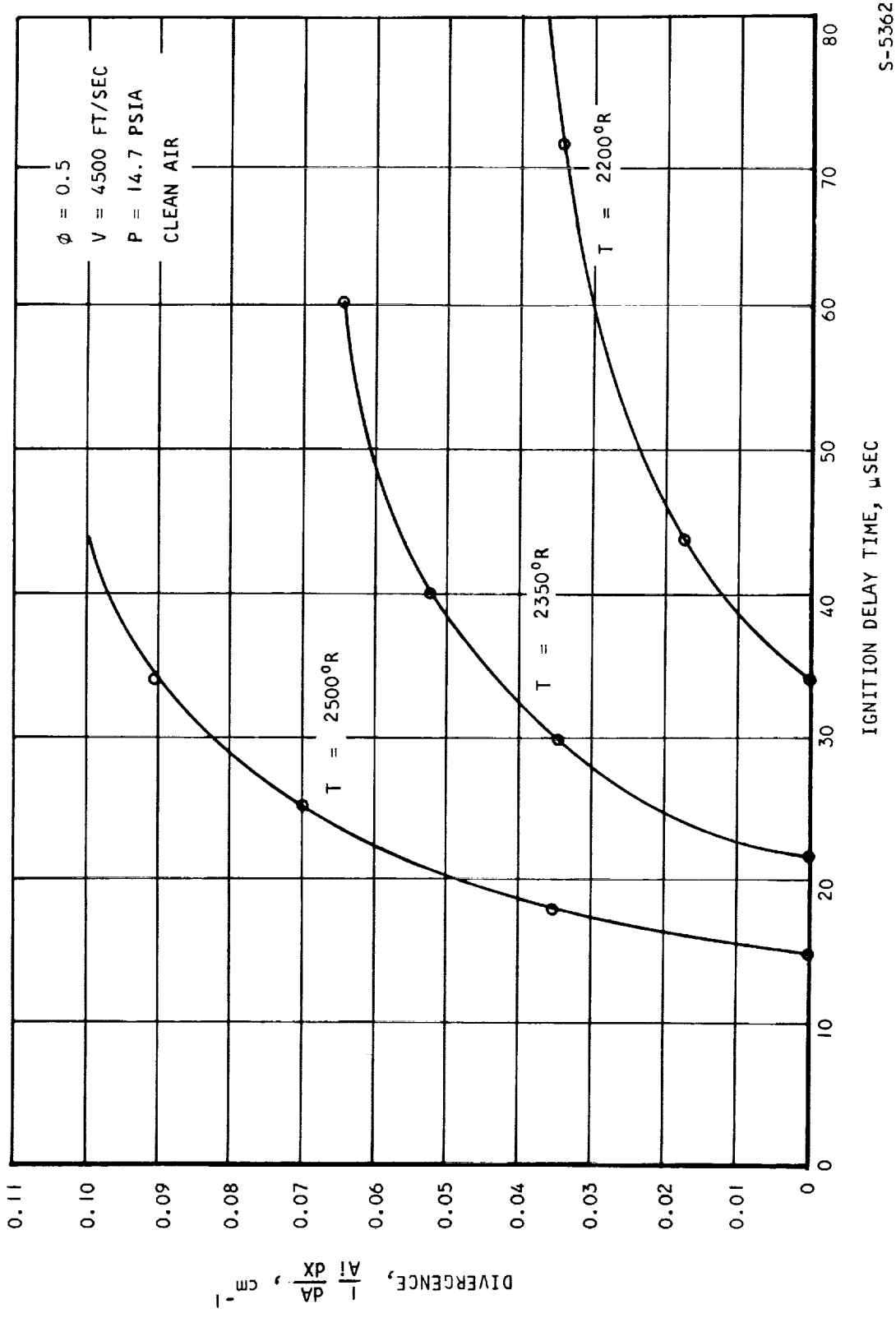

Figure 9.6-5. Effect of Divergence on Ignition Delay as a Function of Initial Static Temperature

9.6.5 Pressure Effects and Vitiation Effects With Nonequilibrium Flow in the Inlet Nozzle

The North American Rockwell (NAR) test facility could provide vitiated air at total pressures up to 300 psia. Flight tests involve combustion with clean air at total pressures sometimes in excess of 1000 psia. In this section the effects of test facility total pressure and of inlet nozzle chemistry on combustion are considered.

Combustor inlet conditions for the Mach 2.9 nozzle were obtained using an inlet total temperature of approximately 4050°R, and 50 percent weight content of vitiating gases. Species concentrations at the nozzle exit were obtained for thee different conditions: (1) frozen flow, (2) equilibrium flow, and (3) equilibrium flow to the throat, followed by frozen flow. The data were based on chemical equilibrium calculations. All heat loss was assumed to occur in the vitiation heater, with no heat loss in the inlet nozzle.

Frozen-flow calculations use the assumption that in the nozzle, reactions are infinitely slow. This results in high dissociation at the nozzle exit corresponding to equilibrium conditions at the upstream plenum of the nozzle. Equilibrium flow calculations use the assumption that the chemical reactions are infinitely fast. This results in a condition of chemical equilibrium which corresponds to the local temperature and pressure at each point in the nozzle.

Calculated static pressure vs combustor axial station is shown in Figure 9.6-6 for the five cases described below. Inlet temperature and velocity were held constant for all cases. The concentrations at the upstream end of the duct were changed to reflect the approximate condition of the inlet gases.

Case 1--corresponds to clean air for flight at a relatively low altitude. Note that the configuration of the combustor's divergent section is unimportant in this case, since combustion is completed within the parallel-walled section. (The calculation was not continued to the end of the combustor because excessive computation time would be required.)

Case 2--Corresponds to clean air at high altitude or in ground testing with a total pressure of approximately 300 psia. This pressure and an exit-to-entrance area ratio of 1.06 (over a 17-in. divergent length) were chosen as a basis for comparison and used in all the cases described below.

Case 3--The inlet concentrations correspond to frozen flow of vitiated air. Heat release in the combustor occurs immediately, due to the high initial radical concentrations.

Case 4--The inlet concentrations correspond to flow which has been frozen at the throat.

Case 5--The inlet concentrations correspond to equilibrium flow of vitiated air.

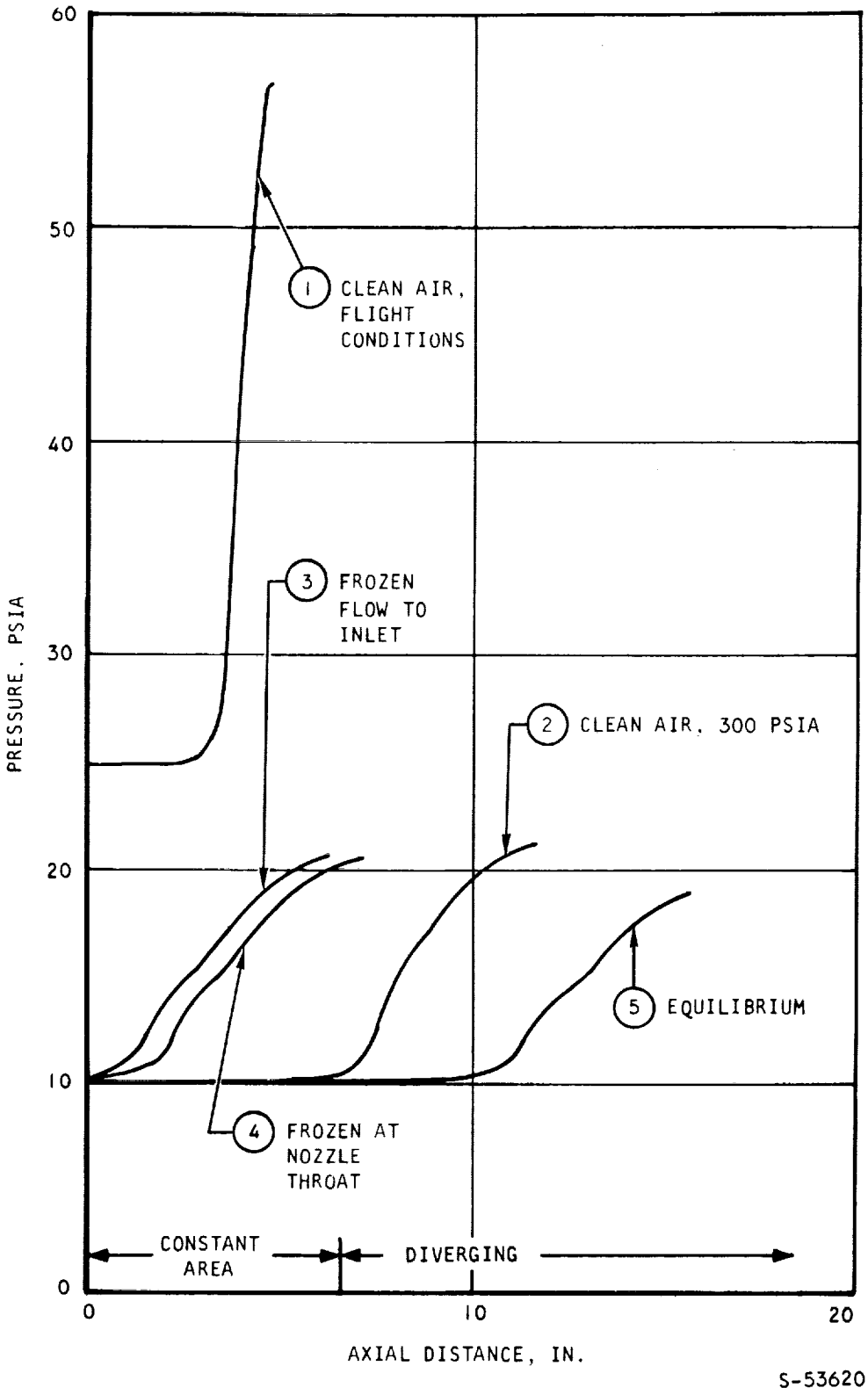

Figure 9.6-6. Calculated Static Pressure vs Combustor Axial Station

The initial conditions used are listed in Table 9.6-4.

TABLE 9.6-4

UPSTREAM BOUNDARY VALUES USED IN CHEMICAL KINETIC CALCULATIONS

Velocity, ft/sec	6464	6464	6464	6464	6464
Temperature, ^0R	2094	2094	2094	2094	2094
Static Pressure, psia	25	10	10	10	10
Mass Fractions:					
H	$1x10^{-9}$	$1x10^{-9}$	$0.1224x10^{-5}$	$0.2637x10^{-6}$	$1x10^{-9}$
O	1.10^{-9}	$1x10^{-9}$	$0.2355x10^{-3}$	$0.7652x10^{-4}$	$1x10^{-9}$
N_2	0.7569	0.7569	0.3890	0.3799	0.3765
H_2	0.0144	0.0144	0.0171	0.01730	0.01727
O_2	0.2287	0.2287	0.2633	0.2697	0.2741
OH	$1x10^{-9}$	$1x10^{-9}$	$0.409x10^{-2}$	$0.1932x10^{-2}$	$.2859x10^{-5}$
H_2O	$1x10^{-9}$	$1x10^{-9}$	0.3262	0.3311	0.3321
HO_2	$1x10^{-9}$	$1x10^{-9}$	$0.2191x10^{-4}$	$0.8767x10^{-5}$	$1x10^{-9}$
H_2O_2	$1x10^{-9}$	$1x10^{-9}$	$1x10^{-9}$	$1x10^{-9}$	$1x10^{-9}$

NOTE: A mass fraction of 10^{-9} was used for those species having negligible concentrations.

The calculations show that not only the low test pressure, but the inlet nozzle kinetics have an appreciable effect on chemical kinetics in the two-dimensional combustor. The conditions of case 4--flow frozen at the nozzle throat--are believed to be most representative of the conditions in the true-scale 2-D combustor. Because the true-scale nozzle had a short, rapidly diverging supersonic section it is likely that the flow was effectively frozen a short distance downstream of the throat.

9.6.6 Effect of Chain Carriers

In order to study further the effect of chain carriers such as H, O, and OH on the chemical reaction as a function of initial static temperature, chemical kinetic studies were made for two vitiated mixtures with initially non-equilibrium free-radical concentrations (see Table 9.6-5).

TABLE 9.6-5

MASS FRACTIONS OF REACTING FLOW WITH INITIAL CARRIERS

(Equivalence Ratio = 0.5)

C_h	2 Percent	10 Percent
H	0.63844118-04	0.30009153-03
O	0.34673790-03	0.16987557-02
N_2	0.75690000-00	0.75690000-00
H_2	0.14104986-01	0.12964130-01
O_2	0.22605520-00	0.21569300-00
OH	0.88783859-04	0.44593853-03
H_2O	0.18617049-02	0.9132536-02
HO_2	0.58185451-03	0.28683717-02
H_2O_2	0.12234745-06	0.64002613-06

Initial concentrations were obtained rather arbitrarily by carrying out a chemical kinetic calculation--for a constant-area process with an initial temperature of 2200°R and an initial pressure of 1 atm--and using the concentrations at various stages of completion of the process. The extent of completion is denoted by C_h, the percentage of hydrogen consumed in this initial process.

The calculation was then re-started at a new temperature. The additional

lengths required for 40 percent and 80 percent of the original H_2 to be consumed are shown in Figure 9.6-7.

Initial presence of chain carriers had the effect of transposing the region of long ignition delay to lower temperatures.

9.6.7 Effect of Divergence

The effect of divergence was calculated for clean air as a function of initial static temperature. In Figure 9.6-5 the ignition delays were plotted versus values of $\frac{1}{Ai}\frac{dA}{dx}$ (change of area ratio per unit length) for initial static temperatures of 2200^0, 2350^0, and 2500^0R. The effect of divergence on ignition delay decreased as initial static temperature was increased. The effect of increasing divergence was to increase the length required for combustion. The increased length is believed to be due mainly to the temperature and pressure effects on ignition delay.

9.7 SEPARATION AT THE COMBUSTOR EXIT

For some of the single-stage supersonic test conditions reported, the flow was separated at the combustor exit because the pressure a few inches upstream of the combustor exit was appreciably lower than the test-cell pressure of 1 atm. This separation may have had beneficial effects on autoignition (Reference 9-19) and chemical efficiency. However, it is believed that the results of the tests were not affected qualitatively by the exit separation because similar effects were produced by the separation associated with second-stage combustion, and these had little effect on first-stage chemical efficiency.

9.8 ANALYTICAL PREDICTION OF COMBUSTOR BEHAVIOR

For preliminary design of combustors and for extrapolation of test results to conditions at which tests cannot be made, it is desirable to have an analytical model in which theory and empirical results are used to predict combustor behavior. In Phase I of the HRE development such a model was used. Results from the two-dimensional combustor tests, and other published experimental results, indicate that combustion-induced boundary layer separation must be considered in the model. In Appendix C results obtained without considering separation are given, and suggested modifications to the model are discussed.

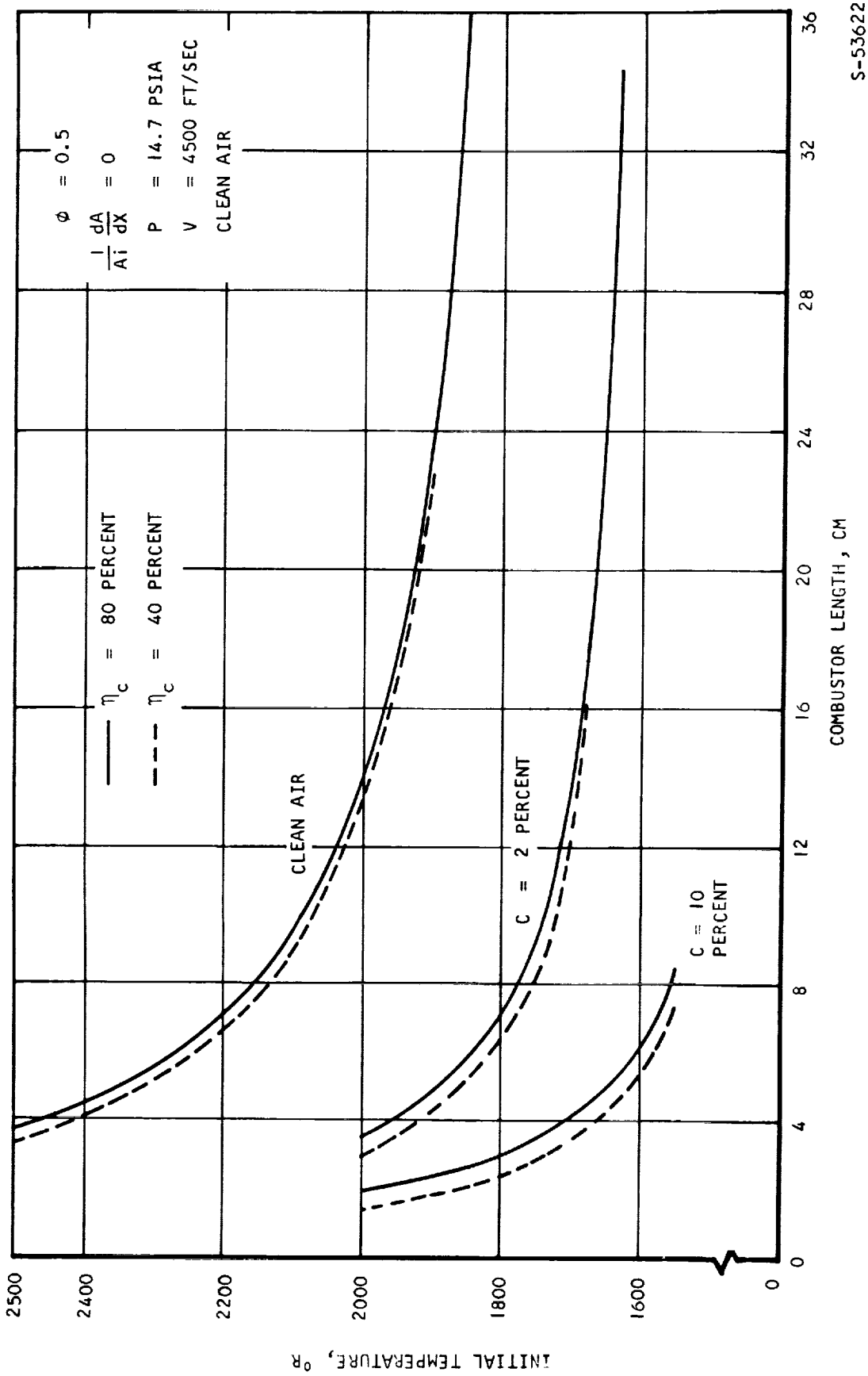

Figure 9.6-7. Effects of Percentage of Carriers on Initial Static Temperature as a Function of Required Combustor Length and Chemical Efficiency

10. CONCLUSIONS

(a) Two-dimensional combustor tests indicated that the backward-facing step created by the trailing edge of the inlet spike would be an effective flameholder for subsonic combustion.

(b) Forced ignition is required for HRE Mach 5 operation. At Mach 6 flight conditions, an igniter is required for equivalence ratios less than 0.2; apparently no igniter is required for Mach 7 flight conditions.

(c) For a one-dimensional analysis, the combustor performance can be uniquely defined by specifying the chemical efficiency and the static pressure rise. It is possible to correlate the first stage chemical efficiency as a function of combustor length in terms of a penetration parameter and a mixing parameter. The use of one-dimensional influence coefficients could yield a useful correlation for static pressure rise in the combustor.

(d) The first stage test results indicate that chemical efficiency increases with penetration parameter, but reaches a plateau at the penetration parameter of 1.7. With the same penetration parameter and orifice spacing-to-diameter ratio, smaller injector orifices give better chemical efficiency.

(e) The low chemical efficiency attained in the second stage is not a chemical kinetics problem, but a mixing problem.

(f) Obtaining adequate jet penetration is not necessarily a difficult design problem for the HRE combustor. Lateral spreading and mixing on the microscopic scale require further study.

(g) The poor chemical efficiency measured at equivalence ratios near unity can be partly attributed to the fact that the mechanical design of the two-dimensional combustor did not provide for fuel injection across the full width of the combustor.

(h) An oversized combustor would not provide true design information because of the scaling effect which is yet to be determined.

II. RECOMMENDATIONS

(a) Because the combustor performance is very sensitive to the combustor geometry, any combustor component test program whose geometry is different from the engine should be aimed at obtaining parametric information rather than verifying an engine design concept or determining engine performance.

(b) The investigation of supersonic combustion and mixing in a diverging duct should be continued.

(c) The development of techniques for gas sampling, enthalpy, and turbulence measurements should be pursued further.

(d) Experiments are needed to clarify the differences in supersonic combustion due to use of vitiated air instead of clean air.

REFERENCES

6-1. Hypersonic Research Engine Project - Phase IIA, Combustor Test Plan For Mach 2.9 Inlet Air Condition, AiResearch Report AP-68-3618, Rev. 1, May 11, 1968.

6-2. Hypersonic Research Engine Project - Phase IIA, Combustor Test Plan For Mach 1.6/Mach 2.3 Inlet Air Conditions and Combustor Inlet Profile Tests, AiResearch Report AP-68-3952, July 1, 1968.

6-3. Hypersonic Research Engine Project - Phase IIA, True-Scale Combustor Test Plan For Mach 2.9 Inlet Air Condition, 2 December 1968.

6-4. Hypersonic Research Engine Project - Phase IIA, True-Scale Combustor Test Plan For Mach 2.9 Inlet Air Condition, Series II., 4 June 1969.

7-1. Engineering Staff, Hypersonic Research Engine Project - Phase IIA, Combustor Program, Third Interim Technical Data Report (U), Data Item No. 55-2.05, AiResearch Report AP-68-3753, 31 May 1968. CONFIDENTIAL.

8-1. Engineering Staff, Hypersonic Research Engine Project - Phase IIA, Combustor Program, Tenth Interim Technical Data Report (U), Data Item No. 55-2.10, AiResearch Report AP-69-5405. CONFIDENTIAL.

8-2. Kepler, C. E., "Hydrocarbon-Fueled Dual-Mode Ramjet Combustor Investigations," Monthly Technical Report No. 36, United Aircraft Research Laboratories, July 1969.

8-3. Vranos, A., and J. J. Nolan, "Supersonic Mixing of Light Gas and Air," AIAA Meeting, Colorado Springs, Colorado, July 1965.

8-4. Schlichting, H., "Boundary Layer Theory," McGraw-Hill, New York, 1962.

8-5. Nicholls, J. A., "Stabilization of Gaseous Detonation Waves with Emphasis on the Ignition Delay Zone," Ph.D. Thesis, University of Michigan, Ann Arbor, Michigan, 1960.

8-6. Shapiro, A. H., "The Dynamics and Thermodynamics of Compressible Fluid Flow," Vol. 1, Ronald Press, New York, 1953.

8-7. Kestin, J., "The Effect of Freestream Turbulence on Heat Transfer Rates," Chapter I of Advances in Heat Transfer, Irvine, Thomas F., Jr., and James P. Hartnett, Academic Press, 1966.

8-8. Knudsen, J. G., and D. L. Katz, Fluid Dynamics and Heat Transfer, McGraw-Hill, New York, 1958, p. 394.

8-9. Eckert, E. R. G., "Survey of Boundary Layer Heat Transfer at High Velocities and High Temperatures," WADC TR 59-624, Wright Air Development Center, April 1960, p. 17.

REFERENCES (Continued)

8-10. Ibid., p. 14.

8-11. Engineering Staff, Hypersonic Research Engine Project Phase IIA, Structures and Cooling Development, Third Interim Technical Data Report, Data Item No. 55-7.03, AiResearch Report AP-67-2833, 4 Dec 1967.

9-1. Hawthorne, W. R., and W. T. Olson, Design and Performance of Gas Turbine Power Plants, Princeton University Press, Princeton, 1960, p. 134.

9-2. Cookson, R. A., P. Flanagan, and G. S. Penney, "A Study of Free-Jet and Enclosed Supersonic Diffusion Flames," Twelfth Symposium (International) on Combustion, the Combustion Institute, Pittsburgh, Pennsylvania.

9-3. "Analytical and Experimental Evaluation of the Supersonic Combustion Ramjet Engine" (U), Component Evaluation, Vol. II, Technical Report AF APL-TR-65-103, General Electric Co., Evendale, Ohio.

9-4. McFarlin, David J., C. Edward Kepler, "Mach 5 Test Results of Hydrogen-Fueled Variable-Geometry Scramjet," United Aircraft Research Laboratories Technical Report AFAPL-TR-68-116.

9-5. Frey, H., J. Kliegel, G. Nickerson, T. Tyson, Shear Layer Computer Program, Vol. I, Dynamic Science, 2400 Michelson Drive, Irvine, California, December 1969.

9-6. Tyson, T., and J. Kliegel, "An Implicit Integration Procedure for Chemical Kinetics," AIAA 6th Aerospace Sciences Meeting, Paper No. 68-180, January 1968.

9-7. Uhl and Gray, Mixing, Vol. I., 1966 Academic Press, N.Y. and London.

9-8. Sovran, Fluid Mechanics of Internal Flow, Elsevier Publishing Company, p. 160.

9-9. Swithenbank, J., and N. A. Chigier, "Vortex Mixing for Supersonic Combustion," Twelfth Symposium on Combustion, The Combustion Institute, Pittsburgh, 1969.

9-10. Schubauer, G. B., and H. K. Skramstad, "Laminar-Boundary-Layer Oscillations and Transition on a Flat Plate," NACA TN 909.

9-11. Orth, R. C. and Funk, John A., "An Experimental and Comparative Study of Jet Penetration in Supersonic Flow," AIAA paper No. 67-225, 1967, p. 3.

9-12. Zeleznik, F. J., and Gordon, S., "A General IBM 704 or 7090 Computer Program for Computation of Chemical Equilibrium Compositions, Rocket Performance, and Chapman-Jouguet Detonations," NASA TN D-1454, October 1962.

REFERENCES (Continued)

9-13. Zupnik, T., E. Nilson, V. Sarli, "Investigation of Non-equilibrium Flow Effects in High Expansion Ratio Nozzles," (Contract NAS3-2572), NASACR-54042, United Aircraft Corporation.

9-14. Schott, G. L., and J. L. Kinsey, Kinetic Studies of Hydroxyl Radicals in Shock Wave. II. Induction Time in the Hydrogen-Oxygen Reaction, Jour. Chem. Phy., Vol. 29, No. 5, Nov. 1958, pp. 1177-1182.

9-15. Momtchiloff, I. N., Taback, E. D., and Buswell, R. F., "An Analytical Method of Computing Reaction Rates for Hydrogen-Air Mixture," Ninth Symposium (International) on Combustion, The Combustion Institute, Pittsburgh, 1963.

9-16. Lezberg, E. A., "Ignition and Chemical Kinetics in Hypersonic Ramjets," Conf. on Hypersonic Aircraft Technology, NASA SP-148, 1967. CONFIDENTIAL.

9-17. Pergament, H. S., "A Theoretical Analysis of Non-Equilibrium Hydrogen-Air Reaction in Flow Systems," AF33(657)-7911.

9-18. Brokaw, R. S., "Analytical Solutions to the Ignition Kinetics of the Hydrogen-Oxygen Reaction," NASA TN D-2542.

9-19. Harsha, P. T., W. C. Colley, and M. J. Kenworthy, "Hypersonic Ramjet Research Engine - Combustor Design," Report No. R66FPD56, General Electric, Cincinnati, Ohio, February, 1966, p. 2.

APPENDIXES

APPENDIX A

DETAILED DESCRIPTION OF THE APPARATUS

APPENDIX A

DETAILED DESCRIPTION OF THE APPARATUS

A.1 TEST FACILITY

The combustor testing was conducted at the North American Rockwell (NAR) Thermophysics Laboratory in El Segundo, California. The layout of the test facility is shown in Figure A-1.

A.1.1 Vitiation Heaters

Tests of the 2-by 6-in. version of the two-dimensional combustor were conducted using vitiated air supplied from a 10-in.-ID water-cooled heater. Water cooling was used because it appeared to be the only way to provide the required life and reliability. The disadvantage with water cooling was that the heat losses were high. This, in turn, required high levels of vitiation resulting in a high water vapor content and a significantly higher enthalpy than clean air, which increased the heat flux in the nozzle, thrust stand, and combustor. Attempts were made to avoid this situation, first by the use of an internal, insulating zirconia liner, and subsequently with an air-regeneratively-cooled vitiation heater.

The use of a zirconia lining in the heater had to be discarded when it was found that excessive dusting of the zirconia occurred, in addition to flaking and cracking. It was concluded that these particles would be deleterious to the combustor model and the intake nozzle, so the zirconia-lining approach was discarded.

The regeneratively-cooled vitiation heater was installed, and a number of tests were conducted. Each time the air-cooled inner liner warped badly and it became apparent that a long development cycle would be involved in bringing the heater to an operational state. A water-cooled liner was installed, replacing the air-cooled liner.

Upon completion of testing with the 2-by 6-in. combustor, a 5-in.-ID heater was fabricated and used for the true-scale tests. The 5-in. vitiation heater was inserted into the 10-in. heater, thereby avoiding major modifications to the existing facility hardware.

A.1.2 Supporting Equipment

Several pieces of support equipment were necessary to conduct the combustor tests and are described in succeeding paragraphs. Figure A-2 is a block diagram showing the various systems.

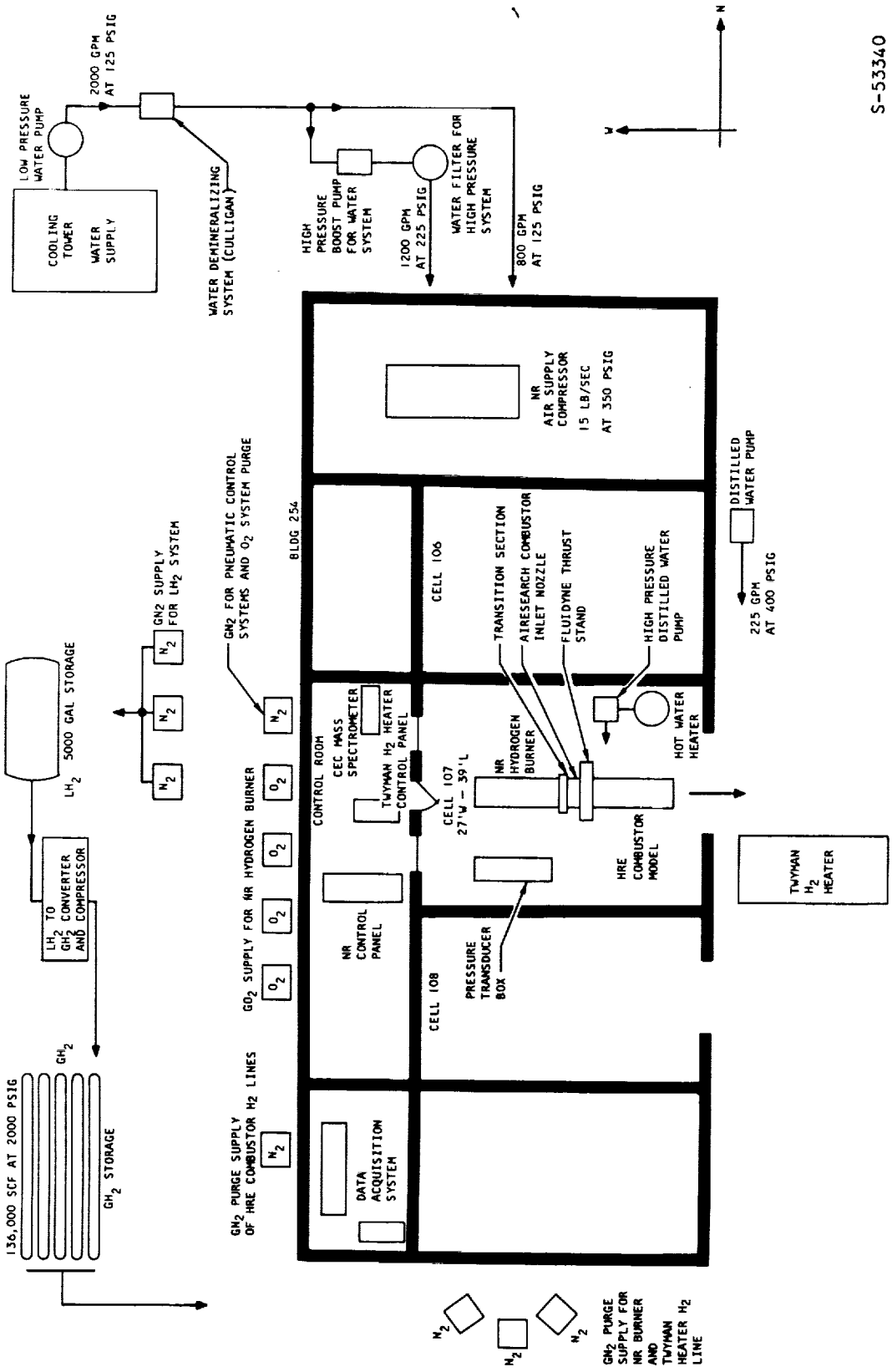

Figure A-1. NAR Combustor Test Facility

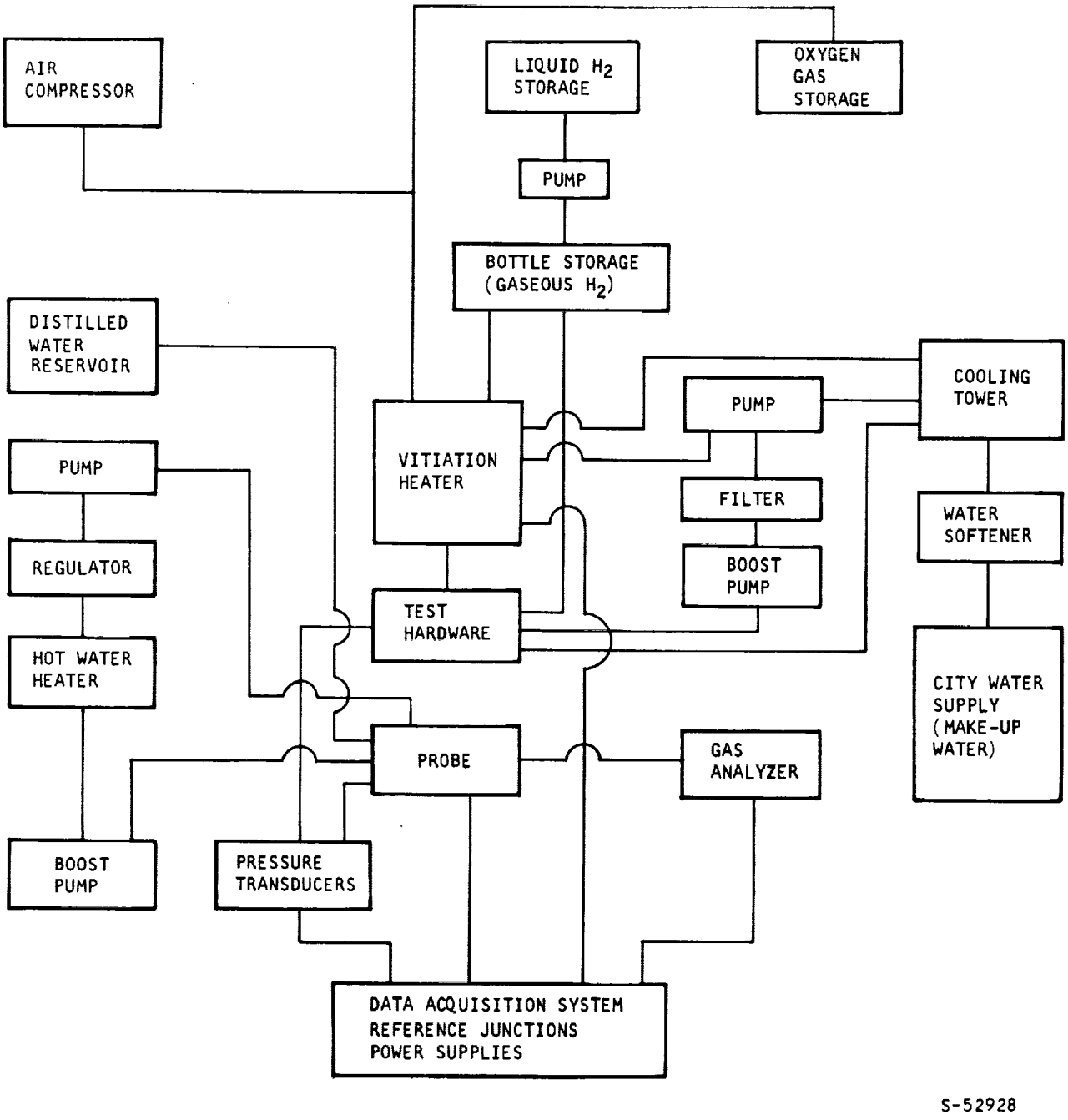

Figure A-2. Block Diagram of the Combustor Test System

Air was supplied to the vitiation heater by means of an electric-motor-driven centrifugal compressor capable of supplying 12 lb per second at 300 psi. The airflow was controlled by the use of pneumatically driven bypass valves. Flow measurement was accomplished by the use of flat-plate orifices constructed in accordance with the ASME power test code. The plumbing was so arranged that the orifices could be cross-checked for accuracy by connecting, or valving, in series with a standard flow nozzle.

Hydrogen was stored in the liquid state in a 5,250 gal cryogenic tank and pumped through a vaporizer into storage bottles at approximately 2,000 psi. The gaseous hydrogen supply was used for both the vitiation heater and the combustor model. The hydrogen used for the combustor model was passed through a hydrogen heater, which was designed for the following parameters:

Hydrogen flow rate	0.1 to 0.7 lb/sec
Hydrogen inlet temperature	70^{0}F
Hydrogen outlet temperature	500^{0} to 1250^{0}F
Hydrogen inlet pressure	700 to 800 psia
Hydrogen pressure drop	150 psi max

The heater employed a temperature-biased, bypass-blending system that mixed cold hydrogen with the hot hydrogen leaving the heater. A period of 20 sec was needed for the system to stabilize when the hydrogen outlet pressure or temperature was changed. The temperature set point was manually variable between 500^{0} and 1200^{0}F ($+10^{0}$, -0^{0}), at pressure levels up to 600 psia. Under operating conditions, flow rate fluctuations were less than one percent. Each test cycle was initiated with a nitrogen purge and preheating of all tubes. All operations were automatic with manual overrides. Automatic and manual abort systems were provided in an integrated package; maximum limits were set on the tube, line and stack temperatures, and on the natural gas inlet pressure.

The measurement of the hydrogen flow rate is discussed in Section A.4.4 of this report.

The cooling water for the combustor model, vitiation heater, and thrust stand was supplied from a system employing an evaporative cooling tower and centrifugal pumps. The primary pump provided a water pressure of 135 psi. A portion of the water was raised to a higher pressure by means of a boost pump that provided a pressure of 210 psi. The water at higher pressure was required for cooling the combustor model and the 5-in.-dia section for the vitiation heater described in paragraph A.1.1. The lower-pressure water was used for the large, 10-in.-dia burner and for the transition sections.

A distilled water loop was also available at 350 psi and flow rates up to 16 gpm. This cooling water system was for the instrumentation probes. In some of the tests the distilled water had to be heated and a domestic electric hot water heater was used. The water heater had a 50-gal capacity and pressure capability of 100 psig, and therefore was placed upstream of the 700 psig pump.

A.2 INTAKE NOZZLE

The exhaust gases from the vitiation heater were subsonic and were accelerated to the required supersonic test Mach number at the entrance to the test combustor. The vitiation heater was connected to the thrust stand via a two-dimensional supersonic nozzle which provided the required flow acceleration.

To provide for several inlet Mach numbers to the combustor model, the nozzle was designed as a box-like structure with interchangeable nozzle blocks that were bolted into the box structure from the top. The nozzle assembly is shown in Drawing ML 2407 attached to the back of this document. Two sets of nozzle blocks were designed and fabricated. The first set provided an exit area of 2 by 6 in. and airflow at subsonic speeds and at Mach 1.6, 2.3, and 2.9. The second set provided an exit area of 0.6 by 6 in. and exit Mach numbers of 2.3 and 2.9. The nozzles were designed for a total pressure of 300 psia and a total temperature of 4660°R.

During the course of the program, two nozzle box structures were built. The first nozzle was constructed by machining copper plates that were brazed together to form the box structure. The second nozzle box was machined from a solid block of copper to eliminate as many braze joints as possible. Figure A-3 depicts the first nozzle box and one of the nozzle inserts.

A.2.1 Box Structure

The box structure was made from copper and stainless steel and was water-cooled. The cooling water for the first nozzle box structure entered through stainless steel manifolds brazed to the sidewall plates, as can be seen in Figure A-3 and in section B-B of Drawing ML 2407. Coolant passages within the copper structure for both the nozzle box and the nozzle block, shown also in section B-B, consisted of drilled holes 0.200 in. in diameter. Prior to the assembly and brazing of the box, these holes were drilled into the flat plates that comprised the structure. The entire exposed inside surface area was cooled by the flow through these drilled passages with the exception of the area immediately adjacent to the inlet flange, which was cooled by conduction. This particular local area is shown in section A-A of Drawing ML 2407. It was necessary to depend on conduction to cool this area because it was impractical to bring the cooling water manifold close to the inlet plane. The low heat flux in this area, in conjunction with the high thermal conductivity of the copper, resulted in an acceptable surface equilibrium temperature.

The inlet side of the nozzle was sealed to the mating part by a flat asbestos gasket and the seal between the nozzle exit and the thrust stand was accomplished by means of an O-ring.

The braze joint locations can be examined by referring to Drawing ML 2407. The various pieces, such as side walls, manifolds, bottom plate, and flange were pre-machined to exact size with the exception of overall length, which was set on final machining. The brazing of the nozzle assembly was performed in steps. The first step was to assemble the two side plates, bottom plate and cross members, and to bolt them together with the copper bolts and brass nuts. Copper

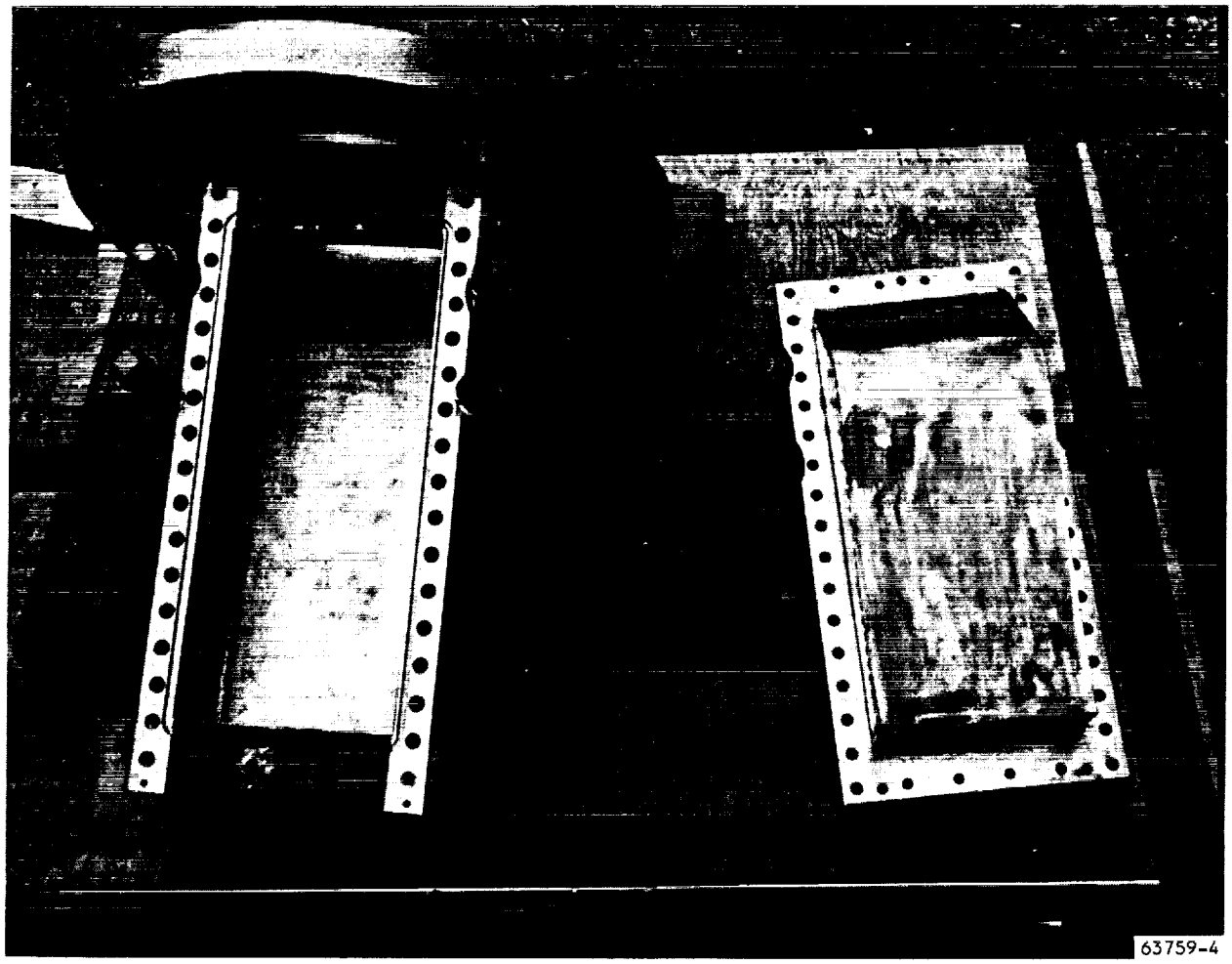

Figure A-3. First Nozzle Box and Insert

bolts were used to eliminate unequal expansion during brazing. After this part was brazed, leak-tested, and dimensionally checked, the flange was added at the second braze cycle. The first braze cycle utilized BAu3 brazing alloy in accordance with ASTM B-260-62T. The second braze cycle required the use of 75Au-20 CU-5Ag braze alloy, which has a lower melting point, to preclude remelting of the alloy used in the first braze cycle. During the brazing operations, the two side plates warped slightly so that the width of the nozzle at the exit plane was 6.040 in. rather than 6.000 in., as specified by the drawing. The width at the exit was brought back to the specified dimensions by plasma-spraying copper on the walls and tapering it to a feather edge. A straight sidewall was thus achieved with a finished width of 6.000 in. at the outlet plane. The sprayed material remained completely intact and in good condition throughout the test program.

As previously mentioned, two nozzle box structures were constructed. The second structure was identified as Part No. SK 55212 and differed from the first one only in that all copper-to-copper braze joints were eliminated, except for the plugs required for the open holes left from the drilling of the coolant passages. The coolant passages in the sidewalls were drilled from the bottom of the part to the required depth. The holes across the bottom plate were drilled from the outside surface of the side plate of the nozzle. The entry to the holes then had to be plugged, which was accomplished through the use of small copper plugs that were brazed in place. The manifolds, flange, and bars were brazed on in the same manner as was done for the first nozzle box structure.

After approximately 140 test runs, the throat area of this nozzle became eroded, perhaps because of particles in the supply air, or due to steel particles burned off the vitiation heater interior. The depressed area in the throat was restored to its original flatness through the application of plasma-sprayed copper.

A.2.2 Nozzle Inserts

Water cooled nozzle inserts (or blocks) were designed as interchangeable parts. Sections A-A and B-B of Drawing ML 2407 show the geometry of the nozzle insert. Inserts for the 2- by 6-in. nozzle were designed with area ratios for Mach 1.6, 2.3, and 2.9. A flat nozzle insert yielded subsonic flow at the nozzle discharge. True-scale nozzle inserts provided Mach numbers 2.3 and 2.6. The same hole size and spacing was used for the coolant passages of the nozzle inserts as was used for the flat section in the box structure. The brazing of the nozzle insert was performed in one step by which both the water manifolds and the contoured copper block were brazed to the steel plate that bolted to the top of the box structure. A typical insert is shown in Figure A-4.

A.2.3 Support Tube

The support tube was a weldment, made from carbon steel, which bolted to the nozzle inlet flange, to the vitiation heater transition section, and to the thrust stand. The purpose of the support tube was to transmit forces from the thrust stand directly to the vitiation heater to avoid stressing the nozzle

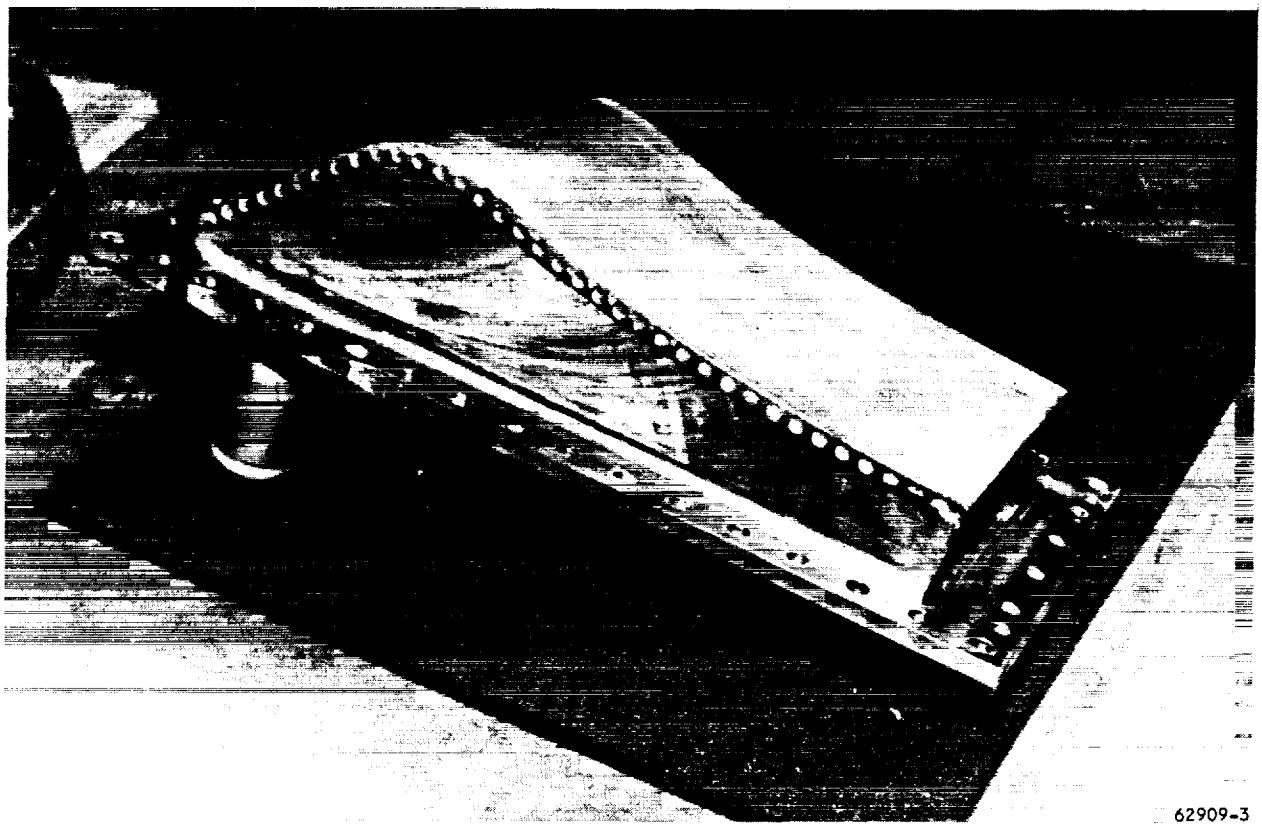

Figure A-4. Typical Nozzle Insert

unnecessarily. The thrust stand was mounted on wheels and was free to move to allow for thermal expansion. As a consequence, the thrust forces generated by the combustor would bear directly on the box of the nozzle were it not for the support tube. Drawing ML 2407 shows the flanges, and section B-B shows a cross section of the tube and the overall view.

A.2.4 Post-Test Examinations of Intake Nozzles

After each test series, the nozzle was removed from the test setup and examined for possible damage and a general assessment of its condition. In all cases, it was found that some amount of throat erosion had taken place, as discussed in paragraph A.2.1. This was apparently caused--at least in part--by particulate matter in the vitiated air that passed through the nozzle. The throat area was not significantly changed in the case of the 2- by 6-in. combustor tests. When the nozzle box was required for the true-scale tests (0.125-in.-high throat), it became evident that the nozzle box was unsuitable without re-machining. This would have destroyed the interchangeability feature. Also, the durability of plasma-sprayed copper in the throat was unproven at the time; therefore, the nozzle insert for the true-scale tests was precision-fitted to the new one-piece nozzle box. The first nozzle box (ML 2407) was relegated for exclusive use in strut testing in an adjacent test cell. After 139 test runs were conducted with the true-scale nozzle, it was found that both the nozzle insert and the nozzle box were eroded to such an extent that a repair was in order. The true contours were restored by plasma-spraying copper onto the nozzle box bottom plate in the throat area and on the nozzle insert as well. This rework rendered the nozzle acceptable for the remainder of the test program.

During the last series of tests, and after contour restoration, leakage started across the seal between the insert and the box. It was assumed that the thrust stand seal had begun to leak, but upon disassembly of the test hardware it was found that the seal in the thrust stand was still in good condition and that the leakage had occurred on the intake nozzle. The O-ring which sealed the nozzle insert to the nozzle box had failed. Hot gases passing through the nozzle could escape in relatively small quantities through the O-ring seal groove to the atmosphere. Figure A-5 shows the exit area of the hot gases from the nozzle.

The nozzle was sufficiently cooled by conduction in the leak area to keep the metal below its melting point; however, erosion and oxidation were evident. One can also observe in Figure A-5 that large quantities of particulate matter (mostly iron) had accumulated at the inlet side of the nozzle. Some of this particle contamination also accumulated in the throat; however, the throat area was cleared mechanically after each test.

An additional observation was that significant grain growth had occurred throughout the heated area, although the design surface temperature was not necessarily exceeded. Grain growth is a function of both time and temperature, and the nozzles were in service for an extended period. A good example of grain growth is shown in Figure A-6, which depicts the nozzle insert after all testing was completed.

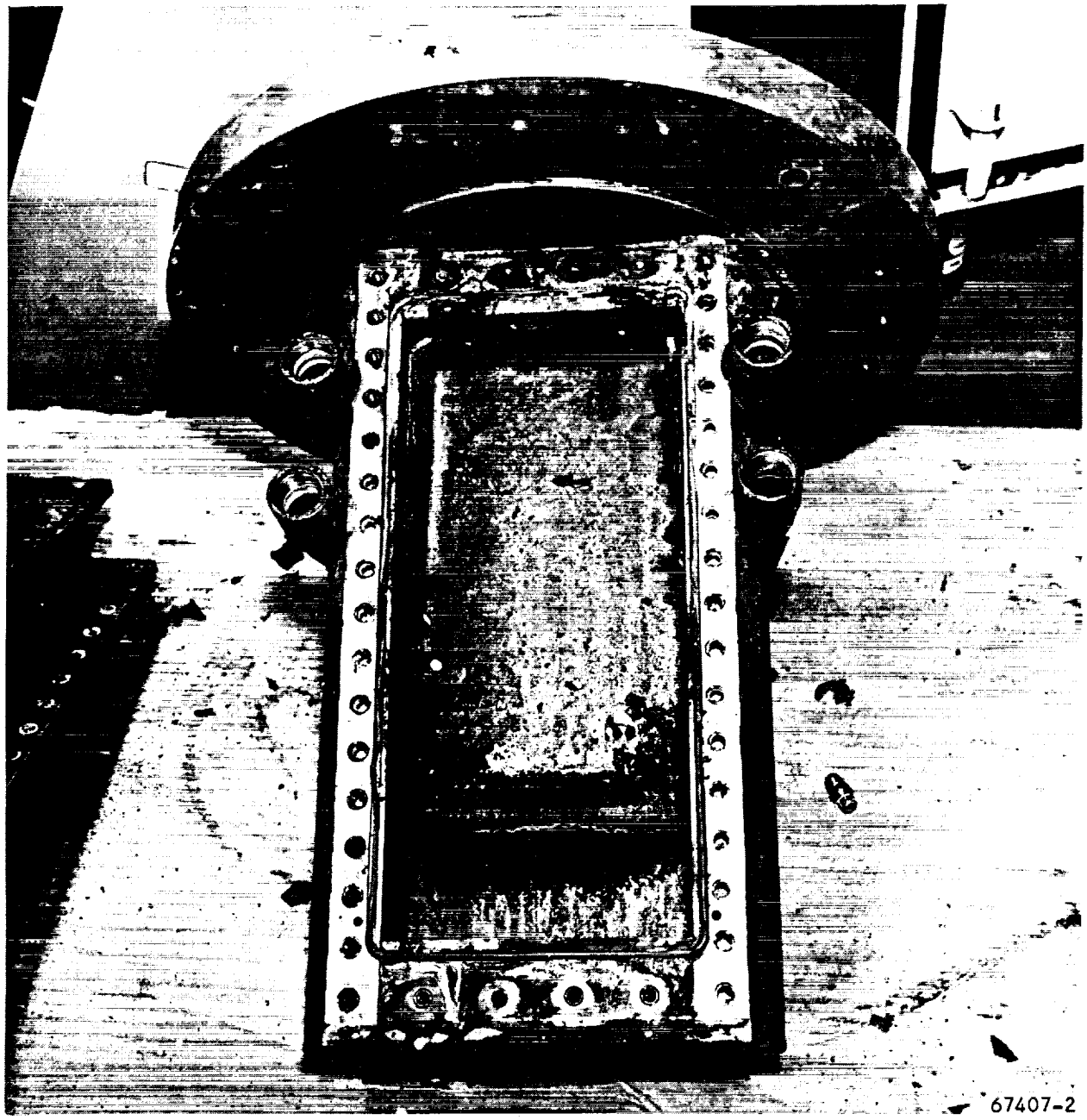

Figure A-5. Nozzle Box Hot-Gas-Exit Area After Test

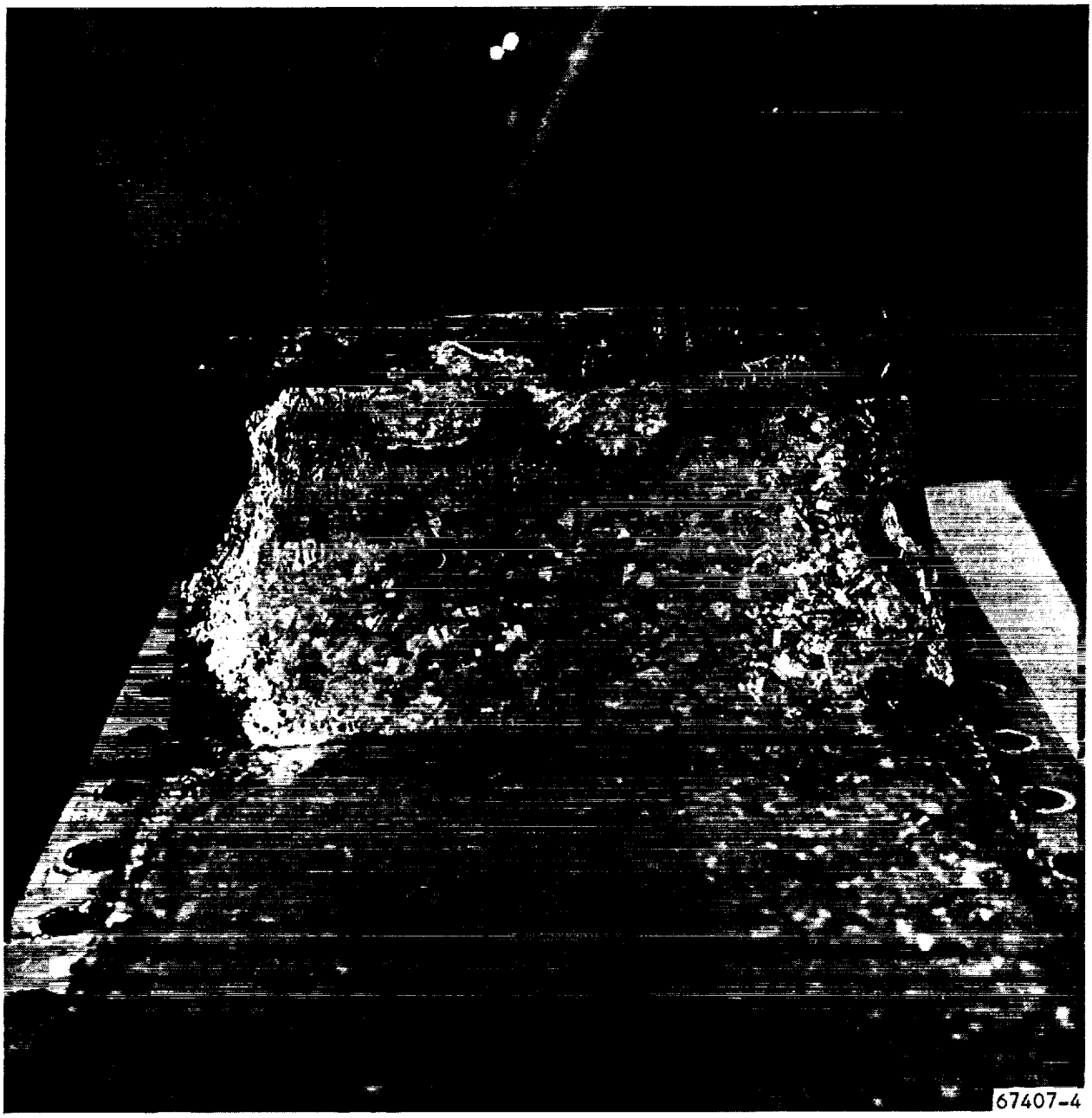

Figure A-6. Nozzle Insert After Testing

Subsequent to completion of the second series of true-scale tests, it was discovered that the alloy used to braze the plugs into the water passage holes had been almost entirely eaten away, although leakage did not occur. The observable alloy (or the alloy close enough to the surface to be seen) had disappeared during the period the nozzle was in use. When this nozzle was disassembled, the plugs were coated with plasma-sprayed copper in order to extend the life of the part. The addition of the plasma-sprayed copper did not aid in maintaining a seal, but merely kept hot gas from further eroding the braze joints. The damage described here was primarily of a dimensional nature and superficial with the exception of two small water leaks that developed in the nozzle box.

A.3 THRUST STAND

The thrust stand used for the two-dimensional combustor tests was designed and fabricated by FluiDyne Engineering Corporation of Minneapolis, Minnesota. FluiDyne Drawing 0565-901, attached at the end of this report, is an assembly drawing of the thrust stand which shows in detail the water-cooled air passage through which the vitiated air passed before entering the combustor, the seal area, and the upper and lower service blocks.

Figure A-7 is a photograph of the test installation showing the combustor cantilevered off the downstream side of the thrust stand. The ring to which the combustor was bolted was supported entirely by the load cell and formed a part of the "floating" section of the thrust stand. The lower service block, also part of the "floating" section, was connected by pipes and lines to the upper service block located at the top of the large cylindrical section on the upper side of the thrust stand. O-ring seals were provided at each end of the pipes, i.e., at the upper and lower service blocks. The high length-to-diameter ratio provided flexibility over the small load cell displacement required. No axial forces were introduced into the floating section by the water flow, as the water pipes were perpendicular to the combustor axis. Hydrogen was carried from the upper to the lower service block through a smaller diameter line (one line was used for the first stage and another line for the second stage) with sufficient length per unit diameter so that negligible forces were introduced with small load cell displacement. The upper service block was connected physically to the fixed portion of the thrust stand, which included the upper service block, the tower (or cylinder), a massive flange, and the basic framework of the thrust stand. A number of modifications were made to the thrust stand during the course of the program. These modifications are discussed below.

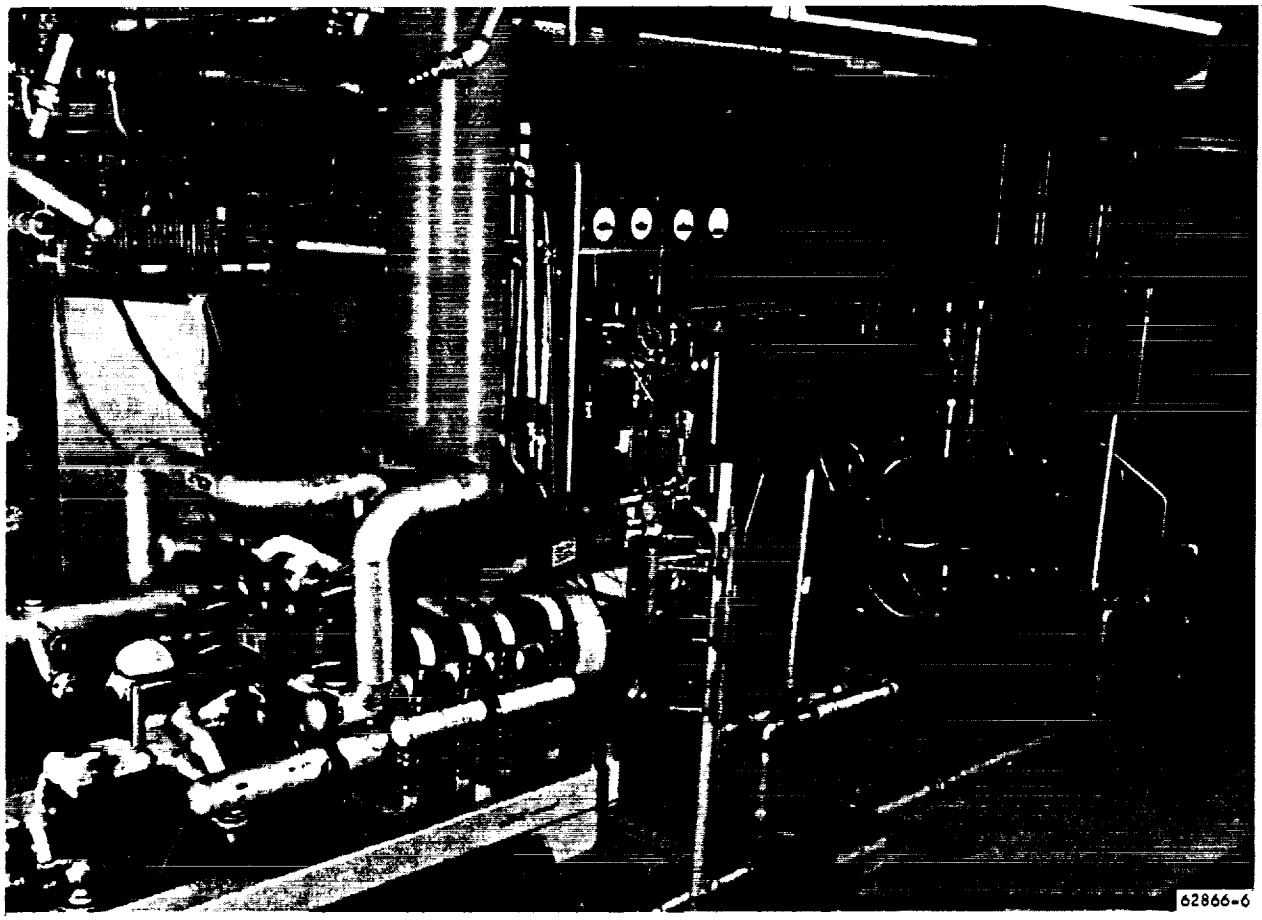

Figure A-7. Combustor Test Installation

A.3.1 Load Cell Replacement

The load cell that was provided with the thrust stand is shown in Figure A-8. Using this load cell, the overall thrust stand error, without water or hydrogen flowing, was less than one pound in 300, but the cell had a very low overload capability such that the combustor model could not be installed on the thrust stand without incurring a failure in the strain gage element. The destruction of the strain gage element occurred three times, despite the caution exercised.*

The overload/impact problem was eliminated by replacing internal elements with a capacity-type displacement sensor. This consisted of parallel plates attached to the machined block, as shown in Figure A-9. When a load was applied to the block, the resulting deflection changed the relative position of the plates, thereby changing the capacitance. An electronic circuit was fabricated with a dc output voltage proportional to the force applied to the load cell. The use of the capacitance load cell gave excellent overload capability at a relatively small sacrifice in accuracy. The stand calibration with no water or hydrogen flowing showed an error of 1.4 lb.

A.3.2 Changes To The Seal

In addition to modifications made to the thrust stand load cell, the seal area was subject to several changes. During the first supersonic 2- by 6-in. combustor tests the rubber seal developed a leak and burned out. At the time, it was not clear why this had occurred, but it was assumed that over-pressure had been at least partly responsible. After the first seal failure, the kit that was provided by the manufacturer to convert the thrust stand for use with the true-scale combustor experiments was installed and the stand again placed in service.

The true-scale tests commenced and the seal was destroyed after a very short time. Based on the events that had occurred and the condition of the seal assembly, it was assumed that over-pressure had caused the failure. A seal with a double wall thickness was installed. The seal plates that held the rubber seal in place were maintained at 0.009 in. apart. Drawing 0565-901, showing the thrust stand, is included for reference at the end of this report. The seal thickness was increased to 0.040 in. so that it could not possibly be extruded into the 0.009-in. gap between the sealer plates without extreme pressure. As an added precaution, an over-pressure abort system was installed that would cut off all hydrogen flow if the static pressure at the seal exceeded 60 psig. In addition to the hypothesis that over-pressure had destroyed the seal, consideration was also given to the possibility that there could have been a circumferential flow field set up in the thrust stand seal cavity.

---

*HRE Program Trouble Analysis Report No. 17126 (Data Item 26.07), No. 17563 (Data Item 26.10), and No. 17647 (Data Item 26.11).

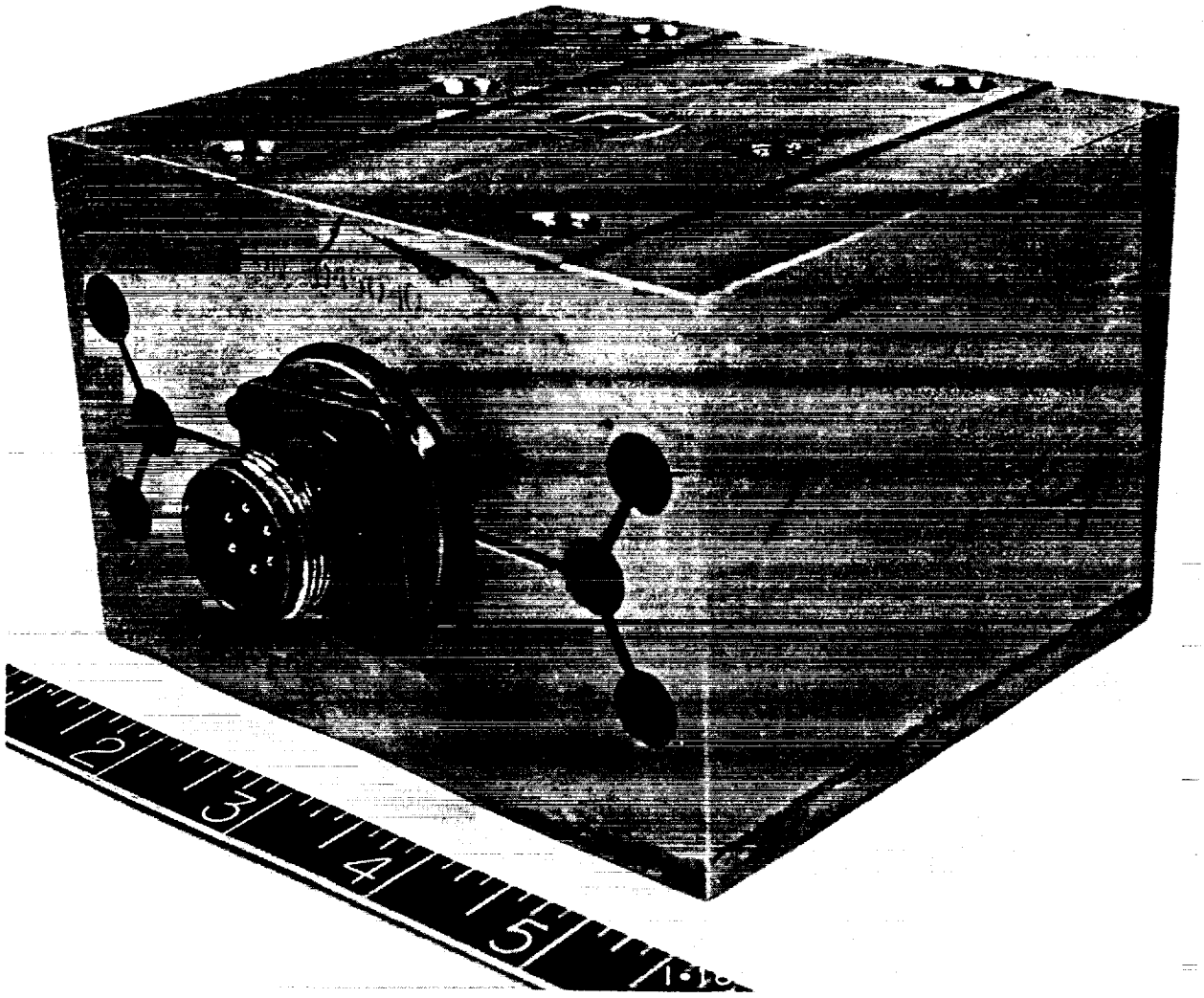

F-11459

Figure A-8. Thrust Stand Load Cell

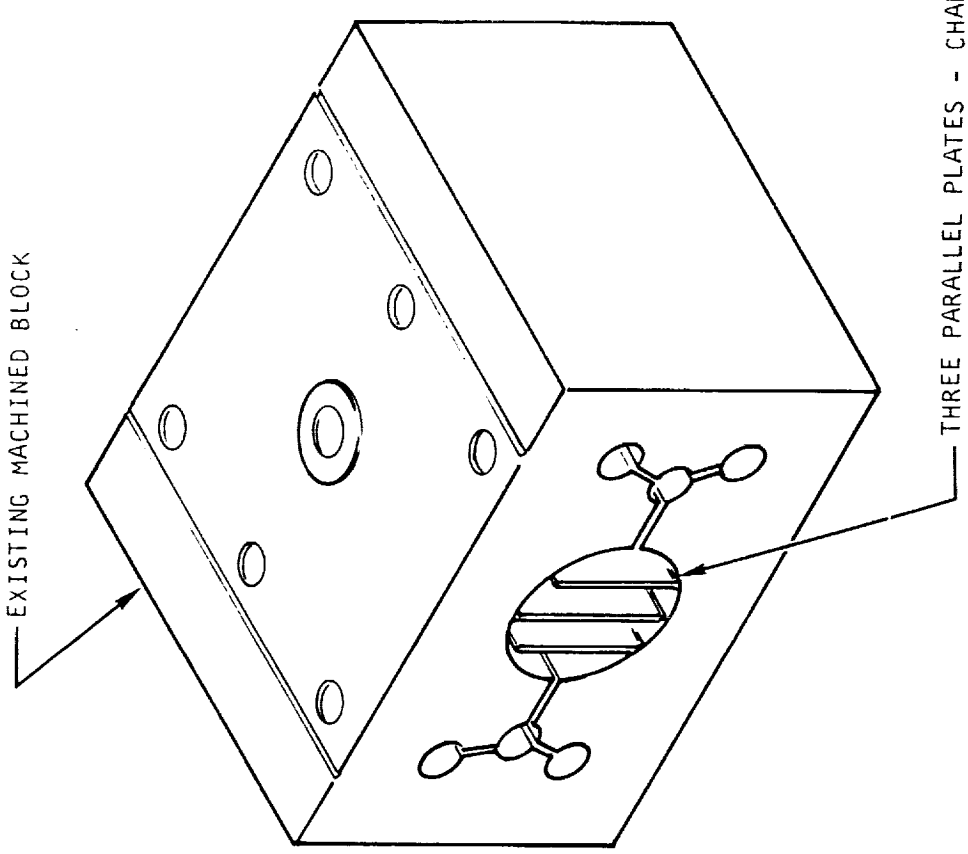

Figure A-9. AiResearch Modification to Load Cell

Assuming that this was the case, a nitrogen bleed system was installed. This bleed system consisted of eight 0.125 OD tubes which delivered gaseous nitrogen to the seal area at a flow rate such that the seal cavity was maintained at a higher static pressure than the air that passed through the thrust stand. The objective in installing this bleed system was to guarantee that a flow of cool nitrogen would be leaving the seal area, eliminating the possibility that hot gas could enter. The modified seal assembly is shown by Figure A-10. The bleed system was operated during vitiation heater startup, and all changes in equivalence ratio in the combustor, but not during test points.

The bleed system did, of course, have a finite volume. Therefore, a sudden increase in static pressure in the duct could cause a back flow of hot gas across the seal area. As a failure mode, this possibility was considered remote, because any gas entering the seal area would be cooled by the water-cooled plates present. The seal again failed and it was apparent that over-pressure was not the cause, because the abort system never actuated. The failed seal assembly is shown in Figure A-11.

It was seen at this point that the modification adding the seal-bleed system had been ineffective, and therefore, this system was removed completely. The formerly used Buna-N seal was replaced by a silicone rubber seal of precisely the same dimensions. The silicone rubber seal, according to the manufacturer, had a short-term temperature capability of 600°F. When the silicone rubber seal was installed, there were four thermocouples installed in the seal area in order to monitor the gas temperature to which the seal was exposed. The temperatures were read in the control area so that a test could be terminated if the seal temperature became excessive. A number of test runs were nearly terminated for reasons of high seal temperature; however, no further seal failures occurred.

A.3.3 Design and Fabrication of a Metal Seal

Since a sudden and significant temperature rise in the seal area seemed to be a common occurrence, it became apparent that a seal of higher temperature capability was highly desirable, if not mandatory, particularly if it became necessary to run higher fuel/air ratios than were required at that time. To run excessive fuel/air ratios enhanced the chances of an occurrence of a sudden over-temperature situation.

An all-metal seal was designed and fabricated in order to provide a higher temperature capability. The design concept, suggested by NASA and shown in Figure A-12, is one in which two thicknesses of 0.006-in. Inconel-X were formed into a bellows of one convolution. The bellows constituted flexible seal with a calculated spring constant of 2250 lb/in. Since the maximum anticipated displacement was 0.003 in., the developed force would be only 6.75 lb, which would be absorbed into the calibration of the thrust stand prior to a combustor test. The seal assembly is shown in Figure A-13. Figure A-14 shows the four Inconel-X leaves, and the welded, one-convolution bellows used in the seal assembly is shown laying on the machined type 321 stainless steel seal plates.

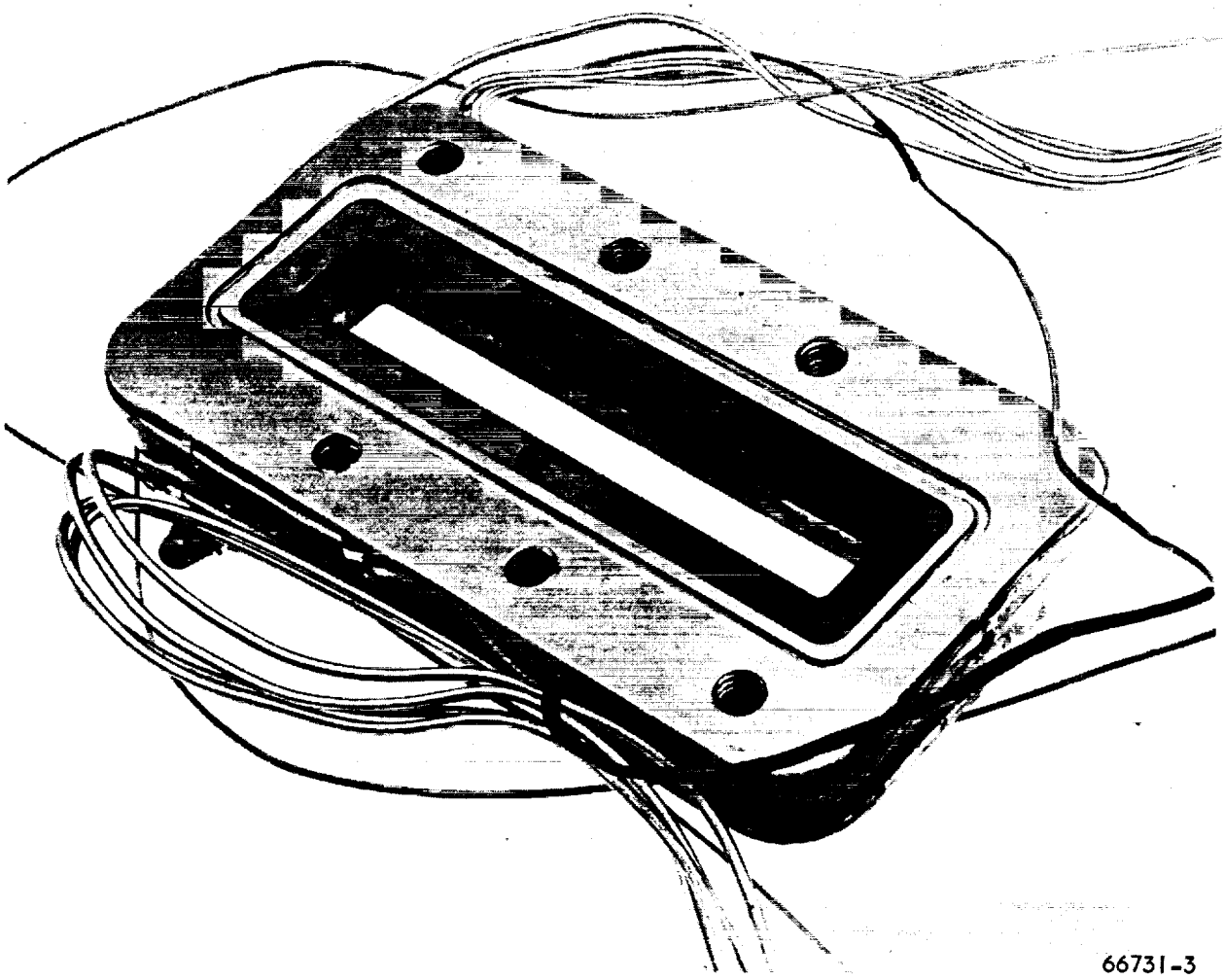

Figure A-10. Seal Assembly With Bleed Lines and Thermocouples Before Use

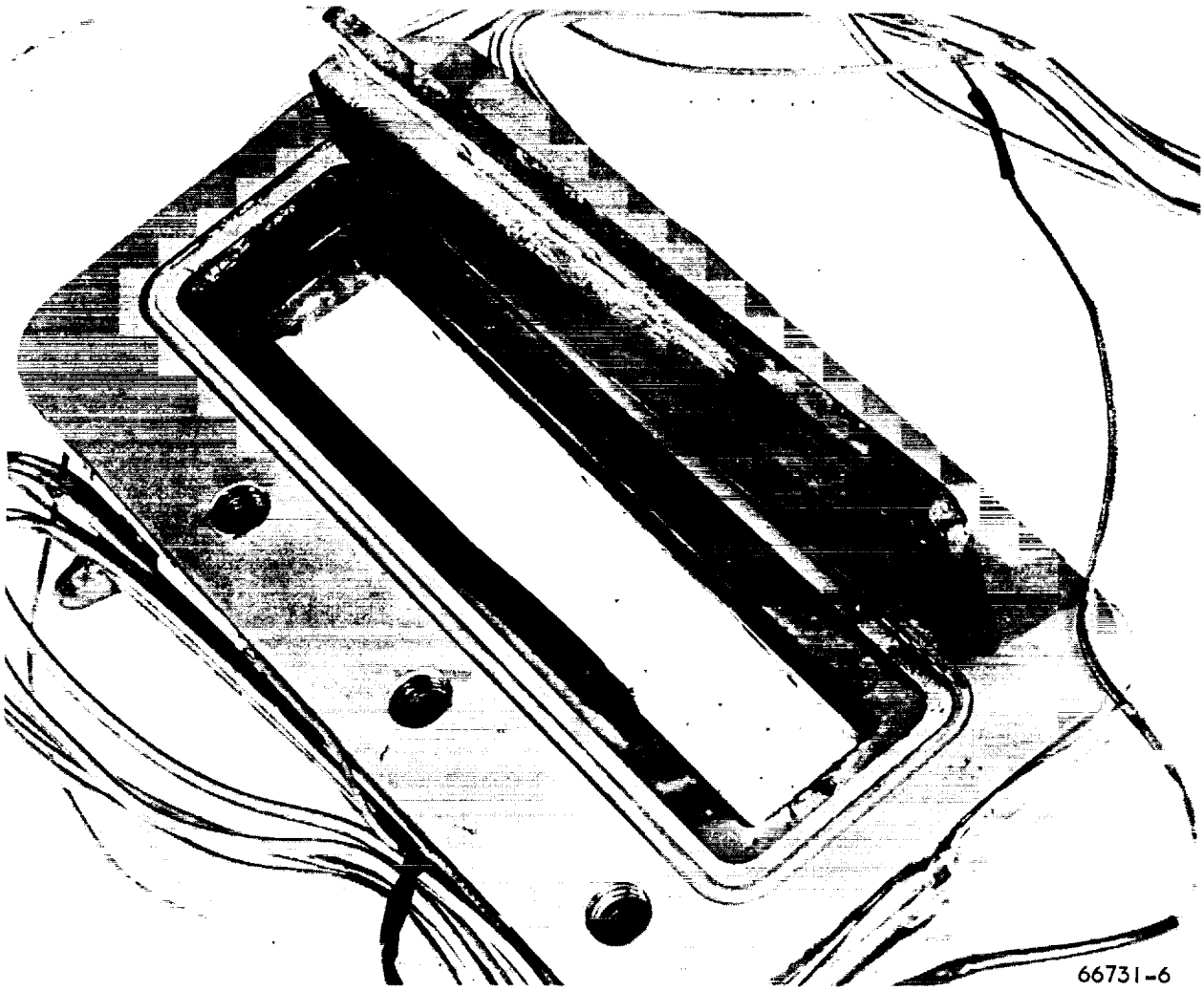

Figure A-11. Seal Assembly After Test

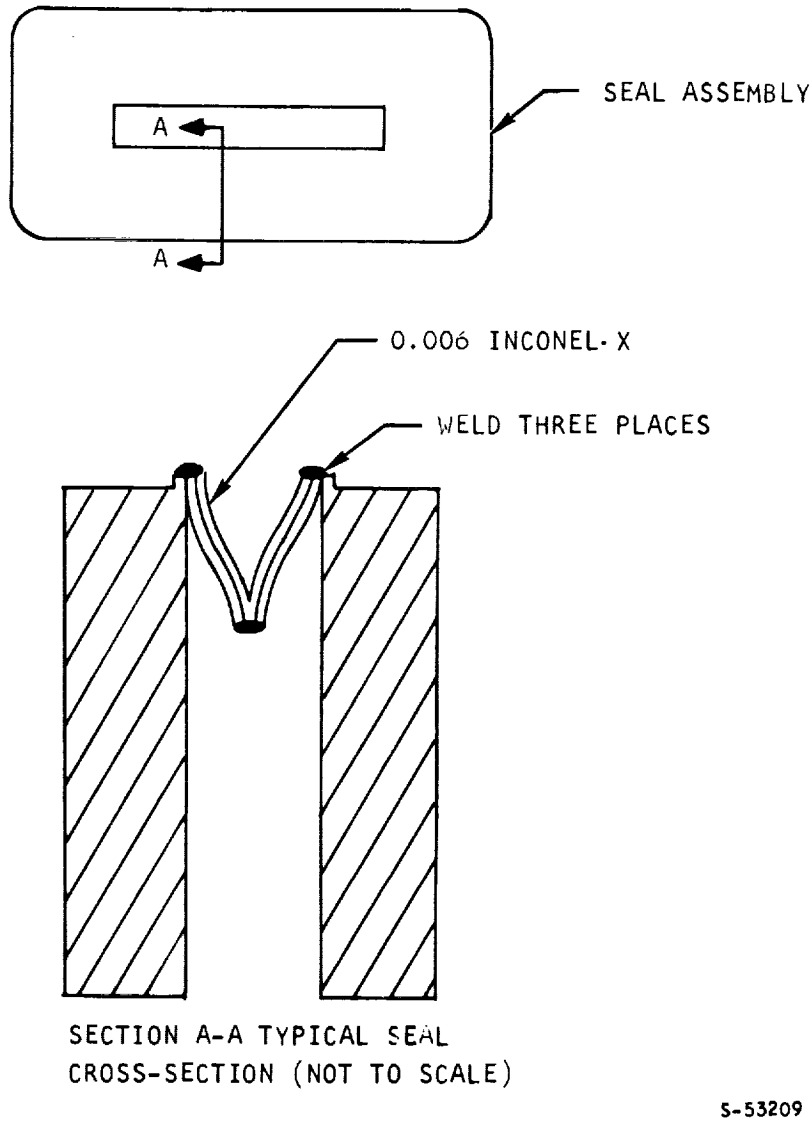

Figure A-12. Design Concept of Metal Seal Cross Section

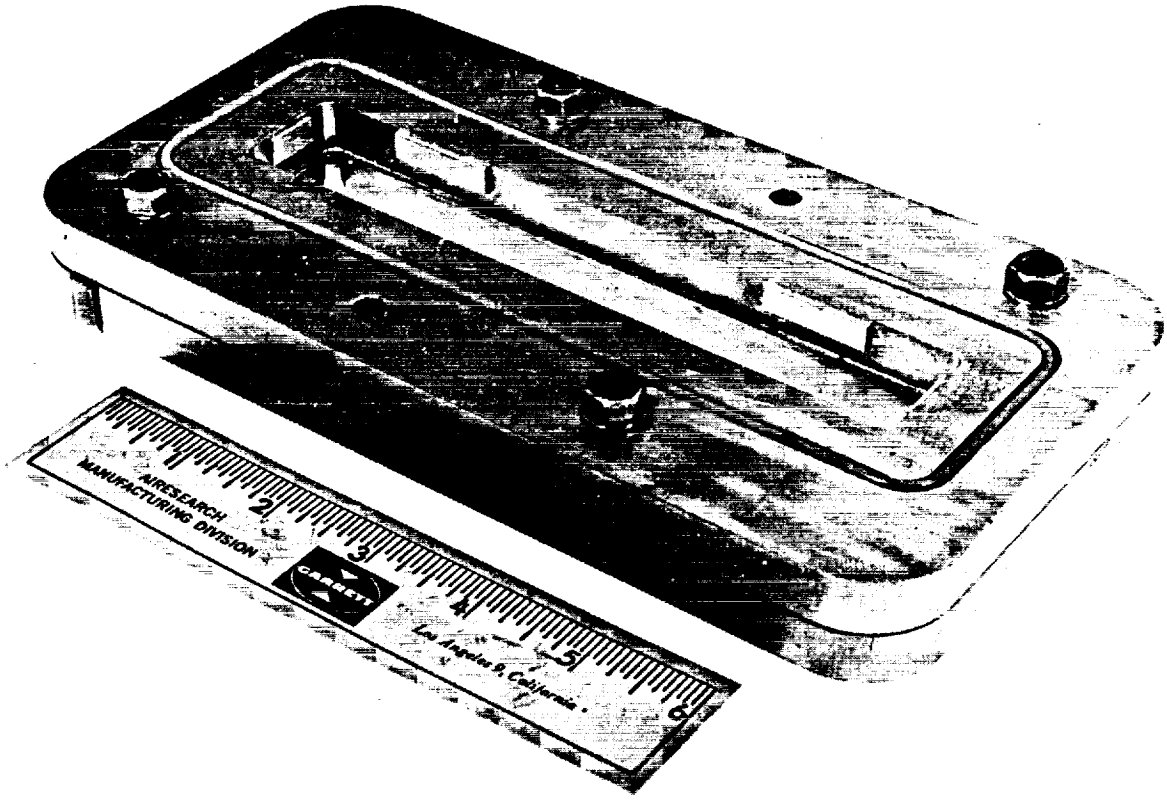

67118

Figure A-13. Completed Metal Seal

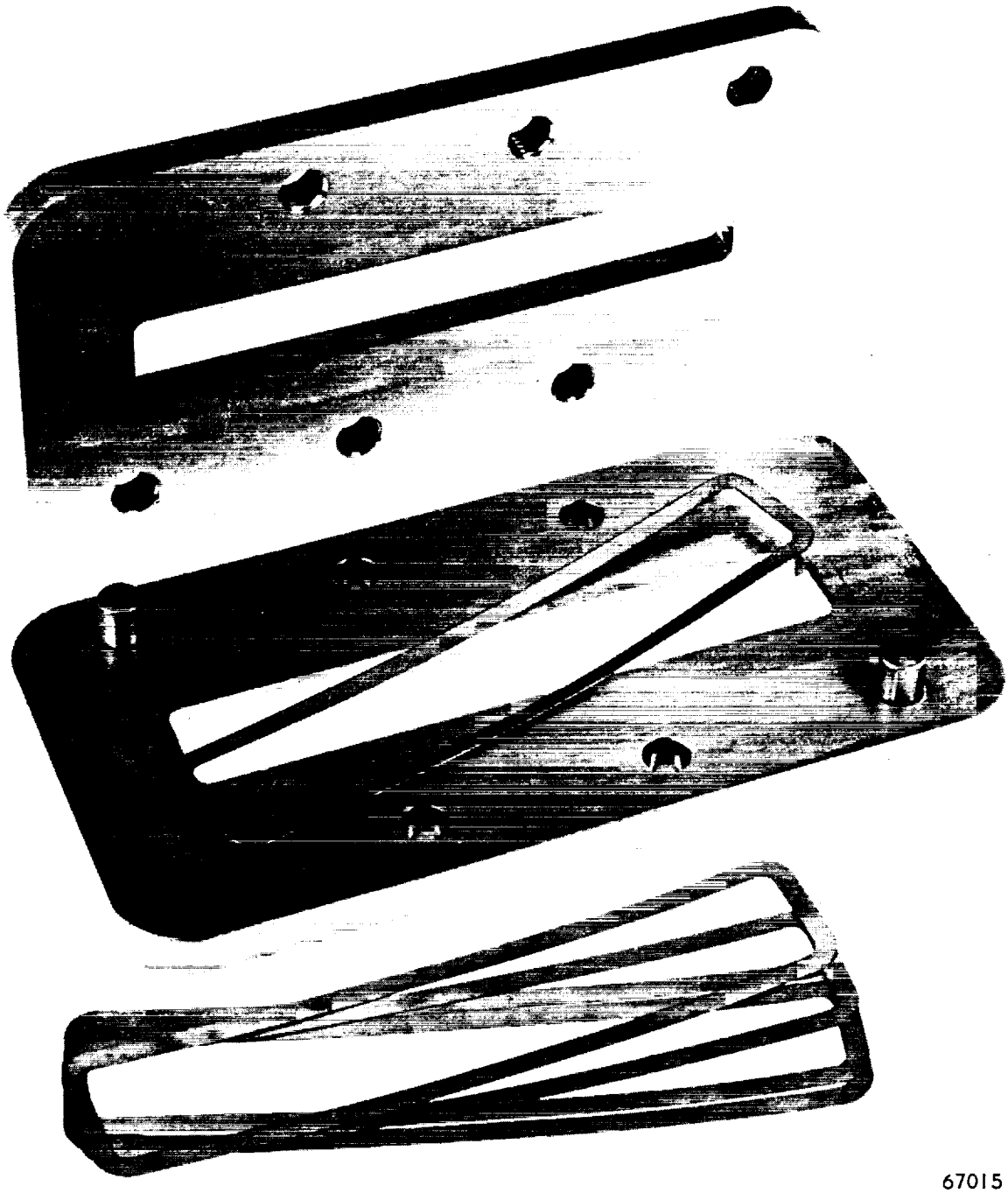

67015

Figure A-14. Metal Seal Component Parts

After the fabrication of the seal assembly was completed, it was pressure tested at 100 psia. A small leak of undeterminable location existed in one of the welds. The leak rate was measured 1.6×10^{-7} lb/sec at 100 psia.

The metal seal was never actually installed and used due to the subsequent termination of the combustor testing.

A.3.4 Modifications to the Hydrogen Entry

The final modification to the thrust stand was the change in the plumbing where the hydrogen fuel entered the stand. It was found that heating of the lines, to provide hydrogen fuel at the combustor at the correct temperature, caused a drift in force of up to 15 lb. This occurred despite the fact that one could easily move hydrogen supply lines by hand, before they were connected to the thrust stand. Figure A-15 shows the modification that was made. The lines were brought in as shown, in order to eliminate any axial force on the load cell. The brace was installed to take out any applied forces at the fixed side of the thrust stand. It had been found, by experiment, that to apply an axial force to the thrust stand hydrogen inlet line (at the top) was changing the reading on the load cell in direct proportion.

A.4 COMBUSTOR

The combustor model was a rectangular duct designed to provide both a 2-in. and a 0.6-in. entrance height, with a 6-in. width. The 2-in.-high configuration was to be used to study combustion to accumulate data for the development of design technique.

The 2-in.-high combustor configuration is depicted in Drawing ML 2340 attached at the end of this report. It was desirable to maximize combustor height in order to effectively probe the combustor exit plane and interior with gas sampling and pitot pressure probes. In order to obtain a mass flow per unit area of 1 lb/sec/sq in., the cross-sectional area of the duct had to be no more than 12 sq in., since the test facility compressor was capable of supplying air at the desired total pressure of 300 psia at a maximum rate of 12 lb/sec. The mass flow of 1 lb/sec/sq in. was the maximum expected mass flux based on the understanding of the HRE inlet at the time.

The true-scale dimensions of the combustor model were established to be 0.6 in. high and 29 in. long. These values provided a close hydraulic simulation of an actual segment of the expected combustor for the HRE.

The 0.6-in-high configuration was intended for tests to verify predicted performance, or expose discrepancies incurred in scaling down from 2 in. to 0.6 in. The model simulated a segment of an annular combustor such as the combustion chamber of the HRE. Variation in divergence angle was available as well as five locations where fuel injectors, plugs or igniters could be installed. The model was built in three sections so that up to three combustor lengths were available (12 in., 29 in., and 40 in.).

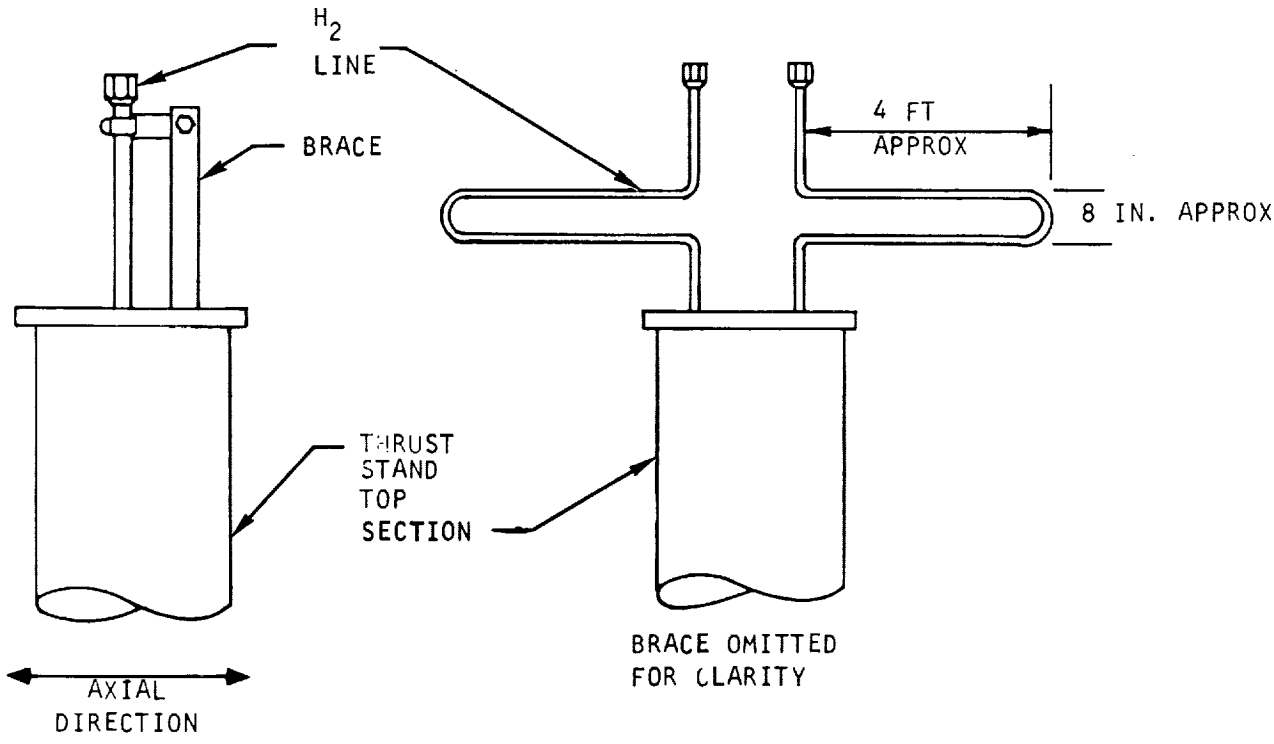

UPPER PORTION OF THRUST STAND WITH HYDROGEN CONNECTIONS, AS INSTALLED TO ELIMINATE TRANSMITTED FORCES DUE TO LINE HEATING

Figure A-15. Modifications to Hydrogen Lines on Thrust Stand

The model provided flexibility in length, height, and divergence angle with five fuel injection stations. Figure A-16 shows the combustor with the appropriate dimensions, fuel injector locations, etc. Drawing No. ML 2340 is an assembly drawing showing the entire combustor with fuel injectors installed. Note that the hinge point is 12-in. downstream from the combustor inlet. The first section, 12 in. in length, was of constant area. The side plates of the combustor remained stationary, while the top and bottom plates downstream of the first section were movable. The movable plates were held in place by turn-buckles to permit setting of the divergence half-angle at any value between 0 and 3.6 deg.

The use of flat plates presented a sealing problem, since a continuous O-ring or gasket could not be expected to seal at each point where more than two plates joined; therefore, cavities were provided in these areas into which RTV sealant could be forced to seal the joint.

The fuel injectors, plugs, igniters, and a high-frequency pressure transducer plug were interchangeable in the various locations provided. The injectors, etc., were bolted into position; a seal was provided by an O-ring, with the O-ring groove machined into the fuel injector flange. The O-ring groove was in a cooled area so that the use of special high-temperature seals was avoided.

The various cooling water inlet and outlet manifolds are depicted on Drawing ML 2340, and water distribution manifolds and connections on Drawing ML 2409, also attached at end of report. The water manifolds were aluminum piping, elbows, and reducers welded together to form the various shapes required to deliver water to numerous points on the combustor. These manifolds connected the combustor to the thrust stand lower service block.

Lateral cooling (crossflow) was employed in the injector blocks and the first two sections of the combustion chamber. Longitudinal cooling was employed in the third section and in the side plates. Approximately 30 skin thermocouples and 100 wall-static taps were spaced throughout the three sections. The water-flow schematic is shown in Figure A-17; the wall static pressure tap locations are shown in Figure A-18. Figure A-19 locates the wall temperature thermocouples.

A.4.1 Combustor Plates

As previously stated, the combustor consisted of flat plates. These plates were held together by brackets and sealed along the edges with O-rings and RTV sealant to provide a rectangular duct of the required size. To provide the necessary rigidity, the plates were machined out of type 347 stainless steel to a thickness of 1.0 in. Rectangular, 0.153-in.-high offset fins, and a 0.030-in.-thick skin were brazed on to form a sandwich structure.

Once the brazement was complete, final machining took place to provide the required overall length and width tolerances. Type 347 stainless steel was used for plates, fins, and header bars, primarily because it has superior qualities for brazing. The flatness requirement imposed on the machined plates was relaxed

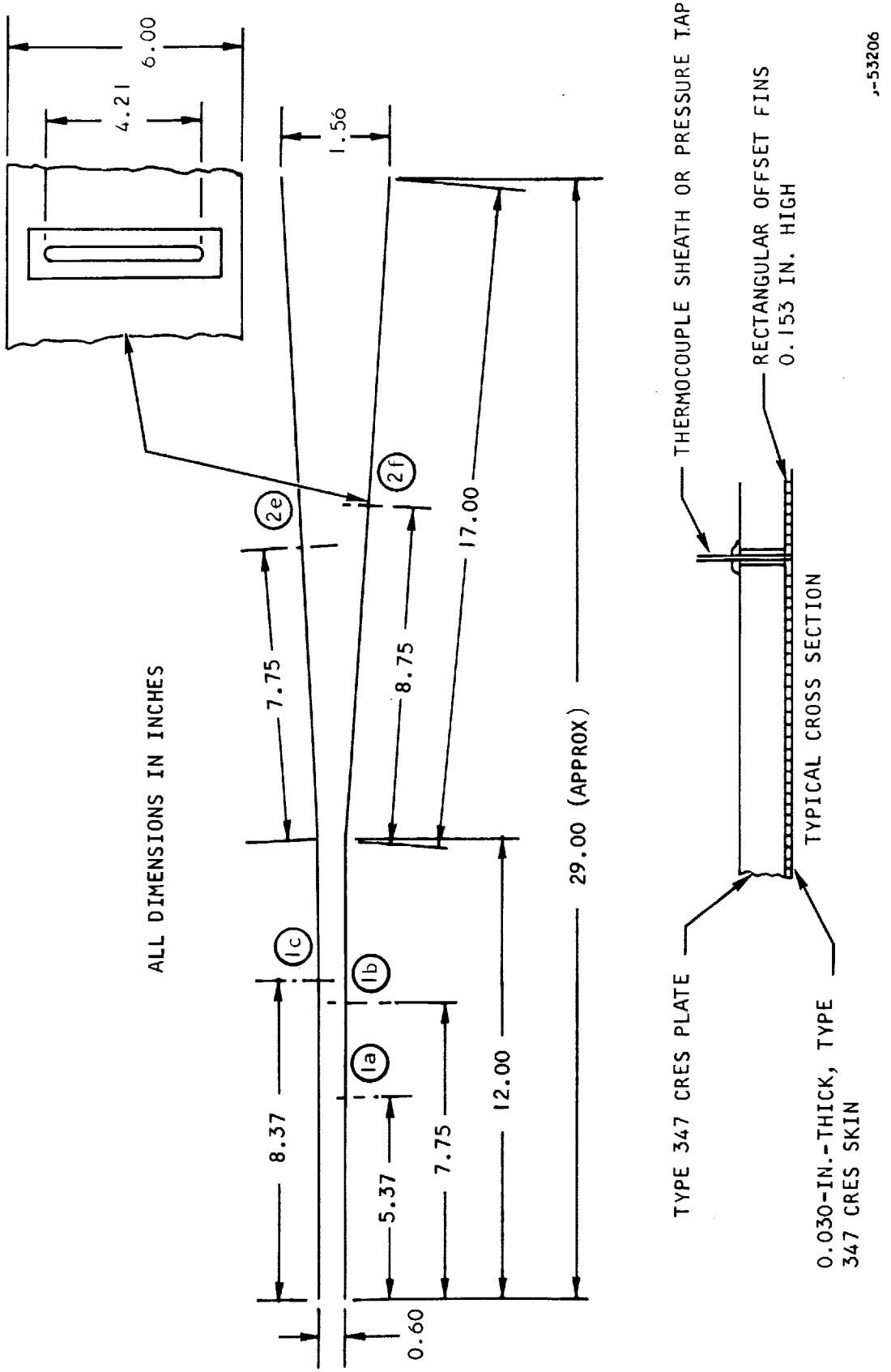

Figure A-16. Combustor Model Dimensions

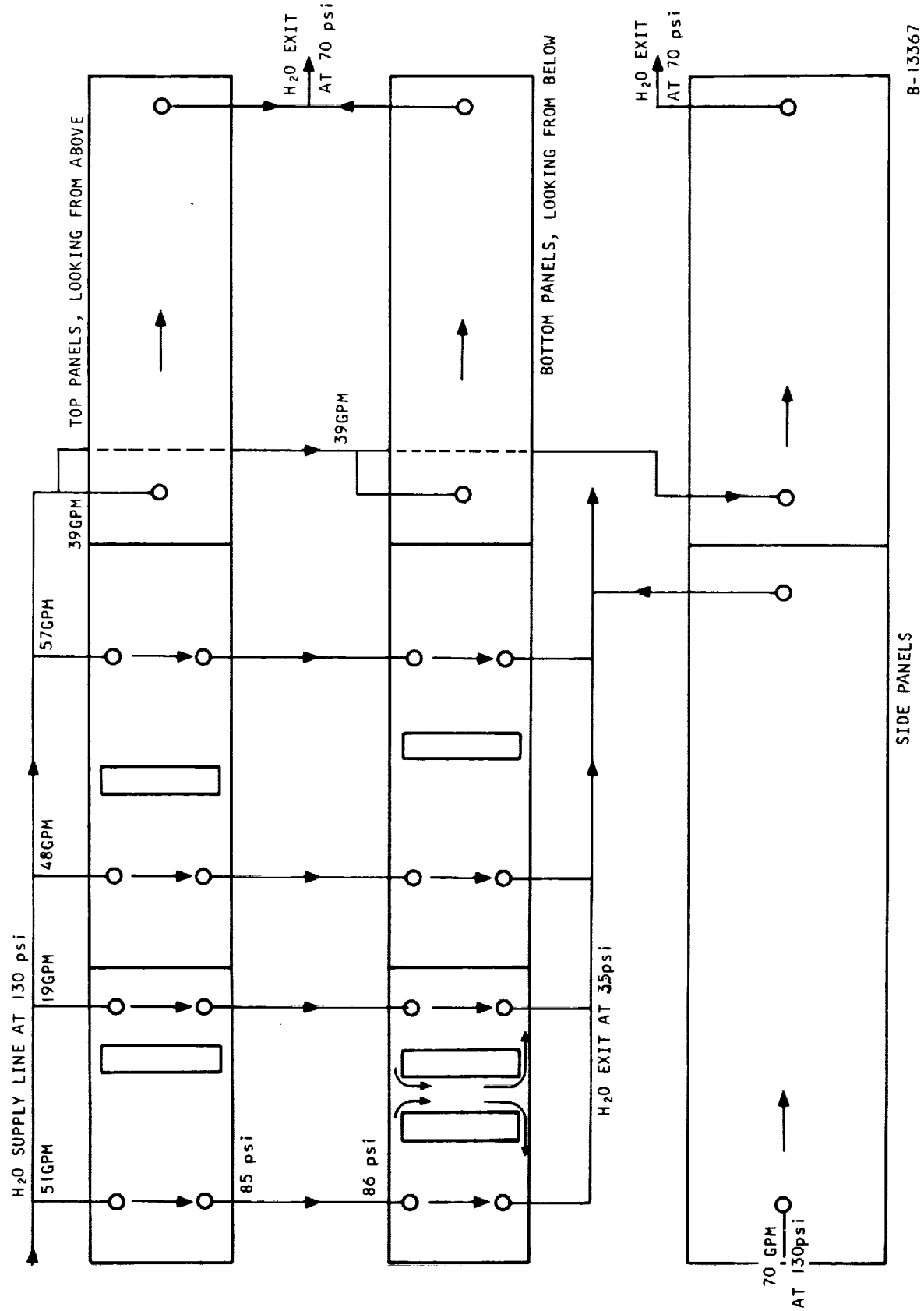

Figure A-17. Schematic Showing Flow Sequence and Flow Rates

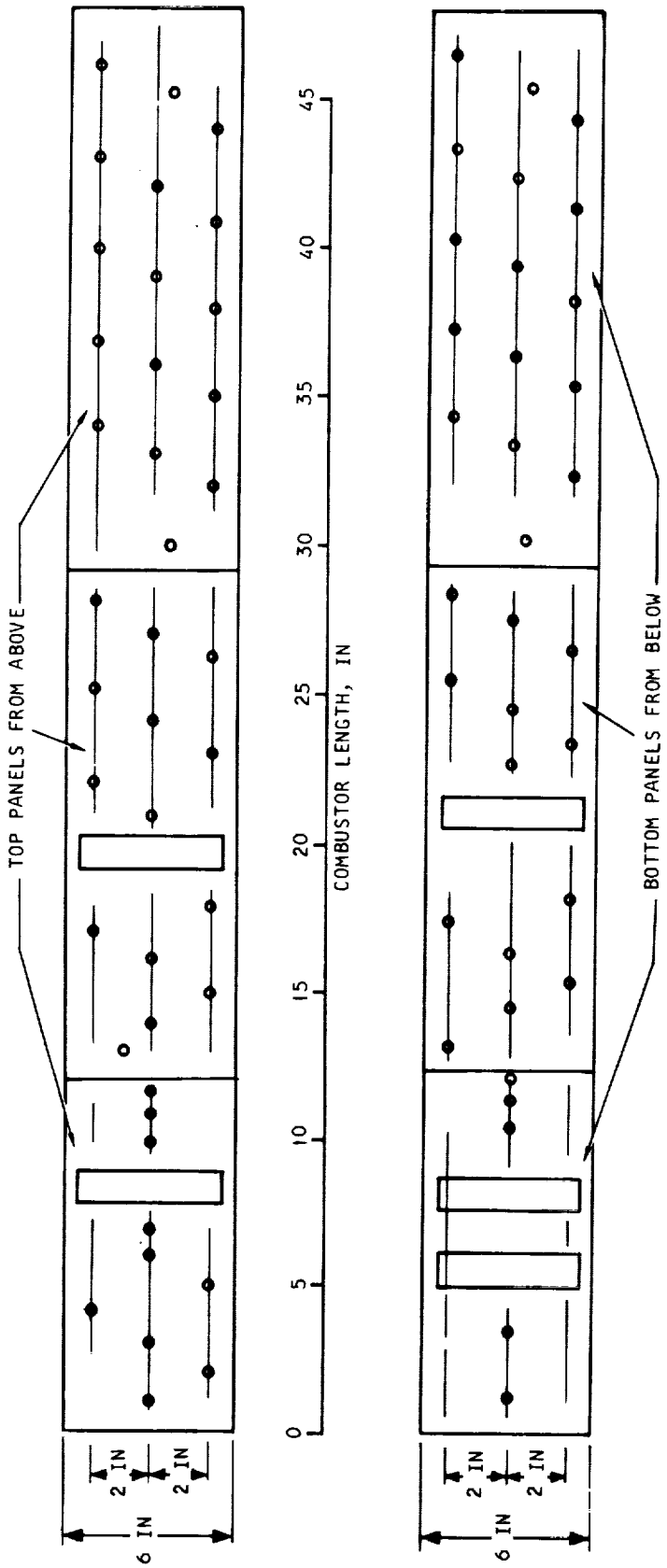

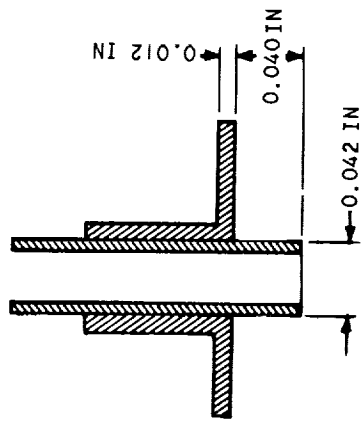

B-13365

Figure A-18. Schematic Showing Wall Static Pressure Locations

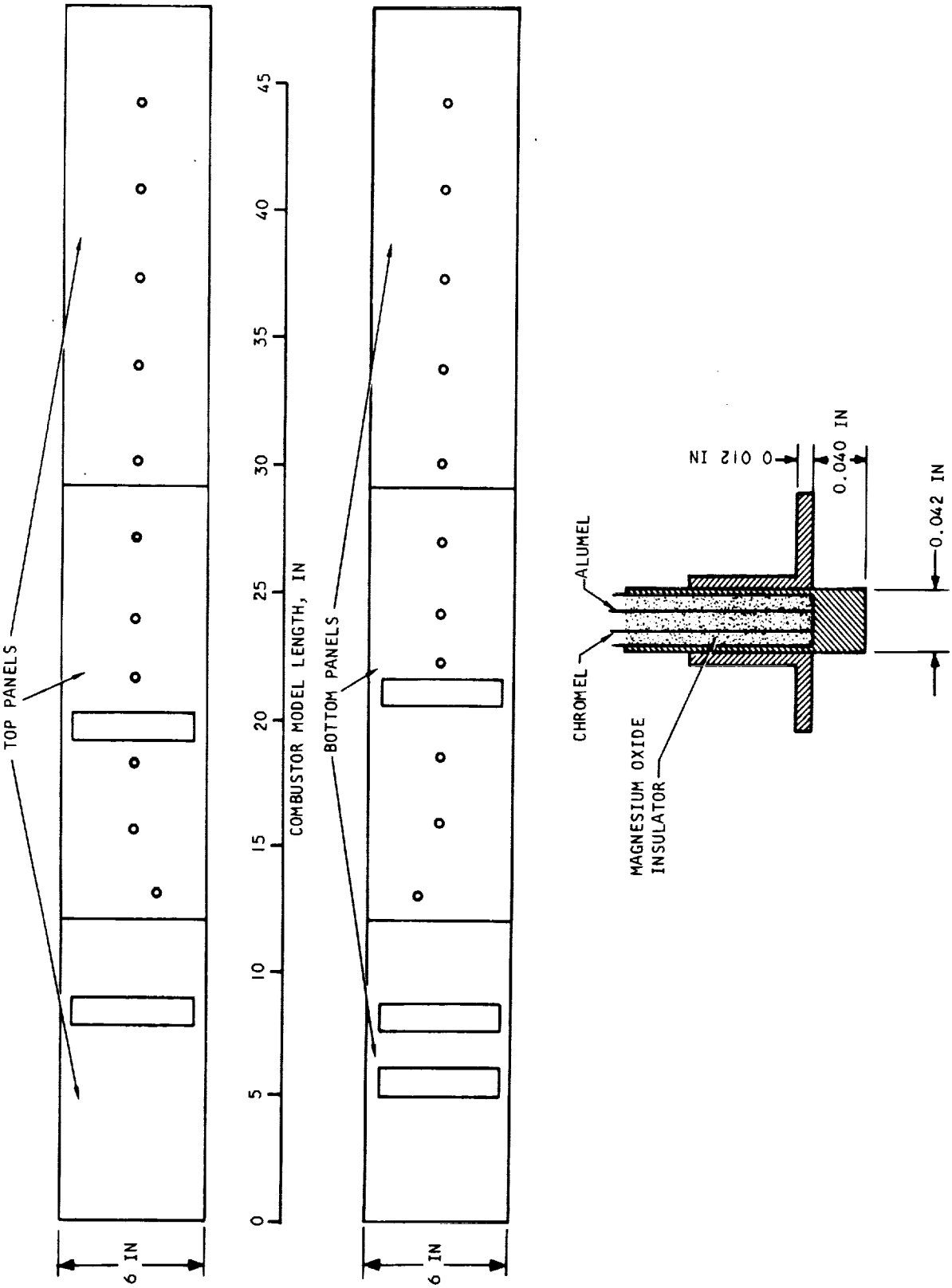

Figure A-19. Schematic Showing Skin Temperature Locations

to 0.020 in. for the 6-in.-wide plates that went on the upper and lower surfaces of the combustor. The side, or vertical, panels on the combustor were held within 0.001 in. flatness, since a seal had to be maintained for the entire length of the panel on both the upper and lower sides. Type 347 stainless steel plate stock, while an excellent alloy for brazing and for corrosion resistance, has the undesirable characteristic of warping after machining and during brazing. For this reason, it was difficult to maintain the flatness required. To achieve a flatness of 0.001 in., the surface on the hot-air side, i.e., the skin, was surface-ground after all other operations had been completed.

To connect the panels, flanges were bolted into the 1-in.-thick plate and then to each other. Prior to initial assembly, all flanges were doweled in place and the periphery of the assembly machined square with the skin surface. The panels were then doweled to each other to ensure a correct fit. The combustor model shown is composed of 10 such panels, called out as items 11, 12, 14, 16, 18, 19, 20, and 34. On ML 2340 the model is 48 in. long and broken into three sections with top and bottom panels of 12 in., 17 in., and 19 in. These are bordered by side panels 17 in. and 29 in. in length.

Also shown in Figures A-18 and A-19 are typical thermocouple and pressure tap installations. The heat transfer rate through the skin was of such a magnitude that the exact location of the thermocouple junction was important. The small "hat" that can be seen in the figures was placed on the thermocouple sheath to determine the location of the thermocouple junction with respect to the skin. The location of the junction with respect to the end of the thermocouple was measured by taking an X-ray of the thermocouple. This same hat was used in installing the pressure taps, not because precision in height was important, but because a straightforward, simple means of providing a good braze joint was readily available by using this existing part. Each of the flat combustor plates was provided with inlet and exit water manifolds. The water manifolds were connected by rubber hose to large aluminum manifolds leading to the thrust stand service block.

A series of feeder holes was drilled through the 1.0-in.-thick plates to deliver water from a water manifold directly to the fins. Sealing was accomplished by a flat gasket between the water manifold and the plate.

Attention is directed to Figures A-20 through A-23, which are photographs showing typical plates, a partial assembly, and a fully assembled combustor.

A.4.2 Fuel Injectors

The hydrogen fuel was injected into the vitiated air stream through fuel injectors shown on Drawing ML 2499, attached at the end of this report. The holes through which the hydrogen passed were drilled through the copper plugs brazed into the injector assembly. To change injector configuration required that the copper plug be machined out and a new drilled plug be brazed into place.

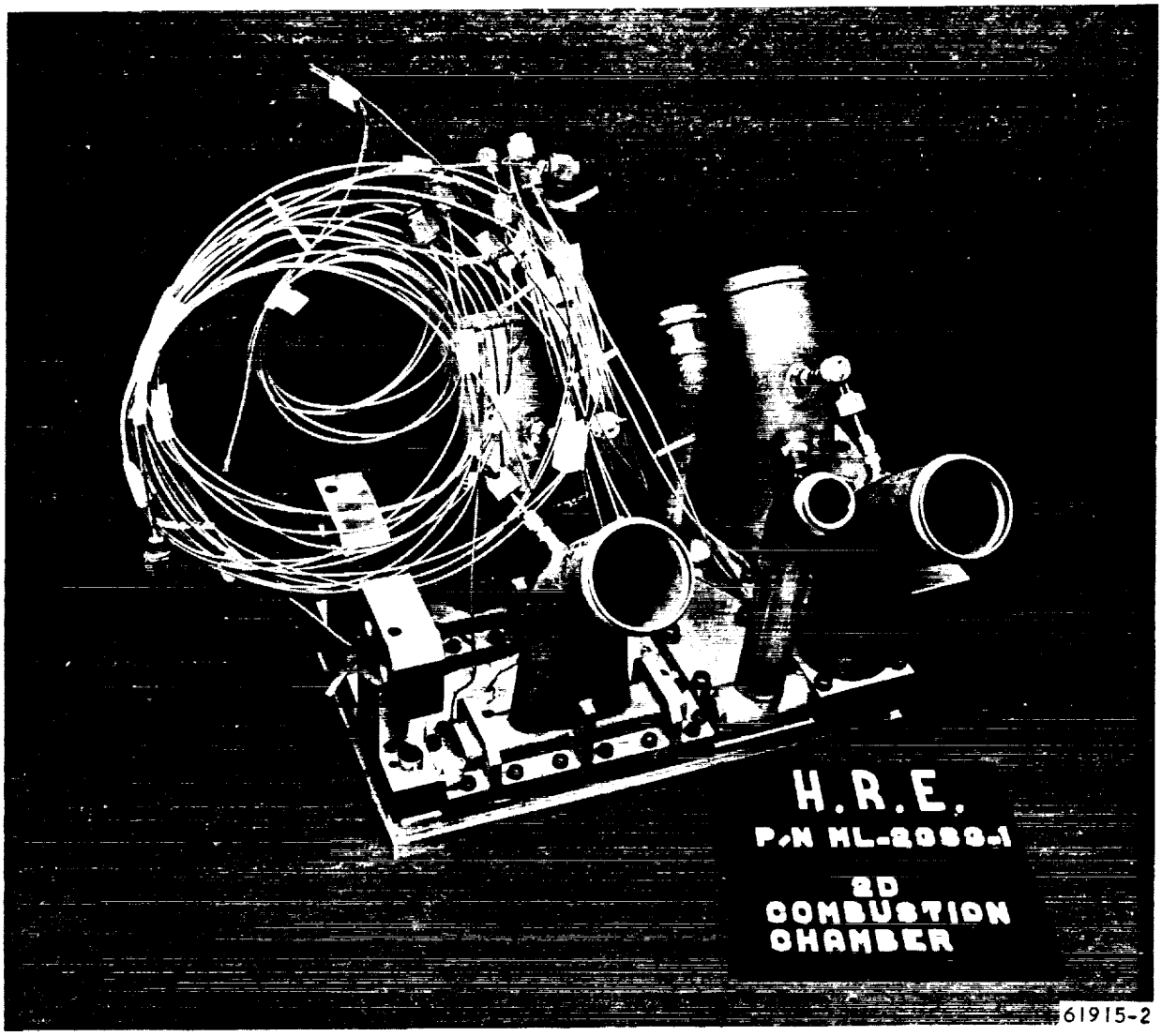

Figure A-20. Typical Combustor Plate

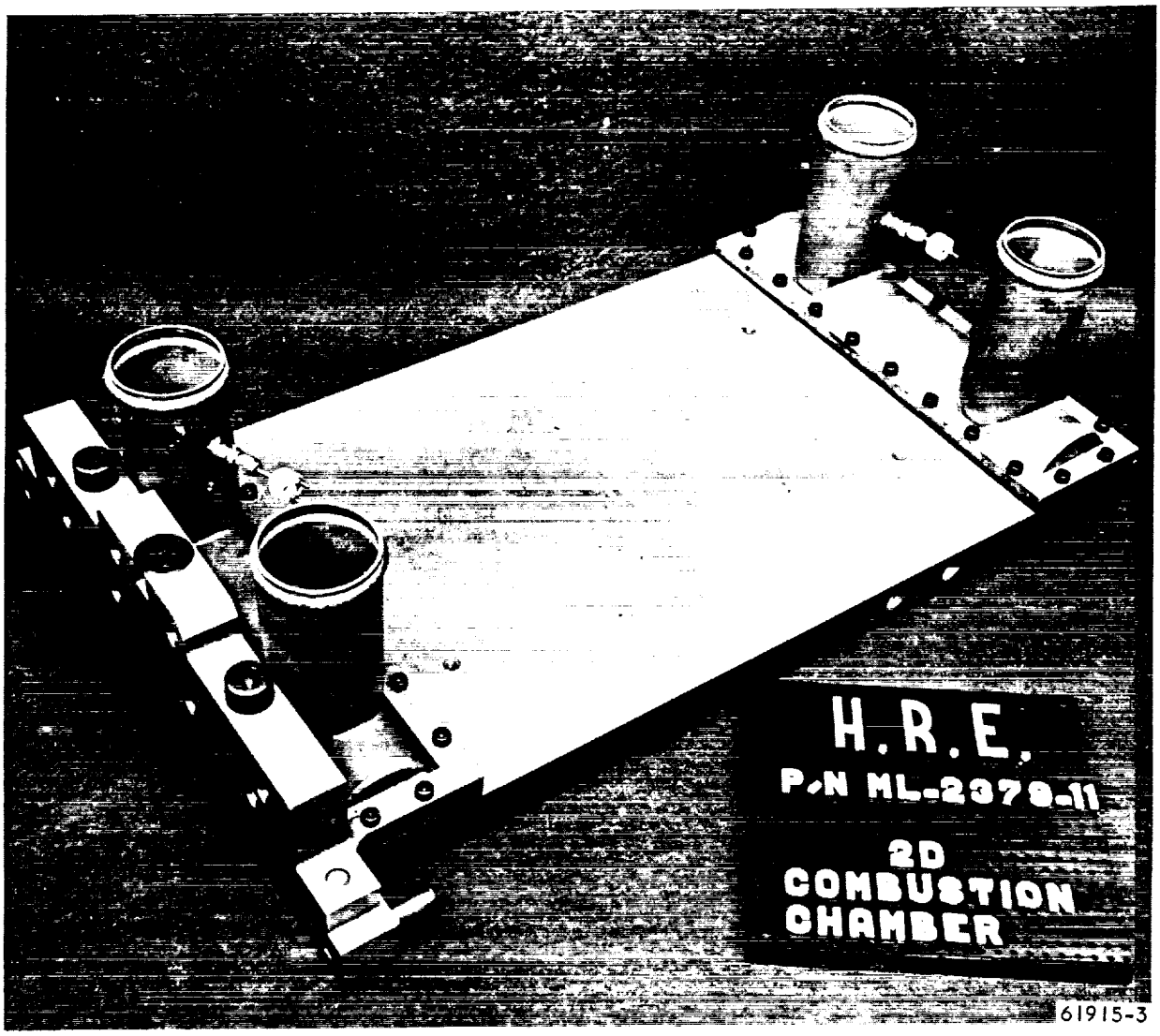

Figure A-21. Typical Combustor Plate

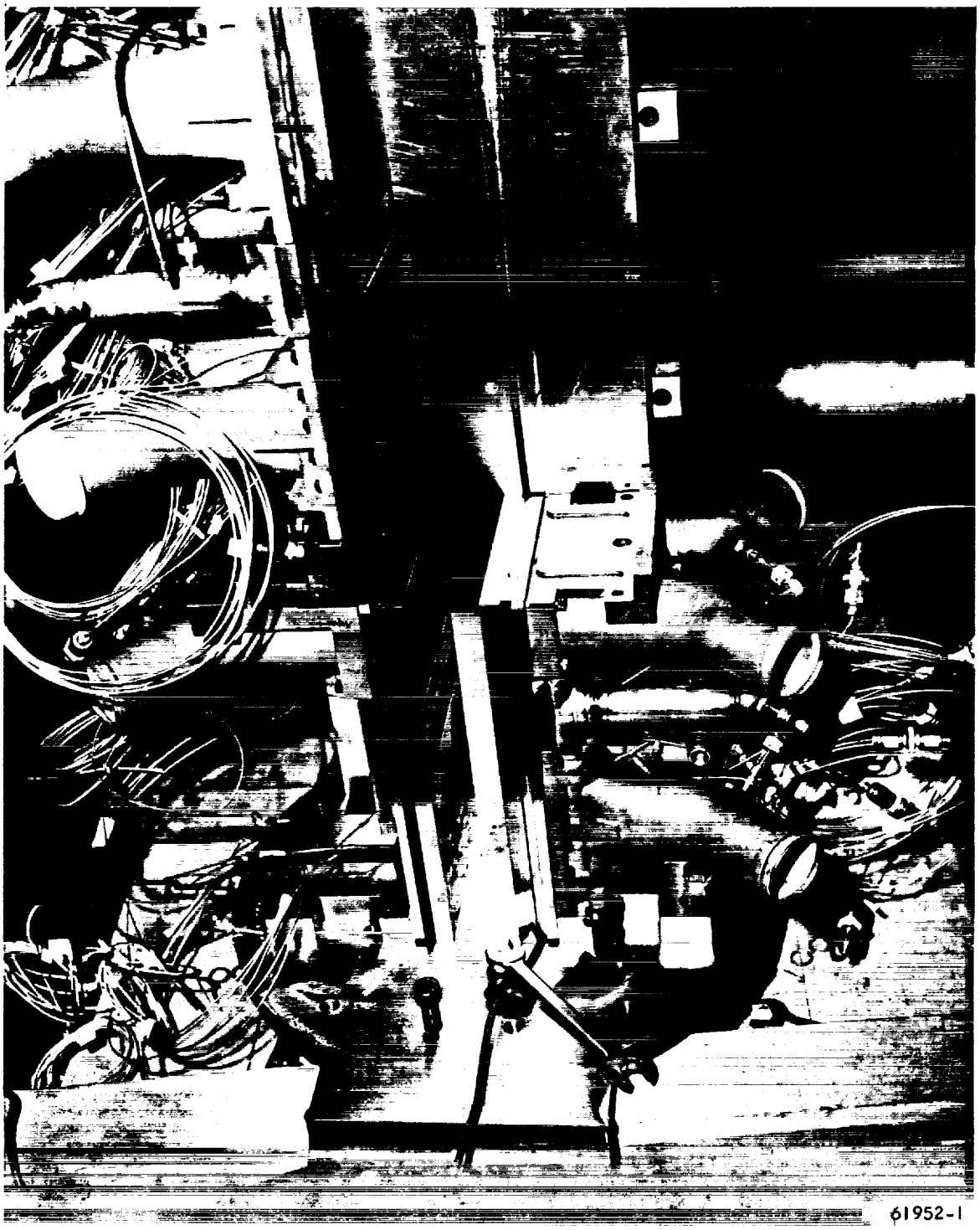

Figure A-22. Combustor, Partially Assembled

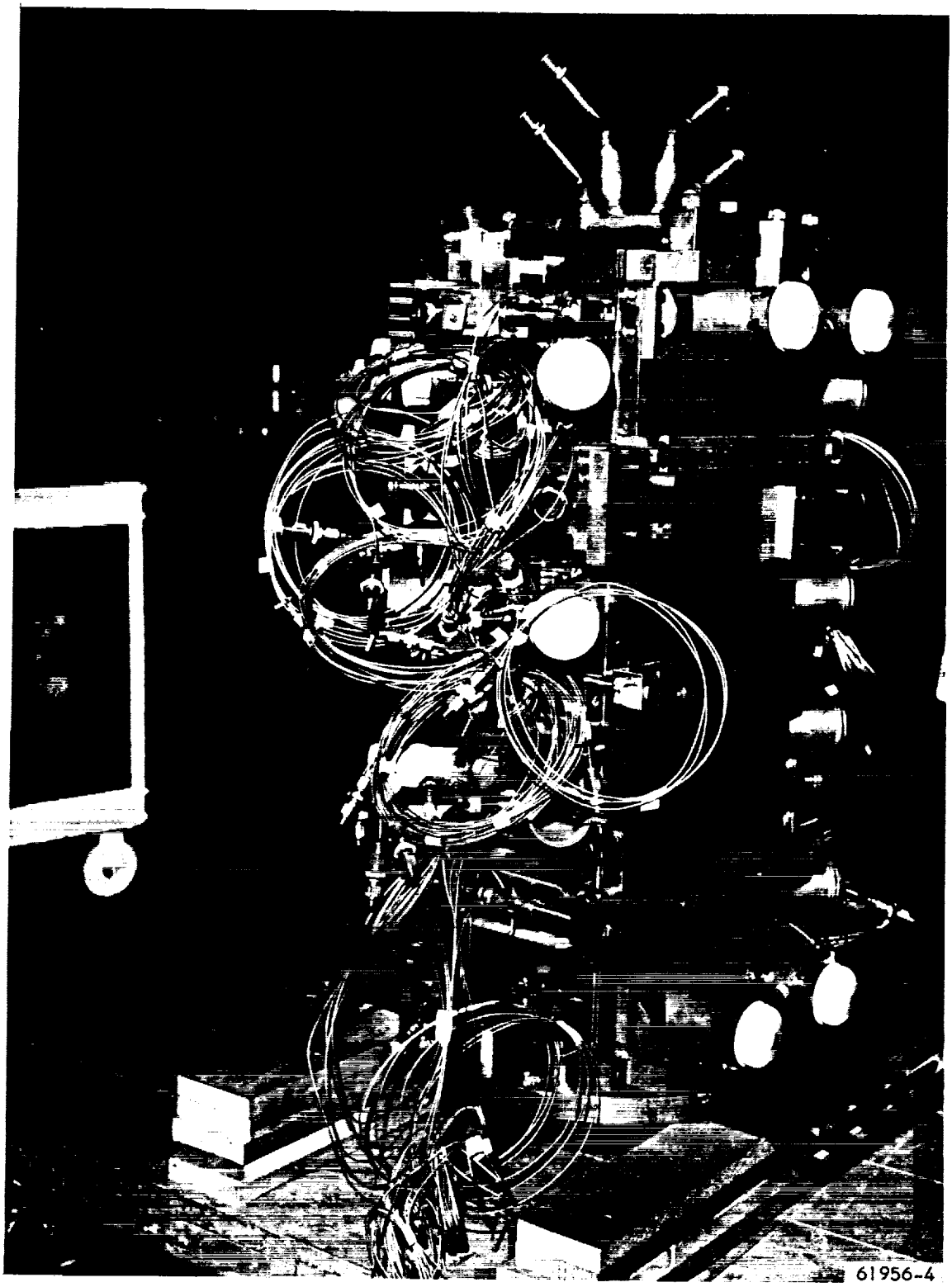

Figure A-23. Combustor, Fully Assembled

A.4.3 Igniter

Many of the combustor tests required positive ignition. Accordingly, a hydrogen-oxygen torch igniter was acquired and installed for that purpose, and is shown in operation during a bench test in Figure A-24. A block diagram of the igniter installation is shown by Figure A-25.

Hydrogen gas entered the igniter through a standard AN fitting, passed through a choked orifice, and was finally injected into the combustion chamber through a tube that also served as a spark electrode. The oxygen gas passed through a choked orifice, into a plenum, then through an annular passage containing swirl vanes, and finally into the combustion chamber. The disk on which the swirl vanes were mounted also served as a spark electrode. The circular combustion chamber wall did not require external cooling because of the oxygen swirl.

The use of choked orifices in the igniter provided mass flow measurement of the gases and stability.

Burning was spark-initiated. Energy for the spark was provided by using a high voltage power supply.

The igniter was fitted into a water-cooled plug that was interchangeable in the combustor with the fuel injectors so that it could be placed in any one of five locations.

A.4.4 Combustor Model Instrumentation

The instrumentation installation is best understood by examining Figures A-18 and A-19. The static pressures in the nozzle and in the combustor were measured by means of strain gage pressure transducers mounted in the cell. The wall thermocouples were used with 150°F-reference junctions and connected to the data acquisition system. The fuel flow to the combustor was measured using flat-plate orifices that were fabricated in accordance with ASME standards. The appropriate parameters regarding flow were fed into the data acquisition system, and the information was returned in the form of pressures, temperatures, and calculated flow rates; all in engineering units. The computer program used for data reduction also contained the necessary subroutines for calculating various parameters such as flow rates and equivalence ratios.

The wall static pressure transducers were all mounted in one container, or rack, and manifolded together so that they could be calibrated simultaneously. The line to the pressure tap was small (approximately 0.030 in. ID) and the lines between the transducers and the combustor were standard size 1/4-in. lines. The resulting value of rise time required that each test point be held steady for at least 15 to 20 seconds. As a precaution, each point was held for 50 seconds to one minute. The absolute error in the pressure measurements, including transducer hysteresis, non linearity, and zero shift, was estimated to be within 0.08 psi. The lowest values of static pressure in the combustor were in the order of 10 psia; therefore the maximum error was 0.8 percent.

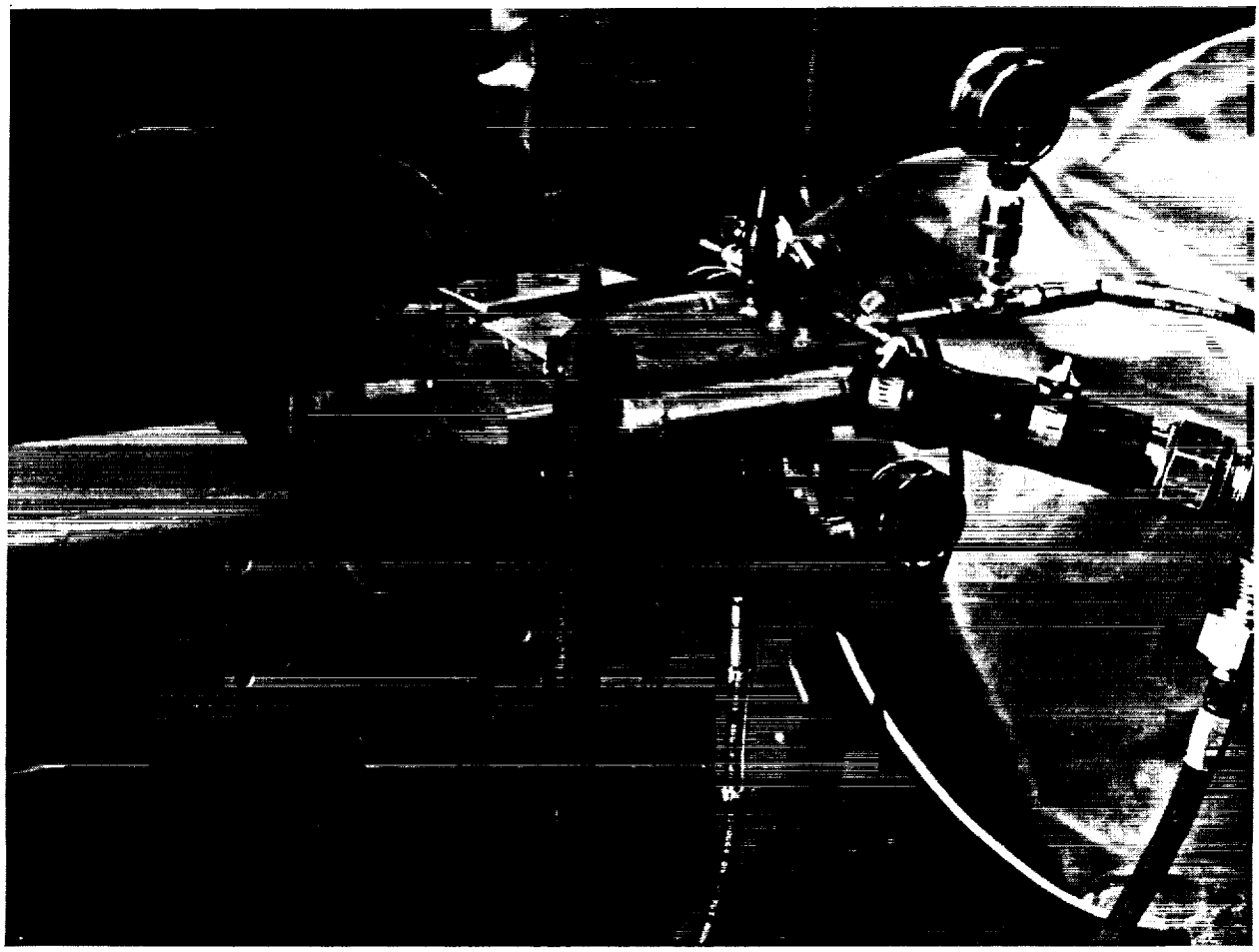

F-11461

Figure A-24. Bench Testing the Hydrogen/Oxygen Torch Igniter

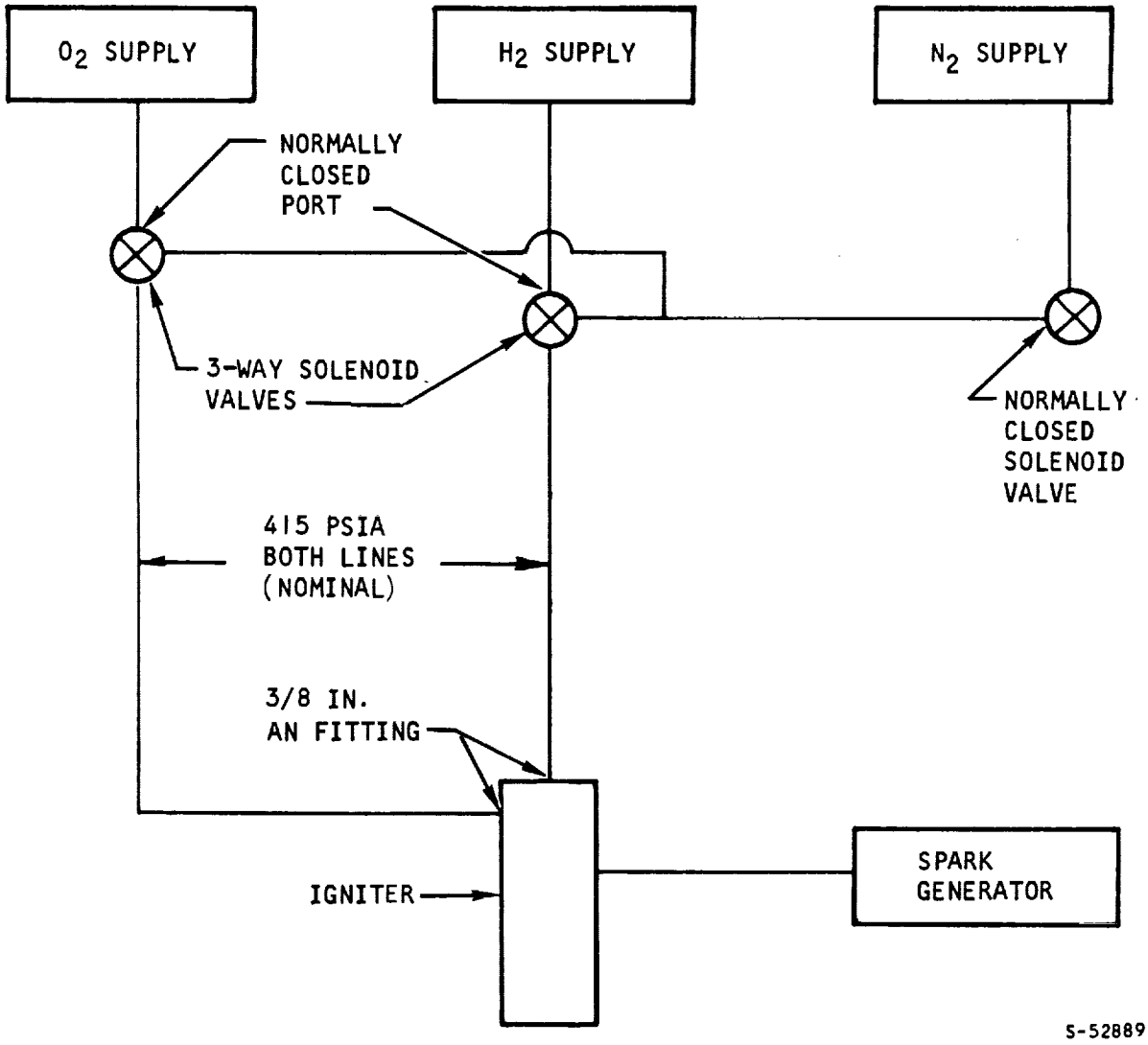

SOLENOID VALVES TO BE WIRED TO OPEN AND CLOSE SIMULTANEOUSLY ON THE H_2 AND O_2 VALVES. N_2 VALVE TO BE ON AN INDIVIDUAL SWITCH. THE THREE-WAY VALVES HAVE "OFF", "ON", AND "PURGE" POSITIONS.

Figure A-25. Igniter Installation - Block Diagram

The wall static temperatures in the combustor were measured by means of chromel-alumel thermocouples, insulated with magnesium oxide and sheathed with type 347 stainless steel. The sheathed thermocouples were brazed into the combustor as described in paragraph A.4.1. The thermocouples were connected to a 150°F-reference junction and the resultant signal fed into the data acquisition system. The temperature data had to be corrected to account for the difference between the temperature of the junction and the temperature of the skin surface, due to the high heat flux through the skin.

In order to measure the heat transferred to the cooling water from the hot gases, the water flow rate and the water temperature rise in each panel of the combustor were measured. The water temperature rise was measured by inserting sheathed, ungrounded copper-constantan thermocouples at the inlet and outlet manifolds, and the temperature differential was measured by connecting the constantan sides of the thermocouples directly together and the copper sides to the data acquisition system. This arrangement recorded an emf proportional to the temperature differential, and avoided the use of cold junctions. The thermocouple output was in the order of one millivolt. The cooling water flow rate was found by having flow-calibrated each panel prior to its installation in the combustor system and measuring the pressure differential across the panel before each test.

The mass flow rate of the hydrogen fuel was measured using a flat-plate orifice that was mounted in the fuel delivery system as follows: The total flow rate was measured upstream (on the cool side) of the hydrogen heater. The pressure differential, the static pressure, and the temperature of the hydrogen were monitored at the flat-plate orifice. Since the flow rate of fuel was required at two points for the two-stage combustion tests, a second measuring station downstream of the hydrogen heater was required to account for the fuel flow split. The second fuel metering point was in the first-stage fuel line. By installing the fuel flowmeter in this way, two flowmeters in series were available for tests that were conducted with only the first stage. During two-stage combustion, the second-stage fuel flow rate was obtained by subtracting the first-stage flow rate (which was measured with the hot flat-plate orifice station) from the total flow, which was measured upstream of the hydrogen heater. This installation is shown schematically by Figure A-2.

A.5 GAS SAMPLING SYSTEM

Gas sampling was accomplished using the wedge-shaped probe depicted by drawing PA 106772 (see back of report). The design of the wedge probe was initiated in order to deal with the specific problem of providing a gas sampling probe that would withstand the environment both from the standpoint of an impinging high temperature gas stream and incurred aerodynamic loading. A number of ground rules were established at the outset in order to design the probe to accomplish the tasks with a minimal amount of corrections required to the data. These ground rules were as follows:

(a) The probe must be able to withstand the following test environment:

Total temperature	-	5470°R
Total pressure	-	69 psia (downstream of bow shock)
	-	100 psia (upstream of bow shock)
Stagnation enthalpy	-	4200 Btu/lb
Drag force	-	200 lb

(b) Condensation of water vapor in the gas sample must be avoided or eliminated.

(c) The probe was to be a calorimetric probe and a pitot-pressure probe, as well as a gas sampling probe.

(d) When using the probe as a calorimetric probe, the tare measurement must be as close to zero as possible.

(e) The probe must be compatible with existing equipment in the test facility.

The details of the probe are shown in the included drawings PA 106770 and PA 106772.

A constraint was placed on the cooling of the gas sample due to the desirability of preventing condensation in the gas sample, while using the existing water-cooling facilities and the existing gas-analysis method.

The gas-analysis system included a relief valve which maintained a pressure of 18.1 psia at a point some 30 ft downstream of the probe's gas-sampling port. The static pressure in the probe could not be predicted accurately, but due to the high water vapor content of the samples it was estimated that the saturation temperature of the sample might be as high as 225°F. It was, therefore, desirable to keep the gas sample tube's inside wall temperature at or above this value at the design condition. On the other hand, the temperature difference across the wall must be kept low (approximately 10°F), if boiling in the coolant circuit is to be avoided. The design-point water-flow rate for the calorimeter is 0.6 gpm at a velocity of 15 ft/sec with an inlet pressure of 350 psia and an inlet temperature of 185°F. The water temperature was to be raised beyond 185°F by its passage through a tube placed on the back of the probe.

In order to prevent condensation, a delicate balance must be struck between overheating the calorimeter and overcooling the sample. The calorimeter water flow was to be adjusted for each run, once experimental data had been accumulated, thereby allowing a more accurate estimation of the heat flux and the static pressure of the sample for a given set of test conditions.

A.5.1 Mechanical Design of the Probe

In order to keep the tare measurement as small as possible, the probe was designed with two water circuits; one for the cooling of the probe and the other exclusively for the calorimeter. Figure A-26 is an enlargement of the cross section of the probe. The combustor exhaust gas that enters the probe goes down through the innermost tube (1), giving up heat to the water passing through the annular passage (2). This constitutes the calorimeter section, which is insulated from wedge-cooling water by means of an air gap (3). The wedge-cooling water passes through the area (4) between the copper wedge and the steel tube. The various tubes shown are standard sizes.

The brazed assembly of the probe is shown in drawing PA 106772. The brazed assembly mounted on a fixture is shown in drawing PA 106770. This assembly, in turn, is mounted on the existing probe-traversing mechanism.

Relative motion between the calorimeter section and the "wedge" is taken up by a slip-type fitting at the upper end of the probe. This joint was sealed with packing.

For design purposes, it was assumed that the largest aerodynamic load exerted on the probe would be 200 lb. This corresponds, for example, to the approximate drag in a gas stream at a total pressure of 100 psia and a Mach number of 1.40, if the probe is assumed to have a drag coefficient of two and to present a 3- by 3/4-in. cross-section area to the flow. In order to control deflection of the low-strength, high-conductivity copper wedge under this load, it is necessary to support the probe at both top and bottom. The top support was merely a beam, with simple supports designed for minimal deflection. The temperature rise of the copper wedge and the stiffness of the beam dictated that the support allow for growth. This was done by designing a slip joint that allowed vertical relative movement.

A second area requiring particular attention to stress analysis was that of differential thermal growth. The growth of the copper wedge mentioned above would have placed tension beyond the yield point on the steel tubes inside, because of the much higher cross-sectional area. Accordingly, the growth was allowed for by providing a slip-joint, or sliding seal. The area where thermal growth was allowed to result in deformation was in the hot-gas-sampling tube. The deformation was calculated as 0.010 in. (maximum) and is taken up both by buckling of the tube, in a noncritical area, and by bending, where the tube bends 90 deg to connect to the copper wedge.

A cycle life calculation indicated that the life would be a minimum of 100 cycles with maximum deformation.

The design condition used for heat transfer purposes corresponded to Mach 8 simulation with a combustor equivalence ratio of unity and 100 percent chemical efficiency. A combustor exit Mach number of 1.9 and an exit total pressure of 100 psia were assumed. The high heat fluxes which the probe must withstand are due to the combination of high total enthalpy (4200 Btu/lb based on an enthalpy of zero at $0^{\circ}R$), high flow per unit area, and shock interaction. The equilibrium stagnation temperature of the gases, circa $5400^{\circ}R$, is deceptively low in that it does not reveal the heating potential of the gases.

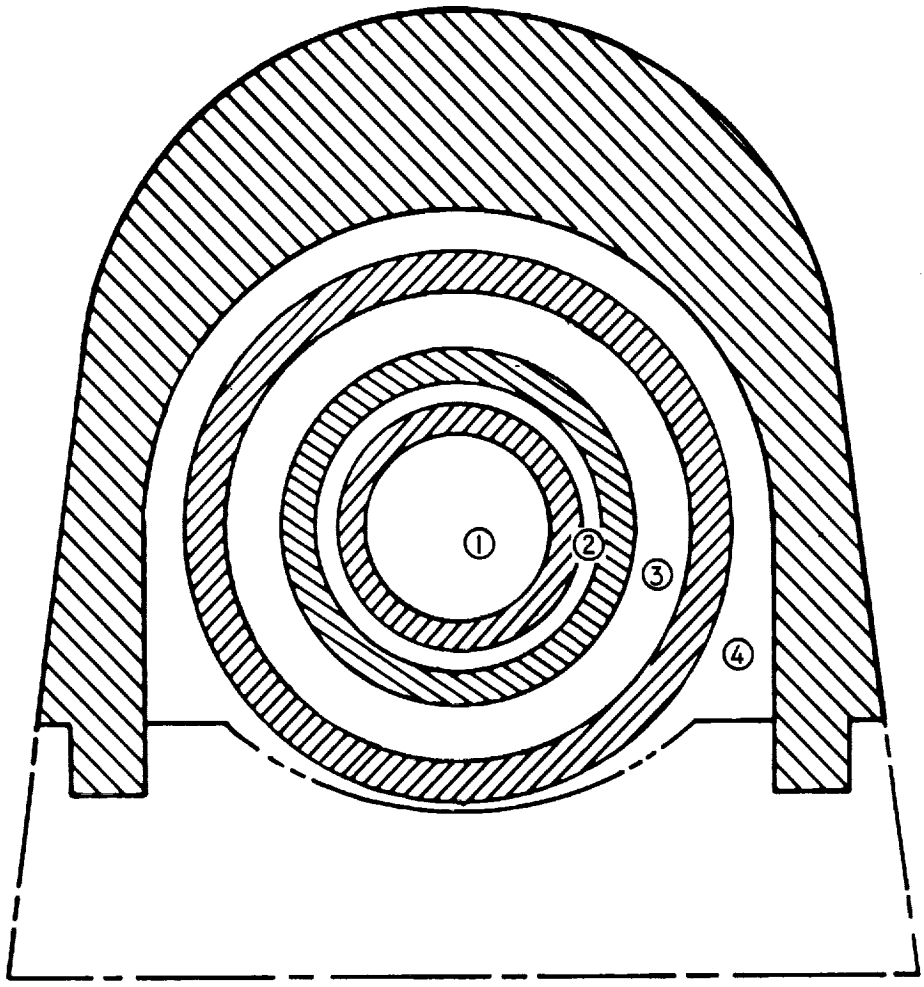

Figure A-26. Enlarged View of the Wedge Probe Cross Section

The copper wedge had a leading edge radius of 0.3 in. The wedge coolant flow rate for the design condition is 14 gpm at a velocity of 100 ft/sec. The theoretical water temperature rise for this circuit is approximately 10^{0}F and the stagnation-line heat flux is 2200 Btu/ft^2 sec. The estimated stagnation line temperature of the copper at these conditions is 900^{0}F.

The gas flow through the calorimeter was calculated based on a total pressure of 69.5 psia behind the bow shock, a total temperature of 5476^{0}R, a specific heat ratio of 1.12, and a gas constant of 89 ft/^{0}R. The result was 5.7×10^{-4} lb/sec. The water temperature rise in the calorimeter at this maximum condition would be 24^{0}F. The calorimeter length was set to prevent condensation on the walls, i.e., made short enough so that the walls would remain hot. The calorimeter water inlet temperature was specified as 185^{0} to 195^{0}F.

Most of the fabrication of the wedge probe utilized straightforward, common techniques. The welding and brazing, however, are worthy of a brief description.

The inner portion of the wedge probe, which consists only of stainless steel tubes, was fitted together and welded, making a complete tube assembly (weldment). The weldment was then brazed to the leading edge section with the back plate in place to insure proper alignment of the weldment in the copper wedge. The only joint brazed in this first cycle was between the gas sample tube and the leading edge. The second braze cycle completed the brazing by the addition of the end caps. Alloy placement and type was specified on the drawings.

Figures A-27 and A-28 show the probe details and the partial assembly, respectively.

A.5.2 Probe-Traversing Mechanism

In order to survey the exit plane of the combustor with the gas sampling probe during the course of an individual combustor test run it was necessary to design and fabricate a device to move the probe about, as well as provide a means of determining the location of the probe at any given time. Accordingly, a probe traversing mechanism was designed that provided vertical and horizontal movement and rotation (variable angle of attack) so that the probe could remain connected during a test and still survey the exit plane or interior of the combustor at one of three available axial positions.

Electric-drive motors with gear boxes moved the mechanism, and potentiometers were installed such that the position of the probe would cause a proportional change in resistance. The probe position could be calibrated into the data acquisition system at the test site so that data showing its horizontal and vertical position, in inches, was obtained. The rate of travel of the probe traversing mechanism was 6 in./min. The traversing mechanism is shown in Drawing ML 2485 at the end of this report.

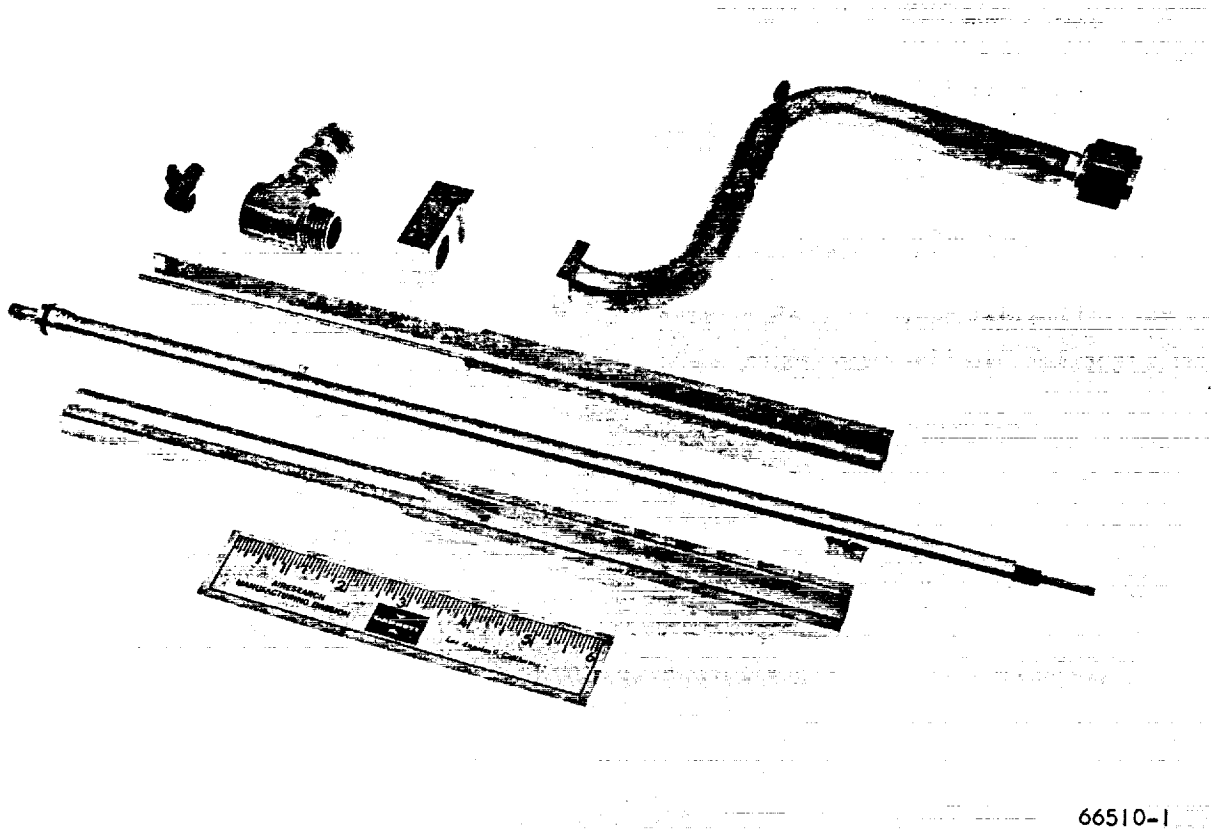

Figure A-27. Wedge Probe No. 1 Before First Braze Attempt (Disassembled)

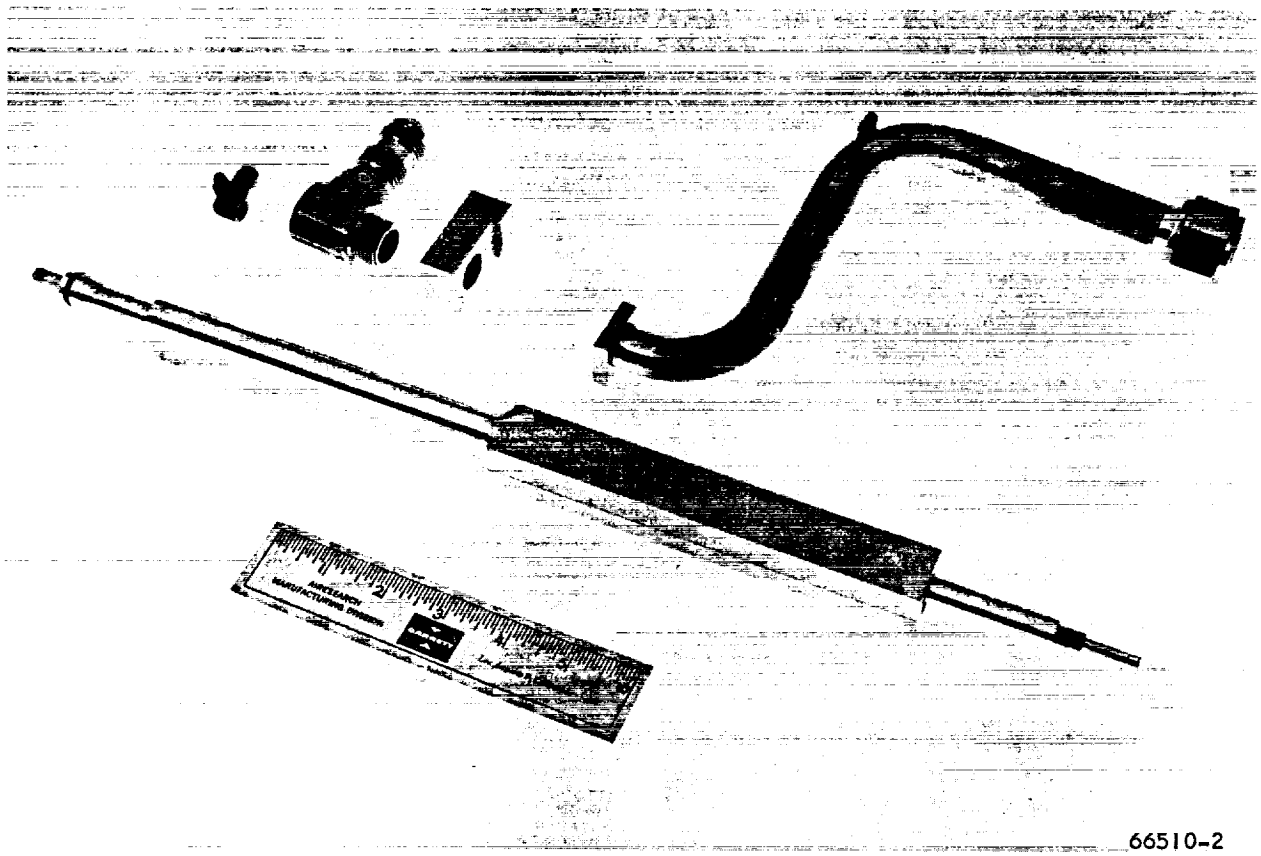

Figure A-28. Wedge Probe No. 1 Before First Braze Attempt (Partially Assembled)

When gas sampling of the exhaust stream was performed, it was necessary that the position of the probe inlet be known. This was accomplished by the use of potentiometers connected to the gear boxes on the probe traversing mechanism. A constant-voltage power supply was connected to the potentiometers such that the position of the probe was a linear function of resistance, and therefore voltage was proportional to position. This voltage was fed into the data acquisition system and the probe position was established by a calibration which was also fed into the data acquisition system. The data was returned in terms of X and Y coordinates from a pre-established datum.

A.5.3 Mass Spectrometer

The cooled exhaust passed from the probe to the gas analyzer by way of an electrically heated line. The line was heated to prevent condensation and thereby preserve the composition of the sample. The mass spectrometer, which is described fully in Reference A-1, was used to measure the mole fractions of N_2, H_2, O_2, and H_2O in the gas sample. Generally, the mass spectrometer operated as follows: gas entered a capillary inlet at near ambient pressure and was pulled by a vacuum pump through capillary tubes into the gold-leak area where the pressure was about 2 mm Hg. It passed through 0.0004-in.-dia holes in the gold foil into an ionizing region where electrons were stripped off. The charged gas molecules then moved, under the influence of static electric fields and the magnetic field of a permanent magnet, through slits, arriving at the collector. Many ions piling up on the collector, created a small current which was amplified and finally displayed on a recorder and fed into the data acquisition system. The mass spectrometer was calibrated using gases of known composition.

A.6 INLET-AIR TEMPERATURE MEASUREMENT

Knowledge of the total temperature of the inlet air supplied to the combustor was of sufficient importance to warrant devoting a significant amount of time and effort to its determination. Because of the very high temperatures involved direct measurement of the air total temperature was impractical. Indirect approaches appeared to be quite unwieldy insofar as on-line test operations were concerned, so the best alternative was to calibrate the vitiation heater and run the tests based on the calibration. Therefore, each vitiation heater configuration that was employed was calibrated at the test conditions.

The vitiation heaters were operated at temperatures sufficiently low so that chromel-alumel thermocouples could be used to provide a direct measurement. Before the temperature was increased, it was verified that the direct measurement agreed with the total temperature calculated from an energy balance. Once agreement was obtained, the temperature was increased and assumed to be the value as determined from the continuity and energy equations if the two determinations agreed within five percent.

A.6.1 Test Results - Ten-Inch Vitiation Heater

During the first series of heater tests the thermocouple measurements, uncorrected for radiation, gave an indicated vitiated air temperature greater than the adiabatic flame temperature. These measurements were made along a radial line but at only one circumferential location. The problem of disagreement was resolved after finding and correcting a circumferential temperature nonuniformity. The heater test results are shown in Figures A-29 and A-30. It is noteworthy that the temperature calculated by continuity in Figure A-30 is consistently lower than the temperature calculated by energy. This is due almost entirely to the fact that the nozzle was fabricated in two pieces and air could leak along the side and not entirely pass through the nozzle throat, as shown below.

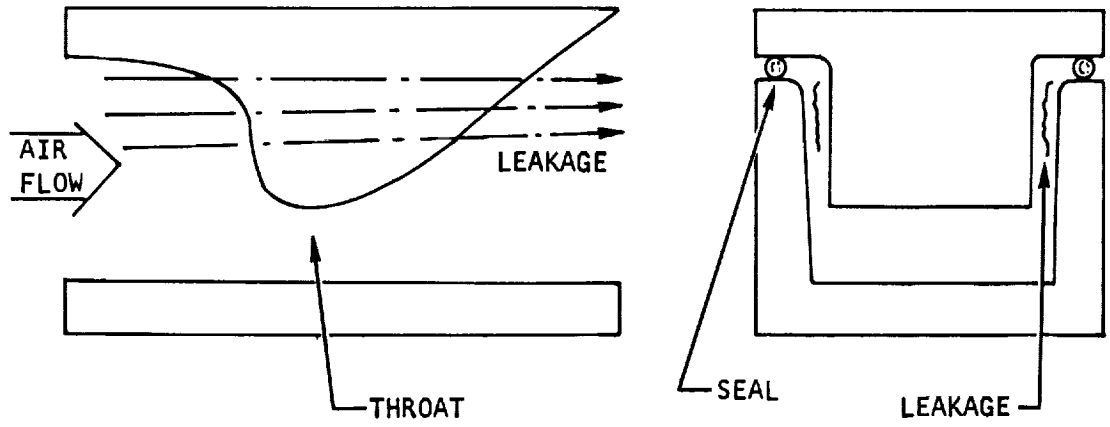

As shown in Equation (A-1), the air total temperature at the throat is inversely proportional to the square of mass flow passing through the throat.

$$T_{TO} = \left[\frac{\left(P/P_t \, \dot{m} \right)_* \, P_{TO} \, A_* \, C_D}{\dot{W}_T} \right]^2 \qquad (A-1)$$

where $\left(\frac{P}{P_t} \dot{m} \right)_* = f(\gamma, \text{M.W.})$

C_D = discharge coefficient

P_{TO} = measured total pressure

A_* = nozzle throat area

$\dot{W}_T$ = total mass flow = $\dot{W}_{air} + \dot{W}_{O_2} + \dot{W}_{H_2}$

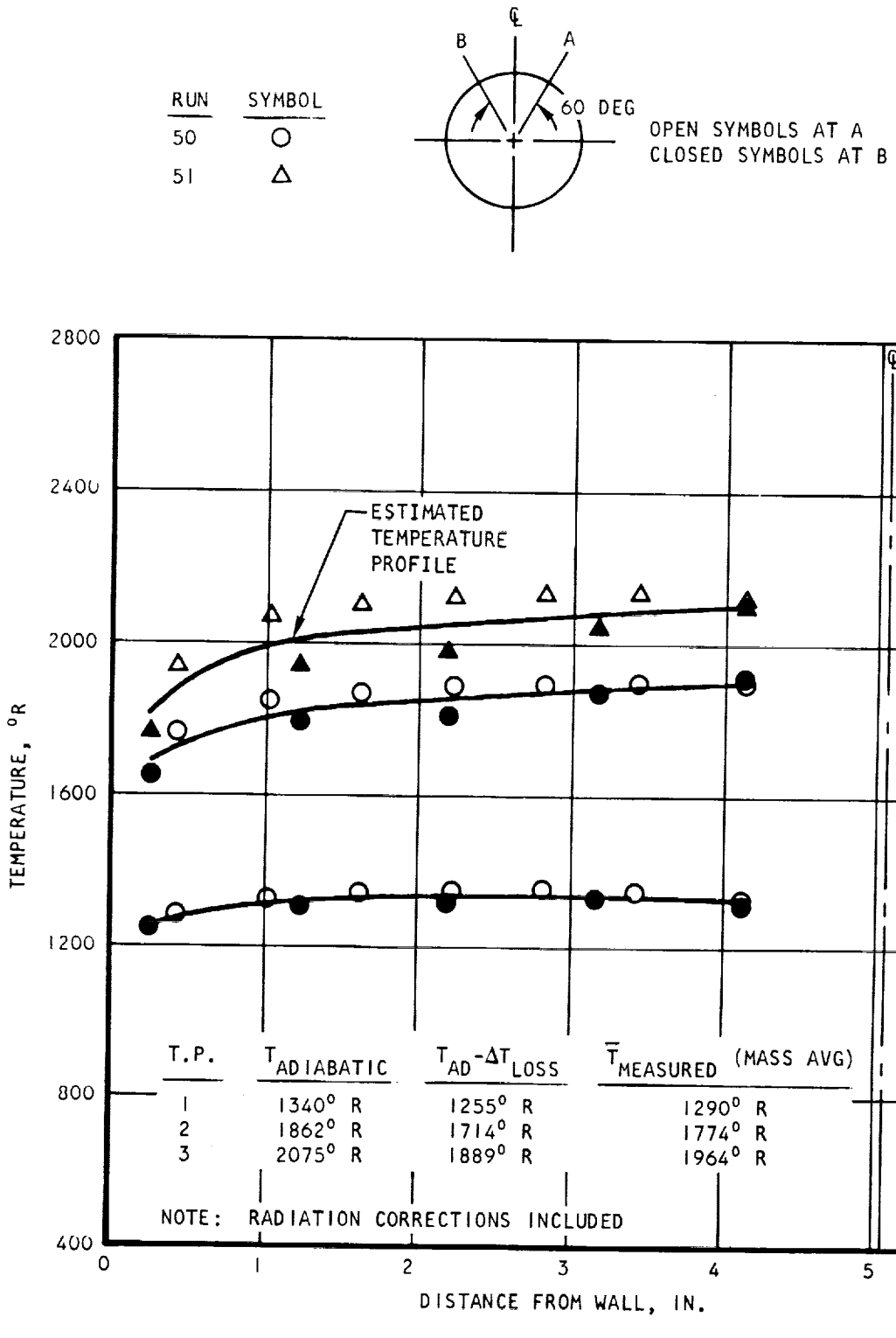

Figure A-29. Vitiation Heater Temperature Profile Test Results

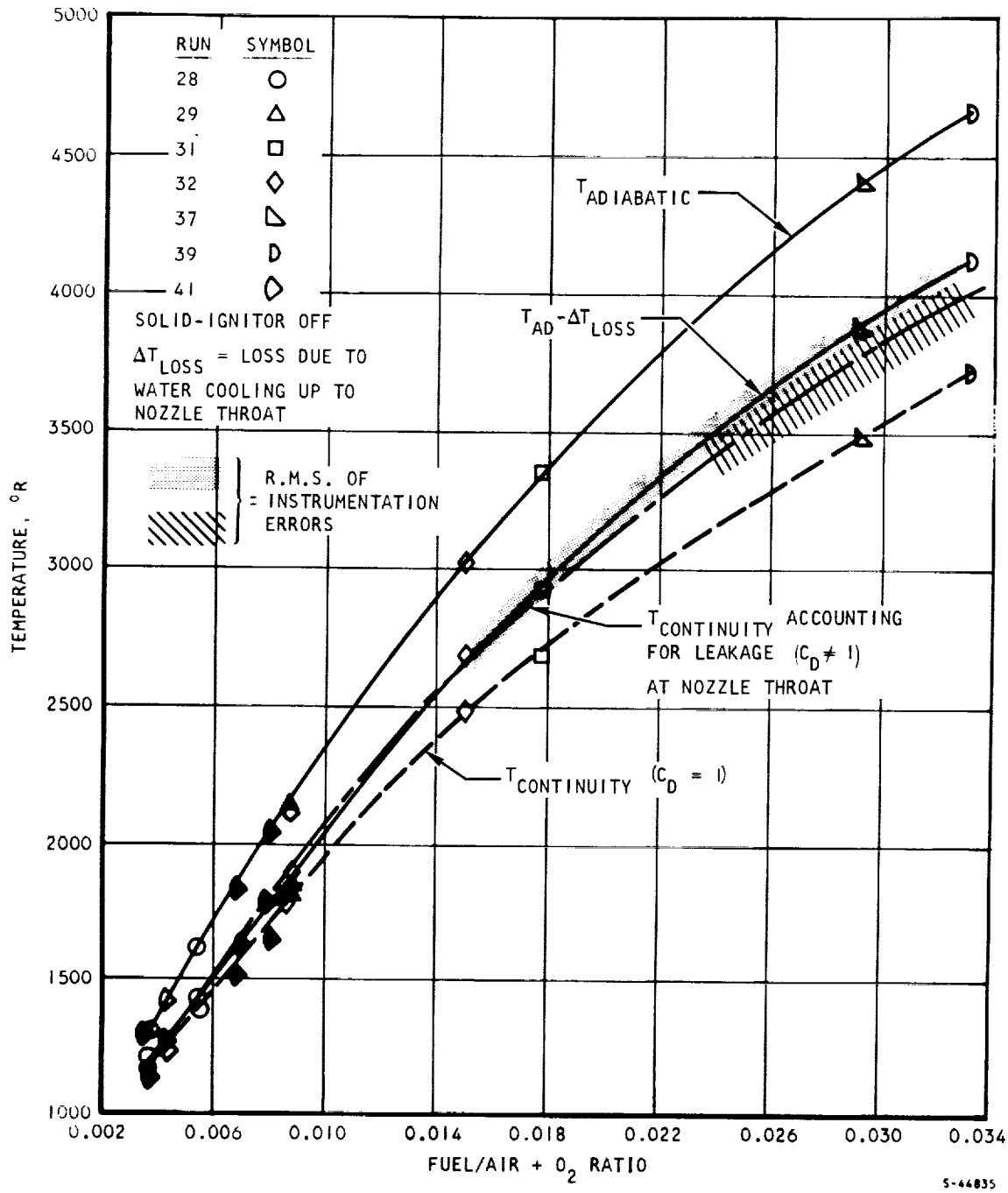

Figure A-30. Ten-Inch-Diameter Vitiation Heater Calibration

The nozzle throat geometry was accurately measured and the heater operated at room temperature, f/a = 0. When the continuity equation was applied at the throat, a leakage of air equivalent area did not change, and that air leakage occurred at the nozzle wall temperature. Reducing the mass flow passing through the nozzle throat due to leakage made the difference between the two calculations decrease considerably at high temperatures, and provided agreement at lower temperatures.

Additionally, if measurement errors were included, the two calculation methods overlapped when accuracies as listed below were used. Again refer to Figure A-30.

W_{air} = ±1 1/2 percent

W_{H_2O} = ±1 percent

W_{H_2} = ±1 percent

P_{T0} = ±1/2 percent

Δt = ±1/2°F (cooling water)

The calculated flame temperature seemed to be the best value to use as the actual test temperature. There was agreement, when leakage was accounted for as shown in Figure A-31, when temperatures calculated by energy and continuity were compared.

A.6.2 Five-Inch-Diameter Vitiation Heater

A 5-in.-ID vitiation heater was designed and fabricated for the true-scale combustor tests. The calibration testing of this vitiation heater was conducted in the same manner as for the 10-in. heater. Figure A-32 shows the calibration test results.

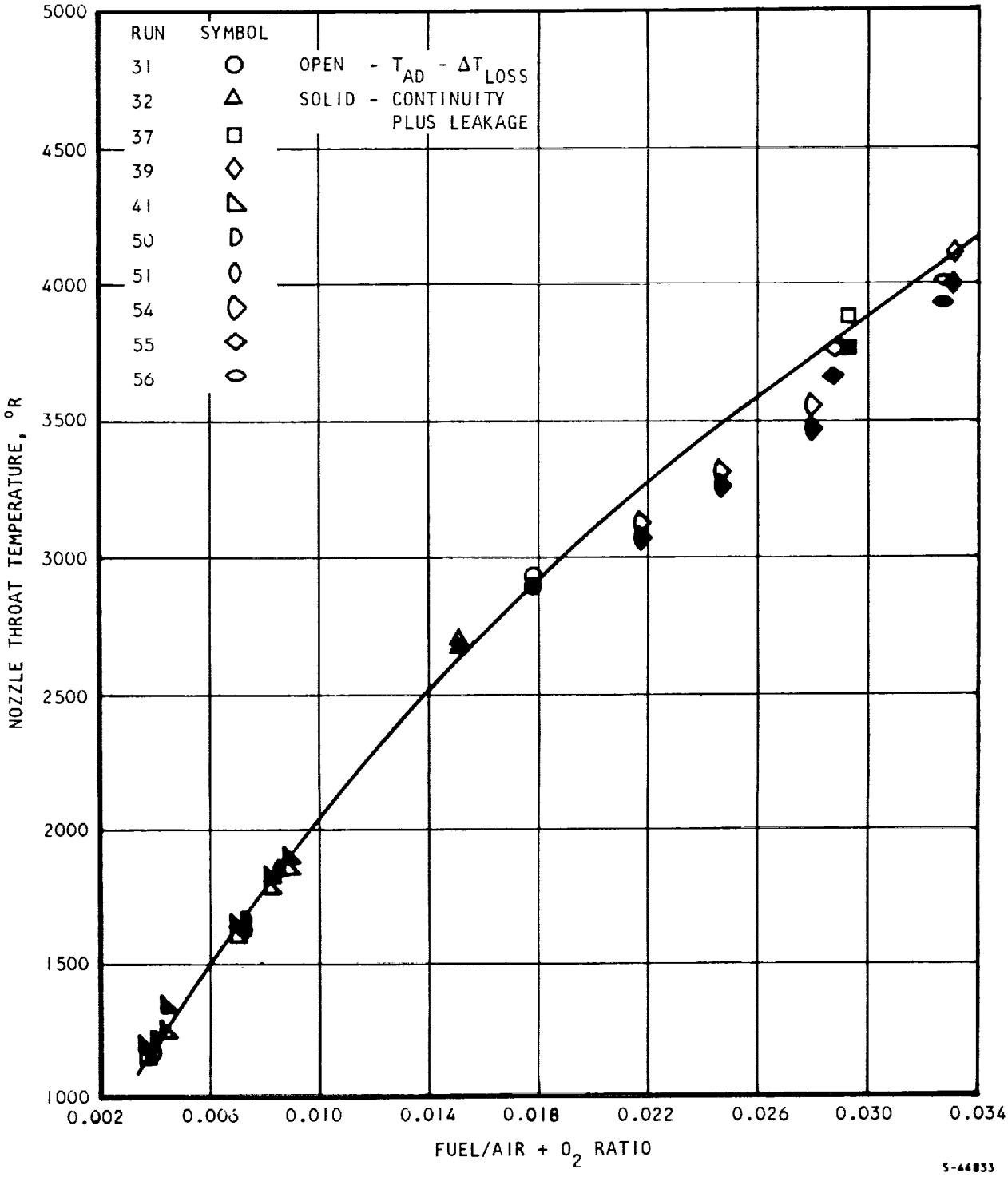

Figure A-31. Ten-Inch-Diameter Vitiation Heater Test Results

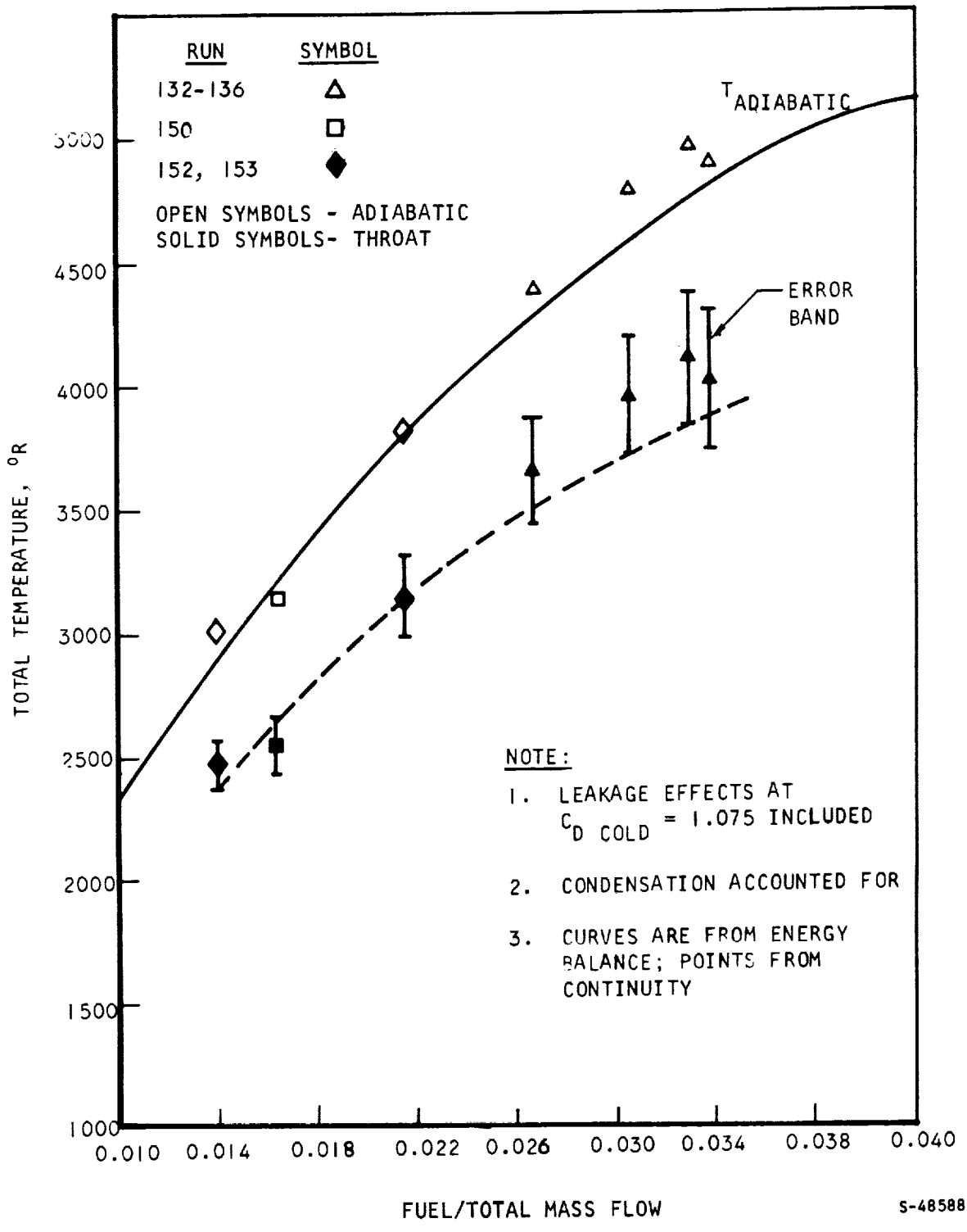

Figure A-32. Vitiation Heater Calibration - Five-Inch Diameter

REFERENCES
(Appendix A)

A-1 Engineering Staff, Hypersonic Research Engine - Phase IIA, Instrumentation Program Third Interim Technical Data Report, Data Item No. 55-8.03, AiResearch Report AP-67-3020, 21 December 1967

APPENDIX B

HEAT TRANSFER ANALYSIS FOR NOZZLE AND COMBUSTOR DESIGN

APPENDIX B

HEAT TRANSFER ANALYSIS FOR NOZZLE AND COMBUSTOR DESIGN

B.I INTAKE NOZZLE COOLING

This section presents the results of the thermal analysis of the combustor intake nozzle cooling system. The cooling system is designed so that both the curved and flat sides of the intake nozzle are cooled by water flowing through a number of small holes along the contour of the nozzle. All the materials are copper. Results of the heat transfer analysis of the nozzle cooling system and the coolant operating conditions are tabulated below. Pertinent dimensions of the nozzle flow passages are shown in Figure B-I.

	Curved Side of Nozzle	Flat Side of Nozzle
Water flow rate, gpm	125	180
Inlet water temperature, ^{0}F	70	70
Outlet water temperature, ^{0}F	85	85
Inlet water pressure, psia	200	200
Outlet water pressure, psia	130	80
Maximum wall temperature in contact with hot gas which occurs near the throat, ^{0}F	440	440
Maximum water-wetted wall temperature which occurs near the throat, ^{0}F	318	318

B.I.I Hot Gas Conditions

The following case of entering-gas conditions was thought to give the highest cooling load of the anticipated test cases:

T_T = 4660^{0}R

P_T = 300 psia

Y = I.2

Water vapor content = 35 percent by weight

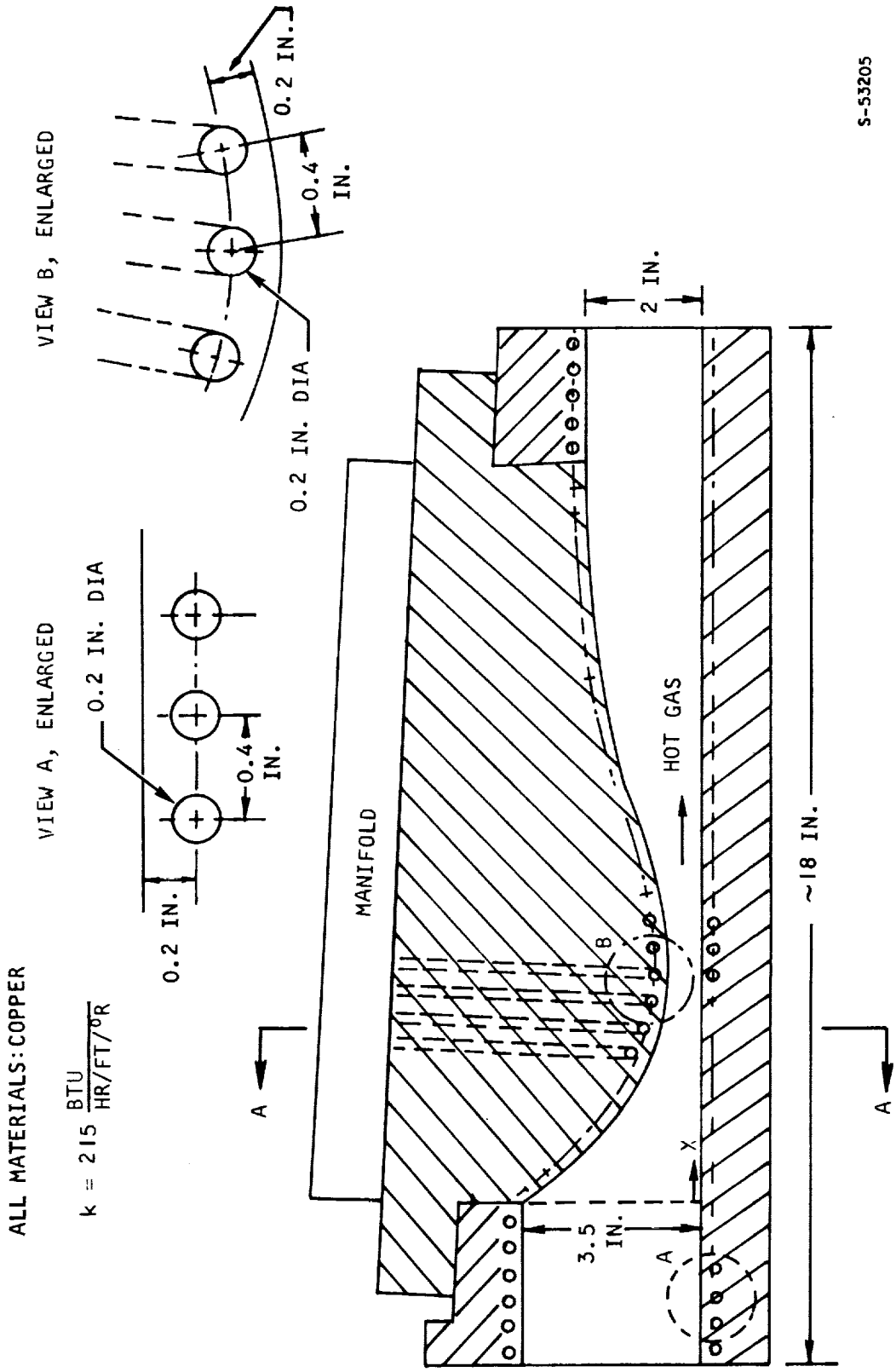

Figure B-1. Configuration and Dimensions of Cooling System

Based on these gas conditions, the local heat fluxes were calculated and are shown in Figure B-2. Also shown in this figure are the local wall temperatures as well as the local coolant temperature. The total cooling load on both sides of the nozzle is about 450 Btu/sec. The peak heat flux near the nozzle throat indicates that the maximum wall temperatures on both hot-gas and coolant sides will occur near the throat as tabulated and shown in Figure B-2.

B.1.2 Coolant Flow

Both sides of the nozzle are cooled by running water through a number of holes drilled in a copper block (Figure B-1). Since copper is a very good thermal conductor, there was no local hot spot found by a two-dimensional heat flow analysis along the surface in contact with hot gas.

The overall pressure drops for the curved and flat side coolants are 70 and 120 psi, respectively. The water flow rate could be increased if necessary as long as the exit pressure was maintained above approximately 70 psia.

B.2 COMBUSTOR WALL COOLING

B.2.1 Configuration With 2-In. Combustor Height

Figure B-3 shows the predicted heat fluxes as a function of the combustor length for different test conditions. The maximum heat flux is about 210 Btu/sec ft^2. For design margin, a heat flux of 300 Btu/sec ft^2 was used and a maximum water-wetted-wall surface temperature of 250°F resulted. The 0.030-in.-thick stainless steel skin had a predicted temperature differential of 300°F and a maximum temperature of 550°F at this condition. The predicted total heat load for the case of $M_\infty = 8$ supersonic combustion, which gave the highest heat load among the cases analyzed, was about 1,200 Btu/sec.

The test results indicate peak heat fluxes of up to 700 Btu/ft^2-sec due to the occurrence of a shock train. This heat flux did not produce any damage because the cooling coefficient increases when the water boiling temperature is reached.

B.2.2 True-Scale Configuration

Analysis of the true-scale combustor cooling system is summarized in Table B-I. This analysis was carried out based on the following main assumptions:

(1) The hot gas flow rate per unit cross-sectional area and the variations of the total gas temperature along the duct length are approximately the same as those in the 2-in.-high combustor.

(2) Gas properties such as specific heat and viscosity do not differ appreciably from those used in the subscale combustor.

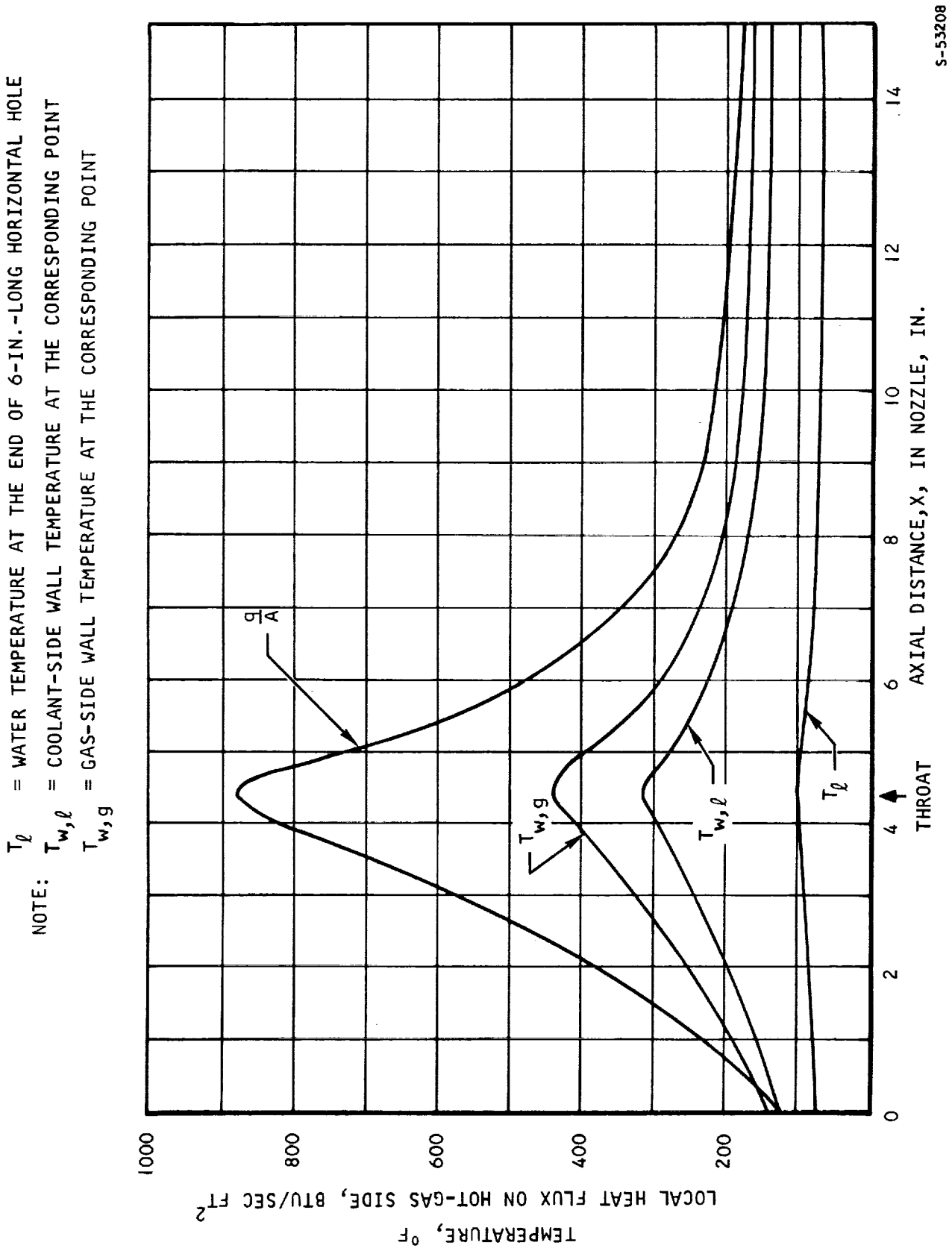

Figure B-2. Heat Fluxes vs X

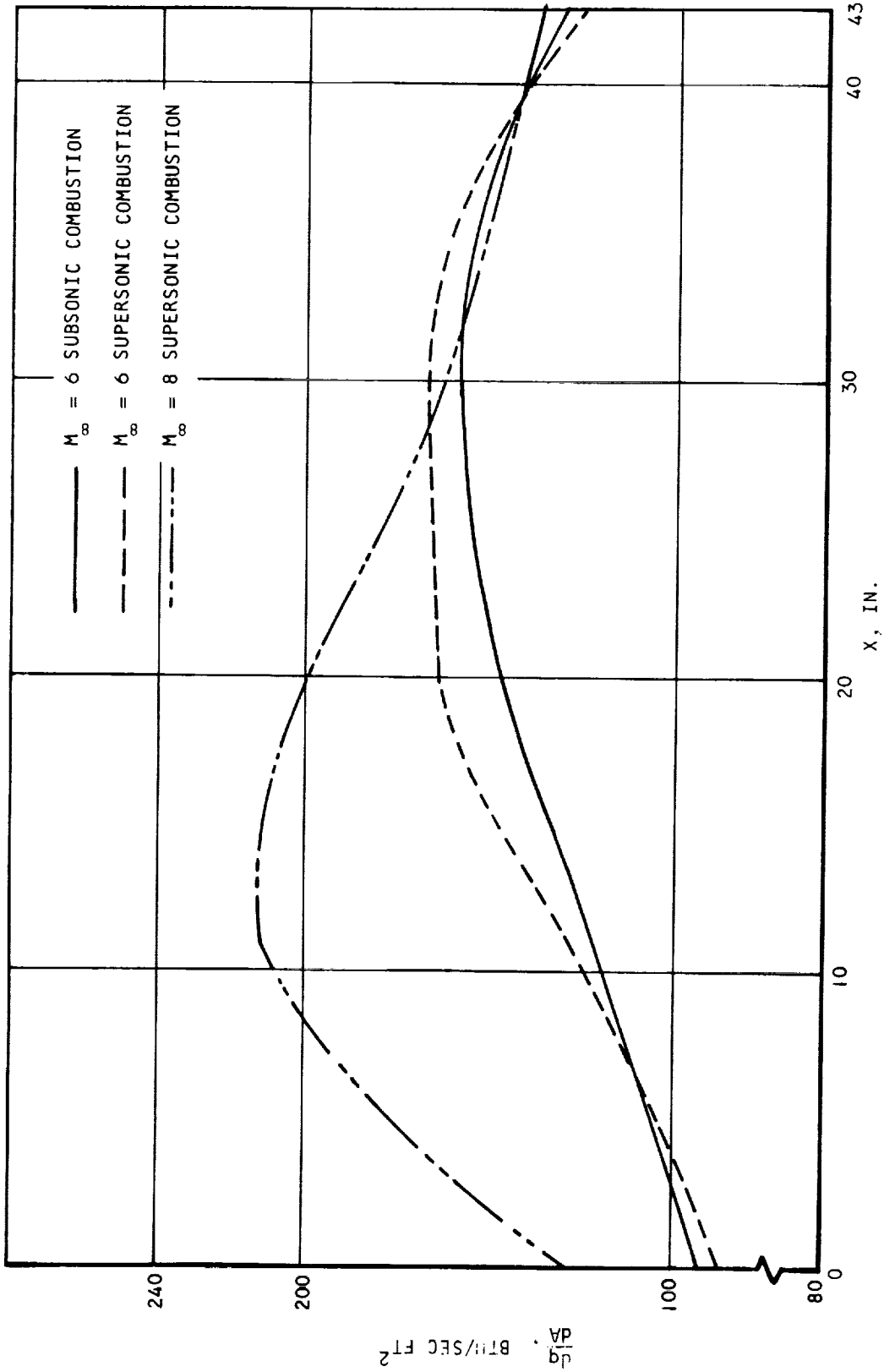

S-53623

Figure B-3. Predicted Heat Fluxes vs Combustor Length

TABLE B-I

SUMMARY OF ANALYSIS

Intake Nozzle

$\left(\frac{q}{A}\right)_{max} = 1100 \frac{Btu}{sec\ ft^2}$ at throat

$(T_{w,g})_{max} = 500^{\circ}F$ at throat

$(T_{w,\ell})_{max} = 350^{\circ}F$ at throat

$V\ (H_2O)$ = 34 fps (coolant flows through small holes drilled in in copper blocks)

Minimum Outlet Water Pressure = 70 psia

Rectangular Duct (except at locations described in other sections of this table):

$\frac{q}{A} = 350 \frac{Btu}{sec\ ft^2}$

$T_{w,g} = 570^{\circ}F$

$T_{w,\ell} = 270^{\circ}F$

$V(H_2O)$ = 15 fps (coolant flows through fin channels)

Minimum Outlet Water Pressure = 40 psia

Near end of shock train (between First and Second Injectors):

$\frac{h_{max}}{h_o} = 4.85$

$\frac{q}{A} = 1300 \frac{Btu}{sec\ ft^2}$ (1220, 1270)

$T_{w,g} = 1460^{\circ}F$ (1670, 1550)

$T_{w,\ell} = 310^{\circ}F$ (582, 410)

The heat flux in the true-scale combustor was estimated from the 2-in.-high combustor analysis with the inclusion of effects of area reduction and water vapor content. The average predicted heat flux on the rectangular duct was 350 Btu/sec ft^2 except in the intake nozzle near the end of a shock train, and on the fuel injector where associated shock structures bring local peak heat fluxes. The heat flux in the intake nozzle was increased by 25 percent over that for the subscale case. The approximate cooling conditions are shown in Table B-I.

B.3 COMBUSTOR FUEL INJECTOR RELATED HEAT TRANSFER

This section covers the effects of fuel injection on heat transfer in the combustor. The jet-like injection of the hydrogen fuel into the supersonic gas stream causes the heat transfer rate in the combustor to increase.

B.3.1 Peak Heat Flux

Since the injectant pressure was higher than the static combustor pressure at the corresponding location, an underexpanded jet appeared and a typical flow pattern (Reference B-I) is shown in Figure B-4 (Reference B-2). The pressure rise associated with the shock structure (Figure B-4) results in the increase of heat transfer coefficient (Reference B-3) near the region where the interaction shock meets the surface (position marked as "A" in Figure B-4). The most severe localized high heating rate was found to occur at the injectors for the case of M = 8 supersonic combustion simulation in which the local peak (or maximum) heat transfer coefficient became approximately 6 times as great as that of the corresponding shockless system. The predicted temperature distribution in the injector block for this case is shown in Figure B-5 for the design coolant flow rate. The maximum local copper temperature is 1040°F at the corner between the main stream hot gas and the injected hydrogen fuel, and local boiling of water may have occurred near the corners along the line D-D' in Figure B-5. The maximum stainless steel temperature was 1400°F and local boiling of water was expected to have occurred if the peak heat flux occurred over the stainless steel portion of the injector block. A minimum water exit pressure of about 55 psia with a water velocity of 34 ft/sec was sufficient to assure avoiding burnout.

The maximum rise in heat transfer coefficient may be correlated to the maximum rise in pressure as follows:

$$\frac{h_{max}}{h_o} = \left(\frac{P_{max}}{P_o} \right)^n \qquad (B-1)$$

where the subscript (o) refers to the attached flow upstream of the separation region and n is a constant with a value between 0.80 and 0.93 (n = 0.9 was used in the subsequent computation).

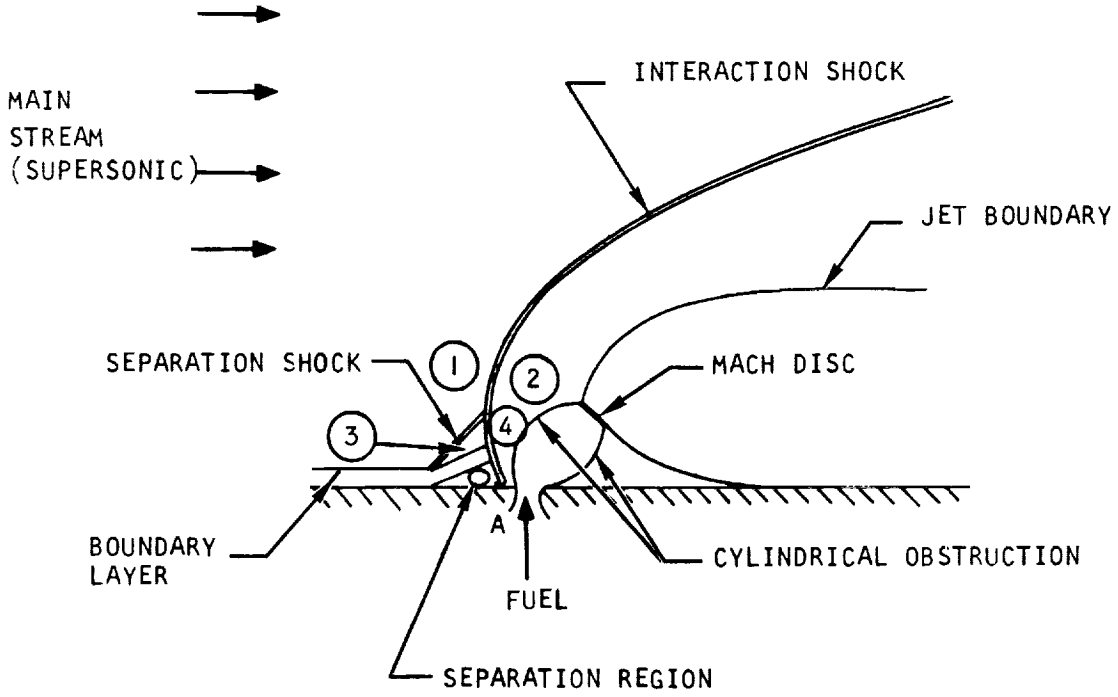

Figure B-4. Schematic Representation of an Under-Expanded Jet Injected Normally into a Supersonic Freestream

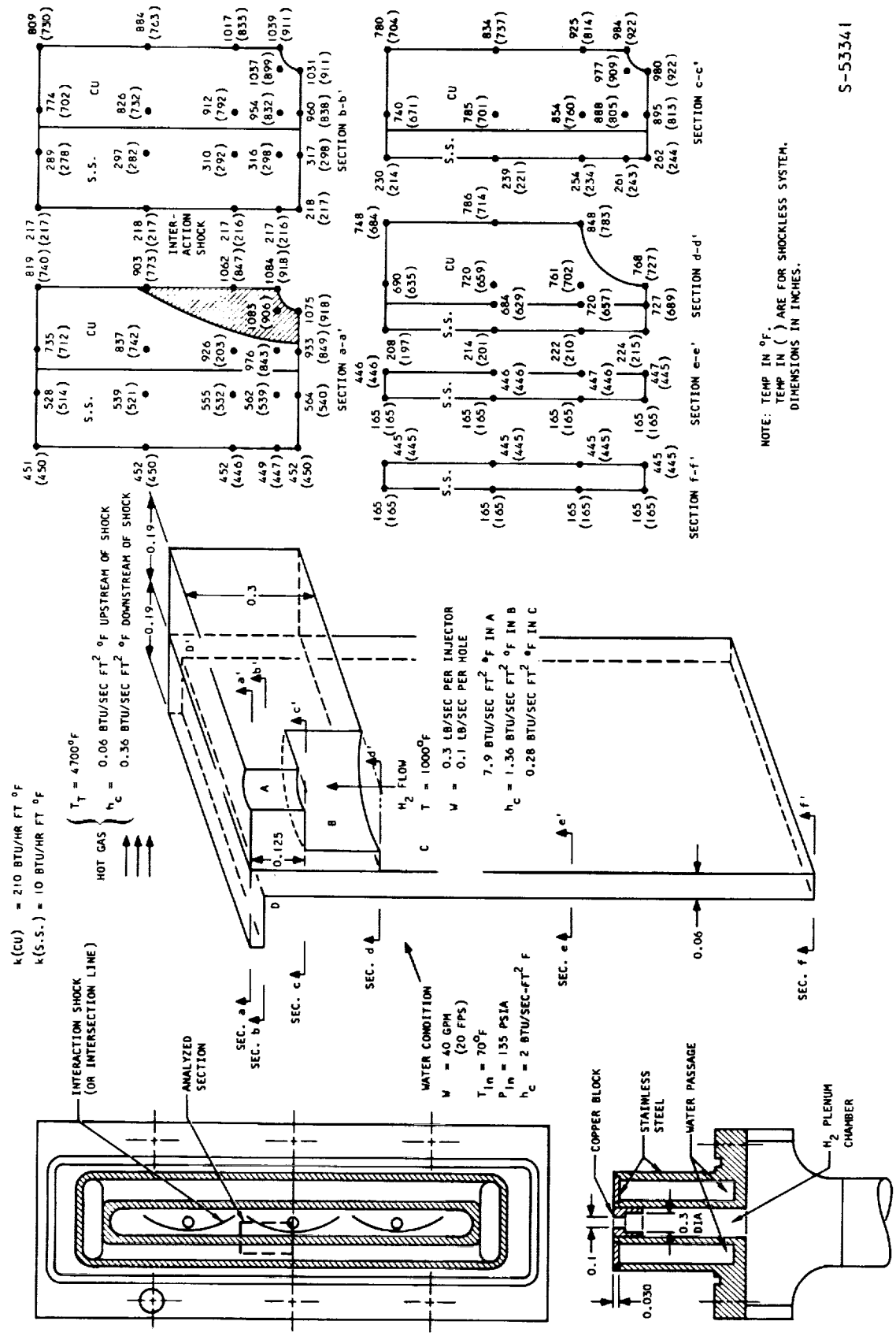

Figure B-5. Injector Block

B.3.2 Temperature Distribution

The region subject to local high heating rate was the small area right after the intersection line between the interaction shock and the surface, whose location and shape were generally unknown. However, an analogy was made between the location and shape of the intersection line under consideration and those of a detached shock in front of a circular cylinder the diameter of which is the same as that of the injector hole. With this assumption, the desired location and shape of the intersection line were found by a method described in Reference B-4 and shown in Figure B-5.

A three-dimensional, steady-state analysis was made for a temperature distribution in the injector block with side conditions for the case of $M_\infty = 8$ supersonic combustion simulation and the results are shown in Figure B-5. Since copper is a very good heat conducting material, it tends to spread the peak heat flux applied locally to the hatched region in Figure B-5 and results in only 130^0F increase in the maximum local temperature, when compared with that in the corresponding shockless system. The temperature distribution on the water wetted surface indicates that local boiling of water may occur at the corners marked as D-D' in Figure B-5. As far as local boiling is concerned, the worst case may come when the intersection line between the interaction shock and the surface lies on the stainless steel part of the injector rather than the copper block as it is shown in Figure B-5. Since there was uncertainty in the analogy used for determining the location of the intersection line, particularly the apex of its seemingly hyperbolic shape where the heat flux is maximum, consideration was given to this latter case in which local boiling of water is expected. The forced convection burnout correlation for water was used here to compare the burnout heat flux with the peak heat flux. The results indicate that the maximum heat flux of 4.3×10^6 Btu/hr ft^2 is smaller than the burnout heat flux of 8.6×10^6 Btu/hr ft^2 and thus no burnout would occur. But it should be noted that a rather large percentage-of-spread of data around a correlated equation is usually associated with boiling data correlation. Therefore, the precaution of increasing water flow or exit pressure was taken since the interaction shock may lie on the stainless steel rather than the copper block. In any case, the exit water pressure should be kept over 55 psia.

REFERENCES

(Appendix B)

B-1 Dowdy, M. W. and Newton, J. F., Jr., "Investigation of Liquid and Gaseous Secondary Injection Phenomena on a Flat Plate with M = 2.01 to M = 4.54", JPL Technical Report No. 32-542, December, 1963.

B-2 Orth, R. C. and Funk, J. A., "An Experimental and Comparative Study of Jet Penetration in Supersonic Flow", John Hopkins University, Maryland.

B-3 Wuerer, J. E., and Clayton, F. I., "Flow Separation in High Speed Flight", Douglas Report SM-46429, April, 1965.

B-4 Love, E. S., "A Re-examination of the Use of Simple Concepts for Predicting the Shape and Location of Detached Shock Waves", NACA TN 4170, December, 1957.

APPENDIX C

COMPUTATION OF LOCAL EQUIVALENCE RATIO USING GAS ANALYSIS DATA

NOMENCLATURE

(Appendix C)

A	Atomic ratio of hydrogen to oxygen
B	Molar percentage of vitiating gases in vitiated air
C	O/N
H	Concentration of hydrogen atoms in any form
N	Concentration of nitrogen atoms in any form
O	Concentration of oxygen atoms in any form
W	Weight flow rate into vitiation heater
X_z	Mole fraction of species z
ϕ	Equivalence ratio
ϕ_L	Local equivalence ratio at the sampling point

Subscripts

c	Removed by condensation
corr	Corrected
s	Sample as analyzed
va	Vitiated air

Superscript

~	Sample as analyzed

APPENDIX C

COMPUTATION OF LOCAL EQUIVALENCE RATIO USING GAS ANALYSIS DATA

Three different methods were used in computing local mixture ratio at the exit plane of the two-dimensional combustor using the gas sampling data. Since each method has proven useful, all three will be described. The "quick-look" method, described in Section C.1, was used for reducing data from strip charts and allowed evaluation of the fuel distribution pattern within minutes after the end of a test run. Thus, the results could be used in assessing the value of the data and determining whether any further data were needed before making hardware changes.

The more exact method described in Section C.2 was used principally for assessing whether the sample composition was preserved in the sampling system. This was done by comparison with the results from the method described in Section C.3, in which correction is made for the effects of evaporation and condensation in the sampling system. In most cases all three methods gave essentially the same answer; however, where there was a discrepancy, the method of Section C.3 was preferred. Section C.4 gives an error analysis for this method, while Section C.5 describes the data reduction method used for the special case where nitrogen is injected into the combustor, with or without simultaneous hydrogen injection.

C.1 "QUICK-LOOK" METHOD

The local equivalence ratio can, in many cases, be quickly found as a function only of the volume percent of hydrogen or the volume percent of oxygen in the sample.

The following assumptions were made:

(a) The vitiation heater hydrogen and oxygen flows are in the correct ratio to give 21 percent free oxygen.

(b) The vitiation heater exit gases are perfectly mixed.

(c) All species other than H_2, O_2, H_2O, Ar, and N_2 are present only in negligible amounts when the sample reaches the mass spectrometer.

(d) The composition of the sample is preserved in the sampling system.

(e) Hydrogen and oxygen do not coexist in the sample.

The last assumption is not restrictive because if hydrogen and oxygen do coexist in the sample as analyzed, it is a simple exercise in chemical stoichiometry to convert the sample composition to a fully reacted mixture which contains either hydrogen or oxygen, but not both.

Assumptions (a) and (b) imply that the N_2 and H_2O from the vitiation heater are present in the sample in the ratio of 3.76 moles per two moles of the oxygen atoms which originate from the free oxygen in the vitiation heater. In other words, the ratio of "inert" (N_2 + H_2O + Ar) to oxygen in the vitiation heater is the same as that in air (0.79/0.21 = 3.76).

The stoichiometric equation for a local equivalence ratio ϕ_L, less than unity and with the gases at chemical equilibrium when analyzed can be written, using assumption (c), as

$$\phi\ H_2 + O_2 + 3.76\ \text{inert} = (1-0.5\ \phi)\ O_2 + \phi\ H_2O + 3.76\ \text{inert}.$$

Therefore, the mole percentage of oxygen X_{O_2} in the sample is

$$X_{O_2} = \frac{1-0.5\phi_L}{(1-0.5\phi_L) + \phi_L + 3.76} = \frac{1-\phi_L}{4.76 + \phi_L} \qquad \text{(C-1)}$$

For a rich mixture, the stoichiometric equation can be written as

$$2\phi H_2 + O_2 + 3.76\ \text{inert} + (2\phi - 2)\ H_2 + 2H_2O + 3.76\ \text{inert}$$

and the hydrogen percentage of the sample X_{H_2} is related to local equivalence ratio by the equation

$$\phi_L = 2.88\ \frac{X_{H_2}}{100 - X_{H_2}} + 1 \qquad \text{(C-2)}$$

Equations (C-1) and (C-2) are plotted in Figure C-1. Since the mass spectrometer directly measures percentages of hydrogen and oxygen in the sample, the plot in Figure C-1 was useful in performing rapid data reduction for gas analysis runs.

C.2 DETERMINATION OF LOCAL EQUIVALENCE RATIO WHEN THE COMPOSITION OF THE SAMPLE IS PRESERVED

In deriving this method, only assumptions (b), (c), and (d) from Section C.1 are used. The elimination of assumption (a) through use of measured vitiation heater flow rates makes this method more general than the "quick-look" method.

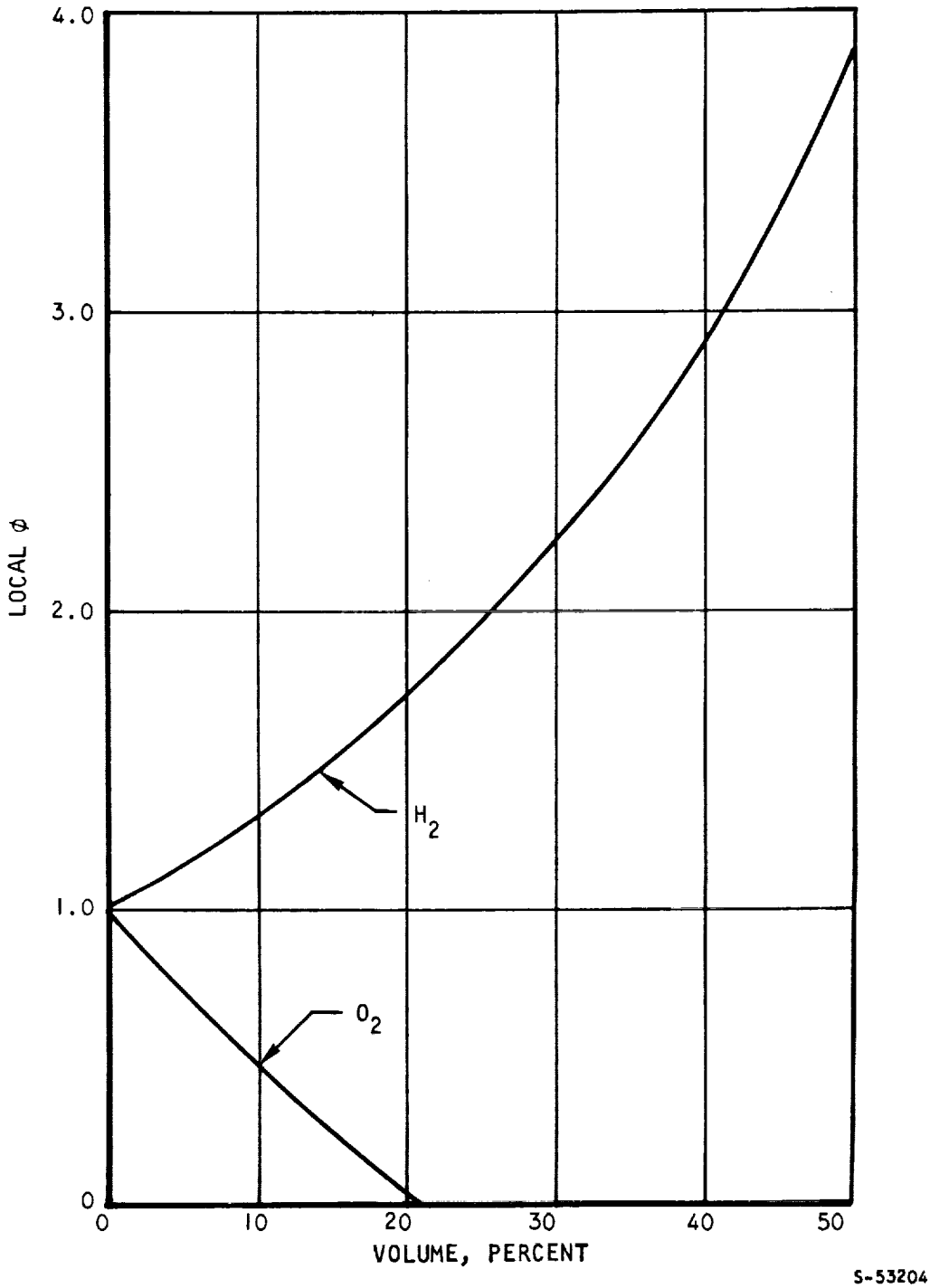

Figure C-1. Equivalence Ratio as a Function of Gas Sample Composition

The first step in the calculation is to find A_s, the atomic ratio of hydrogen to oxygen in the combustor gas sample which entered the probe. If the composition of the combustor gas is preserved (no evaporation, condensation, or coolant leakage), the ratio is obtained from the gas analysis using

$$A_s = \frac{2X_{H_2} + 2X_{H_2O}}{2X_{O_2} + X_{H_2O}} = \frac{X_{H_2} + X_{H_2O}}{X_{O_2} + 0.5\, X_{H_2O}} \qquad (C\text{-}3)$$

where X is mole percent, and the subscripts give the chemical formulas of the species. It is assumed that the only gases present in significant amounts at the mass spectrometer are H_2, O_2, H_2O, N_2, and Ar. The atomic ratio of nitrogen to oxygen in the inlet gases is known from flow rate measurements and should agree with that of the sample.

The atomic ratio of hydrogen to oxygen, A_{va}, in the vitiated air is found next. Humidity is assumed to be negligible, and the air is considered to include 21.0 percent oxygen by volume. Using weight flows, W_l, and molecular weights, the atomic balance is given in the form

$$A_{va} = \frac{\dfrac{W_{H_2,vit}}{2.016}}{\dfrac{0.21\, W_{air}}{28.9} + \dfrac{W_{O_2}}{32}} = \frac{W_{H_2,vit}}{0.01465\, W_{air} + 0.06300 W_{O_2}} \qquad (C\text{-}4)$$

where subscripts $(H_{2,vit})$ and (O_2) denote the hydrogen and oxygen flows in the vitiation heater.

The effective local equivalence ratio, ϕ_L, is given by the amount of fuel which has been mixed with the vitiated air, divided by the amount which it would have had to mix with it in order to give a stoichiometric mixture. Since the reaction of interest is

$$2H_2 + O_2 = 2H_2O$$

(reactions of N_2 are ignored), ϕ_L is given by

$$\phi_L = \frac{A_s - A_{va}}{2 - A_{va}} \qquad (C\text{-}5)$$

Note that if the vitiation heater flow rates are varying with time, the measurement of A_s may be slightly displaced in time relative to the appropriate value

of A_{va}; transport time through the vitiation heater, the combustor, and the gas sampling system should be recognized, since for low pressures it may total as much as two seconds. Most of this time is spent in travel from the probe to the mass spectrometer. For the two-dimensional combustor tests, vitiation heater conditions were held steady and no correction for transport time was made.

Next, the effects of condensation in the probe or water leaks in the system will be considered. These require that a different procedure be used to calculate A_s.

C.3 COMPUTATION OF LOCAL EQUIVALENCE RATIO WHEN THE ATOMIC COMPOSITION OF THE SAMPLE IS NOT PRESERVED

This analysis is based upon the fact that the vitiated air contains the elements oxygen and nitrogen in a known ratio and is homogeneous; that is, each 100 atoms of nitrogen (in the form of N_2) are accompanied by a known number of oxygen atoms in one type of molecule or another. When the combustor gas sample reaches the mass spectrometer, the nitrogen atoms will be detected as N_2 and some of the oxygen atoms will be detected as O_2. An O/N ratio can be calculated from the concentrations of these two species. The difference between this and the vitiated-air-O/N ratio is due to the participation of some atoms in water formation. For each such atom, there are also two hydrogen atoms in the water; therefore, from this knowledge and the amount of free H_2 found in the gas analysis, the effective equivalence ratio of the combustor gases can be found.

The following assumptions are made:

(a) Flow of the sample gas into the mass spectrometer is continuous and finite at all times; that is, the flow is not interrupted by slugs of water which have entered the probe or have been flash-vaporized within the sampling system.

(b) The vitiating gases were well-mixed with the clean air, at least down to the scale of the probe's capture area.

(c) The flow rates of air and vitiating gases are accurately known.

(d) Leaks of air into the combustor and gas sampling system are negligible.

Assuming that the humidity in the compressed air is negligible, the atomic ratio of oxygen (O) to nitrogen (N) in the vitiated air is

$$\frac{O}{N} = \frac{W_{air} + 4.357\, W_{O_2}}{3.729\, W_{air}} = 0.2682 + 1.168\, \frac{W_{O_2}}{W_{air}} \qquad (C\text{-}6)$$

The $\frac{O}{N}$ ratio of the sample <u>as analyzed</u> is denoted by $\widetilde{O}/\widetilde{N}$:

$$\frac{\widetilde{O}}{\widetilde{N}} = \frac{2X_{O_2} + X_{H_2O}}{2X_{N_2}} = \frac{X_{O_2} + 0.5\, X_{H_2O}}{X_{N_2}} \qquad (C\text{-}7)$$

and the sample's hydrogen-to-nitrogen ratio $\widetilde{H}/\widetilde{N}$ is given by

$$\frac{\widetilde{H}}{\widetilde{N}} = \frac{X_{H_2} + X_{H_2O}}{X_{N_2}} \qquad (C\text{-}8)$$

From the above information it is possible to compute the true local H/O, since

$$\frac{H}{O} = \frac{H}{N} \times \frac{N}{O} = \frac{\widetilde{H} + H_c}{\widetilde{N}} \times \frac{N}{O} \qquad (C\text{-}9)$$

Where H_c is the hydrogen in that part of the water vapor which has been removed through condensation. Note the use of

$$\frac{H}{N} = \frac{\widetilde{H} + H_c}{N} = \frac{\widetilde{H} + H_c}{\widetilde{N}}$$

which holds since atomic species are conserved and the gases at the mass spectrometer are considered to be well-mixed.

Since $H_c = 2O_c$, and

$$\frac{O}{N} = \frac{\widetilde{O} + O_c}{\widetilde{N}}$$

$$\frac{O_c}{N} = \frac{O}{N} - \frac{\widetilde{O}}{\widetilde{N}}$$

we see that

$$\frac{H_c}{\widetilde{N}} = 2\left(\frac{O}{N} - \frac{\widetilde{O}}{\widetilde{N}}\right)$$

and Equation (C-9) becomes

$$\frac{H}{O} = \left[\frac{\tilde{H}}{\tilde{N}} + 2\left(\frac{O}{N} - \frac{\tilde{O}}{\tilde{N}}\right)\right] \times \frac{N}{O} \qquad (C\text{-}10)$$

which can be computed from the flow rates and gas analysis using Equations (C-6), (C-7), and (C-8). Before proceeding further, however, we note that in this equation the gas analysis data will appear in the term

$$\frac{\tilde{H}}{\tilde{N}} - 2\frac{\tilde{O}}{\tilde{N}}$$

and that the species H_2O makes no net contribution to this term. Thus, we expect to find that the percentage of water vapor in the analyzed gas will not appear explicitly in the calculation of local equivalence ratio.

The equations may be simplified. First we rewrite (C-10) using (C-7) and (C-8):

$$\frac{H}{O} = \left[\frac{X_{H_2} + X_{H_2O}}{X_{N_2}} + 2\left(\frac{O}{N} - \frac{X_{O_2} + 0.5\, X_{H_2O}}{X_{N_2}}\right)\right] \times \frac{N}{O}$$

Combining terms gives

$$\frac{H}{O} = \frac{X_{H_2} - 2\, X_{O_2}}{\left(\frac{O}{N}\right) X_{N_2}} + 2$$

For convenience, the corrected $\frac{H}{O}$ is represented by A_{corr}, and $\frac{O}{N}$ from Equation (C-6) by C, where

$$C = 0.2682 + 1.168\, \frac{W_{O_2}}{W_{air}} \qquad (C\text{-}11)$$

$$A_{corr} = \frac{X_{H_2} - 2\, X_{O_2}}{C X_{N_2}} + 2 \qquad (C\text{-}12)$$

The local equivalence ratio is found by using A_{corr} in place of A_s in Equation (C-5). Since A_{corr} does not include the mole fraction of water in

the analyzed gas, and includes the other mole fractions only in ratios, the calculation ideally is not affected by condensation or evaporation within the gas sampling system, or by leakage of water from coolant passages anywhere in the system. As the mole fraction of water in the sample approaches unity, however, the ratios between the other three constituents will suffer increasingly from normal experimental inaccuracies. It seems advisable that data points which show a high percentage of water be rejected or, at best, regarded with suspicion. Therefore, the method of Equation (C-12) fails in cases where vitiation is extremely heavy or in circumstances where coolant leakage predominates.

A further disadvantage of the method is that the oxygen-to-nitrogen ratio becomes a primary measurement and can no longer be used as a check on the validity of the data.

C.4 EFFECT OF GAS ANALYSIS ERRORS

This section considers the effect on ϕ_L, as computed by Equation (C-11), of errors in the measured composition of the sampled gas. These errors might arise in either the sampling process or the gas analysis. It will be assumed that the composition of the vitiated air contained in the sample is accurately known from measured flow rates in the vitiation heater.

Using Equations (C-5) and (C-11) yields ϕ_L in the form

$$\phi_L = \frac{A_{corr}}{(2-A_{va})} - \frac{A_{va}}{(2-A_{va})}$$

$$= \frac{X_{H_2} - 2X_{O_2}}{CX_{N_2}(2 - A_{va})} + \frac{2}{2-A_{va}} - \frac{A_{va}}{2-A_{va}}$$

For any given point, A_{va} and C will be treated as known constants so that the above equation can be reduced to

$$\phi_L = \frac{X_{H_2} - 2X_{O_2}}{CX_{N_2}(2-A_{va})} + k_1 + k_2 \qquad (C-12)$$

where k_1 and k_2 are constants. At this point we can make several observations:

(a) As already mentioned, the computed ϕ_L is not explicitly dependent upon X_{H_2O}, the mole percent of water in the sample; thus ϕ_L is not directly affected by any error in X_{H_2O}.

(b) If the values of X_{H_2}, X_{O_2}, X_{N_2} are all in error by the same factor, ϕ_L is not affected.

(c) If the absolute error in X_{H_2} happens to be equal to twice the absolute error in X_{O_2}, ϕ_L is not affected.

The calculation of the differential of ϕ_L is as follows:

$$d\phi_L = \frac{\partial \phi_L}{\partial (X_{H_2}/X_{N_2})} \; d(X_{H_2}/X_{N_2}) + \frac{\partial \phi_L}{\partial (X_{O_2}/X_{N_2})} \; d(X_{O_2}/X_{N_2}) \qquad (C\text{-}13)$$

$$= \frac{1}{C(2 - A_{va})} \left[d(X_{H_2}/X_{N_2}) - 2\, d(X_{O_2}/X_{N_2}) \right]$$

and note that

$$d(X_{H_2}/X_{N_2}) = \frac{dX_{H_2}}{X_{N_2}} - \frac{X_{H_2}}{(X_{N_2})} \, dX_{N_2}$$

$$d(X_{O_2}/X_{N_2}) = \frac{dX_{O_2}}{X_{N_2}} - \frac{X_{O_2}}{(X_{N_2})} \; dX_{N_2}$$

so that Equation (C-13) becomes

$$d\phi_L = \frac{1}{X_{N_2} \, C(2-A_{va})} \left[dX_{H_2} - 2dX_{O_2} + \frac{(2X_{O_2} - X_{H_2})}{X_{N_2}} \; dX_{N_2} \right] \qquad (C\text{-}14)$$

Now we examine the factor $C(2-A_{va})$. If the vitiation process has been correctly controlled, the molar composition of the vitiated air can be represented by

$$O_2 + 3.76 \left[(1\text{-}0.01B)\, N_2 + (0.01B)\, H_2O \right]$$

where B is the molar percentage of vitiating gases (added oxygen and water) in the vitiated air. The H/O ratio of the vitiated air, A_{va}, is then

$$A_{va} = \frac{3.76\ (0.02B)}{(3.76 \times 0.01B) + 2} = \frac{0.0752B}{0.0376B + 2}$$

and the O/N ratio, C, is

$$C = \frac{(3.76 \times 0.01B) + 2}{2 \times 3.76\ (1-0.01B)} = \frac{0.0376B + 2}{7.52\ (1-0.01B)}$$

The factor $C(2-A_{va})$ then becomes

$$C(2-A_{va}) = \frac{1}{0.0188(100-B)}$$

Returning to Equation (C-14), we have

$$d\phi_L = \frac{0.0188(100-B)}{X_{N_2}} \left[dX_{H_2} - 2dX_{O_2} + \frac{2X_{O_2} - X_{H_2}}{X_{N_2}}\ dX_{N_2} \right] \qquad (C\text{-}15)$$

Thus for constant B, as X_{N_2} approaches zero, ϕ_L generally becomes highly sensitive to small errors in X_{H_2}, X_{O_2}, and X_{N_2}. Condensation in the sampling system increases the magnitude of X_{N_2} and thus tends to decrease the effect of experimental errors when this computation method is used. Evaporation and coolant leakage, on the other hand, increase the effect of errors on ϕ_L. The disadvantage of condensing all water before analyzing the sample is that the O/N ratio can no longer be used as a check on the validity of the measurements.

Small errors in either X_{O_2} or X_{H_2}, assuming the other mole percentages to be correct, affect ϕ_L in a relatively simple way, as given by Equation (C-15) and shown graphically in Figure C-2. Accuracy in X_{O_2} is seen to be more critical than accuracy in X_{H_2}. However, the O_2 content can in practice be determined more accurately because $X_{O_2} < 25$ and $X_{H_2} \leq 100$.

The effect of an error in X_{N_2} is slightly more complex and is shown in Figure C-3 for the specific case where $(2X_{O_2} - X_{H_2}) = 21$. When $(2X_{O_2} - X_{H_2}) = 0$, then $\phi = 1$ and all three data reduction methods described in this appendix agree.

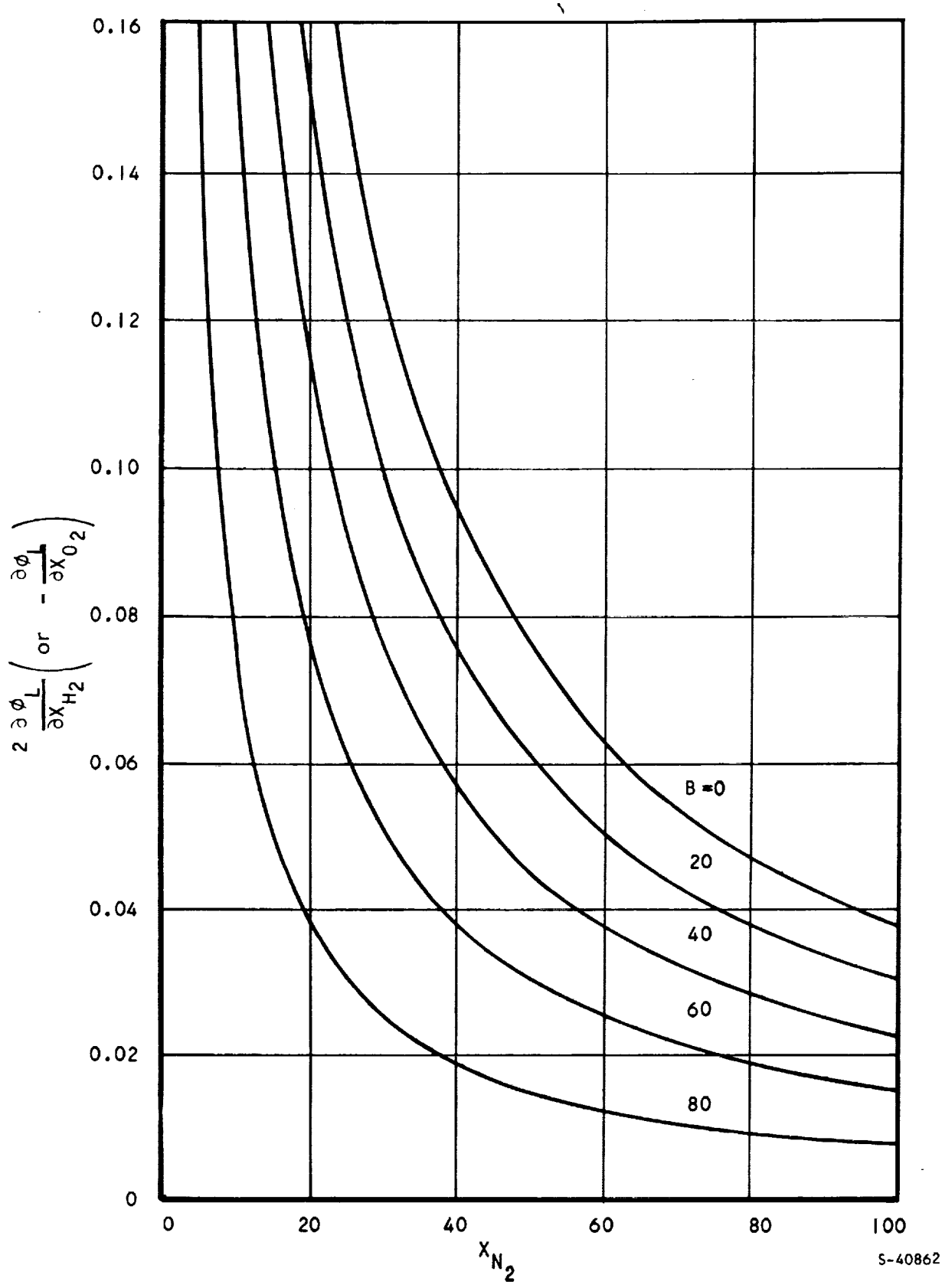

Figure C-2. Effect of Errors in X_{H_2} and X_{O_2}

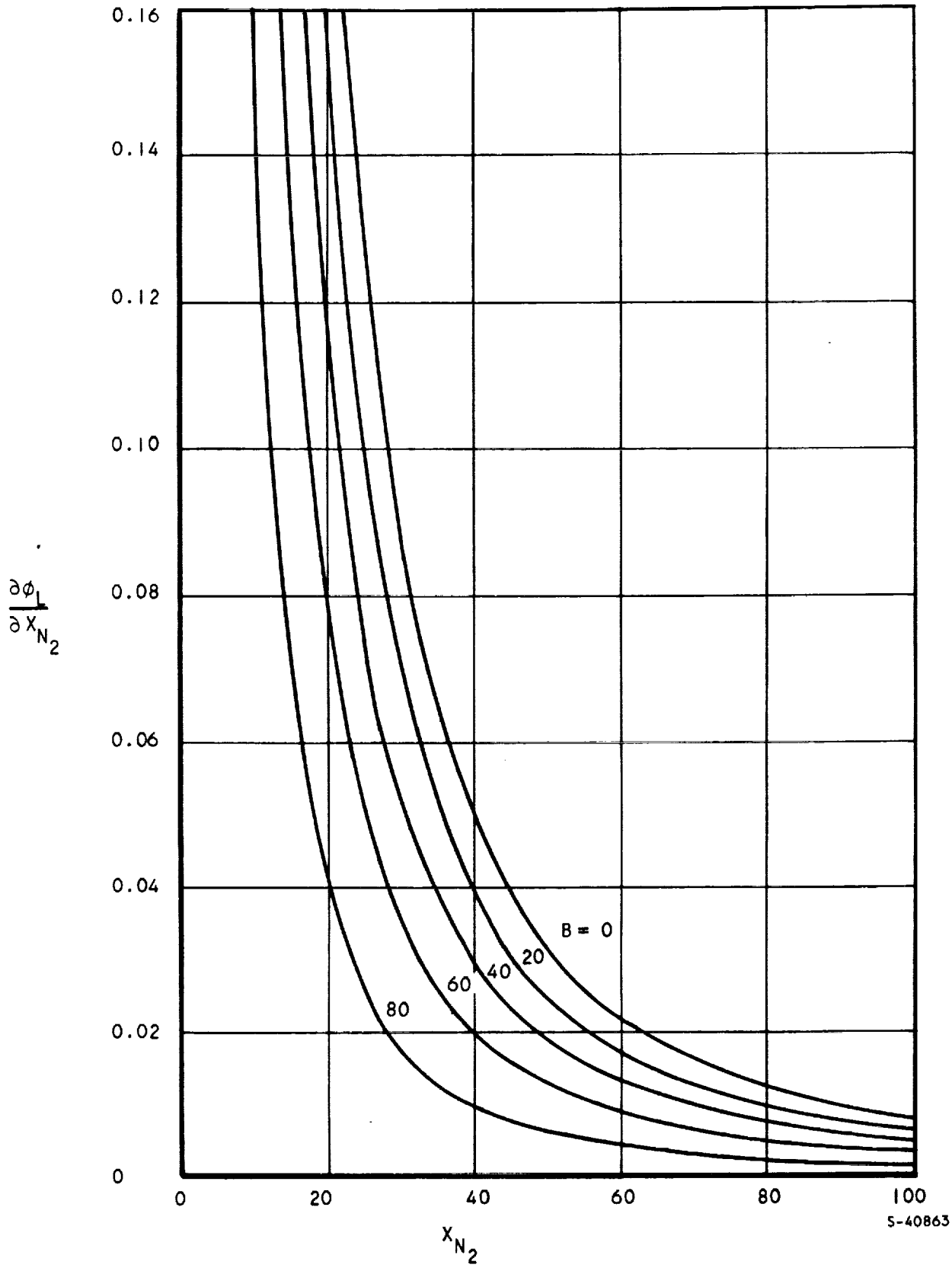

Figure C-3. Effect of Errors in X_{N_2} for $(2X_{O_2} - X_{H_2}) = 42$

Another singularity occurs when the sampled stream is pure hydrogen; in that case the local equivalence ratio is infinite and the method in this section cannot be used because $X_{N_2} = 0$.

The case where B = 100 (so that $X_{N_2} = 0$) was not of interest in the present investigation. The value of B was typically in the range 20 to 50.

For the majority of the points sampled, the data indicate that $\partial\phi_L/\partial X < 0.10$ for each species X. In a few cases $\partial\phi_L/\partial X_{O_2}$ may have been as high as 0.14; however, these were cases with $\phi_L > 2$, where accuracy was not as important. Moreover, as mentioned above, the determination of X_{O_2} was more accurate than those of X_{H_2} and X_{N_2}. In general, it is believed that the determination of the equivalence ratio of the sampled gas was accurate to within 0.06 for $\phi_L < 1.2$ and within 5 percent for higher equivalence ratios. This order of accuracy is considered adequate for the present investigation.

C.5 SIMULTANEOUS NITROGEN AND HYDROGEN INJECTION

In run 248, nitrogen was injected through the second-stage orifices while hydrogen was being injected at the first stage. In this case it was desired to determine, for each point sampled, an equivalence ratio using the assumption that each nitrogen molecule was equivalent to a hydrogen molecule. In addition, first and second stage injection patterns were to be differentiated. For this analysis assumptions (b) through (e) in Section C.1 were made. The first stage equivalence ratio was obtained from Equations (C-3) and (C-5). The "nitrogen equivalence ratio" ϕ_{N_2} was obtained, by analogy with Equation (C-5), from the equation -

$$\phi_{N_2} = \frac{X_{N_2} \Big/ \left(X_{O_2} + 0.5\, X_{H_2O} \right) - 1/C}{2 - A_{va}} \qquad \text{(C-12)}$$

where C is given by Equation (C-11). The numerator of Equation (C-12) gives the moles of N, per mole of O, added to the vitiated air by injection in the combustor. The denominator gives the number of H atoms, per mole O, which must be added to the vitiated air in order to give a stoichiometric mixture.

APPENDIX D

QUASI-TWO-DIMENSIONAL ANALYTICAL MODEL OF SUPERSONIC COMBUSTOR

APPENDIX D

QUASI-TWO-DIMENSIONAL ANALYTICAL MODEL OF SUPERSONIC COMBUSTOR

The complete theoretical analysis of a flow with chemical reaction requires the successful solution of the combined effects of chemical reactions and equations of aerodynamics. The chemical reaction rates are determined from the concentration of each constituent and its temperature and pressure; in turn, these characteristics are determined from the chemical kinetics and the flow processes. The transport properties associated with basic conservation laws are not yet known for turbulent mixing with chemical reactions. Furthermore, the complex physical nature of shock interaction and boundary layer separation due to fuel injection and combustion has not been fully established. These complicated and interacted phenomena make pure theoretical analysis very difficult.

An analysis was made using simplified assumptions combined with emperical correlations. The analysis was divided into two parts. The first part consisted of developing an integral method to handle the mixing of well-injected hydrogen with a supersonic airstream in a two-dimensional or annular channel. The second part involved development of a simplified analytical model for predicting supersonic combustion characteristics.

For mixing, a numerical analysis was used to solve the integral conservation equations using similar velocity, concentration and total enthalpy profiles. Calculations were made at various downstream stations. The results were in the form of concentration profiles across the flow channel at different stations. These profiles were used in calculating the reactive flow in the combustor.

The constant-mass-tube technique was used for the combustion analysis. The flow field was divided into a number of tubes small enough so that one-dimensional analysis was acceptable. In each constant-mass tube the hydrogen mass-flow prifile from the mixing analysis, along with the empirical correlation of ignition delay and reaction time were used, with conservation laws, to solve flow properties at various stations in each tube.

Two separate computer programs were written to solve the mixing and combustion equations. Comparison of the analytical pressure distribution with test data (0.6 x 6 in. combustor test model) showed that the pressure and temperature rise, due to shock boundary interaction cannot be ignored.

D.1 METHODS OF ANALYSIS

D.1.1 Mixing

The mixing analysis makes use of the integral method in which all the conservation equations are satisfied. The following approaches and assumptions are used:

(a) All flow profiles such as velocity, concentration and total enthalpy are similar. These profiles are defined by the conservation laws as mixing progresses downstream of injection.

(b) A correlation from test data is used to define the injected hydrogen jet boundary and maximum concentration. This avoids using empirical constants to establish the spreading rate of mixing.

(c) Static pressure is assumed constant across the combustor duct, but varies with the combustor length.

(d) Only two constituents (hydrogen and air) are considered and they are nonreacting.

(e) Radial momentum is assumed negligible in comparison with axial momentum.

(f) Heat transfer at the wall is calculated assuming that the boundary layer total enthalpy profile is similar to the velocity profile for the case of a cold wall (Figure D-1).

(g) Skin friction on the wall is approximated by smooth-pipe data.

(h) At the starting station only axial momentum of the injectant is considered.

(i) Shock wave interaction and boundary layer separation due to injection are not considered. The fuel jet boundary is derived from Reference D-1; the nondimensional concentration profiles are obtained from Reference D-2; and the combustor inlet velocity profile is assumed to follow the 1/7th power distribution (Figures D-2 and D-3).

As indicated above, the main approach in the study of mixing was to use correlations from tests instead of using empirical models.

Semiempirical models for eddy viscosity have been suggested by many investigators including Prandtl (Reference D-3), Ferri, et al. (Reference D-4), Alpinieri (Reference D-5), Ragsdale, et al. (Reference D-6), Peters, et al. (Reference D-7) and Schetz (Reference D-8). Each model has been successfully employed to correlate experimental mixing-rate data for a limited range of initial conditions. However, no one formulation has been shown applicable for the case of compressible turbulent mixing, and in particular, noncoaxial turbulent mixing.

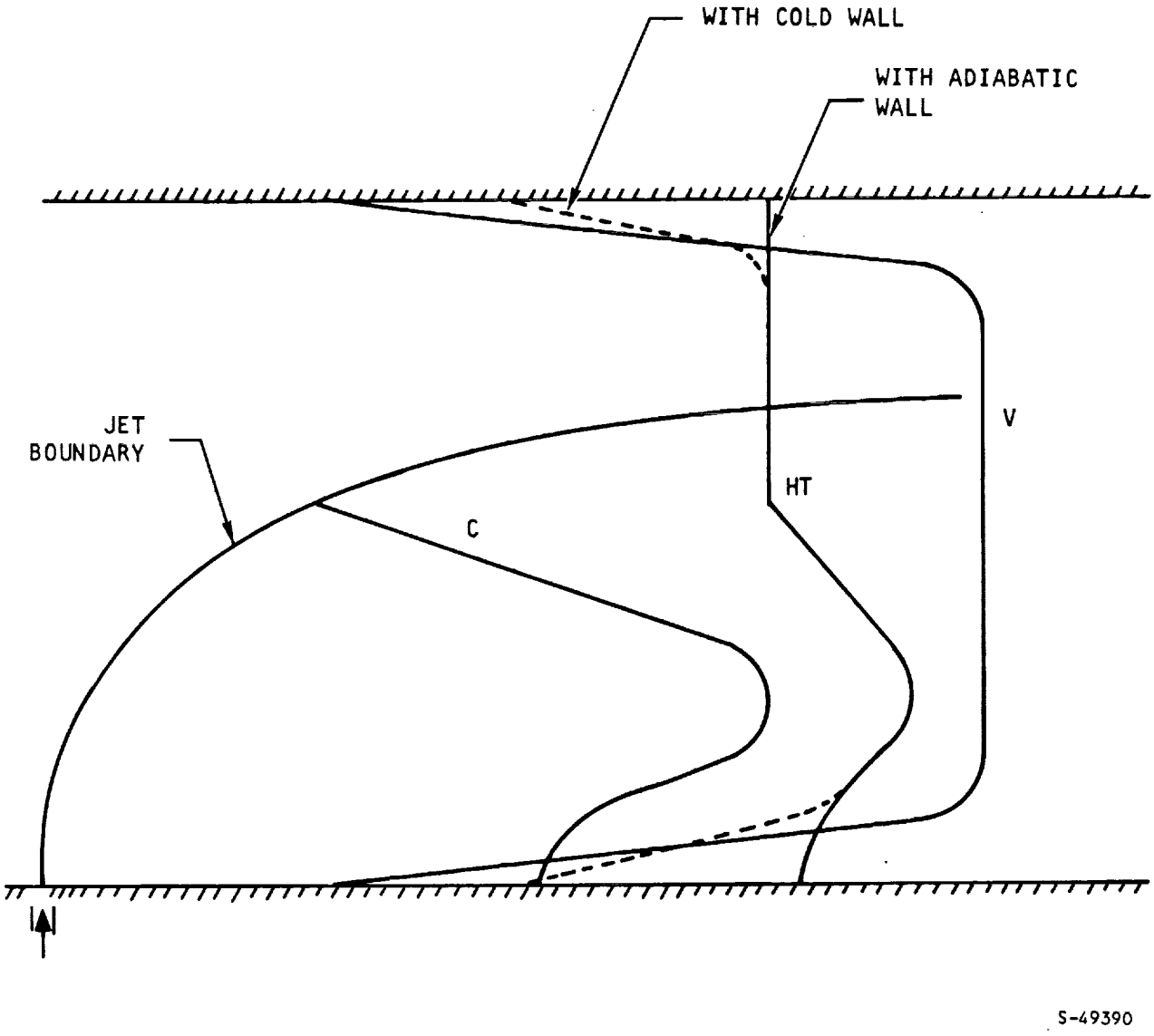

Figure D-1. Initial Profiles of Concentration, Velocity, and Total Enthalpy

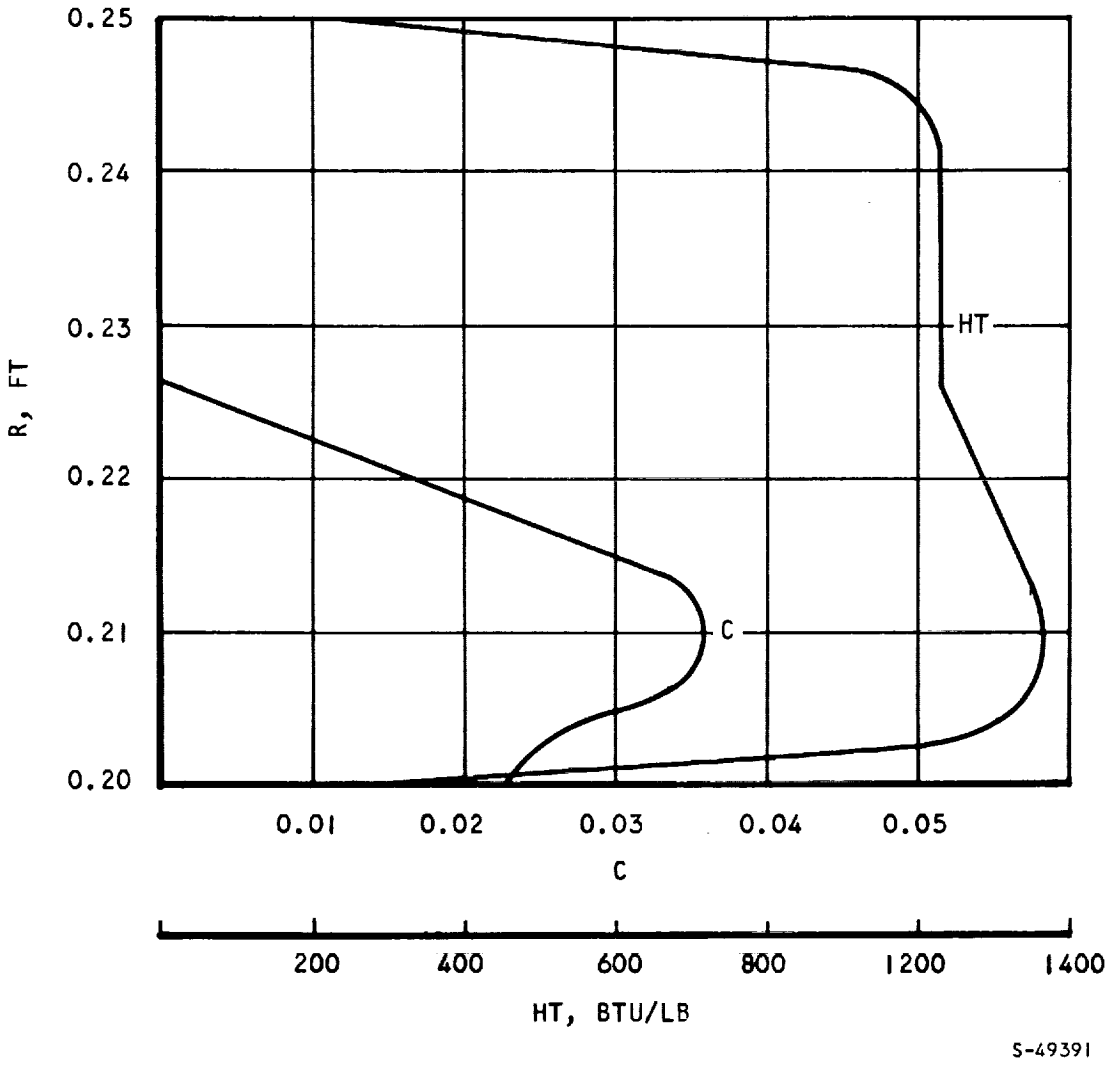

Figure D-2. Concentration and Total-Enthalpy Profiles

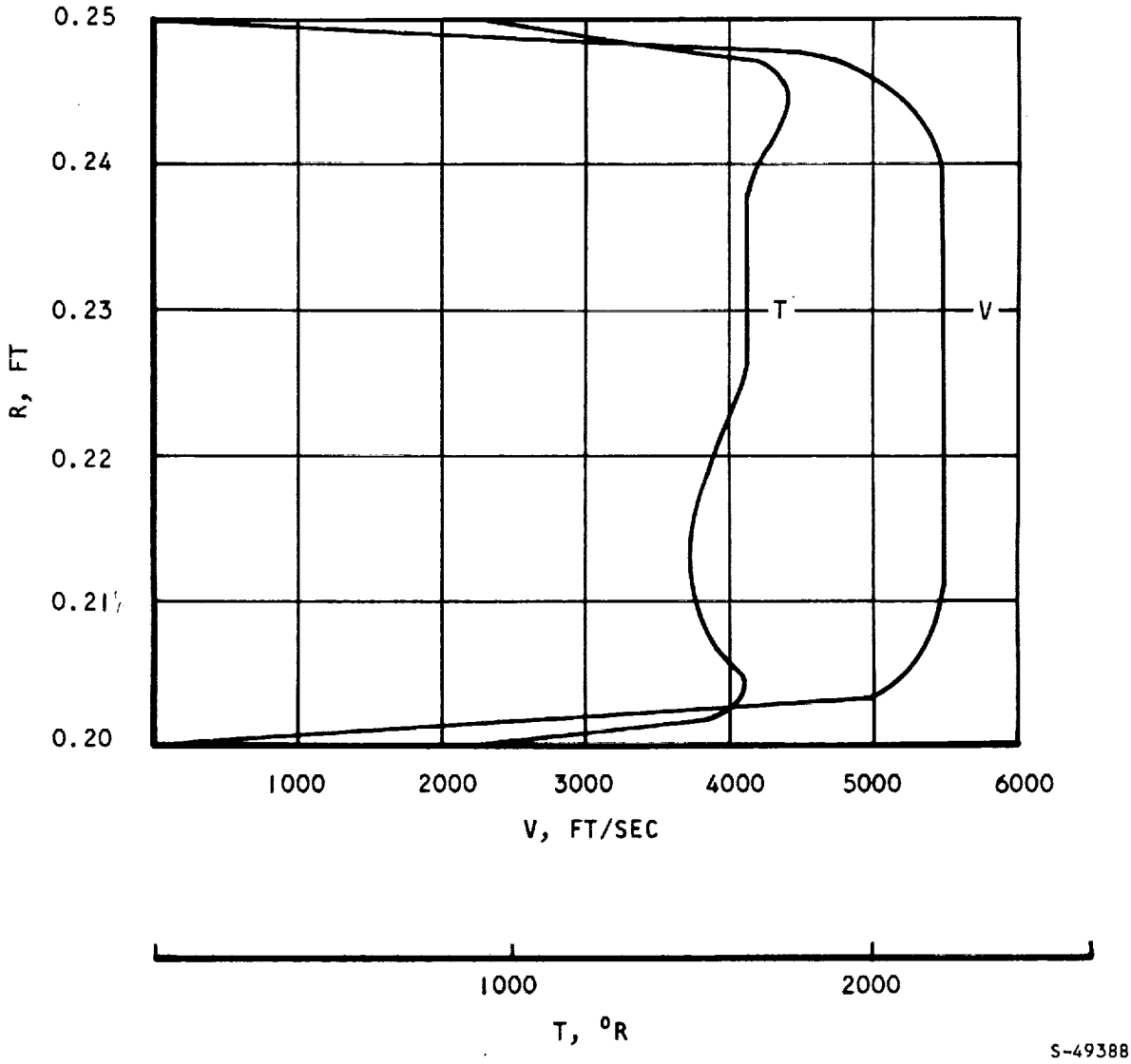

Figure D-3. Velocity and Static-Pressure Profiles

Instead of using an eddy viscosity model, the mixing analysis used the jet-mixing boundary and similar concentration profiles to describe the turbulent mixing processes.

The jet penetration was based on the results from Vranos (Reference D-1). Vranos correlated penetration as:

$$\frac{P}{d} = 2.91\left(\frac{\rho_a v_a^2}{\rho_o v_o^2}\right)\left[\frac{x}{d}\right]^{0.0866} \cos\theta \qquad (D\text{-}1)$$

where P is the penetration height, defined as the vertical distance above the plane of the source where the mole fraction of injected fluid is 0.005; and d is the injection hole diameter. The subscripts j and o refer to injector and freestream conditions, respectively.

The concentration profile is assumed to be characterized by two parameters, defined as follows:

$$\alpha(x) = \frac{Cw\ (x)}{C_M\ (x)} \qquad (D\text{-}2)$$

$$\eta(x) = \frac{Y_M\ (x)}{P\ (x)} \qquad (D\text{-}3)$$

where C_M and Cw are the maximum concentration and concentration at the wall, respectively. Y_M is the location of the maximum concentration measured from the injecting wall. The correlations obtained for $\alpha(x)$ and $\eta(x)$ using the experimental results of Torrence (Reference D-2) are shown in Figures D-4 and D-5. Using the boundary conditions of correlations (D-1, D-2, and D-3), the initial concentration profile (obtained also from Reference D-2) is shaped by the conservation laws as mixing progresses downstream of fuel injection.

D.1.2 Combustion

In the combustion analysis, the flow field is divided into a number of tubes sufficiently small so that one-dimensional analysis is applicable. The following procedures and assumptions are used:

(a) The total mass through each tube is kept constant with mass transfer between the adjoining tubes permitted.

(b) In each tube, the hydrogen mass-flow-rate profile from the mixing analysis is used as the elementary mass concentration in determining heat release.

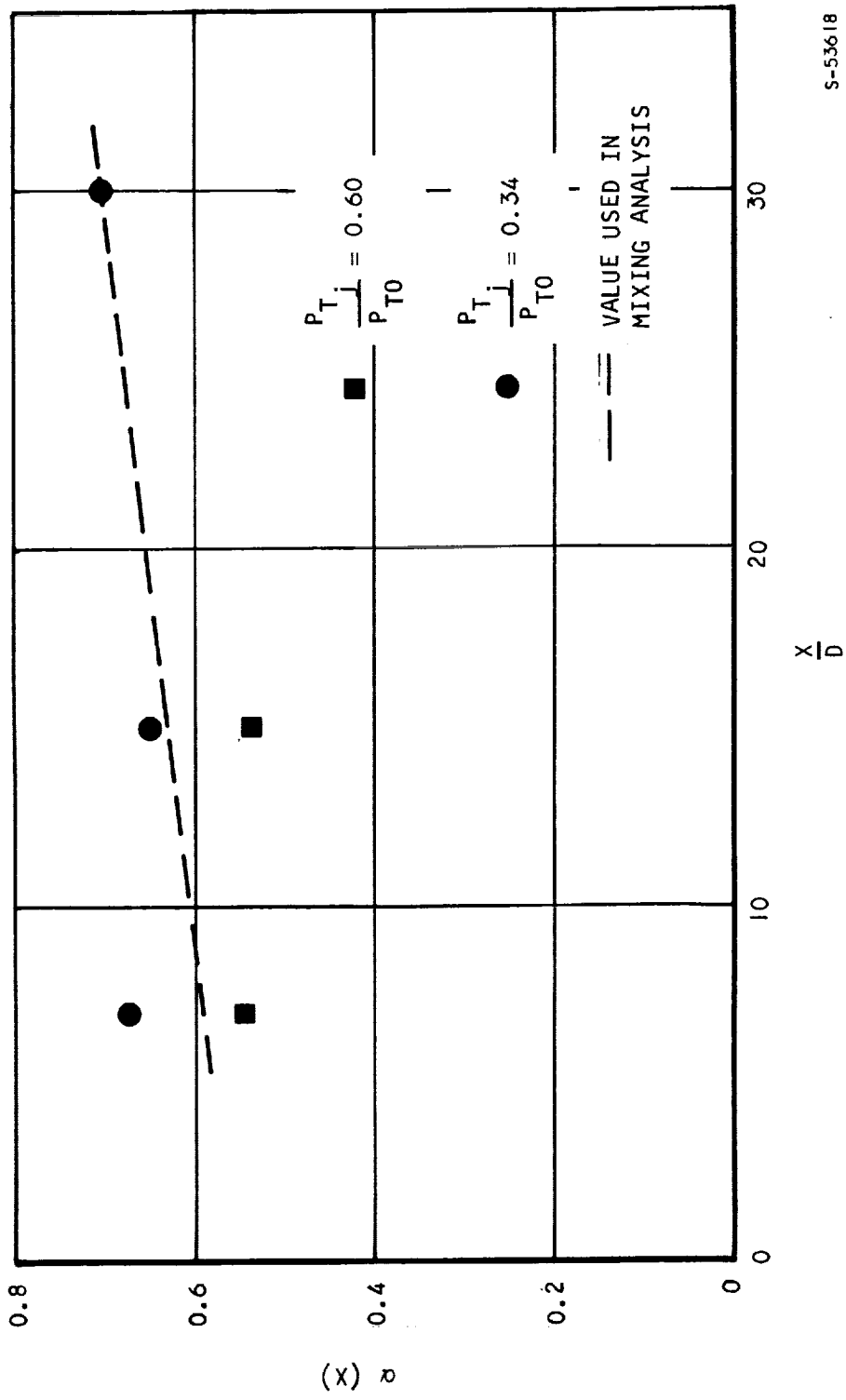

Figure D-4. Concentration at the Wall vs Peak Concentration

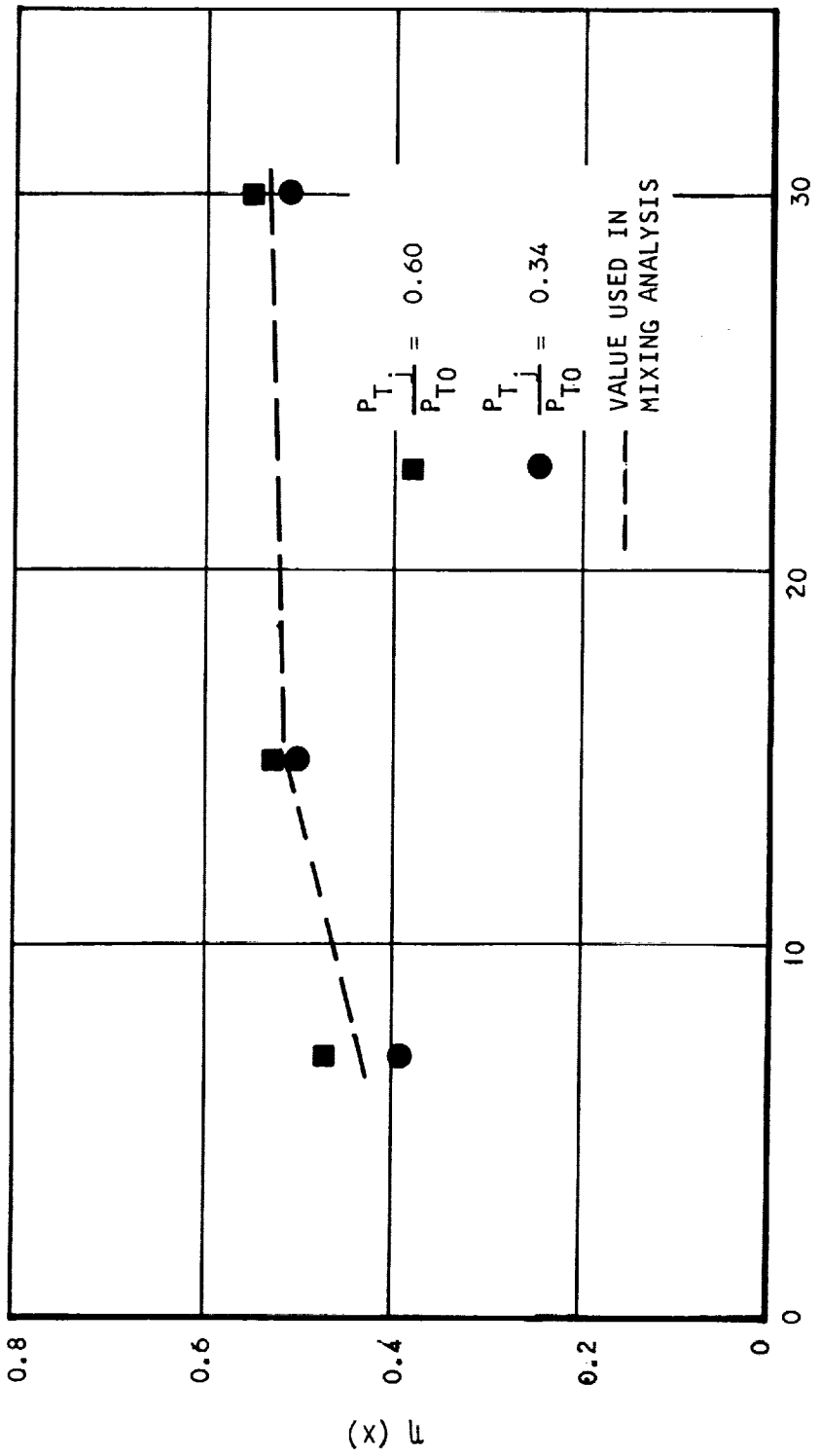

Figure D-5. Peak Concentration Distance vs Jet Boundary Distance from the Wall

(c) Chemical kinetic effects are taken into account with an ignition delay and chemical reaction time, using empirical correlations as a function of local temperature and pressure (References D-9 and D-10) The ignition delay time τ_{ID} and the chemical reaction time τ_R as suggested are:

$$\tau_{ID} = \frac{9.522}{P} \exp\left(\frac{18000}{T}\right)$$

$$\tau_R = 105 \left(\frac{2116}{P}\right)^{1.7} \exp\left(\frac{0.622T}{1000}\right)$$

where τ_{ID} = ignition delay time in ms

τ_R = chemical reacting time in ms

P = pressure in psf

T = temperature, ^0R

(d) The static pressure gradient in a direction normal to the flow is assumed negligible (Reference D-11 and D-12).

(e) In the analysis of each constant-mass tube, the frozen-flow concentration from the mixing program is used as the elemental concentration in determining the heat release. Total mass through this tube is kept constant, with mass transfer of combustion products, air, or hydrogen between the adjoining tubes considered and the associated momentum and energy transfer accounted for. The net total energy in i-th mass tube is equal to the sum of the energy produced by the combustion and the energy transferred due to mass diffusion process, i.e.:

$$Q(i) = HR_i WC_{P_i} + DWA_i\ (HT)_{air} + DWH_i (HT)_{H_2} + (0.74350\ HT_{N_2} + 0.2560\ HT_{H_2O}) DWC_{P_i}$$

where HR_i = heat release

WC_{P_i} = combustion produce produced in i-th mass tube

DWA_i = net mass diffusion of air

DWH_i = net mass diffusion of hydrogen

DWC_{P_i} = net mass diffusion of combustion product

$(HT)_j$ = total enthalpy of j-th constituent

And the energy balance between two stations in each mass tube is

$$HT(2) = HT(1) - Q(i) - Q_i(tr)/w_i$$

where $HT(2)$ = total enthalpy at station 2

$HT(1)$ = total enthalpy at station 1

$Q(tr)$ = net heat transfer in i-th mass tube

W_i = constant mass in i-th mass tube

(f) Due to the lack of experimental confirmation, it is assumed that momentum and energy are transferred between tubes according to their driving potentials at a mass-averaged value. The momentum and heat transfer in each mass tube are assumed to have the following forms:

$$\Delta D_i = D_w \left[\frac{1}{N} + \frac{W_i V_i^{\epsilon_M} - W_i \overline{V}}{\sum_i W_i} \right]$$

$$\Delta Q_i = Q_w \left[\frac{1}{N} + \frac{W_i T_i^{\epsilon_H} - W_i \overline{T}}{\sum_i W_i} \right]$$

where $$\overline{V} = \frac{\sum_i^N W_i V_i^{\epsilon_M}}{\sum_i^N W_i}$$

$$\overline{T} = \frac{\sum_i^N W_i T_i^{\epsilon_H}}{\sum_i^N W_i}$$

W_i = constant mass in each tube

N = number of tubes

ϵ_M = parameter for eddy diffusion of momentum

ϵ_H = parameter for eddy diffusion of heat

D_w = total drag force at the wall = $\tau_{w_1} A_1 + \tau_{w_2} A_2$

Q_w = $q_{w_1} A_1 + q_{w_2} A_2$

τ_{w_1} and τ_{w_2} are the shear stresses at lower and upper walls of combustor, respectively. q_{w_1} and q_{w_2} are the heat transfer at lower and upper walls of combustor, respectively. A_1 and A_2 are the area of lower and upper walls.

(g) The interaction of combustion and boundary layer separation is not considered.

The frozen-flow concentration, total enthalpy, velocity, pressure, and static temperature from the two-dimensional mixing program are used as initial input for combustion analysis.

D.2 ANALYTICAL RESULTS AND DISCUSSION

Computer runs were made for the two-dimensional, true-scale combustor (Figure D-6) at an inlet Mach number of 2.9. The inlet conditions are shown below:

(a) Inlet total pressure = 300 psia

(b) Inlet total temperature = 3830°R

(c) Inlet Mach number = 2.9

(d) Clean air mass-flow rate = 2.00 lb/sec

(e) Injection fuel total temperature = 1460°R

(f) Equivalence ratio = 0.8

(g) Angle of injection = 90 deg

(h) Combustor wall temperature = 960°R

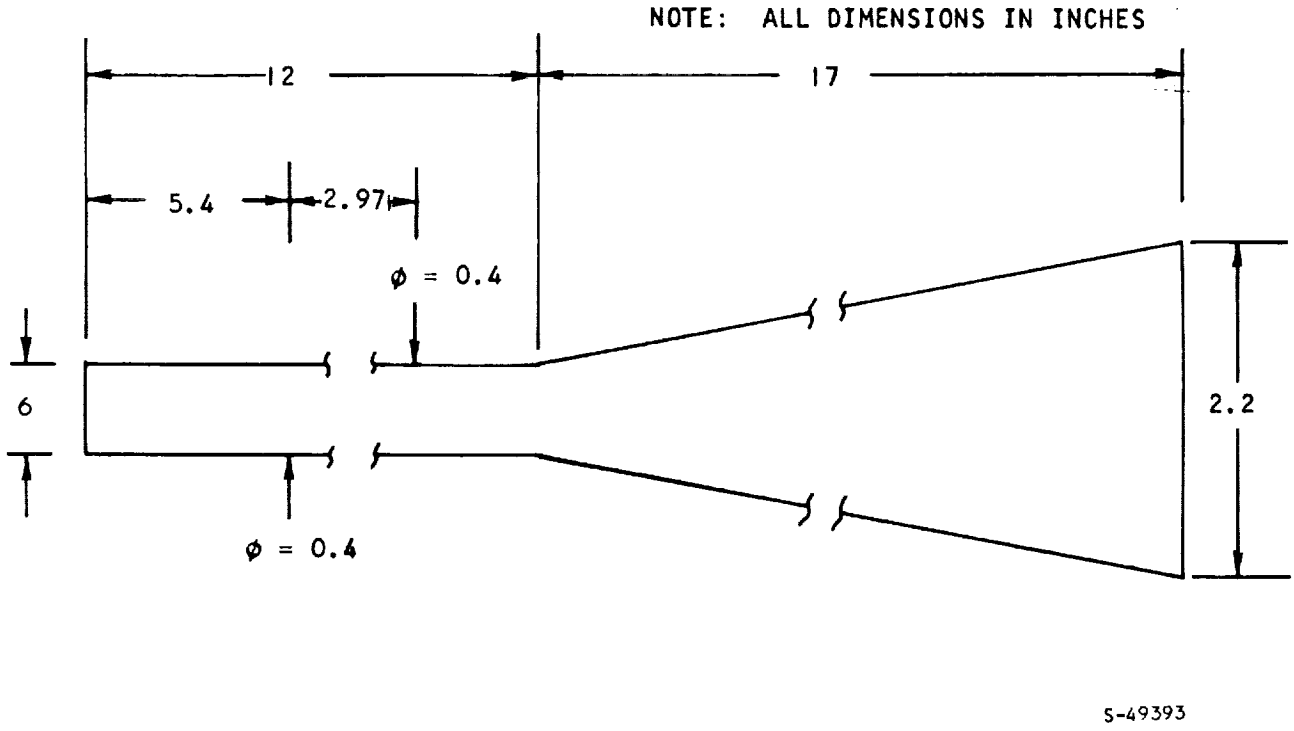

Figure D-6. Schematic Diagram of the True-Scale Combustor

The calculated chemical efficiency and pressures along the combustor wall were as shown in Figures D-7 and D-8, respectively. Figure D-7 indicates that fuel is not reacted within the first five inches downstream of the first injector row. The mainstream temperature and pressure were low and the flow velocity was high which prolonged ignition delay and chemical reaction time. At a distance 8.5 in. downstream of the injector row all of the fuel reacted. The pressure rises at six and nine inches from the combustor entrance were due mainly to fuel injection (Figure D-8). The pressure rose rapidly after combustion began; it then gradually decreased because of the effect of increasing area became more dominant than that due to combustion. The maximum pressure was about four-times that at the inlet.

The concentration, static temperature,and velocity profiles at three axial stations are plotted in Figures D-9, D-10, and D-11, respectively. The static temperature profile shown in Figure D-10b indicates that combustion starts near the boundary layer edge, raising the static temperature and pressure of the mainstream. This promotes combustion. The fast turbulent momentum and heat transfer are clearly observed from the nearly uniform profiles of velocity (shown in Figure D-11) and static temperature (shown in Figure D-10c).

The results from the two-dimensional analysis indicated a general trend for supersonic combustion. However, comparing analytical results with experimental data (different inlet conditions) showed that considerable disagreement existed between the two results. As shown in Figure D-12, this disagreement occurred mainly in the pressure distribution upstream of, and in the vicinity of, the fuel injector.

The discrepancy was believed to be caused by two main factors:

(a) The complex interaction between the two fluid streams was not accounted for in the analytical model. When a secondary flow is injected into a supersonic primary stream, this flow acts as an obstacle inducing a strong bow shock on the upstream side of the injector. The shock-induced pressure field turns the injectant until it moves approximately parallel to the wall. This bow-shock wave also interacts with the boundary layer on the wall; the pressure is propagated through the boundary layer upstream of the shock, producing boundary layer separation. The fluid behind the shock then has a higher static pressure and temperature, causing combustion of the injected fuel.

    The significant pressure rise upstream of the fuel injectors in the test data is believed to be caused partially by this jet-induced boundary layer separation as shown in Figure D-13. This complicated phenomenon cannot be predicted with the present model.

(b) The interaction of combustion and boundary layer separation was not considered in the current analysis. The primary stream, with higher static pressure and temperature (caused by jet-induced separation), should mix instantaneously with hydrogen and react

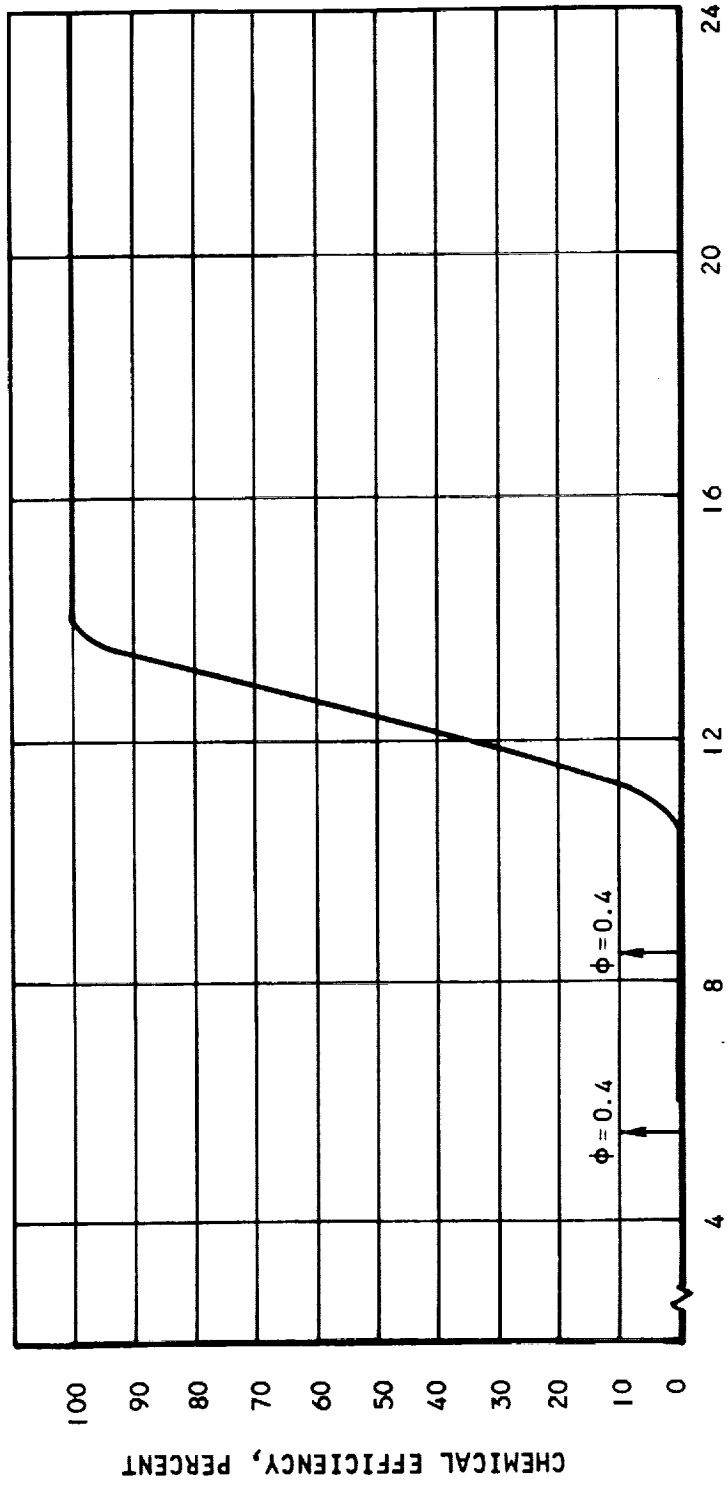

Figure D-7. Chemical Efficiency

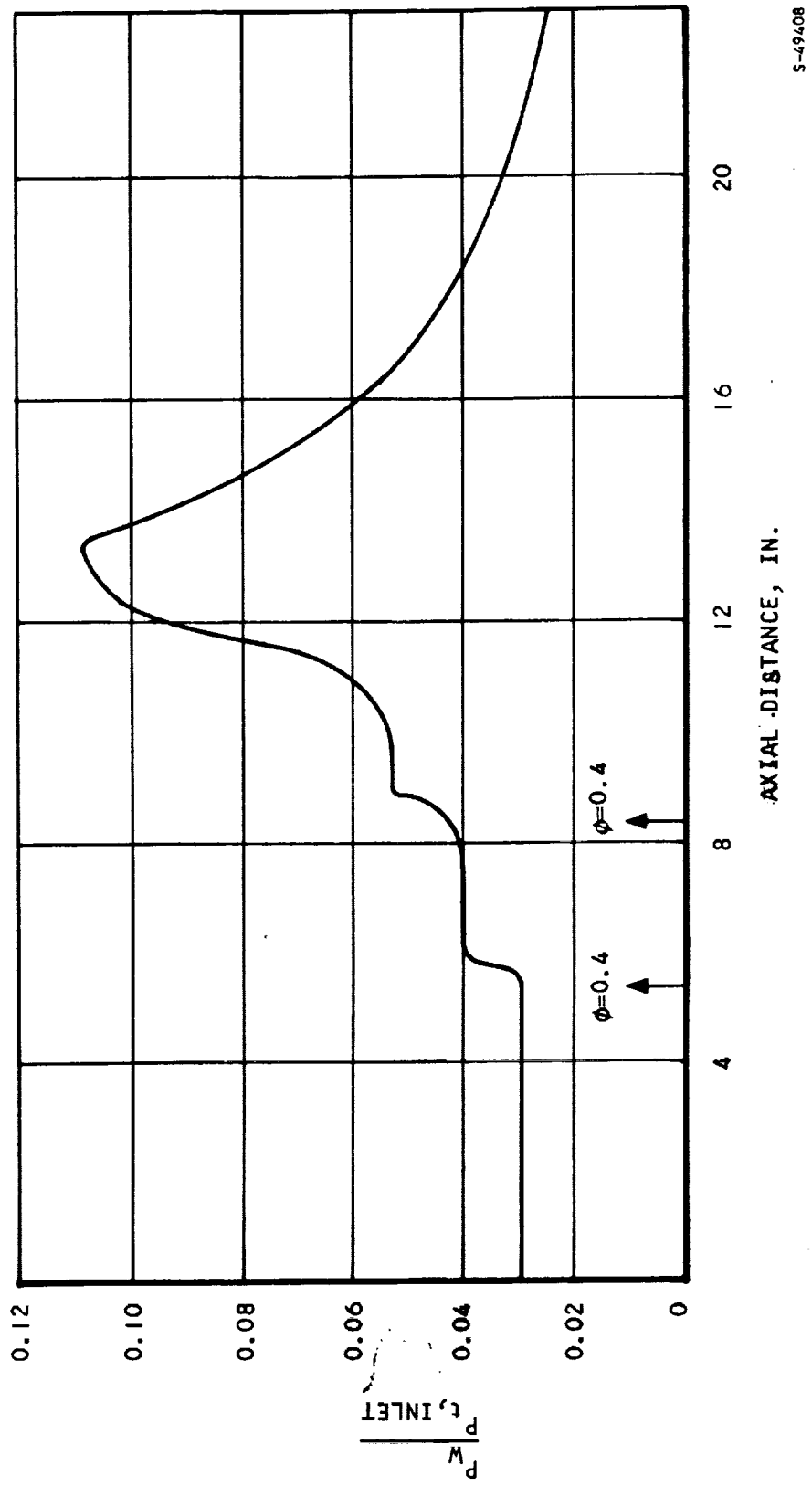

Figure D-8. Pressure Distributions

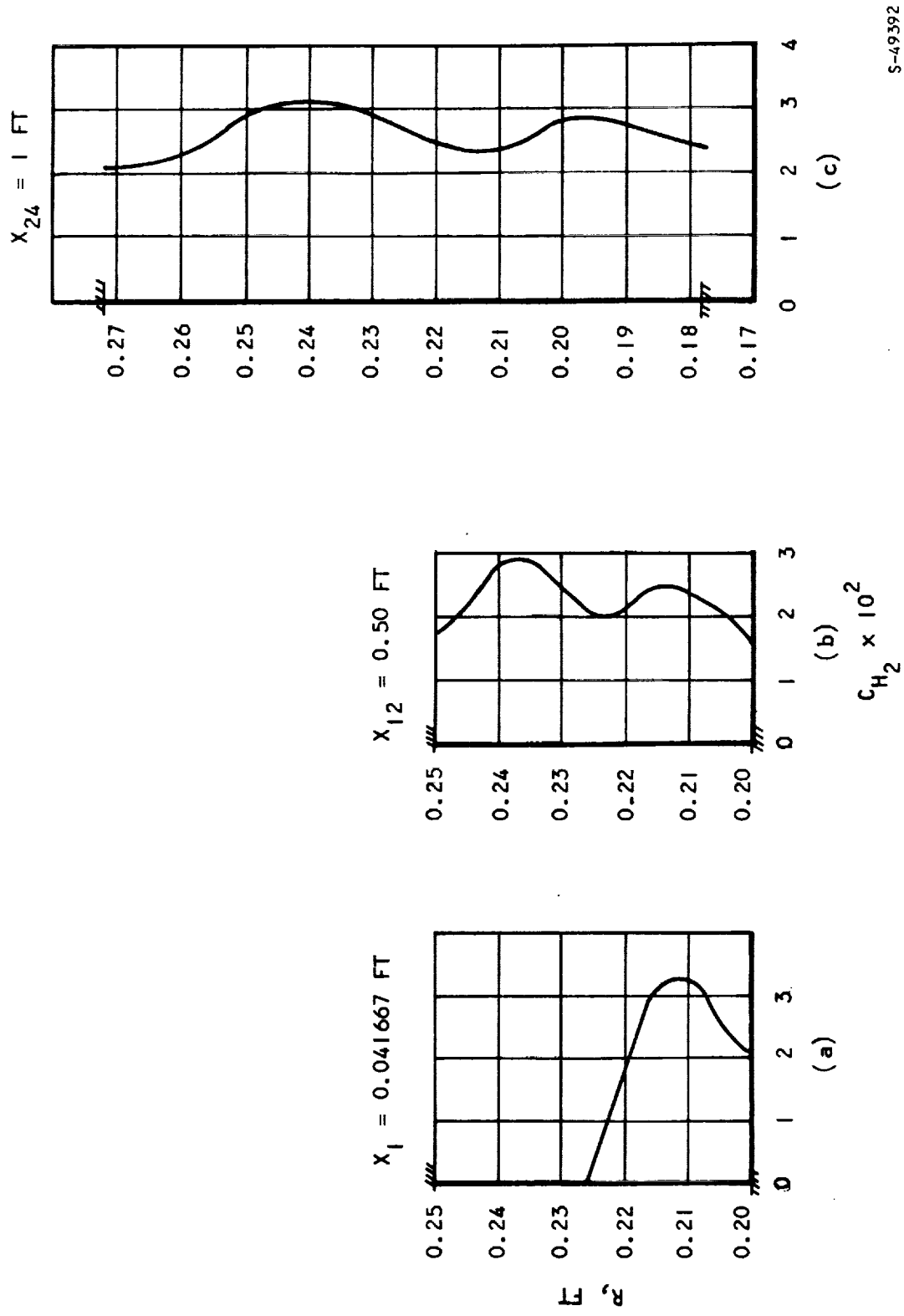

Figure D-9. Concentration Profiles

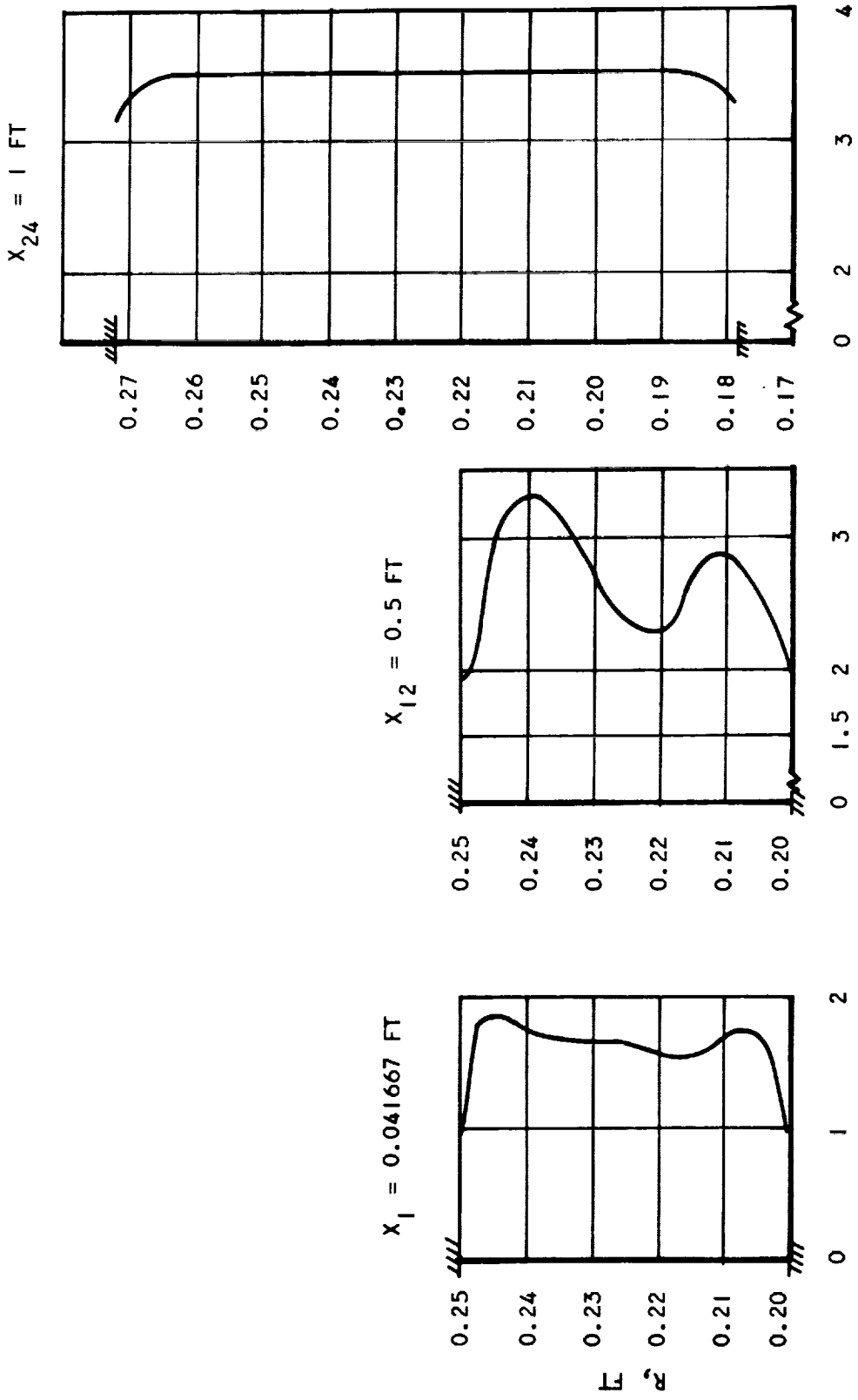

Figure D-10. Static-Temperature Profiles

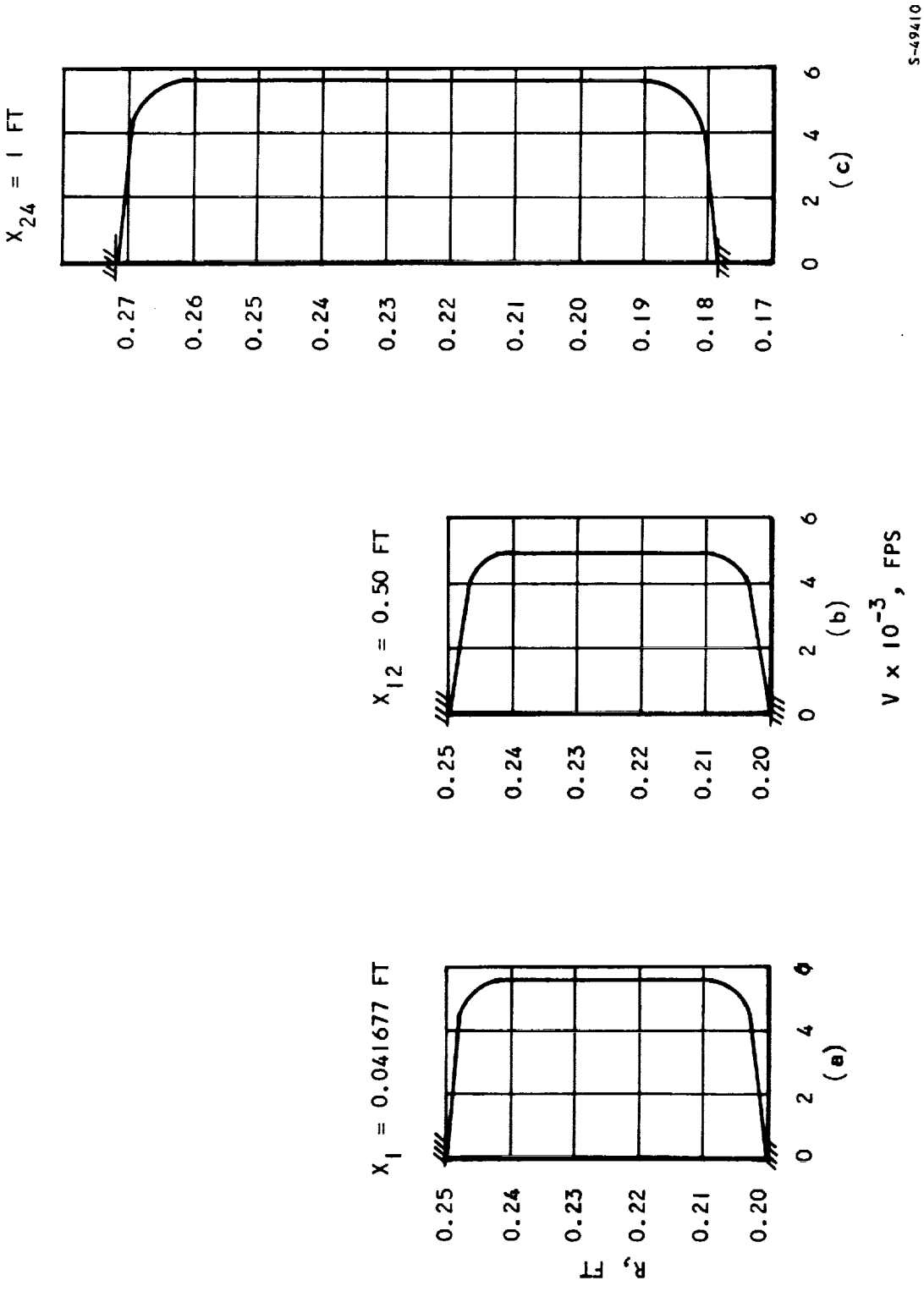

Figure D-11. Velocity Profiles

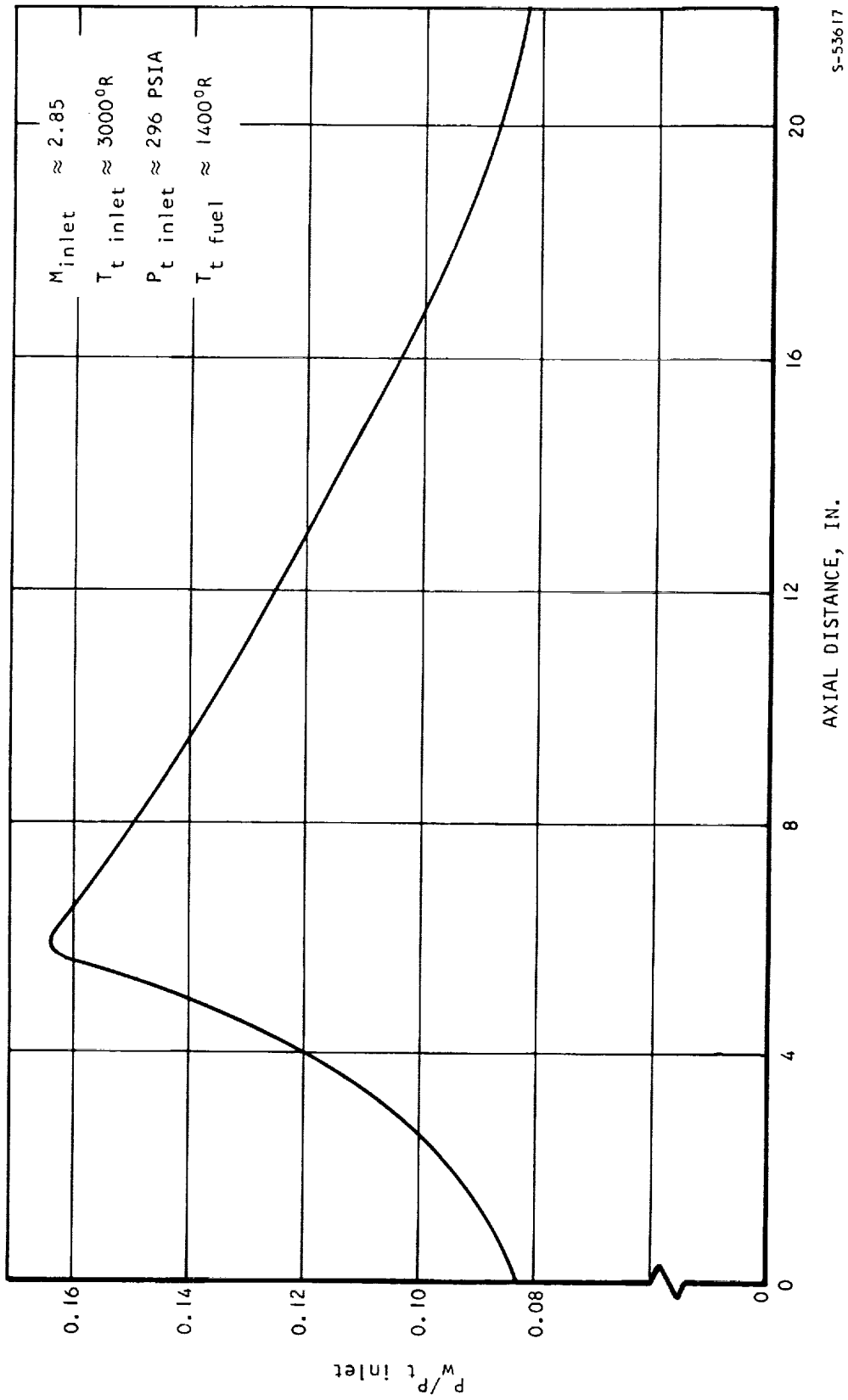

Figure D-12. Pressure Distribution

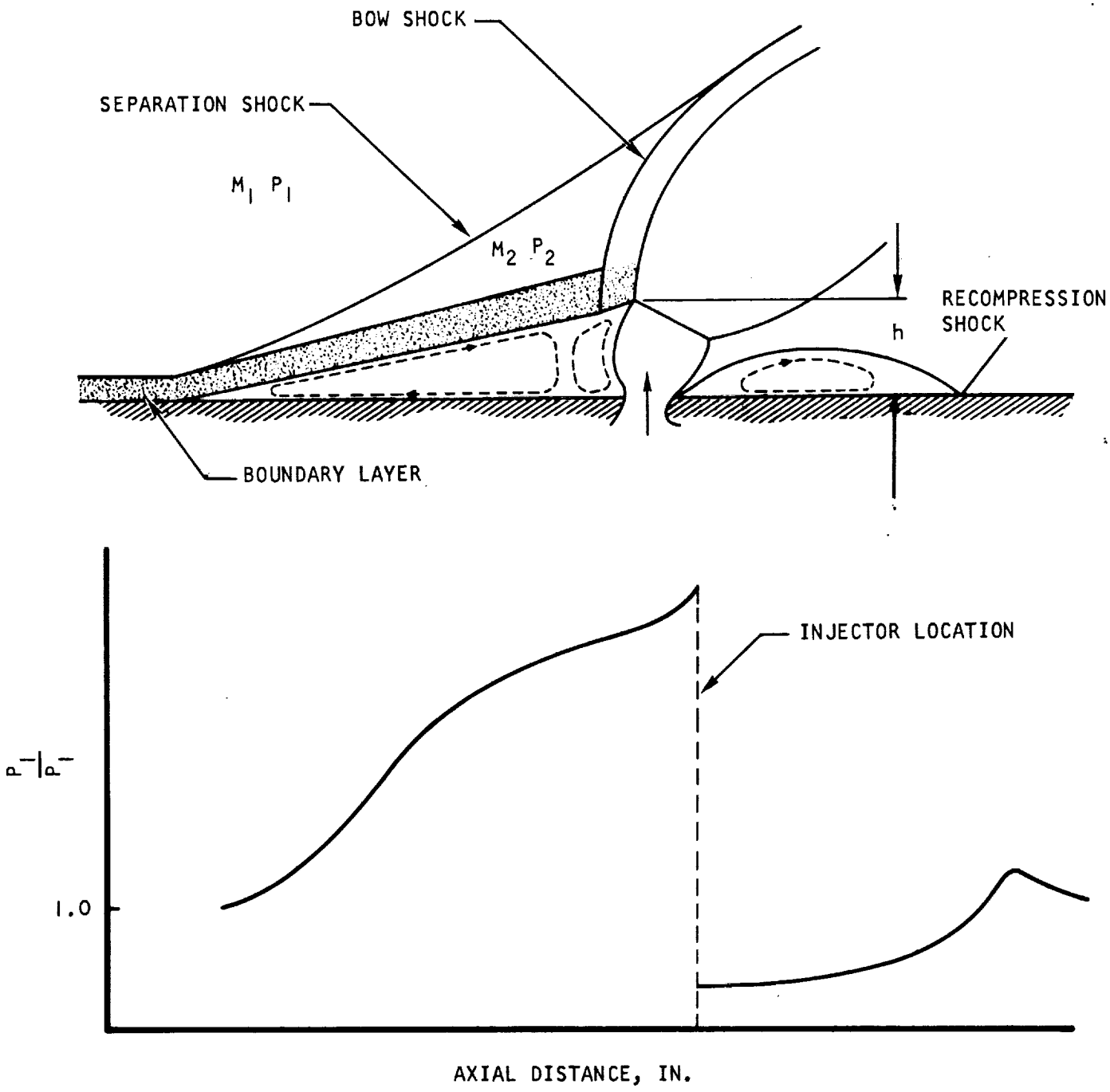

Figure D-13. Sketches of Flowfield and Pressure Distribution

spontaneously. Local burning increases the static pressure and temperature. This disturbance will also be propagated upstream through the boundary layer, producing additional boundary layer separation.

D.3 RECOMMENDATION

A complete understanding of flow separation was not established. The large number of variables involved made satisfactory theoretical solutions and generalization of experimental results difficult to achieve. However, if an improved simplified model could be constructed, the prediction of combustion in supersonic flow could be improved. Data presented by Sterrett and Holloway (Reference D-13) indicate that the two-dimensional turbulent boundary layer separation produced by the flow over a forward-facing step is similar to the separation flow field produced by a jet. Therefore, it should be possible to use results obtained from studies of flow over forward-facing steps to describe separation induced by jet penetration.

The general approach would be as follows:

(a) Select a simple body shape to represent the dividing streamline between the injected and primary flows (Figure D-14a).

(b) Calculate the equivalent height of the body used to define the separation produced by jet injection, using the equation obtained from a momentum balance (References D-14 and D-15).

(c) Correlate the equivalent height (h), and estimate the separation distance (X_s) from information obtained in the studies of flow over forward-facing steps (Reference D-16).

(d) Assume that the lower boundary of the shear layer in the separated region is roughly linear and extends from the separation point to the corner of the equivalent step. The pressure rise is therefore assumed to correspond to that produced by flow over a wedge of angle $\theta = \cot^{-1}\left(\frac{X_s}{h}\right)$ (Reference D-16).

(e) Use the wedge (θ, X_s, h) to represent the separation region; i.e., the combustor wall upstream of the injector (the injection side) is displaced by an angle θ.

The above suggested model could then account for the jet-induced-separation flow field.

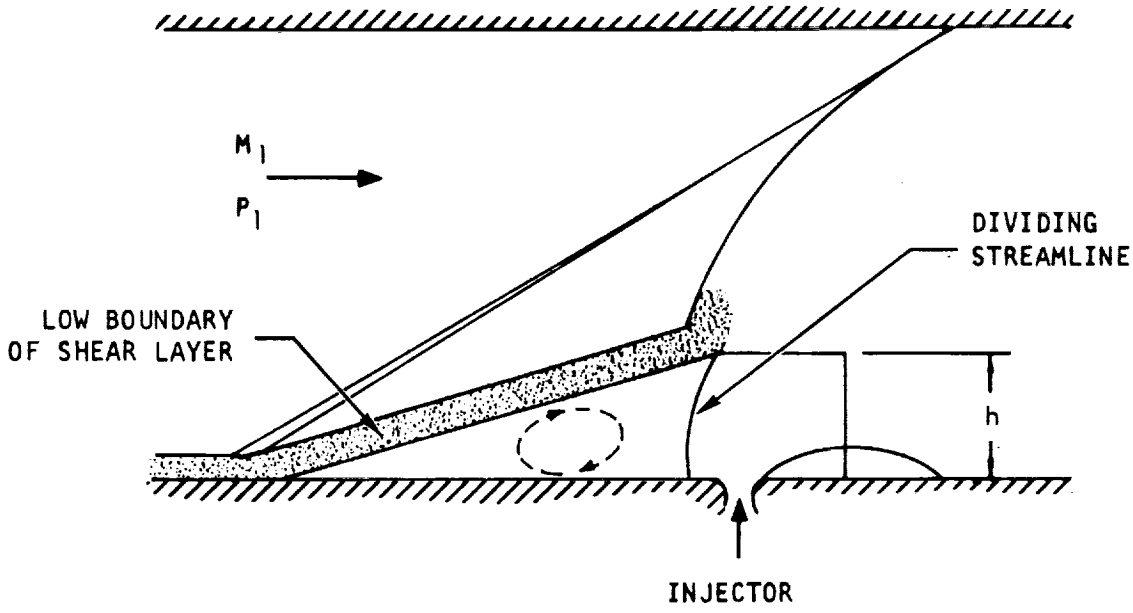

(a) Simplified Flowfield Used in Analysis

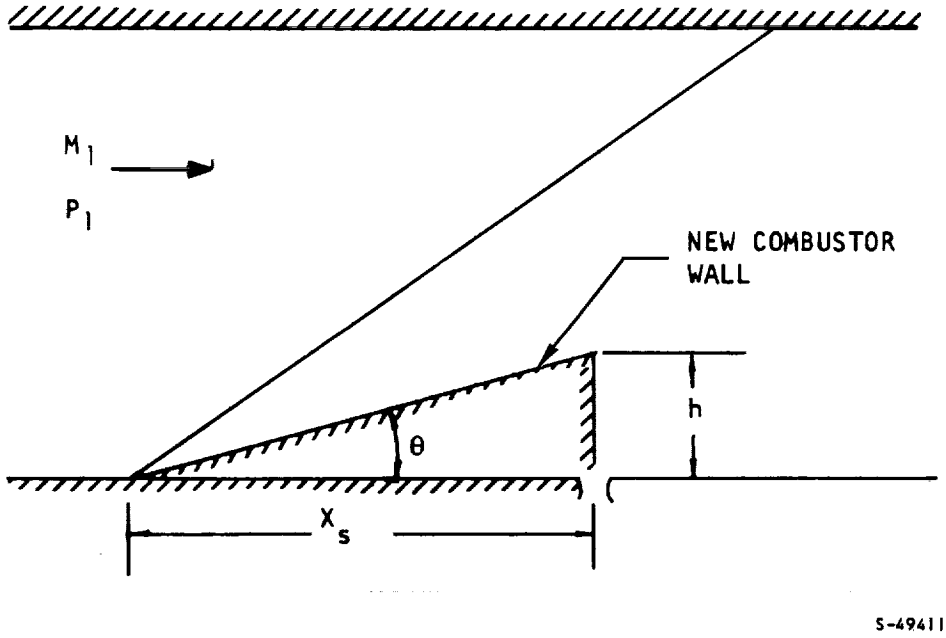

(b) Simplified Separation Region Upstream of the Injector

Figure D-14. Comparison of Flowfield and Separation Region

REFERENCES
(Appendix D)

D-1. Vranos, A., and J. J. Nolan, "Supersonic Mixing of Light Gas and Air," AIAA Meeting, Colorado Springs, July 1965.

D-2. Torrence, M. G., "Concentration Measurement of an Injected Gas in Supersonic Streams," NASA TND-3860, April 1967.

D-3. Schlichting, H. B., "Boundary Layer Theory," McGraw-Hill Book Co., Inc., 1960.

D-4. Ferri, A., P. A. Libby, and V. Zakkay, "Theoretical and Experimental Investigation of Supersonic Combustion," Polytechnical Institute of Brooklyn, PIBAL Report No. 713, ARL 62-467 AD 271712, September, 1962.

D-5. Alpinieri, L. J., "An Experimental Investigation of the Turbulent Mixing of Nonhomogeneous Coaxial Jets." Polytechnic Institute of Brooklyn, PIBAL Report No. 789, AFOSR, November 1965.

D-6. Ragsdale, R. G., and O. J. Edwards, "Data Comparisons and Photographic Observations of Coaxial Mixing of Dissimilar Gases at Nearly Equal Stream Velocities." NASA TN D-3131, December 1965.

D-7. Peters, C. E., T. Peters, and R. B. Billings, "Mixing and Burning of Bounded Coaxial Streams," ARO, Inc., Arnold Engineering Development Center, AEDC-TR-65-4, March 1965.

D-8. Schetz, J. A., "Analysis of the Mixing and Combustion of Gaseous and Particle-Laden Jets in an Air Stream," AIAA 7th Aerospace Sciences Meeting, New York City, January 1969.

D-9. Nicholls, J. A., "Stabilization of Gaseous Detonation Waves with Emphasis on the Ignition Delay Zone," PhD. Thesis, University of Michigan, 1960.

D-10. Perganent, H. S., "A Theoretical Analysis of Non-Equilibrium Hydrogen Air Reactions in Flow System," Paper No. 63-113, AIAA-ASME Hypersonic Ramjet Conference, April 23 - 25, 1963.

D-11. Ferri, A., "Review of Problems in Application of Supersonic Combustion," GASL Seventh Lanchester Memorial Lecture Paper presented at Journal of the Royal Aeronautical Society, September 1964.

D-12. Moretti, G., "Analysis of Two-Dimensional Problems of Supersonic Combustion Controlled by Mixing," AIAA Aerospace Science Meeting, New York, N. Y., January 1964.

D-13. Sterrett, J. R., and P. F. Holloway, "On the Effect of Transition on Parameters Within a Separation Region at Hypersonic Speeds - with Emphasis on Heat Transfer," Symposium on Fully Separated Flow, American Society of Mechanical Engineers, May 1964, pp. 15-26.

D-14. Zukoski, E. E., and F. W. Spaid, "Secondary Injection of Gases into a Supersonic Flow," AIAA Journal, Vol 2, No. 10, October 1964, pp 1689-1696.

D-15. Spaid, F. W., and E. E. Zukoski, "A Study of the Interaction of Gaseous Jets from Transverse Slots with Supersonic External Flows," AIAA Journal, Vol. 6, No. 2, February 1968, pp. 205 - 212.

D-16. Zukoski, E. E., "Turbulent Boundary Layer Separation in Front of a Forward-Facing Step," AIAA Journal, Vol. 5, No. 10, October 1967, pp. 1746 - 1752.

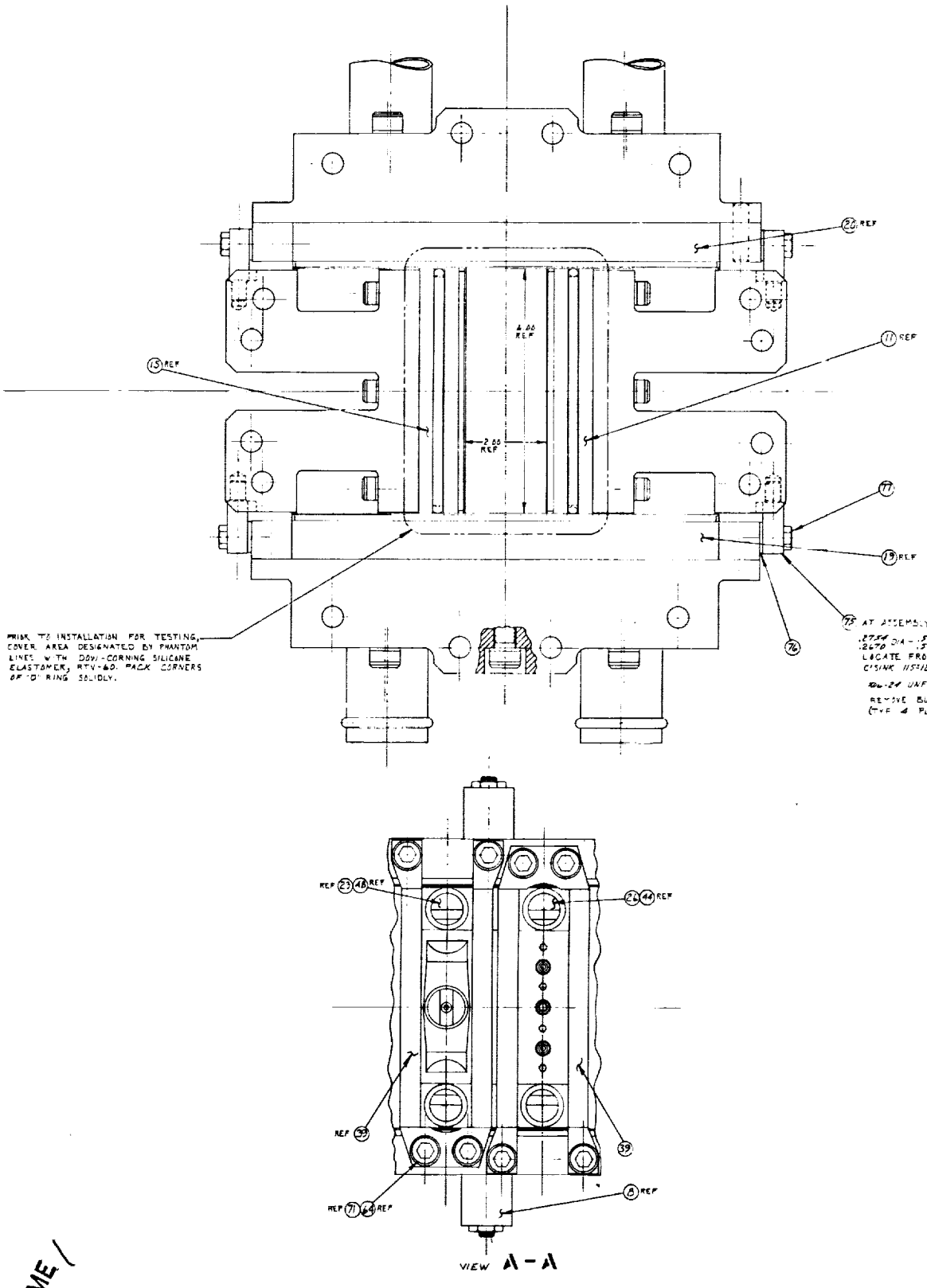

FOLDOUT FRAME 1

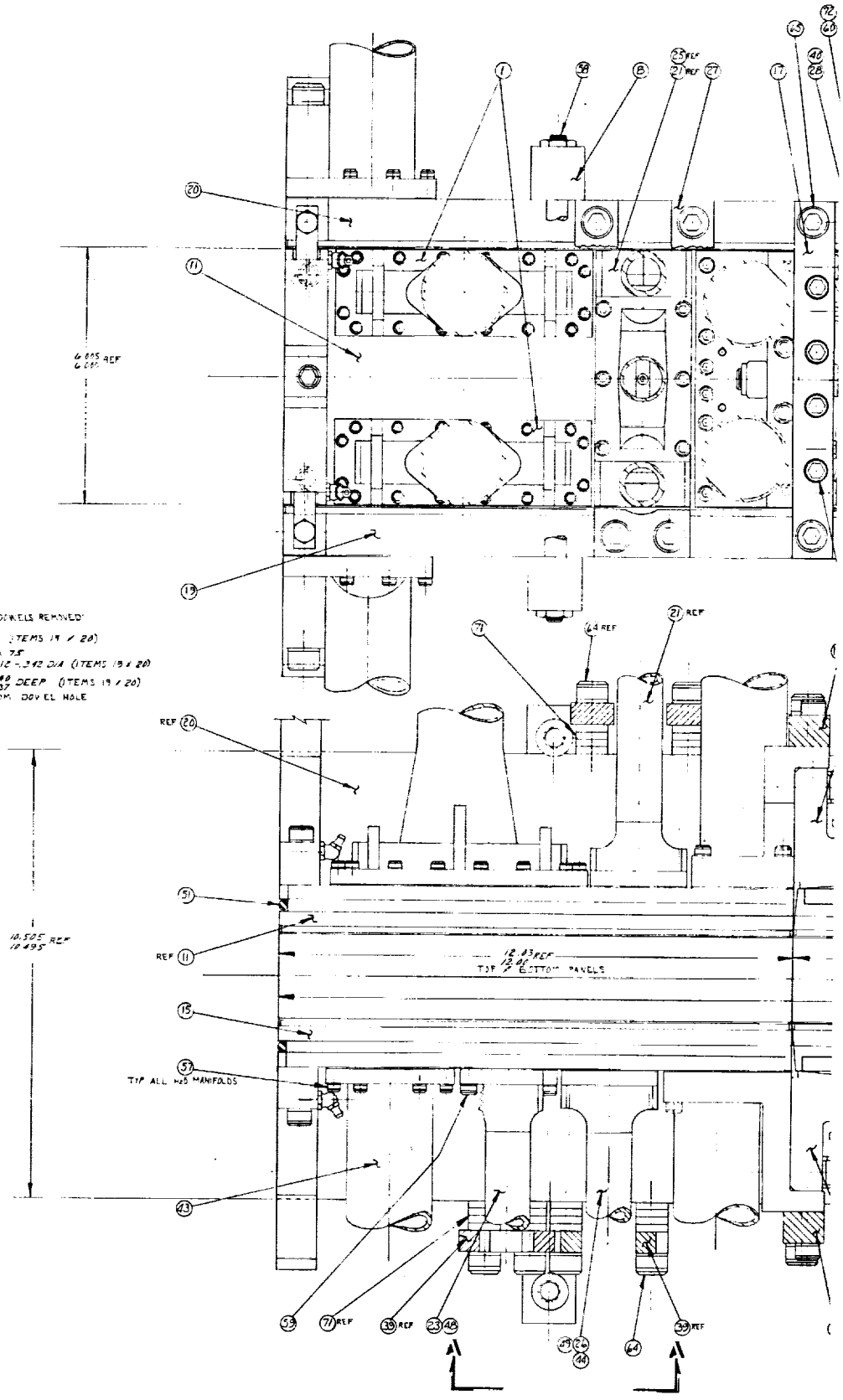

FOLDOUT FRAME 2

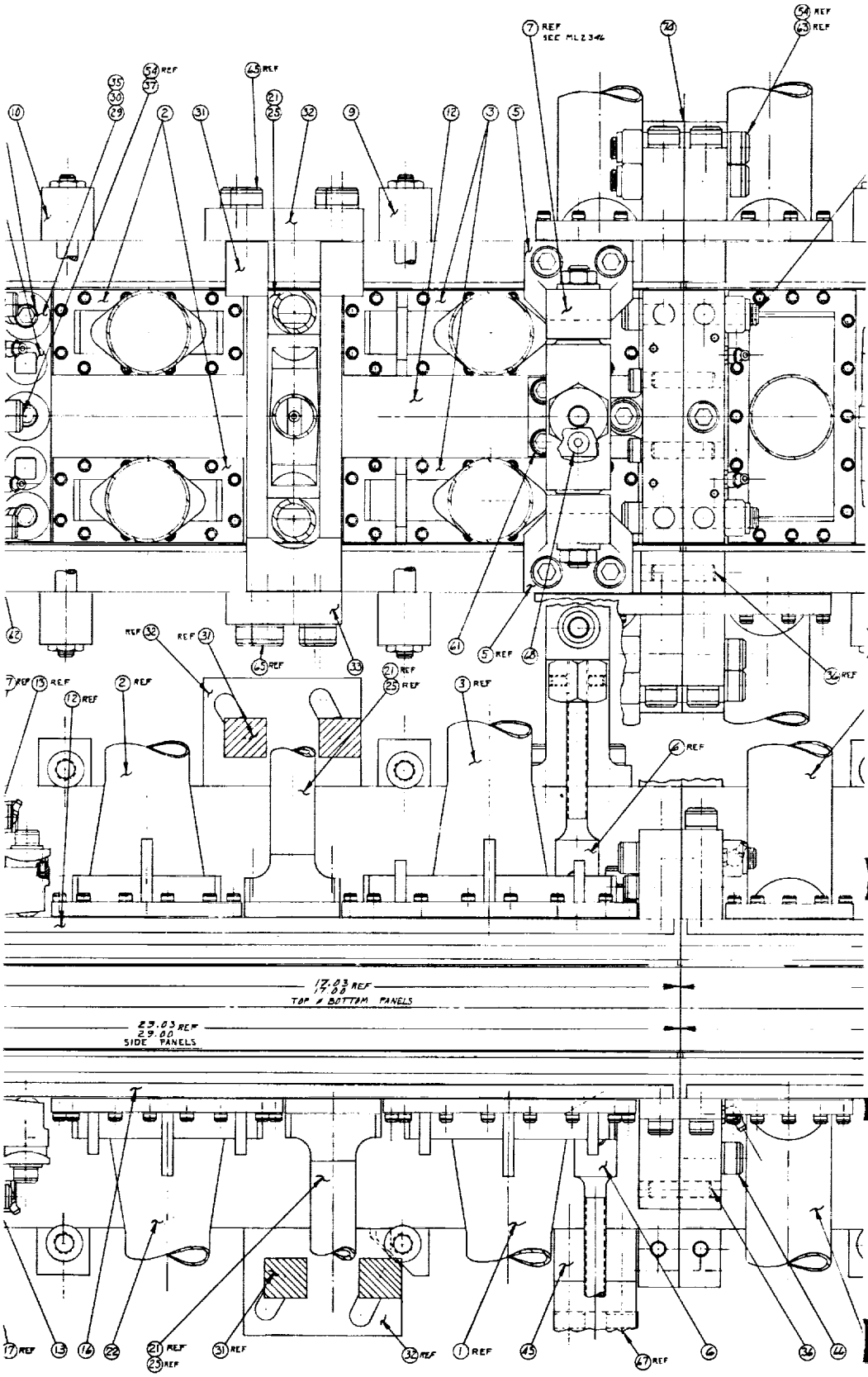

FOLDOUT FRAME

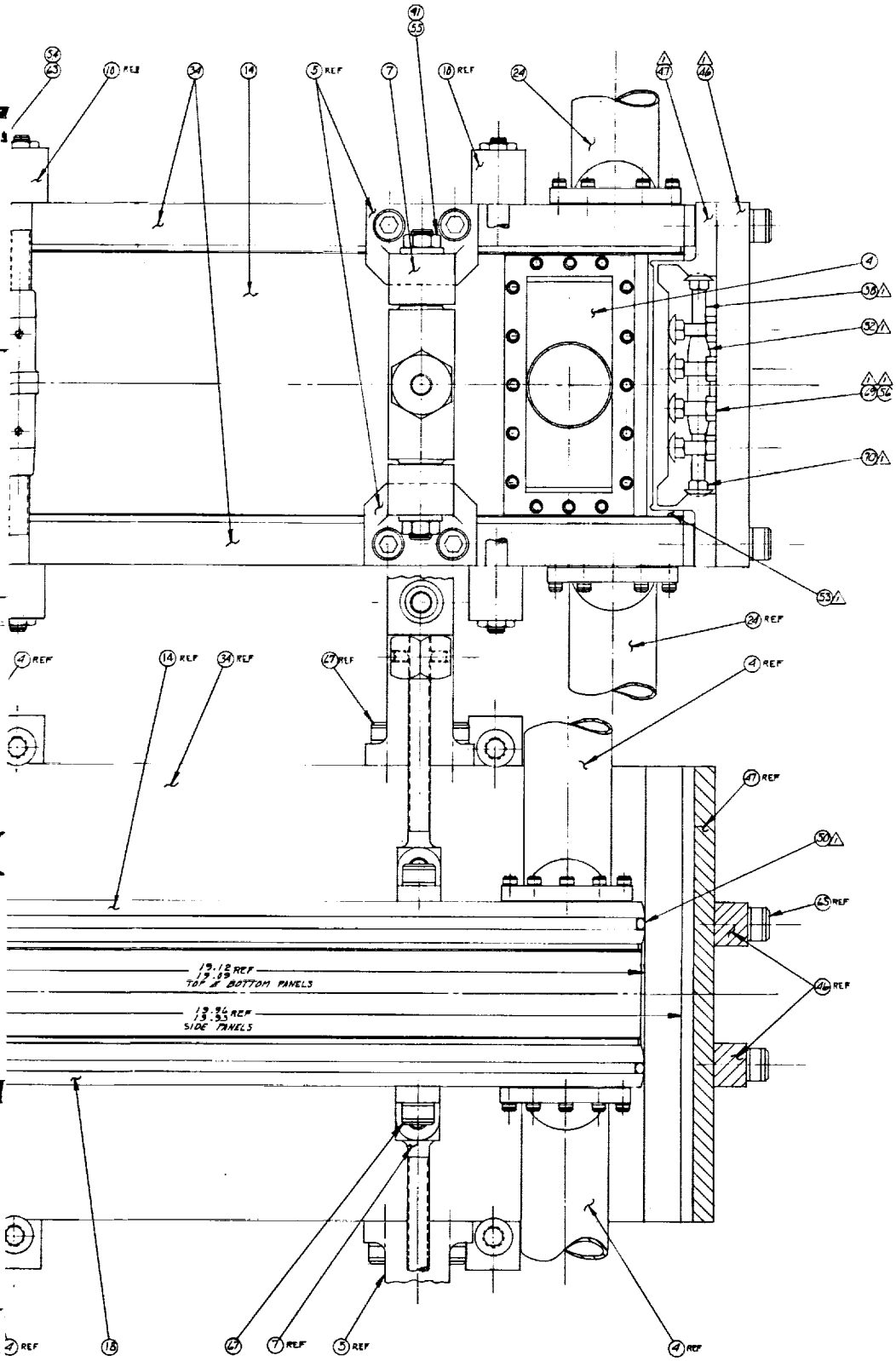

FOLDOUT FRAME 3

REV	ZONE	DESCRIPTION	DATE	APPROVED
A		1. REMOVED: ITEM 42 2. ADDED: ITEM 73 3. ITEM 21 WAS ML2359-1 4. ITEM 23 WAS ML2361-1 5. ITEM 26 WAS ML2364-1 6. ITEM 49 WAS MS29513-014 7. ITEM 49 WAS QTY. 2 8. ITEM 59 WAS 1/4-28 x 1 1/4 LG 9. ITEM 60 WAS 5/16-24 x 2 1/4 LG 10. ADDED: ITEM 74	[illegible]	
B		ADDED: ITEMS 75, 76 & 77	[illegible]	

	4	77	5/16-24 X 7/8 LG	BOLT - HEX. HD. C1038 ⅜ STL. OR EQUAL			
	AR	76	.005 LAM.	SHIM - CRES			
	4	75	ML2481	CLAMP			
	2	74	ML2555	GASKET			
(OPTIONAL)	1	73	ML2499-21	ASSY - FUEL INJECTOR			
	6	72	5815?NILL-125	WASHER			
	44	71	5815?N229-475	WASHER			
△1	6	70	5/16-24 x 2 LG	STEEL CARRIAGE BOLT LT. H. THD			
△1	8	69	5/16-24 x 1½ LG	STEEL CARRIAGE BOLT RT. H. THD			
	4	68	1/4-28 x 5/8 LG	NYLOK FLAT HD. STL. SOCKET ⅜ ...		ALLOY STEEL	MIL-B-933
	16	67	1/2-20 x 2.00 LG	NYLOK KNURLED ⅜ CAP SCREW			
	2	66	1/2-20 x 2.00 LG	↓		↓	↓
	36	65	1/2-20 x 1¼ LG	↓		↓	↓
	12	64	1/2-20 x 1¾ LG	↓		↓	↓
	10	63	1/2-20 x 3.00 LG	↓		↓	↓
	8	62	5/16-24 x 1¾ LG	↓		↓	↓
	4	61	5/16-24 x ¾ LG	↓		↓	↓
	6	60	5/16-24 x 2 LG	↓		↓	↓
	30	59	1/4-28 x ¾ LG	↓		↓	↓
	20	58	1/4-28 x 1¼ LG	↓		↓	↓
	274	57	#10-32 x ⅝ LG	NYLOK KNURLED ⅜ CAP SCREW		ALLOY STEEL	MIL-B-933
△1	8	56	AN345C516	NUT			
	8	55	525-518-9...	NUT			
	12	54	MS21044C8	NUT			
△1	1	53	.125 x 7⅛ x 10⅞	GASKET		BUTYL OR VITON	
△1	6	52	MS21251-6S	TURNBUCKLE BODY			
	2	51	.210 w x 102.00 LG	"O" RING GASKET		BUTYL OR VITON	
△1	2	50	.210 w x 6.00 LG	"O" RING GASKET		BUTYL OR VITON	
	5	49	4.250 I.D. x .070	"O" RING GASKET		SILICONE RUBBER	
	1	48	ML2388-1	PLUG - FUEL INJECTOR			
△1	1	47	ML2387	PLATE - SEAL			
△1	2	46	ML2386	BAR CLAMP			
	2	45	ML2384	BRACKET - JOURNAL			
	1	44	ML2389-1	PLUG - FUEL INJECTOR			
	1	43	ML2381-1	MANIFOLD - WATER			
	[illegible]	[illegible]	[illegible]	[illegible]			
	8	41	5815?N3?3-??	WASHER			
	4	40	MS51964-64	SET SCREW			
	2	39	ML2376-1	BRACKET			
△1	6	38	5/16-24 x 2.00 LG	STEEL CARRIAGE BOLT RT. H. THD			
	2	37	1/2-20 x 2½ LG	NYLOK KNURLED ⅜ CAP SCREW		ALLOY STEEL	MIL-B-933
	8	36	AN122748	DOWEL			
	6	35	AN122691	DOWEL			
	2	34	ML2416-1	ASSY - SIDES, SECT. 2			
	2	33	ML2371	PLATE			
	2	32	ML2370	PLATE			
	2	31	ML2369-1	BRACKET			
	6	30	ML2368	PIVOT			
	6	29	ML2367	PIVOT			
	4	28	ML2366	SCREW - ADJUSTMENT			
	1	27	ML2365-1	BRACKET			
	1	26	ML2518	ASSEMBLY - IGNITER BLOCK			
	1	25	ML2363-1	PLUG - FUEL INJECTOR			
	2	24	ML2362-1	MANIFOLD - WATER			
	1	23	ML2499-11	ASSEMBLY - FUEL INJECTOR			
	2	22	ML2360-1	MANIFOLD - WATER			
	3	21	ML2499-1	ASSY - FUEL INJECTOR			
	1	20	ML2405-11	ASSY - SIDE, SECT. 1, LT			
	1	19	ML2405-1	ASSY. - SIDE, SECT. 1, RT.			
	1	18	ML2404-1	ASSY - BOTTOM SECT. 3			
	2	17	ML2355	BAR CLAMP			
	1	16	ML2403-1	ASSY - BOTTOM, SECT. 2			
	1	15	ML2402-1	ASSY - BOTTOM, SECT. 1			
	1	14	ML2401-1	ASSY - TOP, SECTION 3			
	2	13	ML2351	FLANGE			
	1	12	ML2400-1	ASSY - TOP, SECTION 2			
	1	11	ML2399-1	ASSY - TOP, SECTION 1			
	3	10	ML2348-1	ASSY. - BAR CLAMP			
	1	9	ML2348-21	ASSY. - BAR CLAMP			
	1	8	ML2348-11	ASSY. - BAR CLAMP			
	2	7	ML2347-1	ASSY. - JACK SCREW			
	2	6	ML2346-1	ASSY. - JACK SCREW			
	6	5	ML2345	BRACKET - JOURNAL			
	4	4	ML2344-1	MANIFOLD - WATER			
	2	3	ML2343-1	MANIFOLD - WATER			
	2	2	ML2342-1	MANIFOLD - WATER			
	4	1	ML2341-1	MANIFOLD - WATER			

LIST OF MATERIAL

4. TORQUE ALL BOLTS TO THE FOLLOWING REQUIREMENTS:

#10-32	28-32 IN. LBS.
1/4-28	85-100 IN. LBS.
5/16-24	140-150 IN. LBS.
3/8-24	250-275 IN. LBS.
1/2-20	550-575 IN. LBS.

3. USE JOHNS-MANSVILLE .032 GASKET MATERIAL, (OR EQUAL) SUITABLE FOR WATER SERVICE, BETWEEN ALL H_2O MANIFOLDS AND PANELS.

2. USE DOW-CORNING SILICONE ELASTOMER, RTV-60, TO SEAL FLANGED JOINTS. FILL TO OVERFLOW USING ALEMITE FITTINGS PROVIDED.

△1 THESE ITEMS USED FOR PRESSURE TEST ONLY, PRIOR TO EACH HOT FIRE TEST.

NOTES: UNLESS OTHERWISE SPECIFIED

2-5-67

ASSEMBLY - 2-D NOZZLE & COMBUSTOR TEST CHAMBER

70210 | J | ML2340

SCALE FULL | SHEET 1

76-4-6

FOLDOUT FRAME 4

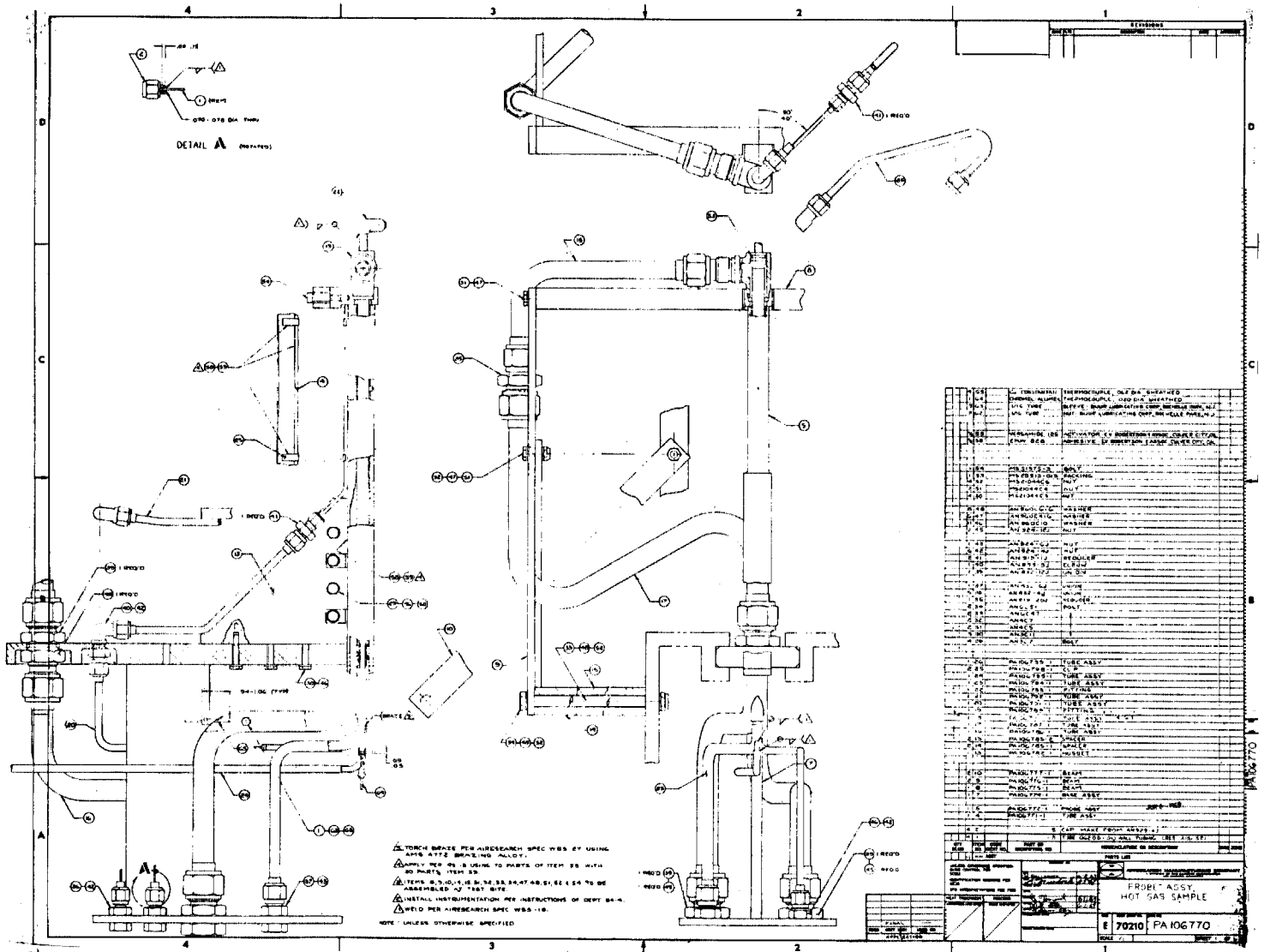

FOLDOUT FRAME

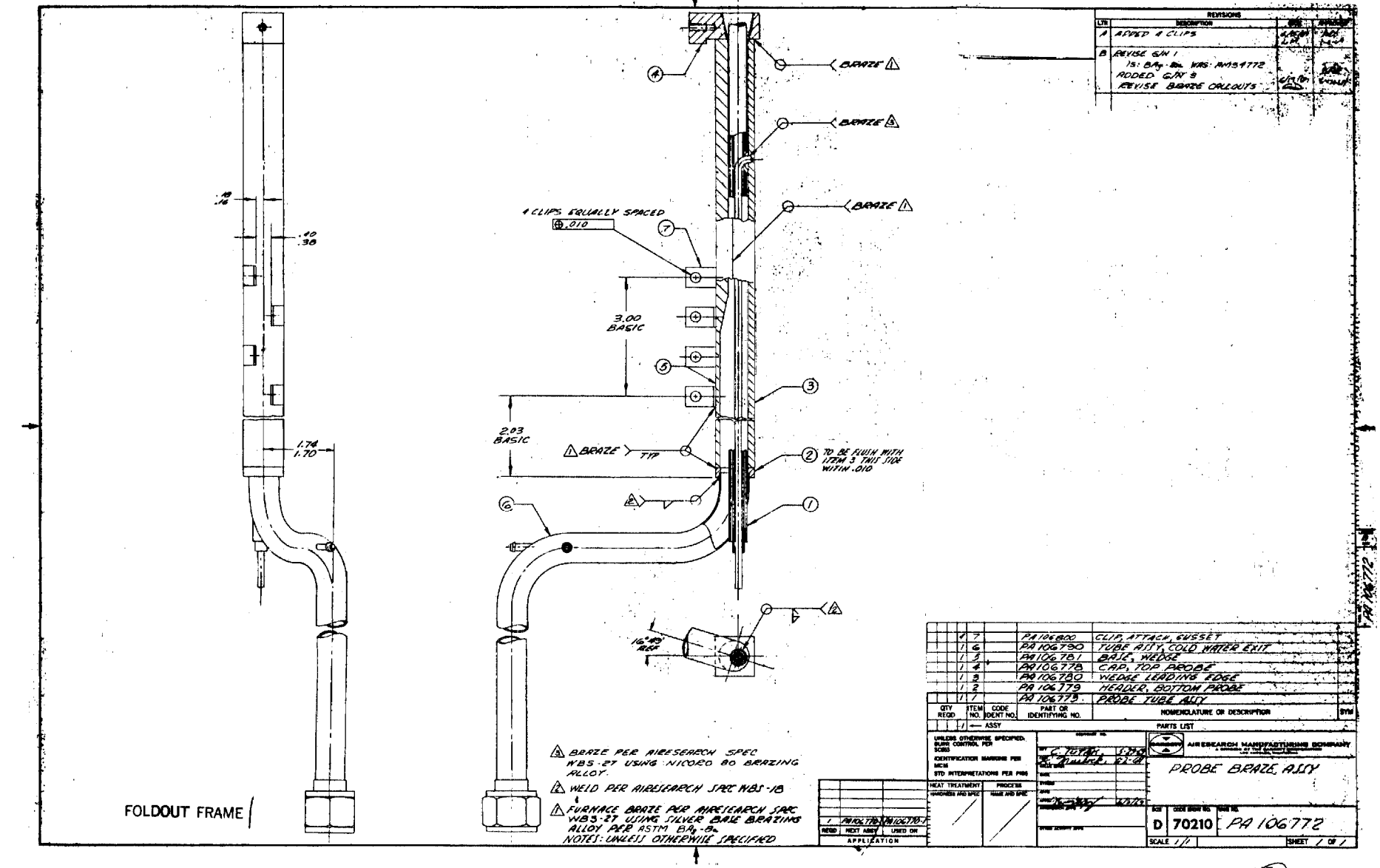

LTR	DESCRIPTION	DATE	APPROVED
A	ADDED 4 CLIPS	4-26-64	
B	REVISE G/N 1 TO: BAg-8a VICE: AMS4772 ADDED G/N 9 REVISE BRAZE CALLOUTS	6-8-64	

QTY REQD	ITEM NO.	CODE IDENT NO.	PART OR IDENTIFYING NO.	NOMENCLATURE OR DESCRIPTION
1	7		PA 106800	CLIP, ATTACH, GUSSET
1	6		PA 106790	TUBE ASY, COLD WATER EXIT
1	5		PA 106781	BASE, WEDGE
1	4		PA 106778	CAP, TOP PROBE
1	3		PA 106780	WEDGE LEADING EDGE
1	2		PA 106779	HEADER, BOTTOM PROBE
1	1		PA 106773	PROBE TUBE ASY
1	—		ASSY	PARTS LIST

△ BRAZE PER AIRESEARCH SPEC MBS-27 USING NICORO 80 BRAZING ALLOY.

△ WELD PER AIRESEARCH SPEC MBS-18

△ FURNACE BRAZE PER AIRESEARCH SPEC MBS-27 USING SILVER BASE BRAZING ALLOY PER ASTM BAg-8a.

NOTES: UNLESS OTHERWISE SPECIFIED

UNLESS OTHERWISE SPECIFIED, SUBJ CONTROL PER SCRS

IDENTIFICATION MARKING PER MCMS

STD INTERPRETATIONS PER PRS

HEAT TREATMENT — HARDNESS AND SPEC

PROCESS — ISSUE AND SPEC

AIRESEARCH MANUFACTURING COMPANY

PROBE BRAZE ASY

D | 70210 | PA 106772

SCALE 1/1 | SHEET 1 OF 1

PA 106772

FOLDOUT FRAME 1

FOLDOUT FRAME 2

AIRESEARCH MANUFACTURING COMPANY
Los Angeles, California

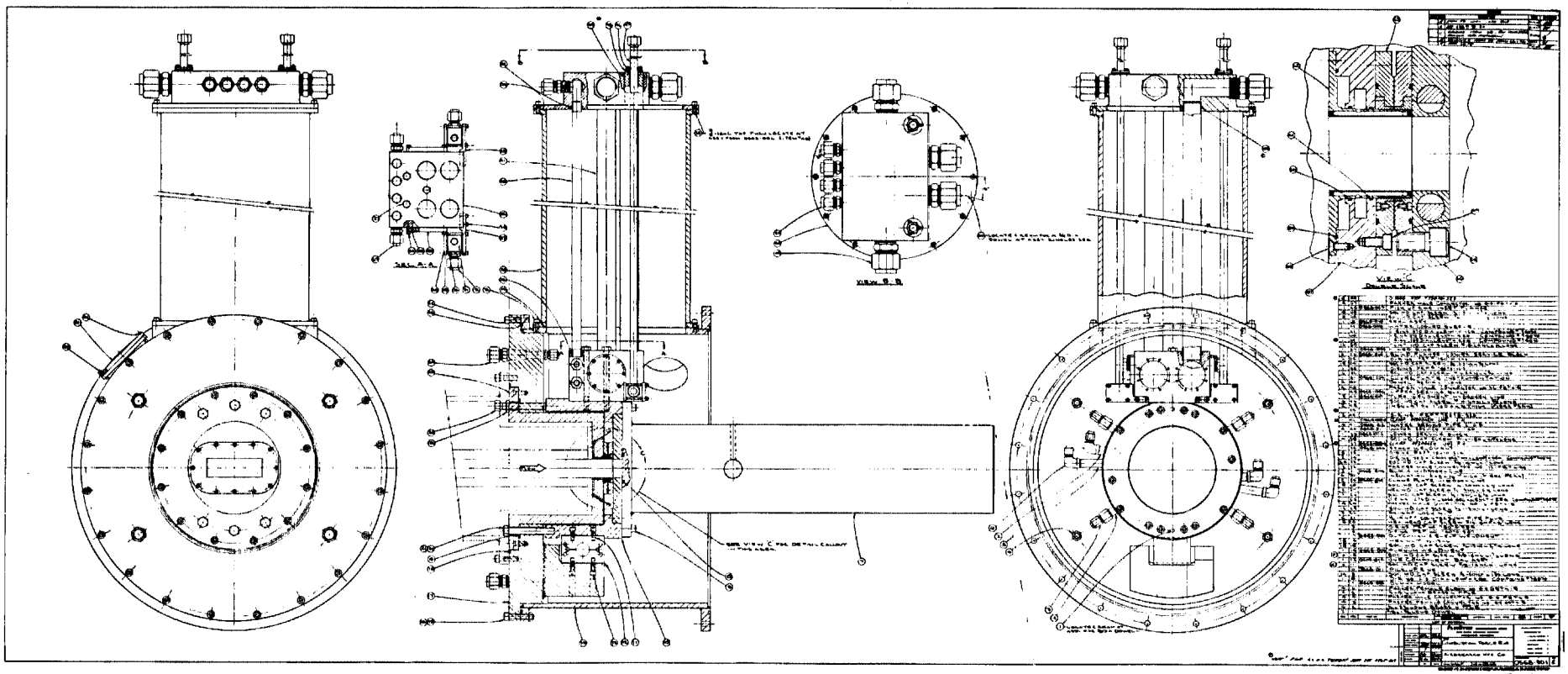

FOLDOUT FRAME 2

FOLDOUT FRAME 1

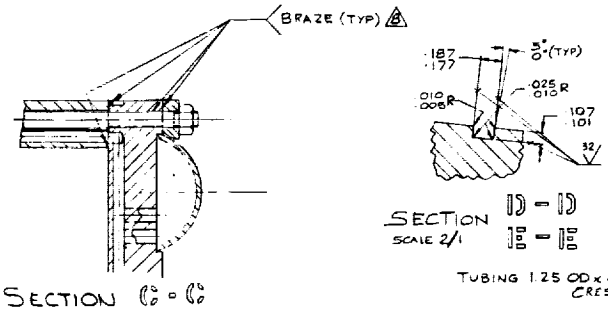

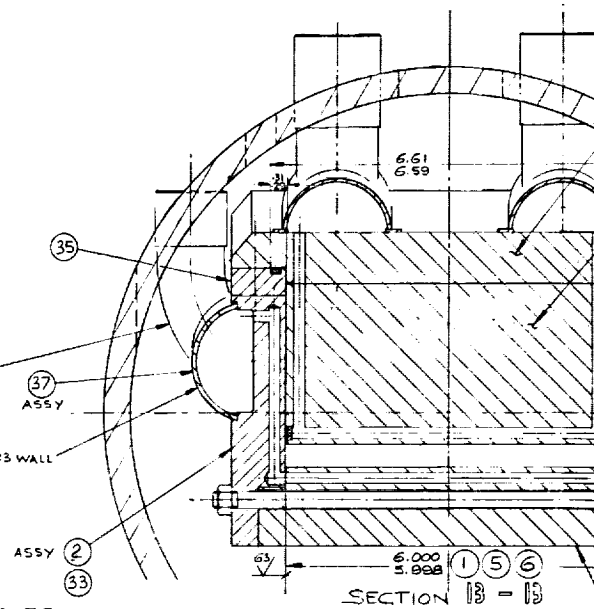

COORDINATES NOZZLE CONTOURS

TOL BAND ± .005 ON 'Y' DIMENSIONS (REF).

NOZZLE																									
8 M 2.9	R 4.50	Z = 4.769																							
	X	-.500	0	.036	.060	.096	.148	.206	.278	.453	.545	.669	.765	.930	1.082	1.311	1.470	1.779	2.202	2.711	3.324	4.063	4.953	6.026	7.187
	Y	.422	.422	.424	.425	.427	.433	.442	.457	.499	.525	.563	.595	.650	.702	.783	.839	.943	1.070	1.205	1.355	1.488	1.630	1.762	1.878
9 M 2.3 Y=1.37	R 4.00	Z = 4.410																							
	X	-.650	0	.220	.317	.407	.495	1.090	1.202	1.538	1.796	2.224	2.608	3.161	3.532	3.753	4.623	5.659	6.888	8.345					
	Y	.864	.864	.865	.865	.866	.868	.907	.920	.967	1.009	1.087	1.161	1.271	1.346	1.389	1.541	1.686	1.816	1.921					
10 M 1.6	R 4.00	Z = 4.440																							
	X	-1.00	0	.450	.541	.665	.834	.958	2.221	2.458	2.846	3.165	3.442	3.701	4.161	4.582	4.975	5.634	6.729	7.709	8.780				
	Y	1.541	1.541	1.542	1.542	1.542	1.543	1.544	1.576	1.589	1.614	1.637	1.657	1.680	1.718	1.756	1.792	1.858	1.914	1.958	1.988				
11 M 2.3 Y=1.28	R 2.00	Z = 3.890																							
	X	-1.00	0	.095	.146	.186	.240	.282	.318	.574	.722	.919	1.071	1.324	1.550	1.715	1.879	2.101	2.244	2.734	3.349	4.081	4.949	5.965	7.194
	Y	.538	.538	.538	.538	.538	.538	.540	.541	.542	.561	.580	.612	.639	.696	.738	.774	.810	.858	.883	.983	1.082	1.172	1.251	1.308	1.335

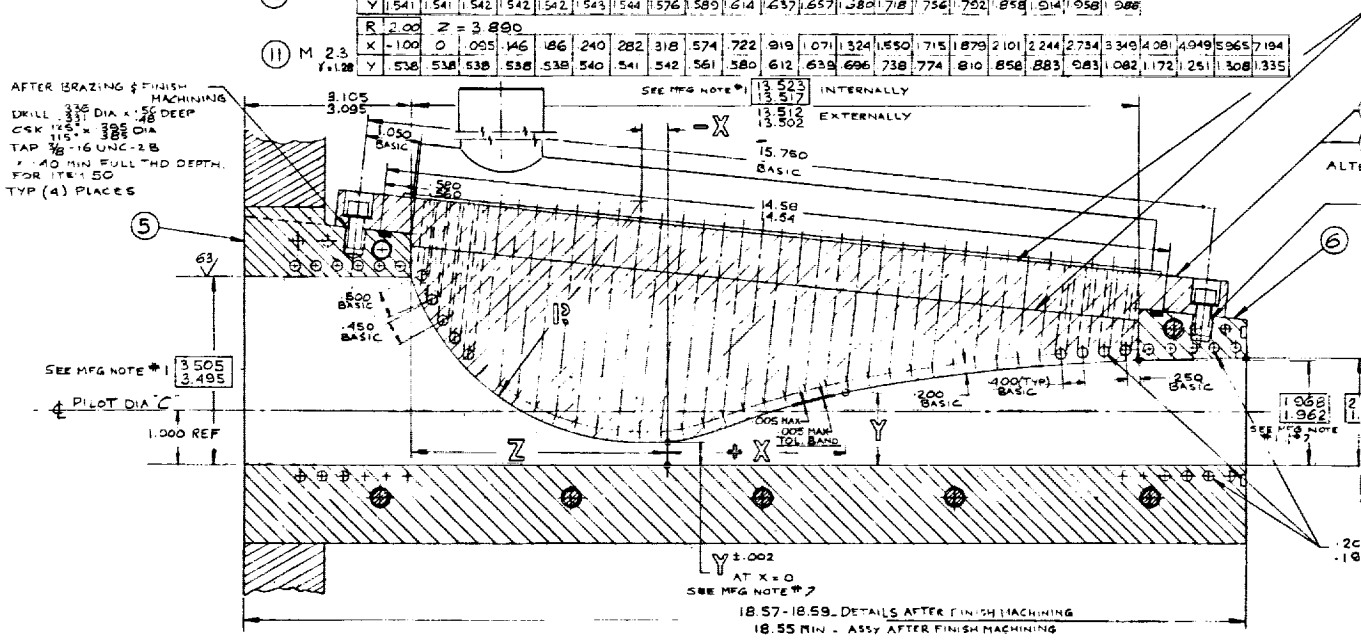

SECTION A - A

FOLDOUT FRAME 1

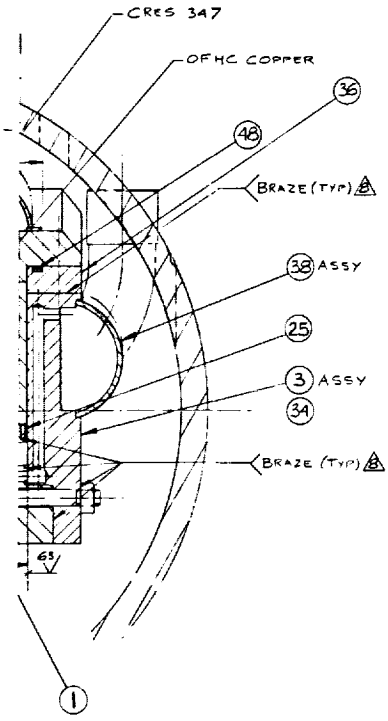

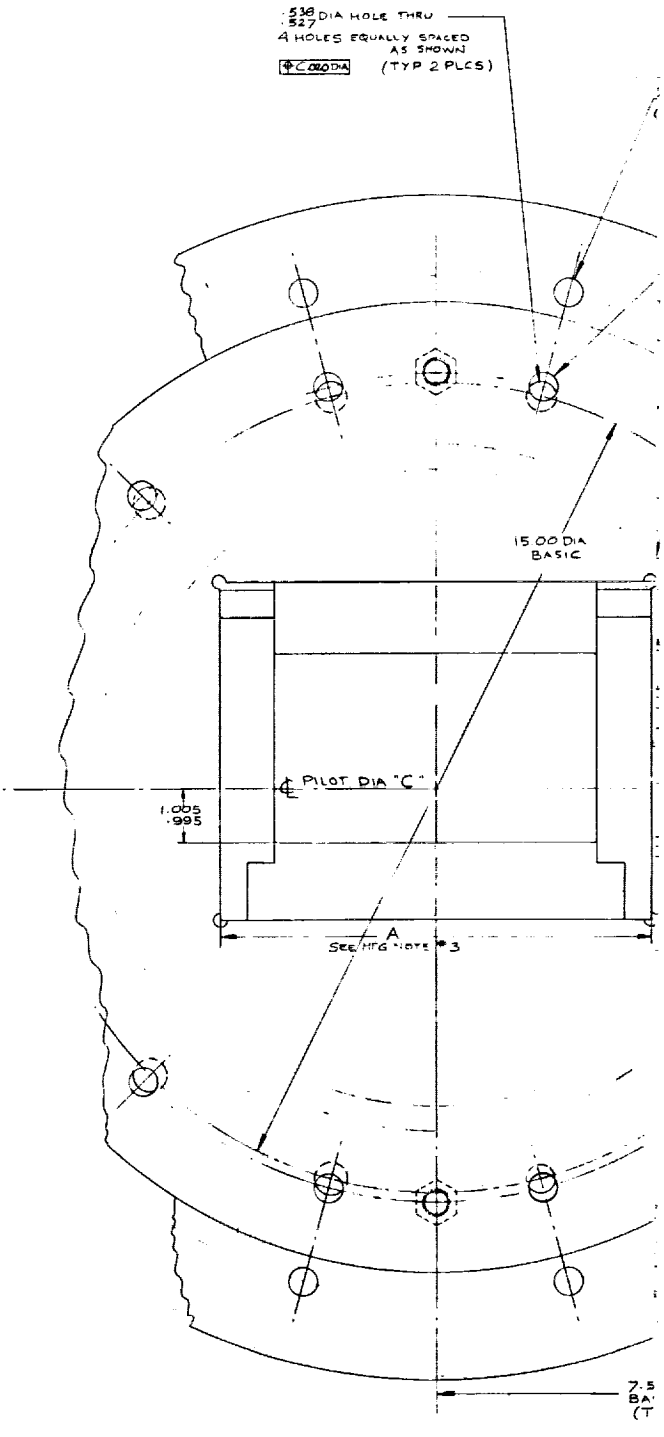

BRAZE 11

3 ASSY SHOWN

9 10 11 12 52 53 ASSEMBLIES

RNATIVE ITEMS

AFTER BRAZING & FINISH MACHINING
DRILL .336 DIA x .50 DEEP - FLAT BOTTOM
CSK 125° x .398 .388 DIA
TAP 3/8-16 UNC-2B x .40 MIN FULL THD DEPTH FOR ITEM 50
TYP (4) PLACES

63

.003 .997
SEE MFG NOTE #1

63

7 DIA HOLES

FOLDOUT FRAME 2

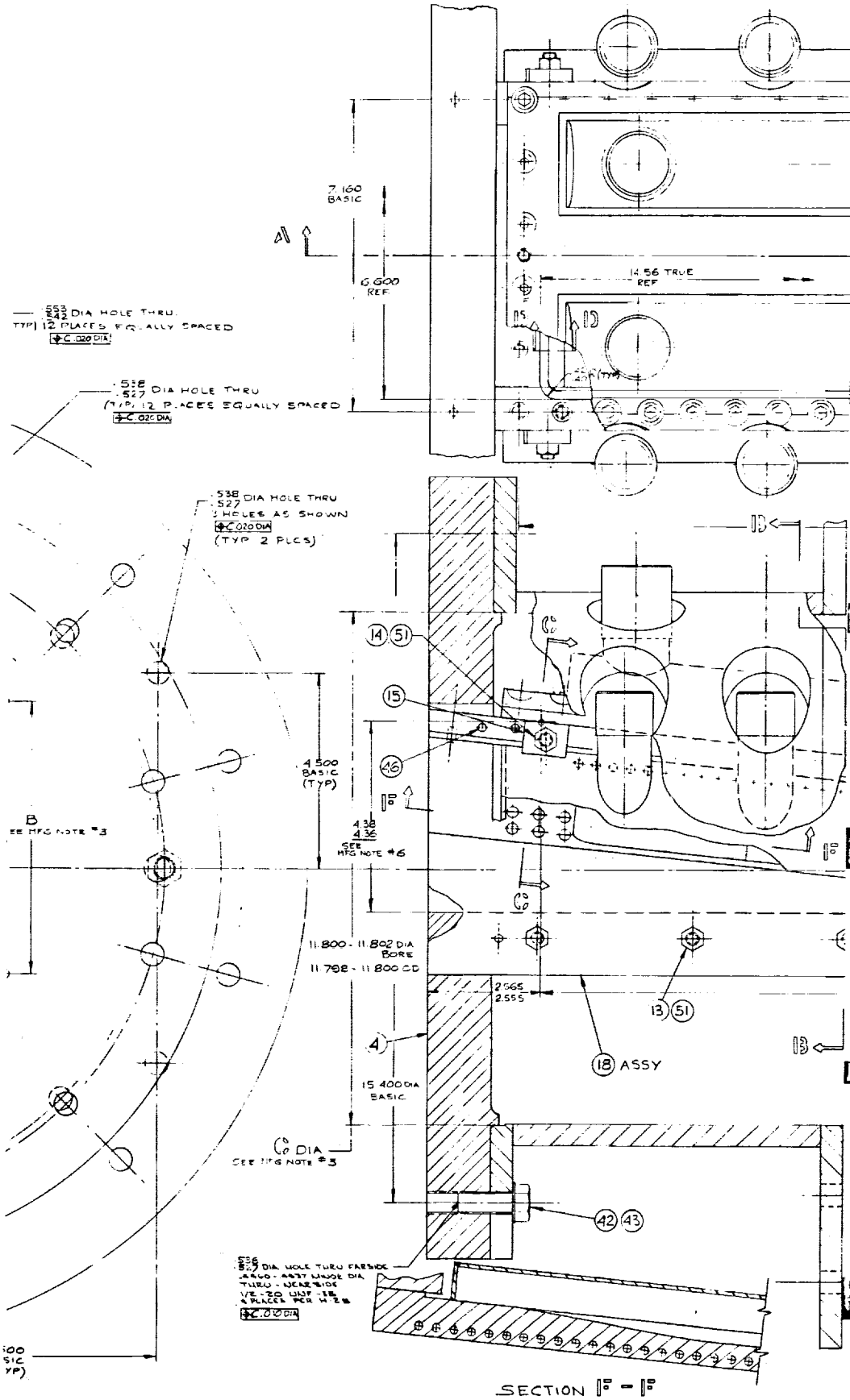

FOLDOUT FRAME 3

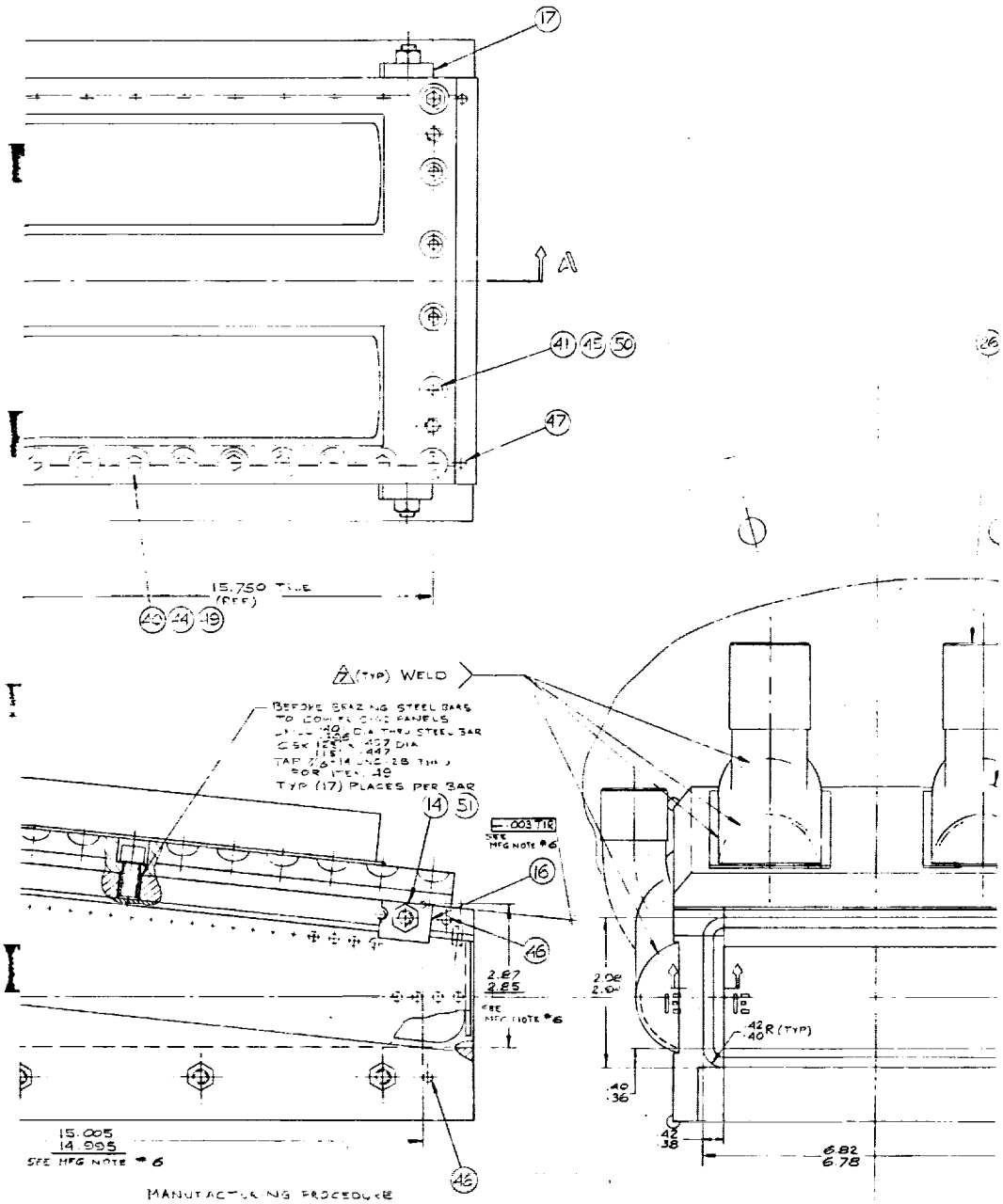

MANUFACTURING PROCEDURE

7 ASSY

1) BOLT ITEMS 1, 4, 5, 6 & 8 TOGETHER AS REQUIRED TO ACHIEVE CRITICAL DIMENSIONS AS SHOWN IN SECTION A-A (ENCLOSED DIMENSIONS)
2) DRILL DOWEL PILOT HOLES (5/16 DIA) THRU IN MATING PARTS
   40 DEEP (TYP 12 PLACES)
   DRILL & REAM .1570 DIA X .40 DEEP .36 IN ITEMS 1, 5 & 6
   DRILL & REAM .1600 DIA THRU IN ITEMS 2 & 3
   .1581
   PRESS ITEM 28 IN ITEMS 1, 5 & 6
3) RE-ASSEMBLE WITH BRAZING MATERIAL (FOIL) IN PLACE
   MEASURE A & B OF HOLE IN MOUNTING FLANGE (ITEM 4) & MATING END OF UNIT TO DETERMINE REQUIRED INCREASE IN FITTING SIZE TO GIVE AN INTERFACE CLEARANCE OF .004 TO .005
   • TAKE EQUAL AMOUNTS OFF VERTICAL SIDES OF HOLE — (REFERENCE ℄ TO BE WITHIN .000 AND .002 FROM ℄ OF DIA "C" (SEE SIDE AND
   • BOTTOM OF FLOW PATH TO BE .005-.010 BELOW ℄ OF THIS VIEWS) DIA "C" (SEE SIDE-& END VIEWS)
4) FURNACE BRAZE ENTIRE UNIT (ITEM 4 INCL)
5) FINISH MACHINE END SURFACES SMOOTH
   MACHINE O-RING GROOVE AS SHOWN
6) FINISH MACHINE UPPER SURFACE TO DIMENSIONS SHOWN (UNDERLINED DIMENSIONS) & MACHINE HOLES FOR INSERTS (ITEMS 31 & 32) & O-RING GROOVE
7) MACHINE NOZZLE BLOCKS TO MEET SPECIFIED DIMENSIONS SHOWN IN SECTION A-A (Y DIMENSION AT K=0)

18.000 DIA BASIC

⚠ BRAZE PER WBS BAU 3 PER AMS 4190 75 Au-20 Cu
10 PRESSURE TEST 15 MINUT
9 MACHINED SURF
⚠ BRAZE PER WBS
⚠ WELD PER WBS

FOLDOUT FRAME 3

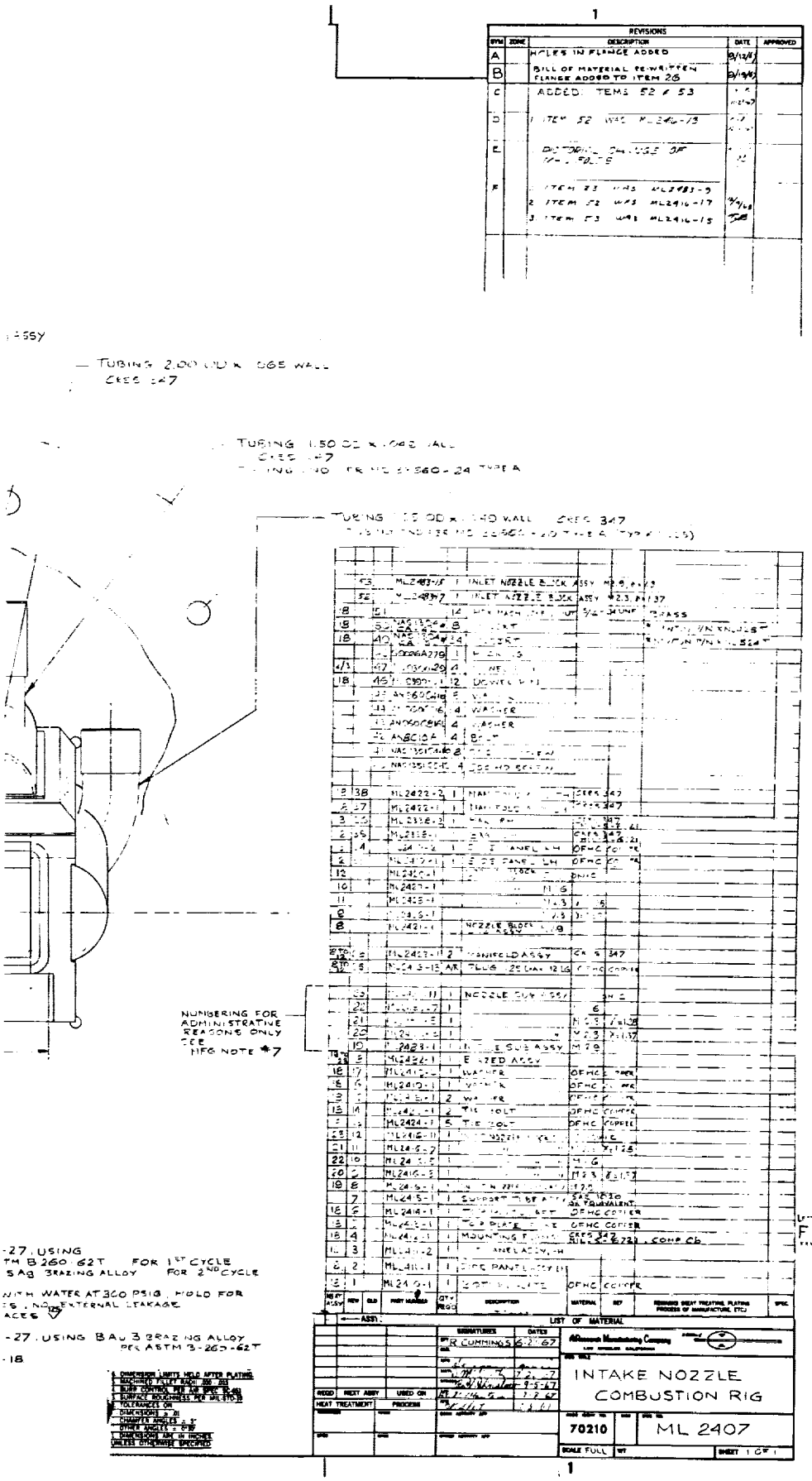

FOLDOUT FRAME 5

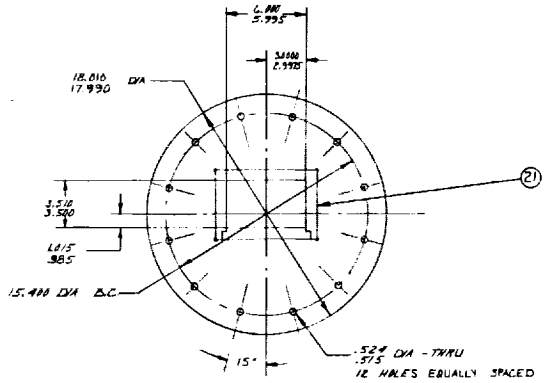

VIEW H-H
NAA INTERFACE

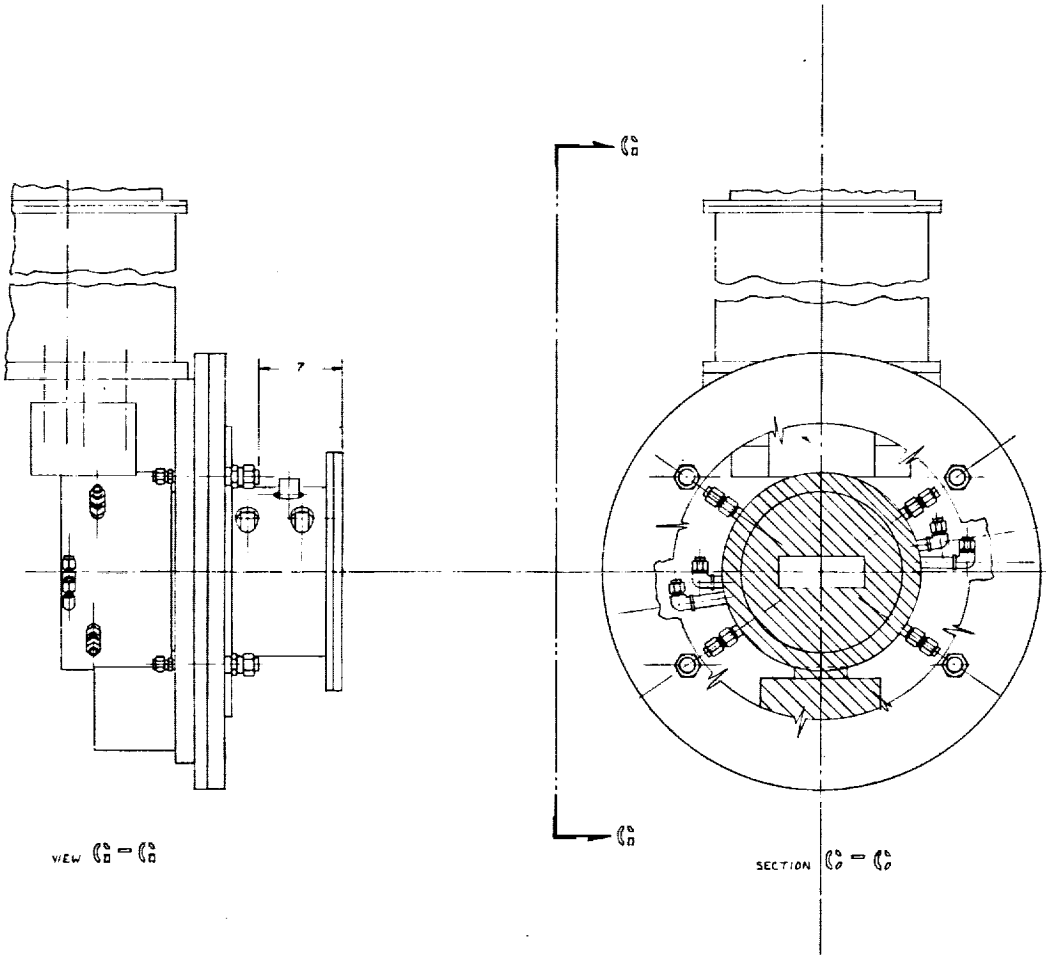

VIEW C-C

SECTION C-C

FOLDOUT FRAME 1

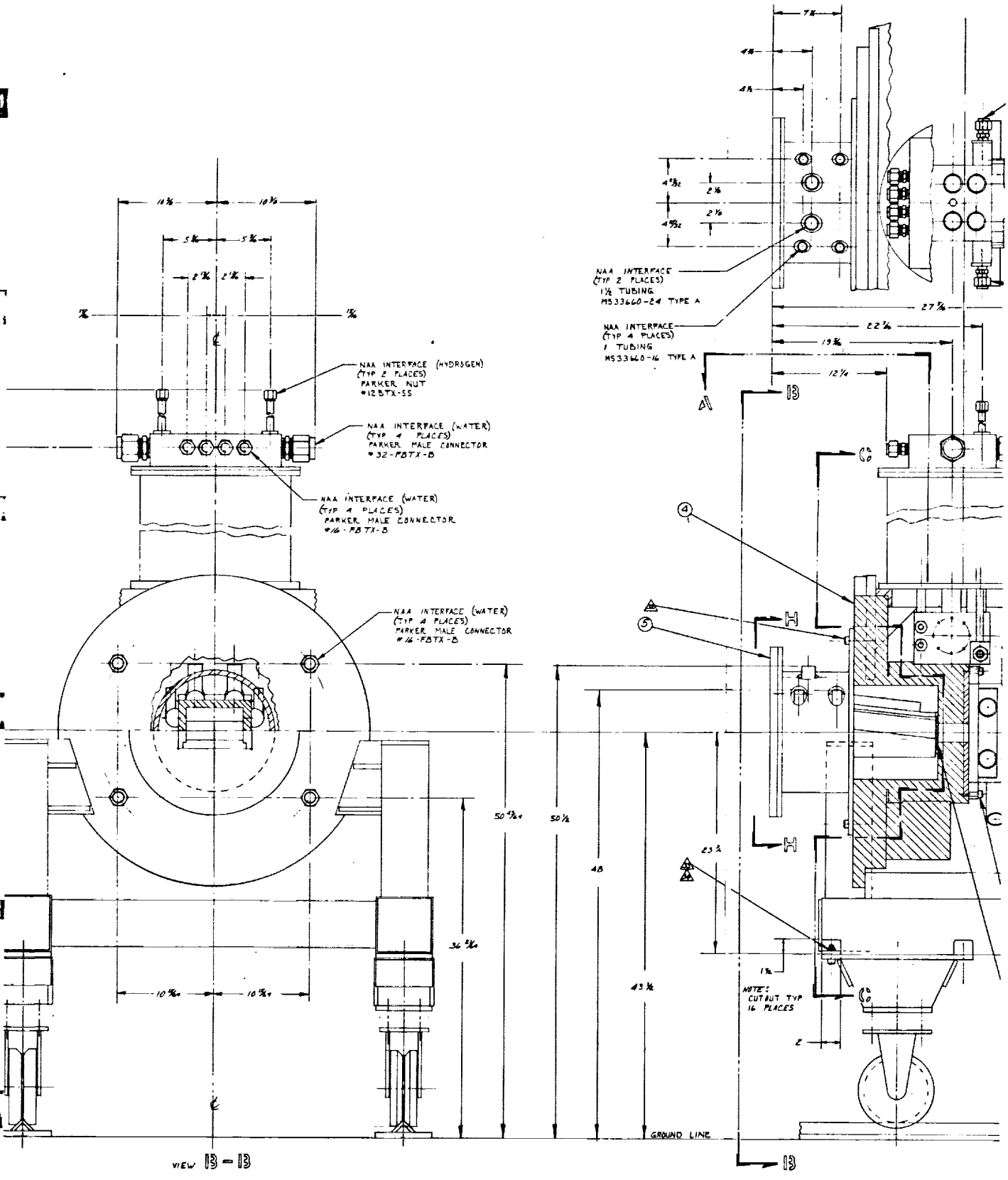

FOLDOUT FRAME 2

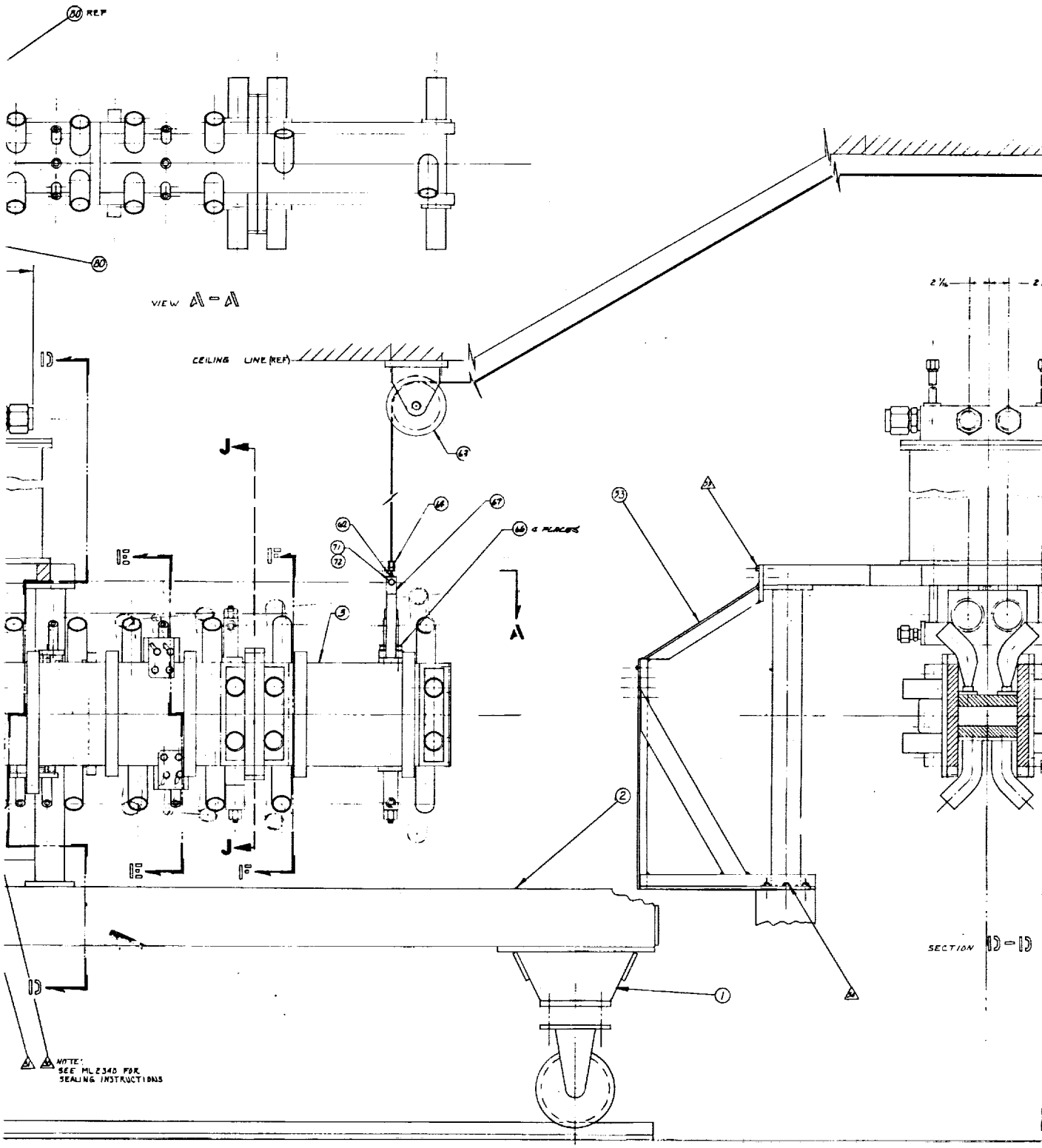

FOLDOUT FRAME 3

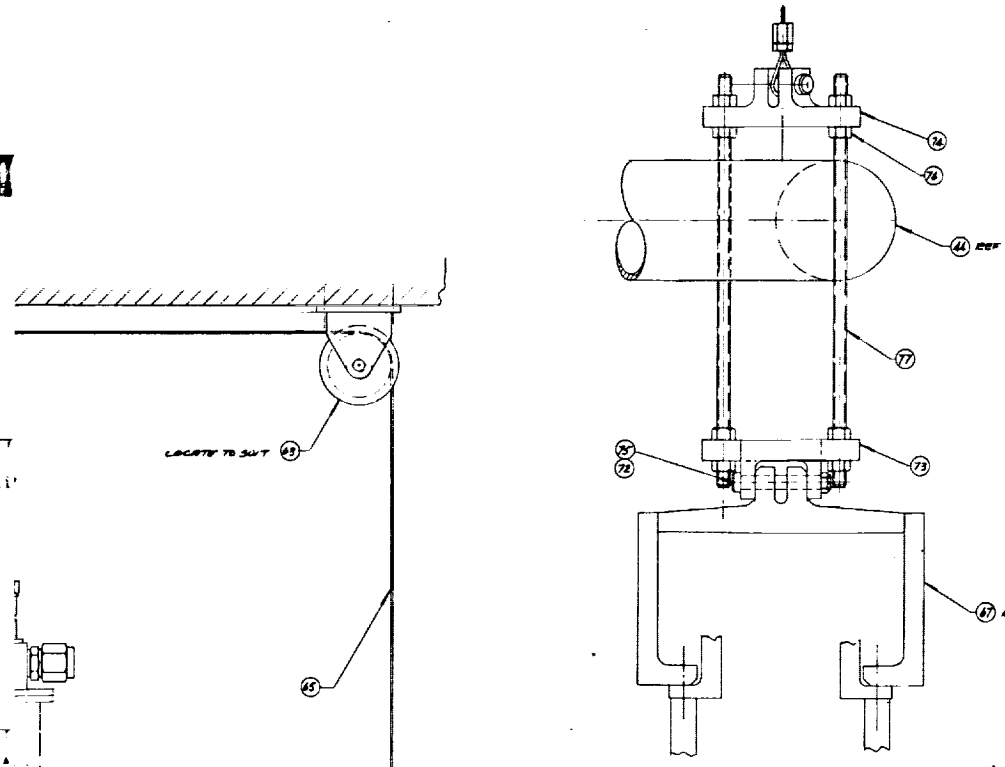

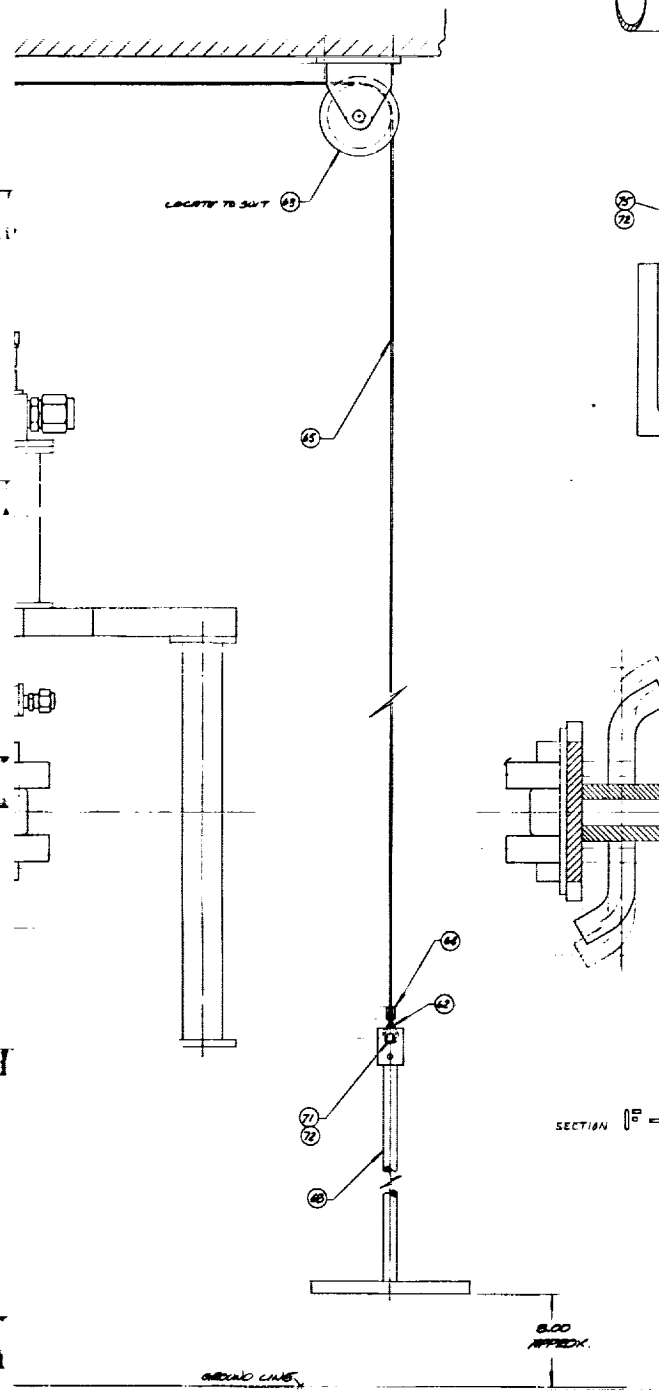

VIEW **J-J**
SCALE: 1/8
THIS ARRANGEMENT IS UTILIZED WHEN SECTION "B" IS REMOVED AS CENTER BALANCING ASSY IS DELIVERED TO SECTION "E".

SECTION

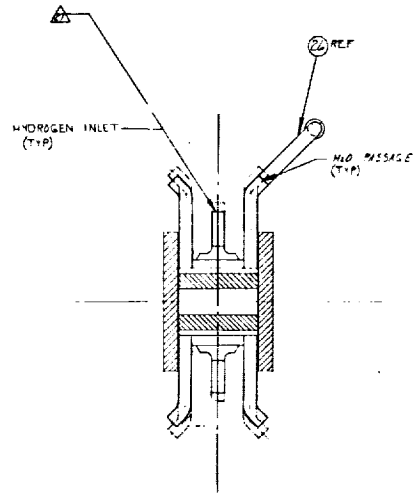

SECTION

FOLDOUT FRAME 4

REVISIONS				
SYM	ZONE	DESCRIPTION	DATE	APPROVED
F		1. REMOVED: ITEMS 28 & 29 2. ADDED: ITEM 80 3. ITEM 27 WAS MS21902-16C 4. ADDED: G/N #1.	[illegible]	

REVISIONS				
SYM	ZONE	DESCRIPTION	DATE	APPROVED
A		1. ADDED: ITEM 61 2. ITEM 46 WAS ML2546 3. ITEM 23 WAS ML2522	[illegible]	
B		1. ITEM 53 WAS ML2546 2. ITEM 42 WAS QTY. 90 3. ITEM 48 WAS ML2528 4. ITEM 52 WAS ML2532 5. ADDED: ITEMS 62 THRU 68	11-[illegible]	
C		1. ITEM 17 WAS ML2439 2. ITEM 40 WAS 3 DIA X 5 ¼ HOSE 3. ITEM 44 WAS 3 DIA HOSE CLAMP 4. ADDED: ITEM 69 5. ADDED: ITEM 70 6. REVISED ITEM 20 7. REMOVED: ITEM 22	[illegible]	
D		(1) ITEM 62 "WAS" [illegible] (2) ITEM 63 "WAS" [illegible] (3) ITEM 64 "WAS" MS21256-[illegible] CLAMP (4) ITEM 65 "WAS" [illegible] (5) ITEM 66 "WAS" ML25[illegible] MOUNT (6) ITEM 67 "WAS" ML256[illegible]-1 ASSY, SUPP (7) ITEM 68 "WAS" ML25[illegible]-11 ASSY, SUPP (8) ADDED: ITEMS 71, 72, 73, 74, 75, 76, 77 (9) DELETED: ITEM 13 (ML2[illegible]) (10) ADDED: [illegible] J-J	[illegible]	
E		1. REVISED TO INCLUDE ITEMS 78 & 79	[illegible]	

ITEM	OLD	PART NUMBER	NO. REQ.	DESCRIPTION	MATERIAL	REF	REMARKS (HEAT TREATING, PLATING PROCESS OF MANUFACTURE, ETC.)	SPEC.	DRAFT	CHECK	APPROVAL
	75	—	1	[illegible] ⅛ [illegible] x 8" BODY LENGTH	ALY STL [illegible]						
	76	MS51971-[illegible]	8	HEX NUT							
	77	⅝-3 x 15½ LG	8	THREADED ROD	STEEL		[illegible] METALS & SUPPLY [illegible]				
78		ML 3163	1	ASSY - UPPER H_2 MANIF LEFT SIDE							
79		ML 3164	1	ASSY - LOWER H_2 MANIF LEFT SIDE							
	80	16-12-FBZ-SS	2	MALE CONNECTOR			PARKER HANNIFIN CORP				

ITEM	OLD	PART NUMBER	NO. REQ.	DESCRIPTION	MATERIAL	REF	REMARKS (HEAT TREATING, PLATING PROCESS OF MANUFACTURE, ETC.)	SPEC.	DRAFT	CHECK	APPROVAL
1		ML2398	4	CARRIAGE							
2		0565-903	1	SUPPORT, STAND							
3		ML2340	1	ASSY - 2-D COMBUSTOR							
4		0565-901	1	ASSY - COMB. FORCE RIG							
5		ML2407	1	ASSY - INTAKE NOZZLE							
6		ML2501	1	ASSY - INTERMEDIATE							
7		ML2500	8	TUBE - EXT. INTER.							
8		ML2441	4	TUBE - EXTENSION							
9		ML2444	1	ASSY - INLET, PRIM.							
10		ML2440	4	TUBE - EXTENSION							
11		ML2447	1	ASSY - OUTLET, SEC.							
12		ML2442	16	TUBE - EXTENSION							
13											
14		ML2445	1	ASSY - INLET, EXT.							
15		ML2443	1	ASSY - OUTLET, EXT.							
16		ML2437	1	ASSY - OUTLET, EXT.							
17		ML3025	2	ASSY - INLET/OUTLET							
18		ML2438	1	ASSY - INLET, SEC.							
19		ML2436	1	ASSY - H_2 MANIF.							
20		ML2502	1	ASSY - H_2 MANIF.							
21		ML2430	1	GASKET							
22											
23		ML2526	6	ELBOW 45°							
24		ML2523	1	ELBOW - 180°							
25		ML2524	2	ELBOW - 90°							
26		ML2525	2	ELBOW - 90°							
	27	16-16-HBZ-SS	8	UNION			PARKER HANNIFIN CORP				
[redacted]							[redacted]				
	30	½-20 x 2 LG	14	NYLOK (OR EQUAL) [illegible] SCREW							
	31	S9026-259	1	"O" RING							
	32	[illegible]-13 x 1½ LG	12	NYLOK (OR EQUAL) [illegible] SCREW							
	33	[illegible]-20 x 1½ LG	16	KNURLED [illegible] CAP SCREW							
	34	AN364-820	16	FLEXLOC THIN NUT							
	35	2 DIA x 9 LG	36	(24HB) HOSE COUPLING			GATES RUBBER CO				
	36	[illegible]-20 x [illegible] LG	32	NYLOK (OR EQUAL) [illegible] SCREW							
	37	4½ DIA x 5 LG	1	([illegible] 35W) HOSE COUPLING			GATES RUBBER CO.				
	38	2 DIA x 4[illegible] LG	12	(24HB) HOSE COUPLING			GATES RUBBER CO.				
	39	4½ DIA x 3[illegible]	2	([illegible] 35W) HOSE COUPLING			GATES RUBBER CO.				
40		ML 3027	1	ASSY - SEC. INLET REWK.							
	41	1 DIA x 6 LG	8	(35B) HOSE COUPLING			GATES RUBBER CO.				
	42	2 DIA	156	HOSE CLAMP			SHERMAN (OR EQUAL)				
	43	4½ DIA	6	HOSE CLAMP			SHERMAN (OR EQUAL)				
44		ML 3028	1	ASSY - PRIM. OUTLET REWK.							
	45	1 DIA	36	HOSE CLAMP			SHERMAN (OR EQUAL)				
	46	1 DIA x 2 LG	10	(35B) HOSE COUPLING			GATES RUBBER CO.				
47		ML2527	1	ASSY - CLAMP 4"-3 WAY							
48		ML2532	1	ASSY - CLAMP 3"-2 WAY							
49		ML2529	1	ASSY - CLAMP 4"-2 WAY							
50		ML2530	2	ASSY - CLAMP 4"-2 WAY							
51		ML2531	2	ASSY - CLAMP 4"-2 WAY							
52		ML2560	2	CLAMP - HALF 3"							
53		ML2533	1	ASSY - INSTRUMENT PANEL							
	54	[illegible]-24 x [illegible] LG	12	NYLOK (OR EQUAL) [illegible] SCREW							
	55	[illegible]-24 x [illegible] LG	4	NYLOK (OR EQUAL) [illegible] SCREW							
	56	[illegible]-32 x [illegible] LG	50	KNURLED [illegible] CAP SCREW							
	57	AN364-1032	50	FLEXLOC THIN NUT							
	58	4 PIPE	7	PIPE HANGER			FEE & MASON #236 (OR EQUAL)				
	59	[illegible]-28 x [illegible] LG	4	KNURLED [illegible] CAP SCREW							
	60	AN364-428	4	FLEXLOC THIN NUT							
	61	2 DIA x 2[illegible] LG	30	(24HB) HOSE COUPLING			GATES RUBBER CO.				
	62	#323 [illegible]	2	[illegible]			[illegible] METALS & SUPPLY CO.				
	63	[illegible]	8	[illegible]							
	64	——	2 [illegible]	CLAMP, [illegible]							
	65	[illegible]	[illegible]	[illegible] CABLE, [illegible] MIL-C-5424			[illegible] METALS & SUPPLY CO.				
	66	[illegible]	4	SOC HD CAP SCREW							
67		ML3055-1	1	ASSY, MOUNT							
68		ML3058-1	1	ASSY, WT. [illegible]							
69		ML 3026	2	ASSY INLET/OUTLET							
70		ML 3030	2	GASKET							
	71	——	2	[illegible] x 2 [illegible] LENGTH	ALY STL [illegible]		[illegible] METALS & SUPPLY [illegible]				
	72	21FB-816	8	FLEXLOC [illegible] LOCKING NUT			[illegible] METALS & SUPPLY [illegible]				
73		ML3061-1	1	BRACKET							
74		ML3062-1	1	BRACKET							

⚠ THE UNION OF ITEM 27 MAY, AT THE OPTION OF THE DEV. ENGINEER, BE WELDED TO H_2 LINE WHERE PRACTICAL.

NOTES: UNLESS OTHERWISE SPECIFIED

SIGNATURES	DATES	DATE STARTED	WITNESSED BY
[illegible]	7-26-67	7-21-67	
[illegible]	10-13-67	DATE COMPLETED	WITNESSED BY
[illegible]	[illegible]	10-5-67	
[illegible]	[illegible]		
[illegible]	[illegible]		

FEATURES

[illegible] MANUFACTURING COMPANY

LAYOUT

INSTALLATION - 2-D COMBUSTION/NOZZLE TEST

SIZE	CODE IDENT NO.	DWG NO.	REV
J	70210	ML 2409	F
SCALE ¼		WT	SHEET 1 OF 2

FOLDOUT FRAME 5

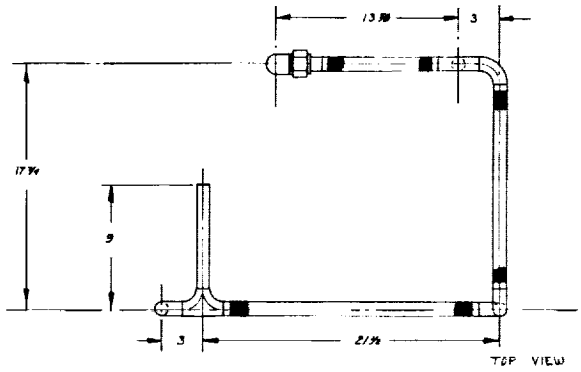

UPPER HYDROGEN MANIFOLD
RIGHT SIDE LOOKING DOWNSTREAM

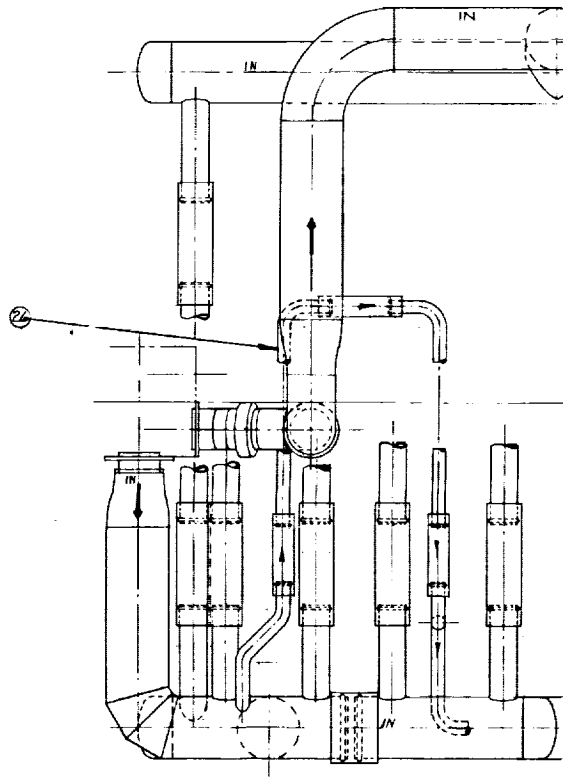

TOP VIEW
INLET MANIFOLD

FOLDOUT FRAME

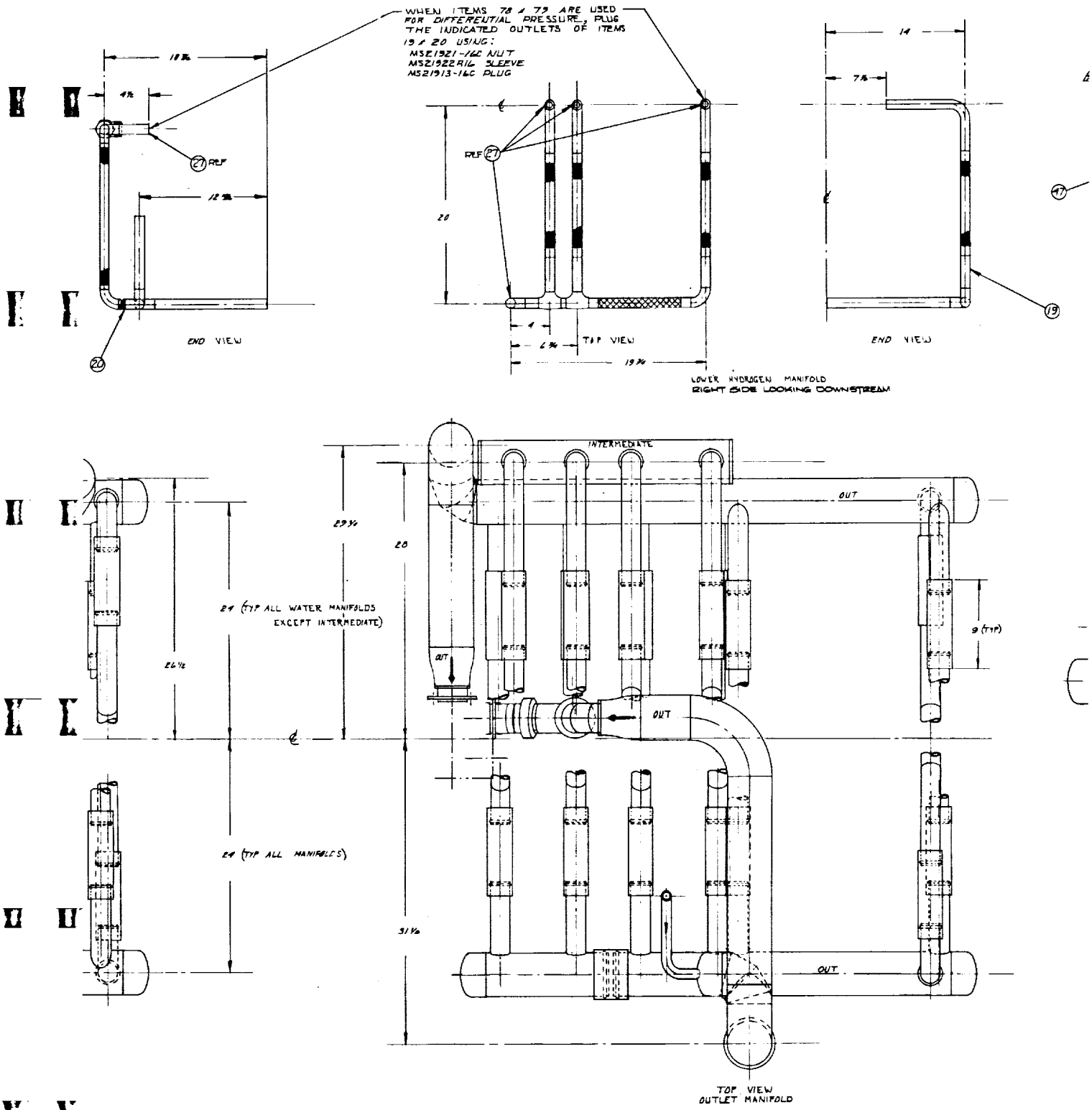

FOLDOUT FRAME

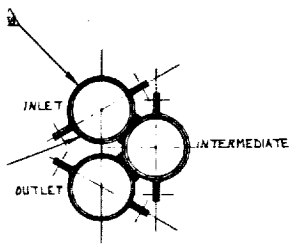

SECTION J – J

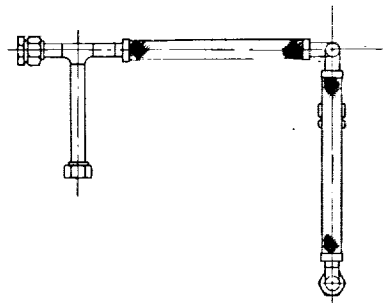

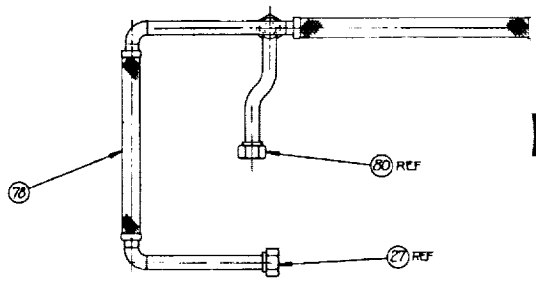

UPPER HYDROGEN MANIFOLD
LEFT SIDE LOOKING DOWNSTREAM

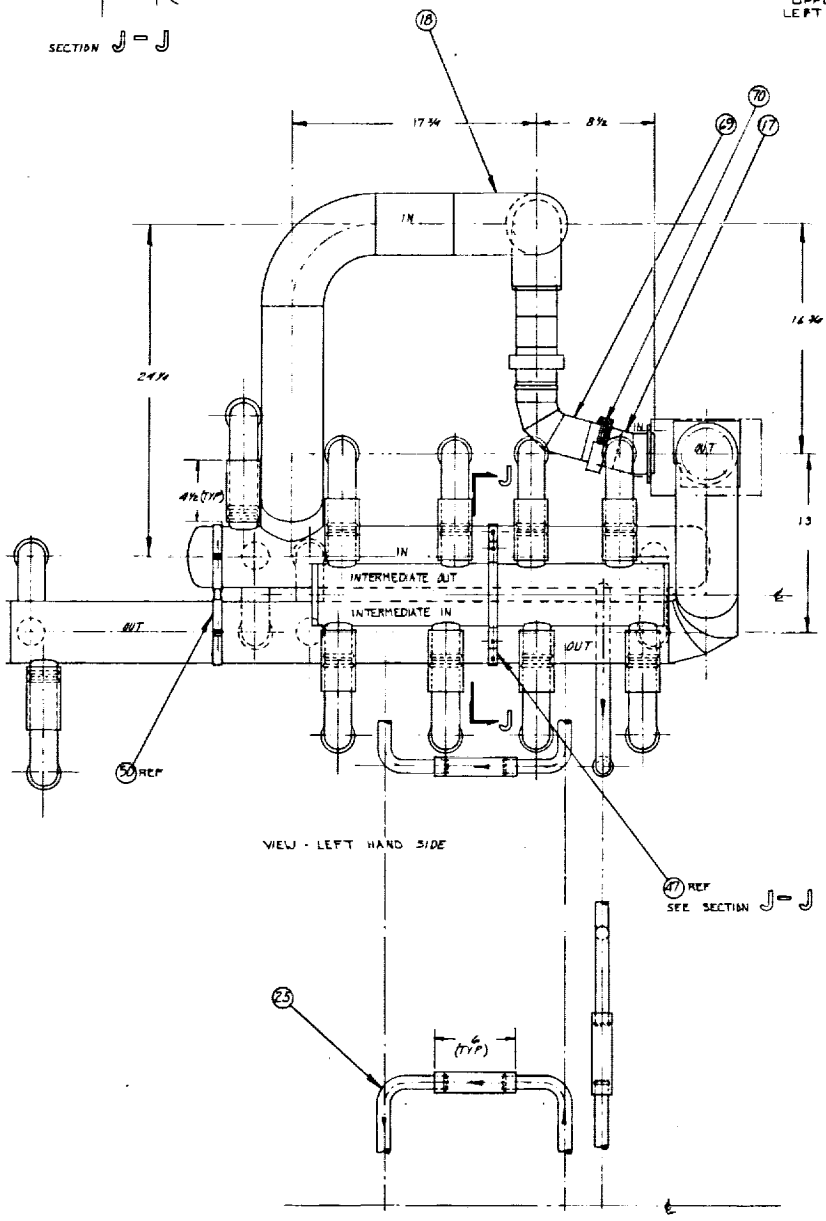

VIEW - LEFT HAND SIDE

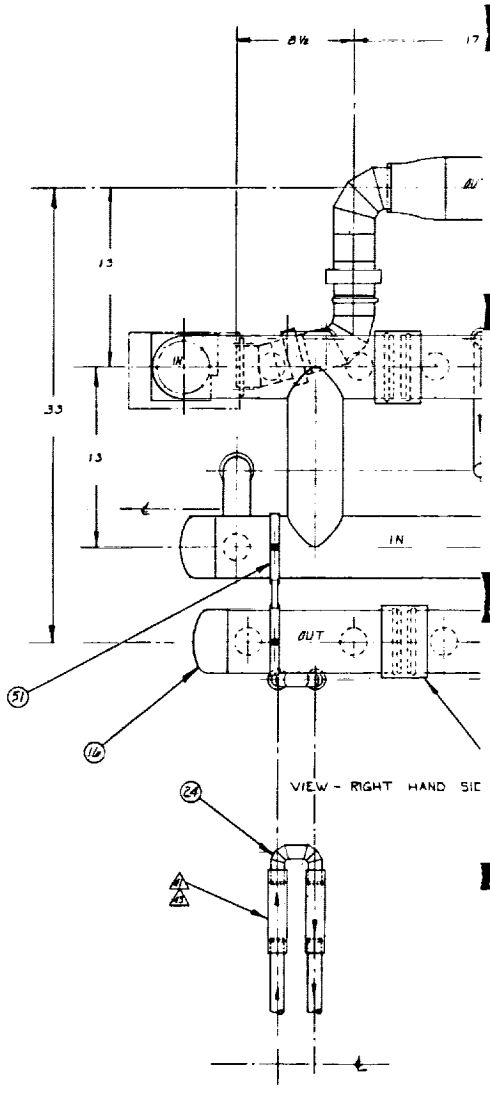

VIEW - RIGHT HAND SIDE

FOLDOUT FRAME 2

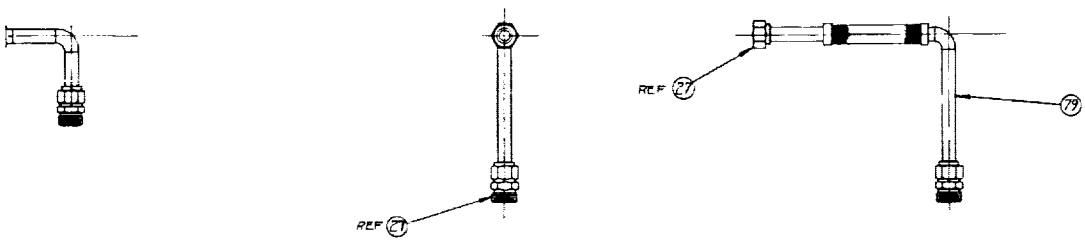

LOWER HYDROGEN MANIFOLD
LEFT SIDE LOOKING DOWNSTREAM

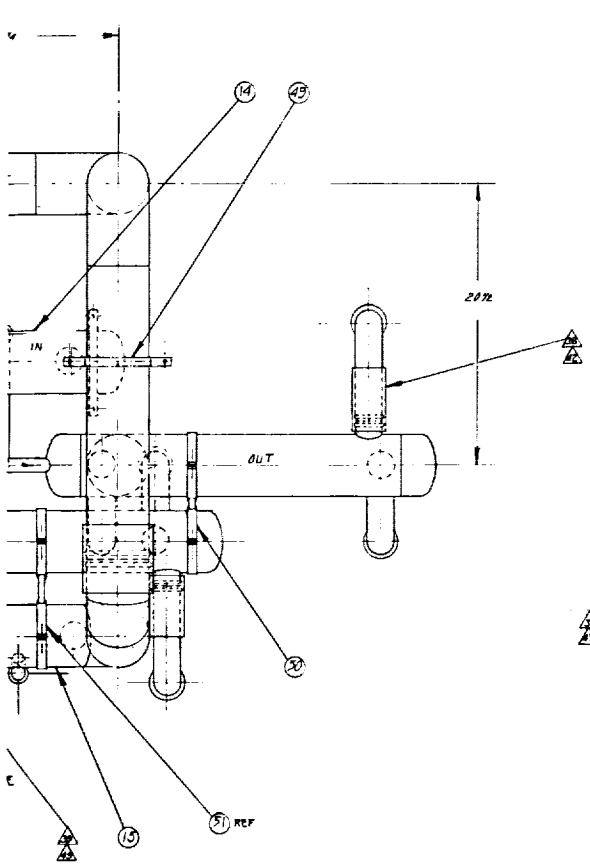

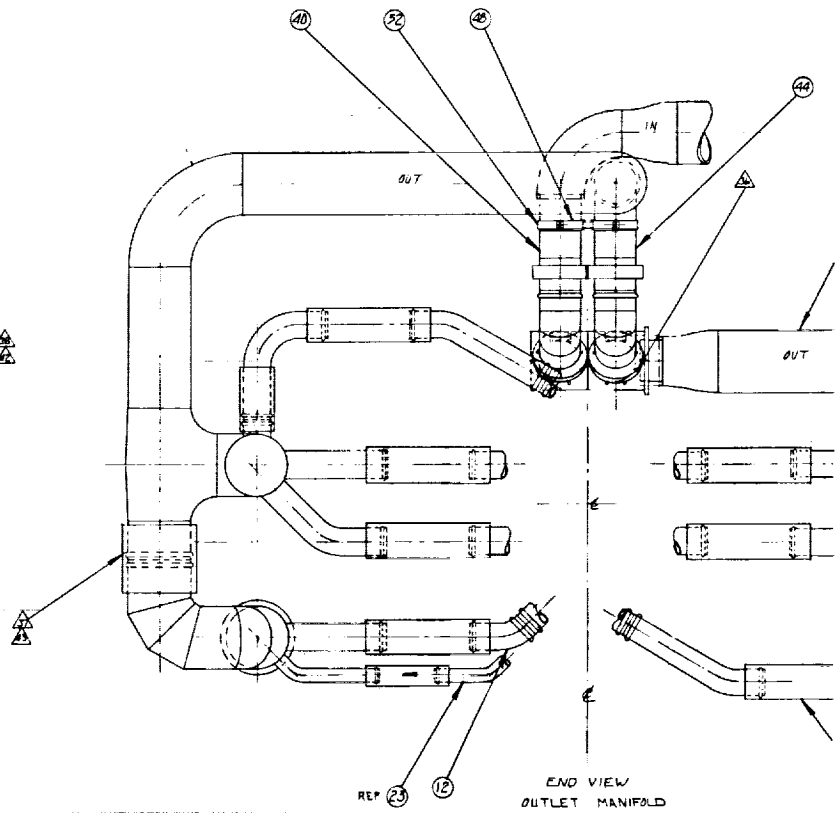

END VIEW
OUTLET MANIFOLD

FOLDOUT FRAME 3

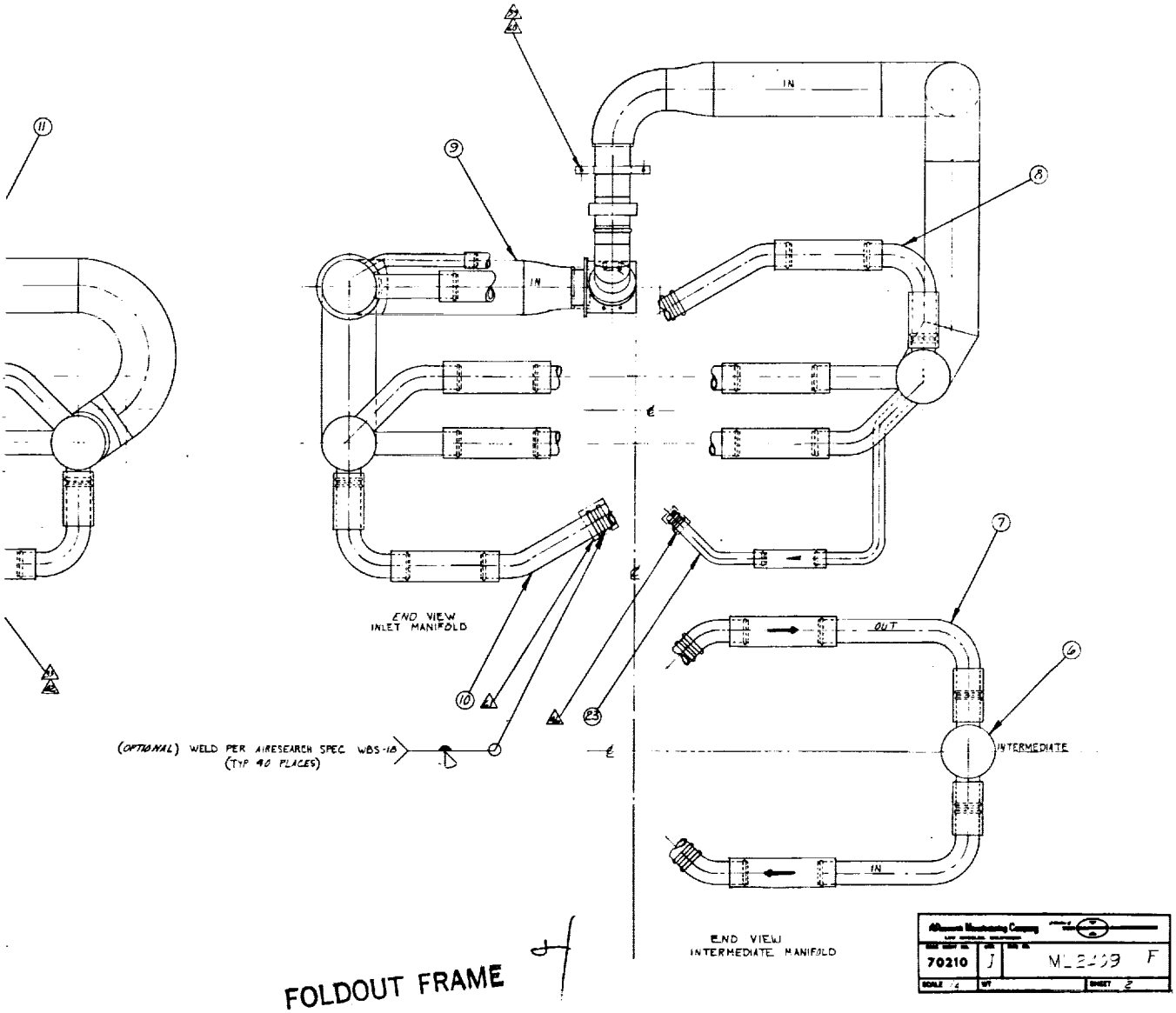

FOLDOUT FRAME

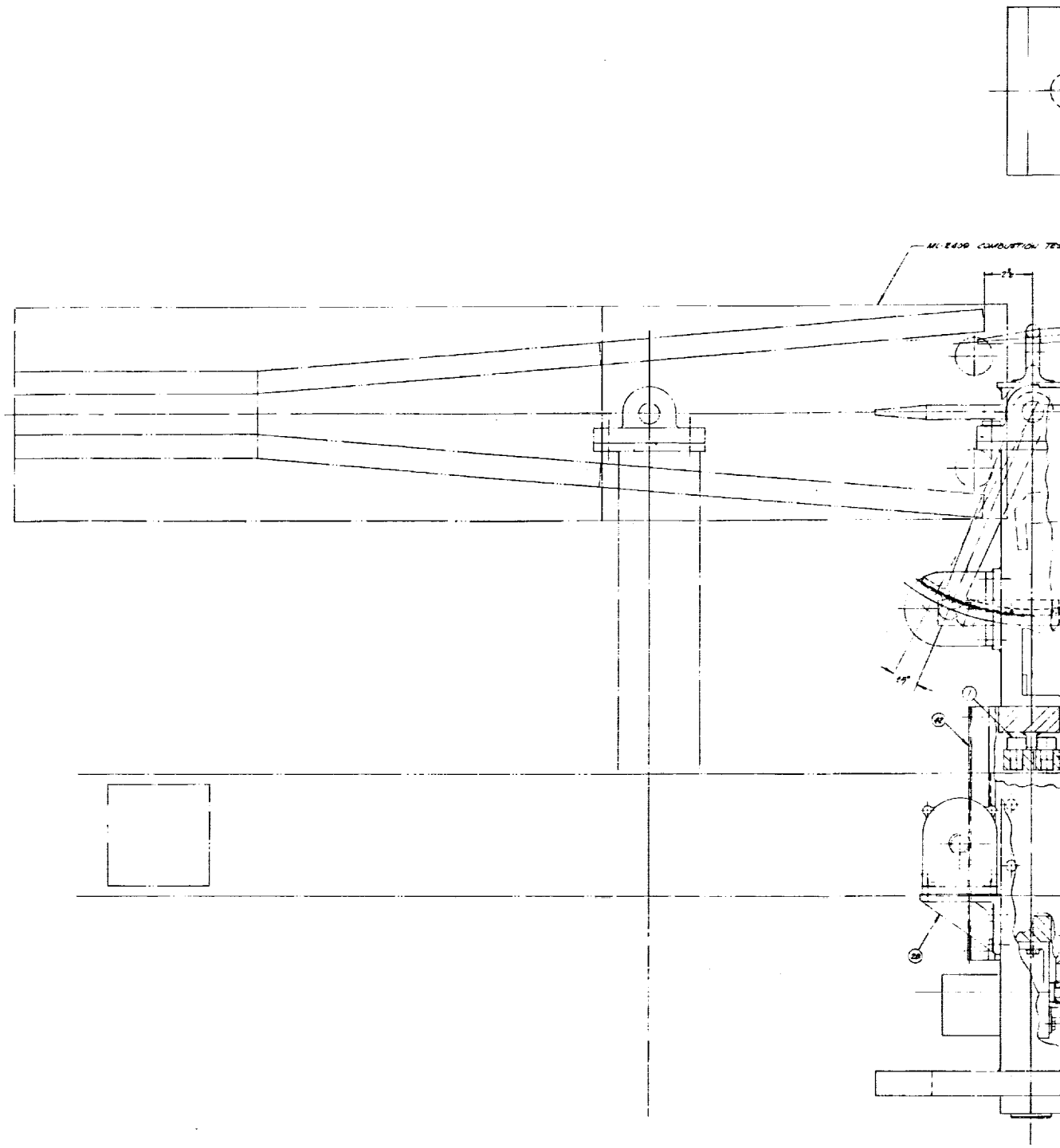

FOLDOUT FRAME

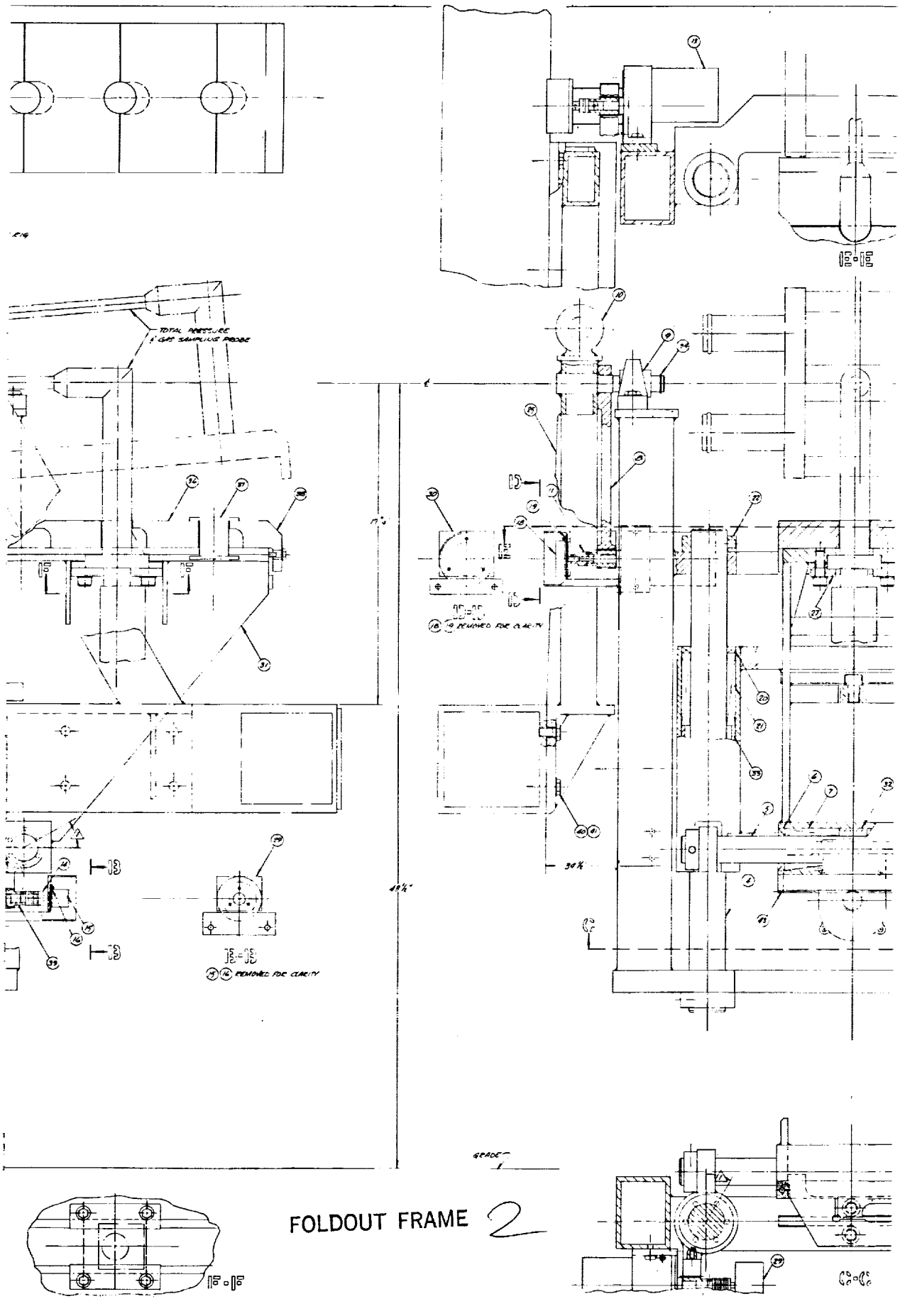

FOLDOUT FRAME 2

REV	ZONE	DESCRIPTION	DATE	APPROVED
A		1. ITEM 27 WAS ML2491	[illegible]	

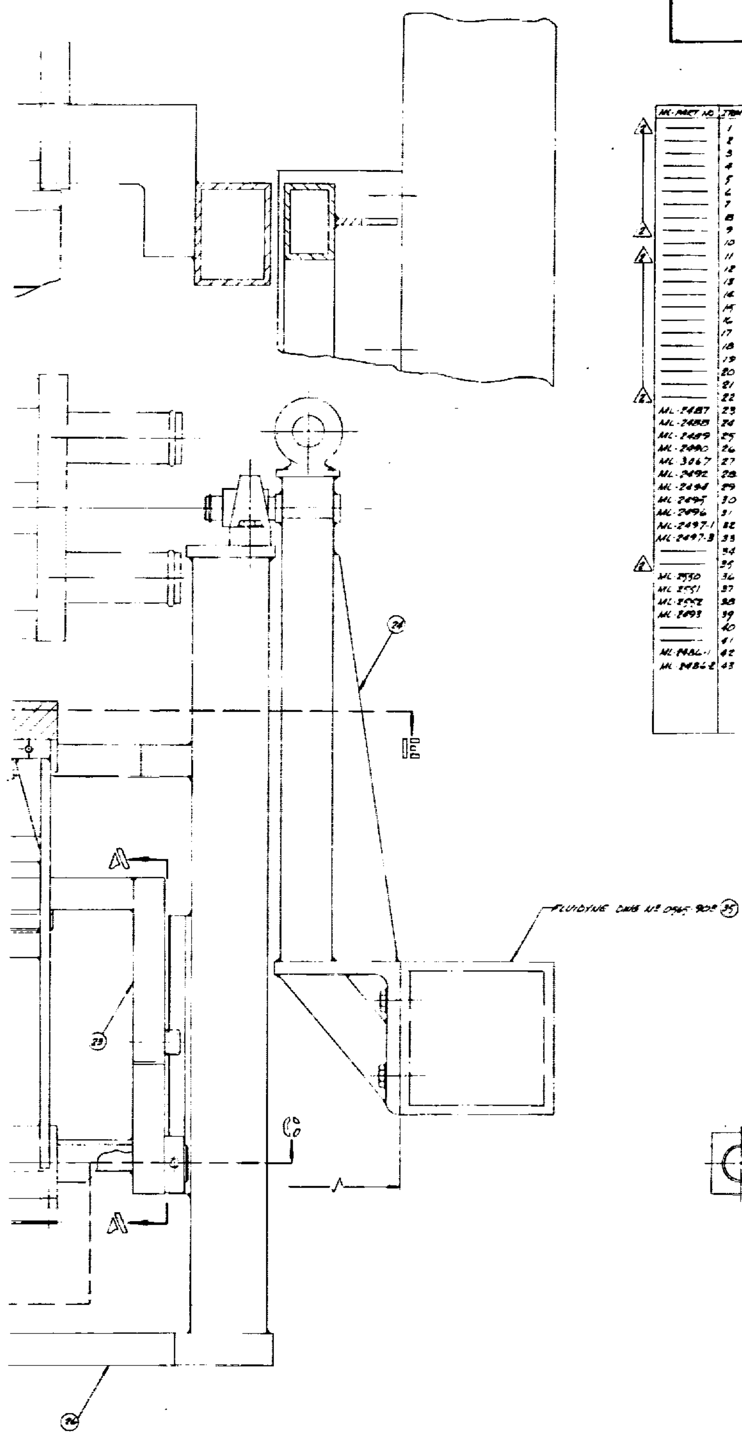

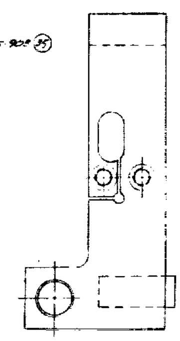

	ML-PART NO	ITEM	REQD	PURCHASED ITEM PART NO	NAME OR PART NAME	ECP #	NEXT ASSY ITEM NO
2	—	1	4	CFN-1-5	M^C GILL MFG CO	49680	23,31
	—	2	1	L2012 x 12¾	BOSTON GEAR	49690	42
	—	3	1	L2012 x 8¼	BOSTON GEAR	49690	43
	—	4	1	2" DIA x 27"	60 CASE ROUND CLASS 3 THOMSON INDUST	49609	26
	—	5	1	1½ DIA x 18¾	60 CASE ROUND CLASS 3 THOMSON INDUST	49609	23
	—	6	2	S-1500	THOMSON INDUST	49609	31
	—	7	2	A 243248	THOMSON INDUST	49609	31
	—	8	1	YC 2408	BOSTON GEAR	49690	25
2	—	9	2	SH ⅝ DIA	BOSTON GEAR	49690	26
	—	10	2	S-364 SIZE 5	CROSBY (AUGMAN)		24,25
2	—	11	1	#164	H H SMITH INC	INST LAB	18,12
	—	12	3	YD12	BOSTON GEAR	49690	39
	—	13	3	ND-PSC 2 RPM	NEW ENGLAND GEAR WORKS	49689	23,26
	—	14	2	TI-5	PIC DESIGN CORP	49693	7,12
	—	15	2	3560-1-102	BOURNS (5 TURN)	INST LAB	29
	—	16	6	C141	STERLING INST	49691	29
	—	17	2	SC150	BOSTON GEAR	49690	23
	—	18	1	MODEL 3460	BOURNS (1 TURN)	INST LAB	30
	—	19	3	C142	STERLING INST	49691	30
	—	20	2	S-2000	THOMSON INDUST	49609	23
	—	21	2	A-324864	THOMSON INDUST	49609	23
2	—	22	2	SC 200	BOSTON GEAR	49696	26
	ML-2487	23	1		CARRIAGE-VERTICAL		26
	ML-2488	24	1		SUPPORT		25
	ML-2489	25	1		SUPPORT		35
	ML-2490	26	1		FRAME		24,25
	ML-3067	27	2		NUT		31
	ML-2492	28	1		BRACKET		26
	ML-2494	29	2		BRACKET		13
	ML-2495	30	1		BRACKET		13
	ML-2496	31	1		CARRIAGE-HORIZONTAL		23
	ML-2497-1	32	1		SPACER		31
	ML-2497-3	33	1		SPACER		23
	—	34	2	MS16624-4093	RETAINING RING		24,25
2	—	35	1		FLUIDYNE #0945-903	—	—
	ML-2550	36	2		SHIELD		31
	ML-2551	37	2		SHIELD		31
	ML-2552	38	2		SHIELD		31
	ML-2493	39	3		GEAR		13
	—	40	12		BOLT-CRES ½-20 x 1" LENGTH HEX HEAD		24,25
	—	41	12		WASHER CRES ½", LOCK		24,25
	ML-2486-1	42	1		RACK		23
	ML-2486-2	43	1		RACK		31

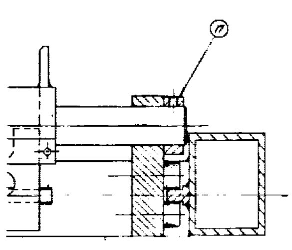

⚠2 FURNISHED BY D/93-17
⚠1 30° (ORIENTATION OF BALL TRACKS)

R Lotz	[signature]	9-13-67	LAYOUT
9-67	[signature]	9-15-67	PROBE TRANSLATING MECHANISM LAYOUT
9-67	[signature]		SCALE ½
AiResearch Manufacturing Company		LAYOUT NO.	ML-2485

FOLDOUT FRAME 3

FOLDOUT FRAME

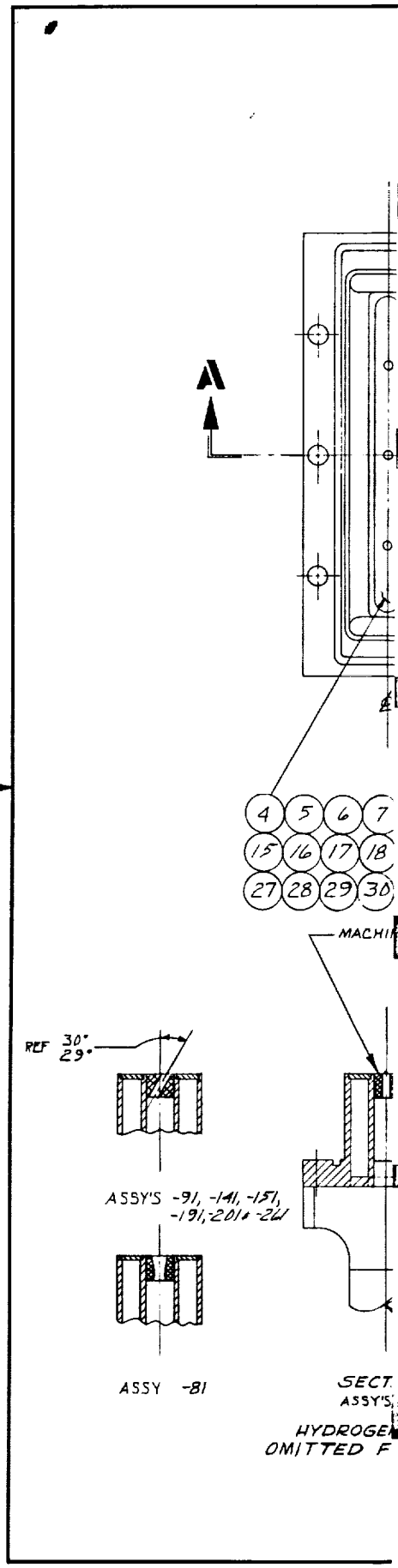

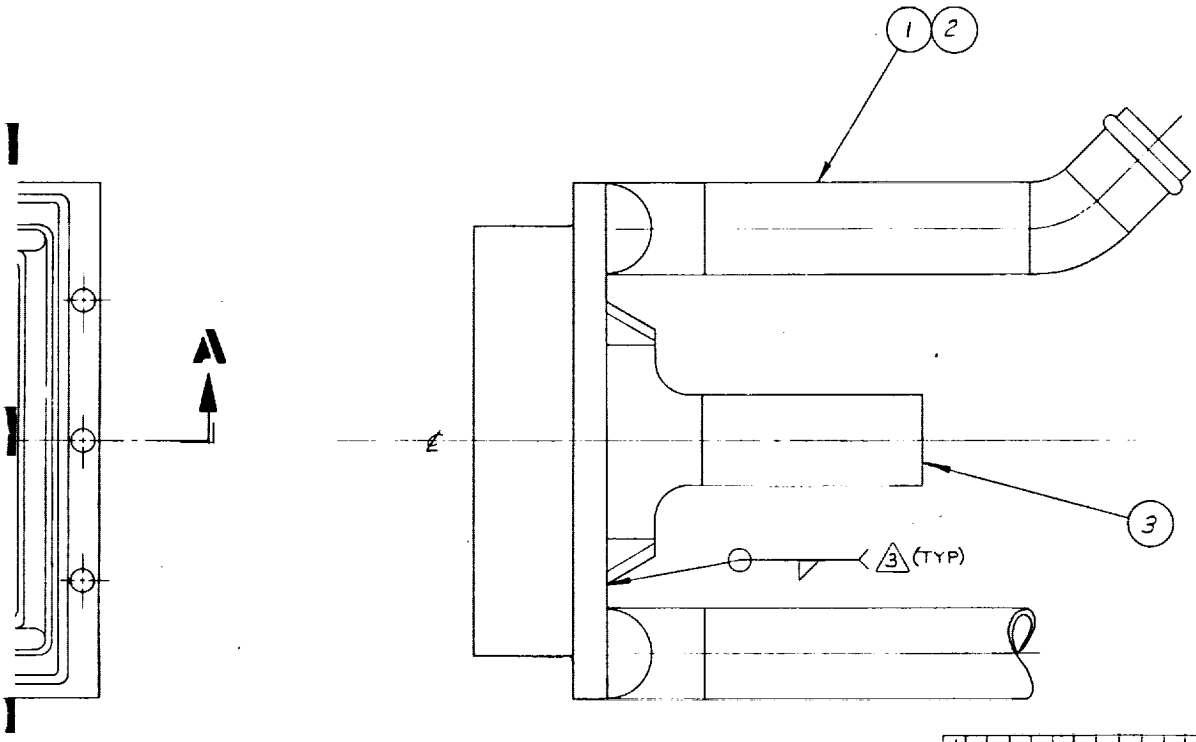

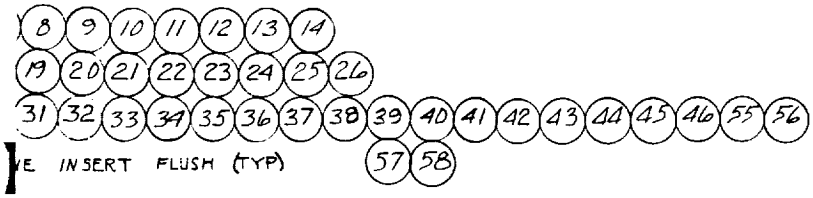

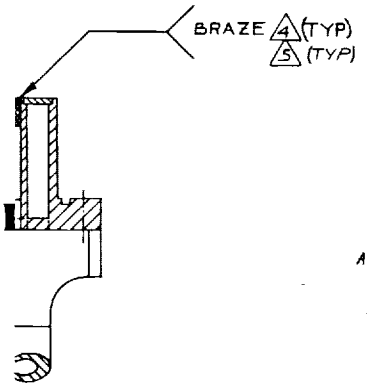

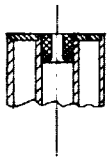

ASSY'S -31 THRU -71 & -381

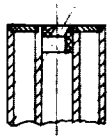

ASSY'S -171, -181, -211, -221, -271 & -281

A-A

-1 THRU -21, -101 THRU -131, -161, -231, -241, -257, -291, -301 MANIFOLD -331, -341, -351 OR CLARITY -391, -401, -911 & -921

(281) 1	ML2340	ML2409
(271) 1		
(261) 1		
(251) 1		
(241) 1		
(231) 1		
(221) 1		
(211) 1		
(201) 1		
(191) 1		
(181) 1		
(171) 1		
(161) 1		
(151) 1		
(141) 1		
(131) 1		
(121)		
(111)		
ADD	ML2340	ML2409
READ	NEXT ASSY	USED ON

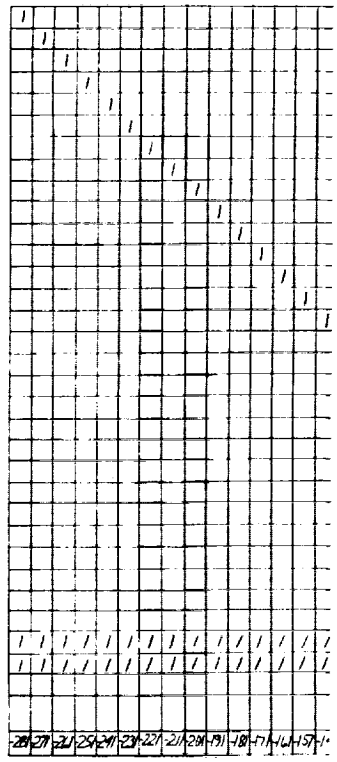

5. BRAZE PER WBS-27 USING NICORO 80 ALLOY, EFFECTIVE ON -101 THRU -911 ASSY'S

4. BRAZE PER WBS-27 USING ASTM B260-62T, BAu-4 ALLOY. EFFECTIVE ON -1 THRU -91 ASSY'S.

3. WELD PER AIRESEARCH SPEC. WBS-18

2. MACHINE SURFACES 125

1. BREAK SHARP EDGES .010 - .015

NOTES: UNLESS OTHERWISE SPECIFIED

6. BRAZE PER WBS-27 USING ASTM B260-62T, BAu-2 ALLOY. (1670° MAX)

FOLDOUT FRAME

REVISIONS			
LTR	DESCRIPTION	DATE	APPROVED
A	1. G/N 4 WAS ---- B AU-3.	11-1-67 TJB	11-1-67
B	1. ADDED: ASSY'S -31 THRU -91	11-9-67 TJB	
C	1. ITEM 2 WAS ML2515-3	11-13-67 TJB	
D	1. ADDED: ASSY'S -101 THRU -201 2. G/N 4 WAS ASTM B260-62T, BAU-4	11/14/67 TJB	RRC 12/1
E	1. ADDED: ITEMS 25 & 26 2. ADDED: EFFECTIVITY TO G/N 4 & G/N 5. 3. ADDED: G/N 5.	11/21/67 TJB	RRC 11/21
F	1. ADDED: ITEMS 27 THRU 32	12/19/67 TJB	
G	1. ADDED: ITEMS 33 THRU 42 & SHEET 2	4-19-68 TJB	RRC 4/19/68
H	1. ADDED: -391 THRU -491 ASSY 2. ADDED: G/N 6 3. G/N 5 WAS ---- -101 ASSY & SUBS	7-2-69 TJB	RRC 7/10/69
I	1. ADDED: -491 & -501 ASSY'S	7-23-69 TJB	

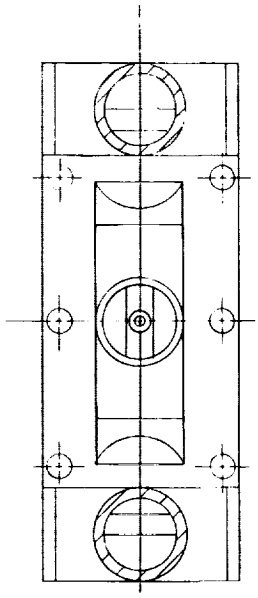

ITEM NO.	QTY REQD -3	-2	-1	CODE IDENT NO.	PART OR IDENTIFYING NO.	NOMENCLATURE OR DESCRIPTION	SYM
32					ML2534-59	PLUG-NOZZLE	
31					ML2534-57		
30					ML2534-55		
29					ML2534-53		
28					ML2534-51		
27					ML2534-49		
26					ML2534-47		
25					ML2534-45		
24					ML2534-43		
23					ML2534-41		
22					ML2534-39		
21					ML2534-37		
20					ML2534-35		
19					ML2534-33		
18					ML2534-31		
17	1				ML2534-29		
16	1				ML2534-27		
15	1				ML2534-25		
14	1				ML2534-23		
13	1				ML2534-21		
12	1				ML2534-19		
11	1				ML2534-17		
10	1				ML2534-15		
9	1				ML2534-13		
8	1				ML2534-11		
7	1	1			ML2534-9		
6	1	1			ML2534-7		
5	1	1			ML2534-5		
4	1	1	1		ML2534-3	PLUG-NOZZLE	
3	1	1	1		ML2516	MANIFOLD-MOD. FUEL	
2	1	1			ML2509-1	BLOCK-MOD. FUEL INJECTOR	
1	1	1	1		ML2515-1	BLOCK-MOD. FUEL INJECTOR	

PARTS LIST

REQD	NEXT ASSY	USED ON
2	ML2340	ML2403
2	ML2340	ML2403
2	ML2340	ML2403
2	ML2340	ML2403
2	ML2340	ML2403
2	ML2340	ML2403
2	ML2340	ML2403
2	ML2340	ML2403
2	ML2340	ML2403
2	ML2340	ML2403

APPLICATION

UNLESS OTHERWISE SPECIFIED:
DIMENSIONS ARE IN INCHES.
MACHINE FILLET RADII .015 — .030
SURFACE ROUGHNESS PER MIL-STD-10
BURR CONTROL PER SC563
DIMENSION LIMITS HELD AFTER PLATING
IDENT MARKING PER MC16
DIMENSIONING AND TOL PER MIL-STD-8

HEAT TREATMENT	PROCESS
HARDNESS AND SPEC	NAME AND SPEC
WBS-18 WBS-27	

CONTRACT NO.

DR	M DE LA ROSA	10-4-67
CHK		
VALUE ENGR		
MATL		10-4-67
STRESS		10-13-67
APPD		10-13-67
APPD		10/13/67
AIRESEARCH APPD		
OTHER ACTIVITY APPD		

AIRESEARCH MANUFACTURING COMPANY
A DIVISION OF THE GARRETT CORPORATION
LOS ANGELES, CALIFORNIA

ASSEMBLY-FUEL INJECTOR 2-D COMBUSTION TEST CHAMBER

SIZE	CODE IDENT NO.	DWG NO.
D	70210	ML 2499

SCALE 1/1 SHEET 1 OF 3

ML 2499

FOLDOUT FRAME 2